

Jonathan Mamou
Michael L. Oelze *Editors*

Quantitative Ultrasound in Soft Tissues

Second Edition

Advances in Experimental Medicine and Biology

Volume 1403

Series Editors

Wim E. Crusio, Institut de Neurosciences Cognitives et Intégratives d'Aquitaine, CNRS and University of Bordeaux, Pessac Cedex, France

Haidong Dong, Departments of Urology and Immunology, Mayo Clinic, Rochester, MN, USA

Heinfried H. Radeke, Institute of Pharmacology and Toxicology, Clinic of the Goethe University Frankfurt Main, Frankfurt am Main, Hessen, Germany

Nima Rezaei , Research Center for Immunodeficiencies, Children's Medical Center, Tehran University of Medical Sciences, Tehran, Iran

Ortrud Steinlein, Institute of Human Genetics, LMU University Hospital, Munich, Germany

Junjie Xiao, Cardiac Regeneration and Ageing Lab, Institute of Cardiovascular Sciences, School of Life Science, Shanghai University, Shanghai, China

Advances in Experimental Medicine and Biology provides a platform for scientific contributions in the main disciplines of the biomedicine and the life sciences. This series publishes thematic volumes on contemporary research in the areas of microbiology, immunology, neurosciences, biochemistry, biomedical engineering, genetics, physiology, and cancer research. Covering emerging topics and techniques in basic and clinical science, it brings together clinicians and researchers from various fields.

Advances in Experimental Medicine and Biology has been publishing exceptional works in the field for over 40 years, and is indexed in SCOPUS, Medline (PubMed), EMBASE, BIOSIS, Reaxys, EMBiology, the Chemical Abstracts Service (CAS), and Pathway Studio.

2021 Impact Factor: 3.650 (no longer indexed in SCIE as of 2022)

Jonathan Mamou • Michael L. Oelze
Editors

Quantitative Ultrasound in Soft Tissues

Second Edition



Editors

Jonathan Mamou
Department of Radiology
Weill Cornell Medicine
New York, NY, USA

Michael L. Oelze
Department of Electrical and Computer Engineering
University of Illinois at Urbana-Champaign
Urbana, IL, USA

ISSN 0065-2598 ISSN 2214-8019 (electronic)
Advances in Experimental Medicine and Biology
ISBN 978-3-031-21986-3 ISBN 978-3-031-21987-0 (eBook)
<https://doi.org/10.1007/978-3-031-21987-0>

1st edition: © Springer Science+Business Media Dordrecht 2013
2nd edition: © The Editor(s) (if applicable) and The Author(s), under exclusive license to Springer
Nature Switzerland AG 2023

This work is subject to copyright. All rights are solely and exclusively licensed by the Publisher, whether the whole or part of the material is concerned, specifically the rights of translation, reprinting, reuse of illustrations, recitation, broadcasting, reproduction on microfilms or in any other physical way, and transmission or information storage and retrieval, electronic adaptation, computer software, or by similar or dissimilar methodology now known or hereafter developed. The use of general descriptive names, registered names, trademarks, service marks, etc. in this publication does not imply, even in the absence of a specific statement, that such names are exempt from the relevant protective laws and regulations and therefore free for general use.

The publisher, the authors, and the editors are safe to assume that the advice and information in this book are believed to be true and accurate at the date of publication. Neither the publisher nor the authors or the editors give a warranty, expressed or implied, with respect to the material contained herein or for any errors or omissions that may have been made. The publisher remains neutral with regard to jurisdictional claims in published maps and institutional affiliations.

This Springer imprint is published by the registered company Springer Nature Switzerland AG
The registered company address is: Gewerbestrasse 11, 6330 Cham, Switzerland

Preface to the Second Edition

Just like all of you, we have been affected by the pandemic and found ourselves stuck at home for an extended period of time asking ourselves what a productive use of our time would be while unable to use equipment in our laboratories or collect new data at our clinical collaborating sites. Of course, we first went back to all the old data sitting on our networks that were meant to be analyzed a while back but for one reason or another were not. But eventually, the idea of putting together a second edition of the book came up. It was briefly discussed and agreed that it would be great idea. And here we are.

As the field of quantitative ultrasound has grown tremendously over the past 10 years with advances in our theoretical understanding, technology in general, and also a greater interest in the biomedical ultrasound research community, we thought the second edition should appropriately reflect the tremendous progress in our field. In addition, our research community includes many new younger professors and researchers, which, as you will be able to tell from the table of contents, were more than eager to contribute to the second edition after having read the first edition arduously – maybe even numerous times!

Upon discussing the project in greater detail between the two of us and, in particular, wondering what this second edition should look like, we decided that we wanted to put together a book with a stronger educational focus than the first edition. In short, something that would present recent advances, state-of-the-art methods, with specific biomedical applications highlighted (but a lesser focus) with a clear delivery of the thinking which went in these advances. Our hope is that this book will bring readers of the first edition up to date with the advances which occurred in the past 10 years, while being comprehensive enough for new readers who are less likely to go back to study the first edition. We are fortunate to dwell in such an interdisciplinary research field, where engineering, physics, biology, and medicine intersect naturally, and this second edition does illustrate nicely this unique fact.

This second edition is organized into 6 parts with a total of 13 chapters.¹ The first part focuses on the backscatter coefficient, the second part on

¹ Note that for completeness, Chaps. 5 (Attenuation Compensation and Estimation) and 7 (Review of Envelope Statistics Models for Quantitative Ultrasound Imaging and Tissue Characterization) of the second edition are identical to Chaps. 4 and 10 of the first edition, respectively.

attenuation estimation, and the third part on envelope statistics. Then, the fourth part proposes three chapters on recent advances in ultrasound tomography – which have been tremendous in the past 10 years. The fifth part is composed of one chapter on recent advances in acoustic microscopy. Finally, the sixth part contains a single, but very interesting, chapter on manufacturing of well-calibrated scattering phantoms. (Just like in the first edition, we did not include a part on elastography methods because of their detailed coverage in other texts.)

I sincerely hope the feedback of the second edition will be as positive as the one we received from the first edition. In a way, putting a book like this together is a gift – at a specific time – to our community. We certainly hope it will be well-received.

New York, NY, USA
Urbana, IL, USA
September 15, 2022

Jonathan Mamou
Michael L. Oelze

Contents

Part I Backscatter Coefficient Methods

1 Quantitative Ultrasound: An Emerging Technology for Detecting, Diagnosing, Imaging, Evaluating, and Monitoring Disease	3
Ernest J. Feleppa	
2 Quantitative Ultrasound: Scattering Theory	19
Michael Oelze	
3 Quantitative Ultrasound: Experimental Implementation	29
Michael Oelze	
4 Extracting Quantitative Ultrasonic Parameters from the Backscatter Coefficient	43
Aiguo Han	

Part II Attenuation Estimation Methods

5 Attenuation Compensation and Estimation	67
Timothy A. Bigelow and Yassin Labyed	
6 Recent Advances in Attenuation Estimation	85
Ivan M. Rosado-Mendez	

Part III Envelope Statistics Methods

7 Review of Envelope Statistics Models for Quantitative Ultrasound Imaging and Tissue Characterization	107
Fran�ois Destrempe and Guy Cloutier	
8 Information Entropy and Its Applications	153
Po-Hsiang Tsui	

Part IV Ultrasound Computed Tomography

9 Ultrasound Tomography	171
Nicole V. Ruiter, Michael Zapf, Torsten Hopp, and Hartmut Gemmeke	
10 Full Wave Inversion and Inverse Scattering in Ultrasound Tomography/Volography	201
James Wiskin	

11 Clinical Importance of 3D Volumography in Breast Imaging	239
John Klock	

Part V Acoustic Microscopy

12 Advanced Topics in Quantitative Acoustic Microscopy	253
Cameron Hoerig and Jonathan Mamou	

Part VI Phantoms for Quantitative Ultrasound

13 Phantoms for Quantitative Ultrasound	281
Timothy A Stiles	

Index	303
------------------------	-----

About the Editors

Jonathan Mamou graduated in 2000 from the Ecole Nationale Supérieure des Télécommunications in Paris, France. In January 2001, he began his graduate studies in Electrical and Computer Engineering at the University of Illinois in Urbana-Champaign, Urbana, IL. He received his M.S. and Ph.D. degrees in May 2002 and 2005, respectively. He previously was the Associate Research Director of the F. L. Lizzi Center for Biomedical Engineering at Riverside Research in New York, NY. He currently holds a faculty position in the Department of Radiology of Weill Cornell Medicine in New York, NY. Dr. Mamou also is an Adjunct Professor in the Department of Electrical Engineering of New York University. His fields of interest include theoretical aspects of ultrasound scattering, ultrasonic medical imaging, quantitative acoustic microscopy, ultrasound contrast agents, and biomedical image processing. Dr. Mamou is a Fellow of the American Institute of Ultrasound in Medicine (AIUM), a Senior member of IEEE, and a member of the Acoustical Society of America. He is coeditor of the book *Quantitative Ultrasound in Soft Tissues* published by Springer, in 2013. In 2022, he was inducted into the Council of Distinguished Investigators of the Academy for Radiology & Biomedical Imaging. He served as the Chair of the AIUM High-Frequency Clinical and Preclinical Imaging Community of Practice. He is an Associate Editor of *Ultrasonic Imaging* and the *IEEE Transactions on Ultrasonics, Ferroelectrics, and Frequency Control*, and a reviewer for numerous journals.

Michael L. Oelze was born in Hamilton, New Zealand, in 1971. He received the B.S. degree in Physics and Mathematics from Harding University, Searcy, AR, USA, in 1994, and the Ph.D. degree in Physics from the University of Mississippi, Oxford, MS, USA. From 2000 to 2002, he was a Post-Doctoral Researcher with the Bioacoustics Research Laboratory, Department of Electrical and Computer Engineering (ECE), University of Illinois at Urbana-Champaign (UIUC), Urbana, IL, USA. From 2002 to 2004, he was an NIH Fellow conducting research in quantitative ultrasound techniques for biomedical ultrasound applications in cancer detection. He is currently a Professor and the Associate Head for Graduate Affairs in ECE at UIUC, the Frederick and Elizabeth Nearing Scholar in the Grainger College of Engineering, and a Health Innovator Professor in the Carle Illinois College of Medicine. His research interests include biomedical ultrasound, quantitative ultrasound imaging for improving cancer diagnostics and monitoring therapy response, ultrasound bioeffects, ultrasound tomography techniques,

ultrasound-based therapy, beamforming, and ultrasound-based medical implants. Dr. Oelze is currently a Fellow of the AIUM, and a member of ASA. He is a member of the Technical Program Committee of the IEEE Ultrasonics Symposium. He currently serves as an Associate Editor of *IEEE Transactions on Ultrasonics, Ferroelectrics, and Frequency Control*, *Ultrasonic Imaging*, and *IEEE Transactions on Biomedical Engineering*.

Part I

Backscatter Coefficient Methods



Quantitative Ultrasound: An Emerging Technology for Detecting, Diagnosing, Imaging, Evaluating, and Monitoring Disease

Ernest J. Feleppa

Abstract

Ultrasound has been a popular clinical imaging modality for decades. It is a well-established means of displaying the macroscopic anatomy of soft-tissue structures. While conventional ultrasound methods, i.e., B-mode and Doppler methods, are well proven and continue to advance technically in many ways, e.g., by extending into higher frequencies and taking advantage of harmonic phenomena in tissues, fundamentally new so-called quantitative ultrasound (QUS) technologies also are emerging and offer exciting promise for making significant improvements in clinical imaging and characterization of disease. These emerging quantitative methods include spectrum analysis, image statistics, elasticity imaging, contrast-agent methods, and flow-detection and -measurement techniques. Each provides independent information. When used alone, each can provide clinically valuable imaging capabilities; when combined with each other, their capabilities may be more powerful in many applications. Furthermore,

all can be used fused with other imaging modalities, such as computed tomography (CT), magnetic-resonance (MR), positron-emission-tomography (PET), or single-photon emission computerized tomography (SPECT) imaging, to offer possibly even greater improvements in detecting, diagnosing, imaging, evaluating, and monitoring disease. This chapter focuses on QUS methods that are based on spectrum analysis and image statistics.

Keywords

Scattering · Spectrum · Envelope statistics · Parametric imaging · Tissue-typing

1.1 Introduction

Ultrasonic imaging has been a widely used and highly regarded method of visualizing anatomic structures for half a century. Two types of conventional ultrasonic imaging are commonly employed: grayscale B-mode imaging and Doppler imaging.

Grayscale B-mode images generated by conventional pulse-echo ultrasound display echo amplitude as a function of position in a scan plane. Echo-signal amplitude is determined by

E. J. Feleppa (✉)

Department of Radiology, Massachusetts General Hospital, Center for Ultrasound Research and Translation (CURT), Boston, MA, USA

Riverside Research, New York, NY, USA

the size, concentration, and relative acoustic impedance of weakly scattering constituents of tissue, such as blood vessels, stromal-tissue elements, and glandular ducts and acini (Lizzi et al. 1983, 1988; Feleppa et al. 1986). Smaller scatterer sizes, lower scatterer concentrations, and lesser acoustic-impedance differences between scatterers and their medium reduce echo-signal amplitude. Attenuation (the decrease in propagated-signal amplitude caused by absorption and scattering) affects echo-signal amplitude and frequency content while refraction (caused by non-uniform propagation velocities) alters ultrasound beam properties and distorts image geometries and relative echo-signal amplitudes. Nevertheless, conventional B-mode ultrasound imaging has proven to be extremely useful in detecting and diagnosing disease, guiding biopsies, planning therapy, and monitoring changes in tissue, e.g., changes occurring as disease progresses or regresses upon treatment.

Doppler images sense the shift in the frequency of echo signals relative to transmitted signals and portray motion, typically blood flow, in color. Color-Doppler imaging typically uses blue and red color encoding to depict the direction of movement parallel to the ultrasound-beam axis; red usually indicates motion toward the transducer and blue indicates motion away from the transducer. Power-Doppler imaging typically uses the intensity of orange color encoding to depict the amplitude of the echo signal from moving scatterers. Such images often are supplemented with graphical displays of Doppler-signal spectra and with acoustic outputs for aurally assessing Doppler information.

While B-mode and Doppler methods of ultrasonic imaging are used widely in medicine and provide clinically important information, emerging quantitative-ultrasound (QUS) methods potentially offer considerable additional information that may prove to be of great value for detecting, diagnosing, imaging, evaluating, and monitoring disease. This chapter focuses on spectrum-analysis and image-statistics QUS methods for assessing tissue micro-architecture

and, hence, for characterizing tissue types and properties (Feleppa et al. 2002c).

1.2 QUS Based on Spectrum Analysis and Envelope Statistics

1.2.1 Spectrum-Analysis Techniques

Spectrum analysis utilizes the power spectra of radiofrequency (RF) echo signals acquired in an ultrasonic scan plane (Lizzi et al. 1983, 1988; Feleppa et al. 1986). Figure 1.1 shows an early PC-based system for acquiring echo-signal data. A Hitachi EUB 525 scanner with two intra-cavity probes (typically used transrectally for prostate examinations) is shown interfaced with a PC-based data-acquisition system. RF data obtained internally from the scanner were digitized within the PC and stored on the hard disk of the computer. Data acquisition was controlled using the keyboard and auxiliary monitor shown at the upper right of the figure.

Tissue spectra typically are computed by applying a set of windows to RF echo-signal data from tissue to define a region of interest (ROI) and to select signals within that region for analysis. Windows within the ROI are applied by multiplying the RF signal with the window function at every window location. The two most common types of ROIs are those that contain windows of uniform size along a specified trajectory with respect to the scan vector (e.g., a rectangular ROI in a linear scan) and those that contain small, fixed-length windows that “slide” at specified range increments along each scan vector within an ROI of arbitrary shape (e.g., a 64-sample window stepping in eight-sample increments along every scan vector within the boundaries of a user-specified lesion). Figure 1.2 shows examples of both ROI types. Figure 1.2a illustrates a constant-length ROI consisting of 58 windows that are 110 samples long; this ROI matches the location of a tissue biopsy in a prostate gland. The grayscale B-mode image of Fig. 1.2a was computer gen-

Fig. 1.1 Clinical scanner configured for data acquisition. A Hitachi EUB 525 instrument provides RF data to the PC computer system on its lower shelf (in the lower left corner of the figure). The keyboard and larger monitor (in the upper right corner of the figure) provide the user interface for the data-acquisition computer. RF signals are acquired from the scanner after summation of the individual array-element signals but prior to non-linear amplification or other processing



erated from the digitized RF echo signals acquired from the entire scan plane. Figure 1.2b shows a calibrated log power spectrum computed from the ROI of Fig. 1.2a. The means of computing the spectrum is described below. Figures 1.2b–d illustrate ROIs of arbitrary shape filled with many small windows; these ROIs match the apparent boundary of cancerous (Fig. 1.2c) and non-cancerous (Fig. 1.2d) breast lesions. Typically, the windows are termed “soft” and consist of cosine-squared, Hamming, or Hanning function to strike a balance between spectral resolution and stability vs. artifacts resulting from abrupt signal-amplitude changes that would be caused by abruptly opening and closing a “hard” window, such as a rectangular-function window.

Once RF data are selected by a window, a Fourier transform is applied to the windowed signals, and the magnitude of the transform is squared. The result is the power spectrum of the windowed RF signals. In most applications, this

result is expressed in decibel units as 10 times the log of the squared magnitude of the Fourier transform, and it is termed the “log power spectrum.” An additional “normalization” or “calibration” step is performed using one of two methods. In one method, the log power spectrum of a reflector with a known reflection coefficient (based on the acoustical impedances of the media on each side of the reflecting surface), e.g., the surface of a glass or stainless-steel block or the interface between water and a high-density silicone oil, is subtracted from the log power spectrum of tissue echo signals. In a second method, the log power spectrum of a fully specified scattering phantom (i.e., specified in terms of scatterer size, scatterer concentration, scatterer acoustic impedance, medium acoustic impedance, and phantom attenuation) is computed and compared to the theoretical log power spectrum for the scattering phantom; the difference between the two spectra serves as the calibration spectrum. In either

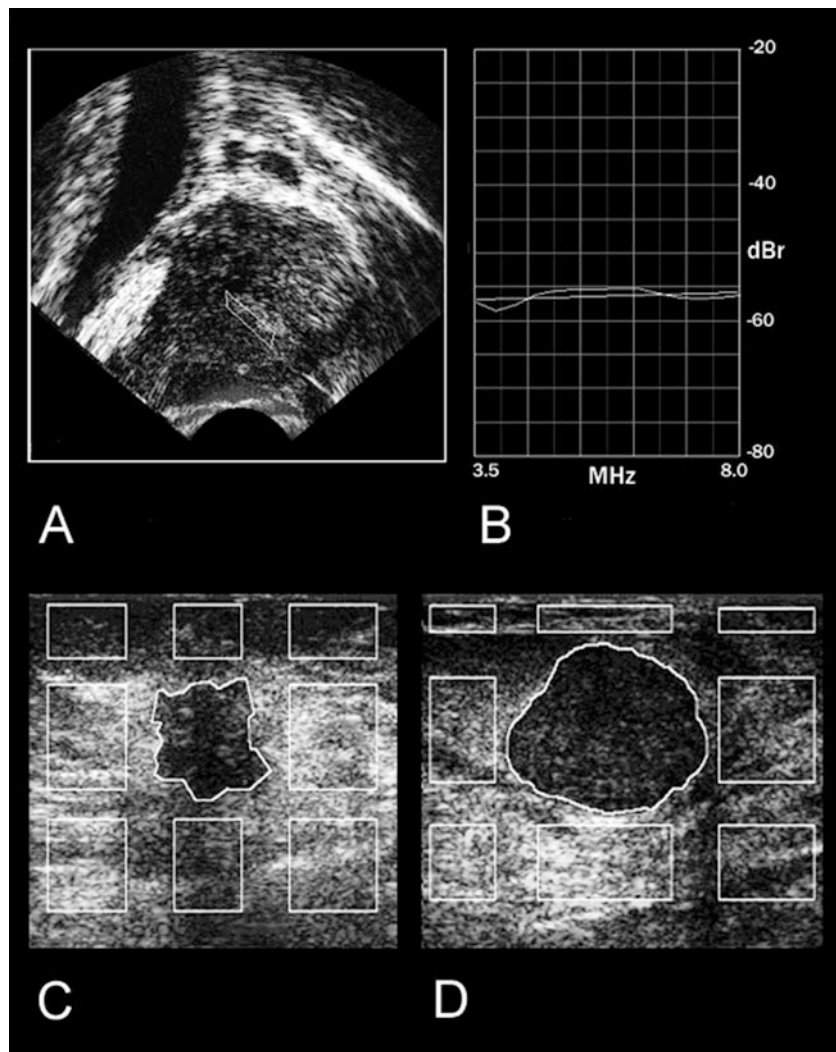


Fig. 1.2 ROIs and a spectrum for prostate and breast studies. **(a)** Rectangular ROI in a longitudinal prostate scan. The ROI is placed where the biopsy needle sampled tissue immediately after RF data were acquired. The prostate is the central circular hypoechogenic region surrounding the ROI, with the seminal vesicles extending to the lower left of the scan. The distance from the inner to the outer arcs of the scan is 3.6 cm. **(b)** Prostate spectrum. The spectrum illustrates the useable bandwidth of prostate RF data acquired with typical prostate scanners,

i.e., from 3.5 to 8.0 MHz in this example. The spectrum is characterized by the slope, intercept, and midband values of its linear-regression approximation. **(c)** An irregular, arbitrary-shape ROI used to compute spectral parameters for a cancerous breast lesion. (Rectangular ROIs are used to characterize disease-free tissue). **(d)** An irregular, arbitrary-shape ROI used to compute spectral parameters for a breast fibroadenoma. (Printed with the permission of Ultrasonic Imaging)

method, the calibration log power spectrum is subtracted from the log power spectrum computed from the tissue echo signals to derive the calibrated log power spectrum of the tissue. Calibration corrects for the transfer function and user-applied settings of the ultrasonic system being

used; it accounts for changes in beam properties as a function of range and changes in the transmitted pulse that occur with different instrument settings. Traditionally, calibration data must be acquired for every instrument setting and probe used for acquiring experimental RF

echo-signal data. Subsequent analysis of the RF echo-signal data must use the matching calibration data. In principle, the resulting calibrated log power spectrum allows computing system-independent spectral parameter values and, furthermore, allows estimating scatterer properties such as effective size and effective concentration combined with relative acoustic impedance (i.e., acoustic impedance of the scatterers relative to the acoustic impedance of the medium) as discussed further below (Lizzi et al. 1983, 1988; Feleppa et al. 1986).

The first theoretically formulated QUS approach based on spectrum analysis is termed the linear approach, and its history can be traced back to the work of Lizzi et al. in the 1980s (Lizzi et al. 1983, 1988; Feleppa et al. 1986). Estimating tissue-scatterer properties using the linear approach begins with calculating calibrated log power spectra and from them deriving spectral-parameter values by performing a linear-regression analysis of the calibrated log power spectrum over the useable bandwidth of the system, i.e., the noise-limited bandwidth. Linear regression provides a “straight-line” approximation to the spectrum in which the spectral-parameter values, i.e., the slope, intercept, and midband values of the linear-regression line, provide a simple means of representing the spectrum. An example is illustrated in Fig. 1.2b. These parameter values then can be related to scatterer properties (Note that only two of these spectral parameters are mathematically independent. The relationship among them is $y = y_0 + mf$, where y is the amplitude value of the line, y_0 is the intercept, m is the slope, and f is the frequency. If $f = f_c$, the center frequency, then $y = y_c$, the midband value). As shown by Lizzi et al., if correction for attenuation is performed, then the value of the spectral slope provides an estimate of effective scatterer size (Lizzi et al. 1983, 1988; Feleppa et al. 1986). Up to the Rayleigh limit, the scatterer-slope value increases as scatterer size decreases. Furthermore, the spectral intercept increases with increases in scatterer size, concentration, and relative acoustic impedance (i.e., the acoustic impedance of the scatterers relative to the

acoustic impedance of the medium). If scatterer size is estimated from the slope value, then the product of scatterer concentration (C) and squared relative acoustic impedance (Q^2) can be computed from the intercept value. Scatterer-property estimation methods depend upon the window function used to select RF signals and upon the two-way-directivity function (beam-profile properties) of the ultrasound beam. See Lizzi et al. for an in-depth discussion of the underlying theoretical framework (Lizzi et al. 1983, 1988; Feleppa et al. 1986).

1.2.1.1 Spectral-Parameter Imaging

Spectral-parameter imaging computes spectral-parameter values at every window location within a specified ROI, or, in the case of multiple small ROIs consisting of multiple windows, the average parameter value computed over each individual ROI, and displays parameter values as grayscale intensity or color value at corresponding pixel locations. In the former case, sliding windows typically are separated in range by distances smaller than half the window length, and grayscale intensity at each pixel is derived as the average of the parameter values computed at several adjacent window positions (This average includes windows on neighboring scan vectors as well as along the scan lines centered on the pixel). The number of windows in the average is a trade-off in which a larger number of windows degrades spatial resolution but improves the statistical validity of the spectral parameter estimates (Lizzi et al. 1997). Figure 1.3 shows examples of B-mode, slope, intercept, and midband images of a prostate gland in a transverse scan. The slope image is quite “noisy” compared to the midband and intercept image. The most stable image is the midband image, which is equivalent to the integrated-backscatter images of Miller et al. (O’Donnell et al. 1979). The B-mode image of Fig. 1.3 is computer generated from the digitized RF echo signals. The B-mode and midband images are quite similar; however, the midband image improves the signal relative to speckle and provides a quantitative, system-independent image at the cost of some spatial resolution (which results from the averaging that

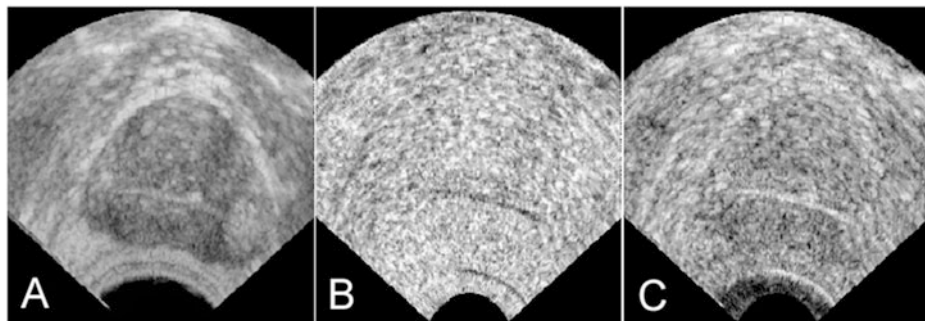


Fig. 1.3 Parameter images of the prostate in a transverse scan. The prostate is the heart-shaped region in the center of each image. The rectal wall is at the apex of the sector.

(a) Midband image. (b) Slope image. (c) Intercept image. Note that the slope image is very “noisy” and would benefit from a greater RF-signal bandwidth

occurs in generating pixel values from midband-parameter values at each window location).

Parameter values computed over a scan plane can be imaged themselves or can be used to generate other image types, such as scatterer-property or tissue-type images. The latter are discussed below. A notable example is the midband value expressed as integrated backscatter by Miller and co-workers, which has proven to be a very useful indicator of myocardial status in numerous studies by these investigators (Lanza et al. 1996, 1998; Miller et al. 1998). Miller and co-workers applied parametric imaging methods to characterization of cardiac tissue, particularly for the purpose of detecting and evaluating ischemia in the myocardium. In Miller’s studies, the time- and angle-dependent characteristics of attenuation-corrected integrated backscatter (which is equivalent mathematically to the midband parameter described above) proved to be a powerful tool in assessing the mechanical properties of the myocardium.

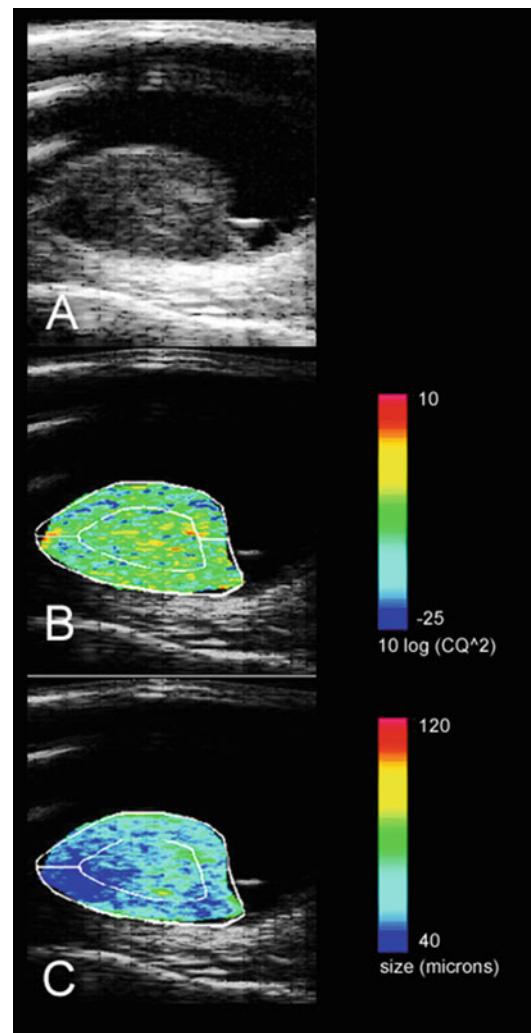
The limitations of these methods are those imposed by the physics of coherent acoustical imaging and the statistics of estimating spectral parameters. The physical limitations arise from well-known propagation and beam phenomena, e.g., limits on lateral resolution associated with transducer aperture and frequency and limits on axial resolution imposed by bandwidth (Feleppa 1996). Frequency-dependent attenuation decreases the signal-to-noise ratio with increasing depth and limits penetration. Furthermore,

because high frequencies are attenuated more rapidly than low frequencies, a downward spectral shift and bandwidth narrowing, and beam broadening occur with increasing depth. Additional limitations result from phase aberrations caused by inhomogeneities in propagation velocity, near-field artifacts, diffraction effects, and band-limiting noise arising from the system and the environment, motion due to respiration, heart contractions, arterial pulses, and the like. Speckle is a well-known phenomenon of coherent-imaging systems; speckle overlays image detail with randomly produced small-scale interference patterns and masks small structures. The statistics of estimating spectral parameters are discussed in detail by Lizzi et al. (1997).

1.2.1.2 Scatterer-Property Imaging

Generating scatterer-property images from parameter-value images requires only a simple algorithm that takes the window and transducer properties along with the system bandwidth into account (Lizzi et al. 1983, 1988; Feleppa et al. 1986). Once parameter values are computed at each pixel location, the algorithm converts the parameter values to values representing estimates of size, d , and the product, CQ^2 , of concentration, C , and squared relative acoustic impedance, Q^2 , which sometimes is termed “acoustic concentration.” Intraocular examples from the early work of Silverman, Coleman, Lizzi, and others are shown in Fig. 1.4. Figure 1.4a shows a scatterer-size (d) image of an

Fig. 1.4 Early scatterer-property images. B-mode and scatterer-property images for a posterior, intra-ocular, choroidal, malignant melanoma. The single-element, mechanical, sector-scanning transducer is above the eye in these images. (The eye appears flattened because the original 30-degree sector geometry is presented in a rectilinear format). (a) B-mode image showing the tumor extending into the vitreous humor from its base in the choroid. (b) CQ^2 image showing a range of values for $10 \log CQ^2$ extending from -25 to $+10$ dB. (c) Scatterer-size image showing scatterers from as small as $40 \mu\text{m}$ to as large as approximately $80 \mu\text{m}$. (Printed with the permission of Ronald Silverman, Department of Ophthalmology, Columbia University Medical Center)



intraocular melanoma; Fig. 1.4b shows an acoustic-concentration (CQ^2) image of ciliary muscles that depicts changes that occur during ocular accommodation (Rondeau et al. 1995; Aslanides et al. 1995). Furthermore, Silverman and co-workers have shown that parameter-value changes follow changes in tissue, specifically in choroidal malignant melanomas, that result from radiation therapy (Coleman et al. 1987).

Insana et al. developed a more-sophisticated method of estimating scatterer size (Insana et al. 1990, 1992, 1995a). This method relates the frequency-dependent backscatter coefficient to f , d , CQ^2 , and a form factor, $F(f,d)$. If scatterers are not spherical, but are symmetric non-

spherical entities, then the form factor becomes a function of scanning angle. In this approach, sizes are estimated by comparing modeled form factors with form factors derived from measured backscatter coefficients. Insana and his collaborators have successfully applied this method to estimating the sizes of kidney structures such as glomeruli, tubules, and arterioles (Insana et al. 1995a).

Oelze et al. investigated parameter and tissue-property techniques based on the form-factor approach in several phantom and animal studies, including characterization of mammary tumors in experimental rats (Oelze and O'Brien 2002; Oelze et al. 2002).

The limitations of scatterer-property imaging derive from those of acoustical imaging and parameter imaging. The statistical aspects are described by Lizzi et al. (1997).

1.2.1.3 Tissue-Type Imaging

Tissue-type imaging requires a database containing spectral-parameter values for the types of tissues that are of interest, e.g., primary choroidal melanomas vs. metastatic choroidal lesions in the eye or adenocarcinomas vs. non-cancerous tissues in the prostate (Coleman et al. 1985a, b, 1987, 1990; Rondeau et al. 1987; Lizzi et al. 1978; Feleppa et al. 2001a, b, c, 2002a, b). A classification tool, such as linear-discriminant, nearest-neighbor, neural-network, or support-vector-machine analysis, is applied to the data to determine what parameter values are associated with each tissue type of interest. In some cases, such as the prostate, including a clinical variable, such as the blood level of prostate-specific antigen (PSA) can improve classification (Feleppa et al. 2001a). Once the optimal classifier is established, that classifier can be applied to an unknown case to translate parameter values at each pixel location into a score to indicate tissue type, e.g., a high score value to indicate a high likelihood of cancer in a prostate image. The score can be depicted in grayscale or using colors to show values within pre-specified score ranges (e.g., red to show very high likelihood of cancer, orange to show a moderate likelihood, yellow to show less likelihood, and green to show minimal likelihood). Figure 1.5 shows examples of early tissue-type images derived from a transverse scan of the prostate. Figure 1.5a shows a grayscale cancer-liability image, and Fig. 1.5b shows a color-encoded image in which red and orange depict the two highest likelihoods of cancer against a midband-value image background. The whole-mount histologic section of the prostatectomy specimen is shown in Fig. 1.5c. The patient's prostate was scanned in a transverse mode immediately prior to prostatectomy surgery using 5-mm spacing between scan planes. The pathologist sectioned the excised prostate using 3-mm spacings between sectioning planes and

then demarcated cancers and pre-cancerous lesions in each whole-mount section. Figure 1.5 shows planes that approximately match, i.e., that have the greatest lateral dimension compared to others in the set of histological and ultrasound-scan planes. The demarcated region at the top of Fig. 1.5c is a 12-mm anterior tumor, which matches the bright anterior region at the top of Fig. 1.5a and the large red and orange region at the top of Fig. 1.5b. Images from adjacent planes are assembled into the 3-D surface rendering of Fig. 1.6. Red depicts the surfaces of high-suspicion regions within the light-gray prostate capsule (The capsule was demarcated manually using computer-generated B-mode images derived from the original RF data).

Parameter imaging can be extended to tissue-type imaging by classifying tissue based on the parameters it manifests. The performance limitations in translating parameter values to tissue type are those associated with the tissue classifier, and these limits are best described in terms of classification sensitivity, specificity, positive or negative predictive values, areas under ROC curves, and the like, in each application (Metz et al. 1990). In most cases, spatial resolution is not likely to be the driving issue in tissue-type imaging compared to the reliability of the tissue-type or tissue-change determination, as is addressed further in the discussion of applications below.

1.2.2 Envelope-Statistics Techniques

The envelope of the backscattered RF echo signal also contains information about the underlying tissue microstructural properties. Several models of the statistics of the envelope have been proposed (Hruska and Oelze 2009). Some of the distributions considered in these models include the Rayleigh, the Rician, the K, the homodyned-K, and the Nakagami distributions; these distributions have been described extensively in the literature (Destrempe and Cloutier 2010; Dutt and Greenleaf 1994). The distributions that cur-

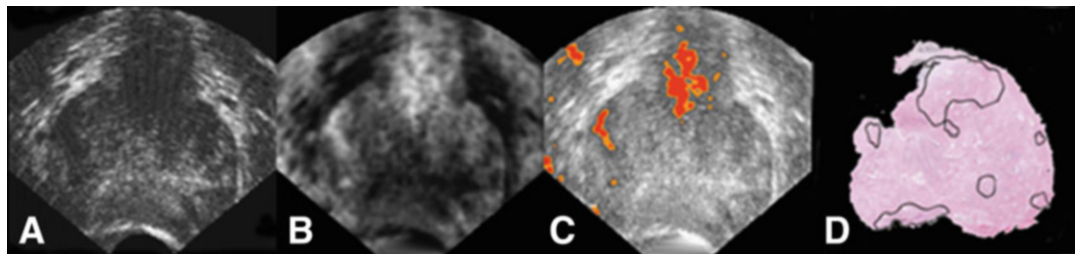
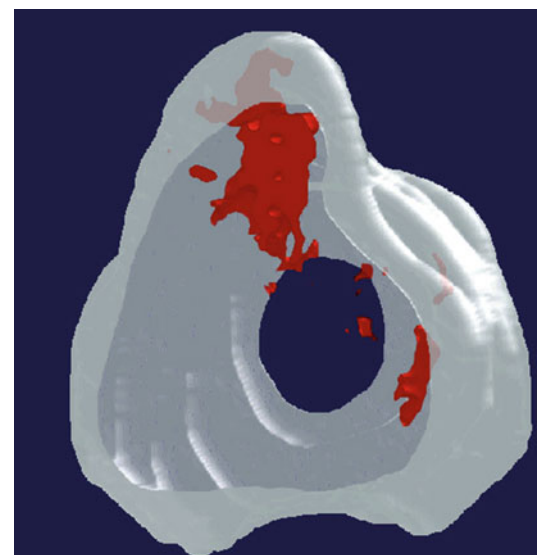


Fig. 1.5 Ultrasonic tissue-type and histologic images of a prostate with an unsuspected anterior tumor. Ultrasonic RF data were acquired immediately prior to prostatectomy for comparison with subsequently obtained whole-mount histology. (a) B-mode image showing artifact-like shadowing that masked the presence of the tumor. (b) Grayscale tissue-type image in which brighter pixels denote higher likelihood of cancer. The bright anterior region is consistent with the subsequent histological determina-

tion that an anterior tumor was present. (c) Color-encoded tissue-type image depicting the highest levels of likelihood for cancer as red and orange superimposed on a midband image. (d) Histological cross-section (in a plane closely matching the ultrasound plane of a, b, and c) that shows a 12-mm anterior tumor along with smaller tumor foci and a posterior pre-cancerous condition. (Note that this figure views the gland from the apex). (Printed with the permission of Ultrasonic Imaging)

Fig. 1.6 3-D rendering of the prostate gland of Fig. 1.5. The 12-mm anterior tumor of Fig. 1.5 is clearly depicted, along with several smaller foci of cancer. (Note that this figure views the gland from the base, i.e., the perspective taken in this figure is the reverse of the perspective taken in Fig. 1.5). (Printed with the permission of Ultrasonic Imaging)



rently are most-commonly used in biomedical applications are the homodyned-K and Nakagami distributions.

Jakeman and Pusey (1976) introduced the K distribution, a generalization of the Rayleigh distribution, in 1976 to model situations where the number of scatterers per resolution-cell volume can be assumed to be small. A parameter introduced by the K distribution is μ , the number of scatterers per resolution cell. The resolution-cell volume is defined as the volume of the point spread function of the imaging system, i.e., the volume of the insonified medium that contributes

to any given point in the echo signal. If the resolution cell of the ultrasound pulse is determined, then the number density of scatterers can be estimated from μ . The K distribution approaches the Rayleigh distribution as μ approaches infinity.

The homodyned-K distribution subsequently was introduced by Jakeman in 1980 (Jakeman 1980). The homodyned-K distribution is more complicated than the K distribution, but it is more versatile. For instance, it can model scattering environments where a coherent signal component exists, e.g., in the presence of periodically located scatterers. It is characterized by several param-

eters including s , σ , μ , and k , where s^2 is the coherent-signal energy, σ^2 is the diffuse-signal energy, and μ is the number of scatterers per resolution cell as defined in the K distribution. A derived parameter, $k = s/\sigma$, is the ratio of the coherent to diffuse signal and can be used to describe the level of organized structure or periodicity in scatterer locations. When using the homodyned-K distribution, the value of μ is an accurate estimate only when the number of scatterers per resolution cell is fewer than 10 (Dutt and Greenleaf 1994).

Nakagami developed the Nakagami distribution in 1960 during studies of long-distance multi-path propagation of radio waves (Nakagami 1960; Suzuki 1977). Shankar and co-workers applied the Nakagami distribution to ultrasound echo signals in 2001 (Shankar et al. 2001; Shankar 2001). The distribution is characterized by the following two parameters: m , the Nakagami parameter, and Ω , the scaling factor. The value of m assigns the distribution in one of the following four categories: $m < 0.5$, a Nakagami-gamma distribution (i.e., only a few scatterers per resolution cell with gamma-distributed scattering cross sections); $0.5 < m < 1$, a pre-Rayleigh distribution; $m = 1$, a Rayleigh distribution; and $m > 1$, a Rician or post-Rayleigh distribution. Maps of the value of the Nakagami parameter can be used for tissue typing based on the underlying scattering properties of the tissue expressed as the statistics of the envelope signal (Ho et al. 2012; Zhou et al. 2015).

Envelope-statistics parameters also depend on the ultrasound frequency and bandwidth, which determine the size of the resolution cell, and they depend on attenuation, which is frequency dependent and increases the size of the resolution cell with depth (Cloutier et al. 2004; Tsui and Tsai 2015).

1.3 Current and Potential Applications of QUS

The emerging QUS methods that are summarized here have a broad range of applications in medicine and biological research and potentially

in clinical practice. Clearly, tissue typing based on spectrum analysis and envelope statistics has enormous potential benefit in detecting, diagnosing, imaging, monitoring, and evaluating many types of diseases. Cancerous lesions, ischemic myocardium, and intra-vascular lesions associated with cardiac and cerebral ischemia are a few obvious examples. Although they now are emerging as exciting tools for detecting early markers of disease, many of these methods have been investigated for several years. Lizzi, Coleman, Silverman, and their co-workers have been developing and refining many of the spectrum-analysis approaches in their foundation ophthalmic intraocular cancer studies that were initiated nearly five decades ago (Coleman et al. 1985a, b, 1987, 1990; Rondeau et al. 1987; Ursea et al. 1998). As described above and as illustrated in Fig. 1.5, Feleppa and co-workers have been investigating the use of spectrum-analysis methods and non-linear classifiers to enable imaging of cancerous lesions of the prostate for the purpose of guiding needle biopsies and for targeting and monitoring therapy (Lizzi et al. 1978; Feleppa et al. 2001a, b, c, 2002a, b). Alam et al. have developed a promising multi-feature approach using spectrum analysis and morphometric parameters for discriminating malignant from benign breast lesions (Noritomi et al. 1997b). Feleppa and co-workers applied spectrum-analysis-based QUS to evaluation of lymph nodes for the purpose of guiding microhistology and immuno-histochemical staining (Noritomi et al. 1998; Tateishi et al. 1998); more recently, these lymph-node studies have been extended to include envelope-statistics methods for detecting and imaging metastatic foci in lymph nodes. Miller, Holland, and others evaluated myocardial status using integrated-backscatter (equivalent to the spectral midband parameter) and attenuation measures (Miller et al. 1998; Sosnovik et al. 2001a, b; Tamirisa et al. 2001; Perez and Miller 2000). Insana and Hall studied changes in renal vasculature using QUS-derived scatterer-size estimates [Insana et al. 1995b]. Insana also investigated limits of scatterer-size estimates in a collaboration with O'Brien and Oelze (Zhu et al. 2017). O'Brien

and Andre are applying QUS to detection and assessment of fatty liver (Andre et al. 2015; Lin et al. 2015). Czarnota, Kolios, and Oelze are using QUS for monitoring and predicting the efficacy of chemotherapy for breast cancer (Sannachi et al. 2015; Sadeghi-Naini et al. 2017; Sharma et al. 2020). Oelze also is investigating QUS for grading fatty liver disease (Nguyen et al. 2019, 2021), for characterizing breast cancer (Insana and Oelze 2006), and for evaluating thyroid nodules (Lavarello et al. 2013). Lee is investigating QUS as a means of distinguishing malignant from benign thyroid nodules (Goundan et al. 2021). Mamou and Raum are applying QUS to detection and assessment of early osteoarthritis (Lye et al. 2020, 2021). Hall and Feltovich are investigating the use of QUS for uterine cervical-ripening assessment associated with pre-term birth and predicting successful inductions (Santoso et al. 2020). These are just a few representative examples of contemporary studies of potential medical applications of QUS. Clearly, considerable exciting research is underway applying these emerging QUS methods to critical issues in detecting, diagnosing, imaging, evaluating, and monitoring disease across an extremely broad range of important medical needs.

1.4 Future Technological Developments

Future technological developments in these emerging technologies can be expected to occur in three general areas: advances within each individual ultrasonic technological area; advances based on combinations of ultrasonic methods with each other; and advances resulting from correlations of information derived by ultrasonic and non-ultrasonic methods.

1.4.1 Advances Within Individual Emerging Ultrasound Technologies

Ultrasound instruments are incorporating a great deal of digital technology in array controls, scanning, gain manipulations, frequency shifting, pulse shaping, speckle suppression, beam formation, dynamic focusing, image enhancement, and the like. Top-of-the-line instruments already are incorporating new imaging modes that only recently were advanced research topics (e.g., harmonic imaging and very-high-frequency intra-vascular imaging). Advances can be expected in all these areas. In addition, array technology constantly is improving in terms of fabrication and materials, which results in increased sensitivity, improved focusing, greater bandwidth, and higher-quality conventional images. Array technology also is extending into higher frequency ranges and providing superior image definition. All these enhancements will advance basic ultrasound imaging and the emerging technologies discussed above.

This chapter summarizes recent developments in spectrum-analysis-based and envelope-statistics-based QUS techniques. However, to utilize fully the potential of technology based on spectrum-analysis and envelope-statistics methods, additional computing power will be required to perform the needed mathematical functions in real time. Improvements will occur by incorporating digital signal-processing capabilities and by developing newer, more-efficient algorithms for processing echo signals. As one example, much of the information extracted from echo signals using Fourier transformation to compute power spectra also may be made available using auto-regression and wavelet methods. The use of deep learning may also impact how spectral-based analysis and envelope-statistics are applied.

1.4.2 Advances Among Emerging Ultrasound Technologies

Images based on spectrum analysis, envelope statistics, elasticity, and ultrasound contrast agents (UCAs) generally provide different information based on the independent properties of tissue. To the extent that information obtained using these methods is truly independent, combining them can permit more-powerful classification and tissue-type differentiation in many applications.

1.4.3 Advances in Combinations of Ultrasonic and Other Technologies

Ultrasonic imaging of any kind is based on the mechanical properties of scatterers in the ultrasound field, i.e., the relative magnitudes and the spatial nature of their acoustical impedances in the case of conventional imaging, spectrum analysis, and envelope-statistics methods. Contrast-agent imaging depends upon the properties of the UCAs themselves. Elastography depicts strains in tissue and, from that, displays relative tissue rigidities over volumes with dimensions that tend to be much larger than a wavelength. Other imaging modalities, such as computed tomography (CT), magnetic-resonance (MR), positron-emission-tomography (PET), or single-photon emission computerized tomography (SPECT) imaging, utilize entirely different types of information. Images generated using these methods display spatial distributions of a variety of tissue properties other than the mechanical properties of constituent scatterers. CT depicts X-ray opacity; MR depicts chemical properties; and PET and SPECT depict metabolic activity. Therefore, if fundamentally independent information from non-ultrasound technologies can be merged with ultrasonically derived information, further substantial improvements in tissue characterization and tissue-type imaging may be realized.

1.5 Conclusion

The emerging QUS technologies discussed in this chapter show exciting potential for detecting disease, assessing disease status, planning therapy, targeting treatment, and following disease progression and regression.

QUS technologies based on spectrum analysis and envelope statistics sense the mechanical properties of microscopic scatterers in tissue. Ultrasonic elastographic methods depict elasticity properties of tissue on a larger scale (de Korte and van der Steen 2002). Ultrasonic contrast agents enhance blood-containing spaces and offer means of assessing flow, perfusion, and the sites of targeted vascular lesions; and advanced flow-measuring methods detect and measure slow flow as well as flow that is detectable and measurable by conventional methods. Spectrum analysis alone and combined with envelope statistics have demonstrated exciting potential for distinguishing cancerous from non-cancerous tissues in a variety of organs, e.g., the eye, prostate gland, and lymph nodes; and for distinguishing among various categories of venous thrombi and arterial plaques (Noritomi et al. 1997a, b). While these applications of spectrum analysis and envelope statistics require a database for characterizing the tissue types of interest, they also simply can depict changes in tissue that occur over time by sensing *changes* in constituent scatterers; in such applications, the organ or lesion of interest provides its own baseline reference for assessing temporal variations.

Elastography clearly presents an enormous potential in cases where a disease process alters the local stiffness or elasticity of tissues. While cancerous lesion detection and evaluation are widely acknowledged candidate applications for elastography, detection and characterization of vascular lesions and evaluation of vessel-wall properties may prove to be additional applications for elastography.

Contrast agents obviously benefit imaging and assessment of large blood-filled volumes such as the cardiac chambers, arteries, and veins, but their greatest future value may lie in their ability to provide perfusion information, e.g., assessing car-

diac ischemia or in revealing and quantitatively evaluating targetable lesions such as atherosclerotic plaque or neo-vasculature associated with some types of cancers. UCAs take advantage of new techniques of harmonic imaging, but also potentially can enhance advanced, correlation-based methods of detecting and measuring slow and chaotic flow, which may be of great value in characterizing neo-vasculature associated either with tissue repair or with developing cancerous lesions.

Combining these emerging QUS technologies with each other or fusing the information provided by each of them may provide even more-powerful quantitative tools for characterizing tissue. In addition, each emerging ultrasound technology potentially can be correlated with other conventional and emerging *non-ultrasound* technologies, such as CT, MR, PET, and SPECT, to synergize the independent types of information provided by each modality and further extend their medical value for detecting, diagnosing, imaging, evaluating, and monitoring disease.

References

- Andre M, Heba E, Han A, Lin S, Wolfson T, Ang B, Gamst A, Erdman J, O'Brien W, Sirlin C, Loomba R (2015) Diagnosis and quantification of liver steatosis with quantitative ultrasound backscatter technique. *Med Phys* 42(6):3684–3684
- Aslanides IM, Rondeau MJ, Silverman RH, Reinstein DZ, Najafi DJ, Lloyd HO, Ursea R, Lizzi FL, Coleman DJ (1995) *In-vivo* functional ultrasound imaging of ciliary muscle response to pharmacological agents. *Invest Ophthalmol Vis Sci* 36(4):S564
- Cloutier G, Daronat M, Savéry D, Garcia D, Durand LG, Foster FS (2004) Non-Gaussian statistics and temporal variations of the ultrasound signal backscattered by blood at frequencies between 10–58 MHz: experimental results. *J Acoust Soc Am* 116:566–577
- Coleman DJ, Lizzi FL, Silverman RH, Helson L, Torpey JH, Rondeau MJ (1985a) A model for acoustic characterization of intraocular tumors. *Invest Ophthalmol Vis Sci* 26:545–550
- Coleman DJ, Lizzi FL, Silverman RH, Ellsworth RM, Haik BG, Abramson DH, Smith ME, Rondeau MJ (1985b) Regression of uveal malignant melanoma following cobalt-60 plaque: correlates between pre-treatment acoustic spectrum analysis and tumor regression. *Retina* 5:73–78
- Coleman DJ, Rondeau MJ, Silverman RH, Lizzi FL (1987) Computerized ultrasonic biometry and imaging of intraocular tumors for the monitoring of therapy. *Trans Am Ophthalmol Soc* LXXXV:49–81
- Coleman DJ, Silverman RH, Rondeau MJ, Lizzi FL, McLean IW, Jakobiec FJ (1990) Correlations of acoustic tissue typing of malignant melanoma and histopathologic features as a predictor of death. *Am J Ophthalmol* 110:380–388
- de Korte CL, van der Steen AF (2002) Intravascular ultrasound elastography: an overview. *Ultrasonics* 40:859–865
- Destrempes F, Cloutier G (2010) A critical review and uniformized representation of statistical distributions modeling the ultrasound echo envelope. *Ultrasound Med Biol* 36:1037–1051
- Dutt V, Greenleaf JF (1994) Ultrasound echo envelope analysis using a homodyned-K distribution signal model. *Ultrason Imaging* 16:265–287
- Feleppa EJ (1996) Physics of diagnostic ultrasound for surgeons. In: Machi J, Sigel B (eds) *Ultrasound for surgeons*. Igaku-Shoin Medical Publishers, New York, pp 7–41
- Feleppa EJ, Lizzi FL, Coleman DJ, Yaremko MM (1986) Diagnostic spectrum analysis in ophthalmology: a physical perspective. *Ultrasound Med Biol* 12(8):623–631
- Feleppa EJ, Ketterling JA, Kalisz A, Urban S, Porter CR, Gillespie J, Schiff PB, Ennis RD, Wuu CS, Moul W, Sesterhenn IA, Scardino PT (2001a) Prostate imaging based on RF spectrum analysis and non-linear classifiers for guiding biopsies and targeting radiotherapy. In: Shung KK, Insana M (eds) *Medical imaging 2001: ultrasonic imaging and signal processing*, vol 4325. Society of Photo-Optical Instrumentation Engineers, Bellingham, pp 371–379
- Feleppa EJ, Ennis RD, Schiff PB, Wuu CS, Kalisz A, Ketterling J, Urban S, Liu T, Fair WR, Porter CR, Gillespie JR (2001b) Spectrum analysis and neural networks for imaging to detect and treat prostate cancer. *Ultrason Imaging* 23:90–106
- Feleppa EJ, Ketterling JA, Kalisz A, Urban S, Porter CR, Gillespie JW, Schiff PB, Ennis RD, Wuu CS, Fair WR (2001c) Advanced ultrasonic tissue-typing and imaging based on radio-frequency spectrum analysis and neural-network classification for guidance of therapy and biopsy procedures. In: Lemke K et al (eds) *Proceedings of CARS 2001-computer assisted radiology and surgery*. Amsterdam, pp 333–337
- Feleppa EJ, Ennis RD, Schiff PB, Wuu CS, Kalisz A, Ketterling JA, Urban S, Liu T, Fair WR, Porter CR, Gillespie JR (2002a) Ultrasonic spectrum analysis and neural-network classification as a basis for Ultrasonic Imaging to target brachytherapy of prostate cancer. *J Brachyther Int* 1(1):1–6
- Feleppa EJ, Urban S, Kalisz A, Porter CR, Gillespie J, Ennis RD, Wuu CS, Schiff PB (2002b) Advances in tissue-type imaging (TTI) for detecting and evaluating prostate cancer. In: *Proceedings of the 2002 ultrason-*

- ics symposium. Institute of Electrical and Electronics Engineers, Piscataway (in press)
- Feleppa EJ, Alam SK, Deng CX (2002c) Emerging ultrasound sound technologies for early markers of disease. *Dis Mark* 18:249–268 with the permission of IOS Press and Hindawi Limited. Portions of this chapter are reproduced from this article
- Goundan PN, Mamou J, Rohrbach D, Smith J, Patel H, Wallace KD, Feleppa EJ, Lee SL (2021) A preliminary study of quantitative ultrasound for cancer-risk assessment of thyroid nodules. *Front Endocrinol (Lausanne)* 12:627698. <https://doi.org/10.3389/fendo.2021.627698>
- Ho MC et al (2012) Using ultrasound Nakagami imaging to assess liver fibrosis in rats. *Ultrasonics* 52:215–222
- Hruska DP, Oelze ML (2009) Improved parameter estimates based on the homodyned K distribution. *IEEE Trans Ultrason Ferroelectr Freq Control* 56(11):2471–2481
- Insana MF, Oelze ML (2006) Advanced ultrasonic imaging techniques for breast cancer research. In: Suri JS, Rangayyan RM, Laxminarayan S (eds) Emerging technologies in breast imaging and mammography. American Scientific Publishers, Valencia
- Insana MF, Wagner RF, Brown DG, Hall TJ (1990) Describing small-scale structure in random media using pulse-echo ultrasound. *J Acoust Soc Am* 87: 179–192
- Insana MF, Wood JG, Hall TJ (1992) Identifying acoustic scattering sources in normal renal parenchyma *in vivo* by varying arterial and ureteral pressures. *Ultrasound Med Biol* 18(7):587–599
- Insana MF, Wood JG, Hall TJ, Cox GG, Harrison LA (1995a) Effects of endothelium-1 on renal microvasculature measured using quantitative ultrasound. *Ultrasound Med Biol* 21:1143–1151
- Insana MF, Wood JG, Hall TJ, Cox GG, Harrison LA (1995b) Effects of endothelin-1 on renal microvascularity measured using quantitative ultrasound. *Ultrasound Med Biol* 21:1143–1151
- Jakeman E (1980) On the statistics of K-distributed noise. *J Phys A Math Gen* 13:31–48
- Jakeman E, Pusey PN (1976) A model for non-Rayleigh sea echo. *IEEE Trans Antennas Propag AP-24(6)*:806–814
- Lanza GM, Wallace K, Scott MJ, Cachetis C, Abendschein D, Christy D, Sharkey A, Miller J, Gaffney P, Wickline SA (1996) A novel site-targeted ultrasonic contrast agent with broad biomedical applications. *Circulation* 94:3334–3340
- Lanza GM, Trousil RL, Wallace KD, Rose JH, Hall CS, Scott MJ, Miller JG, Eisenberg PR, Gaffney PJ, Wickline SA (1998) In vitro characterization of a novel, tissue-targeted ultrasonic contrast system with acoustic microscopy. *J Acoust Soc Am* 104:3665–3672
- Lavarello RJ, Ridgway WR, Sarwate S, Oelze ML (2013) Characterization of thyroid cancer in mouse models using high-frequency quantitative ultrasound techniques. *Ultrasound Med Biol* 12:2333–2341
- Lin SC, Heba E, Wolfson T, Ang B, Gamst A, Han AG, Erdman JW, O'Brien WD, Andre MP, Sirlin CB, Loomba R (2015) Noninvasive diagnosis of nonalcoholic fatty liver disease and quantification of liver fat using a new quantitative ultrasound technique. *Clin Gastroenterol Hepatol* 13(7):1337. <https://doi.org/10.1016/j.cgh.2014.11.027>
- Lizzi FL, Coleman DJ, Franzen L, Feleppa EJ (1978) Use of a spectrum analysis system for characterization of malignant melanoma. In: White D, Lyons EA (eds) *Ultrasound in medicine*. Plenum Press, New York, pp 559–561
- Lizzi FL, Greenebaum M, Feleppa EJ, Elbaum M, Coleman DJ (1983) Theoretical framework for spectrum analysis in ultrasonic tissue characterization. *J Acoust Soc Am* 73(4):1366–1373
- Lizzi FL, King DL, Rorke MC, Hui J, Ostromogilsky M, Yaremko MM, Feleppa EJ, Wai P (1988) Comparison of theoretical scattering results and ultrasonic data from clinical liver examinations. *Ultrasound Med Biol* 14(5):377–385
- Lizzi FL, Feleppa EJ, Astor M, Kalisz A (1997) Statistics of ultrasonic spectral parameters for prostate and liver examinations. *IEEE Trans Ultrason Ferroelectr Freq Control* 44:935–942
- Lye TH, Gachouch O, Renner L, Raum K, Mamou J (2020) Quantitative ultrasound characterization of human articular cartilage. In: 2020 IEEE international ultrasonics symposium
- Lye TH, Gachouch O, Renner L, Elezkurtaj S, Cash H, Messroghli D, Raum K, Mamou J (2021) Quantitative ultrasound assessment of human articular cartilage degeneration with a clinical ultrasound system. *Osteoarthr Cart* [Under Review]
- Metz CE, Shen JH, Herman BA (1990) New methods for estimating a binormal ROC curve from continuously-distributed test results. In: Presented at the 1990 joint meetings of the American Statistical Society and the Biometric Society, Anaheim, August 1990
- Miller JG, Perez S, Wickline SA, Baldwin SL, Barzilai B, Davila-Roman V, Fedewa RJ, Finch-Johnston AE, Hall CS, Handley SM, Huckett FD, Holland MR, Kovacs A, Lanza GM, Lewis SS, Marsh JN, Mobley J, Sosnovik DE, Trousil RL, Wallace KD, Waters KR (1998) Backscatter imaging and myocardial tissue characterization. In: Proceedings of the IEEE ultrasonics symposium, Sendai, Japan, pp 1373–1383
- Nakagami M (1960) The m-distribution: a general formula of intensity distribution of rapid fading. Pergamon, New York
- Nguyen TN, Podkowa A, Arnold E, Miller RJ, Do MN, Oelze ML (2019) Characterizing fatty liver *in vivo* in rabbits using quantitative ultrasound. *Ultrasound Med Biol* 45:2049–2062
- Nguyen TN, Podkowa A, Arnold E, Park T, Miller RJ, Do MN, Oelze ML (2021) Use of a convolutional neural network and quantitative ultrasound for diagnosis of fatty liver. *Ultrasound Med Biol* 47(3):556–568
- Noritomi T, Sigel B, Gahtan V, Swami V, Justin J, Feleppa EJ, Shirouzu K (1997a) In vivo detection of carotid plaque thrombus by ultrasonic tissue characterization. *J Ultrasound Med* 16(2):107–111

- Noritomi T, Sigel B, Swami V, Justin J, Gahtan V, Chen X, Feleppa EJ, Roberts AB, Shirouzu K (1997b) Carotid plaque typing by multiple-parameter ultrasonic tissue characterization. *Ultrasound Med Biol* 23(5):643–650
- Noritomi T, Machi J, Feleppa EJ, Yanagihara E, Shirouzu K (1998) In vitro investigation of lymph node metastasis of colorectal cancer using ultrasonic spectral parameters. *Ultrasound Med Biol* 24:235–243
- O'Donnell M, Bauwens D, Mimbs JW, Miller JG (1979) Broadband integrated backscatter: an approach to spatially localized tissue characterization in vivo. *Proc IEEE Ultrason Symp* 79(CH 1482–1489):175–178
- Oelze ML, O'Brien WD (2002) Method of improved scatterer size estimation and application to parametric imaging using ultrasound. *J Acoust Soc Am* 112(6):3053–3063
- Oelze ML, Zachary JF, O'Brien WD (2002) Characterization of tissue microstructure using ultrasonic backscatter: theory and technique for optimization using a Gaussian form factor. *J Acoust Soc Am* 112(3):1202–1211
- Perez JE, Miller JG (2000) Myocardial tissue characterization: an extension of echocardiography. In: Pohost GM (ed) *Imaging in cardiovascular disease*. Lippincott Williams & Wilkins, Philadelphia, pp 115–120
- Rondeau MJ, Silverman RH, Coleman DJ, Lizzi FL (1987) The acoustic microarchitecture of human malignant melanoma. In: Kessler LW (ed) *Acoustical imaging*, vol 13. Plenum Press, New York
- Rondeau MJ, Silverman RH, Aslanides IM, Lloyd HO, Lizzi FL, Coleman DJ (1995) Functional ultrasound imaging of the ciliary muscle during accommodation. *Invest Ophthalmol Vis Sci* 36(4):S502
- Sadeghi-Naini A, Sannachi L, Tadayyon H, Tran WT, Slodkowska E, Trudeau M, Gandhi S, Pritchard K, Koliou MC, Czarnota GJ (2017) Chemotherapy-response monitoring of breast cancer patients using quantitative ultrasound-based intra-tumour heterogeneities. *Sci Rep* 7(1):10352. <https://doi.org/10.1038/s41598-017-09678-0>. PMID: 28871171
- Sannachi L, Tadayyon H, Sadeghi-Naini A, Tran W, Gandhi S, Wright F, Oelze ML, Czarnota G (2015) Non-invasive evaluation of breast cancer response to chemotherapy using quantitative ultrasonic backscatter parameters. *Med Image Anal* 20:224–236
- Santoso AP, Vink JY, Gallos G, Feltovich H, Hall TJ (2020) Quantitative ultrasound detects smooth muscle activity at the cervical internal Os in vitro. *Ultrasound Med Biol* 46(1):149–155. <https://doi.org/10.1016/j.ultrasmedbio.2019.08.020>. PMCID: PMC6879854
- Shankar PM (2001) Ultrasonic tissue characterization using a generalized Nakagami model. *IEEE Trans Ultrason Ferroelectr Freq Control* 48(6):1716–1720
- Shankar PM, Dumane VA, Ried JM, Genis V (2001) Classification of ultrasonic B-mode images of breast masses using Nakagami distribution. *IEEE Trans Ultrason Ferroelectr Freq Control* 48(2):569–580
- Sharma D, Cartar H, Law N, Giles A, Farhat G, Oelze ML, Czarnota GJ (2020) Optimization of microbubble enhancement of hyperthermia for cancer therapy in an in vivo breast tumour model. *PLoS ONE* 15(8):e0237372
- Sosnovik DE, Baldwin SL, Holland MR, Miller JG (2001a) Transmural variation of myocardial attenuation and its potential effect on contrast-mediated estimates of regional myocardial perfusion. *J Am Soc Echocardiogr* 14:782–788
- Sosnovik DE, Baldwin SL, Lewis SH, Holland MR, Miller JG (2001b) Transmural variation of myocardial attenuation measured with a clinical imager. *Ultrasound Med Biol* 27:1643–1650
- Suzuki H (1977) A statistical model for urban radio propagation. *IEEE Trans Commun* C-25(7):673–680
- Tamirisa PK, Holland MR, Miller JG, Perez JE (2001) Ultrasonic tissue characterization of hypertrophic left ventricular myocardium. *Echocardiography* 18:593–597
- Tateishi T, Machi J, Feleppa EJ, Oishi RH, Jucha J, Yanagihara E, McCarthy LJ, Noritomi T, Shirouzu K (1998) In vitro diagnosis of axillary lymph node metastases in breast cancer by spectrum analysis of radio frequency echo signals. *Ultrasound Med Biol* 24(8):1151–1159
- Tsui PH, Tsai YW (2015) Artifact reduction of ultrasound Nakagami imaging by combining multifocus image reconstruction and the noise-assisted correlation algorithm. *Ultron Imaging* 37:53–69
- Ursea R, Coleman DJ, Silverman RH, Lizzi FL, Harrison W (1998) Correlation of high-frequency ultrasound backscatter with tumor microstructure in iris melanoma. *Ophthalmology* 105:906–912
- Zhou Z, Wu S, Wang CY, Ma HY, Lin CC, Tsui PH (2015) Monitoring radiofrequency ablation using real-time ultra-sound Nakagami imaging combined with frequency and temporal compounding techniques. *PLoS ONE* 10:1–15
- Zhu Y, Han A, O'Brien WD, Oleze ML, Insana MF (2017) Limitations on estimation of effective scatterer diameters. *J Acoust Soc Am* 142(6):3677–3690



Quantitative Ultrasound: Scattering Theory

2

Michael Oelze

Abstract

The radio-frequency ultrasound backscattered data from tissue is rich in information and can provide important information about tissue state that is not obtained through traditional B-mode imaging. To parameterize the ultrasound backscattered data, the frequency spectrum, i.e., the backscatter coefficient, can be modeled using scattering theory. Models of tissue scattering are often represented by simple discrete geometric shapes, i.e., discrete scattering model. The discrete scattering model provides important insights into how the spatial arrangement of scatterers contributes to the signal spectrum. Another competing model is the continuum scattering model. In this model, the tissue is described as a continuous tissue construct with scatterers that have a continuous impedance change from the background. The continuous model provides a form factor description of the underlying tissue scatterers such as an effective scatterer diameter. In this chapter, we will compare and contrast the two underlying tissue scattering models and how they provide

insights into ultrasonic scattering from soft tissues.

Keywords

Backscatter coefficient · Discrete model · Continuous model · Incoherent scatter · Coherent scatter

2.1 Introduction

Mechanical energy can be transported through a medium via an acoustic or ultrasonic wave (Kinsler et al. 2000; Fetter and Walecka 2003). As that energy is transported through a medium, the wave can encounter spatial changes in the mechanical properties of the medium. Because energy must be conserved, at the boundary where mechanical properties change, the energy of the wave outgoing from the interface must equal the energy of the incident wave. If the wave propagates through a fluid medium and encounters a second medium of rigid material, where no energy can be transported into the second medium, all the energy will be directed away from the second medium and the energy in the wave is still conserved.

If the second medium presents as a smooth, flat interface then the wave energy will be redirected

M. Oelze (✉)
Department of Electrical and Computer Engineering and
Carle Illinois College of Medicine, University of Illinois
at Urbana-Champaign, Champaign, IL, USA
e-mail: oelze@illinois.edu

at an angle opposite to its incident angle (assuming a plane wave). If the interface is flat but rough, then some energy will be directed at the angle opposite to its incident angle (i.e., the specular reflection) while some energy will be directed away from the rough interface at different angles (i.e., scattered energy) (Oelze et al. 2001, 2003). The rougher the surface, the larger the amount of energy in the scattered wave versus the specular reflected wave. Similarly, if the interface is not flat but curved, then the direction of the redirected wave will depend on the local curvature of the interface with the plane wave. As the interface takes on a more spherical shape, a plane wave incident on the object can be scattered in all directions, while a specular wave continues to propagate in the forward direction.

If the second medium is not rigid but is fluid, like the incident medium, with properties different from the incident medium, some of the energy can transmit into the second medium. Depending on the incidence angle of the incident wave, the shape and size of the second medium, and the mechanical properties of the second medium (i.e., the density and compressibility of the second medium), the incident energy can be scattered in all directions and inside the second medium (Shung and Thieme 1992). The scattered waves from the second medium, i.e., the scatterer, can be collected with a detector. Information about the size, shape, and mechanical properties of the scatterer are encoded in the scattered waves (Oelze et al. 2002; Oelze and Mamou 2016). Appropriate modeling of the scattered waves can allow the inference of the properties of the scatterer giving rise to the scattered waves.

Typically, a detector is of finite extent and located at some distance from the scatterer. As a result, because the scattered waves are directed into all space, only a limited region of that space is sampled by the detector. This limits the ability to definitively infer properties of the scatterer. Furthermore, any ultrasonic wave that is incident on the scatterer is bandwidth limited, further reducing the information in the scattered waves that are collected. Increasing the complexity of the problem is that multiple scatterers may be embedded in the field resulting in a superpo-

sition of scattered waves at the detector from multiple scatterers. Sometimes, scattered waves can be scattered multiple times from multiple scatterers in the field, i.e., multiple scattering, which further complicates the scattered field from a medium recorded by a detector. Therefore, theoretical modeling of the interaction of an ultrasonic source and detector with a scattering medium is complicated and inverting properties from scattered waves recorded from a detector is not always possible.

To infer properties of the underlying medium, often times simplifications of the scattering medium are assumed and approximations to the scattered field picked up by the detector are adopted. The backscatter coefficient (BSC), or differential backscattered cross section per unit volume, is one parameter that is calculated from the scattered field and is the ratio of the backscattered intensity I_{bsc} in the direction back toward the source to the incident intensity I_0 per unit volume V of the interrogated medium (Insana et al. 1990)

$$\sigma_{BSC} = \frac{R^2}{V} \frac{\langle I_{bsc} \rangle}{I_0}, \quad (2.1)$$

where R is the distance from the scattering volume to the detector. The BSC is often calculated as a function of the frequency. By fitting models to the BSC versus frequency, different features of the scattering medium can be deduced. However, most models used in estimating a theoretical BSC require several simplifying assumptions.

This chapter will focus on theoretical models of scattering with specific applications to ultrasound wave propagation in soft tissue media. The models will assume plane wave or near plane wave incidence on the scattering medium, weak scattering conditions such that multiple scattering can be neglected and weak scattering conditions such that the Born approximation holds, i.e., the total field can be replaced by the incident field driving the sources at each point in the scattering medium. With these approximations, two distinct models of the scattering medium can still hold: the scattering continuum model and the discrete scattering medium model. The continuum model posits that the scattering

medium is a spatially continuous function of changing compressibility and density, i.e., characteristic acoustic impedance. The spatial distribution of changes in acoustic impedance are random. The discrete model posits that discrete well-defined scatterers are embedded in a background medium and their spatial locations in 3D are random. Much literature has been devoted to describing in detail these two models and so the chapter will briefly highlight their implementation. The next sections will discuss the differences in these two models and the important results that come from the applications of these two models.

2.2 Continuum Scatterer Model

The continuum scattering model assumes that the medium is inhomogeneous and wave propagation in the medium is described by the inhomogeneous wave equation (Shung and Thieme 1992; Morse and Uno Ingard 1986)

$$\nabla^2 p + \frac{1}{c^2} \frac{d^2 p}{dt^2} = \nabla \bullet (\gamma_\rho(\vec{x}) \nabla p) + \gamma_\kappa(\vec{x}) \frac{1}{c^2} \frac{d^2 p}{dt^2} \quad (2.2)$$

where p is the acoustic pressure, c is the linear sound speed in the medium, ∇^2 is the Laplacian, and $\gamma_\rho(\vec{x})$ and $\gamma_\kappa(\vec{x})$ represent the fractional changes in the density and compressibility, respectively, and are given by

$$\gamma_\rho(\vec{x}) = \frac{\rho(\vec{x}) - \rho_0}{\rho(\vec{x})} \text{ and } \gamma_\kappa(\vec{x}) = \frac{\kappa_e(\vec{x}) - \kappa_0}{\kappa_0}. \quad (2.3)$$

$\gamma_\rho(\vec{x})$ incorporates the spatially dependent density variations and the compressibility scattering source $\gamma_\kappa(\vec{x})$ incorporates the spatially dependent compressibility variations. Assuming a harmonic wave, i.e., $p(\vec{x}, t) = p(\vec{x}) e^{j\omega t}$, then the inhomogeneous wave equation reduces to

$$\begin{aligned} \nabla^2 p + k^2 p &= \nabla \bullet (\gamma_\rho(\vec{x}) \nabla p) - k^2 \gamma_\kappa(\vec{x}) p \\ &= -f(\vec{r}_0). \end{aligned} \quad (2.4)$$

The inhomogeneous wave equation can be solved using Green's functions by rewriting the inhomogeneous wave equation as an integral. The Green's function $G(\vec{r} | \vec{r}_0)$ describes the observed pressure field at the detector's location \vec{r} resulting from a point source of scattering located at \vec{r}_0 . Therefore, $G(\vec{r} | \vec{r}_0)$ is a solution to the Helmholtz equation for a point source given by

$$\nabla^2 G + k^2 G = -\delta(\vec{x} - \vec{x}_0), \quad (2.5)$$

This equation is satisfied by the free space Green's function $G(\vec{x} | \vec{x}_0) = \frac{1}{4\pi |\vec{x} - \vec{x}_0|} e^{ik|\vec{x} - \vec{x}_0|}$. Combining with the Helmholtz equation defined in Eq. (2.4) provides

$$\begin{aligned} [\nabla^2 p + k^2 p] &= -f(\vec{x}_0) \\ \times [\nabla^2 G + k^2 G] &= -\delta(\vec{x} - \vec{x}_0). \end{aligned} \quad (2.6)$$

Integrating over a volume V containing the scattering sources gives

$$\begin{aligned} \int_V (G \nabla^2 p - p \nabla^2 G) dV_0 &= \int_V p \delta(\vec{x} - \vec{x}_0) dV_0 \\ &\quad - \int_V f(\vec{x}_0) G dV_0 \end{aligned} \quad (2.7)$$

It should be noted that the first integral on the right-hand side is the pressure field at the detector or the so-called total field at the detector consisting of the incident field and scattered field at that location. Rearranging the integral, using the chain rule identity, $G \nabla^2 p - p \nabla^2 G = \nabla \bullet (G \nabla p - p \nabla G)$ along with the divergence theorem gives,

$$p(\vec{x}) = \int_S (G \nabla p - p \nabla G) \bullet dS + \int_V f(\vec{x}_0) G dV_0. \quad (2.8)$$

The first term is the total field, the second term represents fields reflected by a boundary surface, S , and the final term represents the sum of the fields from scattering sources. Assuming an unbounded medium (or a medium where we can

gate out the signals from boundaries), all that is left of the second term is the incident field giving

$$\begin{aligned} p(\vec{x}) &= p_{\text{inc}}(\vec{x}) + \int_V f(\vec{x}_0) G dV_0 \\ &= p_{\text{inc}}(\vec{x}) + p_{sc}(\vec{x}). \end{aligned} \quad (2.9)$$

The scattered pressure is given by

$$p_{sc}(\vec{x}) = \int_V (\nabla \bullet (\gamma_\rho \nabla p) - k^2 \gamma_k p) G(\vec{x} | \vec{x}_0) dV_0. \quad (2.10)$$

Using the divergence theorem on the first term and noting no contribution from scattering sources on the bounded surface of V gives,

$$\begin{aligned} p_{sc}(\vec{x}) &= \int_V [k^2 \gamma_k(\vec{x}_0) p(\vec{x}_0) G(\vec{x} | \vec{x}_0) \\ &\quad + \gamma_\rho(\vec{x}) \nabla p(\vec{x}_0) \bullet G(\vec{x} | \vec{x}_0)] dV_0. \end{aligned} \quad (2.11)$$

Assuming that the scattered field is observed in the far field of the scattering sources, then the Green's function reduces to

$$\begin{aligned} G &\approx \frac{1}{4\pi \vec{x}} e^{jk|\vec{x}|} e^{-j\vec{k}_{sc} \bullet \vec{x}_0} \text{ and} \\ \nabla G &\approx -j\hat{k}_0 G \end{aligned} \quad (2.12)$$

The result of these approximations yields

$$\begin{aligned} p_{sc}(\vec{x}) &= \frac{k^2}{4\pi \vec{x}} e^{jk|\vec{x}|} \left[\int_V [\gamma_k(\vec{x}_0) p(\vec{x}_0) \right. \\ &\quad \left. - j\gamma_\rho(\vec{x}) (\nabla p(\vec{x}_0) \bullet \vec{k})] \right] \\ &\quad e^{-j\vec{k}_{sc} \bullet \vec{x}_0} dV_0 \\ &= \frac{k^2}{4\pi \vec{x}} e^{jk|\vec{x}|} \int_V F(\vec{x}_0) e^{-j\vec{k}_{sc} \bullet \vec{x}_0} dV_0. \end{aligned} \quad (2.13)$$

The integral can be interpreted as the Fourier transform of an object function, $F(\vec{x}_0)$, which is a function of the scattering sources and total pressure field. The integral term is multiplied by the field of a spherical wave from a point source. The

pressure field in the integral is the total field at the location of the scatterer. Assuming a plane wave incidence and invoking the Born approximation for weak scatterers, i.e., $p(\vec{x}_0) = p_{\text{inc}}(\vec{x}_0)$, reduces the scattered field to

$$\begin{aligned} p_{sc}(\vec{x}) &= P_0 \frac{k^2}{4\pi \vec{x}} e^{jk|\vec{x}|} \int_V (\gamma_k(\vec{x}_0) \\ &\quad + \gamma_\rho(\vec{x}_0) (\hat{i} \bullet \hat{r})) e^{-j\vec{k} \bullet \vec{x}_0} dV_0 \\ &= P_0 \frac{k^2}{4\pi \vec{x}} e^{jk|\vec{x}|} \int_V F_p(\vec{x}_0) e^{-j\vec{k} \bullet \vec{x}_0} dV_0 \end{aligned} \quad (2.14)$$

where P_0 is the pressure amplitude of the incident plane wave, $\hat{i} \bullet \hat{r} = \cos \theta$ with θ the angle between the incident direction and the observer (i.e., $\theta = 180^\circ$ is the backscatter direction), $F_p(\vec{x}_0) = \gamma_k(\vec{x}_0) + \gamma_\rho(\vec{x}_0) (\hat{i} \bullet \hat{r})$ and $\vec{k} = \vec{k}_s - \vec{k}_i$ is called the scattering vector. In the backscatter direction $\hat{i} \bullet \hat{r} = -1$ and the density and compressibility contribute equally to the scattered field. Also, for weak scattering assuming backscatter, it can be shown that

$$\gamma_k(\vec{x}_0) - \gamma_\rho(\vec{x}_0) \simeq -2 \frac{\Delta z(\vec{x}_0)}{z_0} \quad (2.15)$$

where z_0 represents the background impedance and $\Delta z(\vec{x}_0)$ is the local change in impedance from the background. Equation (2.14) then reduces to

$$p_{sc}(\vec{x}) = -P_0 \frac{k^2}{2\pi z_0 \vec{x}} e^{jk|\vec{x}|} - \int_V \Delta z(\vec{x}_0) e^{-j\vec{k} \bullet \vec{x}_0} dV_0. \quad (2.16)$$

This suggests that the scattered field in the farfield from the scatterer is directly related to the distribution of impedance in the medium.

The differential power scattered into a spherical surface spanned by $d\Omega$ at \vec{x} is

$$\begin{aligned} d\Pi &= I_s r^2 d\Omega = \frac{|p_{sc}|^2}{2\rho_0 c} r^2 d\Omega \\ &= \frac{|P_0|^2}{2\rho_0 c} \left| \frac{k^2}{2\pi z_0} \mathcal{F}T_k \{ \Delta z \} \right|^2 d\Omega. \end{aligned} \quad (2.17)$$

Therefore, the backscatter coefficient is given by

$$\sigma_b = \frac{d\Pi}{Vl_{\text{inc}}d\Omega} = \frac{1}{V} \left| \frac{k^2}{2\pi z_0} \text{FT}_k \{\Delta z\} \right|^2. \quad (2.18)$$

Assuming that Δz is a continuous random function of position in V , then the scattered field will be a superposition of the incident wave from random fluctuations in the impedance. Treating the scattering as a statistical process,

$$\sigma_b = \frac{k^4}{(2\pi z_0)^2 V} \langle \text{FT}_{k,1} \{\Delta z(\vec{x}_0)\} \text{FT}_{k,2}^* \{\Delta z(\vec{x}_0)\} \rangle, \quad (2.19)$$

where the brackets correspond to an ensemble average. This means that any single measurement of σ_b will yield an estimate that is dependent on the spatial arrangement of the impedance inhomogeneities in the sample. By averaging over independent samples (ensemble) we can estimate σ_b to within a certain precision. We can write a random process as the sum of the mean component plus the fluctuation about the mean component, $\Psi = \langle \Psi \rangle + (\Psi - \langle \Psi \rangle)$. Through some algebraic manipulation and assuming a zero mean random process, Eq. (2.19) can be rewritten as (with $\Psi = \text{FT}_k \{\Delta z(\vec{x}_0)\}$)

$$\sigma_b = \frac{k^4}{(2\pi z_0)^2 V} \langle \Psi_1 \Psi_2^* \rangle = \frac{k^4}{(2\pi z_0)^2 V} \left[\langle \Psi_1 \rangle \langle \Psi_2^* \rangle + \langle (\Psi_1 - \langle \Psi_1 \rangle)(\Psi_2^* - \langle \Psi_2^* \rangle) \rangle \right], \quad (2.20)$$

Or alternatively

$$\sigma_b = \frac{k^4}{(2\pi z_0)^2 V} \left[\begin{array}{l} \left\langle \int_V \Delta z_1 e^{-j\vec{k} \cdot \vec{x}_1} dV_1 \right\rangle \\ \left\langle \left(\int_V \Delta z_2 e^{-j\vec{k} \cdot \vec{x}_2} dV_2 \right)^* \right\rangle \\ + \left\langle \int_V \int_V (\Delta z_1 - \langle \Delta z_1 \rangle)(\Delta z_2 - \langle \Delta z_2 \rangle) e^{-j\vec{k} \cdot (\vec{x}_1 - \vec{x}_2)} dV_1 dV_2 \right\rangle \end{array} \right]. \quad (2.21)$$

Letting $\Delta \vec{x} = \vec{x}_1 - \vec{x}_2$ and noting that $\langle \Delta z_1 \rangle = \langle \Delta z_2 \rangle = \langle \Delta z \rangle$ gives

$$\sigma_b = \frac{k^4}{(2\pi z_0)^2 V} \left[\begin{array}{l} \left| \int_V \langle \Delta z(\vec{x}_0) \rangle e^{-j\vec{k} \cdot \vec{x}_0} dV_0 \right|^2 \\ + \int_V \int_V \langle (\Delta z_1 - \langle \Delta z_1 \rangle)(\Delta z_2 - \langle \Delta z_2 \rangle) \rangle e^{-j\vec{k} \cdot \Delta \vec{x}} dV_1 dV_2 \end{array} \right]. \quad (2.22)$$

The first term represents the coherent scattering term describing the average scattered field and correlation among homogeneities. For a random medium, this term is considered to have a small contribution and is neglected. The second term is the incoherent scattering and describes fluctuations of the scattered field and correlations within inhomogeneities. It is the sum of intensities of the scattered waves without the consideration of position or phase of the scatterers. Furthermore, $\text{cov} \{\Delta z_1, \Delta z_2\} = (\Delta z_1 - \langle \Delta z_1 \rangle)(\Delta z_2 - \langle \Delta z_2 \rangle)$, which results in

$$\sigma_b \simeq \frac{k^4}{(2\pi z_0)^2 V} \int_V \int_V \langle \Delta z^2 \rangle b_z(\Delta \vec{x}) e^{-j\vec{k} \cdot \Delta \vec{x}} dV_1 dV_2. \quad (2.23)$$

where $b_z(\Delta \vec{x})$ is the correlation coefficient of the medium and $\langle \Delta z^2 \rangle$ is the mean squared fluctuations in the medium impedance due to scatterers. Noting that $\Delta \vec{x} = \vec{x}_1 - \vec{x}_2$ and also making an additional change of variables such that $\vec{x}' = \frac{\vec{x}_1 + \vec{x}_2}{2}$ then after identifying $dV_1 dV_2 = d\vec{x}_1 d\vec{x}_2$, Eq. (2.23) can be shown to reduce to

$$\sigma_b \simeq \frac{k^4 \langle \Delta z^2 \rangle}{(2\pi z_0)^2} \int_V b_z(\Delta \vec{x}) e^{-j\vec{k} \cdot \Delta \vec{x}} d\Delta \vec{x}. \quad (2.24)$$

This equation indicates that the BSC is related to the 3D Fourier transform of the autocorrelation function of the medium in terms of the impedance changes due to scattering. That is, if a 3D map of impedance is known for the medium, the BSC can be calculated from the Fourier transform of the map's spatial autocorrelation function.

Assuming the scatterers are isotropic and smaller than a wavelength, i.e., the scatterers can be approximated as spherical, then we can simplify the Eq. (2.24) by expanding in spherical coordinates (Insana et al. 1990),

$$d\Delta \vec{x} = \Delta r^2 \sin \theta dr d\theta d\phi \quad \text{and} \\ \vec{K} \bullet \Delta \vec{x} = 2k\Delta r \cos \theta.$$

Therefore,

$$\sigma_b \simeq \frac{k^4 \langle \Delta z^2 \rangle}{(2\pi z_0)^2} \int_0^{2\pi} d\phi \int_0^\pi \sin \theta d\theta \int_0^\infty b_z(\Delta r) e^{-jk2k\Delta r \cos \theta} \Delta r^2 d\Delta r, \\ \sigma_b \simeq \frac{k^3 \langle \Delta z^2 \rangle}{2\pi z_0^2} \int_0^\infty b_z(\Delta r) \sin(2k\Delta r) \Delta r d\Delta r. \quad (2.25)$$

Consider the case where the medium is made up of identical fluid-filled spherical scatterers of radius a and that there are a number of these spheres per unit volume, \bar{n} . Furthermore, $\langle \Delta z^2 \rangle$ represents the mean square fluctuation in the impedance per particle times the volume fraction of scatterers. If Δz^2 equals the mean square fluctuation in acoustic impedance and the volume fraction of scatterers equals $\bar{n}V_s = \bar{n}\frac{4}{3}\pi a^3$, then $\langle \Delta z^2 \rangle = \bar{n}V_s \Delta z^2$. If the scatterers can be modeled as simple fluid-filled spheres (radius = a) then the BSC can be calculated from the autocorrelation of a sphere which is given by

$$b_z(\Delta r) = 1 - \frac{3\Delta r}{4a} + \frac{(\Delta r)^3}{16a^3} \quad \text{for } 0 \leq \Delta r \leq 2a \\ = 0 \quad \text{for } \Delta r \geq 2a \quad (2.26)$$

Then,

$$\sigma_b = \frac{k^4 V_s^2 n \bar{n} \Delta z^2}{4\pi^2} \left[\frac{3}{2ka} j_1(2ka) \right]^2. \quad (2.27)$$

where j_1 is the spherical Bessel function of the first order. Equation (2.27) represents the BSC from a volume of weak spherical scatterers. The term in brackets is called the form factor. The form factor for the fluid-filled sphere is given by

$$F(ka) = \left[\frac{3}{2ka} j_1(2ka) \right]^2. \quad (2.28)$$

Other form factors can be described by different distributions of the impedance within the sphere or by different shapes (Insana and Hall 1990). Fitting the BSC to the form factor can allow estimation of the size of the scatterers. The form factor is defined as the BSC from the scatterer divided by the BSC from a point scatterer.

2.3 Discrete Scatterer Model

In the discrete model, identifiable objects are embedded in the background. Namely, it is assumed that a harmonic plane wave of radial frequency ω is propagating through a simple fluid medium and then encounters the object at some point in space. The linear wave equation for a fluid governing the wave propagation is given by the 3D wave equation

$$\nabla^2 p = \frac{1}{c^2} \frac{\partial^2 p}{\partial t^2}. \quad (2.29)$$

where p is the acoustic pressure, c is the linear sound speed in the medium, and ∇^2 is the Laplacian. Assuming a fluid model of ultrasonic propagation, the scattered field from an object can be obtained by applying boundary conditions to the object (Anderson 1950). Specifically, at the scatterer boundary both the pressure and the normal component of the particle velocity, u , must be continuous. These boundary conditions give rise to the following equation for the pressure at the boundary (denoted by x_o):

$$p_0(x_o) + p_{sc}(x_o) = p_{int}(x_o). \quad (2.30)$$

where p_0 , p_{sc} , and p_{int} represent the incident pressure wave, the wave scattered external to the object, and the internal wave propagating inside the object, respectively. Likewise, for the normal component of the particle velocity

$$[u_0(x_o) + u_{sc}(x_o)]_\perp = u_{int}(x_o)_\perp \quad (2.31)$$

where u_0 , u_{sc} , and u_{int} correspond to the incident, scattered, and internal particle velocity at the boundary, respectively.

The goal of the ultrasonic interrogation is to quantitatively assess the properties of the scattering medium. Therefore, modeling of the scattered wave and its dependence on the scatterer properties allows relating of the detected scattered fields back to the properties of the scattering medium. Therefore, methods exist for solving the boundary condition equations to obtain p_{sc} at the boundary assuming that the incident wave, p_0 is known. However, from the boundary conditions, five unknown functions are present while only two equations exist. Therefore, to reduce the number of unknowns another equation is employed, namely the linear Euler's eq. [2.1]

$$-\nabla p = \rho \frac{\partial \vec{u}}{\partial t} \quad (2.32)$$

where ρ is the density of the medium. The linear Euler's equation is a restatement of Newton's second Law of motion for constant mass, which states that $F = ma$. By use of the linear Euler's equation, we can rewrite Eq. (2.32) in terms of the pressure. This leaves two unknown values at the boundary, p_{sc} and p_{int} , which can be solved because we have two boundary condition equations.

If the scattering object is of irregular shape and/or is made up of complicated layers, simple solutions for the set of boundary condition equations are not available. In this case, numerical solutions to the boundary equations must be considered, which makes inference of exact medium properties from the scattered field measurement difficult or impractical for real-time QUS imaging. Therefore, to solve the boundary conditions, simplifications to the object shape are required, such that solutions for the boundary conditions are readily available and easily invertible. For example, assuming that the shape of the scattering object is spherical provides simple solutions to scattering (Anderson 1950).

If the object is assumed to be spherical in shape, then natural choice is to use a Laplacian

and the del operator for spherical coordinates. This results in the normal component of the particle velocity being in the radial direction and the linear Euler's equation to simplify to

$$-\frac{\partial}{\partial r} p = j\omega\rho u_r, \quad (2.33)$$

or solving for particle velocity gives

$$u_r = -\frac{1}{j\omega\rho} \frac{\partial}{\partial r} p. \quad (2.34)$$

Furthermore, the incident harmonic plane wave can be represented in spherical harmonics with the assumption of azimuthal symmetry

$$p_0 = P_0 \sum_{m=0}^{\infty} j^m (2m+1) \widehat{P}_m(\cos\theta) \widehat{j}_m(kr) e^{j\omega t}. \quad (2.35)$$

where P_0 is the incident wave pressure amplitude, \widehat{P}_m represent the set of Legendre polynomials, \widehat{j}_m are the spherical Bessel functions, and k is the acoustic wave number. In this case, the plane wave is assumed, without loss of generality, to be propagating along the $-z$ direction toward the spherical scatterer. Choosing the plane wave direction eliminates the dependence on φ . In general, for scattering configurations with azimuthal symmetry solutions in terms of spherical harmonics are given by

$$p = \sum_{m=0}^{\infty} A_m \widehat{P}_m(\cos\theta) \left[\begin{bmatrix} \widehat{j}_m(kr) \\ \widehat{n}_m(kr) \end{bmatrix} \right] e^{j\omega t} \quad (2.36)$$

where \widehat{n}_m are the spherical Neumann functions. Expanding the scattered pressure and internal pressure in terms of spherical harmonics allows for the coefficients for the scattered wave to be solved in terms of the incident wave parameters [see (Anderson 1950) for a full description of the solution to a fluid sphere scatterer]. Assuming that the scattered wave is detected at a region of space far

removed from the scatterer, i.e., $kr \rightarrow \infty$, results in the solution to the scattered wave as

$$p_{sc} = P_0 \frac{1}{jkr} e^{j(\omega t - kr)} \sum_{m=0}^{\infty} (-1)^m (2m+1) \hat{P}_m (\cos \theta) / (1 + jC_m). \quad (2.37)$$

where C_m is a complex function of the radius of the spherical scatterer and the ratios of the densities and sound speeds in the scattering object and background, respectively. For a full description of C_m see (Anderson 1950). C_m is calculated based on the continuity relations and boundary conditions. It is given by

$$\begin{aligned} C_m &= \frac{-[\beta_m(ka)/\alpha_m(ka)]gh}{[\alpha_m(k'a)/\alpha_m(ka)][j_m(ka)/j_m(k'a)] - gh}, \\ \alpha_m(x) &= m j_{m-1}(x) - (m+1) j_{m+1}(x), \\ \beta_m(x) &= n_{m-1}(x) - (m+1) n_{m+1}(x), \end{aligned} \quad (2.38)$$

where $g = \rho'/\rho$, $h = c'/c$, ρ' and ρ are the densities of the fluid inside the sphere and the background, c' and c are the sound speed in the fluid inside the sphere and the background, j_m is the spherical Bessel function and n_m is the spherical Neumann function.

The solution is exact for a fluid sphere scatterer and is a solution for all cases of impedance mismatches and radius to wavelength ratios. If the wavelength is larger than the spherical scatterer and the impedance mismatch is small, such as would be encountered in soft tissue scattering at clinical ultrasound frequencies, then the BSC derived from Eq. (2.37) reduces to the result for the fluid sphere form factor model for the BSC derived from the previous section using the Born model. However, in this case the medium is assumed to be homogeneous except for a spherical scatterer embedded in it.

Based on this assumption, the backscattered field measured by a detector, $r(t)$, at a large

distance from the single spherical scatterer can be written in terms of a convolution (Oelze and Mamou 2016; Oelze and O'Brien Jr 2002)

$$r(t) = h(t) * d(t, \vec{x}) * a(t, \vec{x}) * t_r(t) * s(t, \vec{x}) \quad (2.39)$$

where $h(t)$ is the impulse response of the detector, $d(t, \vec{x})$ represents the spatially-varying diffraction response of the detector (i.e., the field pattern), $a(t, \vec{x})$ attenuation of the signal propagating through the medium to the detector, $t_r(t)$ represents the transmission losses from the detector to the scatterer and $s(t, \vec{x})$ is the scattering function representing the frequency-dependent backscatter from the object. Taking the magnitude-squared of the Fourier transform of the signal received from the scatterer gives

$$|R(f)|^2 = \frac{|H(f)|^2 |D(f, \vec{x})|^2 |A(f, \vec{x})|^2}{|T_r(f)|^2 |S(f, \vec{x})|^2}. \quad (2.40)$$

Relating $|S(f, \vec{x})|^2$ to the scattered intensity in Eq. (2.1) and to the scattered pressure field in Eq. (2.37) allows a direct relationship to the BSC from a fluid sphere scatterer. Essentially, if all the other parameters (H, D, A, T_r) are known or measured through a calibration, then the backscattered intensity divided by the incident intensity is estimated from Eq. (2.40). Correcting for volumetric effects associated with the physical length of the gated signal combined with the 2D cross section of the beam interrogating the region provides an estimate of the BSC. Accounting for volumetric effects is more important when multiple scatterers are within the region interrogated by the ultrasonic scanning system. In that case, assuming N identical scatterers are spatially randomly located within the interrogated volume, then

$$s(t, \vec{x}) = s_0(t-t_1, \vec{x}) + s_0(t-t_2, \vec{x}) + \dots + s_0(t-t_N, \vec{x}), \quad (2.40)$$

and the Fourier transform of this gives

$$S(f, \vec{x}) = S_0(f, \vec{x}) e^{-j2\pi f t_1} + S_0(f, \vec{x}) e^{-j2\pi f t_2} + \dots + S_0(f, \vec{x}) e^{-j2\pi f t_N}. \quad (2.41)$$

By taking the magnitude squared of the Fourier transform the following and after some algebraic manipulation it can be shown that

$$|S(f, \vec{x})|^2 = |S_0(f, \vec{x})|^2 [N+2 \sum_{n \neq m=1}^N \cos(2\pi f[t_n - t_m])]. \quad (2.42)$$

The first term on the right-hand side of Eq. (2.15) represents the incoherent scattering term and the second term represents the coherent scattering. The first term does not depend on the positions of the scatterers relative to each other and the detector but only on the number of scatterers contributing to the windowed signal. The first term is fit to models in order to extract properties of the scatterers. The second term relies on the relative positions of the scatterers with respect to each other and the detector and is most often considered noise in the process of estimating the first term.

The larger the second term the worse the estimates of scatterer properties in terms of both bias and variance. Therefore, by scanning the same region from a different orientation with the detector or by scanning an independent region in the same medium, a different realization of the second term is acquired. Such acquisitions can be compounded to reduce the effects of the second term and improve the bias and variance of scatterer property estimates coming from the first term.

The implications of the discrete model provide a reference for understanding the coherent scattering noise in the estimate of the power spectrum or BSC. Specifically, compounding increases the number of noise terms in the estimation of the power spectrum but reduces the amplitude of the noise terms. Furthermore, high-frequency noise

(i.e., large values of $t_n - t_m$) occurs from scatterers that are spaced far apart in the range gate and low-frequency coherence noise (i.e., small values of $t_n - t_m$) occurs from scatterers that are spaced close together. High-frequency noise can be averaged out by compounding independent realizations. However, low-frequency noise is not well reduced by compounding because the cos terms are slowly varying with small values of $t_n - t_m$ and so they tend to sum with compounding. In other words, when scatterers are close together, they tend to act as a single larger scatterer and so do not average out with compounding.

2.4 Concluding Remarks

The continuum model provides important insights into how the structure of the underlying scatterers leads to the scattered field and the BSC. The discrete model provides important insights into how the spatial arrangement of the scatterers results in the spectral characteristics of the BSC. Both cases indicate that the BSC consists of both an incoherent scattering and a coherent scattering component. Models for scattering that yield information regarding the properties of the underlying scatterers are contained in the incoherent scattering component and the coherent component is considered as noise to any estimation process based on the incoherent scattering component. To reduce the coherent scattering, several methods have been adopted including spatial compounding, Welch's method (Welch 1967), multitaper methods (Liu and Zagzebski 2010), and detection of coherent components and isolation of these components through selective windows (Luchies and Oelze 2015). Each of these methods reduces the spatial resolution associated with imaging or mapping of properties estimated from the BSC. Therefore, a fundamental tradeoff exists between the spatial resolution of QUS imaging based on the BSC and the bias and variance of estimates (Oelze and O'Brien Jr 2004). These tradeoffs are explored further in Chap. 4.

References

- Anderson VC (1950) Sound scattering from a fluid sphere. *J Acoust Soc Am* 22(4):426–431
- Fetter AL, Walecka JD (2003) Theoretical mechanics of particles and continua. Courier Corporation
- Insana MF, Hall TJ (1990) Parametric ultrasound imaging from backscatter coefficient measurements: image formation and interpretation. *Ultrason Imaging* 12(4):245–267
- Insana MF et al (1990) Describing small-scale structure in random media using pulse-echo ultrasound. *J Acoust Soc Am* 87(1):179–192
- Kinsler LE et al (2000) Fundamentals of acoustics. Wiley
- Liu W, Zagzebski JA (2010) Trade-offs in data acquisition and processing parameters for backscatter and scatterer size estimations. *IEEE Trans Ultrason Ferroelectr Freq Control* 57(2):340–352
- Luchies AC, Oelze ML (2015) Backscatter coefficient estimation using tapers with gaps. *Ultrason Imaging* 37(2):117–134
- Morse PMC, Uno Ingard K (1986) Theoretical acoustics. Princeton University Press
- Oelze ML, Mamou J (2016) Review of quantitative ultrasound: envelope statistics and backscatter coefficient imaging and contributions to diagnostic ultrasound. *IEEE Trans Ultrason Ferroelectr Freq Control* 63(2):336–351
- Oelze ML, O'Brien Jr WD (2002) Method of improved scatterer size estimation and application to parametric imaging using ultrasound. *J Acoust Soc Am* 112(6):3053–3063
- Oelze ML, O'Brien WD Jr (2004) Defining optimal axial and lateral resolution for estimating scatterer properties from volumes using ultrasound backscatter. *J Acoust Soc Am* 115(6):3226–3234
- Oelze ML, Sabatier JM, Raspet R (2001) Roughness characterization of porous soil with acoustic backscatter. *J Acoust Soc Am* 109(5):1826–1832
- Oelze ML, Zachary JF, O'Brien WD Jr (2002) Characterization of tissue microstructure using ultrasonic backscatter: theory and technique for optimization using a Gaussian form factor. *J Acoust Soc Am* 112(3):1202–1211
- Oelze ML, Sabatier JM, Raspet R (2003) Roughness measurements of soil surfaces by acoustic backscatter. *Soil Sci Soc Am J* 67(1):241–250
- Shung KK, Thieme GA (1992) Ultrasonic scattering in biological tissues. CRC Press
- Welch P (1967) The use of fast Fourier transform for the estimation of power spectra: a method based on time averaging over short, modified periodograms. *IEEE Trans Audio Electroacoust* 15(2):70–73



Quantitative Ultrasound: Experimental Implementation

3

Michael Oelze

Abstract

The backscatter coefficient is a fundamental property of tissues, much like the attenuation and sound speed. From the backscatter coefficient, different scatterer properties describing the underlying tissue can be used to characterize tissue state. Furthermore, because the backscatter coefficient is a fundamental property of a tissue, estimation of the backscatter coefficient should be able to be computed with system and operator independence. To accomplish system- and operator-independent estimates of the backscatter coefficient, a calibration spectrum must be obtained at the same system settings as the settings used to scan a tissue. In this chapter, we discuss three approaches to obtaining a calibration spectrum and compare the engineering tradeoffs associated with each approach. In addition, methods for reducing deterministic noise in the backscatter coefficient spectrum are considered and implementation of these techniques is discussed.

Keywords

Planar reference · Reference phantom · Calibration · Attenuation compensation · Window functions

3.1 Introduction

The backscatter coefficient (BSC) is defined as the time-averaged scattered intensity in the backward direction per unit solid angle per unit volume normalized by the time-averaged incident intensity. The BSC is a fundamental property of underlying tissues, from which microstructural properties such as shape, size, concentration, and impedance mismatch between scatterers, which make up the tissue microstructure, and the surrounding media can be estimated. This has relevance for tissue characterization and can be used for diagnosing tissue state and disease processes.

Conventional ultrasonic B-mode images are constructed from the envelope-detected, time-domain signals scattered from different tissue structures. In an ultrasonic B-mode image, the frequency-dependent information resulting from the scattering media is not utilized. By transforming the scattered signals in the frequency domain through the BSC estimation,

M. Oelze (✉)

Department of Electrical and Computer Engineering and Carle Illinois College of Medicine, University of Illinois at Urbana-Champaign, Champaign, IL, USA
e-mail: oelze@illinois.edu

the frequency dependence of the scattered signals can be related to the structural properties of the biological media. Often, statistical modeling techniques for the BSC are employed to extract sub-resolution microstructural information using ultrasound with wavelengths larger than the length scale of heterogeneity in the scattering media. Therefore, to extract microstructural features such as the average or effective scatterer size, an accurate estimation of BSC is necessary. The BSC can be used to estimate both the microstructural and acoustical properties of the tissues.

To estimate a system- and user-independent BSC, it is necessary to account for attenuation and system effects accurately. The typical steps involved to estimate BSC are shown in Fig. 3.1. A transducer sends out a broadband ultrasonic pulse, the pulse propagates into the medium, and is reflected/scattered back to the source. This results in a radio frequency (RF) signal recorded by the same transducer, which is then beamformed for lateral localization. From the signal, a B-mode image can be constructed and a region of interest (ROI) for BSC analysis can be chosen consisting of data blocks of RF signal (see Fig. 3.2 for a graphical illustration). A data block consists of

signals that are gated using a windowing function such as Hanning, rectangular, or a tapered window. Next, the power spectrum of each gated signal is estimated using the magnitude squared of the Fourier transform of the gated signal and is averaged from different scan lines in a data block to estimate the average power spectrum. The average power spectrum is then compensated for attenuation and diffraction effects to yield an estimate of the BSC. Therefore, ideally, the BSC is a system-independent quantity that can be used to characterize soft tissue.

The main challenge in BSC estimation is to compensate for diffraction and attenuation effects accurately. Various researchers have developed analytical and numerical methods to accurately compensate for attenuation and diffraction effects. In this chapter, we will discuss current approaches for calibration of the ultrasonic scanning system to produce system- and user-independent BSCs. Currently, there are four methods in use for calibrating an ultrasonic scanning system for BSC estimation: (1) planar reflector technique (Lizzi et al. 1983; Insana et al. 1990), (2) the reference phantom technique (Yao et al. 1990), (3) the in-situ calibration approach (Nguyen et al. 2019;

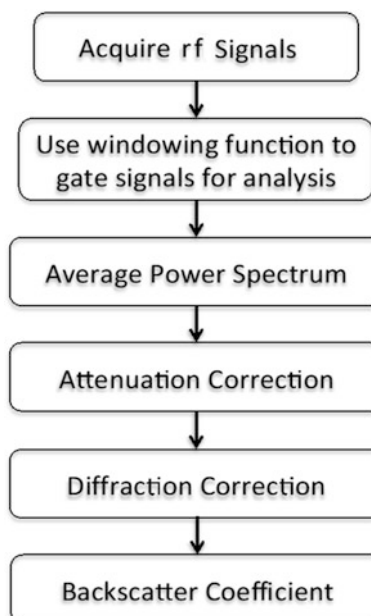


Fig. 3.1 Flowchart for estimating BSC

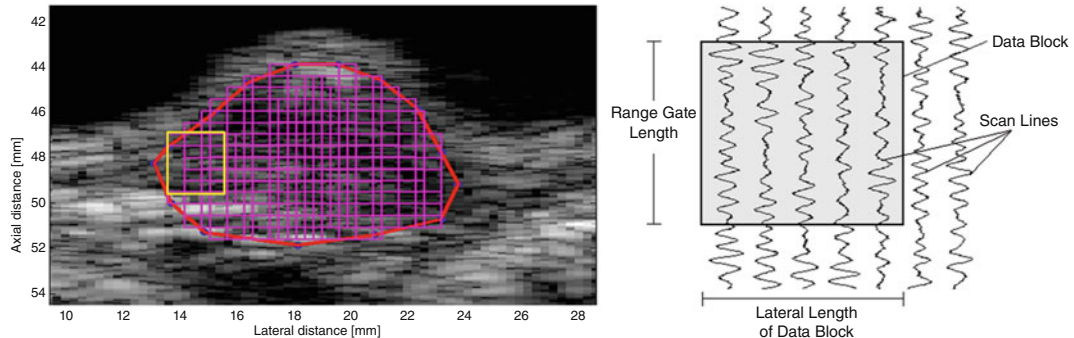


Fig. 3.2 (left) Image from a tumor with ROI outlined and the ROI broken up into overlapping data blocks. The yellow block represents the size of one data block. (right)

A descriptive view of the data block used for estimating the average BSC

Cario et al. 2022) and (4) a reference-free approach.

3.2 The Measurement Terms

Assuming a pulse-echo system, the measurement from a scattering source can be represented by a set of convolutions (Oelze and O'Brien Jr. 2002a, b; Oelze and Mamou 2016),

$$r(t) = h_t(t) * d_t(t, \vec{x}) * a(t, \vec{x}) * tr(t) * s(t, \vec{x}) * d_r(t, \vec{x}) * h_r(t) \quad (3.1)$$

where the t, r subscripts represent the transmit and receive functions, respectively, $h(t)$ is the impulse response function of the transmitter/receiver pair, $d_t(t, \vec{x}), d_r(t, \vec{x})$ are the transmit and receive diffraction patterns, $a(t, \vec{x})$ is the total frequency-dependent attenuation, $tr(t)$ is the total transmission loss due to transmission and reflection at tissue layer boundaries, and $s(t, \vec{x})$ is the scattering function that describes how the ultrasound pulse is modified by the scatterer(s). Taking the magnitude squared of the received signal and grouping the transmit and receive terms for the impulse response and diffraction term together gives

$$|R(f)|^2 = |H_{t,r}(f)|^2 |D_{t,r}(f, \vec{x})|^2 |A(f, \vec{x})|^2 \\ |Tr(f)|^2 |S(f, \vec{x})|^2. \quad (3.2)$$

The BSC comes directly from the $|S(f, \vec{x})|^2$ term. However, in order to extract $|S(f, \vec{x})|^2$ from the measured signal, the other terms must be taken into account either through measurement or approximation. In some applications, the frequency-dependent attenuation $|A(f, \vec{x})|^2$ is also sought for its ability to classify tissues. In order for the BSC to be system- and user-independent estimate over a particular frequency bandwidth, it is necessary to calibrate the system to account for the $|H_{t,r}(f)|^2$ and $|D_{t,r}(f, \vec{x})|^2$ terms. The attenuation and transmission loss terms require either estimation from the medium or approximation based on assumed values. Subsequent sections will provide actual BSC estimates using different reference methods.

3.3 Attenuation Compensation

Attenuation correction is a major step to estimate BSC accurately as shown in Fig. 3.1. Extensive research has been conducted to develop robust attenuation correction functions. Point attenuation compensation can be used for short-gated segments and low attenuation coefficients given by (Oelze and O'Brien Jr. 2002a, b)

$$|A(f, z)|^2 = e^{4 \int_0^{z_T} \alpha_T(f, z) dz + 2\alpha(f)L}, \quad (3.3)$$

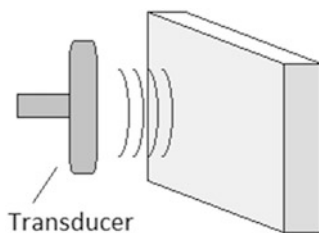


Fig. 3.3 Illustration of the planar reflector technique. The transducer is on the left and emits ultrasound, which is normally incident on the smooth plate. The ultrasound is reflected back towards the transducer and recorded

where z_T is the distance between the source and the gated region, L is the length of the gated region, and $\alpha_T(f, z)$, $\alpha(f)$ are the frequency-dependent attenuation coefficients in Np/cm for the intervening medium and over the gated region, respectively. Specifically, the first term accounts for the round-trip frequency-dependent attenuation losses between the gated region and the source. The attenuation over the gated region is assumed to be constant.

O'Donnell and Miller (1981) used similar approximation of small gate length and low attenuation to derive an attenuation compensation function given by

$$|A_{OM}(f, z)|^2 = \exp \left\{ 4 \int_0^{z_T} \alpha_T(f, z) dz \right\} \left[\frac{4\alpha(f)L}{1 - e^{-4\alpha(f)L}} \right] \quad (3.4)$$

The above attenuation compensation function is derived using a rectangular gating function. The term in the square bracket accounts for frequency-dependent attenuation losses over the gated region.

Oelze and O'Brien Jr. (2002a, b) derived another attenuation compensation function given by

$$|A_{OO}(f, z)|^2 = \exp \left\{ 4 \int_0^{z_T} \alpha_T(f, z) dz \right\} \left[\frac{2\alpha(f)L}{1 - e^{-2\alpha(f)L}} \right]^2. \quad (3.5)$$

The approach of Oelze and O'Brien Jr. (2002a, b) provided better performance than the O'Donnell and Miller (1981) model for $\alpha L < 1$ to estimate the normalized backscatter power spectra. The authors also derived the attenuation

compensation function for a Hanning window given by (Oelze and O'Brien Jr. 2002a, b)

$$|A_{OO}^{\text{Han}}(f, z)|^2 = |A_{OO}(f, z)|^2 \left[1 + \left(\frac{\alpha(f)L}{\pi} \right)^2 \right]^2. \quad (3.6)$$

Bigelow and O'Brien Jr. (2004) derived an attenuation compensation function by coupling the windowing function, beam pattern, and attenuation coefficients. The authors used a single-order Gaussian function to model the transducer beam pattern in the focal region. The attenuation compensation function is given by

$$\begin{aligned} |A_{OB}(f, z)|^2 \\ = \exp \left\{ 4 \int_0^{z_T} \alpha_T(f, z) dz \right\} \\ \left[\int_{-L/2}^{L/2} g_{\text{win}}(z) \exp \left(-4 \frac{z^2}{w_z^2} + 4\alpha(f)z \right) \right]^{-1} \end{aligned} \quad (3.7)$$

where $g_{\text{win}}(z)$ is the windowing function and w_z is the width of the Gaussian beam in the focal region.

Researchers have also developed a technique to estimate BSC and attenuation slopes using the least square method (Nam et al. (2011a)). The authors used a power law model for BSCs and developed a three-parameter model to incorporate backscatter and attenuation coefficients. Then a least square technique was employed to estimate backscatter and attenuation coefficients simultaneously. The authors used a glass bead phantom to compare theoretical and experimental results.

3.4 Calibration Approaches

3.4.1 Planar Reference

One of the earliest methods for calibrating a system for estimation of the BSC was the planar reflector technique. In the planar reflector technique, a smooth plate of material with known acoustic properties is used to reflect the signal from the transducer used to estimate the BSC from a sample. The transducer is aligned so that

the ultrasound is normally incident on the plate and it is assumed that ultrasound is reflected back to the transducer with all frequencies reflected back at the same magnitude. The magnitude of the reflection depends on the impedance mismatch between the planar reflector and the propagation medium, usually assumed to be water. Figure 3.3 shows an illustration of the planar reflector technique.

Based on the formalism adapted from Eq. (3.1), the signal recorded from a planar reflector can be described as,

$$r_{\text{ref}}(t) = h_t(t) * d_t(t, \vec{x}) * s_{\text{re}}(t, \vec{x}) * d_r(t, \vec{x}) * h_r(t), \quad (3.8)$$

where $s_{\text{re}}(t, \vec{x}) = \gamma \delta(\vec{x} - \vec{x}_0)$ is the signal reflected from a planar reflector located at \vec{x}_0 with a reflectivity of γ . This assumes that the propagation medium has negligible attenuation, as would be the case for water at clinical ultrasound frequencies. Taking the magnitude squared of the Fourier transform of the received signal yields

$$|R_{\text{ref}}(f)|^2 = \gamma^2 |H_{t,r}(f)|^2 |D_{t,r}(f, \vec{x})|^2. \quad (3.9)$$

Rearranging the terms,

$$|H_{t,r}(f)|^2 |D_{t,r}(f, \vec{x})|^2 = \frac{|R_{\text{ref}}(f)|^2}{\gamma^2}. \quad (3.10)$$

Substituting into Eq. (3.2) provides,

$$|R(f)|^2 = \frac{|R_{\text{ref}}(f)|^2}{\gamma^2} |A(f, \vec{x})|^2 |Tr(f)|^2 |S(f, \vec{x})|^2. \quad (3.11)$$

or after rearranging,

$$|S(f, \vec{x})|^2 = \frac{\gamma^2 |R(f)|^2}{|A(f, \vec{x})|^2 |Tr(f)|^2 |R_{\text{ref}}(f)|^2}. \quad (3.12)$$

This provides the normalized backscattering spectrum using the planar reflector method for calibrating a system to BSC estimation. However,

Eq. (3.12) does not account for volumetric scattering effects, which is required for BSC estimation and depends on the transducer properties.

Several studies have developed techniques using the planar reflector technique for estimating the BSC and accounting for volumetric scattering effects. The planar reflector technique is the oldest of the techniques used for estimating BSCs. Sigelmann and Reid (1973) developed the method of estimating backscatter power from a volume of randomly distributed scatterers using a single-element planar transducer. The authors used a substitution method where the backscatter signal from a sample and planar rigid reflector were compared to estimate “volumetric backscattering cross-section.” Bamber et al. (1979) used a cylindrical tissue sample positioned with its long axis normal to the sound propagation path and recorded backscatter signal at different angle using a planar transducer that acted both as a source and receiver. The expression for estimating backscatter cross-section from the cylindrical tissue sample is given by (Sigelmann and Reid 1973; Bamber et al. 1979)

$$\sigma_b(f_0) = \frac{4\alpha\xi}{\Omega \exp(-4\alpha)[\exp(c\tau\alpha) - \exp(-c\tau\alpha)]} \frac{W_s}{W_R} \quad (3.13)$$

where α is the frequency-dependent attenuation coefficient, r is the radius of the tissue cylinder, c is the speed of sound in the tissue, τ is the duration of the time gate, Ω is the solid angle subtended by the transducer face at the center of the specimen, W_s and W_R are the measured power scattered from the tissue and the total power returned by a plane reflector and ξ is the reflection coefficient of the plane reflector. Note that the measurement occurs at a single frequency by taking the power of the RF signal without conversion to the frequency domain.

Nicholas et al. (1982) used the substitution method to derive the BSC given by

$$\sigma_b(f) = \frac{2\alpha}{\exp(-2\alpha z_1)[1 - \exp(c\tau\alpha)]} \frac{\frac{2\eta R^2}{\beta^2 A} \left[\frac{\lambda_0}{\lambda} \right]^2 \frac{W_r}{W_i}}{\frac{2\eta R^2}{\beta^2 A} \left[\frac{\lambda_0}{\lambda} \right]^2 \frac{W_r}{W_i}} \quad (3.14)$$

where W_r is the total power received at the transducer face due to scattering, W_i is the total power received from a planar reflector, η is the intensity reflection coefficient for the reference interface, β is the intensity transmission coefficient for the water/tissue interface, τ is the gate duration, c is the sound speed in the tissue, R is the distance from the transducer face to the gated volume, and z_1 is the distance from the surface of the tissue to the beginning of the gated region. The technique could provide BSCs versus frequency, but no analysis using spectral analysis was conducted.

Lizzi et al. (1983) were credited with developing a theoretical framework for spectrum analysis using BSCs for ultrasonic tissue characterization. Based on this work, D'Astous and Foster (1986) developed a method of computing BSCs for focused transducers assuming a plane wave approximation at the focus. The BSC may be written as

$$\sigma_b(f) = \frac{R_q}{2\pi(1 - \cos\theta_T)\Delta z} \frac{|S'(f)|^2}{|S'_0(f)|^2} \quad (3.15)$$

where R_q is the intensity reflectance of the water reflector interface, θ_T is the half angle of the transducer subtended at its focus, $S'(f)$ is the energy spectrum of the gated, attenuation-corrected signal, $S'_0(f)$ is the Fourier transform of the reference echo signal measured using a planar surface, and Δz is the axial length of the range-gated volume.

Ueda and Ozawa (1985) derived the reference power spectrum using the boundary integral wave equation under the first-order Born approximation. An approximate closed-form solution for estimating BSC assuming a Gaussian profile for the transducer radiation pattern was proposed and developed by the authors and is given by

$$\sigma_b^{\text{Gaussian}}(f) = 1.9964 \frac{(G_p/2)^2}{1 + (G_p/2) A_0 \Delta z} \frac{\gamma^2 R_1^2}{A_0 \Delta z} |S(f)|^2 \quad (3.16)$$

where f is the frequency, A_0 is the aperture area of the transducer, Δz is the axial length of the range-gated volume, R_1 is the on-axis distance between the transducer and the proximal surface of the gated volume, γ is the pressure reflection coefficient of the planar reflector, $G_p = kr^2/2R_1$ is the pressure focusing gain of the transducer (Chen et al. 1993a, 1994), and a is the radius of the transducer. The power spectra is defined by

$$|S(f)|^2 = \frac{\langle |S_m(f)|^2 \rangle}{|S_0(f)|^2} \exp\{-4(\alpha_m - \alpha_0)(R_1 + \Delta z/2)\} \quad (3.17)$$

where $S_m(f)$ is the Fourier transform of the sample echo signal, $S_0(f)$ is the Fourier transform of the reference echo signal measured using a planar surface, and $\langle |S_m(f)|^2 \rangle$ is the average of the power spectra of several adjacent, gated scan lines $s_m(t)$. The attenuation coefficients for the sample and the reference media are denoted by α_m and α_0 respectively. The authors also derived the backscatter from circular piston transducer given by

$$\sigma_b(f) = 1.9964 \frac{L(ka, kR_1)}{0.919} \frac{(G_p/2)^2}{1 + (G_p/2) A_0 \Delta z} \frac{\gamma^2 R_1^2}{A_0 \Delta z} |S(f)|^2 \quad (3.18)$$

where $L(ka, kR_1)$ is a frequency-dependent correction factor, which can be calculated numerically for respective transducer characteristics (Ueda and Ozawa 1985).

Insana and co-workers (Insana and Hall 1990; Insana et al. 1990) used a volumetric integral wave equation derived under the first-order Born approximation to estimate the power spectrum of both weakly scattering random media and the planar reflector. From this approach, the BSC can be estimated using

$$\sigma_b^{\text{Hann}}(f) = 0.3625 \frac{\gamma^2 R_1^2}{A_0 \Delta z} |S(f)|^2 \quad (3.19)$$

Equation 3.19 was derived assuming a Hanning window to gate the radiofrequency data.

Researchers determined the theoretical reference power spectrum using the mirror image method assuming a perfectly reflecting plate and derived the BSC using (Chen et al. 1994, 1997)

$$\sigma_b(f) = 2.17 \frac{\nu^2 R_i^2}{A_0 \Delta z} \left\{ \left| \exp(-jG_p) [J_0(G_p) + jJ_1(G_p)] - 1 \right| \right\} \frac{|S(f)|^2}{(3.20)}$$

where J_m is the m th order Bessel function, and $|S(f)|^2$ is given in Eq. 3.17.

These represent different methodologies used to develop the planar reflector technique for calculating the BSC from the scattering samples. The planar reflector technique requires large f-number focusing transducers, i.e., weakly focused sources, and is more difficult to implement for transducer arrays. The planar reflector technique does not account for attenuation or transmission losses in the sample and the typical water path can lead to high nonlinear distortion of waveforms that can affect the estimation of BSCs and attenuation (Coila and Oelze 2019, 2020).

3.4.2 Reference Phantom

In the reference phantom technique, a well-characterized reference material with known attenuation and BSC is used to obtain a calibration spectrum. Figure 3.4 shows an illustration of the reference phantom technique. A transducer is used to propagate ultrasound into a phantom and the ultrasound scattered from the phantom is recorded by the transducer. The same system settings used in the sample are used to scan the reference phantom. The reference phantom is well-characterized so that the BSC and attenuation are known for the phantom.

The reference phantom technique for BSC estimation was first proposed by Yao et al. (1990). The BSC from a sample using the reference phan-

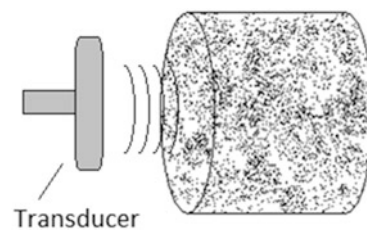


Fig. 3.4 Illustration of the reference phantom technique. The transducer is on the left and emits ultrasound, which propagates into the phantom and scatters ultrasound back to the transducer

tom technique is given by

$$\sigma_b^s(f) = \sigma_b^{\text{RPM}}(f) e^{-4z[\alpha_{\text{RPM}}(f) - \alpha_s(f)]} \frac{|S_s(f)|^2}{|S_{\text{RPM}}(f)|^2} \quad (3.21)$$

where z is the depth, $\sigma_b^s(f)$ and $\alpha_s(f)$ are the BSC and attenuation coefficients of the sample, respectively. Similarly, $\sigma_b^{\text{RPM}}(f)$ and $\alpha_{\text{RPM}}(f)$ are the known BSC and attenuation coefficients of the reference material, respectively. The averaged power spectrum from the sample and the reference phantom are denoted by $S_s(f)$ and $S_{\text{RPM}}(f)$, respectively. The data acquired from the sample and reference phantom are presumed to come from the same range depth using the same system settings. This technique is applicable for any transducer geometry such as single-element focused/unfocused transducers and array systems. The reference phantom technique also allows for multiple transmission approaches to be used including coherent plane-wave compounding (Garcia-Duitama et al. 2015).

The BSC for the reference material, $\sigma_b^{\text{RPM}}(f)$, is usually estimated by taking backscatter measurements from the reference material and calibrating with a reference planar technique. Furthermore, the BSC is often calculated for the reference phantom by using multiple single-element transducers to span a larger frequency range. The reference material should

be homogeneous in its scattering properties and the frequency-dependent transmission effects of any acoustic scan window over the phantom material should be taken into account. The BSC estimate is taken from a large number of scan lines to produce a smoothed BSC estimate through ensemble averaging. Smoothing the reference BSC improves the variance of the sample estimate.

Similarly, the estimate of the power spectrum from the reference material, $S_{\text{RPM}}(f)$, should be estimated from a large number of scan lines. This will allow ensemble averaging of the different spectral estimates resulting in a smoother power spectrum estimate. Lack of averaging will result in a larger variance of the estimate of the BSC from a sample because the reference spectrum, $S_{\text{RPM}}(f)$, is noisy. However, because the reference material is not being mapped or imaged, there is no loss of spatial resolution when averaging a larger number of scan lines and multiple planes of a phantom can be used to get a smooth estimate of $S_{\text{RPM}}(f)$. While the reference phantom method allows a larger range of sources and focusing parameters to be used, the reference phantom method does add additional variance to the estimates of BSC because of the variance inherent in the estimate of $S_{\text{RPM}}(f)$.

3.4.3 In Situ Calibration

A more recent approach to calibration is to find and use a target inside the sample to be interrogated as a calibration source (Nguyen et al. 2019; Cario et al. 2022). In this instance, the in-situ calibration target provides the reference signal during the scan of the sample. The approach can be used with all types of sources, i.e., single-element transducers and arrays. The approach has the advantage that it also accounts for transmission and attenuation losses down to the level of the calibration target, reducing bias and error that results from either guessing the losses or estimating them separately with an attenuation estimation algorithm, which are known to have large variances.

The calibration target could be a known structure in the sample or it could be a target embedded

in the sample. One clinical application would be radiological clips that are often inserted into tumors, lymph nodes, and surrounding tissues for keeping track of the tissues during and after therapy. Ideally, the calibration target should have a shape that does not change when the orientation of scattering with respect to the source changes, i.e., a sphere. Other shapes, like a cylinder or ellipse, would have different backscatter versus frequency depending on the orientation of the target with the source. Therefore, spherical targets or small beads embedded in tissue represent the ideal calibration target.

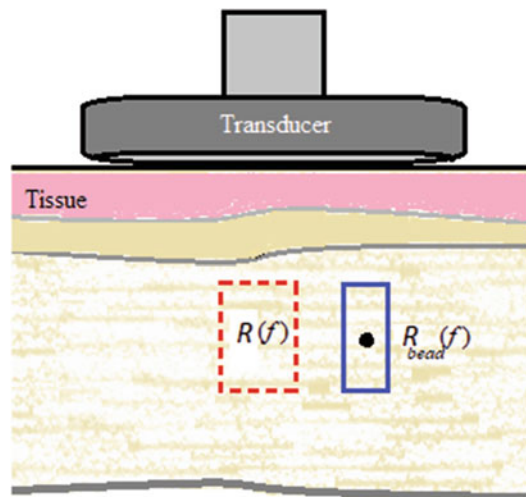
For an in situ calibration approach using a single spherical bead, several assumptions are imposed. First, it is assumed that the signal, i.e., scattered intensity, from the calibration bead is much larger than the signal from soft tissues. Assuming the bead is made out of metal, e.g., titanium or gold, then the signal from the bead should be much larger than the signal from the tissue. Second, the bead is large enough to be used as a radiological clip but small enough for scanning with ultrasound. In experiments, it was observed that beads of 2-mm diameter and larger were good candidates for an in-situ calibration target. Even if the bead is larger than a wavelength or beamwidth, consistent spectra from the beads can be obtained. Third, transmission and attenuation losses to the bead location in the tissue are close to transmission and attenuation losses encountered at a similar depth in the tissue not containing the bead.

Figure 3.5 illustrates how the in-situ calibration bead works in practice. The power spectrum from the bead is first acquired and then a power spectrum from a data block near the same depth as the bead in the sample is acquired. Under the three assumptions stated above, the power spectrum from the bead is

$$|R_{\text{bead}}(f, x)|^2 \approx |T_r(f, x)|^2 |A(f, x)|^2 |D(f, x)|^2 \\ |H(f)|^2 |S_{\text{bead}}(f, x)|^2 \quad (3.22)$$

where $S_{\text{bead}}(f, x)$ is the scattering function from the calibration bead. Therefore, dividing Eq. (3.2) by (3.22) results in a cancellation of the attenua-

Fig. 3.5 Illustration of the in-situ calibration technique. The transducer is on the top and emits ultrasound, which propagates into the sample and scatters ultrasound back to the transducer from the sample and from the bead embedded in the sample. Losses to the data block are similar to losses encountered by the bead



tion term, the transmission loss term, diffraction term, and the impulse response,

$$\frac{|R(f, x)|^2}{|R_{\text{bead}}(f, x)|^2} = \frac{|S(f, x)|^2}{|S_{\text{bead}}(f, x)|^2}. \quad (3.23)$$

Solving for $S(f, x)$ gives

$$|S(f, x)|^2 = \left| \frac{R(f, x)}{R_{\text{bead}}(f, x)} \right|^2 |S_{\text{bead}}(f, x)|^2. \quad (3.24)$$

Or alternatively

$$\sigma_{\text{bsc}}(f, x) = \left| \frac{R(f, x)}{R_{\text{bead}}(f, x)} \right|^2 \sigma_{\text{bsc}}^{\text{bead}}(f, x). \quad (3.25)$$

By estimating the power spectrum from the bead in the sample and utilizing the known BSC from the bead, the BSC from the sample can be estimated. The known BSC from the bead can be calculated using a planar reference technique to compare the ultrasonic signals from a transducer over a chosen frequency range to the signals scattered from the calibration bead. Losses in the signals due to attenuation and transmission losses are approximately taken into account because the calibration bead would face the same losses as the sample around it, at least to its depth. At different depths, the attenuation can still be compensated

based on the estimated attenuation in the sample. The in-situ calibration approach is the only approach that can account for all losses to the bead depth when estimating the BSC. However, there are limited clinical applications where placing a small bead as a calibration target is feasible. The in-situ calibration technique also allows for multiple transmission approaches to be used including coherent plane-wave compounding.

3.4.4 Reference Free

An alternative approach, which does not require a calibration signal, is the reference-free method for estimating tissue state based on the RF backscattered signal (Nguyen et al. 2018, 2021; Nguyen and Oelze 2019; Han et al. 2020). In a reference-free approach to QUS, the BSC is not actually calculated. Rather a machine/deep learning approach is used to separate the tissue signal from the system signal in order to characterize the tissue state. Essentially, the same system and system settings are used to acquire a large amount of sample data with labels. The RF signals from the data are fed into a learning approach, such as a convolutional neural network (CNN). The CNN learns the tissue signals corresponding to different tissue states. Then, when scanning a tissue sample with unknown state, the CNN can predict the state

of the tissue based on the learned data. In this approach, no separate reference scan is required because the CNN would differentiate between the tissue signal and the system signal. However, this approach requires that the same system is used over and over again with the same system settings. Departure from the system settings would change the system signal and throw off the CNN (Soylu and Oelze 2023a, b). Furthermore, the CNN is trained only on a set of tissue disease states. Tissue states that have not been observed by the training data may not provide accurate prediction of the tissue state. Finally, the training of a CNN would require a large amount of data to provide good classification accuracy.

3.5 Windowing Functions

The use of different windowing functions and gate lengths may lead to different BSC estimates due to windowing effects and spatial variation of the tissue microstructure. Spatially, tissue microstructure consists of various length scales. Therefore, the results of BSC estimates from larger data blocks may not yield similar scatterer properties as compared to smaller data blocks. For tissues with a higher degree of spatial variation in the microstructure, larger data blocks will result in estimating average properties of the varied microstructure. Therefore, smaller data blocks are often beneficial to better resolve regions of distinct tissue microstructure. By selecting smaller data blocks, the effects of spatial variation of tissue microstructure are smaller than for larger data blocks. If the gate length used is too small compared to the incidence pulse then a bias in the estimate is introduced (Oelze and O'Brian Jr. 2004; Huisman and Thijssen 1996). Higher axial resolution can be achieved with a smaller data block size, but there exists a trade-off between the block size and accurate estimation of scatterer properties.

Various studies have been conducted to examine the effects of data block size and windowing function on the bias and variance of the scatterer property estimates based on the BSC. Chen et al. (1993b) showed that the gate length less than

5 times the wavelength at a center frequency of the input wave resulted in inaccurate estimation of scatterer properties without respect of the gating window type used. Usually, with longer gate length the theoretical model fits the experimental data with less mean square error. A Hanning window with length greater than 12.5 times the incident pulse length resulted in a better fit to the experimental power spectrum. Typically, the data block size cannot be smaller than the spatial pulse length (SPL) of the input wave. Studies have also shown larger data block size compared to SPL reduces the contribution from the coherent scattering improving the accuracy and variance of the scatterer property estimates (Madsen et al. 1984; Insana et al. 1986). With axial ROI size comparable to the SPL the effects of the input pulse need to be incorporated (Ueda and Ozawa 1985). Akita and Ueda (1988) used deconvolution methods to account for gate edge truncation error which worked only for limited cases. Therefore, if the effects due to the truncation of the signals can be accounted, then improved axial resolution can be achieved.

In another study, the optimal data block size of 4–5 beamwidths laterally and 15–20 SPL axially was suggested to predict scatterer properties within 10% accuracy (Oelze and O'Brian Jr. 2004). Using lateral length of data blocks to 5 beamwidths, the spatial variation of the noise was reduced by 1/e by averaging backscattered power spectra from individual A-lines. Here A-line is referred to an individual time domain signal. Therefore, large numbers of A-lines should be acquired to have large size data blocks in the lateral directions. Also, it should be noted that spacing between any adjacent A-lines should be large enough to have independent signals.

The choice of the windowing function affects the bias and variance of the BSC estimate and scatterer property estimates coming from the BSC. Specifically, a simple rectangular windowing function provides lower variance of BSC estimates compared to a Hanning window of the same length. This occurs because a tapered windowing function, like the Hanning window, reduces the effective length of the data segment because of the tapering at the edges of the window

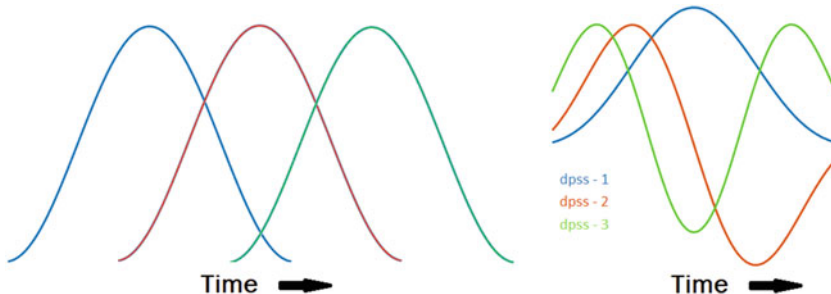


Fig. 3.6 (Left) Illustration of the Welch's method sequence using overlapping Hanning windows to range gate out the ultrasonic signal and compound the resulting power spectra for smoothing. (Right) Illustration of a

dpss (first three windows) that is used to range gate out the ultrasonic signal and subsequent compounding of the power spectra for smoothing

reducing the contribution of data at the edges. However, the bias introduced by the rectangular window is increased due to the sharp edge of the rectangular window resulting in ringing in the spectrum and BSC estimate, i.e., the Gibbs phenomenon. Other windowing functions, such as the Tukey-cosine window, provide a tradeoff between the bias and variance of estimates by allowing the tuning of the window between a rectangular to a Hanning window.

The Welch's technique can also be used to improve the bias and variance of BSC estimates and associated scatterer properties (Welch 1967). Figure 3.6 shows an illustration of the Welch's technique. In the Welch's technique, the axial extent of the data block is broken into overlapping Hanning windows and the spectra from each overlapping window are averaged together to provide a smoothed BSC (Liu et al. 2006). The smoother power spectra, i.e., BSC estimate, resulted in estimates of effective scatterer size with better accuracy. Liu and Zagzebski (2010) investigated the effects of various windowing functions such as rectangular, Hanning, Hamming, and Welch's technique. The authors suggested that Welch's technique yielded more accurate BSCs compared to other windowing functions. The authors also provided recommendation on the size of the region of interest to estimate BSCs accurately under various conditions. Ghoshal and Oelze (2010) combined gate edge correction factor and Welch's technique to improve scatterer property estimates using short gate lengths to improve

biases introduced by small gate lengths. Finally, Liu and Zagzebski used a multitaper method to reduce the coherence noise in the estimate of the BSC. The multitaper method makes use of multiple time windows, e.g., discrete prolate spherical sequences (dpss), applied to the same data segments. These windows are orthogonal and provide pseudo-independent estimates of the BSC that can be averaged together to smooth the BSC estimate from a time segment. Figure 3.6 also provides a graph of the dpss sequences used in the multitaper method.

3.6 Conclusion

The obvious step to translate ultrasound tissue characterization techniques based on the BSC to the clinics is to test the feasibility of estimated parameters to be reproducible across different transducers and systems. Several studies have been conducted to compare BSC-based parameters by different systems and users from the same sample. Ten laboratories participated in an interlaboratory study to estimate BSCs from tissue-mimicking phantoms using individual laboratory systems, operators, and techniques (Madsen et al. 1999). The final conclusion of the early study resulted in considerable differences in BSC estimates between laboratories, which may be related to the accuracy of the techniques used by each group. A better agreement was observed in a subsequent interlaboratory study to compare BSCs from tissue-mimicking phantoms (Wear et

al. 2005). In this study, the estimated BSCs were compared with theoretical values. The theoretical BSCs were calculated using Born approximation and the properties of the phantoms. The American Institute of Ultrasound in Medicine (AIUM) sponsored both studies (Madsen et al. 1999; Wear et al. 2005). Another interlaboratory study of BSCs from tissue-mimicking phantoms where glass beads were used as scatterers was conducted between two laboratories (Anderson et al. 2010). The main aim was to investigate the interlaboratory comparison of Faran's theoretical model (Faran 1951) to predict BSCs in the frequency range 1–12 MHz from glass spheres embedded in a uniform agar-based background. The study resulted in good agreement between the two laboratory results and the theoretical model except for one tissue-mimicking phantom (Anderson et al. 2010). Further interlaboratory comparison of BSCs from tissue-mimicking phantoms with glass beads as scatterers were conducted using four different clinical array-based imaging systems (Nam et al. 2011b, 2012).

Interlaboratory studies to estimate BSC from in vivo spontaneous rat mammary tumors (fibroadenoma and carcinoma) acquired by different research groups using three clinical array systems and a single-element laboratory scanner system were conducted (Wirtzfeld et al. 2010). The results were encouraging from this first in vivo study to compare quantitative ultrasound parameter estimates by different laboratories and systems scanning the same tumor in vivo. Better agreement in BSCs was observed from in vivo spontaneous rat mammary tumors in the second joint study by the same group of laboratories (Wirtzfeld et al. 2013). In this study, the researchers used functional ANOVA to compare the frequency dependence of the BSCs across different systems (Wirtzfeld et al. 2013).

Ultrasonic BSC is a fundamental system-independent material quantity that can be used to characterize tissues and monitor and assess therapies. Researchers have used BSCs to characterize different organs/tissues of the body, and published results from various mammalian tissues are available for reference at both in

vitro and in vivo experimental configurations. For the quantitative ultrasound technique to be successful, the BSC is one of the major parameters that needs to be estimated accurately. This is due to the fact that BSCs can be used to infer microstructural parameters such as correlation length and scattering strength. Often correlation length can be related to the cell size as various researchers hypothesized cells as the dominating scattering component in tissue. The scattering strength can be related to the acoustical properties of the tissue.

Due to the importance of estimating system and user-independent BSC accurately, a large amount of research has been conducted to compensate for system effects and attenuation effects. Some of the analytical models developed by various researchers are explained briefly in this chapter. Over the years, authors developed models to predict BSCs accurately based on their experimental configurations. Lavarello et al. (2011) recently showed a comparison of using three different techniques to estimate BSCs from glass bead phantoms using multiple transducers with a wide range of f-numbers and frequency bandwidths. The authors showed different estimation methods introduced varying frequency-dependent effects, which could have noticeable effects to estimate other parameters such as correlation length and scattering strength from BSCs.

Depending on the application, particular methods to estimate BSC may be more appropriate based on experimental configuration and tissue types. We hypothesize that coupling attenuation and diffraction effects in an integral form (Bigelow and O'Brien Jr. 2004) may be used to estimate BSC accurately. In every model, there are certain assumptions and limitations. The reference phantom technique (Yao et al. 1990) is a very powerful technique because modeling of the diffraction pattern of the beam is not required. The evidence of vast experimental and theoretical investigations conducted to estimate BSC to infer tissue properties suggests that it may be used for diagnostic and therapeutic applications.

References

- Akita M, Ueda (1988) The effect of windowing on spectral estimation of echoes by a random medium. *J Acoust Soc Am* 83:1243–1248
- Anderson JJ, Herd MT, King MR, Haak A, Hafez ZT, Song J, Oelze ML, Madsen EL, Zagzebski JA, O'Brien WD Jr, Hall TJ (2010) Interlaboratory comparison of BSC estimates for tissue-mimicking phantoms. *Ultrasound Imaging* 32(1):48–64
- Bamber JC, Hill CR, King JA, Dunn F (1979) Ultrasonic propagation through fixed and unfixed tissues. *Ultrasound Med Biol* 5:159–165
- Bigelow TA, O'Brien WD Jr (2004) Scatterer size estimation in pulse-echo ultrasound using focused sources: theoretical approximations and simulation analysis. *J Acoust Soc Am* 116(1):578–593
- Cario J et al (2022) Identifying and overcoming limitations with *in situ* calibration beads for quantitative ultrasound. *J Acoust Soc Am* 151(4):2701–2711
- Chen X, Schwarz KQ, Parker KJ (1993a) Radiation pattern of a focused transducer: a numerically convergent solution. *J Acoust Soc Am* 94:2979–2991
- Chen JF, Zagzebski JA, Madsen EL (1993b) Tests of BSC measurement using broadband pulses. *IEEE Trans Ultrason Ferroelectr Freq Control* 40:603–607
- Chen X, Schwarz KQ, Parker KJ (1994) Acoustic coupling from a focused transducer to a flat plate and back to the transducer. *J Acoust Soc Am* 95: 3049–3054
- Chen X, Phillips D, Schwarz KQ, Mottley JG, Parker KJ (1997) The measurement of BSC from a broadband pulse-echo system: a new formulation. *IEEE Trans Ultrason Ferroelectr Freq Control* 44:515–525
- Coila A, Oelze ML (2019) Effects of acoustic nonlinearities on the ultrasonic backscatter coefficient estimation. *J Acoust Soc Am* 146(1):85–94
- Coila A, Oelze ML (2020) Effects of acoustic nonlinearity on pulse-echo attenuation coefficient estimation from tissue-mimicking phantoms. *J Acoust Soc Am* 148(2):805–814
- D'Astous FT, Foster FS (1986) Frequency dependence of ultrasound attenuation and backscatter in breast tissue. *Ultrasound Med Biol* 12:795–808
- Faran JJ (1951) Sound scattering by solid cylinders and spheres. *J Acoust Soc Am* 23:405–418
- Garcia-Duitama J et al (2015) Experimental application of ultrafast imaging to spectral tissue characterization. *Ultrasound Med Biol* 41(9):2506–2519
- Ghoshal G, Oelze ML (2010) Improved scatterer property estimates from ultrasound backscatter using gate-edge correction and a pseudo-Welch technique. *IEEE Trans Ultrason Ferroelectr Freq Control* 57(12):2828–2832
- Han A et al (2020) Noninvasive diagnosis of nonalcoholic fatty liver disease and quantification of liver fat with radiofrequency ultrasound data using one-dimensional convolutional neural networks. *Radiology* 295(2):342–350
- Huisman HJ, Thijssen JM (1996) Precision and accuracy of acoustospectrographic parameters. *Ultrasound Med Biol* 22(7):855–871
- Insana MF, Hall TJ (1990) Parametric ultrasound imaging from BSC measurements: image formation and interpretation. *Ultrasound Imaging* 12:245–267
- Insana MF, Madsen EL, Hall TJ, Zagzebski (1986) Tests of the accuracy of a data reduction method for determination of acoustic BSCs. *J Acoust Soc Am* 79:1230–1236
- Insana MF, Wagner RF, Brown DG, Hall TJ (1990) Describing small-scale structure in random media using pulse-echo ultrasound. *J Acoust Soc Am* 87(1):179–192
- Lavarello R, Ghoshal G, Oelze ML (2011) On the estimation of BSCs using single-element focused transducers. *J Acoust Soc Am* 129:2903–2911
- Liu W, Zagzebski JA (2010) Trade-offs in data acquisition and processing parameters for backscatter and scatterer size estimation. *IEEE Trans Ultrason Ferroelectr Freq Control* 57(2):340–352
- Liu W, Zagzebski JA, Gerig AL, Varghese T, Marquez EC, Kliewer MA (2006) Methods for improvement on liver scatterer size estimates. In: Proceedings of 2006 IEEE ultrasonic symposium, pp 641–644
- Lizzi FL, Greenebaum M, Feleppa EJ, Elbaum M, Coleman DJ (1983) Theoretical framework for spectrum analysis in ultrasonic tissue characterization. *J Acoust Soc Am* 73(4):1366–1373
- Madsen EL, Insana MF, Zagzebski (1984) Method of data reduction for accurate determination of acoustic BSCs. *J Acoust Soc Am* 76:913–923
- Madsen EL, Dong F, Frank GR, Gara BS, Wear KA, Wilson T, Zagzebski JA, Miller HL, Shung KK, Wang SH, Feleppa EJ, Liu T, O'Brien WD Jr, Topp KA, Sanghvi NT, Zaitsev AV, Hall TJ, Fowlkes JB, Kripfgans OD, Miller JG (1999) Interlaboratory comparison of ultrasonic backscatter, attenuation, and speed measurements. *J Ultrasound Med* 18:615–631
- Nam K, Zagzebski JA, Hall TJ (2011a) Simultaneous backscatter and attenuation estimation using a least square method with constraints. *Ultrasound Med Biol* 37(12):2096–2104
- Nam K, Rosado-Mendex IM, Wirtzfeld LA, Paelicki AD, Kumar V, Madsen EL, Ghoshal G, Lavarello RJ, Oelze ML, Bigelow TA, Zagzebski JA, O'Brien WD Jr, Hall TJ (2011b) Ultrasonic attenuation and BSC estimates of rodent-tumor mimicking structures: comparison of results among clinical scanners. *Ultrasound Imaging* 33(4):233–250
- Nam K, Rosado-Mendex IM, Wirtzfeld LA, Kumar V, Madsen EL, Ghoshal G, Pawlicki AD, Oelze ML, Bigelow TA, Zagzebski JA, O'Brien WD Jr, Hall TJ (2012) Cross-imaging system comparison of BSCs estimates from tissue-mimicking sample. *J Acoust Soc Am Exp Lett* 132(3):1319–1324
- Nguyen T, Oelze M (2019) Reference free quantitative ultrasound classification of fatty liver. In: 2019 IEEE International Ultrasonics Symposium (IUS). IEEE

- Nguyen T, Do M, Oelze ML (2018) Sensitivity analysis of reference-free quantitative ultrasound tissue classification. In: 2018 IEEE International Ultrasonics Symposium (IUS). IEEE
- Nguyen TN et al (2019) Estimation of backscatter coefficients using an in situ calibration source. *IEEE Trans Ultrason Ferroelectr Freq Control* 67(2):308–317
- Nguyen TN et al (2021) Use of a convolutional neural network and quantitative ultrasound for diagnosis of fatty liver. *Ultrasound Med Biol* 47(3):556–568
- Nicholas D, Hill CR, Nassiri (1982) Evaluation of backscattering coefficients for excised human tissues: principles and techniques. *Ultrasound Med Biol* 8(1):7–15
- O'Donnell M, Miller JG (1981) Quantitative broadband ultrasonic backscatter: an approach to nondestructive evaluation in acoustically inhomogeneous materials. *J Appl Phys* 52(2):1056–1064
- Oelze ML, Mamou J (2016) Review of quantitative ultrasound: envelope statistics and backscatter coefficient imaging and contributions to diagnostic ultrasound. *IEEE Trans Ultrason Ferroelectr Freq Control* 63(2):336–351
- Oelze ML, O'Brien WD Jr (2004) Defining optimal axial and lateral resolution for estimating scatter properties from volume using ultrasound backscatter. *J Acoust Soc Am* 115:3226–3234
- Oelze ML, O'Brien WD Jr (2002a) Method of improved scatterer size estimation and application to parametric imaging using ultrasound. *J Acoust Soc Am* 112(6):3053–3063
- Oelze ML, O'Brien WD Jr (2002b) Frequency-dependent attenuation-compensation functions for ultrasonic signals backscattered from random media. *J Acoust Soc Am* 111(5):2308–2319
- Sigelmann RA, Reid JM (1973) Analysis and measurement of ultrasound backscattering from an ensemble of scatterers excited by sine-wave bursts. *J Acoust Soc Am* 53:1351–1355
- Soylu U, Oelze ML (2023a) A Data-Efficient Deep Learning Strategy for Tissue Characterization via Quantitative Ultrasound: Zone Training. *IEEE Transactions on Ultrasonics, Ferroelectrics, and Frequency Control* (in press)
- Soylu U, Oelze ML (2023b) Calibrating Data Mismatches in Deep Learning-Based Quantitative Ultrasound Using Setting Transfer Functions. *IEEE Transactions on Ultrasonics, Ferroelectrics, and Frequency Control* (in press)
- Ueda M, Ozawa Y (1985) Spectral analysis of echoes for backscattering coefficient measurement. *J Acoust Soc Am* 77:38–47
- Wear KA, Stiles TA, Frank GR, Madsen EL, Cheng F, Feleppa EJ, Hall CS, Kim BS, Lee P, O'Brien WD Jr, Oelze ML, Raju BI, Shung KK, Wilson TA, Yuan JR (2005) Interlaboratory comparison of ultrasonic BSC measurements from 2 to 9 MHz. *J Ultrasound Med* 24(9):1235–1250
- Welch PD (1967) The use of fast Fourier transform for the estimation of power spectra: A method based on time averaging over short, modified periodogram. *IEEE Trans Audio Electroacoust AU-15:70–73*
- Wirtzfeld LA, Ghoshal G, Hafez ZT, Nam K, Labyed Y, Anderson JJ, Herd MT, Haak A, He Z, Miller RJ, Sarwate S, Simpson DG, Zagzebski JA, Bigelow TA, Oelze ML, Hall TJ, O'Brien WD Jr (2010) Cross-imaging platform comparison of ultrasonic BSC measurements of live rat tumors. *J Ultrasound Med* 29(7):11117–11123
- Wirtzfeld LA, Hirtz NR, Nam K, Labyed Y, Ghoshal G, Haak A, Sen-Gupta E, He Z, Miller RJ, Sarwate S, Simpson DG, Zagzebski JA, Bigelow TA, Oelze ML, Hall TJ, O'Brien WD Jr (2013) Techniques and evaluation from a cross-platform imaging comparison of quantitative ultrasound parameters in an in vivo rodent fibroadenoma model. *IEEE Trans Ultrason Ferroelectr Freq Control* 60(7):1386–1400
- Yao LX, Zagzebski JA, Madsen EL (1990) Backscatter coefficient measurements using a reference phantom to extract depth-dependent instrumentation factors. *Ultrasound Imaging* 12:58–70



Extracting Quantitative Ultrasonic Parameters from the Backscatter Coefficient

4

Aiguo Han

Abstract

The ultrasonic backscatter coefficient (BSC) is a fundamental quantitative ultrasound (QUS) parameter that contains rich information about the underlying tissue. Deriving parameters from the BSC is essential for fully utilizing the information contained in BSC for tissue characterization. In this chapter, we review two primary approaches for extracting parameters from the BSC versus frequency curve: the model-based approach and the model-free approach, focusing on the model-based approach, where a scattering model is fit to the observed BSC to yield model parameters. For this approach, we will attempt to unite commonly used models under a coherent theoretical framework. We will focus on the underlying assumptions and conditions for various BSC models. Computer code is provided to facilitate the use of some of the models. The strengths and weaknesses of various models are also discussed.

Keywords

Backscatter coefficient · Ultrasonic scattering · Form factor · Structure function

4.1 Introduction

The radiofrequency (RF) ultrasound echo signals backscattered from tissue contain rich information about the tissue properties and microstructure. Much information is lost when the raw RF data are converted into B-mode images displayed on clinical scanners. Quantitative ultrasound (QUS, Oelze and Mamou 2016) techniques attempt to extract useful information about tissue from the raw RF signals. The RF signals result from the complex interaction between the tissue and the ultrasound waves. RF signals encode information about both the tissue (spatially and temporally) and the ultrasound system. A primary objective of QUS is to remove the system effects and extract information that is only related to tissue.

The backscatter coefficient (BSC) is a quantity provided by QUS that contains only information about the tissue. It is a fundamental parameter that describes the tissue's ability to backscatter ultrasound energy. When measured properly, the BSC is system- and operator-independent. Cali-

A. Han (✉)

Department of Biomedical Engineering and Mechanics,
Virginia Polytechnic Institute and State University,
Blacksburg, VA, USA
e-mail: aiguohan@vt.edu

brations are performed during the QUS scans to remove the system and operator dependence. In laboratory settings when a single-element transducer is used in water-tank experiments, system calibration is typically performed by taking a reference scan of a planar reflective surface whose reflection coefficient is known. In clinical settings when an array transducer is used, system calibration is performed by scanning a physical reference phantom whose acoustic properties are known a priori. Other effects such as attenuation are also compensated during the BSC measurement or data processing period.

The BSC can be estimated as a function of frequency. The BSC versus frequency curves can be directly used for tissue characterization. However, the BSC curves can be better interpreted when combined with acoustic scattering models, allowing further extraction of information from the curves. The BSC and parameters derived from the BSC have shown promising potential for tissue characterization and disease diagnosis. Interested readers are referred to Oelze and Mamou 2016 for a review.

The main objective of this chapter is to discuss methods for deriving parameters from the BSC. The methods are broadly classified into two categories: model-based and model-free. The model-based approach requires a scattering model to interpret the observed BSC curve. Fitting the model to the observed BSC yields model parameters related to tissue properties. Those parameters usually have well-defined physical meanings and are easy to interpret. The model-free approach does not require scattering models to interpret the BSC data. Instead, non-acoustic methods, such as linear regression and machine learning, are used to parameterize the BSC. Both approaches are promising, although research has been performed more extensively on the model-based approach. Therefore, we will focus more on the model-based approach in this chapter. In particular, we will attempt to summarize commonly used BSC models in a united, coherent theoretical framework. We will also discuss the assumptions and conditions for various BSC models.

Because this chapter is about deriving parameters from the BSC, other parameter derivation

methods such as envelope statistics (Oelze and Mamou 2016), H-scan (Parker 2016), and deep learning (Han et al. 2020a) are not included in this chapter.

4.2 Definitions

To formally define the BSC for acoustic scattering and intuitively understand the definition, we start by defining the following quantities (Insana and Brown 1993; Cobbald 2007): (i) *scattering cross-section*, (ii) *differential scattering cross-section*, and (iii) *differential scattering coefficient*.

When a plane wave is incident on a discrete scatterer, the intensity of the incident wave will be reduced due to interactions with the scatterer. The energy loss is caused by absorption (i.e., energy absorbed by the scatterer) and scattering (i.e., energy deflected from its original course by the scatterer).

The incident power lost to scattering, divided by the incident intensity, is defined as the *scattering cross-section*,

$$\sigma_s = \frac{W_s}{I_{\text{inc}}} \quad (4.1)$$

where the total scattered power, W_s , and the incident intensity, I_{inc} , are defined as time-averaged quantities. If the intensity is expressed in Watts/m² and power in Watts, then σ_s has the unit m², which is the unit of an area. The scattering cross-section represents the physical cross-sectional area of the portion of the incident wave that is lost to scattering. Therefore, the scattering cross-section is a useful measure of the scattering strength.

The scattered waves are often measured using a finite-aperture detector that only samples a fraction of the total scattered power. Therefore, it is useful to define the *differential scattering cross-section* to describe the variation of the scattered power with angular direction. The differential scattering cross-section is defined as the time-averaged scattered power in the direction (θ, ϕ) per unit solid angle divided by the

incident intensity,

$$\sigma_d(\theta, \varphi) = \frac{dW_s(\theta, \varphi)}{d\Omega} \frac{1}{I_{\text{inc}}} \quad (4.2)$$

where θ and φ represent the polar angle and azimuthal angle, respectively, following the ISO convention of the spherical coordinate system, $dW_s(\theta, \varphi)$ is the differential power scattered in the direction (θ, φ) , and $d\Omega$ is a differential solid angle given by $d\Omega = \sin \theta d\theta d\varphi$. Equation (4.2) is equivalent to

$$\sigma_d(\theta, \varphi) = \frac{d\sigma_s}{d\Omega} \quad (4.3)$$

The above definitions are given with a discrete scatterer in mind. If the scattering volume is an ensemble of discrete scatterers or a continuum with continuously varying density and compressibility, the scattered power received at the detector will increase with the scattering volume, V . The increase is generally nonlinear but linear if only the *incoherent* portion of the scattered power is concerned. Therefore, it is reasonable to quantify the scattering strength of an ensemble of scatterers by the *differential scattering coefficient*, defined as

$$\sigma_{\text{dsc}}(\theta, \varphi) = \frac{\sigma_d(\theta, \varphi)}{V} = \frac{dW_s(\theta, \varphi)}{d\Omega} \frac{1}{I_{\text{inc}} V} \quad (4.4)$$

In pulse-echo ultrasound applications, the same transducer is used for both transmission and reception. The scattering direction opposite to the incident beam is of particular importance. The differential scattering coefficient in the backscattering direction ($\theta = \pi$) is called the (differential) *backscatter coefficient* (BSC)

$$\sigma_{\text{BSC}} = \sigma_{\text{dsc}}(\theta = \pi) \quad (4.5)$$

The MKS units of the BSC are $1/\text{m}\cdot\text{sr}$. However, units $1/\text{cm}\cdot\text{sr}$ are most frequently used in the ultrasound literature.

4.3 Model-Based BSC Parameterization

4.3.1 Assumptions and Notations

Model-based BSC parameterization requires acoustic scattering models appropriate for the tissue being investigated. Understanding the acoustic scattering process in biological tissues is essential to developing and choosing the models. Unfortunately, acoustic scattering in biological tissues is complicated because of the complexity and diversity of tissue structures. It is generally difficult, if feasible at all, to fully model the scattering process in biological tissues. Therefore, it is helpful to make some assumptions to simplify the problem. The following assumptions are used in the BSC models described in this chapter:

Assumption (i): The incident wave is a plane harmonic wave. The plane wave assumption is generally valid near the focal plane of a single-element focused transducer, at the far-field of a single-element unfocused transducer, and at the far-field of an ultrasonic beam generated by an array transducer. The harmonic assumption is convenient for theoretical derivation. Any pulsed wave can be treated as a superposition of harmonic waves.

Assumption (ii): A scattering volume with spatially varying density, ρ , and compressibility, κ , is embedded in a uniform background with density, ρ_o , and compressibility, κ_o . The scattering volume can be modeled as a collection of discrete scatterers or a continuum with continuously varying density and compressibility.

Assumption (iii): The observation point is far from the scattering volume; that is, the observation distance is much larger than the dimension of the scattering volume of interest. This assumption is useful because the scattered wave can be approximated as a spherical wave in the far-field.

Assumption (iv): The ultrasonic waves travel through the tissue without loss. In real-world

scenarios, ultrasonic attenuation does occur in tissues due to absorption and scattering. However, the no-loss assumption is still applicable because attenuation correction is performed during the BSC measurement process.

Assumption (v): Unless otherwise noted, the tissues are assumed to have fluid-like properties without shear wave propagation. Although shear wave is supported in real tissues, any shear waves generated are damped locally. Therefore, the shear wave effects can be included in the attenuation coefficient (Insana and Brown 1993).

Assumption (vi): Only linear wave propagation is considered. This assumption is generally valid when the transmit power of the ultrasound imaging system is moderate or low. This assumption may be violated when high transmit power is used.

We use complex quantities and the engineering convention to represent waves. For example, a unit-amplitude harmonic plane wave propagating toward $+x$ direction is denoted by $p = e^{j(\omega t - kx)}$. Because harmonic waves are assumed in this chapter, the $e^{j\omega t}$ term is omitted in the subsequent discussion.

4.3.2 Relating BSC to Scattered Acoustic Pressure Field

With the above assumptions and notations, we consider the scattering geometry shown in Fig. 4.1 for discussing acoustic scattering models. Although only backscattering is relevant to the analysis of BSC, it is useful to consider the general case where the scattered wave is observed in an arbitrary direction as shown in Fig. 4.1.

Specifically, we consider a harmonic plane wave of amplitude p_{im} and angular frequency ω incident on a scattering volume V that is embedded in a uniform background. The equilibrium density ρ_o and compressibility κ_o of the background are constants. The equilibrium density $\rho(\mathbf{r})$ and compressibility $\kappa(\mathbf{r})$ of the scattering volume are spatially varying. The observation

point is far from the scattering volume. The incident wave direction is denoted by $\hat{\mathbf{i}}$, and the direction of the observer is denoted by $\hat{\mathbf{o}}$. Define the *scattering vector* \mathbf{K} as $\mathbf{K} = \mathbf{k}_s - \mathbf{k}_i = k(\hat{\mathbf{o}} - \hat{\mathbf{i}})$, where $k = \frac{\omega}{c}$ is the wavenumber. The magnitude of \mathbf{K} is given by $|\mathbf{K}| = 2k \sin(\frac{\Theta}{2})$, where Θ is the scattering angle, i.e., the angle between $\hat{\mathbf{i}}$ and $\hat{\mathbf{o}}$. For backscatter, $\hat{\mathbf{o}} = -\hat{\mathbf{i}}$, $\Theta = \pi$, $\mathbf{K} = 2k\hat{\mathbf{o}} = 2\mathbf{k}_s$, and $|\mathbf{K}| = 2k$.

The scattered wave asymptotically behaves as a spherical wave in the far-field, as given by (Morse and Ingard 1968)

$$p_s(\mathbf{r}) = p_{im} \frac{e^{-jkR}}{R} \Phi(\mathbf{K}) \quad (4.6)$$

where $R = |\mathbf{r}|$, and the function $\Phi(\mathbf{K})$ is called the *complex scattering amplitude*, which describes the angular distribution of the scattered wave.

The (time-averaged) intensity of the scattered wave in the far-field is then given by

$$I_s = \frac{|\Phi(\mathbf{K})|^2}{2\rho_0 c_0 R^2} p_{im}^2 \quad (4.7)$$

The differential scattering coefficient defined in Eq. (4.4) becomes

$$\begin{aligned} \sigma_{dsc} &= \frac{dW_s(\theta, \varphi)}{d\Omega} \frac{1}{I_{inc} V} \\ &= \frac{I_s R^2 d\Omega}{d\Omega} \frac{1}{I_{inc} V} \\ &= \frac{|\Phi(\mathbf{K})|^2}{V} \end{aligned} \quad (4.8)$$

The BSC is then expressed by

$$\text{BSC} = \frac{|\Phi(2k)|^2}{V} \quad (4.9)$$

which relates the BSC to the distribution of the scattered wave field. Thus, if the form of $\Phi(2k)$ is known, the BSC could be computed. Different forms of $\Phi(2k)$ yield different BSC models.

Equations (4.8) and (4.9) have been derived with deterministic media in mind, i.e., the spatial distribution of the media's equilibrium density $\rho(\mathbf{r})$ and compressibility $\kappa(\mathbf{r})$ are known precisely. In QUS applications, it is often necessary to model biological tissues as random media,

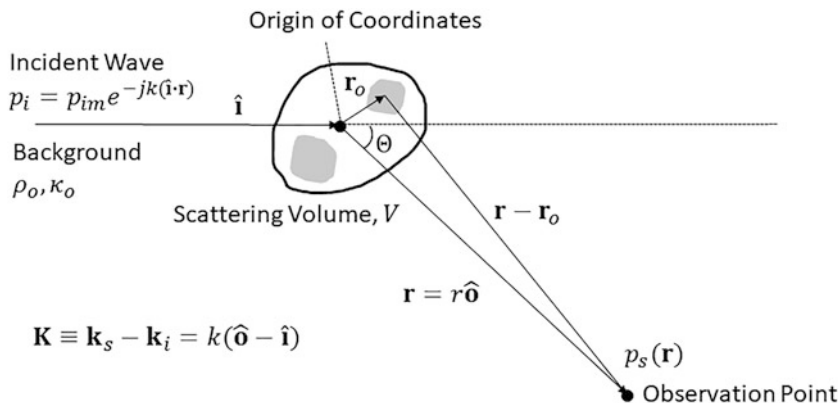


Fig. 4.1 Scattering geometry illustration showing a scattering volume within which the density and compressibility vary, embedded in a uniform background. The

incident wave is a harmonic plane wave propagating in the direction \hat{i} . The observation point is far from the scattering volume

where the functions $\rho(\mathbf{r})$ and $\kappa(\mathbf{r})$ are treated as random processes. Each A-line scan measures a realization of the random media. Thus, the differential scattering coefficient must be obtained by a statistical averaging process,

$$\sigma_{dsc} = \frac{E[\Phi(\mathbf{K})\Phi^*(\mathbf{K})]}{V} \quad (4.10)$$

where $E[\dots]$ represents statistical averaging (also called ensemble averaging), i.e., averaging over many different realizations of the random process, to be distinguished from spatial averaging within the same realization. In practice, however, random processes describing biological media are often assumed to be mean ergodic, i.e., the spatial average asymptotically equals the statistical average.

Similarly, the BSC for random media is expressed as

$$BSC = \frac{E[\Phi(2k)\Phi^*(2k)]}{V} \quad (4.11)$$

4.3.3 Exact BSC Models from Acoustic Scattering Theory

Exact BSC models can be obtained by using acoustic scattering theory for simple discrete scatterers such as spheres and cylinders. The word

“exact” refers to the fact that the models do not require the Born approximation (discussed later in this chapter) or the long-wavelength assumption (also discussed later).

Simple scatterer geometries are useful for modeling the acoustic scattering sites in various biological tissues. For example, fluid spheres have been used to model cell nuclei (Taggart et al. 2007) and other spherical scatterer sites. Two concentric spheres have been used to model eukaryotic cells, with the inner sphere representing the nucleus and the outer shell representing the cytoplasm (Teisseire et al. 2010; Han et al. 2011). Cylinders have been used to model skeletal muscle (Levinson 1987), myocardium (Shung and Thieme 1993), renal cortical structure (Insana 1995), and trabecular bone (Wear 1999).

For a single scatterer of simple geometry, the form of the complex scattering amplitude $\Phi(\mathbf{K})$ at the far-field can be derived from the exact acoustic scattering solutions. The exact solutions can be obtained using the boundary value method initially used by Rayleigh (Cobbold 2007). The scattering from simple geometries such as spheres and cylinders has been solved by various authors (e.g., fluid sphere by Anderson 1950; concentric spheres by McNew et al. 2009; infinitely long cylinder by Morse and Ingard 1968).

For a scattering volume consisting of a sparse distribution of randomly positioned simple

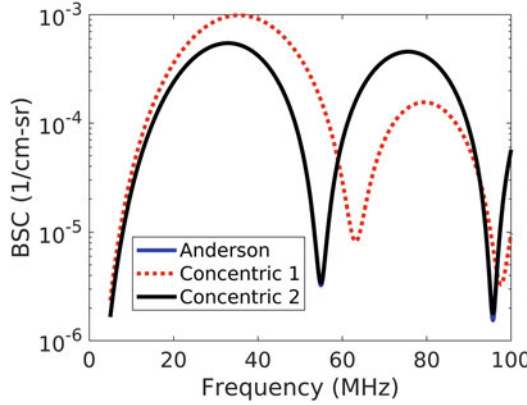


Fig. 4.2 BSC versus frequency curves computed using the Anderson and concentric spheres models with the following parameters: Anderson: $a = 10 \mu\text{m}$, $\rho_0 = 1 \text{ g/cm}^3$, $\rho_1 = 1.02 \text{ g/cm}^3$, $c_0 = 1500 \text{ m/s}$, $c_1 = 1540 \text{ m/s}$, $c_2 = 1560 \text{ m/s}$, and $\bar{n} = 1 \times 10^6 \text{ cm}^{-3}$; Concentric 2: $a_1 = 10 \mu\text{m}$, $a_2 = 6 \mu\text{m}$, $\rho_0 = 1 \text{ g/cm}^3$, $\rho_1 = \rho_2 = 1.02 \text{ g/cm}^3$, $c_0 = 1500 \text{ m/s}$, $c_1 = c_2 = 1540 \text{ m/s}$, and $\bar{n} = 1 \times 10^6 \text{ cm}^{-3}$; Concentric 1: $a_1 = 10 \mu\text{m}$, $a_2 = 6 \mu\text{m}$,

$\rho_0 = 1 \text{ g/cm}^3$, $\rho_1 = 1.02 \text{ g/cm}^3$, $\rho_2 = 1.05 \text{ g/cm}^3$, $c_0 = 1500 \text{ m/s}$, $c_1 = 1540 \text{ m/s}$, $c_2 = 1560 \text{ m/s}$, and $\bar{n} = 1 \times 10^6 \text{ cm}^{-3}$; Concentric 2: $a_1 = 10 \mu\text{m}$, $a_2 = 6 \mu\text{m}$, $\rho_0 = 1 \text{ g/cm}^3$, $\rho_1 = \rho_2 = 1.02 \text{ g/cm}^3$, $c_0 = 1500 \text{ m/s}$, $c_1 = c_2 = 1540 \text{ m/s}$, and $\bar{n} = 1 \times 10^6 \text{ cm}^{-3}$

scatterers, BSC models can be derived by using the exact scattering solutions obtained using the boundary value method, provided that two conditions are satisfied: (i) The scatterers are positioned sufficiently randomly such that there is a negligible correlation between the positions of any pair of scatterers. The scattered signals from different scatterers add *incoherently*. (ii) Multiple scattering effects are negligible. These conditions will often occur when the scatterer concentration is low (i.e., sparse scattering medium). Under these conditions, the total power scattered by all scatterers is equal to the sum of the scattered power of each scatterer in the statistical sense. If the scatterers are assumed to be identical, Eq. (4.10) reduces to

$$\sigma_{\text{dsc,incoherent}} = \bar{n} |\Phi_1(\mathbf{K})|^2 \quad (4.12)$$

and Eq. (4.11) reduces to

$$\text{BSC}_{\text{incoherent}} = \bar{n} |\Phi_1(2k)|^2 \quad (4.13)$$

where $\bar{n} = N/V$ is the number density, and Φ_1 is the complex scattering amplitude of a single scatterer. The subscript incoherent is used to emphasize that incoherent scattering is assumed.

Equation (4.13) can be used to derive the analytical expression of the BSC from exact solutions of $\Phi_1(2k)$. The analytical BSC expressions de-

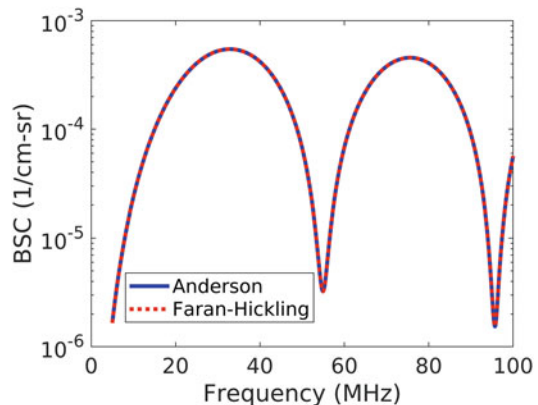
rived from the exact solutions are lengthy in most cases. Matlab code is provided in Appendices A and B for the readers to conveniently compute the BSC using the Anderson model (i.e., fluid sphere scattering solution given by Anderson 1950) and the concentric spheres model (i.e., two concentric spheres scattering solution given by McNew et al. 2009).

The computation of the Anderson BSC at given frequency values requires six parameters: the sphere radius a , the sphere density ρ_1 , the sphere speed of sound c_1 , the background density ρ_0 , the background speed of sound c_0 , and the number density \bar{n} . Nine parameters are required for the concentric spheres model: the outer sphere radius a_1 , the inner sphere radius a_2 , the background density ρ_0 , the outer shell density ρ_1 , the inner shell density ρ_2 , the background speed of sound c_0 , the outer shell speed of sound c_1 , the inner shell speed of sound c_2 , and the number density \bar{n} .

The concentric sphere model reduces to the Anderson model when the inner sphere and outer shell share the same density and sound speed values (Fig. 4.2).

The scatterers are assumed to have fluid-like properties in the Anderson and concentric sphere models. The fluid-scatterer assumption is often considered appropriate to model the scattering in soft tissues. However, this assumption ignores the

Fig. 4.3 BSC versus frequency curves computed using the Anderson and Faran-Hickling models with the following parameters: $a = 10 \mu\text{m}$, $\rho_0 = 1 \text{ g/cm}^3$, $\rho_1 = 1.02 \text{ g/cm}^3$, $c_0 = 1500 \text{ m/s}$, $c_1 = 1540 \text{ m/s}$, and $\bar{n} = 1 \times 10^6 \text{ cm}^{-3}$. The Poisson's ratio was set to $0.5 - 10^{-14}$ for the Faran-Hickling model



shear wave motion inside the scatterers. Therefore, the assumption is less appropriate when shear waves are generated inside the scatterers, as is the case for physical phantoms made of solid spheres (e.g., glass beads) embedded in a uniform fluid-like background.

A solid sphere model is needed to more accurately describe the scattering from solid scatterers. The theoretical scattering solution for solid spheres was originally derived by Faran (1951). There was an error in Faran's paper. The error was corrected by Hickling (1962). The Faran-Hickling BSC model reduces to the Anderson model when the Poisson's ratio of the sphere approaches 0.5 (Fig. 4.3).

Quantitative parameters can be extracted by fitting the above-mentioned exact models to the measured BSC versus frequency curves. Model fitting is typically performed by using a least-squares technique. Those exact BSC models have a large number of parameters. It is not practical to fit all parameters at the same time. Several techniques are useful for making the inverse problems practical: (i) Some model parameters can be fixed to reduce the number of variable parameters. For example, the background density and speed of sound values are often fixed with empirical values. (ii) Because the number density only affects the BSC magnitude in those models, this parameter can be ignored by fitting the shape of the BSC first. (iii) Constraints (e.g., combining parameters) can be applied to reduce the degree of freedom.

Among the model parameters, the scatterer size is of particular interest. Because the scatterer size is directly related to the frequency location of the BSC peaks (e.g., Figs. 4.2 and 4.3), the scatterer size is easier to estimate than other parameters for the exact BSC models. For example, Teisseire et al. (2010) fitted the concentric spheres model to the BSC versus frequency curves measured from Chinese hamster ovary (CHO) cell pellet biophantoms. They yielded estimated nuclear radii ranging from 0 to 6 μm and estimated cell radii ranging from 6 to 7 μm , which agreed well with those of CHO sizes (nuclear radii typically 2–4.6 μm and cell radii typically 5.7–8.3 μm).

There are several advantages of using the exact BSC models: (i) The models do not require the Born approximation or the long-wavelength assumption. They are applicable for strong scattering (i.e., large impedance mismatch between the scatterer and the background) and applicable in a wide range of frequencies (e.g., not limited to $ka \ll 1$). (ii) The acoustic scattering theories behind those models have been validated by experiments. (iii) The models can be used as a gold standard to evaluate models that use more approximations.

There are also disadvantages of using the exact BSC models: (i) The inverse problem is challenged by the large number of model parameters. (ii) The analytical expressions of the exact models

are complicated. (iii) Exact scattering solutions are only available for simple scatterer geometries.

4.3.4 Approximate BSC Models Using Born Approximation

4.3.4.1 Theoretical Framework

Alternative to the boundary value method of solving the scattering problem, the Green's function approach can be used, where the scattered wave is expressed in an integral solution (Morse and Ingard 1968). The Green's function approach is particularly helpful when the acoustic properties of the scattering medium vary in a continuous manner, although the approach also applies to discrete scatterers. This approach is often used in combination with the Born approximation that assumes the scattered field is small compared to the incident field.

Using the Green's function approach with the Born approximation, the complex scattering amplitude shown in Eq. (4.6) can be expressed as

$$\Phi(\mathbf{K}) = \frac{k^2}{4\pi} \iiint_V [\gamma_\kappa(\mathbf{r}_o) + \gamma_\rho(\mathbf{r}_o) \cos(\Theta)] e^{j\mathbf{K}\cdot\mathbf{r}_o} dV_o \quad (4.14)$$

where $\gamma_\kappa = (\kappa_v - \kappa_o)/\kappa_o$ represents the fractional variation in compressibility and $\gamma_\rho = (\rho_v - \rho_o)/\rho_v$ represents the fractional variation in density, where κ_v and ρ_v are the spatially varying compressibility and density in the scattering volume, respectively. Eq. (4.14) assumes an incident plane wave, far-field observation, and weak scattering (i.e., $\gamma_\kappa \ll 1$, $\gamma_\rho \ll 1$, to satisfy the Born approximation). Define

$$\gamma(\mathbf{r}, \Theta) = \gamma_\kappa(\mathbf{r}) + \gamma_\rho(\mathbf{r}) \cos(\Theta) \quad (4.15)$$

which characterizes the medium inhomogeneity in a single function of two arguments \mathbf{r} (i.e., position in the medium) and Θ (i.e., the scattering angle).

For deterministic media, recognizing the 3-D integral in Eq. (4.14) as 3-D spatial Fourier transform yields

$$\Phi(\mathbf{K}) = \frac{k^2}{4\pi} \text{FT}\{\gamma(\mathbf{r}, \Theta)\} \quad (4.16)$$

where $\text{FT}\{\dots\}$ represents 3-D spatial Fourier transform. Substituting Eq. (4.16) to Eq. (4.8) yields

$$\sigma_{\text{dsc}} = \frac{k^4}{16\pi^2 V} |\text{FT}\{\gamma\}|^2 \quad (4.17)$$

Note that for weak scattering and backscattering ($\Theta = \pi$), $\gamma \approx -2(z_v - z_o)/z_v$, where z is the acoustic impedance and $z = \sqrt{\rho/\kappa}$. Therefore, when considering backscattering, Eq. (4.17) indicates that the BSC can be calculated by taking the squared magnitude of the 3-D spatial Fourier transform of the 3-D map of impedance contrast of the medium. Equation (4.17) is particularly useful for computing the BSC when the 3-D spatial distribution of the impedance is known. Equation (4.17) provides the basis for the 3-D impedance map (3DZM) approach to identifying the scattering sites from 3-D histology (Mamou et al. 2005, 2008).

For random media, $\gamma(\mathbf{r})$ can be theoretically treated as a wide-sense stationary random process, i.e., its mean and autocorrelation function do not vary with respect to spatial location. Therefore, the mean (ensemble average) of $\gamma(\mathbf{r})$ is a constant and the autocorrelation of $\gamma(\mathbf{r})$ is only dependent on the $\Delta\mathbf{r}$. The random process is also assumed to be ergodic; that is, we may replace ensemble average with spatial average performed throughout the medium. These assumptions are reasonable for homogenous tissues.

The wide-sense stationary assumption implies that the medium is infinitely large, which is reasonable if the medium is much larger than the ultrasonic beam. In this case, the scattering volume V in Eq. (4.14) is interpreted as the volume covered by the ultrasonic beam. The 3-D integration in Eq. (4.14) is interpreted as a *truncated*

3-D spatial Fourier transform of $\gamma(\mathbf{r})$, denoted as $\text{FT}_{\text{trunc}}\{\gamma\}$. Substituting Eqs. (4.14) and (4.15) into Eq. (4.10) yields

$$\sigma_{\text{dsc}} = \frac{k^4}{16\pi^2} \frac{E[|\text{FT}_{\text{trunc}}\{\gamma\}|^2]}{V} \quad (4.18)$$

where $E[|\text{FT}_{\text{trunc}}\{\gamma\}|^2]/V$ represents the truncated spectral density of $\gamma(\mathbf{r})$, which approaches the power spectral density of $\gamma(\mathbf{r})$ if V is sufficiently large. Applying the Wiener-Khinchin theorem to Eq. (4.18) yields

$$\sigma_{\text{dsc}} = \frac{k^4}{16\pi^2} \text{FT}\{R_\gamma(\Delta\mathbf{r})\} \quad (4.19)$$

where $R_\gamma(\Delta\mathbf{r})$ represents the spatial autocorrelation function of $\gamma(\mathbf{r})$. The statistical averaging operation does not appear in Eq. (4.19) because $R_\gamma(\Delta\mathbf{r})$ is already a statistical quantity. Also, the 3-D Fourier transform operation in Eq. (4.19) is no longer truncated. Because $\gamma(\mathbf{r})$ is a wide-sense stationary process, we have $R_\gamma(\Delta\mathbf{r}) = (E[\gamma])^2 + E[\gamma^2]b_\gamma(\Delta\mathbf{r})$, where $b_\gamma(\Delta\mathbf{r})$ is the spatial autocorrelation coefficient of $\gamma(\mathbf{r})$. Therefore, Eq. (4.19) can be expressed as

$$\begin{aligned} \sigma_{\text{dsc}} &= \frac{k^4}{16\pi^2} \text{FT}\{(E[\gamma])^2\} \\ &\quad + \frac{k^4 E[\gamma^2]}{16\pi^2} \text{FT}\{b_\gamma(\Delta\mathbf{r})\} \end{aligned} \quad (4.20)$$

The first term on the right-hand side of Eq. (4.20) is the 3-D Fourier transform of a constant, which is Dirac δ function and of no practical interest. Therefore, this term can be ignored, and Eq. (4.20) is reduced to

$$\sigma_{\text{dsc}} = \frac{k^4 E[\gamma^2]}{16\pi^2} \text{FT}\{b_\gamma(\Delta\mathbf{r})\} \quad (4.21)$$

Equivalent forms of Equation (4.21) have been derived in the literature (e.g., Insana and Brown 1993). However, the derivation process introduced herein is new. We applied results from random process theories to facilitate the derivation.

If the random medium is isotropic, the spatial autocorrelation coefficient (also called the correlation coefficient) $b_\gamma(\Delta\mathbf{r})$ depends only on the radial coordinate in the spherical coordinate system. Applying angular symmetry and considering backscattering, Eq. (4.21) reduces to (Insana and Brown 1993)

$$\text{BSC} = \frac{k^3}{8\pi} E[\gamma^2] \int_0^\infty b_\gamma(\Delta r) \sin(2k\Delta r) \Delta r d\Delta r \quad (4.22)$$

where the BSC is expressed in terms of the correlation coefficient, which indicates that different BSC models can be derived from different correlation coefficient models.

4.3.4.2 Correlation Coefficient Models

Three widely used correlation coefficients are fluid sphere, Gaussian, and exponential functions, which are expressed as (Insana and Brown 1993)

$$\begin{aligned} \text{Fluid sphere : } b_\gamma(\Delta r) &= \begin{cases} 1 - \frac{3\Delta r}{4a} + \frac{(\Delta r)^3}{16a^3}, & 0 \leq \Delta r \leq 2a \\ 0, & \Delta r > 2a \end{cases} \end{aligned} \quad (4.23)$$

$$\text{Gaussian : } b_\gamma(\Delta r) = e^{-\frac{(\Delta r)^2}{2a^2}} \quad (4.24)$$

and

$$\text{Exponential : } b_\gamma(\Delta r) = e^{-\frac{\Delta r}{a}}, \Delta r \geq 0 \quad (4.25)$$

respectively. The fluid sphere model describes the correlation coefficient for a medium where identical fluid spheres of radius a are randomly distributed within a uniform fluid background of different compressibility and/or density. The scatterers described by this model are discrete. This model is similar to the Anderson model introduced above. The Gaussian and exponential models describe random media with continuously varying compressibility and/or density.

The corresponding BSCs of the three models are expressed as (Insana and Brown 1993)

$$\text{Fluid sphere : BSC} = \frac{k^4 V_s^2 \bar{n} \gamma_0^2}{16\pi^2} \left[\frac{3}{2ka} j_1(2ka) \right]^2 \quad (4.26)$$

$$\text{Gaussian : BSC} = \frac{k^4 V_s^2 \bar{n} \gamma_0^2}{16\pi^2} e^{-2k^2 d^2} \quad (4.27)$$

$$\text{Exponential : BSC} = \frac{k^4 V_s^2 \bar{n} \gamma_0^2}{16\pi^2} \frac{1}{(1 + 4k^2 d^2)^2} \quad (4.28)$$

where j_1 is the first-order spherical Bessel function of the first kind, γ_0^2 is the mean-square of γ per scatterer, and V_s is the effective scatterer volume, with $V_s = 4\pi a^3/3$ for the fluid sphere model, $V_s = (2\pi d^2)^{3/2}$ for the Gaussian model, and $V_s = \pi(2d)^3$ for the exponential model.

Each of the three BSC models shown in Eqs. (4.26), (4.27), and (4.28) is characterized by two parameters, the scatterer size and the scattering strength. The effective scatterer diameter (ESD) is widely used in the QUS literature to describe the scatterer size. For the fluid sphere model, $ESD = 2a$, because the scatterers are discrete. For the Gaussian and exponential models, the scatterers are continuous and characterized by the correlation distance d . For these two models, the ESD is defined as the value of d that gives the same value of V_s as the fluid sphere model. Under this definition, $ESD = (12\sqrt{2\pi})^{1/3} d \approx 3.11d$ for the Gaussian model, and $ESD = 48^{1/3} d \approx 3.63d$ for the exponential model (Insana and Brown 1993).

The effective acoustic concentration (EAC) is widely used to describe the scattering strength. Several versions of EAC definitions exist in the QUS literature (e.g., Feleppa et al. 1986, 1988; Insana et al. 1990; Oelze and Zachary 2006). Here we adopt the definition given by Insana et al. (1990), where EAC is defined as

$$\text{EAC} = \bar{n} \gamma_0^2 \approx 4\bar{n} \left(\frac{z_v - z_0}{z_v} \right)^2 \quad (4.29)$$

Example BSC versus frequency curves are shown in Fig. 4.4 for the three models (Eqs. (4.26), (4.27), and (4.28)) using the same ESD and EAC parameters. The BSC curves are plotted over a wide frequency range (2–100 MHz), where $f = 24.5$ MHz corresponds to $ka = 1$, assuming the speed of sound to be 1540 m/s. The three models behave similarly at low frequencies (e.g., $ka < 0.5$) and their behaviors start to diverge as the frequency increases.

The three models are applicable to weak scattering because the derivation of the three models requires the Born approximation. As a numerical example, the fluid sphere model shows reasonable agreement with the Anderson model (exact model) for weak scattering for wavelength to scatterer radius ratios up to $ka = 4$ (Fig. 4.5a). The difference between the two models increases at $ka > 1$ as scattering becomes stronger (Fig. 4.5b). However, the fluid sphere model shows reasonable agreement with the Anderson model at $ka < 1$ for both weaker and stronger scattering in Fig. 4.5. Therefore, it is sometimes suggested that the three models [Eqs. (4.26), (4.27), and (4.28)] be used for low frequencies (e.g., $ka < 1$), although the derivation of the three models does not explicitly require low frequencies.

4.3.4.3 Rayleigh Scattering and Form Factor

In the low-frequency limit (or long-wavelength limit; $ka \ll 1$), the fluid sphere, Gaussian, and exponential models all reduce to

$$\text{BSC} = \frac{1}{9} k^4 a_{\text{eff}}^6 \bar{n} \gamma_0^2 \quad (4.30)$$

where $a_{\text{eff}} = \text{ESD}/2$. This equation provides the BSC for the widely known Rayleigh scattering that occurs in the low-frequency limit. The upper limit of ka for Rayleigh scattering is suggested to be $ka = \pi/10$ (Ishimaru 1978; Insana and Brown 1993). The BSC is proportional to the fourth power of the frequency and the sixth power of the scatterer radius for Rayleigh scattering. Rayleigh scattering has a simple form but provides limited information. In particular, information about the scatterer shape and impedance distribution within the scatterer is lost in Rayleigh scattering.

Fig. 4.4 BSC versus frequency curves computed using the fluid sphere [Eq. (4.26)], Gaussian [Eq. (4.27)], and exponential [Eq. (4.28)] models with the same ESD and EAC parameters: ESD = 20 μm and EAC = $8.13 \times 10^6 \text{ mm}^{-3}$, assuming $c = 1540 \text{ m/s}$. For the given ESD value, $ka = 1$ at 24.5 MHz

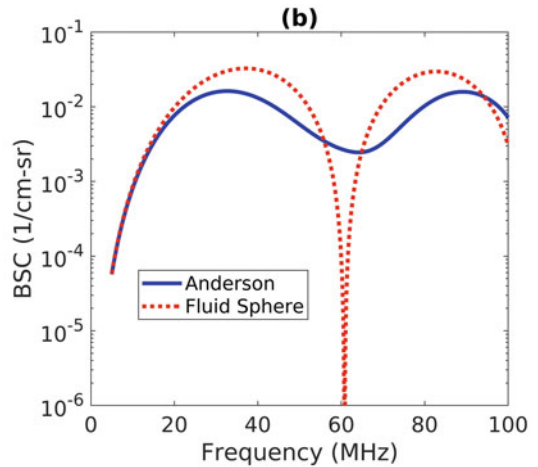
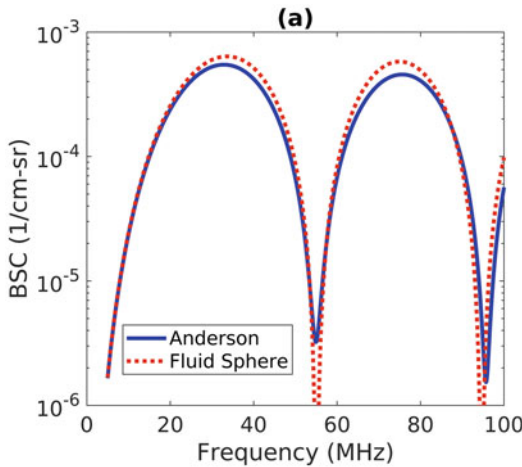
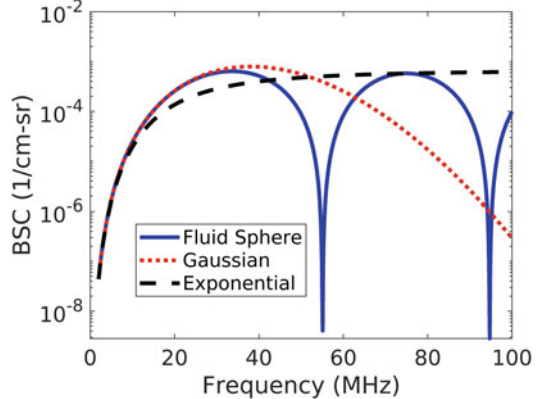


Fig. 4.5 BSC versus frequency curves computed using the Anderson and the fluid sphere [Eq. (4.26)] models with the same sets of parameters: (a) Weak scattering: $a = 10 \mu\text{m}$, $\rho_0 = 1 \text{ g/cm}^3$, $\rho_1 = 1.02 \text{ g/cm}^3$, $c_0 = 1500 \text{ m/s}$, $c_1 = 1540 \text{ m/s}$, and $\bar{n} = 1 \times 10^6 \text{ cm}^{-3}$;

(b) Strong scattering: $a = 10 \mu\text{m}$, $\rho_0 = 1 \text{ g/cm}^3$, $\rho_1 = 1.2 \text{ g/cm}^3$, $c_0 = 1500 \text{ m/s}$, $c_1 = 1700 \text{ m/s}$, and $\bar{n} = 1 \times 10^6 \text{ cm}^{-3}$. For the given scatterer size, $ka = 1$ at 24.5 MHz

Dividing the BSC expressions in Eqs. (4.26), (4.27), and (4.28) by the Rayleigh scattering BSC yields the so-called backscatter *form factor* F (Insana and Brown 1993) that captures the combined information about the scatterer shape and impedance distribution:

$$\text{Fluid sphere : } F = \left[\frac{3}{2ka} j_1(2ka) \right]^2 \quad (4.31)$$

$$\text{Gaussian : } F = e^{-2k^2 d^2} \quad (4.32)$$

$$\text{Exponential : } F = \frac{1}{(1 + 4k^2 d^2)^2} \quad (4.33)$$

In all three cases, the form factor approaches unity at low frequencies and decreases with increasing frequency.

4.3.4.4 Strengths and Weaknesses of Correlation Models

The correlation coefficient models show several strengths: (i) The inverse problem is easy to solve due to the simplicity of the models. For example, the three correlation models discussed above (fluid sphere, Gaussian, and exponential) are determined by two independent parameters, the ESD and the EAC. Least squares techniques can extract the two parameters from

the experimental BSC. The inverse problem can also be performed for the Gaussian model through a linear regression Oelze et al. (2002). (ii) The correlation coefficient method exhibits a high degree of flexibility because developing a new model using this theoretical framework is convenient. One can study tissue histology to develop a spatial autocorrelation coefficient model that matches the tissue structure. For example, Oelze and O'Brien (2006) developed a correlation model to describe the scattering from cells. A cell was modeled as two concentric spheres, with the inner sphere modeling the nucleus with constant impedance and the outer shell modeling the cytoplasm with spatially varying impedance values. This model yielded a statistically significant difference between ESD estimated from two mouse models of mammary cancer (carcinoma and sarcoma).

The correlation coefficient models also have several weaknesses: (i) The models require the Born approximation and are only applicable to weak scattering. (ii) The physical interpretation of the models is not always clear. For example, it is unclear to what anatomic structure the ESD estimated from the Gaussian model corresponds. (iii) If the correlation coefficient is derived by assuming a sparse medium, the derived BSC model may not work for a dense medium. The fluid sphere, Gaussian, and exponential models as given in Eqs. (4.26), (4.27), and (4.28) do not apply to a dense medium.

4.3.5 Scatterer Size Distribution

The BSC models discussed so far are all derived assuming identical scatterers, while scatterers in biological tissues are not identical. The variability in scatterer size is particularly noticeable. For example, we have shown that the cell size follows a Gamma distribution in several cell lines (Fig. 4.6; Han and O'Brien 2015). It has also been well documented that scatterer size estimates are affected by the size distribution (Lavarello and Oelze 2012).

To solve this problem, the BSC models can be updated to consider the scatterer size distribution

while assuming the other acoustic properties are identical among the scatterers. For instance, Eq. (4.13) can be revised as

$$\text{BSC}_{\text{incoherent}} = \int_0^{\infty} \bar{n} |\Phi_1(2k, x)|^2 g(x) dx \quad (4.34)$$

where $g(x)$ is the probability density function of the scatterer size. Some probability distributions (e.g., Gamma size distribution) can yield an analytical expression of the BSC when combined with an appropriate form factor, as shown in the light scattering literature (Aragon and Pecora 1976; Schmitt and Kumar 1998; Wang 2000). In this case, Eq. (4.34) can be used to estimate not only the mean scatterer size, but also the variance of the scatterer size distribution.

4.3.6 Structure Function Models for Dense Media

When the volume fraction of the scatterers in a scattering medium is large, the scatterers cannot be randomly positioned. The scatterer positions become correlated, and the incoherent scattering assumption does not hold anymore. The concept of structure function (or structure factor, SF) originally used in statistical mechanics has been applied by several groups of investigators to model the scattering in dense media (e.g., Twersky 1987, 1988; Fontaine et al. 1999; Savery and Cloutier 2001, 2005; Franceschini et al. 2008, 2011, 2016; Han and O'Brien 2015, 2016; Muleki-Seya et al. 2016; Han 2018) and has shown improved results (e.g., more accurate scatterer size estimates and more QUS parameters) relative to incoherent BSC models. The theory and basic models of SF are discussed herein.

Consider the scattering geometry described in Fig. 4.1. The scattered field from a collection of N scatterers is expressed as (Insana and Brown 1993)

$$p_s(\mathbf{r}) = p_{im} \frac{e^{-jkR}}{R} \sum_{i=1}^N \Phi_i(\mathbf{K}) e^{-j\mathbf{K} \cdot \mathbf{r}_i} \quad (4.35)$$

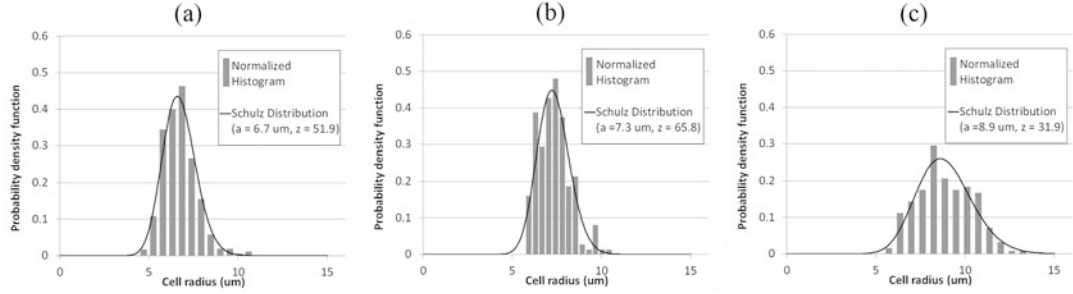


Fig. 4.6 Measured cell radius distribution for three cell lines: (a) Chinese hamster ovary, (b) 13762 MAT B III, and (c) 4T1. Bars represent normalized histograms obtained

from the size measurements. Solid lines represent best fits to the Schulz distribution (i.e., Gamma distribution). (Figure adapted from Han and O'Brien 2015)

where \mathbf{r}_i is the position of the i th scatterer with respect to the origin and Φ_i is the complex scattering amplitude of the i th scatterer. The term $e^{-j\mathbf{K}\bullet\mathbf{r}_i}$ considers the phase delay in the scattering process due to scatterer positioning. Comparing Eqs. (4.6) and (4.35) yields

$$\Phi(\mathbf{K}) = \sum_{i=1}^N \Phi_i(\mathbf{K}) e^{-j\mathbf{K}\bullet\mathbf{r}_i} \quad (4.36)$$

where $\Phi(\mathbf{K})$ is the effective complex scattering amplitude for all N scatterers. Substituting Eq. (4.36) into Eq. (4.10) yields

$$\sigma_{\text{dsc}} = \frac{E \left[\left| \sum_{i=1}^N \Phi_i(\mathbf{K}) e^{-j\mathbf{K}\bullet\mathbf{r}_i} \right|^2 \right]}{V} \quad (4.37)$$

If $\Phi_i(\mathbf{K})$ are identical,

$$\sigma_{\text{dsc}} = \frac{|\Phi_1(\mathbf{K})|^2 E \left[\left| \sum_{i=1}^N e^{-j\mathbf{K}\bullet\mathbf{r}_i} \right|^2 \right]}{V} \quad (4.38)$$

The only difference between Eqs. (4.12) and (4.38) is that Eqs. (4.12) assumes incoherent scattering and Eq. (4.38) considers the coherent scattering caused by the scatterer position correlation. Dividing Eq. (4.38) by Eq. (4.12) yields a ratio that is defined as the SF

$$\text{SF}(\mathbf{K}) = \frac{E \left[\left| \sum_{i=1}^N e^{-j\mathbf{K}\bullet\mathbf{r}_i} \right|^2 \right]}{N} \quad (4.39)$$

The idea is that the SF is unity for incoherent scattering but deviates from unity for a dense medium. To model the scattering more appropriately from dense media, incoherent BSC models must be multiplied by the SF.

Equation (4.39) can be used to calculate the SF from realizations of scatterer positions. However, Eq. (4.39) is not particularly useful for developing analytical SF models. For purposes of model development, note that Eq. (4.39) is mathematically equivalent to (Twersky 1987)

$$S(\mathbf{K}) = 1 + \bar{n} \int [g(\mathbf{r}) - 1] e^{-j\mathbf{K}\bullet\mathbf{r}} d\mathbf{r} \quad (4.40)$$

where the SF is related to the pair correlation function $g(\mathbf{r})$ that describes the spatial distribution of scatterers.

There are various pair correlation function models available in the literature. The most widely used one is the hard-sphere model that assumes the spheres can be randomly distributed in space except that they cannot overlap or deform (Percus and Yevick 1958). The non-overlapping condition leads to correlation in sphere positions when the volume fraction is high. The analytical expression of the SF for this model was given by Wertheim (1963). Considering backscattering, the SF for the monodisperse hard-sphere model is expressed as

$$S(2k) = \frac{1}{1 - \bar{n} C(2k)} \quad (4.41)$$

where

$$C(2k) = -32\pi a^3 \int_0^1 s^2 \frac{\sin(4kas)}{4kas} (\alpha + \beta s + \gamma s^3) ds$$

and

$$\begin{aligned}\alpha &= \frac{(1+2\eta)^2}{(1-\eta)^4}, \quad \beta = -\frac{6\eta(1+\frac{\eta}{2})^2}{(1-\eta)^4}, \\ \gamma &= \frac{\eta(1+2\eta)^2}{2(1-\eta)^4}\end{aligned}$$

where a is the sphere radius and η is the sphere volume fraction.

Matlab code for computing the SF of monodisperse hard-sphere model is available in [Appendix C](#). Example SF curves are shown in Fig. 4.7. The SF approaches unity at a volume fraction of 1%, suggesting incoherent scattering at low volume fractions. The SF starts to show a peak between $ka = 1.5$ to 2.0 as the volume fraction increases, due to the correlation in scatterer positions at higher volume fractions.

The monodisperse hard-sphere SF model has been extended to consider the polydispersity of the spheres for QUS applications (Han and O'Brien [2015](#); Franceschini et al. [2016](#)). Matlab code for the polydisperse hard-sphere SF model developed by Han and O'Brien ([2015](#)) is included in [Appendix D](#). Example SF curves calculated using the polydisperse model are shown in Fig. 4.8 for various sphere size distribution widths. The sphere size distribution width is characterized by the Schulz width factor z (a greater z value representing a narrower distribution). The SF calculated at $z = 10,000$ overlaps with the SF calculated using the monodisperse model. The SF peak starts to reduce as the size distribution becomes wider. As a reference, the Schulz width factor is 52, 66, and 32 for the distribution shown in Fig. 4.6a–c, respectively.

4.4 Model-Free BSC Parameterization

4.4.1 Linear Regression

The BSC versus frequency curve can be parameterized through a linear regression without using

any models. This approach was initially used by Lizzi and Feleppa et al. (Lizzi et al. [1983, 1987, 1997a, b, c](#); Feleppa et al. [1986, 1988](#)). In their original work, Lizzi et al. fitted a line to the calibrated power spectra (similar to BSC) expressed in decibels versus frequency over the transducer bandwidth to yield three summary spectral parameters: spectral slope (dB/MHz), spectral intercept (dB, extrapolation to 0 MHz), and midband fit (dB, fitted value at the center frequency). Only two of the three parameters are independent; however, it is considered to be useful to obtain all three.

Although simple, this approach of BSC parameterization is powerful. Others have widely used this approach. For example, Mamou et al. ([2011](#)) used linear regression parameters to characterize cancerous human lymph nodes. Czarnota and coworkers demonstrated the usefulness of the parameters in monitoring tumor treatment response (e.g., Sannachi et al. [2020](#)). The intercept and midband parameters have been shown to be correlated with live steatosis (Han et al. [2020b](#); Jung et al. [2022](#)).

It is worth noting that the midband fit parameter is equivalent to the integrated-backscatter parameter used by other investigators (O'Donnell et al. [1979](#); Lanza et al. [1996](#); Miller et al. [1998](#)).

4.4.2 Principal Component Analysis

Principal component analysis (PCA) is another model-free approach that has been used to parameterize the BSC. This approach was initially used by Nguyen et al. ([2019](#)) to characterize fatty liver in rabbits. Nguyen et al. showed using their experimental data that the first two components captured 96% of the variance in BSCs. They parameterized the BSC by projecting it onto the first two components to yield two parameters, PCA1 and PCA2. Compared with using ESD and EAC derived from the Gaussian model, they found that the two PCA parameters had similar performance in classifying the rabbits into low-fat and high-fat classes. However, the PCA features were found to be more spatially compact than ESD and EAC,

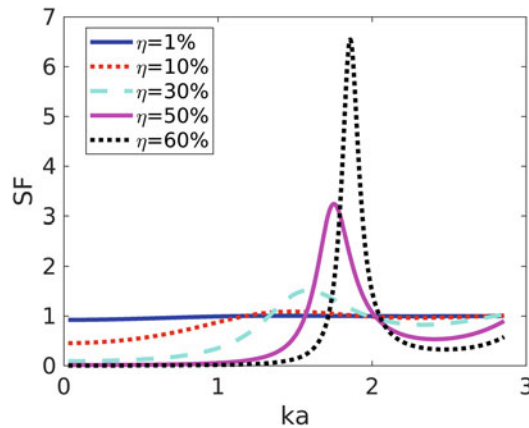


Fig. 4.7 Comparison among SF versus ka curves at five volume fractions: 1%, 10%, 30%, 50%, and 60%, computed by using the monodisperse hard-sphere SF model (Eq. (4.41))

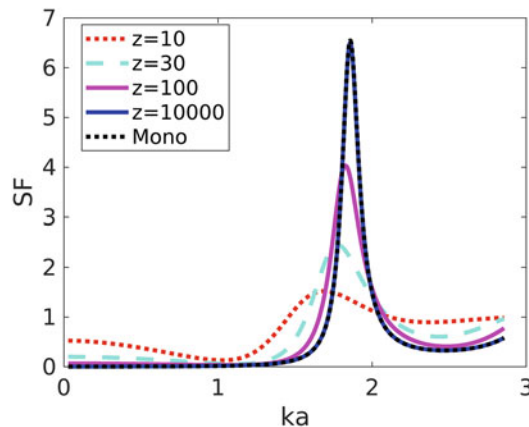


Fig. 4.8 Comparison among SF versus ka curves at four Schulz width factor values: 10, 30, 100, and 10,000, com-

puted by the polydisperse model in [Appendix D](#), compared to the SF versus ka curve computed by the monodisperse model at the same volume fraction 60%

suggesting that the PCA features could be more robust to noisy outliers.

Problems

Problem 1: Show that $\gamma(\mathbf{r}, \Theta)$ defined in Eq. (4.15) is approximately equal to $-2 \frac{z_v - z_0}{z_v}$ for backscatter and weak scattering ($\gamma_\kappa \ll 1$, $\gamma_\rho \ll 1$).

Problem 2: Derive Eq. (4.22) from Eq. (4.21) by assuming the medium to be isotropic.

Problem 3: Using the code provided in [Appendix A](#), plot the Anderson BSC for 1) monodisperse spheres with a radius of 10 μm and 2) poly-

disperse spheres with radius values uniformly distributed between 8 and 12 μm .

Appendices

Appendix A: Matlab Code for the Anderson BSC Model

```
function [bsc] = bsc_Anderson(a, dens0,
dens1, c0, c1, nbar, freq)
```

```
% This function computes the BSC using the Anderson model
```

```
% a: sphere radius (unit: micron)
% dens0: background density (unit: g/mL)
% dens1: sphere density (unit: g/mL)
% c0: background sound speed (unit: m/s)
% c1: sphere sound speed (unit: m/s)
% nbar: number density (unit: million spheres per mL)
% freq: frequency (unit: MHz)
% bsc: backscatter coefficient (unit: 1/cm-sr)

% freq and bsc are column vectors;

N = 25; % number of terms
```

```
freq = freq(:); % Making sure freq is a column vector.
```

```
g = dens1/dens0; h = c1/c0;
k = 2*pi*freq/c0; ka = k*a;
kpa = 2*pi*freq*c1*a; % column vector.
```

```
% All the N terms are calculated simultaneously in matrix form.
```

```
ja = sbessel(-1:N+1, ka);
jpa = sbessel(-1:N+1, kpa);
na = sbessely(-1:N+1, ka);
ja1 = ja(:,1:end-2).*(ones(size(ja,1),1)*[0:N]);
ja2 = ja(:,3:end).*(ones(size(ja,1),1)*[1:N+1]);
jpa1 = jpa(:,1:end-2).*(ones(size(jpa,1),1)*[0:N]);
jpa2 = jpa(:,3:end).*(ones(size(jpa,1),1)*[1:N+1]);
na1 = na(:,1:end-2).*(ones(size(na,1),1)*[0:N]);
na2 = na(:,3:end).*(ones(size(na,1),1)*[1:N+1]);
```

```
% same notation as in Anderson 1950
beta = na1 - na2; alpha = ja1 - ja2; alphap = jpa1 - jpa2;
tmp = alphap./alpha./jpa(:,2:end-1);
num = tmp.*na(:,2:end-1) - beta./alpha*g*h;
den = tmp.*ja(:,2:end-1) - g*h;
C = num./den;
```

```
A = (ones(size(C,1),1)*(((-1).^[0:N]).* ...
(2*[0:N]+1))./(1+i*C));
A(isnan(A)) = 0; % replace NaNs with zeros
A = sum(A,2);
bsc = 1e-2*nbar./k.^2.*abs(A).^2;
end
```

```
function [j] = sbessel(n,x)
% x in column, n in row
j=sqrt(pi./(2*(x*ones(size(n))))).*...
besselj(ones(size(x))*(n+0.5),x*ones(size(n)));
end

function [j] = sbessely(n,x)
% x in column, n in row
j=sqrt(pi./(2*(x*ones(size(n))))).*...
bessely(ones(size(x))*(n+0.5),x*ones(size(n)));
end
```

Appendix B: Matlab Code for the Concentric Spheres BSC Model

```
function bsc = bsc_concentric (a_in, a_out, dens0,
dens1, dens2, c0, c1, c2, nbar, freq)
```

```
% This function computes the BSC using the concentric spheres BSC model
```

```
% a_in: inner sphere radius (unit: micron)
% a_out: outer sphere radius (unit: micron)
% dens0: background density (unit: g/mL)
% dens1: outer shell density (unit: g/mL)
% dens2: inner sphere density (unit: g/mL)
% c0: background sound speed (unit: m/s)
% c1: outer shell sound speed (unit: m/s)
% c2: inner sphere sound speed (unit: m/s)
% nbar: number density (unit: million spheres per mL)
% freq: frequency (unit: MHz)
% bsc: backscatter coefficient (unit: 1/cm-sr)
```

```
% freq and bsc are column vectors;
```

```
freq = freq(:); % Making sure freq is a column vector.
```

```
max_order = 25;
```

```
alph0 = 0.2*freq*1e-4/8.686;
alph1 = 0.2*freq*1e-4/8.686;
alph2 = 0.2*freq*1e-4/8.686;
```

```
w = 2*pi*freq;
```

```

k0 = w/c0; k0_tild = k0+i*alph0;
k1 = w/c1; k1_tild = k1+i*alph1;
k2 = w/c2; k2_tild = k2+i*alph2;

Hk1r1_prime = Jk1r1_prime + i*Yk1r1_prime;
Hk1r2_prime = Jk1r2_prime + i*Yk1r2_prime;
Hk0r1_prime = Jk0r1_prime + i*Yk0r1_prime;

Zr1 = ((dens0*c0)*((1+i*alph1*c1./w)./
(1+i*alph0*c0./w))./(dens1*c1));
Zr2 = ((dens0*c0)*((1+i*alph2*c2./w)./
(1+i*alph0*c0./w))./(dens2*c2));

Num = ((Zr2.*Jk1r2.*Jk2r2_prime - ...
Zr1.*Jk1r2_prime.*Jk2r2) ...
.*(Zr1.*Hk1r1_prime.*Jk0r1 ...
- Hk1r1 .*Jk0r1_prime) ...
- (Zr1.*Hk1r2_prime.*Jk2r2 - ...
Zr2.*Hk1r2 .*Jk2r2_prime) ...
.*(Jk1r1 .*Jk0r1_prime - ...
Zr1.*Jk1r1_prime.*Jk0r1 ));

Denom = ((Zr1.*Hk1r2_prime.*Jk2r2 - ...
Zr2.*Hk1r2 .*Jk2r2_prime) ...
.*(Hk0r1_prime.*Jk1r1 - ...
Zr1.*Hk0r1 .*Jk1r1_prime) ...
- (Zr1.*Jk1r2_prime.*Jk2r2 - ...
Zr2.*Jk1r2 .*Jk2r2_prime) ...
.*(Hk0r1_prime.*Hk1r1 - ...
Zr1.*Hk0r1 .*Hk1r1_prime));

A =((-1).^m)*(2*m+1).*Num./Denom + A;
A(isnan(A)) = 0;
bsc0 = bsc;
bsc = (abs(A./k0_tild/1e6)).^2*nbar*1e10;
if max(abs(bsc(bsc0==0) - ...
bsc0(bsc0==0))/bsc(bsc0==0)) < 1e-12
    flag = 0;
elseif m==max_order
    flag = 0;
end
end

function [j] = sbessel(n,x)
% x in column, n in row

j=sqrt(pi./(2*(x*ones(size(n))))).*...
besselj(ones(size(x))*(n+0.5),x*ones(size(n)));
end

function [j] = sbessely(n,x)
% x in column, n in row
j=sqrt(pi./(2*(x*ones(size(n))))).*...
bessely(ones(size(x))*(n+0.5),x*ones(size(n)));
end

```

Appendix C: Matlab Code for the Monodisperse Hard Sphere SF Model

```

function [sf, ka] = sf_py_mono(a, eta, c, f)
% This function computes the SF of the Percus-Yiveck hard sphere model

% a: sphere radius (unit: micron)
% eta: volumem fraction of spheres
% c: sound speed (unit: m/s)
% f: frequency (unit: MHz)

d = 2*a*1e-6;
m = eta/(4/3*pi*(d/2)^3);
k = 2*pi*f/c*1e6;
ka = k*a*1e-6; kd = 2*ka;
alpha = (1+2*eta)^2/(1-eta)^4;
beta = -6*eta*(1+eta/2)^2/(1-eta)^4;
gamma = eta/2*alpha;

C0 = (alpha*(sin(2*kd) - 2*kd.*cos(2*kd)))./(8*kd.^3) ...
+ (beta*(cos(2*kd) - 2*kd.^2.*cos(2*kd) ...
+ 2*kd.*sin(2*kd) - 1))./(8*kd.^4) ...
+ (gamma*(sin(2*kd).*((1./kd.^2) - 3./(2*kd.^4)) ...
- cos(2*kd).*((1./(2*kd) - 3./(2*kd.^3) + 3./(4*kd.^5))...
+ 3./(4*kd.^5)))./(2.*kd);
Ck = -4*pi*d.^3.*C0;
sf = 1./(1-m*Ck);
end

```

Appendix D: Matlab Code for the Polydisperse Hard Sphere SF Model

```

function [sk, ka] = sf_py_poly(a, eta, c, f, z)

% a: sphere radius (unit: micron)
% eta: volumem fraction of spheres
% c: sound speed (unit: m/s)
% f: frequency (unit: MHz)
% z: Schulz width factor

% Han A and O'Brien WD (2015) Structure function for
% high-concentration biophantoms of polydisperse scatterer sizes.

```

% IEEE Trans Ultrason Ferroelectr Freq Control, 62(2):303–318

```

d_mean = a*1e-6*2;
k = 2*pi*f/c*1e6; K = 2*k;
ka = k*a*1e-6;
b = d_mean./(z + 1); c = z + 1;
% refer to equation 2.2, Aragon and Pecora 1976 JCP
d3_mean = d_mean.*((z+3).*(z+2)./(z+1).^2).^(1/3);
rho = eta/(4/3*pi*(d3_mean/2)^3);
zetap = b.*c; zetapp = b.^2.*c.*(c+1);
zetappp = b.^3.*c.*(c + 1).*((c + 2));
v1 = 1./((1 + (b.*K).^2));
psi = v1.^((c/2).*sin(c.*atan(b.*K)));
psip = b.*c.*v1.^((c+1)/2).*sin((c+1).*atan(b.*K));
psipp = b.^2.*c.*((c+1).*v1.^((c+2)/2).*...
sin((c+2).*atan(b.*K)));
v2 = 1./((2.^2 + (b.*K).^2);
mu = (4*v2).^(c/2).*sin(c.*atan(b.*K/2));
mup = (4*v2).^(c+1)/2).*b.*c.*...
sin((c+1).*atan(b.*K/2)); %%
chi = v1.^((c/2).*cos(c.*atan(b.*K)));
chip = b.*c.*v1.^((c+1)/2).*cos((c+1).*atan(b.*K));
chipp = b.^2.*c.*((c+1).*v1.^((c+2)/2).*...
cos((c+2).*atan(b.*K)));
lambda = (4*v2).^(c/2).*cos(c.*atan(b.*K/2)); %%
lambdap = (4*v2).^(c+1)/2).*b.*c.*...
cos((c+1).*atan(b.*K/2));
xi2 = rho.*b.^2.*c.*((c+1));
xi3 = rho.*b.^3.*c.*((c+1).*((c+2));
delta = 1 - pi*xi3/6;
pd = pi./delta; rK = rho./K;
delta1 = pd.*((2+pd.*((xi3-rK.*((K.*zetapp-psipp))));
delta2 = pd.^2.*rK.*((K.*zetapp-psip));
delta3 = -pd.^2.*rK.*((K.*zetap-psi));
delta4 = pd.*((K-pd.*rK.*((chip-zetap)));
delta5 = pd.^2.*((rK.*((chi-1)+K.*xi2/2));
delta6 = pd.^2.*rK.*((chipp - zetapp);

XI = 1- 2*pd.*((1+xi3.*pd/2).*((rho./K.^3). ...
*(K.*zetap-psi) ...
- 2*pd.*rho./K.^2.*((chip-zetap) + pd.*xi2/4.* ...
(chipp-zetapp)) ...
- pd.^2.*((rho./K.^2).^2.*((chi-1).*((chipp-zetapp) - ...
(chip-zetap).^2 ...
- (K.*zetap - psi).*((K.*zetapp-psipp) ...
+(K.*zetapp-psip).^2);

UPSILON = 2*pd.*((1+xi3.*pd/2).*((rho./K.^3). ...
((chi+K.^2.*zetapp/2-1) ...

```

```

-(2*pi*rho./delta./K.^2).*(K.*zetapp-psip+ ...
pd.*xi2/4.*(K.*zetapp-psipp)) ...
- pd.^2.*((rho./K.^2).^2.*((K.*zetap-psi).*(chipp- ...
zetapp))...
-2.*((K.*zetapp-psip).*(chip-zetap)+(K.*zetapp- ...
psipp).*(chi-1));

```

$hk = -2*\rho.*(\lambda.*(\lambda.* ...$

 $*(\text{UPSILON}.*\delta_1-\text{XI}.*\delta_6) ...$
 $+\lambda\text{bdap}.*(\text{UPSILON}.*\delta_2-\text{XI}.*\delta_4) ...$
 $+\mu_1.*(\text{XI}.*\delta_1+\text{UPSILON}.*\delta_6) ...$
 $+\mu_2.*(\text{XI}.*\delta_2+\text{UPSILON}.*\delta_4) ...$
 $+\lambda\text{bdap}.*(\lambda.*(\text{UPSILON}.*\delta_2- ...$
 $\text{XI}.*\delta_4) ...$
 $+\lambda\text{bdap}.*(\text{UPSILON}.*\delta_3-\text{XI}.*\delta_5) ...$
 $+\mu_1.*(\text{XI}.*\delta_2+\text{UPSILON}.*\delta_4) ...$
 $+\mu_2.*(\text{XI}.*\delta_3+\text{UPSILON}.*\delta_5) ...$
 $+\mu_1.*(\lambda.*(\text{XI}.*\delta_1+\text{UPSILON}.*\delta_6) ...$
 $+\lambda\text{bdap}.*(\text{XI}.*\delta_2+\text{UPSILON}.*\delta_4) ...$
 $+\mu_1.*(\text{XI}.*\delta_6-\text{UPSILON}.*\delta_1) ...$
 $+\mu_2.*(\text{XI}.*\delta_4-\text{UPSILON}.*\delta_2) ...$
 $+\mu_2.*(\lambda.*(\text{XI}.*\delta_2+\text{UPSILON}.*\delta_4) ...$
 $+\lambda\text{bdap}.*(\text{XI}.*\delta_3+\text{UPSILON}.*\delta_5) ...$
 $+\mu_1.*(\text{XI}.*\delta_4-\text{UPSILON}.*\delta_2) ...$
 $+\mu_2.*(\text{XI}.*\delta_5-\text{UPSILON}.*\delta_3))... /(\text{K}.^3.*(\text{XI}.^2+\text{UPSILON}.^2));$

$sk = 1 + hk;$
end

References

- Anderson VC (1950) Sound scattering from a fluid sphere. *J Acoust Soc Am* 22:426–443
- Aragon SR, Pecora R (1976) Theory of dynamic light scattering from polydisperse systems. *J Chem Phys* 64(6):2395–2404
- Cobbold RSC (2007) Foundations of biomedical ultrasound. Oxford University Press, New York
- Faran JJ (1951) Sound scattering by solid cylinders and spheres. *J Acoust Soc Am* 23:405–418
- Feleppa EJ, Lizzi FL, Coleman DJ, Yaremko MM (1986) Diagnostic spectrum analysis in ophthalmology: a physical perspective. *Ultrasound Med Biol* 12:623–631
- Feleppa EJ, Lizzi FL, Coleman DJ (1988) Ultrasonic analysis for ocular tumor characterization and therapy assessment. *Physiology* 3:193–197
- Fontaine I, Bertrand M, Cloutier G (1999) A system-based approach to modeling the ultrasound signal backscattered by red blood cells. *Biophys J* 77:2387–2399
- Franceschini E, Yu FTH, Cloutier G (2008) Simultaneous estimation of attenuation and structure parameters of aggregated red blood cells from backscatter measurements. *J Acoust Soc Am* 123:EL85–EL91
- Franceschini E, Metzger B, Cloutier G (2011) Forward problem study of an effective medium model for ultrasound blood characterization. *IEEE Trans Ultrason Ferroelectr Freq Control* 58:2668–2679
- Franceschini E, Monchy R, Mamou J (2016) Quantitative characterization of tissue microstructure in concentrated cell pellet biophantoms based on the structure factor model. *IEEE Trans Ultrason Ferroelectr Freq Control* 63(9):1321–1334
- Han A (2018) A method for stereological determination of the structure function from histological sections of isotropic scattering media. *IEEE Trans Ultrason Ferroelectr Freq Control* 65(6):1007–1016
- Han A, O'Brien WD Jr (2015) Structure function for high-concentration biophantoms of polydisperse scatterer sizes. *IEEE Trans Ultrason Ferroelectr Freq Control* 62(2):303–318
- Han A, O'Brien WD Jr (2016) Structure function estimated from histological tissue sections. *IEEE Trans Ultrason Ferroelectr Freq Control* 63(9):1296–1305
- Han A, Abuhabash R, Blue JP Jr, Sarwate S, O'Brien WD Jr (2011) Ultrasonic backscatter coefficient quantitative estimates from high-concentration Chinese hamster ovary cell pellet biophantoms. *J Acoust Soc Am* 130(6):4139–4147
- Han A, Byra M, Heba E, Andre MP, Erdman JW Jr, Loomba R, Sirlin CB, O'Brien WD Jr (2020a) Non-invasive diagnosis of nonalcoholic fatty liver disease and quantification of liver fat with radiofrequency ultrasound data using one-dimensional convolutional neural network. *Radiology* 295:342–350
- Han A, Zhang YN, Boehringer AS, Montes V, Andre MP, Erdman JW Jr, Loomba R, Valasek MA, Sirlin CB, O'Brien WD Jr (2020b) Assessment of hepatic steatosis in nonalcoholic fatty liver disease using quantitative ultrasound. *Radiology* 295:106–113
- Hickling R (1962) Analysis of echoes from a solid elastic sphere in water. *J Acoust Soc Am* 34(10):1582–1592
- Insana MF, Wagner RF, Brown DG, Hall TJ (1990) Describing small-scale structure in random media using pulse-echo ultrasound. *J Acoust Soc Am* 87:179–192
- Insana MF (1995) Modeling acoustic backscatter from kidney microstructure using an anisotropic correlation function. *J Acoust Soc Am* 97:649–655
- Insana MF, Brown DG (1993) Acoustic scattering theory applied to soft biological tissues. In: Shung KK, Thieme GA (eds) Ultrasonic scattering in biological tissues. CRC Press, Boca Raton
- Ishimaru A (1978) Wave propagation and scattering in random media. Academic, New York
- Jung J, Han A, Madamba E, Bettencourt R, Loomba RR, Boehringer AS, Andre MP, Erdman JE Jr, O'Brien WD Jr, Fowler KJ, Sirlin CB, Loomba R (2022) Direct comparison of quantitative US versus controlled attenuation parameter for liver fat assessment using MRI proton

- density fat fraction as the reference standard in patients suspected of having NAFLD. *Radiology* 304:75–82
- Lanza GM, Wallace K, Scott MJ, Cachetis C, Abendschein D, Christy D, Sharkey A, Miller J, Gaffney P, Wickline S (1996) A novel site-targeted ultrasonic contrast agent with broad biomedical applications. *Circulation* 94:3334–3340
- Lavarello R, Oelze ML (2012) Quantitative ultrasound estimates from populations of scatterers with continuous size distributions: effects of the size estimator algorithm. *IEEE Trans Ultrason Ferroelectr Freq Control* 59(9):2066–2076
- Levinson SF (1987) Ultrasound propagation in anisotropic soft tissue: the application of linear elastic theory. *J Biomech* 20:251–260
- Lizzi FL, Greenebaum M, Feleppa EJ, Elbaum M, Coleman DJ (1983) Theoretical framework for spectrum analysis in ultrasonic tissue characterization. *J Acoust Soc Am* 73:1366–1373
- Lizzi FL, Ostromogilsky M, Feleppa EJ, Rorke MC, Yaremko MM (1987) Relationship of ultrasonic spectral parameters to features of tissue microstructure. *IEEE Trans Ultrason Ferroelectr Freq Control* 34:319–329
- Lizzi FL, Astor M, Feleppa EJ, Shao M, Kalisz A (1997a) Statistical framework for ultrasonic spectral parameter imaging. *Ultrasound Med Biol* 23:1371–1382
- Lizzi FL, Feleppa EJ, Astor M, Kalisz A (1997b) Statistics of ultrasonic spectral parameters for prostate and liver examinations. *IEEE Trans Ultrason Ferroelectr Freq Control* 44:935–942
- Lizzi FL, Astor M, Liu T, Deng C, Coleman D, Silverman RH (1997c) Ultrasonic spectrum analysis for tissue assays and therapy evaluation. *Int J Imaging Syst Technol* 8:3–10
- Mamou J, Oelze ML, O'Brien WD Jr, Zachary JF (2005) Identifying ultrasonic scattering sites from three-dimensional impedance maps. *J Acoust Soc Am* 117(1):413–423
- Mamou J, Oelze ML, O'Brien WD Jr, Zachary JF (2008) Extended three-dimensional impedance map methods for identifying ultrasonic scattering sites. *J Acoust Soc Am* 123:1195–1208
- Mamou J, Coron A, Oelze ML, Saegusa-Beecroft E, Hata M, Lee P, Machi J, Yanagihara E, Laugier P, Feleppa EJ (2011) Three-dimensional high-frequency backscatter and envelope quantification of cancerous human lymph nodes. *Ultrasound Med Biol* 37(3):2055–2068
- McNew J, Lavarello R, O'Brien WD Jr (2009) Sound scattering from two concentric fluid spheres. *J Acoust Soc Am* 125:1–4
- Miller JG, Perez JE, Wickline SJA, Baldwin SL, Barzilai B, Davila-Roman V, Fedewa RJ, Finch-Johnston AE, Hall CS, Handley SM, Hockett FD, Holland MR, Kovacs A, Lanza GM, Lewis SS, Marsh JN, Mobley J, Sosnovik DE, Trousil RL, Wallace KD, Waters KR (1998) Backscatter imaging and myocardial tissue characterization. In: Proceedings of the IEEE ultrasonics symposium. Sendai, Japan, pp 1373–1383
- Morse P and Ingard K (1968) Theoretical acoustics, International Series in Pure and Applied Physics. Princeton University Press, Princeton
- Muleki-Seya P, Guillermin R, Guglielmi J, Chen J, Pourcher T, Konofagou E, Franceschini E (2016) High-frequency quantitative ultrasound spectroscopy of excised canine livers and mouse tumors using the structure factor model. *IEEE Trans Ultrason Ferroelectr Freq Control* 63:1334–1350
- Nguyen TN, Podkowa AS, Tam AY, Arnold EC, Miller RJ, Park TH, Do MN, Oelze ML (2019) Characterizing fatty liver in vivo in rabbits, using quantitative ultrasound. *Ultrasound Med Biol* 45(8):2049–2062
- O'Donnell M, Bauwens D, Mimbs JW, Miller JG (1979) Broadband integrated backscatter: an approach to spatially localized tissue characterization in vivo. In: Proceedings of the IEEE ultrasonics symposium 79 CH 1482–1489, pp 175–178
- Oelze ML, Mamou J (2016) Review of quantitative ultrasound: envelope statistics and backscatter coefficient imaging and contributions to diagnostic ultrasound. *IEEE Trans Ultrason Ferroelectr Freq Control* 63(2):336–351
- Oelze ML, O'Brien WD Jr (2006) Application of three scattering models to characterization of solid tumors in mice. *Ultrason Imaging* 28(2):83–96
- Oelze ML, Zachary JF (2006) Examination of cancer in mouse models using high frequency quantitative ultrasound. *Ultrasound Med Biol* 32(11):1639–1648
- Oelze ML, Zachary JF, O'Brien WD Jr (2002) Characterization of tissue microstructure using ultrasonic backscatter: theory and technique for optimization using a Gaussian form factor. *J Acoust Soc Am* 112:1202–1211
- Parker KJ (2016) The H-format for classification of ultrasound scattering. *OMICS J Radiol* 5(5):1000236
- Percus JK, Yevick GJ (1958) Analysis of classical statistical mechanics by means of collective coordinates. *Phys Rev* 110(1):1–13
- Sannachi L, Gangeh M, Naini AS, Bhargava P, Jain A, Tran WT, Czarnota GJ (2020) Quantitative ultrasound monitoring of breast tumour response to neoadjuvant chemotherapy: comparison of results among clinical scanners. *Ultrasound Med Biol* 46(5):1142–1157
- Savery D, Cloutier G (2001) A point process approach to assess the frequency dependence of ultrasound backscattering by aggregating red blood cells. *J Acoust Soc Am* 110:3252–3262
- Savery D, Cloutier G (2005) Effect of red cell clustering and anisotropy on ultrasound blood backscatter: a Monte Carlo study. *IEEE Trans Ultrason Ferroelectr Freq Control* 52:94–103
- Schmitt JM, Kumar G (1998) Optical scattering properties of soft tissue: a discrete particle model. *Appl Opt* 37(13):2788–2797
- Shung KK, Thieme GA (1993) Biological tissues as ultrasonic scattering media. In: Shung KK, Thieme GA (eds) Ultrasonic scattering in biological tissues. CRC Press, Boca Raton

- Taggart LR, Baddour RE, Giles A, Czarnota GJ, Kolios MC (2007) Ultrasonic characterization of whole cells and isolated nuclei. *Ultrasound Med Biol* 33(3):389–401
- Teisseire M, Han A, Abuhabssah R, Blue JP Jr, Sarwate S, O'Brien WD Jr (2010) Ultrasonic backscatter coefficient quantitative estimates from Chinese hamster ovary cell pellet biophantoms. *J Acoust Soc Am* 128(5):3175–3180
- Twersky V (1987) Low-frequency scattering by correlated distributions of randomly oriented particles. *J Acoust Soc Am* 81(5):1609–1618
- Twersky V (1988) Low-frequency scattering by mixtures of correlated nonspherical particles. *J Acoust Soc Am* 84(1):409–415
- Wang RK (2000) Modeling optical properties of soft tissue by fractal distribution of scatterers. *J Mod Opt* 47(1):103–120
- Wear KA (1999) Frequency dependence of ultrasonic backscatter from human trabecular bone: theory and experiment. *J Acoust Soc Am* 106(6):3659–3664
- Wertheim MS (1963) Exact solution of the Percus-Yevick integral equation for hard spheres. *Phys Rev Lett* 10(8):321–323

Part II

Attenuation Estimation Methods



Attenuation Compensation and Estimation

5

Timothy A. Bigelow and Yassin Labyed

Abstract

Estimating the loss of ultrasound signal with propagation depth as a function of frequency is essential for quantifying tissue properties. Specifically, ultrasound attenuation is used to correct for spectral distortion prior to estimating quantitative ultrasound parameters to assess the tissue. Ultrasound attenuation can also be used independently to characterize the tissue. In this chapter, we review the primary algorithms for estimating both the local attenuation within a region of interest as well as the total attenuation between a region of interest and an ultrasound source. The strengths and weaknesses of each algorithm are also discussed.

Keywords

Attenuation · Local attenuation · Total attenuation · Spectral difference method · Spectral-log difference method · Hybrid method · Spectral-fit method · Multiple filter method

T. A. Bigelow (✉)
Iowa State University, Ames, IA, USA
e-mail: bigelow@iastate.edu

Y. Labyed
Los Alamos National Lab, Los Alamos, NM, USA

Siemens Healthineers, Issaquah, WA, USA;
yassin.labyed@philips.com;
yassin.labyed@siemens-healthineers.com

5.1 Introduction

When attempting to characterize tissue based on the frequency spectrum of backscattered ultrasound echoes, it is critically important to correctly compensate for attenuation. Because both scattering and attenuation impact the frequency spectrum, the effects of attenuation must be removed before the scattering properties can be extracted for diagnostic purposes. For the purpose of tissue characterization, there are two different attenuation parameters to be considered. First, there is the **local attenuation**. The local attenuation is the attenuation within a region of interest and is used primarily to quantify the tissue properties of that region. It can also be used to improve the accuracy of scatterer property, e.g., scatterer size and acoustic concentration, as will be discussed in more detail later in this chapter. The second and most important type of **attenuation is the total attenuation**. The total attenuation is the effective attenuation along the propagation path from the source thru the intervening tissue layers to the region of interest. Figure 5.1 shows an image of the different regions corresponding to the local and total attenuation. It is impossible to obtain accurate estimates of the backscatter coefficient and corresponding scatterer property estimates derived from the backscatter coefficient without an accurate estimate for the total attenuation. In

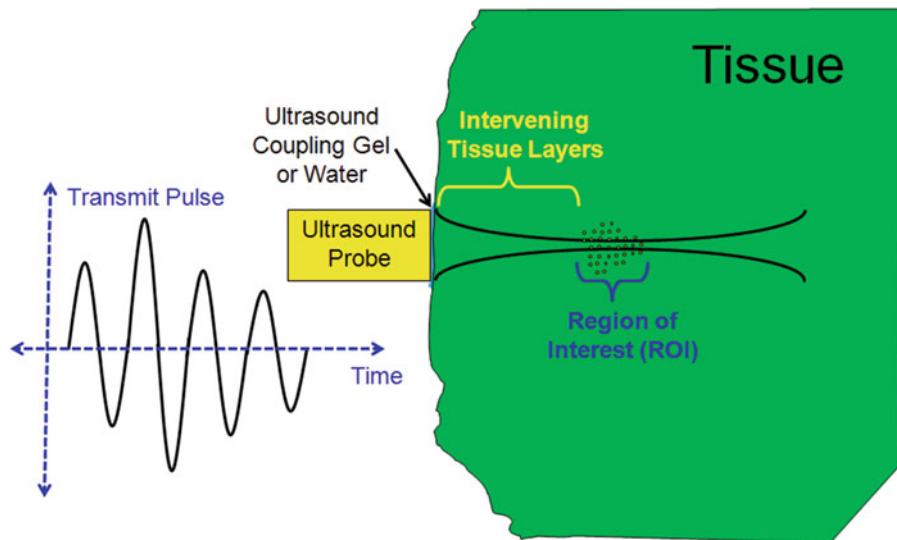


Fig. 5.1 Illustration of tissue when performing ultrasound tissue characterization

this chapter, we will review how the attenuation impacts the backscattered power spectrum as well as summarize the basic algorithms that have been developed to estimate both total and local attenuation.

5.2 Impact of Attenuation on Backscattered Power Spectrum

Before discussing the various algorithms that have been developed to estimate the total and local attenuation, we will briefly review how these attenuation parameters relate to the backscattered power spectrum. The backscattered power spectrum from a region of interest in an unknown sample is given by (Bigelow 2004; Bigelow and O'Brien Jr. 2004a, b)

$$S_s(f) \propto \left[f^4 |H(f)|^4 |V_{\text{inc}}(f)|^2 \exp(-4\alpha_{\text{tot}}(f)z_T) \cdot M_\gamma \cdot F_\gamma(f, a_{\text{eff}}) D(f, \alpha_{\text{loc}}) \right] \quad (5.1)$$

In this equation, f is frequency, $H(f)$ is the dimensionless filtering characteristics of the ultrasound source, $|V_{\text{inc}}(f)|$ is the power spectrum of the voltage pulse applied to the ultrasound source,

and z_T is the distance from the ultrasound source to the beginning of the region of interest in the tissue. The term $\alpha_{\text{tot}}(f)$ is the total attenuation along the propagation path, as was described previously, and is given by

$$\alpha_{\text{tot}}(f) = \left(\sum_{j=1}^{N-1} \alpha_j(f) \frac{\Delta z_j}{z_T} \right) \quad (5.2)$$

where α_j is the attenuation in each of the intervening tissue layers of thickness Δz_j . Also, $F_\gamma(f, a_{\text{eff}})$ is the form factor which captures the frequency dependence of the scattering while M_γ is the acoustic concentration (Insana et al. 1990). Typical form factors for tissue and tissue-mimicking phantoms include the Gaussian form factor, the fluid-filled sphere form factor, and the spherical-shell form factor.

$$\begin{aligned} F_{\gamma\text{-Gaussian}}(f, a_{\text{eff}}) &= \exp(-0.827(k \cdot a_{\text{eff}})) \\ F_{\gamma\text{-Sphere}}(f, a_{\text{eff}}) &= \left[\frac{j_1(2k \cdot a_{\text{eff}})}{(2/3)k \cdot a_{\text{eff}}} \right]^2 \\ F_{\gamma\text{-Shell}}(f, a_{\text{eff}}) &= [j_0(2k \cdot a_{\text{eff}})]^2 \end{aligned} \quad (5.3)$$

The development of more complicated form factors to accurately model tissue is the subject of a recent study (Oelze and O'Brien Jr. 2006).

The remaining term from (5.1), $D(f, \alpha_{\text{loc}})$ takes into account both the diffraction of the acoustic waves (i.e., focusing) and the local attenuation, $\alpha_{\text{loc}}(f)$ of the tissue in the region of interest and is given by

$$D(f, \alpha_{\text{loc}}) = \exp(-4\alpha_{\text{loc}}(f)z_o) \cdot \int_{-L/2}^{L/2} [g_{\text{win}}(s_z) \exp(-4\alpha_{\text{loc}}(f)s_z) D_{\text{focus}}(f, s_z)] ds_z \quad (5.4)$$

where the variable of integration, s_z , increases as we move away from the source. In this equation, g_{win} is the windowing function used to gate the backscattered echoes when selecting an analysis region. Common windowing functions include rectangular, Hamming, and Hanning windows. Also, L is the length of the windowing function expressed as a distance and z_o is the distance from the beginning of the region of interest (ROI) to the center of the current windowed analysis region within the ROI. We distinguish here between the larger ROI, or the region over which the attenuation estimate is obtained, and the smaller windowed analysis region, or the region where the power spectrum is estimated. The attenuation estimation algorithms require finding multiple power spectra from different analysis regions within the ROI in order to find the attenuation of the ROI. The windowed analysis region is illustrated in Fig. 5.2.

The term within the integral $D_{\text{focus}}(f, s_z)$ takes into account focusing and is given by

$$D_{\text{focus}}(f, s_z) = \left[\exp\left(\frac{-2((z_T + z_o - F_{\text{transmit}}) + s_z)^2}{(w_{z_{\text{transmit}}}(f))^2}\right) \cdot \exp\left(\frac{-2((z_T + z_o - F_{\text{recv}}) + s_z)^2}{(w_{z_{\text{recv}}}(f))^2}\right) \right] \quad (5.5)$$

assuming the beam profile on transmit and receive can be approximated by a Gaussian function; an approximation that is reasonable for most sources (Barber 1991; Bigelow 2004; Bigelow and O'Brien Jr. 2004a, b). In this equation, F_{transmit} and F_{recv} are the distance from the aperture

plane to the transmit and receive foci respectively. Also, $w_{z_{\text{transmit}}}(f)$ and $w_{z_{\text{recv}}}(f)$ are the effective Gaussian depths of focus for the transmit and receive foci, respectively. For a spherically focused source, w_z is approximately equal to $6.01\lambda(f\#)^2$ where λ is the wavelength and $f\#$ is the f-number for the source.

From (5.4), it is clear that the impact of local attenuation on the backscattered power spectrum is coupled with the diffraction of the acoustic field via the integral expression. This coupling can make the assessment of backscatter more challenging. As a result, various investigators have attempted to isolate the local attenuation and focusing effects on the spectrum so that each can be corrected independently. The most common approach, termed **point compensation**, assumes that the size of the windowing function is so small that g_{win} can be approximated by an impulse function (Oelze and O'Brien Jr. 2002; Bigelow 2004; Bigelow and O'Brien Jr. 2004a, b). Under this approximation, (5.4) becomes

$$D(f, \alpha_{\text{loc}}) = \exp(-4\alpha_{\text{loc}}(f)z_o) \left[\exp\left(\frac{-2(z_T + z_o - F_{\text{transmit}})^2}{(w_{z_{\text{transmit}}}(f))^2}\right) \cdot \exp\left(\frac{-2(z_T + z_o - F_{\text{recv}})^2}{(w_{z_{\text{recv}}}(f))^2}\right) \right] \quad (5.6)$$

where the local attenuation term and diffraction terms have been decoupled.

Another approach to decouple the local attenuation and diffraction is to use an approximate value for the local attenuation within the integral (Bigelow and O'Brien Jr. 2006). This approach is used in all tissue characterization methods that divide the power spectrum from the sample by the power spectrum from a reference phantom as will be discussed in more detail later in the chapter. Under this approximation (5.4) becomes

$$D(f, \alpha_{\text{loc}}) = \exp(-4\alpha_{\text{loc}}(f)z_o) \cdot \int_{-L/2}^{L/2} [g_{\text{win}}(s_z) \exp(-4\alpha_{\text{approximate}}(f)s_z) D_{\text{focus}}(f, s_z)] ds_z \quad (5.7)$$

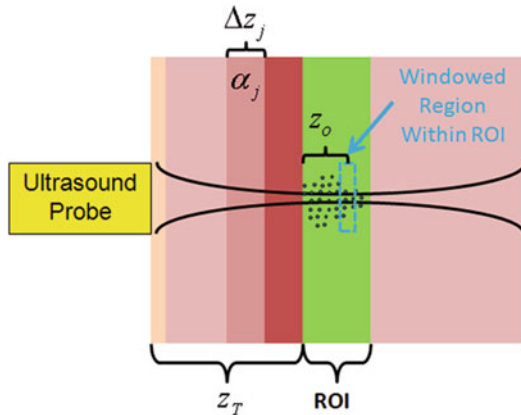


Fig. 5.2 Illustration showing coordinates when defining variables in the backscattered power spectrum

The optimal choice for $\alpha_{\text{approximate}}(f)$ was shown to be given by

$$\alpha_{\text{approximate}}(f) \cong \sqrt{\frac{\alpha_{\text{high}}^2(f) + \alpha_{\text{low}}^2(f)}{2}} \quad (5.8)$$

where $\alpha_{\text{high}}(f)$ and $\alpha_{\text{low}}(f)$ are the largest and smallest attenuation values expected in the tissue region (Bigelow and O'Brien Jr. 2006).

5.3 Local Attenuation Estimation Algorithms

Now that we have reviewed how local and total attenuation impacts the backscattered power spectrum, we can review some of the algorithms used to estimate the attenuation within a region of interest. While this local attenuation can be used to improve the estimate of the scattering properties for the tissue, it is typically used independently to characterize the tissue for diagnostic purposes. We will focus on four of the most common local attenuation estimation algorithms.

5.3.1 Spectral Shift Algorithm for Local Attenuation Estimation

One of the most common algorithms for estimating the attenuation within a region of interest

is the spectral-shift algorithm. This algorithm uses the down shift in the center frequency of the power spectrum versus propagation depth to estimate the attenuation slope, α_0 , where the local attenuation is assumed to have the form $\alpha_{\text{loc}}(f) = \alpha_0 f + \beta_b$ (Narayana and Ophir 1983a, b; Oosterveld et al. 1991; Baldeweck et al. 1993, 1994, 1995; Girault et al. 1998; Kim and Varghese 2007). This algorithm has been implemented in both the frequency and the time domain, where the time-domain implementation requires utilizing an autoregressive approach (Baldeweck et al. 1993, 1994, 1995; Girault et al. 1998). We will derive the algorithm in the frequency domain because focusing has not been accounted for in the autoregressive approach.

The spectral shift algorithm begins by assuming that the backscattered power spectrum can be approximated by a Gaussian function. As a result, (5.1) can be written as

$$S_s(f) \propto \exp\left(-\frac{(f - f_o)^2}{2\sigma_\omega^2}\right) D(f, \alpha_{\text{loc}}). \quad (5.9)$$

Traditionally, the spectral-shift algorithm has been implemented assuming weakly focused sources where diffraction effects in the ROI can be neglected. In addition, small windows are typically used resulting in the assumption that point compensation is valid. Hence, (5.9) can be

written as

$$S_s(f) \propto \exp\left(-\frac{(f - f_o)^2}{2\sigma_\omega^2}\right) \exp(-4\alpha_o \cdot fz_o). \quad (5.10)$$

However, multiplying the Gaussian function by the decaying exponential is just a Gaussian transformation resulting in a new Gaussian function.

$$S_s(f) \propto \exp\left(-\frac{(f - \tilde{f}_o(z_o))^2}{2\sigma_\omega^2}\right) \quad (5.11)$$

where

$$\tilde{f}_o(z_o) = f_o - 4\sigma_\omega^2\alpha_o \cdot z_o. \quad (5.12)$$

Therefore, the attenuation slope can be found by selecting multiple windows within a ROI (i.e., different z_o). The power spectrum for each window is then calculated and fit by a Gaussian function to find the center frequency, \tilde{f}_o , and bandwidth, σ_ω^2 . The attenuation slope can then be calculated from the change in center frequency with depth

$$\alpha_o = -\frac{1}{4\sigma_\omega^2} \frac{\partial \tilde{f}_o}{\partial z_o}. \quad (5.13)$$

$$\text{mse} = \text{mean}_{f_o} \left[\begin{aligned} & \left(\log \left(e^{-\frac{(f - \tilde{f}_o)^2}{2\sigma_\omega^2}} \right) \right) - \log \left(\frac{S_s(f)}{\max_f(S_s(f))} \right) \right]^2 \\ & - \text{mean}_{f_o} \left(\log \left(e^{-\frac{(f - \tilde{f}_o)^2}{2\sigma_\omega^2}} \right) \right) \\ & - \log \left(\frac{S_s(f)}{\max_f(S_s(f))} \right) \end{aligned} \right]. \quad (5.14)$$

Importance of Finding the Usable Frequency Range:

When fitting a function to a spectrum it is critically important to perform the fit only with values from the spectrum that are not dominated by noise. Therefore, the first step in any frequency domain algorithm is to first find the usable frequency range from the power spectrum. One can do this from either a visible inspection of the spectrum or using a computer program that identifies the noise floor for the spectral data and always operates above this noise floor.

Hint on Finding Center Frequency and Bandwidth:

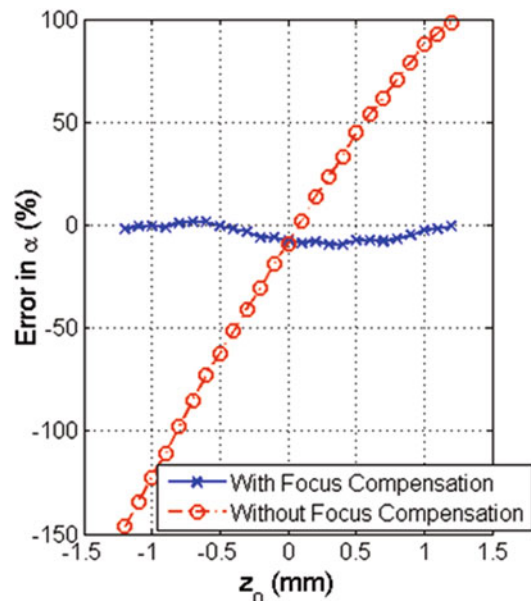
When finding the center frequency and bandwidth from a fit to a Gaussian function, we have found that a more accurate fit can be obtained by performing the fit in the log domain. Therefore, we find the values of \tilde{f}_o and σ_ω^2 that minimize the function in (5.14).

The expression derived in (5.13) is valid only when diffraction effects can be neglected (Bigelow et al. 2008; Kim and Varghese 2008). Otherwise, a correction needs to be applied as indicated in Fig. 5.3 taken from (Bigelow et al. 2008).

From this figure, it is clear that without focusing compensation, ROIs before the focus underestimate the attenuation slope while ROIs beyond the focus overestimate the attenuation slope. When the windowed region is close to the focus, we use the following correction

$$\left[\begin{aligned} & \exp\left(\frac{2(z_T + z_o - F_{\text{transmit}})^2}{(w_{z_{\text{transmit}}}(f))^2}\right) \\ & \cdot \exp\left(\frac{2(z_T + z_o - F_{\text{recv}})^2}{(w_{z_{\text{recv}}}(f))^2}\right) \end{aligned} \right] \quad (5.15)$$

Fig. 5.3 Error in attenuation estimate both with and without focusing compensation for a simulated 33 MHz spherically focused transducer intended to assess cervical ripening in rats taken from (Bigelow et al. 2008). The source had a focal length 9 mm and $z_0 = 0$ in this figure corresponds to the focus



before finding the center frequency. This correction is based on the assumption that the beam can be approximated by a Gaussian function in the focal region (Bigelow et al. 2008).

5.3.2 Spectral Difference Method for Local Attenuation Estimation

Another common algorithm for estimating the local attenuation from an ROI is the spectral difference method (Parker and Waag 1983; Parker et al. 1988; Yao et al. 1990). The spectral difference method is sometimes referred to as the reference-phantom method because it uses a well-characterized reference phantom to correct for diffraction effects. In the spectral difference method, multiple overlapping windows are positioned throughout the ROI as shown in Fig. 5.4. An overlap of 50% between adjacent windows is common; however, other overlap values have been used. Power spectra from corresponding windows in a reference phantom are also acquired.

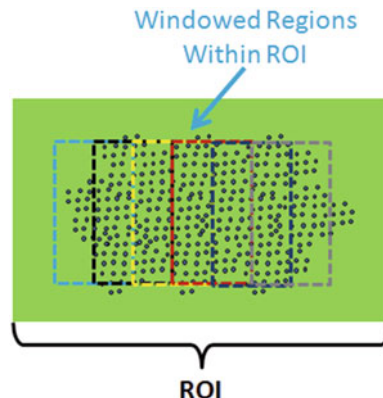


Fig. 5.4 Illustration of windowed regions within ROI when implementing the spectral difference algorithm

Importance of Sound Speed

It is important to use a tissue-mimicking phantom with a sound speed similar to the expected sound speed of the tissue so that the diffraction properties are similar when estimating the attenuation.

After obtaining the power spectrum from each window for the sample and the reference, the

power spectra are divided to give

$$\frac{S_s(f)}{S_{\text{ref}}(f)} \propto \left[\frac{\exp(-4\alpha_{\text{tot}}(f)z_T) \cdot M_\gamma F_\gamma(f) D(f, \alpha_{\text{loc}})}{\exp(-4\alpha_{\text{ref}}(f)z_T) \cdot M_{\gamma\text{-ref}} F_{\gamma\text{-ref}}(f) D(f, \alpha_{\text{ref}})} \right] \quad (5.16)$$

where $\alpha_{\text{ref}}(f)$ is the attenuation of the reference phantom and $F_{\gamma\text{-ref}}(f)$ is the form factor describing the frequency dependence of the scattering from the phantom. Using the approximation in (5.7), (5.16) simplifies to

$$\frac{S_s(f)}{S_{\text{ref}}(f)} \propto \left[\frac{\exp(-4(\alpha_{\text{tot}}(f) - \alpha_{\text{ref}}(f))z_T)}{\exp(-4(\alpha_{\text{loc}}(f) - \alpha_{\text{ref}}(f))z_o) \cdot \frac{M_\gamma F_\gamma(f)}{M_{\gamma\text{-ref}} F_{\gamma\text{-ref}}(f)}} \right]. \quad (5.17)$$

Taking the natural logarithm of the above relation gives

$$\begin{aligned} S(f) &= \ln \left(\frac{S_s(f)}{S_{\text{ref}}(f)} \right) \\ &= 4(\alpha_{\text{ref}}(f) - \alpha_{\text{loc}}(f))z_o + C(f) \end{aligned} \quad (5.18)$$

where $C(f)$ is a function of frequency that depends on the scattering properties and total attenuation of the sample and reference phantoms. $C(f)$ does not depend on z_o provided the ROI is homogeneous. The attenuation of the sample is calculated from the change in $S(f)$ with z_o , i.e.,

$$\alpha_{\text{loc}}(f) = \alpha_{\text{ref}}(f) - \frac{1}{4} \frac{\partial S(f)}{\partial z_o}. \quad (5.19)$$

Importance of Homogeneous Region

The spectral difference method cannot be used to estimate the attenuation when the scattering properties change within the ROI as this would make $C(f)$ also a function of z_o (Labyed and Bigelow 2011).

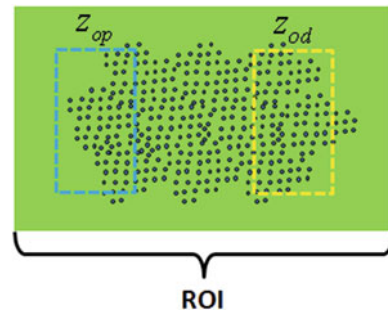


Fig. 5.5 Illustration of windowed regions within ROI when implementing the spectral log difference algorithm

5.3.3 Spectral Log Difference Method for Local Attenuation Estimation

A slightly modified form of the spectral-difference method is the spectral-log-difference method (Kuc and Schwartz 1979; Kuc 1980, 1984; Insana et al. 1983). This method is slightly less dependent on changes in the scattering properties of the medium (Labyed and Bigelow 2011). The method begins by finding the backscattered power spectrum from two windowed regions within an ROI; one at the proximal edge of the ROI, z_{op} , and one at the distal edge of the ROI, z_{od} , as shown in Fig. 5.5. Once again the power spectra from the windowed regions of the sample are divided by corresponding spectra from a reference phantom yielding

$$\begin{aligned} S_p(f) &= \ln \left(\frac{S_s(f, z_{op})}{S_{\text{ref}}(f, z_{op})} \right) \\ &= 4(\alpha_{\text{ref}}(f) - \alpha_{\text{loc}}(f))z_{op} + C(f, z_{op}) \end{aligned} \quad (5.20)$$

$$\begin{aligned} S_d(f) &= \ln \left(\frac{S_s(f, z_{od})}{S_{\text{ref}}(f, z_{od})} \right) \\ &= 4(\alpha_{\text{ref}}(f) - \alpha_{\text{loc}}(f))z_{od} + C(f, z_{od}) \end{aligned} \quad (5.21)$$

where the subscript p refers to the proximal windowed region and the subscript d refers to the distal windowed region. Subtracting (5.20) and

(5.21) yields

$$\begin{aligned} S_\Delta(f) &= S_p(f) - S_d(f) \\ &= \left[4(\alpha_{\text{ref}}(f) - \alpha_{\text{loc}}(f))(z_{op} - z_{od}) \right. \\ &\quad \left. + C(f, z_{op}) - C(f, z_{od}) \right]. \end{aligned} \quad (5.22)$$

Also, if we assume that the frequency dependence of the scattering does not change within the ROI for the sample (only possibly the acoustic concentration), then

$$C(f, z_{op}) - C(f, z_{od}) \cong C_\Delta(z_{op}, z_{od}) \quad (5.23)$$

which is independent of frequency (Labyed and Bigelow 2011). Therefore, the local attenuation within the ROI can be estimated by finding

$$\begin{aligned} &\left[\frac{S_\Delta(f)}{4(z_{od} - z_{op})} + \alpha_{\text{ref}}(f) \right] \\ &= \alpha_{\text{loc}}(f) + \frac{C_\Delta(z_{op}, z_{od})}{4(z_{od} - z_{op})} \end{aligned} \quad (5.24)$$

and then performing a fit as a function of frequency to eliminate the C_Δ term. The most common approach is to assume a frequency dependence of $\alpha_{\text{loc}}(f) = \alpha_0 f + \beta_b$, and then perform a linear fit as a function of frequency to determine α_0 .

ROI Size Needed for Spectral Log Difference Method

A good rule of thumb is to have $(z_{od} - z_{op}) > 15$ pulse lengths and at least 15 independent echoes when using a linear approximation for the attenuation with the spectral-log-difference method. Smaller values tend to produce large variance of the estimates. However, these values are also dependent on the frequency range available for obtaining the estimates.

5.3.4 Hybrid Method for Local Attenuation Estimation

A third method for estimating the attenuation within an ROI is the hybrid method (Kim and Varghese 2008). The hybrid method has very similar performance to the spectral log-difference method (Labyed and Bigelow 2011). The hybrid method once again begins by calculating the power spectra for multiple windowed regions within an ROI and a corresponding reference phantom. The sample and reference power spectra are then divided yielding

$$\frac{S_s(f, z_o)}{S_{\text{ref}}(f, z_o)} \propto \left[\frac{\exp(-4(\alpha_{\text{tot}}(f) - \alpha_{\text{ref}}(f))z_T)}{\frac{\exp(-4(\alpha_{\text{loc}}(f) - \alpha_{\text{ref}}(f))z_o)}{\frac{M_\gamma(z_o)F_\gamma(f)}{M_{\gamma_ref}(z_o)F_{\gamma_ref}(f)}}} \right] \quad (5.25)$$

where once again we have assumed that the frequency dependence of the scattering **does not change** within the ROI. Note that a change in the acoustic concentration $M_\gamma(z_o)$ within the ROI does not impact the attenuation estimate. The power-spectra ratio for each window is then multiplied by a Gaussian function and corrected for the attenuation of the reference phantom to yield

$$\begin{aligned} &\text{GRS}(f, z_o) \\ &= \exp\left(-\frac{(f-f_c)^2}{2\sigma_c^2}\right) \frac{S_s(f, z_o)}{S_{\text{ref}}(f, z_o)} \exp(-4\alpha_{\text{ref}}(f)z_o) \\ &\propto \left[\frac{\exp\left(-\frac{(f-f_c)^2}{2\sigma_c^2}\right) \exp(-4(\alpha_{\text{tot}}(f) - \alpha_{\text{ref}}(f))z_T)}{\exp(-4\alpha_{\text{loc}}(f)z_o) \frac{M_\gamma(z_o)F_\gamma(f)}{M_{\gamma_ref}(z_o)F_{\gamma_ref}(f)}} \right] \end{aligned} \quad (5.26)$$

which is approximately equal to

$$\text{GRS}(f, z_o) \propto \left[\frac{\exp\left(-\frac{(f-\tilde{f}_c)^2}{2\tilde{\sigma}_c^2}\right)}{\exp(-4\alpha_{\text{loc}}(f)z_o)} \right] \quad (5.27)$$

because of the frequency dependence of total attenuation and scattering. If we assume that

the attenuation within the ROI has the form $\alpha_{\text{loc}}(f) = \alpha_0 f + \beta_b$, then (5.27) becomes

$$\begin{aligned} \text{GRS}(f, z_o) &\propto e^{-\frac{(f-\tilde{f}_c)^2}{2\tilde{\sigma}_c^2}} e^{-4\alpha_o f z_o} \\ &\propto \exp\left(-\frac{(f-\tilde{f}'_c(z_o))^2}{2\tilde{\sigma}_c^2}\right) \end{aligned} \quad (5.28)$$

where

$$\tilde{f}'_c(z_o) = \tilde{f}_c - 4\tilde{\sigma}_c^2 \alpha_o \cdot z_o. \quad (5.29)$$

Therefore, the attenuation slope can be calculated as

$$\alpha_o = -\frac{1}{4\tilde{\sigma}_c^2} \frac{\partial \tilde{f}'_c}{\partial z_o}. \quad (5.30)$$

Selection of f_c and $\tilde{\sigma}_c$ for Hybrid Method

f_c is often chosen as the frequency where the spectral peak of $\text{GRS}(f, z_o)$ is approximately in the middle of the usable frequency range. Similarly, $\tilde{\sigma}_c$ is chosen as the bandwidth of the received echoes from the ROI.

5.3.5 Comparison of Spectral Difference, Spectral Log-Difference, and Hybrid Methods for Local Attenuation Estimation

Before concluding our discussion of local attenuation estimation, we will briefly compare the performance of the three algorithms that utilize a reference phantom as was originally reported in (Labyed and Bigelow 2011). These algorithms were selected for comparison because they are the easiest to implement when using modern ultrasound clinical array transducers. We use computer simulations to evaluate the dependence of the algorithms on the number of independent echoes and the number of pulse lengths utilized

to obtain the estimates. The simulations utilized a 10 MHz source with a 5 cm focal length and a 50% –3-dB bandwidth. We assume that the local attenuation has the form $\alpha_{\text{loc}}(f) = \alpha_0 f$. Figure 5.6 shows the variance of the estimates as a function of ROI size.

From this figure, it is clear that for any given ROI size, the spectral-difference method has the lowest variance. However, the spectral-difference method is also significantly impacted by any heterogeneities in the tissue (Kim and Varghese 2008; Labyed and Bigelow 2011). The spectral-log difference method and the hybrid method have comparable performance both in terms of variance (Fig. 5.6) and in terms of their robustness to tissue heterogeneity (Labyed and Bigelow 2011). Neither the spectral log-difference nor the hybrid method are impacted by changes in acoustic concentration within the ROI. However, a bias will be introduced when there is a change in the frequency dependence of the scattering. If we assume that the change in frequency dependence results from a variation in the effective scatterer diameter, then the bias is approximately given by

$$\begin{aligned} \text{Error (Np/cm} &-\text{MHz)} \\ &\approx \frac{16.32 f_{\text{mid}} (a_{\text{eff}}^2(z_p) - a_{\text{eff}}^2(z_d))}{c^2(z_p - z_d)} \end{aligned} \quad (5.31)$$

where f_{mid} is the middle frequency of the usable frequency range.

5.4 Total Attenuation Estimation Algorithms

When performing ultrasound tissue characterization, it is critically important to correct for the frequency dependence of the attenuation along the propagation path. Therefore, in this section, we will summarize the two types of algorithms that have been proposed for this purpose. Both of these algorithms assume that the **total attenuation for the sample has a linear frequency dependence** given by $\alpha_{\text{tot}}(f) = \alpha_s f$. A third approach, which will not be discussed in detail, would be to use estimates of local attenuation in each of the intervening tissue layers and then

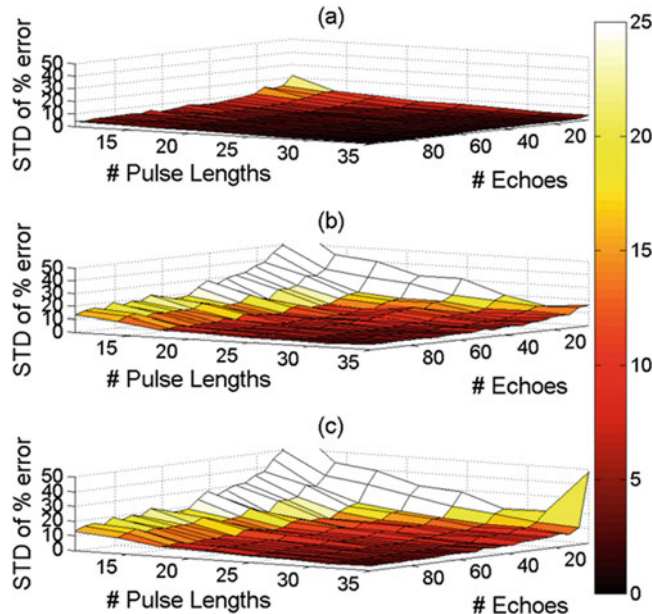


Fig. 5.6 The standard deviation (STD) in the percent error of the attenuation coefficient estimates that were obtained using the spectral difference method from the homogeneous sample, versus the number of pulse lengths

and the number of echoes per ROI for the (a) spectral difference algorithm, (b) the spectral-log difference algorithm, and (c) the hybrid algorithm

sum the estimates to calculate the total attenuation from (5.2) directly. While this third approach works for some applications with clearly identifiable and relatively thick layers, it tends to have problems when the intervening tissue layers are more complex.

5.4.1 Multiple Filter Algorithm for Total Attenuation Estimation

The first type of algorithm that will be discussed is the multiple-filter algorithm. This algorithm requires either applying multiple Gaussian filters to the backscattered waveforms or using multiple transmit frequencies that span the bandwidth of the transducer (Bigelow 2008, 2010a, b; Labyed and Bigelow 2010). Because most modern tissue characterization applications utilize a clinical array transducer, we will focus our discussion on the use of multiple filters. We use echoes from a reference phantom to correct for diffraction effects.

The algorithm begins with finding the power spectra from a single windowed region in the tissue sample and from the corresponding region in a well-characterized reference phantom. After correcting for the attenuation in the reference phantom, the ratio of the spectra is given by

$$\frac{S_s(f)}{S_{\text{ref}}(f)} e^{-\alpha_{\text{ref}}(f)z_T} \propto \exp(-4\alpha_s f z_T) \frac{F_\gamma(f)}{F_{\gamma_{\text{ref}}}(f)} \quad (5.32)$$

where we can assume that the window is located at $z_0 = 0$ without loss of generality. We then assume that the frequency dependence of the scattering is approximately given by $F_\gamma(f) \propto \exp(-Af^n)$ where n is approximately equal to 2. While this is clearly true for the Gaussian form factor, it is also true over a limited ka_{eff} range for other common form factors as shown in Fig. 5.7 taken from (Bigelow 2010a, b).

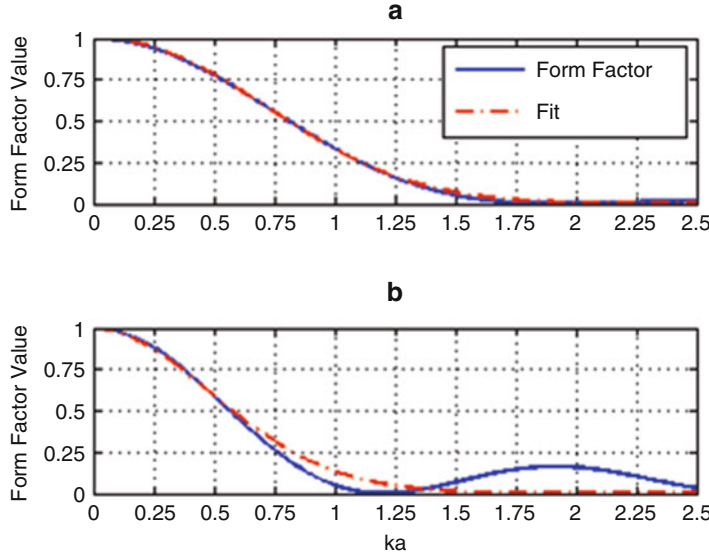


Fig. 5.7 Form factor with fit of the form $\exp(-Af^n)$ for (a) fluid-filled sphere and (b) spherical shell taken from (Bigelow 2010a, b)

In this figure, the fits for each form factor are given by

$$\begin{aligned} F_{\gamma_Sphere}(f, a_{\text{eff}}) &\cong \exp(-1.11(ka_{\text{eff}})^{2.167}), \\ F_{\gamma_Shell}(f, a_{\text{eff}}) &\cong \exp(-2(ka_{\text{eff}})^{1.914}) \end{aligned} \quad (5.33)$$

and the fit was performed for ka_{eff} from 0 to 1.2 because ka_{eff} values less than 1.2 are of the greatest interest when quantifying the tissue microstructure.

If we then multiply (5.32) by a series of Gaussian filters, we can show that

$$\frac{S_s(f)}{S_{\text{ref}}(f)} e^{-\alpha_{\text{ref}}(f)z_T} \exp\left(-\frac{(f-f_c)^2}{2\sigma_c^2}\right) \cong C_1 \exp\left(-\frac{(f-\tilde{f}_c)^2}{2\sigma_c^2}\right) \quad (5.34)$$

where

$$\begin{aligned} \tilde{f}_c &\cong [1 - 2\tilde{\sigma}_c^2(A_s - A_r)] f_c + 4\tilde{\sigma}_c^2 z_T \alpha_s \\ \tilde{\sigma}_c^2 &= \frac{\sigma_c^2}{1 - 2\tilde{\sigma}_c^2(A_s - A_r)} \end{aligned} \quad (5.35)$$

using a derivation similar to that performed for the hybrid method discussed previously. Therefore,

for each filter applied, we can find

$$\xi(f_c) = \frac{(f_c - \tilde{f}_c)}{4\tilde{\sigma}_c^2 z_T} \cong \frac{(A_s - A_r)}{2z_T} f_c - \alpha_s. \quad (5.36)$$

The intercept of $\xi(f_c)$ with respect to f_c will give the slope of the frequency dependence for the total attenuation.

One of the challenges when using the multiple-filter method is determining the optimal number of filters. In an early work, the use of four filters was examined (Bigelow 2010a, b; Labyed and Bigelow 2010). For the first three filters, the center frequency of each filter was calculated as

$$\begin{aligned} f_{c1} &= f_{\min} + \frac{f_{\max} - f_{\min}}{4} \\ f_{c2} &= f_{c1} + \frac{f_{\max} - f_{\min}}{4} \\ f_{c3} &= f_{c2} + \frac{f_{\max} - f_{\min}}{4} \end{aligned} \quad (5.37)$$

where f_{\min} and f_{\max} were the smallest and largest frequencies of the usable frequency range, respectively. The usable frequency range is the range of frequencies in the power spectrum for which the power spectrum exceeds some level (e.g., -20 dB) based on the noise level of the received echoes. Once these center frequencies

were set, the bandwidths were determined by finding the percent bandwidth such that f_{\min} corresponded to the -10 dB to -15 dB bandwidth for the filter as calculated from

$$\sigma_{c1}^2 = \left(\frac{10(f_{c1} - f_{\min})^2}{2 \ln(10) (-BW_{dB})} \right) \quad (5.38)$$

where BW_{dB} is the desired bandwidth (i.e., -10 dB or -15 dB) for the first filter that would correspond with f_{\min} . The bandwidths of the other three filters were then selected to have the same -3 -dB percent bandwidth as the first filter. The remaining fourth filter was then selected to span the entire usable frequency range of the backscattered echoes.

Recently, a statistical analysis study was performed on the multiple-filter algorithm to derive an expression for the standard deviation of the total attenuation estimate as a function of ROI size, bandwidth, and number of Gaussian filters (Labyed 2010). The focus was on the variance of the estimates as this is the limiting criterion when estimating the total attenuation (Bigelow and O'Brien Jr. 2005a, b; Bigelow et al. 2005; Bigelow 2008, 2010a, b; Labyed and Bigelow 2010). While it is trivial to get the attenuation correct on average, it is much more challenging to obtain precise estimates especially when the ROI is small. The statistical analysis used non-overlapping (independent) filters to simplify the mathematics and found that the variance in the total attenuation estimate was proportional to

$$\text{var}(\alpha_s) \propto \frac{(N_s + N_r)}{N_s N_r} \cdot \frac{1}{\left\{ \sum_{j=1}^K \left[\sum_{i=1}^M (f_i - f_c(j))^2 \right] \right\} - \frac{\left\{ \sum_{j=1}^K \left[\sum_{i=1}^M (f_i - f_c(j))^2 \right] f_c(j) \right\}^2}{\sum_{j=1}^K \left\{ \left[\sum_{i=1}^M (f_i - f_c(j))^2 \right] f_c(j)^2 \right\}}} \quad (5.39)$$

where f_i are the individual frequency components of the spectrum, $f_c(j)$ is the center frequency of the j^{th} Gaussian filter when a total of K filters are used, and N_s and N_r are the number of independent echoes used to estimate the power spectra of the sample and reference, respectively.

Precision of Total Attenuation Estimation Algorithms

The precision of the total attenuation estimation algorithms is strongly influenced by the bandwidth of the source and the number of independent echoes used to obtain the estimate. There is also some dependence on the size of the windowed region used to estimate the power spectrum as this can influence the accuracy of the power spectra estimate.

The results of the statistical analysis also revealed that the optimal number of non-overlapping filters is equal to two. In addition, the standard deviation of the total attenuation estimate decreases with increasing ROI size, i.e., with increasing number of independent echo lines used to compute the power spectra, and increasing time window length used to gate the echo lines. Note that the total attenuation is estimated from the power spectrum that is obtained by averaging the power spectra of the windows within the ROI. Therefore, using a large number of echo lines improves the estimate of the power spectrum, and hence improves the estimate of the total attenuation.

The results of the statistical analysis were validated using numerical simulations. Backscattered signals were simulated for a sample and a reference that had attenuation coefficients of 0.7 dB/cm-MHz and 0.5 dB/cm-MHz, respectively. The sample scatterers had a Gaussian Form Factor with a 20 μm effective radius, while the reference had spherical shell scatterers with 10 μm radii. Both the sample and the reference had a scattering density of 100 mm^{-3} , corresponding to approximately 10 scatterers per resolution cell, which is adequate for fully developed speckle.

Figure 5.8 shows plots of the theoretical and calculated standard deviation of the total attenuation estimate from the simulated backscattered signals as a function of the number of non-overlapping filters. It is clear

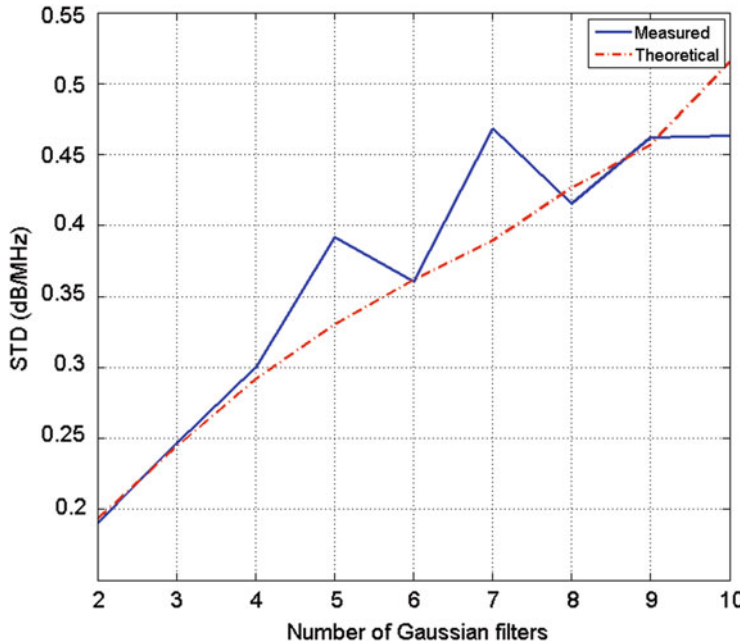


Fig. 5.8 Plots of the theoretical and calculated standard deviation of the total attenuation estimate from the simulated backscattered signals, obtained with the multiple-

filter method using an ROI length of 10 pulse lengths and an ROI width of 60 independent echo lines, with respect to the number of non-overlapping filters

that using two independent Gaussian filters yields the smallest standard deviation in the estimate of the total attenuation. As shown in Fig. 5.9, the STD in the total attenuation estimate decreased with increasing number of independent echoes.

5.4.2 Spectral Fit Algorithm for Total Attenuation Estimation

The second type of algorithm used for obtaining the frequency-dependent attenuation along the propagation path involves estimating the frequency dependence of the backscatter and the attenuation simultaneously. Initially, the tissue was assumed to satisfy a Gaussian form factor ($F_{\gamma_Gaussian}(f, a_{eff}) = \exp(-0.827(k \cdot a_{eff}))$) and a fit was performed to estimate both α_s and a_{eff} (Bigelow and O'Brien Jr. 2005a, b; Bigelow et al. 2005). Other authors have extended the algorithm to allow for a more general form for the backscatter ($BSC(f) = b^{\mu}$) and then perform a fit for b, n ,

and α_s (Nam et al. 2011). However, we will focus on the original spectral fit algorithm where only two parameters were estimated.

The spectral fit algorithm begins by dividing the spectra from the windowed region of the sample by the spectra from the windowed region of a known reference. Initially, a planar target was used as a reference, but a reference phantom has also been used. Our derivation here will assume a reference phantom is used. After dividing the spectra, the result is multiplied by the attenuation and backscatter terms for the reference as given by

$$S_{fit}(f) = \frac{S_s(f)}{S_{ref}(f)} e^{-\alpha_{ref}(f)z_T} BSC_{ref}(f) \propto \exp(-4\alpha_s f z_T) F_{\gamma}(f). \quad (5.40)$$

Assuming a Gaussian form factor for $F_{\gamma}(f)$, the natural log of (5.40) will yield

$$-\ln(S_{fit}(f)) = 0.827 \left(\frac{2\pi}{c} a_{eff} \right)^2 f^2 + 4\alpha_s f z_T + \text{Constant} \quad (5.41)$$

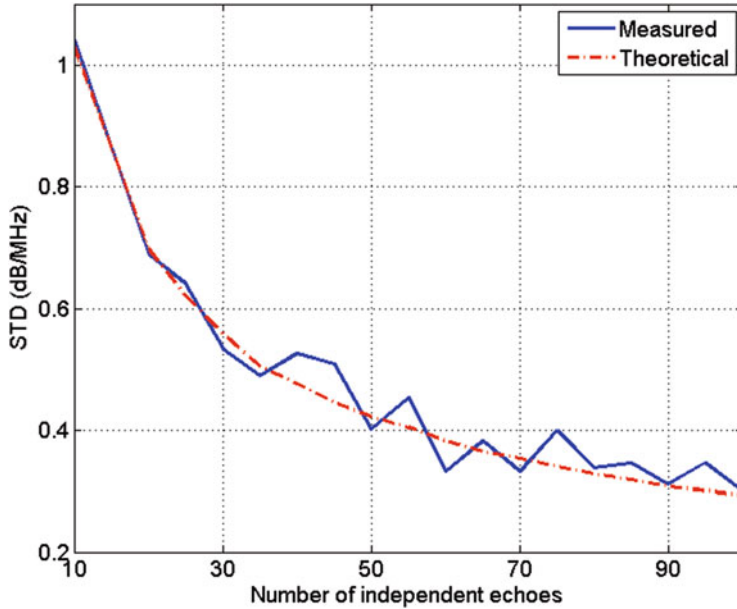


Fig. 5.9 Plots of the theoretical and calculated standard deviation of the total attenuation estimate from the simulated backscattered signals, obtained using the multiple

filter method with two Gaussian filters and an ROI length (time window size) of 10 pulse lengths with respect to the number of independent echoes per ROI

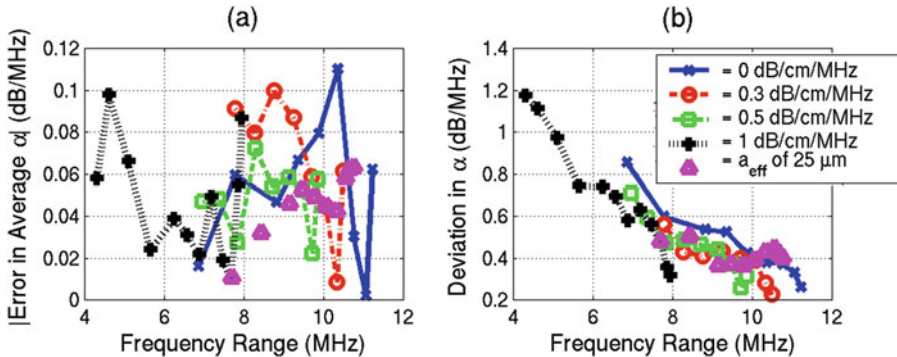


Fig. 5.10 Plots of the (a) accuracy and (b) precision for a range of attenuations and scatterer sizes taken from (Bigelow and O'Brien Jr. 2005a, b) estimated from sim-

ulated backscattered signals illustrating the importance of the frequency bandwidth when estimating the total attenuation using the spectral fit algorithm

where a simple polynomial fit will yield both the total attenuation slope, α_s , and the effective scatterer radius, a_{eff} .

When implementing the spectral fit algorithm, more accurate and precise estimates are obtained as the frequency range ($\Delta f = f_{\max} - f_{\min}$) used to obtain the attenuation estimate increases, similar to the case for the multiple filter method (Labyed 2010). Figure 5.10 shows average error and the deviation as a function of frequency

range for attenuation values of 0, 0.3, 0.5, and 1 dB/cm-MHz with a_{eff} of 5–105 μm , 5–75 μm , 5–85 μm , and 5–150 μm , respectively taken from (Bigelow and O'Brien Jr. 2005a, b). Also, shown are the results for a 25 μm a_{eff} and attenuation values varying from 0 to 1 dB/cm-MHz. The results were obtained using a 3 mm hamming window (13.5 pulse lengths) and 25 independent echoes. Regardless of the scattering and attenuation properties of the sample, a consistent vari-

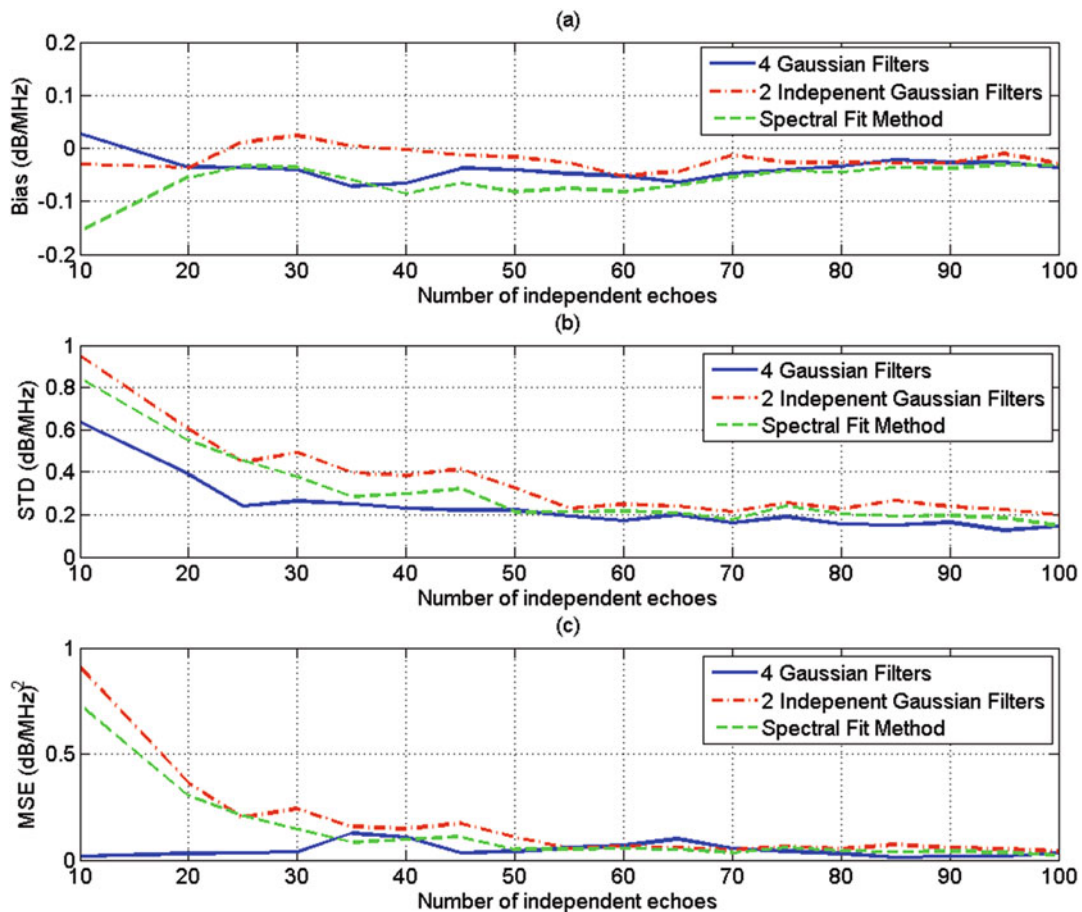


Fig. 5.11 Plots of the (a) bias (b) STD, and (c) MSE of the estimate α_s , which was obtained using the multiple filter method with two independent Gaussian filters, the multiple filter method with four overlapping Gaussian

filters, and the spectral-fit method, with respect to the number of independent of echoes per ROI for an ROI length of 10 pulse lengths

ance is achieved provided the same Δf is used to obtain the estimates. Figure 5.10 also reiterates that when finding the total attenuation, achieving good accuracy is much easier than achieving small variance.

Methods to Improve Usable Frequency Range

Because the total attenuation estimation algorithms are highly dependent on bandwidth. One way of increasing the bandwidth is to use higher frequency transducers. Using higher frequency transducers

however limits the penetration depth into the tissue. Recently, methods that are based on coded excitation and pulse compression have been shown to improve the bandwidth and penetration depth (Oelze 2007). Surface micro-machined capacitive ultrasonic transducers are new designs that demonstrated a big improvement in the bandwidth (Ladabaum et al. 1998; Ergun et al. 2003). Some ultrasound clinical systems, however, allow the transducer to be excited at three different center frequencies. This

(continued)

(continued)

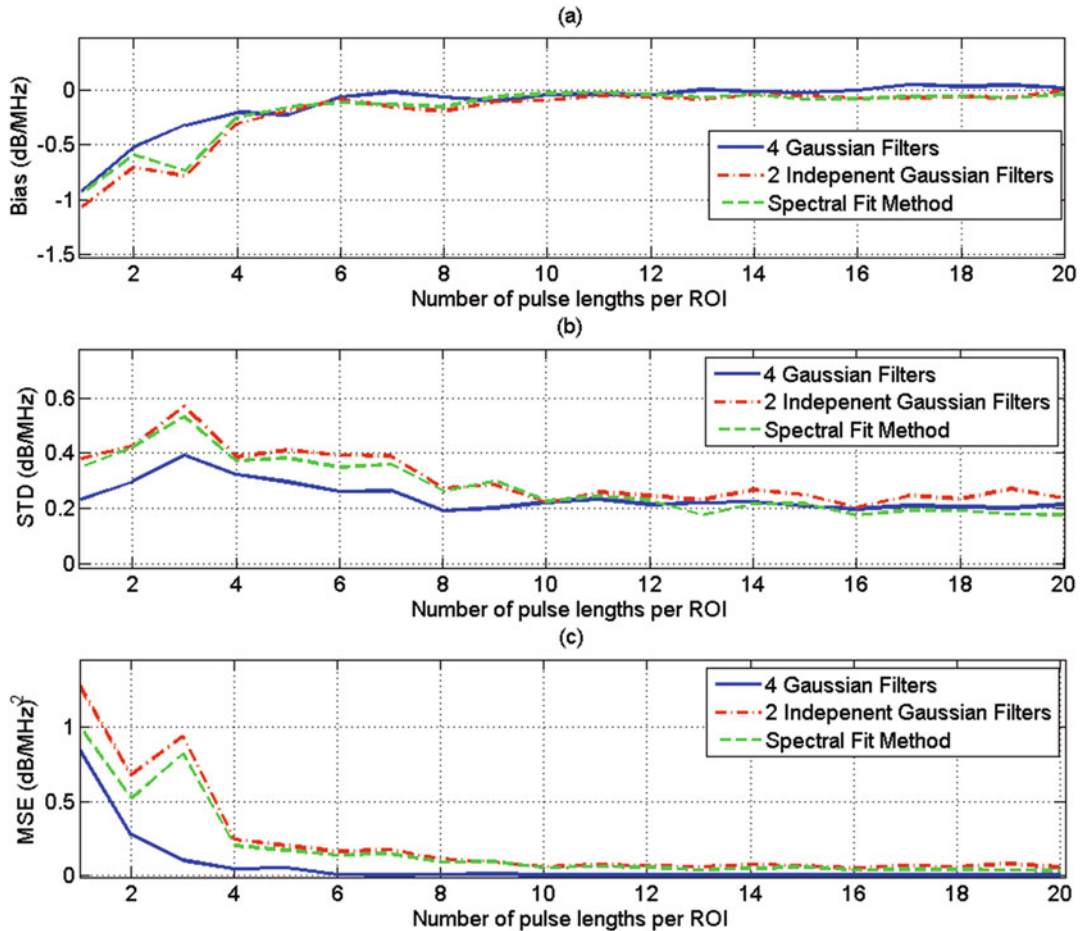


Fig. 5.12 Plots of the (a) bias (b) STD, and (c) MSE of the estimate α_s , which was obtained using the multiple filter method with two independent Gaussian filters, the multiple filter method with four overlapping Gaussian

filters, and the spectral-fit method, with respect the number of pulse lengths per ROI for an ROI that has 50 independent echo lines

feature can be used to increase the usable frequency range in the power spectrum of the backscattered signal.

5.4.3 Comparison of Spectral Fit Algorithm and Multiple Filter Algorithm

As described in Sect. 5.4.1, the optimal number of filters for the multiple-filter method is two. However, that result was only valid when the Gaussian filters were non-overlapping. Therefore, it is im-

portant to test whether using overlapping filters can improve the attenuation estimates. A comparison of the performance between the multiple-filter method and the spectral-fit method is also important to consider.

In this section, we compare the bias, STD, and mean squared error (MSE) of the total attenuation estimates obtained with the spectral-fit method, the multiple-filter method that uses two non-overlapping filters, and the multiple-filter method that uses four overlapping filters as described in (see Sect. 5.4.1). We use the numerical simulations described in Sect. 5.4.1 to perform these tests. Figure 5.11 shows the results as a function of number of independent echoes in the sample while Fig. 5.12 gives the results as a func-

tion of number of pulse lengths used to estimate the backscattered power spectrum. The results indicate that the variance strongly depends on the number of echoes with only a weak dependence on the number of pulse lengths. However, a slight bias is introduced for smaller pulse lengths that is not observed when the number of independent echoes tends toward zero.

ROI Size Needed for Total Attenuation Algorithms

A good rule of thumb is to have a windowed region of at least 10 pulse lengths and at least 25 to 35 independent echoes. However, these values are also dependent on the frequency range available for obtaining the estimates.

Based on Figs. 5.11 and 5.12, the MSE is comparable for both the spectral fit method and the multiple filter method with two independent Gaussian filters. However, the spectral fit method provides a slightly smaller STD and a slightly larger bias compared to the two independent filter method. The figures also show in the multiple filter method that using three overlapping Gaussian filters and a fourth filter that spans the entire usable frequency range gives better results than using only two independent Gaussian filters. This latter result demonstrates that the multiple filter method could potentially be improved to yield smaller errors in the attenuation estimates by using two overlapping filters.

References

- Baldeweck T, Laugier P et al (1993) Application of autoregressive spectral analysis for ultrasound attenuation: interest in highly attenuating medium. Proc IEEE Ultrason Symp 1182:1181–1186
- Baldeweck T, Herment A et al (1994) Attenuation estimation in highly attenuating media using high frequencies: a comparison study between different mean frequency estimators. Proc IEEE Ultrason Symp 1783:1783–1786
- Baldeweck T, Laugier P et al (1995) Application of autoregressive spectral analysis for ultrasound attenuation estimation: interest in highly attenuating medium. IEEE Trans Ultrason Ferroelectr Freq Control 42(1):99–110
- Barber FE (1991) The scanning acoustic microprobe: I. analysis and synthesis of a spherically symmetric point spread function. J Acoust Soc Am 90(1):1–10
- Bigelow TA (2004) Estimating the medical ultrasound *in vivo* power spectrum. PhD Electrical Engineering. Urbana, University of Illinois, p 243
- Bigelow TA (2008) Ultrasound attenuation estimation using backscattered echoes from multiple sources. J Acoust Soc Am 124(2):1367–1373
- Bigelow TA (2010a) Estimating the total ultrasound attenuation along the propagation path by applying multiple filters to backscattered echoes from a single spherically focused source. IEEE Trans Ultrason Ferroelectr Freq Control 57(4):900–907
- Bigelow TA (2010b) Improved algorithm for estimation of attenuation along propagation path using backscattered echoes from multiple sources. Ultrasonics 50(4–5):496–501
- Bigelow TA, O'Brien WD Jr (2004a) Scatterer size estimation in pulse-echo ultrasound using focused sources: calibration measurements and phantom experiments. J Acoust Soc Am 116(1):594–602
- Bigelow TA, O'Brien WD Jr (2004b) Scatterer size estimation in pulse-echo ultrasound using focused sources: theoretical approximations and simulation analysis. J Acoust Soc Am 116(1):578–593
- Bigelow TA, O'Brien WD Jr (2005a) Evaluation of the spectral fit algorithm as functions of frequency range and Dk_{eff} . IEEE Trans Ultrason Ferroelectr Freq Control 52(11):2003–2010
- Bigelow TA, O'Brien WD Jr (2005b) Signal processing strategies that improve performance and understanding of the quantitative ultrasound SPECTRAL FIT algorithm. J Acoust Soc Am 118(3):1808–1819
- Bigelow TA, O'Brien WD Jr (2006) Impact of local attenuation approximations when estimating correlation length from backscattered ultrasound echoes. J Acoust Soc Am 120(1):546–553
- Bigelow TA, Oelze ML et al (2005) Estimation of total attenuation and scatterer size from backscattered ultrasound waveforms. J Acoust Soc Am 117(3):1431–1439
- Bigelow TA, McFarlin BL et al (2008) In vivo ultrasonic attenuation slope estimates for detecting cervical ripening in rats: preliminary results. J Acoust Soc Am 123(3):1794–1800
- Ergun AS, Yaralioglu GG et al (2003) Capacitive micro-machined ultrasonic transducers: theory and technology. J Aerosp Eng 16(2):76–84
- Girault JM, Ossant F et al (1998) Time-varying autoregressive spectral estimation for ultrasound attenuation in tissue characterization. IEEE Trans Ultrason Ferroelectr Freq Control 45(3):650–659
- Insana M, Zagzebski J et al (1983) Improvements in the spectral difference method for measuring ultrasonic attenuation. Ultrason Imaging 5(4):331–345
- Insana MF, Wagner RF et al (1990) Describing small-scale structure in random media using pulse-echo ultrasound. J Acoust Soc Am 87(1):179–192
- Kim H, Varghese T (2007) Attenuation estimation using spectral cross-correlation. IEEE Trans Ultrason Ferroelectr Freq Control 54(3):510–519

- Kim H, Varghese T (2008) Hybrid spectral domain method for attenuation slope estimation. *Ultrasound Med Biol* 34(11):1808–1819
- Kuc R (1980) Clinical application of an ultrasound attenuation coefficient estimation technique for liver pathology characterization. *IEEE Trans Biomed Eng BME-27(6)*:312–319
- Kuc R (1984) Estimating acoustic attenuation from reflected ultrasound signals: comparison of spectral-shift and spectral-difference approaches. *IEEE Trans Acoust Speech Signal Process* 32(1):1–6
- Kuc R, Schwartz M (1979) Estimating the acoustic attenuation coefficient slope for liver from reflected ultrasound signals. *IEEE Trans Sonics Ultrason* 26(5):353–361
- Labyed Y (2010) Optimization and application of ultrasound attenuation estimation algorithms. PhD Electrical and Computer Engineering. Ames, Iowa State University, p 179
- Labyed Y, Bigelow TA (2010) Estimating the total ultrasound attenuation along the propagation path by using a reference phantom. *J Acoust Soc Am* 128(5):3232–3238
- Labyed Y, Bigelow TA (2011) A theoretical comparison of attenuation measurement techniques from backscattered ultrasound echoes. *J Acoust Soc Am* 129(4):2316–2324
- Ladabaum I, Xuecheng J et al (1998) Surface micromachined capacitive ultrasonic transducers. *IEEE Trans Ultrason Ferroelectr Freq Control* 45(3):678–690
- Nam K, Zagzebski JA et al (2011) Simultaneous backscatter and attenuation estimation using a least squares method with constraints. *Ultrasound Med Biol* 37(12):2096–2104
- Narayana PA, Ophir J (1983a) A closed form method for the measurement of attenuation in nonlinearly dispersive media. *Ultrason Imaging* 5:17–21
- Narayana PA, Ophir J (1983b) On the validity of the linear approximation in the parametric measurement of attenuation in tissues. *Ultrasound Med Biol* 9(4):357–361
- Oelze ML (2007) Bandwidth and resolution enhancement through pulse compression. *IEEE Trans Ultrason Ferroelectr Freq Control* 54(4):768–781
- Oelze ML, O'Brien WD Jr (2002) Frequency-dependent attenuation-compensation functions for ultrasonic signals backscattered from random media. *J Acoust Soc Am* 111(5 I):2308–2319
- Oelze ML, O'Brien WD Jr (2006) Application of three scattering models to characterization of solid tumors in mice. *Ultrason Imaging* 28(2):83–96
- Oosterveld BJ, Thijssen JM et al (1991) Ultrasound attenuation and texture analysis of diffuse liver disease: methods and preliminary results. *Phys Med Biol* 36(8):1039–1064
- Parker KJ, Waag RC (1983) Measurement of ultrasonic attenuation within regions selected from B-scan images. *IEEE Trans Biomed Eng BME-30(8)*:431–437
- Parker KJ, Lerner RM et al (1988) Comparison of techniques for in vivo attenuation measurements. *IEEE Trans Biomed Eng* 35(12):1064–1068
- Yao LX, Zagzebski JA et al (1990) Backscatter coefficient measurements using a reference phantom to extract depth-dependent instrumentation factors. *Ultrason Imaging* 12(1):58–70



Recent Advances in Attenuation Estimation

6

Ivan M. Rosado-Mendez

Abstract

This chapter reviews some of the recent advances in the estimation of the local and the total attenuation, with an emphasis on reducing the bias and variance of the estimates. A special focus is put on describing the effect of power spectrum estimation on bias and variance, the introduction of regularization strategies, as well as on eliminating the need to use reference phantoms for compensating for system dependent effects.

Keywords

Attenuation · Local attenuation · Total attenuation · Bias · Precision · Regularization · Cost function · Reference phantom

motivated efforts to gain a deeper understanding on the different sources of error that affect the accuracy and precision of estimates of the local and the total attenuation. As a reminder from the previous chapter, the local attenuation coefficient, identified here as $\alpha_{loc}(f)$, where f indicates frequency, refers to the value of the attenuation coefficient within a small (10 mm^2 for a 10 MHz ultrasound pulse), macroscopically homogeneous section of tissue; the total attenuation coefficient $\alpha_{tot}(f)$ refers to the effective or cumulative attenuation from tissues between the transducer and the location of interest, and is used to compensate for attenuation losses in the estimation of the backscatter coefficient. The total attenuation is obtained by averaging the local attenuation across depth-varying local attenuation values $\alpha_{loc}(f, z')$ corresponding to different tissues between the transducer and a location of interest at depth z :

$$\alpha_{tot}(f) = \frac{1}{z} \int_0^{z'} \alpha_{loc}(f, z') dz'. \quad (6.1)$$

6.1 Introduction

During the past decade, quantitative ultrasound has seen a resurgence in clinical interest and its commercial implementation. This interest has

When a linear relationship is assumed between the attenuation coefficient (either α_{loc} or α_{tot}) and frequency, the constant of proportionality between α_{loc} or α_{tot} and the frequency is referred to as the specific attenuation coefficient (IEC

I. M. Rosado-Mendez (✉)
Medical Physics, University of Wisconsin-Madison,
Madison, WI, USA
e-mail: rosadomendez@wisc.edu

2010),¹ with units dB/cm-MHz, and indicated by $\alpha_{0,\text{loc}}$ or $\alpha_{0,\text{tot}}$, respectively. The following sections present an overview of recent research efforts focused on reducing sources of error in the estimates of α_{loc} and α_{tot} , aimed at facilitating their successful incorporation into clinical practice. Of note, this chapter builds on the descriptions of different attenuation estimation methods described by Labyed and Bigelow in the previous chapter.

6.2 Bias Reduction

Bias refers to the difference between the expected value of the estimated quantity, in this chapter either $\alpha_{0,\text{loc}}$ or $\alpha_{0,\text{tot}}$, and the true value. Bias in attenuation estimation is assessed under conditions in which a true value is available, such as in simulated echo signals from computational tissue-mimicking media with specified attenuation values, or in tissue-mimicking phantoms or ex vivo tissue samples in which attenuation is measured with independent techniques such as through-transmission immersion methods (Madsen et al. 1999). The sources of bias in the quantification of $\alpha_{0,\text{loc}}$ or $\alpha_{0,\text{tot}}$ depend on the specific assumptions and signal processing steps used in their estimation method, such as the spectral shift, the spectral difference, the spectral log-difference, and the hybrid methods.

In the case of the spectral shift method, one important source of bias is the presence of factors affecting the center frequency of the radiofrequency (RF) echo signal spectrum other than the frequency-dependent attenuation. Two of these factors are the axial variations of acoustic intensity caused by diffraction, and the high-frequency

noise associated with the limited response bandwidth of the transducer. To reduce the influence of these factors on the calculation of the center frequency of the RF signal spectrum, Klimonda et al. (2016) developed a bandwidth correction method based on determining the mean spectral frequency after applying a bandpass-filter to the echo signal spectrum and then computing the center frequency numerically by solving the following equation:

$$f_m = f_c - \frac{\sigma}{\sqrt{\pi}} \frac{\exp\left[-\left(\frac{f_2-f_c}{\sigma}\right)^2\right] - \exp\left[-\left(\frac{f_1-f_c}{\sigma}\right)^2\right]}{\operatorname{erf}\left[\frac{f_2-f_c}{\sigma}\right] - \operatorname{erf}\left[\frac{f_1-f_c}{\sigma}\right]} \quad (6.2)$$

where erf is the error function, f_1 and f_2 are the low- and high-frequency cutoffs of the bandpass filter, f_m is the mean spectral frequency, f_c is the center frequency, and σ is a bandwidth parameter of a Gaussian model of the spectrum. With this approach, the authors reported a maximum reduction of the bias of $\alpha_{0,\text{loc}}$ in a phantom with 0.7 dB/cm-MHz scanned with a 5.6 MHz center frequency single element transducer ($\sigma = 1.68$ MHz, bandpass filter 2–8 MHz) from approximately 0.3 dB/cm-MHz to approximately 0.1 dB/cm-MHz (Fig. 6.1). This approach is limited by the assumption of a Gaussian-shaped spectrum and a linear dependence of the local attenuation coefficient versus frequency.

In the case of the spectral difference method based on a reference phantom normalization, the bias can significantly increase when the tissue under characterization and the reference phantom have different sound speeds. This error is accentuated when a discrepancy exists between the tissue sound speed and the sound speed value assumed by the scanner's beamformer. These sound speed discrepancies produce a flawed compensation of spatial variations in echo amplitude caused by diffraction. Furthermore, the displayed distances would not correspond to actual distances in the tissue, and the spatial resolution would be degraded because of flawed focusing (Chen and Zagzebski 2004). Figure 6.2 reported by Nam et al. (2011a) shows the absolute error (expressed as a percentage) of the expected value of $\alpha_{0,\text{loc}}$

¹ Here, the attenuation coefficient in dB/cm-MHz is referred to as the specific attenuation coefficient, following the nomenclature of the International Electrotechnical Commission (IEC 2010). Of note, the units dB/cm-MHz value can be obtained in various ways, e.g., by dividing α_{tot} or α_{loc} by the frequency, by reporting the slope of a linear fit applied to the attenuation coefficient vs. frequency, or by explicitly incorporating a linear frequency dependence in the estimation method. The reader is referred to the original references for the exact method of computing the specific attenuation coefficient.

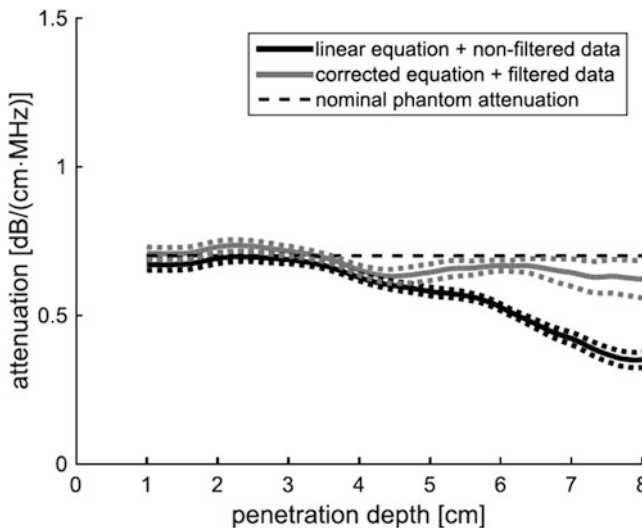


Fig. 6.1 Estimates of $\alpha_{0, \text{loc}}$ with (gray line) and without (black line) bandwidth correction in a homogeneous phantom. The dashed line indicates the expected attenuation

value of 0.7 dB/cm-MHz. (Reproduced with permission from Klimonda et al. 2016)

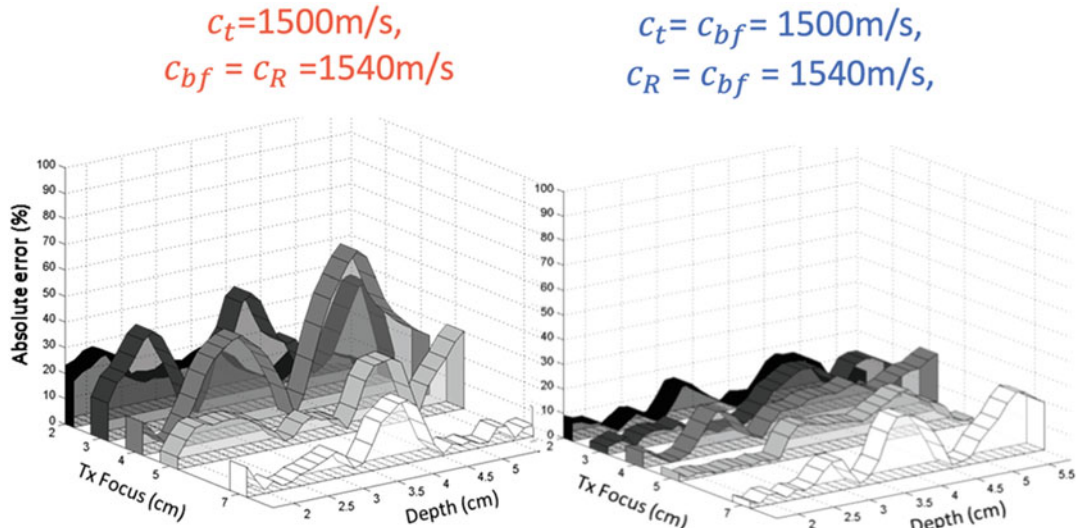


Fig. 6.2 Percent error of $\alpha_{0, \text{loc}}$ estimated using the spectral difference method with a reference phantom normalization in a tissue-mimicking phantom with a sound speed of 1500 m/s and $\alpha_{0, \text{loc}} = 0.56 \text{ dB/cm-MHz}$. Left side: Beamformer and reference phantom with sound speed of 1540 m/s. Right side: Beamformer sound speed matched

independently to the sample and the reference phantoms sound speeds. c_t = tissue (or sample phantom) sound speed, c_{bf} = beamformer sound speed, c_R = reference phantom sound speed. (Reproduced with permission of Nam et al. 2011a)

estimated from a tissue-mimicking phantom with a specific attenuation of 0.56 dB/cm-MHz and sound speed c_t (subscript t for “tissue” or “tissue-mimicking phantom”) 40 m/s lower than the scanner beamformer sound speed c_{bf} (subscripts bf

for “beamformer”) and the one of the reference phantom c_R (subscript R for “Reference”). The error is shown for different focal configurations and as a function of depth. When there is discrepancy between the sound speed values (left figure), the

largest error occurs near the transmit focus. The errors are minimized by adjusting the sound speed value assumed in the scanner beamformer to that of the sample or when placing the transmit focus at a depth greater than the transmit aperture. The bias caused by sound speed mismatch between the sample, reference, and scanner beamformer is relevant for various clinical applications. For example, in the context of breast lesion classification, Nasief et al. (2019) reported differences in the specific attenuation coefficient between fibroadenomas (most typical benign lesion) and carcinomas (most typical malignant lesion) of 0.3 dB/cm-MHz. Based on Fig. 6.2, errors in $\alpha_{0,\text{loc}}$ estimation of the order of 50% for an expected value of 0.56 dB/cm-MHz and caused by the sound speed mismatch among subcutaneous breast fat above the lesion, the reference phantom, and the beamformer sound speed (e.g., due to the presence of subcutaneous fat in the breast), could hide differences in $\alpha_{0,\text{loc}}$ between benign and malignant breast lesions.

The bias in the estimations of $\alpha_{\text{loc}}(f)$ can also be affected by nonlinear wave propagation, which refers to the nonlinear relationship between variations in pressure and density that occur as ultrasound waves of increasing amplitudes travel through a medium (Szabo 2014; Hamilton and Blackstock 1998). The nonlinear response of a material depends on the value of the B/A parameter, where B and A are the coefficients of the second- and first-order terms of a Taylor's series expansion of the equation of state relating acoustic pressure to the density (Duck 2002). B/A ranges from 6 to 8 in non-fatty soft tissues and up to 9 to 11 for fatty tissues (Dong et al. 1999). As a consequence of the nonlinear wave propagation, as the ultrasound pulse travels through tissue, its shape transitions from a sinusoid into a nonsymmetric, sawtooth shape that can eventually form a shock wave (Duck 2002). In the frequency domain, the formation of the shock wave results in the appearance of harmonics of the fundamental frequency. The tradeoff between the generation of harmonics due to nonlinearity and their higher absorption rate compared to the fundamental frequency is described (for plane waves) by the Gol'dberg number, Γ , which is

proportional to the nonlinear coefficient $\beta = 1 + \frac{B}{2A}$, and inversely proportional to the attenuation coefficient at the center frequency (Hamilton and Blackstock 1998). Although this phenomenon is the basis of tissue-harmonic imaging techniques aimed at improving the quality of conventional B-mode images (Tranquart et al. 1999; Anvari et al. 2015), it can also severely alter the shape of the RF signal spectrum obtained from common broadband pulses used in clinical ultrasound imaging. These effects can bias and increase the variance of $\alpha_{\text{loc}}(f)$ estimates as the amplitude of the ultrasound pulse increases. In a recent study, Coila and Oelze (2020) investigated errors in the estimation of $\alpha_{0,\text{loc}}$ using the spectral log difference method when gradually increasing the ultrasound pulse amplitude and, therefore, augmenting the effects of nonlinear wave propagation. To this end, the authors implemented the spectral log difference method in simulated and experimental backscattered echo signals produced with a 5 MHz single-element transducer and three phantoms: a sample phantom ($\alpha_{\text{loc}}(f) = 0.27f^{1.32}$, or 2.3 dB/cm @ 5 MHz, and $B/A = 6.8$), a high-attenuation reference phantom ($\alpha_{\text{loc}}(f) = 0.7f^{1.1}$, or 4.1 dB/cm @ 5 MHz, and $B/A = 6.9$) and a low-attenuation reference phantom ($\alpha_{\text{loc}}(f) = 0.028f^{1.75}$, or 0.47 dB/cm @ 5 MHz, and $B/A = 6.0$). The authors observed a larger bias in the estimates of $\alpha_{0,\text{loc}}$ as the pulse pressure amplitude increased, and that the absolute value of the bias was larger when using the low-attenuation phantom as a reference than when using the high-attenuation phantom. This finding was attributed to the difference in the rate of second harmonic generation and absorption between the sample and the reference as the ultrasound pulse amplitude increased. The authors recommended the use of a reference phantom with similar Gol'dberg number to that of the sample to reduce the effects of nonlinear wave propagation in the estimates of $\alpha_{0,\text{loc}}$ obtained with spectral log-difference method. In the clinical context, this problem may be particularly important in abnormal processes that involve fat infiltration, such as hepatic steatosis, due to the higher B/A value of fatty compared to non-fatty soft tissues. In a recent review, Ferraioli et al. (2022) reported

a range of attenuation values between 0.5 and 1.1 dB/cm-MHz from normal to steatotic liver. Therefore, the bias levels reported by Coila and Oelze (2020) of the order of 0.14 dB/cm-MHz represent 23% of the reported range of attenuation values in the liver.

Reducing the bias caused by nonlinear wave propagation can be particularly challenging in liver imaging because of the need to use lower frequencies to penetrate deep into the abdominal cavity. This makes it necessary to rely on other strategies to reduce the effects of nonlinear wave propagation, such as reducing transmit power or using shallow focal configurations. This could lead to noisier RF echo signals and, therefore, noisier attenuation estimates. In these scenarios, robust power spectrum estimators, such as Thomson's multitaper approach (described below) as well as angular compounding strategies (Gerig et al. 2004) could prove valuable.

Another source of bias when using the spectral difference and spectral shift methods is the violation of the assumption that the tissue scattering characteristics (either magnitude and/or frequency dependence) within the estimation region are diffuse (incoherent scattering) and homogeneous. Complex tissues such as breast impose a challenge to this assumption due to the presence of zones with different echogenicity as well as tissue interfaces and strong reflectors. To deal with this challenge, Civale et al. (2021) proposed a method to reduce the effects of the presence of atypically strong reflections in the estimates of $\alpha_{loc}(f)$. Segments of the RF echo signals containing these atypical echoes were identified using a depth-dependent echo amplitude threshold and then ignored in the estimation of $\alpha_{loc}(f)$. The threshold function was based on determining a depth- and frequency-dependent diffraction function, which was attenuation-corrected with a preliminary estimate of $\alpha_{loc}(f)$ by fitting an exponential decay to the acoustic power vs. depth. The threshold was then applied iteratively by adjusting the scaling parameter while minimizing a residual difference between the fit of the exponential decay to the diffraction-corrected spectrum considering a mean residual limit of 5.6–6 dB

based on the expected speckle component of the spectral variance. The authors tested the method on a gelatin-based phantom with pieces of leek that provided localized sources of strong scattering and reported a reduction between 60% and 80% in the errors of the estimated values of $\alpha_{loc}(f)$. Preliminary applications on *in vivo* images of normal breasts showed that the standard deviation of the attenuation coefficient estimated across different parts of the breast was reduced between 30% and 50%. An important challenge in the implementation of this algorithm is the need to independently characterize the diffraction field and obtain an initial estimate of the $\alpha_{loc}(f)$. This is particularly difficult when applying the method to clinical images where unknown values of the tissue sound speed could produce complicated diffraction patterns. Furthermore, the algorithm has a basic tradeoff between bias reduction from ignoring the presence of scattering outliers and increased variance from the reduction of echo information used in the estimation of $\alpha_{loc}(f)$.

Other methods have been devised to reduce the bias of estimates obtained from the spectral difference method caused by the presence of masses or inclusions with different echogenicity. The presence of such structures can cause a large overestimation of the attenuation coefficient in a transition from high to low echogenicity, and an underestimation in the opposite case. Rosado-Mendez et al. (2012) proposed to reduce this type of bias by combining estimates from overlapping estimation regions while ignoring atypically large or negative values. Figure 6.3 shows B-mode and attenuation coefficient maps of inclusions in a rodent-tumor-mimicking phantom described by Nam et al. (2011b). Inclusion A had $\alpha_{0,loc} = 1.02$ dB/cm-MHz and a backscatter coefficient on average -5.6 dB lower than the background within the analysis bandwidth (3.5–10 MHz); inclusion B had $\alpha_{0,loc} = 1.58$ dB/cm-MHz and a backscatter coefficient on average -1.3 dB lower than the background; the background had $\alpha_{0,loc} = 0.51$ dB/cm-MHz. Method 1 is the conventional spectral difference method and

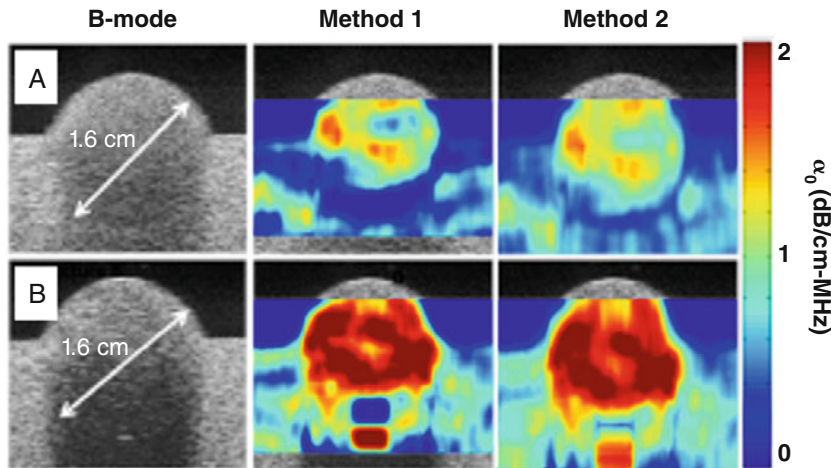


Fig. 6.3 Attenuation maps of the attenuation coefficient of a rodent-tumor mimicking phantom using the conventional spectral difference method (Method 1) and

the constrained-average version (Method 2). (Reproduced with permission of Rosado-Mendez et al. 2012)

Method 2 is the constrained-average version. The constrained approach reduced the average $\alpha_{0,\text{loc}}$ bias by 24% in inclusion A and by 11% in inclusion B compared to the conventional spectral difference method.

Other segmentation approaches have been proposed to identify regions in the RF echo signal field presenting conditions other than diffuse scattering. Luchies and Oelze (2015) proposed the use of spectral estimators with gaps to remove echo signals from specular reflectors in the estimation of the RF signal spectrum. Tests on tissue-mimicking phantoms demonstrated a significant reduction of mean square errors in the estimates of the backscatter coefficient. Although not evaluated by the authors, the spectral estimator with gaps could also be used to estimate first the attenuation coefficient, and then using these estimates in the calculation of the backscatter coefficient. This scenario would be more representative of the clinical application in which the attenuation value of tissue is not known *a priori*; in this case, the reduction in bias and variance provided by the spectral estimator with gaps could be even more valuable. Rosado-Mendez et al. (2016) proposed an automated algorithm that classifies each estimation region in one of five different scattering conditions: diffuse scattering, low scatterer number density, strong scatterer or

specular reflector, and periodic scatterers. This was achieved by performing joint comparisons of various parameters including the echo-amplitude signal-to-noise ratio, the generalized spectrum, and the uniformity of the phase distribution to values obtained in a phantom fabricated to provide diffuse scattering conditions. The authors suggested that this algorithm could be implemented as a step prior to the estimation of the attenuation coefficient for testing the assumption of diffuse scattering. More recently, Tehrani et al. (2021) proposed the use of convolutional neural networks to identify regions in the RF echo signal field with scatterer number densities not large enough to produce diffuse scattering, a condition identified by Rubert and Varghese (2014) to increase the variance of attenuation estimates compared to values obtained under diffuse scattering conditions.

This section discussed various sources of bias in the estimation of the local attenuation coefficient, such as the effects of sound speed mismatch between the tissue sample and the reference phantom, the presence of harmonics in the RF signal spectrum caused by nonlinear wave propagation, among others, as well as different ways to mitigate them. These challenges demonstrate the important tradeoffs among different sources of error and the need to reach a consensus on the best

strategies to estimate QUS features, in particular attenuation.

6.3 Elimination of a Reference Phantom Normalization

An aspect related to bias estimation in the quantification of the attenuation coefficient is the need to remove diffraction and system-dependent effects from the RF signal spectrum. This need is behind the normalization of the RF signal spectrum from the tissue sample with respect to the spectrum obtained from a reference phantom scanned under the same system settings as the tissue of interest (Yao et al. 1990). The need to scan a well-calibrated reference phantom to compensate for diffraction and system-dependent effects can represent significant extra work for the user, which could limit the practicality and clinical adoption of attenuation estimation methods based on a reference phantom normalization. Based on prior evidence of the reproducibility of echo signal power spectra among scanners and transducers of the same model (Guerrero et al. 2018), Labyed and Milkowski (2020) estimated the local attenuation in the human liver *in vivo* using reference spectra pre-stored in the scanner. Although this approach removed the need of scanning a reference phantom after acquiring data from the patient, it is still limited by the sources of bias associated with the use of a reference phantom described in the previous subsection.

An alternative approach is to remove the reference phantom normalization completely. To this end, Gong et al. (2019) proposed a frequency normalization method by which each frequency component of the spectrum is normalized by the value of the spectrum at the immediately adjacent lower frequency. In this approach, the power spectrum of the RF echo signal $S(f, z)$ is modeled as:

$$S(f, z) = G(f)TGC(z)D(f, z)A(f, z)BSC(f) \quad (6.3)$$

where $G(f)$ is the transducer's pulse-echo response, $TGC(z)$ is the time gain compensation,

$D(f, z)$ is a diffraction function, $A(f, z)$ is the exponential attenuation function, and $BSC(f)$ is the backscatter coefficient. Note that this model assumes that the TGC is frequency independent, that the BSC does not vary with depth, and that the attenuation coefficient is assumed to be homogeneous within the estimation region ($\alpha_{loc} = \alpha_{tot}$). By computing the log-ratio of the power spectrum values at frequencies f_{i-1} and f_i at depth z , $J(f_i, f_{i-1}, z) = \ln\left(\frac{S(f_i, z_r)}{S(f_{i-1}, z_r)}\right)$, the dependence on the TGC is eliminated. Next, by computing the difference $Y(f_i, f_{i-1}, z_k, z_r)$ of the log-ratio spectrum $J(f_i, f_{i-1}, z)$ at depths z_r and z_k separated by Δz , the terms related to the system transfer function $G(f)$ and the backscatter coefficient $BSC(f)$ are eliminated, leaving a model $Y_{model}(f_i, f_{i-1}, z_k, z_r | \alpha_s)$ that depends only on the local specific attenuation coefficient $\alpha_{0, loc}$ of the tissue sample:

$$\begin{aligned} Y_{model}(f_i, f_{i-1}, z_k, z_r | \alpha_{0, loc}) \\ = J(f_i, f_{i-1}, z_r) - J(f_i, f_{i-1}, z_k) \quad (6.4) \\ = 4\alpha_{0, loc}(f_i - f_{i-1})(\Delta z) \end{aligned}$$

The value of $\alpha_{0, loc}$ is estimated through a least squares approach:

$$\widehat{\alpha_{0, loc}} = \arg \min \sum_{r=1}^R \sum_{k=1}^K \sum_{i=1}^I \left(Y_{meas}(f_i, f_{i-1}, z_k, z_r) - Y_{model}(f_i, f_{i-1}, z_k, z_r | \alpha_{0, loc}) \right)^2 \quad (6.5)$$

The equation above is solved through a constrained least-squares minimization approach where the constraints on the values of $\alpha_{0, loc}$ are determined by solving eq. 6.4, substituting Y_{meas} for Y_{model} , and getting a distribution of estimates for different values of i , r , and k . The constraints are defined as the 12.5% and 87.5% quantiles. Tests on tissue-mimicking phantoms demonstrated reproducible attenuation estimates using echo signals acquired using systems with different beamforming strategies (plane-wave compounding and conventional focused ray line-based imaging). The method showed reduced accuracy in the focal region

when using tightly focused beams due to the violation of the assumption of a slowly varying diffraction function between adjacent frequency components. The authors recommended using plane wave imaging or focused ray-line-based imaging with a f-number ≥ 4 or higher to limit the estimation error of $\alpha_{0,\text{loc}}$ below 10%. The performance of the method was limited by the need of large estimation regions because of the need to compare the log-normalized spectra at two different depths (z_r and z_p , separated by at least one pulse length). This requirement restricted the application to tissues with relatively homogeneous attenuation, such as liver.

Another reference-free approach was proposed by Khan and Hasan (2019), which relied on bandpass filtering and exponentially weighting the cepstrum (the real part of the inverse Fourier transform of the logarithm of the RF signal spectrum) to separate the system-dependent effects, in particular the point spread function (PSF), and the tissue reflectivity function which included the exponential attenuation. The spectrum of the tissue reflectivity function was obtained by removing the effects of the PSF, and then further filtered to reduce noise and remaining diffraction effects. Finally, a linear regression of the filtered spectrum as a function of depth was used to determine $\alpha_{0,\text{loc}}$. The authors compared the proposed reference-free methods to reference-based ones including the spectral difference, the spectral shift, and the hybrid methods, as well as more recent ones based on spectral normalization and spectral cross-correlation methods (Fig. 6.4).

In homogeneous phantoms, the accuracy and precision of the proposed method were similar to those obtained with compounding strategies based on nearest neighbor averaging. In phantoms with inclusions, on average, the bias of the proposed method was 5% and 6% in inclusions with $\alpha_{0,\text{loc}} = 0.95 \text{ dB/cm-MHz}$ and 0.7 dB/cm-MHz , respectively, within a homogeneous background with $\alpha_{0,\text{loc}} = 0.5 \text{ dB/cm-MHz}$, compared to 25% and 3% with the hybrid method, and 24% and 17% with the spectral difference method. The standard deviation achieved with the proposed method was 23% and 26% in each inclusion, compared to 23% and 39% with the hybrid method, and 31% and 76% with the spectral difference method. A limitation of this method is that it assumes that the spatial variation of diffraction within the region of interest in which $\alpha_{0,\text{loc}}$ is estimated is negligible.

6.4 Variance Reduction

In addition to the reduction of bias, many efforts have focused on improving the tradeoff between variance and spatial resolution. This tradeoff is based on the need of a sufficiently large number of realizations of the scattering process to obtain a robust estimate of the acoustic property of interest. Here, we discuss four strategies to reduce the variance of the attenuation estimate: (1) use of low noise power spectrum estimators, (2) development of estimators based on the Cramer-Rao lower bound, (3) frequency compounding, and (4) regularization.

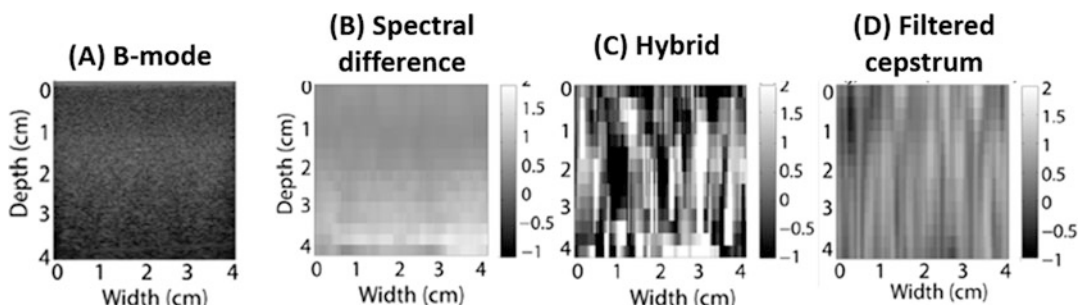


Fig. 6.4 (a) B-mode and $\alpha_{0,\text{loc}}$ maps obtained with (b) the spectral difference method, (c) the hybrid method, and (d) the filtered cepstrum. (Modified with permission from Khan and Hassan 2019)

6.4.1 Power-Spectrum Estimation

There are many methods to estimate the power spectrum of the RF echo signals, each one with its own tradeoff between bias and variance, such as the periodogram with rectangular (REC) and Hann (HAN) windows, Welch's method (WELCH), and Thomson's multitaper method (MTM) (Percival and Walden 1993). Figure 6.5a from Rosado-Mendez et al. (2013) compares power spectra obtained using the REC, HAN, WELCH, and MTM approaches on echo signals from a tissue-mimicking phantom. The gray curve shows the spectrum from a single estimation region, while the black curve is the average of 60 regions. The WELCH and MTM methods produce single-estimation region power spectra with less noise compared with the single periodogram. Figure 6.5b shows the normalized standard deviation of estimates of the constant of a power-law fit to $\alpha_{loc}(f)$ obtained from the spectra on the left, plotted as a function of the axial length of the estimation region. In each panel, each curve corresponds to the number of uncorrelated scanlines used to estimate the power spectrum (which defines the estimation region's

lateral width). For these conditions, the MTM method produced the least noisy estimates of the specific attenuation for a given size of the estimation region.

6.4.2 Cramer-Rao Lower Bound

Samimi and Varghese (2015, 2016, 2017) developed a theoretical framework to study the precision of estimates of $\alpha_{0,loc}$ obtained with the hybrid method and the spectral difference method with a reference phantom normalization. An important result of this approach was the derivation of an expression of the Cramer-Rao lower bound (CRLB) of the variance of estimates of $\alpha_{0,loc}$, which provides a theoretical lower bound to the variance of an unbiased estimator of $\alpha_{0,loc}$ based on a statistical model of the random components of the RF echo signals. The derivation was based on the assumptions of (i) diffuse scattering conditions, (ii) homogeneous attenuation and backscatter statistics within the estimation region, (iii) a linear dependence of α_{loc} vs frequency, and (iv) a sufficiently large (>30) number of uncorrelated A-lines within the spectrum region in order to

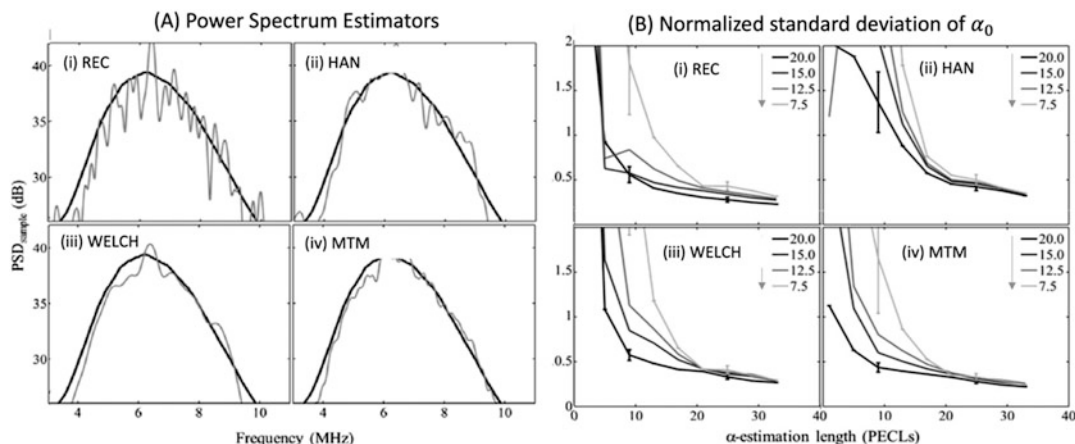


Fig. 6.5 (a) Power spectra obtained in a tissue-mimicking phantom from a single estimation region (gray curve) and the average of 60 estimation regions (black curve). (b) Normalized standard deviation of estimates of the coefficient of a power-law fit to $\alpha_{loc}(f)$ as a function of estimation region length (pulse-echo correlation length, or PECL), and for various widths indicated by different

curves (where the width is expressed in the number of uncorrelated scanlines within the estimation region). Power spectrum estimation methods: periodogram with rectangular (REC) and Hann (HAN) windows, Welch's method (WEL), and Thomson's multitaper method (MTM). (Reproduced from permission of Rosado-Mendez et al. 2013)

apply the central limit theorem to model the probability density function of the reference-phantom normalized power spectrum. In the case of the hybrid method, the CRLB is given by:

$$\text{Var}(\widehat{\alpha_{0,\text{loc}}}) = \frac{3\widehat{\sigma}_S^2}{4\sigma_{BW}^4 \Delta z^2 N (N^2 - 1)} \quad (6.6)$$

where N is the number of spectral estimation regions with centers separated by an axial distance Δz over which the centroid shift is estimated, $\widehat{\sigma}_S^2$ is the estimated variance of the spectral noise, and σ_{BW} is the spectrum bandwidth parameter. This expression was validated in simulations of homogeneous phantoms, which confirmed the expected trends of the CRLB: lower estimation variance can be achieved with higher signal-to-noise ratios, wider bandwidths, longer window lengths while avoiding non-stationarities, and the use of more uncorrelated scanlines.

The derivation of the CRLB for the hybrid method was then extended by the same authors (Samimi and Varghese 2016) to optimize the estimation of the centroid frequency in the hybrid method using a Maximum Likelihood Estimator based on spectral cross-correlation. The optimum estimator was derived by finding the zero value of the correlation between the echo signal spectrum and a weighting function $B(f)$ given by the frequency derivative of the reciprocal of the spectrum. Assuming a Gaussian-shaped spectrum, this results in the correlation of the spectrum with the following function:

$$B(f) = C \frac{(f - f_c)}{\sigma^2} \exp \left[\frac{(f - f_c)^2}{2\sigma^2} \right] \quad (6.7)$$

where C is an arbitrary constant, f_c is the centroid frequency, and σ is a spectral width parameter. Figure 6.6a–c show the B-mode image and $\alpha_{0,\text{loc}}$ maps obtained with the optimum estimator and the conventional hybrid method on a simulated phantom with 0.7 dB/cm-MHz. The figures demonstrate the significant reduction in variance (at least 3 times smaller) of the $\alpha_{0,\text{loc}}$ estimates when using the optimum estimator compared to the conventional approach. Of note is the increase

in the bias of the estimates beyond a depth of 42 mm caused by the weak echo signals.

In the case of the spectral difference method (Samimi and Varghese 2017), the CRLB for the variance of $\alpha_{0,\text{loc}}$ obtained from a linear regression to the attenuation vs frequency is given by:

$$\text{Var}(\widehat{\alpha_{0,\text{loc}}}) \geq \frac{\frac{N_t + N_R}{N_t N_R}}{\frac{4}{9} \Delta f^2 \Delta z^2 (L-1)(2L-1)(M-1)(2M-1)} \quad (6.8)$$

where N_t and N_r are the number of independent acoustic lines used to compute the RF signal power spectrum of the tissue sample and the reference, respectively; L and Δz are the axial number of spectra within the estimation region and the depth span over which the spectral power loss is analyzed to estimate the attenuation, Δf is the spectrum frequency resolution (inversely related to the RF signal segment length), and M is the number of independent frequency bins used to compute the regression of the attenuation vs. frequency. The authors compared the predicted CRLB of the $\alpha_{0,\text{loc}}$ variance to the variance obtained from $\alpha_{0,\text{loc}}$ estimates in a simulated phantom with 0.7 dB/cm-MHz obtained from the spectral difference method. As the number of independent scanlines was reduced from 100 to 10, the CRLB increased. The variance of the $\alpha_{0,\text{loc}}$ estimates was above the CRLB values, as expected. These observations were confirmed in experimental phantoms.

6.4.3 Frequency Compounding

Another approach to reduce the variance of attenuation estimates is the use of compounding approaches that combine estimates from different beam angles (Tu et al., 2003; Zenteno et al., 2014), or at different frequencies (Tu et al. 2003; Kim et al. 2018). Recently, Kim et al. (2018) developed a frequency-compounding strategy of the spectral log difference method in which estimates of $\alpha_{0,\text{loc}}$ obtained at different frequencies were combined within the available bandwidth by weighting each frequency estimate by the strength of the backscattered signal. This

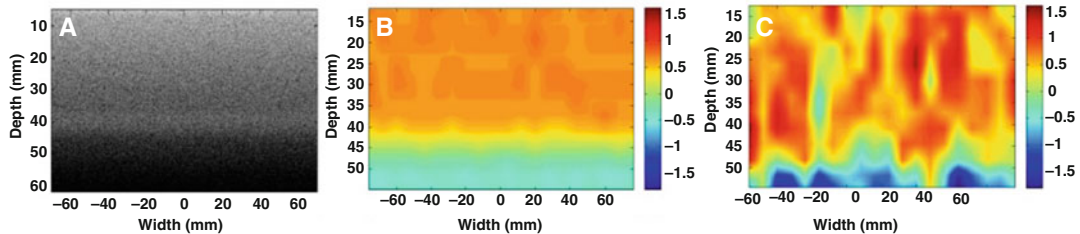


Fig. 6.6 (a) B-mode and $\alpha_{0, \text{loc}}$ maps produced with (b) the optimized and (c) the conventional hybrid methods on a phantom with 0.7 dB/cm-MHz. (Reproduced with permission from Samimi and Varghese 2016)

weighting strategy was derived by maximizing the signal-to-noise ratio of $\alpha_{0, \text{loc}}$ estimates assuming an additive white Gaussian noise model that was inversely proportional to the backscatter intensity factor. Tests on simulated phantoms demonstrated a variance reduction of 84% over conventional estimators, and of 32% over a uniform-weight compounding strategy.

6.4.4 Regularization Methods

Another successful approach to reduce the variance of attenuation estimates consists of using regularization approaches. In general, these approaches are based on minimizing a cost function defined as the sum of a data fidelity term $F[S_{\text{meas}}(x, z, f); S_{\text{model}}(x, z, f| \mathbf{v})]$ that fits a model function $S_{\text{model}}(x, z, f| \mathbf{v})$ of the echo signal power spectrum expressed in terms of the parameters of interest (represented by a vector \mathbf{v}) to the measured echo signal spectrum $S_{\text{meas}}(x, z, f)$ at lateral location x , depth z , and frequency f , and a regularization term $R(\mathbf{v})$ that constrains the spatial variability of the estimates by minimizing differences between estimates from adjacent estimation regions. The hypothesis behind these approaches is that attenuation varies smoothly within a single tissue, and has piecewise-continuity across different tissues (Coila and Lavarello 2017). Based on this hypothesis, and assuming (1) a linear frequency dependence of the attenuation, (2) that the ratio of the backscatter coefficients in the two spectral estimation regions does not vary with frequency, and (3) a zero-mean Gaussian noise of the logarithmic transform of the power spectrum, Coila and Lavarello (2017) introduced a regular-

ization term to the spectral log difference method based on the incorporation of isotropic total variation. In this approach, the log ratio of the power spectra at two depths separated by a distance Δz was modeled as $y_{\text{model}} = 4\Delta z \alpha_{0, \text{loc}} f + c$, where c is the log-ratio of the backscatter coefficients. This expression can be represented in matrix form as $\mathbf{y}_{\text{model}} = \mathbf{A}\mathbf{v}$, where \mathbf{A} is a mapping matrix transforming the parameter space to the signal model,² and \mathbf{v} is a vector with the parameters $\alpha_{0, \text{loc}}$ and c at different axial and lateral locations. Using an L2-norm minimization strategy, the data fidelity term was defined as:

$$F(\mathbf{y}|\mathbf{A}, \mathbf{v}) = \frac{1}{2} \|\mathbf{y}_{\text{meas}} - \mathbf{A}\mathbf{v}\|_2^2, \quad (6.9)$$

and the data regularization term was defined as:

$$R(\mu, \mathbf{v}) = \mu [TV_{2D}(\alpha_{0, \text{loc}}) + TV_{2D}(c)] \quad (6.10)$$

where μ is the regularization weight, and the 2D total variation terms $TV_{2D}(p)$ of parameters $p = \alpha_{0, \text{loc}}$ and c evaluated at axial location z_i and lateral location x_j are given by

$$\begin{aligned} TV_{2D}(p) \\ = \sum_{i,j} \sqrt{(p_{i+1,j} - p_{i,j})^2 + (p_{i,j+1} - p_{i,j})^2} \end{aligned} \quad (6.11)$$

²The elements of matrix \mathbf{A} vary depending on the model of the backscatter echo signal spectrum used in each publication. Here, for the sake of reducing the number of mathematical variables, the matrix \mathbf{A} will be used to indicate any mapping matrix from the parameter space to the signal space, regardless of the model.

The minimization of the cost function was achieved by using the alternating direction method of multipliers. The authors reported values of the standard deviation of the percentage error (a metric of the estimation variability) of less than 20% for simulated phantoms with $\alpha_{0, \text{loc}} = 0.5$ and 1.0 dB/cm-MHz, respectively, and estimation regions on the order of 11 pulse lengths and 32 uncorrelated scan lines with the non-regularized approach, while achieving similar levels of precision with an estimation region of about half the axial and lateral size with the regularized approach. This indicates the potential of using the regularized approach for improving the spatial resolution of attenuation coefficient images or improving the precision when using the same resolution. In simulated phantoms with inclusions with different attenuation coefficients, the authors reported values of the standard deviation of the percent error up to 220% for the non-regularized spectral log difference method and of 14% for the regularized version. Similar improvements in precision were observed in physical phantoms, and tests on ex vivo chicken breast. Furthermore, the reduction of variance achieved with the regularized approach resulted in an increase by up to a factor of 30 in the contrast-to-noise ratio of $\alpha_{0, \text{loc}}$ maps of an in vivo human breast fibroadenoma. An important consideration of this method is the need to define the regularization weight μ .

To improve the computation time of regularized attenuation estimators, Muraleedharan et al. (2019) proposed a closed-form solution of the minimization of the cost function based on a linear least-squares approach for estimating $\alpha_{0, \text{loc}}$ from backscattered echo signals. In this approach, the closed-form solution for $\hat{\mathbf{v}}$ is given by:

$$\hat{\mathbf{v}} = (\mathbf{H}^T \mathbf{H})^{-1} \mathbf{H}^T \tilde{\mathbf{q}} \quad (6.12)$$

where \mathbf{H} is a mapping matrix similar to \mathbf{A} in Eq. 6.9 and containing frequency and depth information, $\tilde{\mathbf{q}}$ is a vector containing the difference between the logarithm of the echo signal spectrum and the logarithm of the spectrum of the electric pulse and combined effects of the electromechanical and mechano-electric coupling of the transducer, and subscripts T and -1 indicate the matrix transpose and inverse, respectively. Some limitations of this method are that it ignores the diffraction effects from focusing, the frequency dependence of backscatter, and the reflection and transmission losses at tissue interfaces.

More recently, Romero et al. (2020) extended the work by Coila and Lavarello (2017) by simultaneously estimating the local attenuation and backscatter coefficients using a regularized power law method. The method assumes a linear dependence of the attenuation coefficient vs frequency and uses a reference phantom for normalization. The total attenuation is represented as a discrete sum of local attenuation terms starting with the total attenuation at the initial estimation depth z_1 , followed by local estimates within spectral estimation windows. The proposed solution is based on a regularized least-squares minimization approach

$$\hat{\mathbf{v}} = \arg \min \left[\frac{1}{2} \|\mathbf{y}_{\text{meas}} - \mathbf{M}\mathbf{v}\|_2^2 + \mu\phi(\mathbf{v}) \right] \quad (6.13)$$

where \mathbf{M} is a matrix similar to \mathbf{A} in Eq. 6.9 formed with the constants of the model mapping the parameter vector \mathbf{v} to the measured log-ratio of sample-to-reference power spectra \mathbf{y}_{meas} . Note that in this new formulation, the parameter vector \mathbf{v} now considers the $\alpha_{0, \text{loc}}$ as well as the magnitude β and frequency dependence ν of a power law model βf^ν to the frequency dependence of the backscatter coefficient. The second term $\mu\phi(\mathbf{v})$ represents a total variation-based regularization term. As in Coila and Lavarello (2017), the minimization in Eq. 6.13 was done using the alternating direction method of multipliers. Tests in homogeneous phantoms reported a reduction of the coefficient of variation of more than 400%. In simulated phantoms with an inclusion with different backscatter coefficient than the background, the resulting $\alpha_{0, \text{loc}}$ showed artifacts at the top and bottom of the circular inclusion, which were attributed to the change in echogenicity at the boundary of the inclusion. In a simulated phantom with an inclusion with

different attenuation than the background, no artifacts were observed in the image of the attenuation coefficient. Bias of $\alpha_{0,\text{loc}}$ of the inclusion increased with regularization weight (from 11.40% to 33.21%), while the coefficient of variation decreased from 25.03% to 3.38%. Preliminary applications on breast fibroadenoma produced $\alpha_{0,\text{loc}}$ values comparable to those reported in previous works (1.90 \pm 0.31 dB/cm-MHz for fibroadenoma, and 0.62 \pm 20 dB/cm-MHz for healthy breast tissue). The method was later refined by Chahuara et al. (2020), who proposed the use of a regularized power law by total variation based on an iteratively reweighted least squares method (IRLS) and solved with the conjugate gradient method to reduce computation times. The authors concluded that the proposed method outperformed the previous version reported by Romero et al. (2020) in terms of providing similar levels of bias and variance but at significantly shorter computation times.

In parallel, Destrempe et al. (2019) proposed the use of the least absolute shrinkage and selection operator (LASSO) for regularizing the estimates of $\alpha_{0,\text{loc}}$ with a Lagrangian multiplier for the regularization coefficients selected through the Bayesian Information Criterion. Assuming that the values of the backscatter coefficient at two depths are proportional to each other (no change in the frequency dependence) and using a reference phantom-based normalization, the data fidelity term becomes:

$$F(\mathbf{y}|\mathbf{U}, \mathbf{v}) = \frac{1}{2} \|\mathbf{y}_{\text{meas}} - \mathbf{U}\mathbf{v}\|_2^2 \quad (6.14)$$

where, in this case, the components of the parameter vector \mathbf{v} and the mapping matrix \mathbf{U} varied depending on the model chosen. Two models were investigated; the first one based on a reference phantom-based normalization with a backscatter coefficient parameterized in terms of a Gaussian form factor, in which case the vector \mathbf{v} had the form:

$$\mathbf{v} = \left[\Delta\alpha_{0,\text{tot}} \ 0.827 \frac{4\pi^2}{c^2} \Delta a_{\text{eff}}^2 \ \Delta \log \vartheta \right]^2 \quad (6.15)$$

where $\Delta\alpha_{0,\text{tot}}$ is difference in total attenuation coefficients between sample and reference, Δa_{eff}^2 is the difference in the square of the effective scatterer radius, ϑ is a constant related to the acoustic concentration. A second model was based on the spectral difference method, which considered the difference in the log-normalized power spectra from two, non-overlapping spectral estimation regions. In this case the parameter vector \mathbf{v} was

$$\mathbf{v} = [\Delta\alpha_{0,\text{loc}} \ \Delta\chi]^2 \quad (6.16)$$

where $\Delta\alpha_{0,\text{loc}}$ is the difference in $\alpha_{0,\text{loc}}$ between the reference and the sample, and χ is a constant related to the difference in backscatter. The regularization term used in this approach was:

$$R(\beta, \lambda) = \lambda \sum_{r=1}^{N_{\text{ROI}}} \sum_{k=1}^d \sum_{s \in N(r)} |v_{r,k} - v_{s,k}| \quad (6.17)$$

where λ is a Lagrangian multiplier, N_{ROI} is the number of axial and lateral estimation regions in which the attenuation coefficient is estimated, $N(r)$ is the number of estimation regions preceding the one indicated by index r , and d is the number of parameters being estimated. The value of λ was selected using the Bayesian information criterion. The Gaussian model was tested on a phantom with an inclusion with a higher scatterer number density. The use of the proposed regularization approach increased the contrast-to-noise ratio of the estimate of the acoustic concentration between the inclusion and the background by a factor of 2.8. The spectral log different regularization was tested on phantoms with a side-by-side difference in the $\alpha_{0,\text{loc}}$ obtaining a reduction of the standard deviation of, at least, 76% without increasing levels of bias. This reduction in variance is evident in the attenuation maps of the phantom shown in Fig. 6.7.

An alternative approach based on the application of compressed sensing was proposed by Shim et al. (2019). In this approach, a compressed or undersampled version \mathbf{x}_u of the RF echo signal \mathbf{x} can be modeled as:

$$\mathbf{x}_u = \mathbf{WZx} \quad (6.18)$$

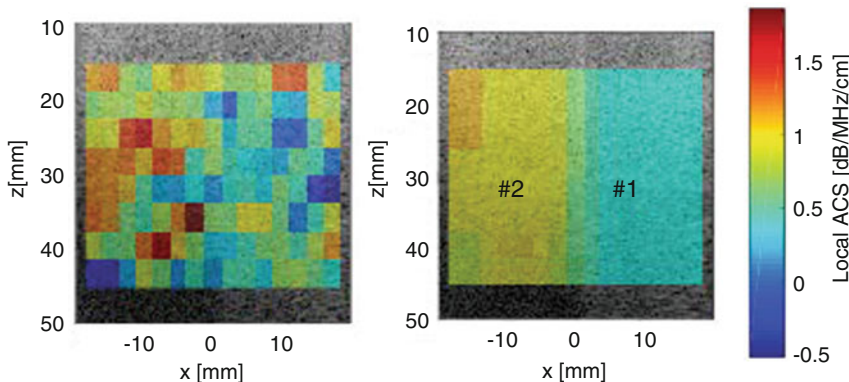


Fig. 6.7 Maps of $\alpha_{0,loc}$ obtained with (left) the conventional and (right) the regularized versions of the spectral difference method in a tissue-mimicking phantom with

side-by-side variations of the attenuation coefficient. (Reproduced with permission of Destrempe et al. 2019)

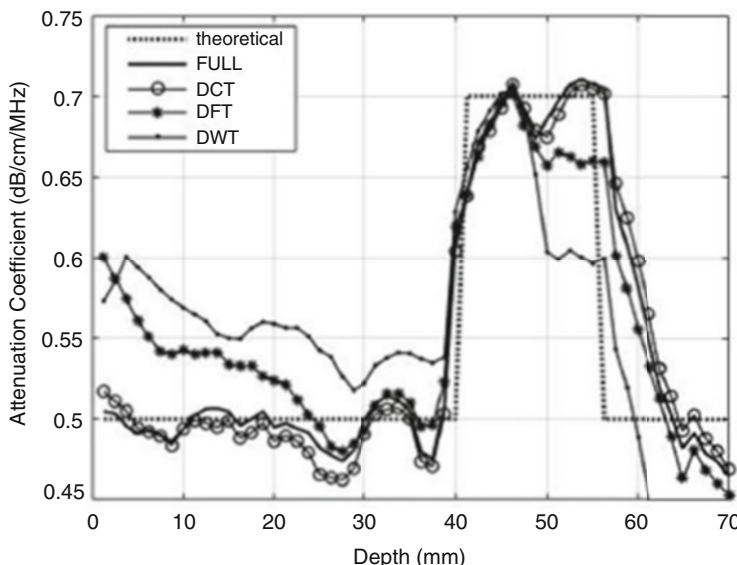


Fig. 6.8 Estimates of $\alpha_{0,loc}$ in a simulated tissue-mimicking phantom with a central layer with 0.2 dB/cm-MHz higher attenuation than the background. Estimation methods include the conventional spectral difference method with full signal sampling (FULL) and with com-

pressed sensing using discrete cosine (DCT), discrete Fourier (DFT), and discrete wavelet (DWT) domain transformations. (Reproduced with permission of Shim et al. 2019)

where \mathbf{W} is an incoherent sampling matrix (i.e., Gaussian random sampling) and \mathbf{Z} is a domain transformation defined to make the original echo signal sparse. The motivation behind this approach is the reduction of the number of echo signal samples needed to obtain quantitative ultrasound parameters. In simulations of a phantom with a higher attenuation layer (Fig. 6.8), the authors demon-

strated that using the spectral difference method on echo signals compressed with the discrete cosine domain transform (DCT) produced the lowest root mean square error compared to other domain transformations such as the discrete Fourier transform (DFT) and the discrete wavelet transform (DWT) or the conventional method without any signal compression.

Rafati et al. (2020) adapted the reference frequency-normalization strategy introduced by Gong et al. (2019) to include regularization. As a reminder, this normalization approach compensates for TGC and the system transfer function by normalizing the RF echo signal power spectrum at frequency f_i with respect to the value of the spectrum at f_{i-1} . Differently from Gong et al. (2019), Rafati et al. (2020) applied a Gaussian model to the log-transformed spectrum, restricted the analysis bandwidth to be within $\pm 25\%$ of the frequency with maximum power, and introduced LASSO regularization with a Lagrangian multiplier. The authors reported levels of bias below $8.2 \pm 4.1\%$ and $7.0 \pm 1.5\%$ in homogeneous phantoms with $\alpha_{0,\text{loc}} = 0.54$ and 1.27 dB/cm-MHz , respectively. In phantoms with two side-by-side media with different attenuation, the contrast-to-noise ratio of the $\alpha_{0,\text{loc}}$ maps was $1.69 \pm 0.65\%$ times larger with the regularization approach than without it.

Other approaches have focused on simultaneously estimating the total attenuation and the backscatter coefficient. Simultaneous estimation of the backscatter coefficient and the total attenuation coefficient was addressed by Nam et al. (2011c) through a least-squares minimization of a three-parameter model of a reference-normalized power spectrum that included the total attenuation and the backscatter coefficient. Assuming a power law model to the frequency of the backscatter coefficient $\text{BSC}(f) = \beta f^\nu$ and a linear frequency dependence of the total attenuation, the reference phantom-normalized power spectrum could be expressed as:

$$\frac{S_t(f, z)}{S_R(f, z)} = \frac{\beta_t(z) f^{\nu_t(z)}}{\beta_R f^{\nu_R}} \frac{e^{-4\alpha_{0,\text{tot}}(z) f z}}{e^{-4\alpha_R f z}} \quad (6.19)$$

where $\alpha_{0,\text{tot}}$ is the total attenuation slope of the tissue sample (subscript t), and subscript R indicates the reference phantom. Applying a natural logarithm to both sides of Eq. 6.19, the log-normalized power spectrum can be expressed as a three-parameter model:

$$L_{\text{model}}(f, z | b, n, a) = b(z) + n(z) \ln f - 4a(z) f z \quad (6.20)$$

where $b(z) = \ln(\beta_t(z)/\beta_R)$, $n(z) = \nu_t(z) - \nu_R$, and $a(z) = \alpha_{0,\text{tot}}(z) - \alpha_R$. This model was fit to the log-normalized power spectrum $L_{\text{meas}}(f_k, z_i)$ measured at N_f frequency components f_k (determined by the spectrum bandwidth) and discrete depth locations z_i at which the power spectra were computed by minimizing a data fidelity term through a least-squares approach:

$$\begin{aligned} F(j | b(z_i), n(z_i), a(z_i)) \\ = \sum_{k=1}^{N_f} [L_{\text{meas}}(f_k, z_i) - L_{\text{model}}(f_k, z_i | b(z_i), \\ n(z_i), a(z_i))]^2 \end{aligned} \quad (6.21)$$

Tests on a uniform phantom with an attenuation of 0.54 dB/cm-MHz produced average percent errors of 4% and 6.9% in $\alpha_{0,\text{tot}}$ estimates using the least squares method and the conventional spectral difference approach, respectively. In layered phantoms with depth-dependent changes in the local attenuation coefficient, the least squares approach produced a similar percent error as the spectral difference method (on average, 1.8% and 2.0% , respectively), while the least squares method produced smaller percent error in a phantom with a depth-dependent variation of the backscatter coefficient (9.1% vs. 12.5%). One advantage of the least squares method is that it only requires one power spectrum estimate, compared to the spectral difference method that requires estimating the local attenuation at various depths to compensate for the total attenuation and estimate the backscatter coefficient. An important limitation of Nam et al. (2011c)'s least squares approach, namely the assumption of a linear frequency dependence of the attenuation coefficient, was later addressed by Nasief et al. (2015), who proposed applying the least squares method over overlapping frequency sub-bands, and then combining estimates at the center frequencies of the sub-bands to reconstruct the frequency dependence of the attenuation.

Vajahi et al. (2018) introduced the use of regularization into Nam et al. (2011c)'s least squares approach by minimizing a cost function using dynamic programming. The cost function incor-

porated the data fidelity in Eq. 6.21 plus a L2-norm regularization term:

$$R = w_a(a_i - a_{i-1})^2 + w_b(b_i - b_{i-1})^2 + w_n(n_i - n_{i-1})^2 \quad (6.22)$$

where w_a , w_b , and w_n are the regularization weights of parameters a , b , and n defined in Eq. 6.20, and indices i refer to consecutive depth locations in which the power spectrum is estimated. Combining the three parameters in a single vector $\mathbf{v} = [\mathbf{a}, \mathbf{b}, \mathbf{n}]$, the parameter vector was estimated by minimizing the following recursive cost function:

$$C(i, v_i) = \min_{\mathbf{v}} \{C(i-1, v_{i-1}) + R(i, i-1)\} + D(i|v_i) \quad (6.23)$$

The cost function was minimized using a dynamic programming approach that stored pre-computed values of the cost function at previous depths to avoid redundancy in calculations and accelerate the estimation process. Tests in tissue-mimicking phantoms with a central layer with higher attenuation (0.78 dB/cm-MHz) than the background (0.51 dB/cm-MHz) and the same value of the backscatter coefficient at the center frequency demonstrated an average reduction by a factor of 20 in the standard deviation of the estimates of the total attenuation, a factor of 70 in the standard deviation of the magnitude of the backscatter coefficient, and a factor of 18 in the standard deviation of the power of the backscatter coefficient, without increasing the bias in the estimates (Fig. 6.9). The approach was later improved by the same group with the incorporation of an L1 norm that further reduced the standard deviation of the magnitude of the backscatter coefficient by an order of magnitude (Vajahi et al. 2019). Important limitations of this approach were the need to define a discrete search range for the total attenuation and the parameters of the backscatter coefficient, the lack of an automated criterion to select the weights of the regularization term, and the use of a power-law model for the frequency dependence of the backscatter coefficient. This latter limitation was

addressed in a later publication that incorporated a Gaussian form factor for the estimation of the effective scatterer size instead of the power-law model (Jafarpisheh et al. 2020a, b). Using simulated noisy spectra from phantoms with layers with different scatterer sizes and numbers of scatterers per resolution cell, the authors demonstrated that the dynamic programming regularization with the Gaussian form factor model was able to reduce the variance of estimates of attenuation, magnitude of the backscatter coefficient and the scatterer size by 88%, 75%, and 32%, respectively, compared to a non-regularized least-squares approach. Further tests in a phantom with 8-mm diameter cylindrical inclusions with different values of the backscatter coefficient demonstrated larger values of the contrast-to-noise ratio in parametric images of the acoustic concentration (Jafarpisheh et al. 2020b). The authors also compared the use of the dynamic programming approach for the compensation for total attenuation in the estimation of the backscatter coefficient with estimates of the total attenuation obtained from the local estimation obtained from a constrained-averaged spectral difference method (Rosado-Mendez et al. 2012). Tests in layered phantoms and phantoms with specular reflectors demonstrated that the constrained spectral difference method provided more accurate values of the local attenuation than those achieved by using spatial differentiation of total attenuation values obtained with dynamic programming. On the contrary, the dynamic programming approach was more accurate at estimating the total attenuation compared to spatially accumulating the local attenuation estimates obtained with the constrained-averaged spectral log difference method to compensate for attenuation in the estimation of the backscatter coefficient (Castañeda-Martinez et al. 2021).

The need to define a discrete search range of the three parameters in the dynamic programming approach limited the accuracy with which the total attenuation and the backscatter coefficient could be estimated, and introduced a degree of complexity because of the need to define criteria for selecting the regularization steps, search ranges, and steps. To address this limitation, Ja-

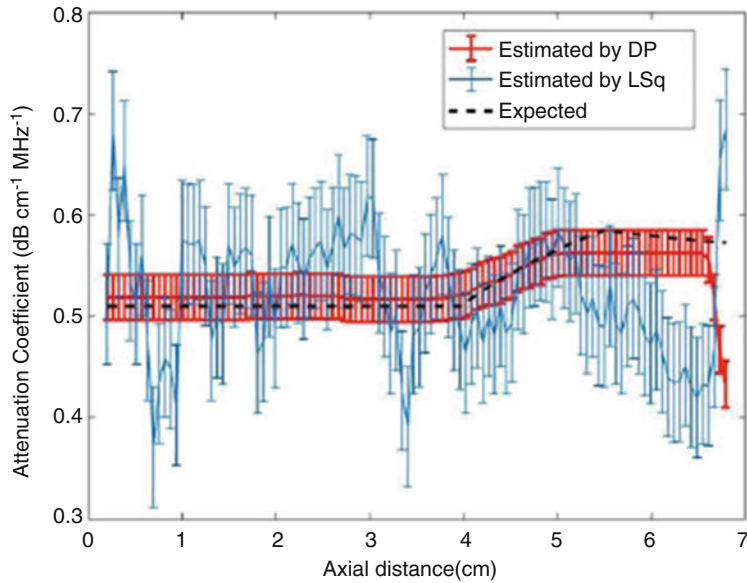


Fig. 6.9 Estimates of the total attenuation in a tissue-mimicking phantom with a middle layer with 0.27 dB/cm-MHz higher than the background. Dashed line: expected value, Blue line: least-squares approach (LSq), red line

(DP): dynamic programming approach. Errors bars indicate standard deviations across 10 uncorrelated frames. (Reproduced with permission from Vajihi et al. 2018)

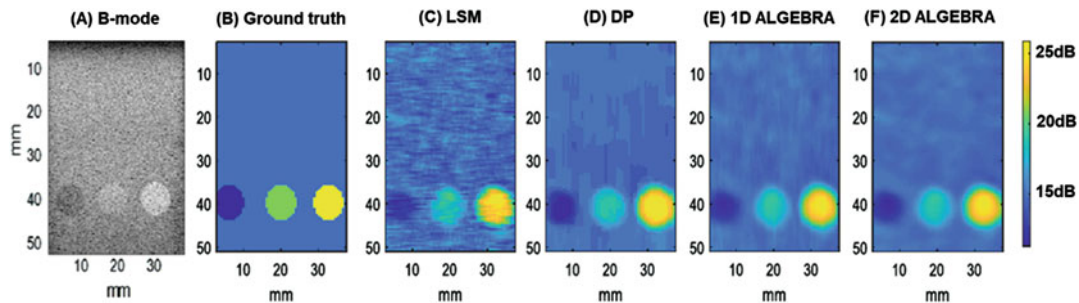


Fig. 6.10 (a) B-mode and parametric images of the backscatter coefficient at the center frequency of a tissue-mimicking phantom with inclusions with different echogenicity. (b) Ground truth values, (c) Least-squares

Method, (d) Dynamic programming, (e) 1D ALGEBRA, and (f) 2D ALGEBRA. (Reproduced with permission from Jafarpisheh et al. 2020a, b, c)

farpisheh et al. (2020c) developed an analytic approach for the minimization of the cost function named AnaLytical Global rEgularized BackscatteR quAntitative ultrasound, or ALGEBRA. This approach was based on obtaining the derivative of the cost function with respect to each of the parameters and equaling to zero, which resulted in a system of linear equations. The close-form solution of the system of equations eliminated the need to define a discrete search range. Another advantage of this approach was the possibility to

extend the regularization to 2D, i.e., also considering the lateral direction in the regularization. Tests in a tissue-mimicking phantom with inclusions with different backscatter coefficients demonstrated a significant reduction of variance in the estimates of the backscatter coefficient with the analytical approach, either 1D or 2D, compared to dynamic programming and the non-regularized method (Fig. 6.10). However, similar to the dynamic programming method, ALGEBRA is also limited by the need to optimize

the weights of the regularization function and its reliance on a power law model to the backscatter coefficient.

6.5 Summary and Conclusion

This chapter discussed several recent efforts to improve the accuracy and precision of estimates of the local and total acoustic attenuation. Although by no means extensive, this review demonstrates that the field of ultrasound attenuation imaging and quantification is active and growing. Continuous improvements in attenuation estimation algorithms during the past 40 years, as well as increasing interest in using acoustic properties of tissue as potential imaging biomarkers of fat infiltration in the liver, have resulted in several commercial implementations of attenuation coefficient quantification by major ultrasound scanner manufacturers. In this expanding context, the diversity of methods to estimate the attenuation coefficient has made evident the need to standardize the way the acoustic attenuation is being reported and used. This need is now being addressed by the Liver Fat Quantification Task Force of the American Institute of Ultrasound in Medicine and the Pulse-Echo Quantitative Ultrasound Biomarker Committee (PEQUS), hosted jointly by the AIUM and the Quantitative Imaging Biomarkers Alliance of the Radiological Society of North-America. Recently, the attenuation working group within the PEQUS biomarker committee published an overview of attenuation imaging and quantification in the context of liver fat assessment (Ferraioli et al. 2022). As applications diversify to address different clinical problems, the need to overcome challenges such as the quantification of attenuation in macroscopically heterogeneous and anisotropic tissues, as well as the need to further the understanding of the underlying physical mechanisms behind ultrasound attenuation will continue sparking interest in the quantitative ultrasound community.

References

- Anvari A, Forsberg F, Samir AE (2015) A primer on the physical principles of tissue harmonic imaging. *Radio-graphics* 35(7):1955–1964
- Castañeda-Martínez L, Rivaz H, Rosado-Mendez IM (2021) Comparison of different attenuation compensation methods in the estimation of the ultrasound backscatter coefficient. *AIP Conf Proc* 2348(1):040001
- Chahuara H, Basarab A, Lavarello R (2020) Regularized framework for simultaneous estimation of ultrasonic attenuation and backscatter coefficients. In: 2020 IEEE international ultrasonics symposium (IUS), pp 1–4
- Chen Q, Zagzebski JA (2004) Simulation study of effects of speed of sound and attenuation on ultrasound lateral resolution. *Ultrasound Med Biol* 30(10):1297–1306
- Civale J, Bamber J, Harris E (2021) Amplitude based segmentation of ultrasound echoes for attenuation coefficient estimation. *Ultrasonics* 111:106302
- Coila AL, Lavarello R (2017) Regularized spectral log difference technique for ultrasonic attenuation imaging. *IEEE Trans Ultrason Ferroelectr Freq Control* 65(3):378–389
- Coila AL, Oelze ML (2020) Effects of acoustic nonlinearity on pulse-echo attenuation coefficient estimation from tissue-mimicking phantoms. *J Acoust Soc Am* 148(2):805–814
- Destrempe F, Gesnik M, Cloutier G (2019) Construction of adaptively regularized parametric maps for quantitative ultrasound imaging. In: 2019 IEEE international ultrasonics symposium (IUS), pp 2027–2030
- Dong F, Madsen EL, MacDonald MC, Zagzebski JA (1999) Nonlinearity parameter for tissue-mimicking materials. *Ultrasound Med Biol* 25(5):831–838
- Duck FA (2002) Nonlinear acoustics in diagnostic ultrasound. *Ultrasound Med Biol* 28(1):1–18
- Ferraioli G, Kumar V, Ozturk A, Nam K, de Korte CL, Barr RG (2022) US attenuation for liver fat quantification: an AIUM-RSNA QIBA pulse-echo quantitative ultrasound initiative. *Radiology* 302:495
- Gerig AL, Varghese T, Zagzebski JA (2004) Improved parametric imaging of scatterer size estimates using angular compounding. *IEEE Trans Ultrason Ferroelectr Freq Control* 51(6):708–715
- Gong P, Song P, Huang C, Trzasko J, Chen S (2019) System-independent ultrasound attenuation coefficient estimation using spectra normalization. *IEEE Trans Ultrason Ferroelectr Freq Control* 66(5):867–875
- Guerrero QW, Fan L, Brunke S, Milkowski A, Rosado-Mendez IM, Hall TJ (2018) Power spectrum consistency among systems and transducers. *Ultrasound Med Biol* 44(11):2358–2370
- Hamilton MF, Blackstock DT (1998) Nonlinear acoustics. Academic, San Diego
- International Electrotechnical Commission (2010) Standard I. Ultrasonics – Pulse-echo scanners – Part 2:

- measurement of maximum depth of penetration and local dynamic range (IEC 61391-2)
- Jafarpisheh N, Rosado-Mendez IM, Hall TJ, Rivaz H (2020a) Evaluation of contrast to noise ratio of parametric images of regularized estimates of quantitative ultrasound. In: 2020 IEEE international ultrasonics symposium (IUS), pp 1–4
- Jafarpisheh N, Rosado-Mendez IM, Hall TJ, Rivaz H (2020b) Regularized estimation of effective scatterer size and acoustic concentration quantitative ultrasound parameters using dynamic programming. In: 2020 42nd annual international conference of the IEEE engineering in medicine & biology society (EMBC), pp 13–16
- Jafarpisheh N, Hall TJ, Rivaz H, Rosado-Mendez IM (2020c) Analytic global regularized backscatter quantitative ultrasound. *IEEE Trans Ultrason Ferroelectr Freq Control* 68(5):1605–1617
- Khan MH, Hasan MK (2019) Attenuation estimation of soft tissue with reference-free minimization of system effects. *Biomed Signal Process Control* 50:121–133
- Kim H, Shim J, Heo SW (2018) Improved attenuation estimation of ultrasonic signals using frequency compounding method. *J Electr Eng Technol* 13(1):430–437
- Klimonda Z, Postema M, Nowicki A, Litniewski J (2016) Tissue attenuation estimation by mean frequency downshift and bandwidth limitation. *IEEE Trans Ultrason Ferroelectr Freq Control* 63(8):1107–1115
- Labyed Y, Milkowski A (2020) Novel method for ultrasound-derived fat fraction using an integrated phantom. *J Ultrasound Med* 39(12):2427–2438
- Luchies AC, Oelze ML (2015) Backscatter coefficient estimation using tapers with gaps. *Ultrason Imaging* 37(2):117–134
- Madsen EL, Dong F, Frank GR, Garra BS, Wear KA et al (1999) Interlaboratory comparison of ultrasonic backscatter, attenuation, and speed measurements. *J Ultrasound Med* 18(9):615–631
- Muraleedharan A, Bertrand A, D'hooge J. (2019) A linear least squares based estimation of spatial variation of the attenuation coefficient from ultrasound backscatter signals. *Proc Meet Acoust ICU* 38(1):020016
- Nam K, Rosado-Mendez IM, Rubert NC, Madsen EL, Zagzebski JA, Hall TJ (2011a) Ultrasound attenuation measurements using a reference phantom with sound speed mismatch. *Ultrason Imaging* 33(4):251–263
- Nam K, Rosado-Mendez IM, Wirtzfeld LA, Pawlicki AD, Kumar V et al (2011b) Ultrasonic attenuation and backscatter coefficient estimates of rodent-tumor-mimicking structures: comparison of results among clinical scanners. *Ultrason Imaging* 33(4):233–250
- Nam K, Zagzebski JA et al (2011c) Simultaneous backscatter and attenuation estimation using a least squares method with constraints. *Ultrasound Med Biol* 37(12):2096–2104
- Nasief HG, Rosado-Mendez IM, Zagzebski JA, Hall TJ (2015) Acoustic properties of breast fat. *J Ultrasound Med* 34(11):2007–2016
- Nasief HG, Rosado-Mendez IM, Zagzebski JA, Hall TJ (2019) A quantitative ultrasound-based multi-parameter classifier for breast masses. *Ultrasound Med Biol* 45(7):1603–1616
- Percival DB, Walden AT (1993) Spectral analysis for physical applications. Cambridge University Press, Cambridge
- Rafati I, Destrempe F, Cloutier G (2020) Regularized phantom-free construction of local attenuation coefficient slope maps for quantitative ultrasound imaging. In: 2020 IEEE international ultrasonics symposium (IUS), pp 1–3
- Romero SE, Coila A, Lavarello RJ (2020) A regularized quantitative ultrasound method for simultaneous calculation of backscatter and attenuation coefficients. In: 15th international symposium on medical information processing and analysis, vol 11330, p 113300T
- Rosado-Mendez IM, Nam K, Hall TJ, Zagzebski JA (2012) A constrained-average strategy for reduction of artifacts from scattering in homogeneities in parametric images of the attenuation coefficient. In: 2012 IEEE international ultrasonics symposium, pp 2380–2383
- Rosado-Mendez IM, Nam K, Hall TJ, Zagzebski JA (2013) Task-oriented comparison of power spectral density estimation methods for quantifying acoustic attenuation in diagnostic ultrasound using a reference phantom method. *Ultrason Imaging* 35(3):214–234
- Rosado-Mendez IM, Drehfal LC, Zagzebski JA, Hall TJ (2016) Analysis of coherent and diffuse scattering using a reference phantom. *IEEE Trans Ultrason Ferroelectr Freq Control* 63(9):1306–1320
- Rubert N, Varghese T (2014) Scatterer number density considerations in reference phantom-based attenuation estimation. *Ultrasound Med Biol* 40(7):1680–1696
- Samimi K, Varghese T (2015) Performance evaluation of the spectral centroid downshift method for attenuation estimation. *IEEE Trans Ultrason Ferroelectr Freq Control* 62(5):871–880
- Samimi K, Varghese T (2016) Optimum diffraction-corrected frequency-shift estimator of the ultrasonic attenuation coefficient. *IEEE Trans Ultrason Ferroelectr Freq Control* 63(5):691–702
- Samimi K, Varghese T (2017) Lower bound on estimation variance of the ultrasonic attenuation coefficient using the spectral-difference reference-phantom method. *Ultrason Imaging* 39(3):151–171
- Shim J, Hur D, Kim H (2019) Spectral analysis framework for compressed sensing ultrasound signals. *J Med Ultrason* 46(4):367–375
- Szabo TL (2014) Chapter 12 – Nonlinear acoustics and imaging. In: Diagnostic ultrasound imaging inside out. Elsevier/Academic, Oxford, pp 501–563
- Tehrani AK, Amiri M, Rosado-Mendez IM, Hall TJ, Rivaz H (2021) Ultrasound scatterer density classification using convolutional neural networks and patch statistics. *IEEE Trans Ultrason Ferroelectr Freq Control* 68(8):2697–2706
- Tranquart F, Grenier N, Eder V, Pourcelot L (1999) Clinical use of ultrasound tissue harmonic imaging. *Ultrasound Med Biol* 25(6):889–894
- Tu H, Varghese T, Madsen EL, Chen Q, Zagzebski JA (2003) Ultrasound attenuation imaging using com-

- pound acquisition and processing. *Ultrason Imaging* 25(4):245–261
- Vajahi Z, Rosado-Mendez IM, Hall TJ, Rivaz H (2018) Low variance estimation of backscatter quantitative ultrasound parameters using dynamic programming. *IEEE Trans Ultrason Ferroelectr Freq Control* 65(11):2042–2053
- Vajahi Z, Rosado-Mendez I, Hall TJ, Rivaz H (2019) L1 and L2 norm depth-regularized estimation of the acoustic attenuation and backscatter coefficients using dynamic programming. In: 2019 IEEE 16th international symposium on biomedical imaging (ISBI 2019), pp 1749–1752
- Yao LX, Zagzebski JA et al (1990) Backscatter coefficient measurements using a reference phantom to extract depth-dependent instrumentation factors. *Ultrason Imaging* 12(1):58–70
- Zenteno O, Luchies A, Oelze M, Lavarello R (2014) Improving the quality of attenuation imaging using full angular spatial compounding. In: 2014 IEEE international ultrasonics symposium, pp 2426–2429

Part III

Envelope Statistics Methods



Review of Envelope Statistics Models for Quantitative Ultrasound Imaging and Tissue Characterization

7

François Destrempes and Guy Cloutier

Abstract

The homodyned K-distribution and the K-distribution, viewed as a special case, as well as the Rayleigh and the Rice distributions, viewed as limit cases, are discussed in the context of quantitative ultrasound (QUS) imaging. The Nakagami distribution is presented as an approximation of the homodyned K-distribution. The main assumptions made are (1) the absence of log-compression or application of nonlinear filtering on the echo envelope of the radiofrequency signal and (2) the randomness and independence of the diffuse scatterers. We explain why other available models are less amenable to a physical interpretation of their parameters.

We also present the main methods for the estimation of the statistical parameters of these distributions. We explain why we advocate the methods based on the X -statistics for the Rice and the Nakagami distributions and the K-distribution. The limitations of the proposed models are presented. Several new results are included in the discussion sections, with proofs in the appendix.

Keywords

Quantitative ultrasound (QUS) · Ultrasound tissue characterization · Ultrasound imaging · Echo envelope · Homodyned K-distribution · K-distribution · Rice distribution · Rayleigh distribution · Nakagami distribution · Parameters estimation · Moments · Log-moments

F. Destrempes

Laboratory of Biorheology and Medical Ultrasonics,
University of Montreal Hospital Research Center
(CRCHUM), Montréal, QC, Canada
e-mail: francois.destrempes@crchum.qc.ca

G. Cloutier (✉)

Laboratory of Biorheology and Medical Ultrasonics,
University of Montreal Hospital Research Center
(CRCHUM), Montréal, QC, Canada

The Department of Radiology, Radio-Oncology and
Nuclear Medicine, University of Montreal, Montréal, QC,
Canada

The Institute of Biomedical Engineering, University of
Montreal, Montréal, QC, Canada
e-mail: guy.cloutier@umontreal.ca

7.1 Introduction

The statistical distributions presented here appeared in the context of various applications in the past 130 years or so. The Rayleigh distribution was introduced in Rayleigh (1880) in the context of sound propagation. The Rice distribution appeared in Nakagami (1940) and Rice (1945) as a model of wave propagation. The K-distribution

was first introduced (Lord 1954) in the context of random walks and then in the context of sea echo (Jakeman and Pusey 1976). The homodyned K-distribution was introduced and studied in Jakeman (1980) and Jakeman and Tough (1987) as a model of weak scattering. The Nakagami distribution was defined in Nakagami (1943) in the field of wave propagation.

In ultrasound imaging, the Rayleigh distribution appeared as a model of the gray level (also called amplitude) in an unfiltered B-mode image, viewed as the envelope of the radiofrequency (RF) image, in the case of a high density of random scatterers with no coherent signal component (Burckhardt 1978; Wagner et al. 1983). The Rice distribution corresponds to a high density of random scatterers (the diffuse signal component) but combined with the presence of a coherent signal component (Insana et al. 1986). Non-Rayleigh distributions were considered in ultrasound imaging as early as the pioneer article (Burckhardt 1978) in 1978. The K-distribution corresponds to a variable (effective) density α of random scatterers, with no coherent signal component, and was introduced in ultrasound imaging by Shankar et al. (1993), Molthen et al. (1993), Narayanan et al. (1994), Shankar (1995), and Molthen et al. (1995). The homodyned K-distribution corresponds to the general case of a variable effective density of random scatterers with or without a coherent signal component (Dutt and Greenleaf 1994). A simpler model consists in modeling the gray level of the speckle pattern in a B-mode image by a Nakagami distribution (Shankar 2000; Dumane and Shankar 2001). In the context of QUS, the estimated parameters of the statistical distribution of the echo envelope play the role of quantitative measures that give information about the underlying tissues of interest.

The Nakagami distribution has been the most frequently adopted model in the context of tissue characterization, probably due to its simplicity. As the pioneer work, let us mention (Shankar et al. 2001) in the context of breast tumor classification. The Nakagami model was then systematically used in various medical ultrasound imaging fields, including ophthalmology (Tsui

et al. 2007), vascular flow applications (Huang et al. 2007; Huang and Wang 2007; Tsui et al. 2008b; Tsui et al. 2009a,b), and breast cancer (Tsui et al. 2008a, 2010a,b,c). The K-distribution was used in the context of breast cancer classification in the pioneer work of Shankar et al. (1993). More recently, the homodyned K-distribution was used for cardiac tissue characterization (Hao et al. 2002) and cancerous lesion classification (Oelze and O'Brien 2007; Hruska et al. 1959; Mamou et al. 2010; Mamou et al. 2011), and a model of mixtures of Rayleigh distributions was adopted for liver fibrosis quantification (Yamaguchi et al. 2011).

Whereas at the time of Shankar et al. (1993) and Dutt and Greenleaf (1994), the estimation of the (homodyned) K-distribution was a problem, since then, several estimation methods have been published. In particular, the K-distribution can be estimated using the simple and reliable X -statistics (Blacknell and Tough 2001) (defined as the log-moment $E[I \log I]/E[I] - E[\log I]$, where I denotes the square of the echo envelope amplitude), and a method (Hruska and Oelze 2009) was proposed for the estimation of the homodyned K-distribution. Thus, the use of the Nakagami model does not seem justified text of QUS, since it reduces the information carried by the homodyned K-distribution model.

7.2 Chapter Content

The remaining part of this chapter is organized as follows. Section 7.3 presents in detail the various models mentioned in the introduction, as well as other available models. A physical underlying model is also presented to help with the interpretation of the various parameters. In Sect. 7.4, the most frequently used estimation methods for the main distributions are presented. Finally, Sect. 7.5 presents the limitations of the main models and hints to future work on that matter.

In Sect. 7.4.1, various estimation methods are explained: (1) the Maximum Likelihood Estimator (MLE) and the Maximum A Posteriori (MAP), (2) moments-based methods, and (3) log-moments-based methods. Then, in Sects. 7.4.2

Table 7.1 Main distributions discussed in this chapter and the relations among them

Distribution	Notation	Relation
gamma	$\mathcal{G}(w \alpha, 1)$	
Rice	$P_{\text{Ri}}(A \varepsilon, \sigma^2)$	
Rayleigh	$P_{\text{Ra}}(A \sigma^2)$	$= P_{\text{Ri}}(A 0, \sigma^2)$
Homodyned K	$P_{\text{HK}}(A \varepsilon, \sigma^2, \alpha)$	$= \int_0^\infty P_{\text{Ri}}(A \varepsilon, \sigma^2 w) \mathcal{G}(w \alpha, 1) dw$
K	$P_{\text{K}}(A \sigma^2, \alpha)$	$= \int_0^\infty P_{\text{Ra}}(A \sigma^2 w) \mathcal{G}(w \alpha, 1) dw$ $= P_{\text{HK}}(A 0, \sigma^2, \alpha)$
Rice	$P_{\text{Ri}}(A \varepsilon, " \sigma^2 ")$	$= \lim_{\alpha \rightarrow \infty} P_{\text{HK}}(A \varepsilon, " \sigma^2 " / \alpha, \alpha)$
Rayleigh	$P_{\text{Ra}}(A " \sigma^2 ")$	$= \lim_{\alpha \rightarrow \infty} P_{\text{K}}(A " \sigma^2 " / \alpha, \alpha)$
Nakagami	$\text{N}(A m, \Omega)$	Approximation of the homodyned K-distribution

to 7.4.6, we kept the same structure in the presentation of the estimation methods for each of the five distributions presented in Sects. 7.3.1 and 7.3.3, whenever possible (according to the literature).

In Sects. 7.3 and 7.4, various remarks and additional results are mentioned in the subsections entitled “discussion.” As far as we know, most of these results are new (Theorems 8–12, 18–23, and 25–26, Corollary 2, and Lemmas 4 and 5), except probably Lemmas 1–3, although we did not find references. Theorem 28 was used explicitly in Destrempe et al. (2009, Table 1), but without proof. The proofs of the new results are postponed to the appendix. The purpose of these new results is to deepen the understanding of the published methods mentioned in this chapter.

same constraint. The parameter α is related to the homogeneity of the diffuse scattering medium and the density of the scatterers. It is called the *scatterer clustering parameter* (Dutt and Greenleaf 1994). In the context of the K-distribution, it is also called the *effective number of scatterers* (Narayanan et al. 1994). The parameter ε is called the *coherent component* and is related to the strength of specular reflection or the periodic organization of the scatterers. The diffuse signal power can be viewed as $2\sigma^2\alpha$ for the homodyned K-distribution (and K-distribution), whereas ε^2 can be viewed as the coherent signal power. In Sect. 7.3.2, an underlying physical model is presented. In Sect. 7.3.3, the Nakagami distribution is described as an approximation of the homodyned K-distribution. Finally, in Sect. 7.3.4, the relevance of these distributions compared to other available models is discussed (see Destrempe and Cloutier 2010 for further reading on that topic). The reader may refer to Table 7.1 for a summarize of the main distributions discussed here and the relations among them.

7.3 Statistical Models

We first present in Sect. 7.3.1 various models for the first-order statistics of the amplitude of the echo envelope. The most general of these models is the homodyned K-distribution that depends on three parameters $\varepsilon \geq 0$, $\sigma^2 > 0$, and $\alpha \geq 0$. The Rice distribution with parameter $\sigma^2 = \bar{a}^2/2$ is viewed as the limiting case of the homodyned K-distribution with parameter σ^2 of the form $\bar{a}^2/(2\alpha)$ when $\alpha \rightarrow \infty$. The K-distribution is a special case of the homodyned K-distribution with $\varepsilon = 0$, whereas the Rayleigh distribution is a special case of the Rice distribution with the

7.3.1 The Homodyned K-Distribution and Related Distributions

7.3.1.1 The Rayleigh Distribution

The (two-dimensional) Rayleigh distribution (Rayleigh 1880) is defined by

$$P_{\text{Ra}}(A | \sigma^2) = \frac{A}{\sigma^2} \exp\left(-\frac{A^2}{2\sigma^2}\right), \quad (7.1)$$

where A represents the amplitude of the signal. In Jakeman and Tough (1987), the distribution is expressed, in the context of n -dimensional random walks, in terms of the variable $\bar{a}^2 = n\sigma^2$. The case $n = 2$ corresponds to Eq. (7.1). Equivalently, the intensity I , i.e., the square of the amplitude A , is distributed according to an exponential distribution.

7.3.1.2 The Rice Distribution

The (two-dimensional) Rice distribution is expressed as

$$P_{\text{Ri}}(A|\varepsilon, \sigma^2) = \frac{A}{\sigma^2} I_0\left(\frac{\varepsilon}{\sigma^2} A\right) \exp\left(-\frac{(\varepsilon^2 + A^2)}{2\sigma^2}\right), \quad (7.2)$$

where $\sigma > 0$ and $\varepsilon \geq 0$ are real numbers and I_0 denotes the modified Bessel function of the first kind of order 0 (the intensity I should not be confused with the Bessel function I_0). See Jakeman and Tough (1987, Eq. 2.16) for a generalization in dimension $n \geq 2$. The special case where $\varepsilon \rightarrow 0$ yields the Rayleigh distribution. The case $n = 2$ corresponds to Nakagami (1940) and Rice (1945). In Nakagami (1960, p. 4, Eq. 5), the Rice distribution is called the “ n -distribution” (Nakagami 1940).

7.3.1.3 The K-Distribution

The (two-dimensional) K-distribution (Lord 1954; Jakeman and Pusey 1976) is defined by

$$P_K(A|\sigma^2, \alpha) = \frac{4A^\alpha}{(2\sigma^2)^{(\alpha+1)/2} \Gamma(\alpha)} \times K_{\alpha-1}\left(\sqrt{\frac{2}{\sigma^2}} A\right), \quad (7.3)$$

where $\alpha > 0$, $\sigma^2 > 0$, Γ is the Euler gamma function, and K_p denotes the modified Bessel function of the second kind of order p . In Jakeman and Tough (1987, Eq. 2.11), the distribution is expressed in terms of the parameters α and $b = \sqrt{\frac{2}{\sigma^2}}$. In view of the compound representation presented below, we find the proposed parametrization more convenient.

Theorem 1 (Jakeman and Tough 1987) *The compound representation of the K-distribution is*

$$P_K(A|\sigma^2, \alpha) = \int_0^\infty P_{\text{Ra}}(A|\sigma^2 w) \times \mathcal{G}(w|\alpha, 1) dw, \quad (7.4)$$

where P_{Ra} denotes the Rayleigh distribution, and $\mathcal{G}(w|\alpha, 1)$ is the gamma distribution $w^{\alpha-1} \exp(-w)/\Gamma(\alpha)$ of mean and variance equal to α .

The compound representation is useful to simulate the K-distribution and in the evaluation of its value. A K-distribution with parameters $\sigma^2 = \bar{a}^2/(2\alpha)$ and α yields the Rayleigh distribution with parameter “ σ^2 ” = $\bar{a}^2/2$, as $\alpha \rightarrow \infty$; see Jakeman and Tough (1987, Eq. 2.12). Thus, the parameter “ σ^2 ” of the limiting Rayleigh distribution is $\bar{a}^2/2$ and should not be confused with the parameter σ^2 of the K-distribution. The relation between these two quantities is “ σ^2 ” = $\bar{a}^2/2 = \sigma^2\alpha$.

7.3.1.4 The Homodyned K-Distribution

The (two-dimensional) homodyned K-distribution (Jakeman 1980; Jakeman and Tough 1987) is defined by

$$P_{\text{HK}}(A|\varepsilon, \sigma^2, \alpha) = A \int_0^\infty u J_0(u\varepsilon) J_0(uA) \times \left(1 + \frac{u^2 \sigma^2}{2}\right)^{-\alpha} du, \quad (7.5)$$

where $\sigma^2 > 0$, $\alpha > 0$, $\varepsilon \geq 0$, and J_0 denotes the Bessel function of the first kind of order 0. In Jakeman and Tough (1987, Eq. 4.13), the homodyned K-distribution is expressed in terms of the parameters α , $\bar{a}^2 = n\sigma^2\alpha$, and $a_0 = \varepsilon$, in the context of n -dimensional random walks.

Theorem 2 (Jakeman and Tough 1987) *The compound representation of the homodyned*

K-distribution is

$$P_{HK}(A | \varepsilon, \sigma^2, \alpha) = \int_0^\infty P_{Ri}(A | \varepsilon, \sigma^2 w) \mathcal{G}(w | \alpha, 1) d w, \quad (7.6)$$

where P_{Ri} denotes the Rice distribution and $\mathcal{G}(w | \alpha, 1)$ is the gamma distribution with mean and variance equal to α .

The case $\varepsilon \rightarrow 0$ yields the K-distribution (with parameters σ^2 and α). In particular, the compound representation of the homodyned K-distribution is consistent with Eq. (7.4), upon taking $\varepsilon \rightarrow 0$. A homodyned K-distribution with parameters ε , $\sigma^2 = \overline{a^2}/(2\alpha)$ and α yields the Rice distribution with parameters ε and “ σ^2 ” = $\overline{a^2}/2$, as $\alpha \rightarrow \infty$. Thus, if in addition, $\varepsilon \rightarrow 0$, then one obtains the Rayleigh distribution with parameter “ σ^2 ” = $\overline{a^2}/2$, as $\alpha \rightarrow \infty$. Figure 7.1 illustrates four representative examples of the homodyned K-distribution (including two examples of the K-distribution, as a special case).

Two functions of the three parameters of the homodyned K-distribution are invariant under scaling of the intensity (Dutt and Greenleaf 1994): (1) the parameter α , and (2) the structure parameter $\kappa = \varepsilon^2/(2\sigma^2\alpha)$, i.e., the ratio of the coherent signal power ε^2 with the diffuse signal power $\overline{a^2} = 2\sigma^2\alpha$. Other parameters of the homodyned K-distribution were considered in the literature: the coherent to diffuse signal ratio $k = \sqrt{2\kappa} = \varepsilon/(\sigma\sqrt{\alpha})$ (Dutt and Greenleaf 1994; Hruska and Oelze 2009; Dutt 1995) and the parameter β equal to $1/\alpha$ (Dutt 1995; Dutt and Greenleaf 1994).

Considering $\sigma^2 = \overline{a^2}/(2\alpha)$ and letting α tend to infinity, one obtains a Rice distribution for which the diffuse signal power is also $\overline{a^2}$ and the structure parameter κ is also equal to $\varepsilon^2/\overline{a^2}$.

7.3.2 Interpretation of the Distributions in the Context of Ultrasound Imaging

In Shankar et al. (1993), Molthen et al. (1993, 1995), Narayanan et al. (1994), Shankar (1995), one considers N_s scatterers lying in an ambient scattering medium within the resolution cell. Each scatterer corresponds to a phasor $a_j e^{i\phi_j}$ with two elements: (1) an amplitude a_j depending on the scattering properties (i.e., the scattering cross section) and the position of the scatterer with respect to the ultrasound beam, the instrumentation, and the attenuation and (2) a phase ϕ_j that depends on the scatterer's position. One then postulates (Narayanan et al. 1994) a K-distribution with parameters σ^2 and α_s for each amplitude and considers uniformly distributed independent phases for each scatterer. The choice of the K-distribution was motivated in Narayanan et al. (1994) by its good modeling properties of the first-order statistics of the echo envelope in the case where the Rayleigh distribution model (corresponding to infinitely many scatterers of identical cross sections) breaks down, as explained in the next paragraph. Assuming weak scattering, the resulting complex signal is expressed as

$$\mathbf{A} = \sum_{j=1}^{N_s} a_j e^{i\phi_j}. \quad (7.7)$$

Then, its amplitude A is viewed as the norm of the complex signal.

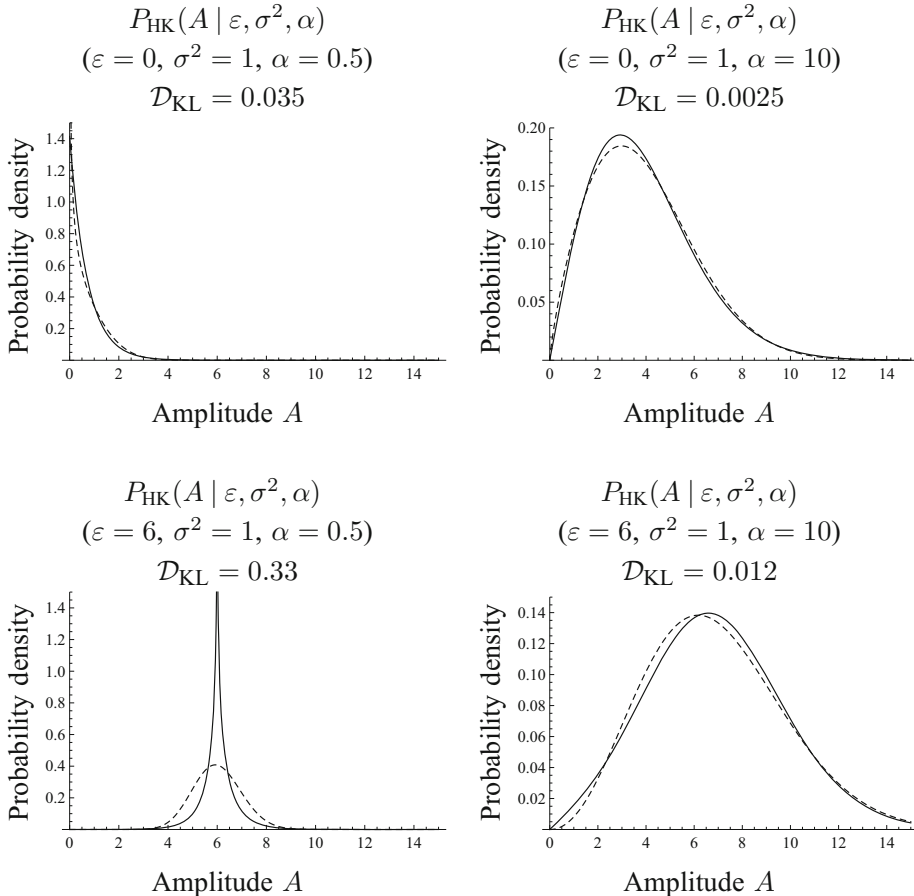


Fig. 7.1 Typical examples of the homodyned K-distribution. Top row: K-distribution ($\varepsilon = 0$). Bottom row: $\varepsilon > 0$. The dashed curves represent the approximating Nakagami distributions. The Kullback–Leibler distance

values between the two distributions were (top left) 0.035, (top right) 0.0025, (bottom left) 0.33 (with a coherent to diffuse signal ratio $k = \varepsilon/(\sigma\sqrt{\alpha})$ equal to 8.5), and (bottom right) 0.012 (with $k \approx 1.9$)

Note that Eq. (7.7) can be viewed as a random walk in the Euclidean plane (corresponding to $n = 2$), since the complex number $e^{i\phi_j}$ corresponds to the vector $(\cos(\phi_j), \sin(\phi_j))$. Thus,¹ the amplitude $A = \|\mathbf{A}\|$ corresponding to Eq. (7.7) follows a K-distribution with parameter $\alpha = \alpha_s N_s$. In that context, α is called the *effective number of scatterers* because the number of scatterers N_s is multiplied by the parameter α_s . For instance, if N_s is large, but α_s is so small that $\alpha_s N_s \ll 10$, then the resulting distribution is a K-distribution rather than a Rayleigh distribution. For the same reason, even

if N_s is small, but α_s is so large that $\alpha_s N_s \geq 10$, then one obtains a Rayleigh distribution. The parameter α_s is a parameter describing the lack of uniformity of the scattering cross sections in the range cell (cf. Narayanan et al. 1994, Eq. (6)). A small value of α_s corresponds to a great variability, whereas a large value of α_s corresponds to a small variability. Thus, the parameter α_s is viewed as a measure of homogeneity of the scattering medium. The choice of the K-distribution is also consistent with the observation that the higher order moments of the intensity of the echo envelope may be larger than the ones predicted by the Rayleigh distribution model in the case of pathological

¹ Correction of a typo (“ $A = \mathbf{A}$ ”) in the first edition.

tissues (Shankar et al. 1993). For instance, under the Rayleigh model, one would have $E[I^2]/E[I]^2 = 2$, whereas the K-distribution model yields $E[I^2]/E[I]^2 = 2(1 + 1/\alpha)$, which corresponds to observed values upon taking α sufficiently small. So, the statistics of the echo envelope depart from the Rayleigh model if the number of scatterers is small and α_s is not too large or if the cross sections are heterogeneous and N_s is not too large.

Adding a coherent component $\boldsymbol{\varepsilon}$, with constant amplitude ε and either a constant phase or a uniformly distributed phase, then yields a homodyned K-distribution with parameters ε, σ^2 , and $\alpha = \alpha_s N_s$, for the amplitude $A = \|\boldsymbol{\varepsilon} + \mathbf{A}\|$. Since a coherent component may arise when the scatterers are organized periodically, the parameter α does not quite represent the effective number of scatterers in that context, but it may still be viewed as a scatterer clustering parameter. The coherent component may also be caused by specular reflection.

7.3.3 The Nakagami Distribution as an Approximation

The Nakagami distribution (Nakagami 1943, 1960) is defined by

$$N(A | m, \Omega) = \frac{2m^m}{\Gamma(m)\Omega^m} A^{2m-1} e^{-mA^2/\Omega}, \quad (7.8)$$

where Γ is the Euler gamma function. The real numbers $m > 0$ and $\Omega > 0$ are called the shape parameter and the scaling parameter, respectively. Equivalently, the intensity $I = A^2$ follows a gamma distribution, with shape parameter m and scale parameter Ω/m .

The shape parameter m can be interpreted as the square of the intensity signal-to-noise ratio (SNR), i.e., $m = \frac{E[I]^2}{Var(I)}$ and Ω represents the mean intensity $E[I]$ (i.e., the total signal power). The intensity SNR should not be confused with the amplitude SNR. For instance, when $m = 1$, one retrieves the Rayleigh distribution. This observation can be found in Nakagami (1960, p.

17, Eqs. 50 and 51). In that case, the intensity SNR is equal to 1, whereas the amplitude SNR is about 1.91.

The Nakagami distribution can be viewed as an approximation of the homodyned K-distribution. First of all, we have the limiting case where $\alpha \rightarrow \infty$, which yields the Rice distribution and corresponds to the case $m \geq 1$.

Theorem 3 (Destrempe and Cloutier 2010)

Let $m = \frac{(\varepsilon^2 + 2\sigma^2)^2}{4\sigma^2(\varepsilon^2 + \sigma^2)}$ and $\Omega = \varepsilon^2 + 2\sigma^2$. Then,

$$\mathcal{D}_{KL}(P_{\text{Ri}}(\varepsilon, \sigma^2), N(m, \Omega)) \leq 0.02, \quad (7.9)$$

where \mathcal{D}_{KL} denotes the Kullback-Leibler distance (Kullback and Leibler 1951) between two distributions.

Recall that the Kullback-Leibler distance (also called Kullback-Leibler divergence because it is non-symmetric) is a measure of the difference between two probability distribution functions (PDFs) $f(x)$ and $g(x)$ in the continuous random variable x and is defined by $\int f(x) \log \frac{f(x)}{g(x)} dx$. It has the properties: (1) $\mathcal{D}_{KL}(f, g) \geq 0$ for any PDFs f and g and (2) $\mathcal{D}_{KL}(f, g) = 0$ if and only if $f \equiv g$. However, it is a non-symmetric measure (i.e., $\mathcal{D}_{KL}(f, g)$ is not necessarily equal to $\mathcal{D}_{KL}(g, f)$). The choice of m and Ω in Theorem 3 is consistent with the identities $SNR^2 = \frac{(\varepsilon^2 + 2\sigma^2)^2}{4\sigma^2(\varepsilon^2 + \sigma^2)}$ and $E[I] = \varepsilon^2 + 2\sigma^2$ valid for the Rice distribution; see also Nakagami (1960, p. 18, Eq. (55)).

We also have the following approximation result in the case of the K-distribution ($\varepsilon \rightarrow 0$), which corresponds to the case $m < 1$.

Theorem 4 (Destrempe and Cloutier 2010)

Let $m = \frac{\alpha}{(\alpha+1)}$ and $\Omega = 2\sigma^2\alpha$. Then,

$$\mathcal{D}_{KL}(P_K(\sigma^2, \alpha), N(m, \Omega)) \leq 0.0325. \quad (7.10)$$

For Theorem 4, the choice of m and Ω is consistent with the identities $E[I \log I]/E[I] - E[\log I] = 1/m$ and $E[I \log I]/E[I] - E[\log I] = 1 + 1/\alpha$ valid for the Nakagami

distribution and the K-distribution, respectively (see Sects. 7.4.6.3 and 7.4.4.5).

7.3.4 Discussion

In this section, a new result on the Nakagami distribution as an approximation of the homodyned K-distribution is introduced (in greater generality than Theorems 3 and 4). We then discuss the consistency of the distributions presented in Sect. 7.3.1 in the limit case of a vanishing diffuse signal power, and we explain why other models available in the literature fail to have this feature (Destrempe and Cloutier 2010). Finally, as a new result, that

property is shown to hold for the Nakagami distribution.

Considering the general case of a homodyned K-distribution with parameters ε , σ^2 , and α , the $M^{(1)}$ -statistics $E[A]/\sqrt{E[I]}$ is expressed explicitly in Theorem 7.44 as a function $M_{HK}^{(1)}(\gamma, \alpha)$, where $\gamma = \kappa\alpha$. Using the identity $M_{Na}^{(1)}(m) = \frac{\Gamma(1/2+m)}{\sqrt{m}\Gamma(m)}$ of Theorem 30, one then solves the equation $M_{Na}^{(1)}(m) = M_{HK}^{(1)}(\gamma, \alpha)$ in the variable m , using a binary search algorithm based on Theorem 31. This yields a function $m = m(\gamma, \alpha)$. Moreover, considering $E[I]$, one is led to the identity $\Omega = \varepsilon^2 + 2\sigma^2\alpha = \mu$ (the average value of the intensity). So, one is interested in the Kullback-Leibler distance

$$\mathcal{D}_{KL}\left(P_{HK}(\varepsilon = \sqrt{\frac{\mu\gamma}{(\gamma + \alpha)}}, \sigma^2 = \frac{\mu}{2(\gamma + \alpha)}, \alpha), N(m = m(\gamma, \alpha), \Omega = \mu)\right), \quad (7.11)$$

as a function of γ , α , and μ . It can be seen that this function is independent of the scaling factor μ (this is actually a general property of the Kullback-Leibler distance).

We computed Eq. (7.11) for $k = \varepsilon/(\sigma\sqrt{\alpha}) = 0.0, 0.1, \dots, 2.0$, $\alpha = 1, 2, \dots, 20$, taking $\sigma^2 = 1/\alpha$. For each value of k and α , a sample set of size $N = 1000$ was simulated according to the corresponding homodyned K-distribution. The Kullback-Leibler distance was then estimated as the average over the simulated set of $\log(P_{HK}(A_i | \varepsilon = k, \sigma^2 = 1/\alpha, \alpha)/N(A_i | m = m(\gamma, \alpha), \Omega = k^2 + 2))$. The maximal value was 0.072 (this result could be slightly improved upon considering the X -statistics instead of the $M^{(1)}$ -statistics). So, the Nakagami is a satisfying approximation in that range of the parameters k and α . See Fig. 7.1 for examples of approximating Nakagami distributions. In that figure, we included an example of a value of k much larger than 2; in that case, the KL distance is quite large (0.33).

Theorem 2 states that the homodyned K-distribution corresponds to a model in which the diffuse signal power $2\sigma^2$ of a Rice distribution is modulated by a gamma distribution, but not its coherent signal component ε . As mentioned in Destrempe and Cloutier (2010), there are several more models for the first-order statistics of the echo envelope. One modeling possibility introduced in Barakat (1986) and further developed in Jakeman and Tough (1987) is equivalent to modulate both the coherent signal component ε and the diffuse signal power $2\sigma^2$ of the Rice distribution by a gamma distribution. This gives rise to the generalized K-distribution. Note that this distribution has not been used in ultrasound imaging as of now. However, in Eltoft (2005), the Rician Inverse Gaussian (RiIG) distribution is introduced, and it corresponds to a model in which both the coherent signal component ε and the diffuse signal power $2\sigma^2$ of a Rice distribution are modulated by an Inverse Gaussian (IG) distribution, instead of a gamma distribution. Thus, this model is related to the generalized K-distribution, as

further discussed in Destrempe and Cloutier (2010).

Three other distributions were introduced in the context of ultrasound imaging. The first one is called the generalized Nakagami distribution (Shankar 2000) and is obtained from the Nakagami distribution by a change of variable of the form $y = A^{1/s}$, where s is a shape adjustment parameter and A is the amplitude of the signal. This distribution was also proposed in Raju and Srinivasan (2002) (in the equivalent form of a generalized gamma distribution). The second other distribution is called the Nakagami-gamma distribution (Shankar 2003). That distribution can be viewed as a model in which the Rice distribution is approximated by a Nakagami distribution, and in which its total signal power Ω is modulated by a gamma distribution. The third distribution is called the Nakagami-generalized inverse Gaussian (NGIG) distribution (Agrawal and Karmeshu 2006), and it corresponds to a model in which the (approximating) Nakagami distribution has its total signal power Ω modulated by a Generalized Inverse Gaussian (GIG) distribution instead of a gamma distribution.

As shown in Destrempe and Cloutier (2010), none of these five other models is compatible with the limit case of a vanishing diffuse signal power $2\sigma^2\alpha_s$. Indeed, in that case, one should obtain an infinite intensity SNR (if $\varepsilon > 0$). It turns out that only the homodyned K-distribution and its related distributions satisfy that property. In fact, keeping α_s (the scattering cross sections homogeneity) and N_s (the number of random scatterers within the resolution cell) constant (see Sect. 7.3.2), one must have $\sigma^2 \rightarrow 0$ if the diffuse signal power $2\sigma^2\alpha_s N_s$ vanishes. Then, as computed in Destrempe and Cloutier (2010), one obtains an infinite intensity SNR if $\varepsilon > 0$, either for the Rice distribution or for the homodyned K-distribution. Moreover, it was shown in Destrempe and Cloutier (2010) that the total signal power depends only on the coherent component in that case, which is a desirable property. Since the other distributions do not have these two properties, it makes the interpretation of their parameters more delicate, even if goodness-of-fit tests with data might be satisfying.

Finally, let us show that the Nakagami distribution also has these two properties. For that purpose, we consider a homodyned K-distribution with parameters ε , σ^2 , and α and its approximating Nakagami distribution with parameters $m = m(\varepsilon^2/(2\sigma^2), \alpha)$ and $\Omega = \varepsilon^2 + 2\sigma^2\alpha$ as at the beginning of this section. If $\varepsilon > 0$ and α are fixed and $\sigma^2 \rightarrow 0$, then, the parameter $\gamma = \varepsilon^2/(2\sigma^2) \rightarrow \infty$. From Theorem 26, part (b), one has $\lim_{\gamma \rightarrow \infty} M_{HK}^{(1)}(\gamma, \alpha) = 1$ (α being fixed). Thus, from Theorem 31, part (b), one concludes that $m(\gamma, \alpha) \rightarrow \infty$. Therefore, one obtains $SNR = \sqrt{m(\gamma, \alpha)} \rightarrow \infty$. Moreover, if $\sigma^2 \rightarrow 0$, then $\Omega = \varepsilon^2 + 2\sigma^2\alpha \rightarrow \varepsilon^2$, which is independent of the diffuse signal parameters σ^2 and α . Therefore, the Nakagami, just as the Rice distribution and the homodyned K-distribution, is compatible with the limit case of a vanishing diffuse signal.

7.4 Parameter Estimation Methods

We discuss various known methods for the estimation of the parameters of the distributions presented in Sect. 7.3 based on an independent and identically distributed (i.i.d.) sample set (A_1, \dots, A_N) of positive real numbers (representing the amplitude).

7.4.1 Overview of a Few Estimation Methods

7.4.1.1 The MLE and the MAP

The MLE is defined as a critical point of the log-likelihood function (Edgeworth 1908, 1909; Fisher 1912, 1922, 1925) (the reader may consult Pratt 1976)

$$L(\theta) = \sum_{i=1}^N \log P(A_i | \theta), \quad (7.12)$$

where θ represents the vector of parameters of the distribution and $\{A_1, \dots, A_N\}$ is the sample data of size N . Actually, there might be multiple critical points and no global maximum (on the

entire parameter domain). However, if the true value of the parameters is in the interior of a compact subset of the parameter domain, then the global maximum of the log-likelihood on that compact set converges to the true value of the parameters as the size of the sample tends to infinity (Redner 1981). Thus, one can define the MLE as the critical point with the largest log-likelihood value (Redner and Walker 1984). A major difficulty lies in the analysis of the critical points: how many are there and which one coincides with the MLE? In fact, if the sample size is not sufficiently large, there might be no critical point of the log-likelihood function. Thus, one needs to address this issue before applying any numerical method to find the MLE.

One may also wish to impose a prior $\pi(\theta)$ on the parameters of the distribution. In that case, one considers the critical points of the constrained log-likelihood function

$$L(\theta) + \log \pi(\theta), \quad (7.13)$$

where $\log \pi(\theta)$ is viewed as a regularizing term. The MAP can then be defined as the critical point with the largest value of the constrained log-likelihood function.

7.4.1.2 Moments-Based Methods

Moments' methods have the advantage, over the MLE, of resulting into simpler and faster algorithms. On the other hand, the resulting systems of equations do not always admit a solution.

The simplest of these methods is based on the first few moments of the intensity. The number of moments considered is then equal to the number of parameters in the estimated distribution: one for the Rayleigh distribution, two for the Rice distribution, the K-distribution or the Nakagami distribution, and three for the homodyned K-distribution. Thus, one solves the system of equations

$$E[I^\nu] = \bar{I}^\nu, \quad \nu = 1, \dots, r, \quad (7.14)$$

where r is the number of parameters of the distribution. In Eq. (7.14), the left-hand side $E[I^\nu]$

represents a function of the parameters of the distribution, whereas the right-hand side \bar{I}^ν is the empirical moment computed from the data.

A slightly more complex method is based on the first few moments of the amplitude. Thus, one solves the system of equations

$$E[A^\nu] = \bar{A}^\nu, \quad \nu = 1, \dots, r. \quad (7.15)$$

Since the intensity is the square of the amplitude, such methods use lower orders of the intensity and, thus, are likely to be less sensitive to noise. On the other hand, the analytical expressions of those moments are typically more complex than integral order moments of the intensity.

One may also use arbitrary fractional order moments of the intensity. For later reference, we find convenient to introduce the $M^{(\nu)}$ -statistics, defined as

$$M^{(\nu)} = \frac{\bar{A}^\nu}{(\bar{I})^{\nu/2}}, \quad (7.16)$$

where $\nu > 0$. That statistic is the fractional moment of order ν of the amplitude normalized so that it becomes invariant under multiplication of the signal by a positive scaling constant.

Lemma 1 *For any non-constant random variable, $0 < M^{(\nu)} < 1$, if $0 < \nu < 2$, whereas $M^{(\nu)} > 1$, if $\nu > 2$.*

Proof If $\nu < 2$, the function $I^{\nu/2}$ is convex. Therefore, by Jensen's inequality (Jensen 1906), we have $E[A^\nu] = E[I^{\nu/2}] < (E[I])^{\nu/2}$ since the random variable I is non-constant. If $\nu > 2$, the function $I^{\nu/2}$ is concave and we obtain the reversed inequality. ■

If the number of parameters r is at least 2, the method based on the first few moments of the intensity is equivalent to solving the system

$$E[I] = \bar{I}; \quad \frac{E[A^\nu]}{(E[I])^{\nu/2}} = \frac{\bar{A}^\nu}{(\bar{I})^{\nu/2}}, \quad \nu = 4, 6 \quad (7.17)$$

and thus amounts to working with the $M^{(4)}$ and $M^{(6)}$ statistics. Similarly, the method based on the first few moments of the amplitude is equivalent to solving the system

$$E[I] = \bar{I}; \quad \frac{E[A^v]}{(E[I])^{v/2}} = \frac{\bar{A}^v}{(\bar{I})^{v/2}}, \quad v = 1, 3 \quad (7.18)$$

and thus amounts to working with the $M^{(1)}$ and $M^{(3)}$ statistics.

One may also combine various moments in the form of the SNR of a fractional order of the amplitude

$$R^{(v)} = \frac{\bar{A}^v}{(\bar{A}^{2v} - (\bar{A}^v)^2)^{1/2}}, \quad (7.19)$$

or the skewness

$$S^{(v)} = \frac{\bar{A}^{3v} - 3\bar{A}^v \bar{A}^{2v} + 2(\bar{A}^v)^3}{(\bar{A}^{2v} - (\bar{A}^v)^2)^{3/2}}, \quad (7.20)$$

or the kurtosis

$$K^{(v)} = \frac{\bar{A}^{4v} - 4\bar{A}^v \bar{A}^{3v} + 6\bar{A}^{2v} (\bar{A}^v)^2 - 3(\bar{A}^v)^4}{(\bar{A}^{2v} - (\bar{A}^v)^2)^2}. \quad (7.21)$$

Note that these three statistics can be expressed in terms of the family of $M^{(v)}$ -statistics. For instance, we have $R^{(v)} = \frac{M^{(v)}}{(M^{(2v)} - (M^{(v)})^2)^{1/2}}$.

Considering more equations than the number of parameters of the distribution yields an overdetermined system of (nonlinear) equations that may be solved in the sense of the least mean square (LMS). Thus, overall, all these methods amount to considering various combinations of the $M^{(v)}$ -statistics.

7.4.1.3 Log-Moments-Based Methods

One may also work with moments of functions of the intensity that involve its logarithm. Ideally,

one would consider powers of the logarithm of the intensity. But powers greater than 1 appear to be intractable for the distributions considered in this chapter because the resulting integrals are not known explicitly as far as we can tell. Moreover, one may want to obtain functions that are invariant under a change of the intensity by a scaling factor. Thus, one is lead to the so-called U -statistics (Oliver 1993)

$$U = \bar{\log I} - \log \bar{I} \quad (7.22)$$

and the X -statistics (Blacknell and Tough 2001)

$$X = \bar{I \log I / \bar{I}} - \bar{\log I}. \quad (7.23)$$

Lemma 2 *For any non-constant random variable, $U < 0$.*

Proof The function $\log I$ is convex. Therefore, from Jensen's inequality, we obtain $E[\log I] < \log E[I]$, since the random variable I is non-constant. ■

Lemma 3 *For any non-constant random variable, $X > 0$.*

Proof The function $I \log I$ is concave. Thus, $E[I \log I] > E[I] \log E[I]$. From Lemma 2, we conclude that $E[I \log I] > E[I]E[\log I]$. ■

7.4.2 Parameter Estimation Method for the Rayleigh Distribution

Since a Rayleigh distribution with parameter σ^2 on the amplitude A is equivalent to an exponential distribution with parameter $2\sigma^2$ on the intensity $I = A^2$, the MLE of the parameter σ^2 is equal to $\bar{I}/2$. Note that, in this special case, the MLE coincides with the estimator based on the first moment of the intensity.

7.4.3 Parameter Estimation Methods for the Rice Distribution

7.4.3.1 The MLE for the Rice Distribution

In Talukdar and Lawding (1991), the Rice distribution is estimated in the sense of the MLE, as follows.

Theorem 5 (Talukdar and Lawding 1991) *Let A_1, \dots, A_N be a finite sample set of positive numbers. Let $\varepsilon \geq 0$ and $\sigma^2 > 0$ be the parameters of the Rice distribution. Let $\mu = \varepsilon^2 + 2\sigma^2$, and $\kappa = \varepsilon^2/(2\sigma^2)$. Let $y_i = A_i/\sqrt{\bar{I}}$, where $\bar{I} = 1/N \sum_{i=1}^N A_i^2$. Then, the critical points of the log-likelihood function $L_{\text{Ri}}(\varepsilon, \sigma^2)$ of the Rice distribution are the points of the form*

$$\varepsilon = \sqrt{\mu\kappa/(\kappa + 1)}; \quad \sigma^2 = \mu/(2(\kappa + 1)), \quad (7.24)$$

where $\mu = \bar{I}$ and $\kappa \geq 0$ is any root of the function $f(\kappa)$ defined by

$$\frac{1}{(1+\kappa)} + \frac{(1+2\kappa)}{N\sqrt{\kappa(1+\kappa)}} \sum_{i=1}^N y_i \frac{I_1(2y_i\sqrt{\kappa(1+\kappa)})}{I_0(2y_i\sqrt{\kappa(1+\kappa)})} - 2. \quad (7.25)$$

Here, I_p denotes the modified Bessel function of the first kind of order p (the subscript avoids the confusion with the intensity I).

Theorem 5 gives a useful information on the value of μ for the critical points of the log-likelihood function. It also introduces a one-variable function $f(\kappa)$. But the main drawback is the lack of information on the roots of f . Fortunately, a more recent result gives complete information about the critical points of the log-likelihood function of the Rice distribution in the following form.

Theorem 6 (Carrobi and Cati 2008) *Let A_1, \dots, A_N be a finite sample set of positive numbers. Let $\varepsilon \geq 0$ and $\sigma^2 > 0$ be the parameters of the Rice distribution. Let $\bar{I} = 1/N \sum_{i=1}^N A_i^2$. Assume that the elements A_i are not all identical. Then, the log-likelihood function $L_{\text{Ri}}(\varepsilon, \sigma^2)$ of the Rice distribution has exactly two critical points: $(0, \bar{I}/2)$ and another one, denoted $(\hat{\varepsilon}, \hat{\sigma}^2)$, that satisfies $\hat{\varepsilon} > 0$ and $\hat{\sigma}^2 > 0$. Moreover, the MLE is the second one. In fact, the MLE is actually an absolute maximum of the log-likelihood function on its domain.*

Thus, the MLE $(\hat{\varepsilon}, \hat{\sigma}^2)$ consists in the unique critical point of the log-likelihood function $L_{\text{Ri}}(\varepsilon, \sigma^2)$ for which both coordinates are positive.

7.4.3.2 Expression of Fractional Order Moments of the Amplitude

The $M^{(v)}$ -statistics is explicitly known for the Rice distribution.

Theorem 7 (Rice 1954) *Assume that $A = \sqrt{I}$ is distributed according to the Rice distribution, with parameters $\varepsilon \geq 0$ and $\sigma^2 > 0$. Set $\kappa = \varepsilon^2/(2\sigma^2)$. Then, the $M^{(v)}$ -statistics $E[A^v]/E[I]^{v/2}$ is equal to*

$$M_{\text{Ri}}^{(v)}(\kappa) = \frac{\Gamma(v/2 + 1)}{(\kappa + 1)^{v/2}} {}_1F_1(-v/2, 1, -\kappa), \quad (7.26)$$

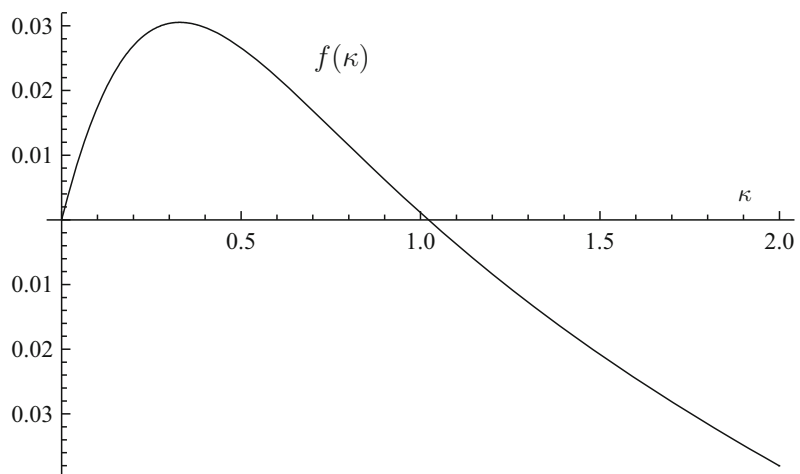
where ${}_pF_q(a_1, \dots, a_p; b_1, \dots, b_q; z)$ is the generalized hypergeometric series (here $p = q = 1$).

7.4.3.3 Method Based on the Moments of the Amplitude

In Talukdar and Lawding (1991), an estimation method of the Rice distribution based on the first two moments of the amplitude is proposed as an alternative to the MLE. The method consists in solving the system of equations

$$E[A] = \bar{A}; \quad E[A^2] = \bar{A}^2. \quad (7.27)$$

Fig. 7.2 Typical behavior of the function $f(\kappa)$ defined in Eq. (7.25), assuming that the data elements are not all identical. The function f has two non-negative roots (0 and $\kappa_* > 0$); $f(\kappa) > 0$ for $0 < \kappa < \kappa_*$, and $f(\kappa) < 0$ for $\kappa > \kappa_*$ (here, $N = 2$, $y_1 = 0.5$, $y_2 = \sqrt{2 - (0.5)^2}$, so that $\frac{1}{2}(y_1^2 + y_2^2) = 1$)



For that purpose, it is proposed to consider the equivalent system $E[I] = \bar{I}$ and $\frac{E[A]}{E[I]^{1/2}} = M^{(1)}$. The point of using this equivalent system is that the $M^{(1)}$ -statistics for the Rice distribution depends only on the parameter κ . As a special case of Theorem 7, we have the $M^{(1)}$ -statistics.

Corollary 1 (Talukdar and Lawding 1991)

Assume that $A = \sqrt{I}$ is distributed according to the Rice distribution, with parameters $\varepsilon \geq 0$ and $\sigma^2 > 0$. Set $\kappa = \varepsilon^2/(2\sigma^2)$. Then, the $M^{(1)}$ -statistics $E[A]/E[I]^{1/2}$ is equal to

$$\begin{aligned} M_{\text{Ri}}^{(1)}(\kappa) &= \frac{\Gamma(3/2)}{\sqrt{\kappa+1}} \\ &\times e^{-\kappa/2} \left((1+\kappa)I_0(\kappa/2) \right. \\ &\quad \left. + \kappa I_1(\kappa/2) \right), \end{aligned} \quad (7.28)$$

where I_p denotes the modified Bessel function of the first kind of order p .

7.4.3.4 Discussion

In this section, we present a new result on the computation of the MLE of the Rice distribution. We show that the Talukdar–Lawing estimator of Sect. 7.4.3.3 can be computed with a

binary search algorithm. We introduce two log-moments-based methods for the Rice distribution. Finally, we compare these estimators on simulated data.

Concerning the MLE computation, a little more work allows to combine Theorems 5 and 6 into the following result. See Fig. 7.2 for an illustration of the function $f(\kappa)$.

Theorem 8 Notation as in Theorem 5. Assume that the data elements A_i are not all identical. Then, the function $f(\kappa)$ of Eq. (7.25) has exactly two non-negative roots: 0 and a unique positive root, denoted κ_* . The MLE is expressed as in Eq. (7.24), with $\kappa = \kappa_*$ (i.e., the unique positive root of the function f). Moreover, $f(\kappa) > 0$ on the interval $(0, \kappa_*)$, and $f(\kappa) < 0$ on the interval (κ_*, ∞) .

Theorem 8 implies that an efficient binary search algorithm can be used for the computation of the MLE of the Rice distribution.

Concerning the estimation method based on the $M^{(v)}$ -statistics, in general, there is no closed form for a solution to Eq. $M_{\text{Ri}}^{(v)}(\kappa) = M$, but one can use the following result, relevant for any $v \neq 2$. See Fig. 7.3, right column, for an illustration of the function $M_{\text{Ri}}^{(v)}(\kappa)$.

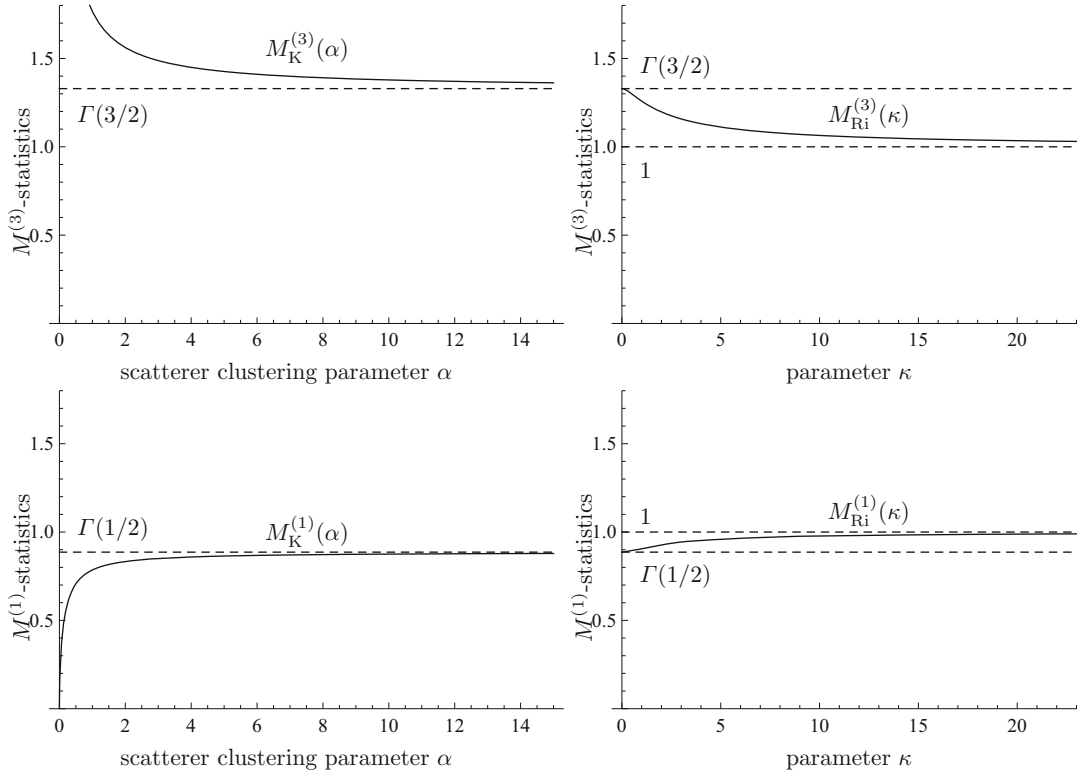


Fig. 7.3 Typical behavior of the $M^{(v)}$ -statistics for the K-distribution (left column) and the Rice distribution (right column), when $v < 2$ (bottom row) and $v > 2$ (top row)

Theorem 9 Let $v > 0$. Then,

- $\lim_{\kappa \rightarrow 0} M_{\text{Ri}}^{(v)}(\kappa) = \Gamma(v/2 + 1)$.
- $\lim_{\kappa \rightarrow \infty} M_{\text{Ri}}^{(v)}(\kappa) = 1$.
- If $v < 2$, the function $M_{\text{Ri}}^{(v)}(\kappa)$ is an increasing function, and if $v > 2$, the function $M_{\text{Ri}}^{(v)}(\kappa)$ is a decreasing function.

Thus, let $M > 0$ be a real number (playing the role of the $M^{(v)}$ -statistics). If $v < 2$ and $\Gamma(v/2 + 1) \leq M < 1$, then an efficient binary search algorithm yields the unique solution to the equation $M_{\text{Ri}}^{(v)}(\kappa) = M$. Indeed, from Theorem 9, the function $M_{\text{Ri}}^{(v)}(\kappa)$ is increasing in that case and its range is the interval $[\Gamma(v/2 + 1), 1]$. On the other hand, if $v < 2$ and $M < \Gamma(v/2 + 1)$, then

there is no solution to the equation $M_{\text{Ri}}^{(v)}(\kappa) = M$. Nevertheless, in that case, the value $\kappa = 0$ minimizes the distance between $M_{\text{Ri}}^{(v)}(\kappa)$ and M . Thus, it makes sense to take $\kappa = 0$. Similarly, if $v > 2$ and $1 < M \leq \Gamma(v/2 + 1)$, then there is a unique solution to the equation $M_{\text{Ri}}^{(v)}(\kappa) = M$, and this solution can be found efficiently with a binary search algorithm. On the other hand, if $v > 2$ and $M > \Gamma(v/2 + 1)$, one may take $\kappa = 0$. Thus, it makes sense to switch to the Rayleigh model (corresponding to $\kappa = 0$), whenever the equation $M_{\text{Ri}}^{(v)}(\kappa) = M$ has no solution. This argument applies to the special case where $v = 1$, which corresponds to the Talukdar–Lawing method of Corollary 1. For later reference, we introduce here

what we call the Rice conditions

$$\nu < 2 \text{ and } \Gamma(\nu/2 + 1) \leq M < 1, \text{ or } \nu > 2 \text{ and } 1 < M \leq \Gamma(\nu/2 + 1). \quad (7.29)$$

Thus, as explained above, the equation $M_{\text{Ri}}^{(\nu)}(\kappa) = M$ has a solution if and only if the Rice conditions are satisfied. Note that the U and X -statistics can be computed analytically for the Rice distribution.

Theorem 10 Assume that $A = \sqrt{I}$ is distributed according to the Rice distribution, with parameters $\varepsilon \geq 0$ and $\sigma^2 > 0$. Set $\kappa = \varepsilon^2/(2\sigma^2)$. Then,

- (a) The U -statistics $E[\log I] - \log E[I]$ is equal to

$$U_{\text{Ri}}(\kappa) = \Gamma(0, \kappa) + \log \frac{\kappa}{\kappa + 1}, \quad (7.30)$$

where $\Gamma(0, x)$ is the incomplete gamma function $\int_x^\infty \frac{e^{-t}}{t} dt$.

- (b) The X -statistics $E[I \log I]/E[I] - E[\log I]$ is equal to

$$X_{\text{Ri}}(\kappa) = \frac{1}{\kappa + 1}(2 - e^{-\kappa}). \quad (7.31)$$

Theorem 11 below shows that a binary search algorithm can be used to solve the equation $U_{\text{Ri}} = U$ if and only if $U \geq -\gamma_E$, where γ_E is Euler's constant. If ever $U < -\gamma_E$, one may switch to the Rayleigh model ($\kappa = 0$). Similarly, Theorem 12 shows that the equation $X_{\text{Ri}} = X$ has a solution (which is then unique and can be found with a binary search algorithm) if and only if $X < 4$. If ever $X \geq 4$, one may switch to the Rayleigh model.

Theorem 11 (a) $\lim_{\kappa \rightarrow 0} U_{\text{Ri}}(\kappa) = -\gamma_E$, where γ_E is Euler's constant.

- (b) $\lim_{\kappa \rightarrow \infty} U_{\text{Ri}}(\kappa) = 0$.
(c) The function $U_{\text{Ri}}(\kappa)$ is an increasing function.

Theorem 12 (a) $\lim_{\kappa \rightarrow 0} X_{\text{Ri}}(\kappa) = 1$.

- (b) $\lim_{\kappa \rightarrow \infty} X_{\text{Ri}}(\kappa) = 0$.
(c) The function $X_{\text{Ri}}(\kappa)$ is a decreasing function.

See Fig. 7.4, right column, for an illustration of the X -statistics for the Rice distribution.

In order to compare these four estimators, we considered the parameter $k = \sqrt{2\kappa} = \varepsilon/\sigma$ with values in the set $\{0.1, 0.2, \dots, 2.0\}$. For each value of k , 1000 datasets of $N = 1000$ elements each were simulated according to the corresponding Rice distribution. Thus, we could estimate the normalized mean squared error (MSE) of the estimator \hat{k} as $\sqrt{E[(\hat{k} - k)^2]}/k$. The resulting normalized MSE curves are presented in Fig. 7.5. As one can see, the MLE is slightly better than the estimators based on the $M^{(1)}$ or the X -statistics. The method based on the U -statistics is slightly worse than the other estimators. The two estimators based on the $M^{(1)}$ and the X -statistics are practically equivalent.

7.4.4 Parameter Estimation Methods for the K-Distribution

7.4.4.1 The MLE for the K-Distribution

The partial derivatives of the log-likelihood function of the K-distribution with respect to α and σ^2 are equal to

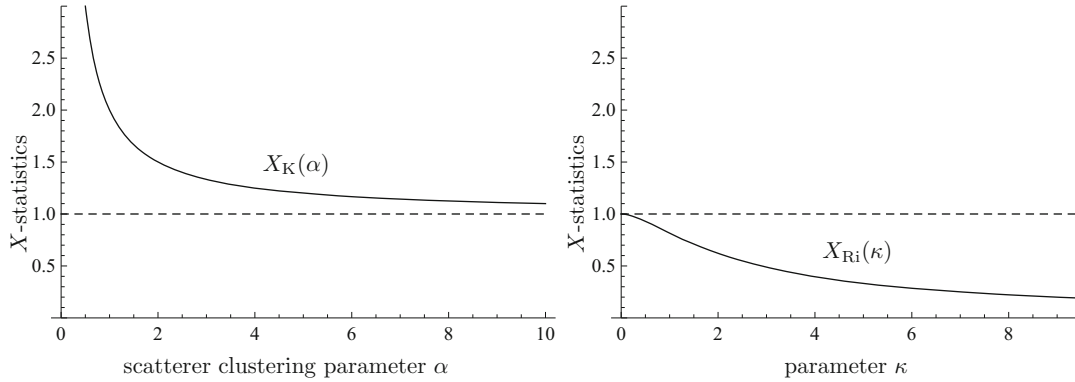


Fig. 7.4 Typical behavior of the X -statistics for the K-distribution (left column) and the Rice distribution (right column)

$$\frac{\partial}{\partial \alpha} L_K(\sigma^2, \alpha) = -N\psi(\alpha) + \sum_{i=1}^N \log\left(\frac{1}{\sqrt{2\sigma^2}} A_i\right) + \frac{\frac{\partial}{\partial \alpha} K_{\alpha-1}\left(\sqrt{\frac{2}{\sigma^2}} A_i\right)}{K_{\alpha-1}\left(\sqrt{\frac{2}{\sigma^2}} A_i\right)}; \quad (7.32)$$

$$\frac{\partial}{\partial \sigma^2} L_K(\sigma^2, \alpha) = -\frac{N\alpha}{\sigma^2} + \sum_{i=1}^N \frac{1}{\sigma^2} \left(\frac{1}{\sqrt{2\sigma^2}} A_i\right) \frac{K_\alpha\left(\sqrt{\frac{2}{\sigma^2}} A_i\right)}{K_{\alpha-1}\left(\sqrt{\frac{2}{\sigma^2}} A_i\right)}. \quad (7.33)$$

Solutions to this system of two nonlinear equations are found numerically in Joughin et al. (1993). In Roberts and Furui (2000), an Expectation-Maximization (EM) algorithm is proposed for finding the MLE. In that context, the variable w of Eq. (7.4) is viewed as the latent variable. A variant of the EM algorithm is used in Chung et al. (2005) in place of the standard EM algorithm.

However, none of the methods (Joughin et al. 1993; Roberts and Furui 2000; Chung et al. 2005) can be used in full generality because the MLE is not always well defined for the K-distribution. See Sect. 7.4.4.6 for a discussion on that issue.

7.4.4.2 Expression of Fractional Order Moments of the Amplitude

The $M^{(v)}$ -statistics is explicitly known for the K-distribution.

Theorem 13 (Dutt and Greenleaf 1995)
Assume that $A = \sqrt{I}$ is distributed according to the K-distribution, with parameters $\sigma^2 > 0$ and $\alpha > 0$. Then, the $M^{(v)}$ -statistics $E[A^v]/E[I]^{v/2}$ is equal to

$$M_K^{(v)}(\alpha) = \Gamma(v/2 + 1) \frac{\Gamma(v/2 + \alpha)}{\alpha^{v/2} \Gamma(\alpha)}. \quad (7.34)$$

7.4.4.3 A Method Based on the Moments of the Intensity

The simplest moments method consists in solving the system of equations

$$E[I] = \bar{I}; \quad E[I^2] = \bar{I}^2. \quad (7.35)$$

Equivalently, that method is based on the mean intensity and the $M^{(4)}$ -statistics (that statistics is called the V -statistics in Blacknell and Tough

(2001)). One computes for the K-distribution $V_K(\alpha) = E[I^2]/E[I]^2 = 2\left(1 + \frac{1}{\alpha}\right)$. Thus, there is a solution to the system (7.35) if and only if $V > 2$, in which case the solution is equal to $\alpha = 2/(V - 2)$.

7.4.4.4 Two Methods Based on Fractional Order Moments of the Amplitude

In Dutt and Greenleaf (1995), the authors suggest to use the SNR based on fractional order moments in the form of the $R^{(v)}$ -statistics, where $v > 0$. In

$$R_K^{(v)}(\alpha) = \frac{\Gamma(v/2 + 1)\Gamma(v/2 + \alpha)}{\sqrt{\Gamma(v + 1)\Gamma(v + \alpha)\Gamma(\alpha) - \Gamma^2(v/2 + 1)\Gamma^2(v/2 + \alpha)}}. \quad (7.36)$$

In Iskander and Zoubir (1999), the authors suggest the use of fractional order moments in the form of the Y -statistics $\frac{E[A^{2r+2s}]}{E[A^{2r}]E[A^{2s}]}$, where $s > 0$, and $r \in \mathbb{N}$. It is shown that a value of $s < 2$ yields lower variance of the resulting estimator, taking $r = 1$. The following result holds.

Theorem 15 (Iskander and Zoubir 1999) Assume that A is distributed according to the K-distribution, with parameters $\sigma^2 > 0$ and $\alpha > 0$. Then, the Y -statistics $\frac{E[A^{2r+2s}]}{E[A^{2r}]E[A^{2s}]}$ is expressed as

$$Y_K(\alpha) = (1 + s)(1 + \frac{s}{\alpha}). \quad (7.37)$$

Using Theorem 15, there is a solution to the equation $Y_K(\alpha) = Y$ if and only if $Y > 1 + s$. In that case, $\alpha = \frac{s(1+s)}{Y-(1+s)}$ is the unique solution. Note that the V -statistics corresponds to the special case where $s = 1$.

7.4.4.5 Two Log-Moments Methods

In the case of the K-distribution, it has been proposed (Oliver 1993) to use the U -statistics in order to estimate α .

that study, it is shown that a value of $v = 1/4$ yields a reliable estimator. We have the following result (note that there is a typo in Dutt and Greenleaf (1995, Eq. (6), p. 253)).

Theorem 14 (Dutt and Greenleaf 1995)

Assume that A is distributed according to the K-distribution, with parameters $\sigma^2 > 0$ and $\alpha > 0$. Then, the $R^{(v)}$ -statistics $\frac{E[A^v]}{\sqrt{E[A^{2v}] - E[A^v]^2}}$ is expressed as

Theorem 16 (Oliver 1993) Assume that \sqrt{I} is distributed according to the K-distribution, with parameters $\sigma^2 > 0$ and $\alpha > 0$. Then, the U -statistics $E[\log I] - \log E[I]$ is expressed as

$$U_K(\alpha) = -\gamma_E + \psi(\alpha) - \log \alpha, \quad (7.38)$$

where γ_E is Euler's constant and $\psi(z) = d[\log \Gamma(z)]/dz$ is the digamma function (Abramowitz and Stegun 1972, (6.3.1)).

There is also a method (Blacknell and Tough 2001) based on the X -statistics.

Theorem 17 (Blacknell and Tough 2001) Assume that \sqrt{I} is distributed according to the K-distribution, with parameters $\sigma^2 > 0$ and $\alpha > 0$. Then, the X -statistics $E[I \log I]/E[I] - E[\log I]$ is expressed as

$$X_K(\alpha) = 1 + \frac{1}{\alpha}. \quad (7.39)$$

Lemma 3 guarantees that X is non-negative. Thus, there is a solution to the equation $X_K(\alpha) = X$ if and only if $X > 1$, in which case the unique solution is equal to $\alpha = 1/(X - 1)$. See Fig. 7.4, left column, for an illustration of the X -statistics for the K-distribution.

7.4.4.6 Discussion

In this section, we present further results on the MLE and the MAP of the K-distribution. We then show that the methods introduced in Sects. 7.4.4.3 to 7.4.4.5 can be solved with a binary search algorithm. Finally, we present a comparison of these estimators on simulated data.

Arguing that the existing methods for computing the MLE are time consuming and that moments-based methods do not always lead to a solution of the resulting equations, a Bayesian estimation method of the SNR (denoted D and called the detection index) was proposed in Abraham and Lyons (2010).

To clarify the notion of MLE for the K-distribution, we present the following two results.

Theorem 18 Let $\alpha > 0$ be fixed. Then, there exists a root $\sigma^2(\alpha, \tilde{A}) > 0$ of $\frac{\partial}{\partial \sigma^2} L_K(\sigma^2, \alpha)$.

Theorem 19 Let $N \geq 1$ be the sample size and $\sigma^2(\alpha, \tilde{A})$ denote any root of $\frac{\partial}{\partial \sigma^2} L_K(\sigma^2, \alpha)$. Then,

- (a) $\lim_{\alpha \rightarrow 0} \alpha \frac{\partial}{\partial \alpha} L_K(\sigma^2(\alpha, \tilde{A}), \alpha) \geq N$.
- (b) $\lim_{\alpha \rightarrow \infty} \alpha \frac{\partial}{\partial \alpha} L_K(\sigma^2(\alpha, \tilde{A}), \alpha) = 0$.

Thus, if ever the function $\frac{\partial}{\partial \alpha} L_K(\sigma^2(\alpha, \tilde{A}), \alpha)$ is decreasing for some sample set, then there is no MLE. This is the case, for instance, if $\{A_1, A_2\} = \{\frac{1}{2}, \frac{\sqrt{7}}{2}\}$ (see Fig. 7.6). So, the point in considering other estimators than the MLE is not so much that its computation is time consuming, but rather that it is not always well defined for the K-distribution.

However, one may set a prior on the parameters σ^2 and α and see if the maximum

a posteriori (MAP) is well defined. For the K-distribution, let us consider the prior $\pi(\alpha) = 1/\alpha$ (so, this prior does not depend on σ^2 for simplicity of technical considerations). This amounts to setting the Jeffreys non-informative prior (Jeffreys 1946) on the parameter α . Recall that the Jeffreys prior is defined as $\pi(\alpha) = (I_F(\alpha))^{1/2}$, where $I_F(\alpha)$ denotes the Fisher information (Fisher 1956), namely $I_F(\alpha) = -E[\frac{\partial^2}{\partial \alpha^2} \log P(A | \sigma^2, \alpha)] = E[(\frac{\partial}{\partial \alpha} \log P(A | \sigma^2, \alpha))^2]$. In Abraham and Lyons (2010), it is shown that $\pi(\alpha) \sim 1/\alpha$ for large values of α . Then, the MAP corresponds to a solution to the system of equations

$$\frac{\partial}{\partial \alpha} L_K(\sigma^2, \alpha) + \frac{\partial}{\partial \alpha} \log \pi(\alpha) = 0; \quad (7.40)$$

$$\frac{\partial}{\partial \sigma^2} L_K(\sigma^2, \alpha) = 0. \quad (7.41)$$

Now, with the proposed prior, we obtain $\frac{\partial}{\partial \alpha} \log \pi(\alpha) = -1/\alpha$. Then, from Theorem 19, we know that $\frac{\partial}{\partial \sigma^2} L_K(\sigma^2(\alpha, \tilde{A}), \alpha) - 1/\alpha \geq (N - 1)/\alpha > 0$, for α sufficiently small and $N > 1$, and that $\frac{\partial}{\partial \alpha} L_K(\sigma^2(\alpha, \tilde{A}), \alpha) - 1/\alpha < 0$ for α sufficiently large. Therefore, the Intermediate Value Theorem implies that there is $\alpha > 0$ for which $\frac{\partial}{\partial \alpha} L_K(\sigma^2(\alpha, \tilde{A}), \alpha) - 1/\alpha = 0$. Thus, this MAP estimator is well defined for the K-distribution. Furthermore, its computation is amenable to a binary search algorithm. Note that one may have chosen the prior $\pi(\sigma^2, \alpha) = \frac{1}{\sigma}$ because it is *scale-invariant* (i.e., $P_K(A | \sigma^2, \alpha) = \frac{1}{\sigma} P_K(\frac{A}{\sigma} | 1, \alpha)$). However, with that choice of prior, one may have an undefined MAP estimator. Other priors are possible, but we have not explored that avenue here.

Note that in Abraham and Lyons (2010), it is advocated to take the non-informative prior $1/\alpha^2$ instead of the Jeffreys prior $1/\alpha$, in order to obtain a posterior distribution with a well-defined mean, i.e., such that $\int_0^\infty \alpha P(\alpha | \tilde{A}) d\alpha < \infty$. But there is no need to require a finite

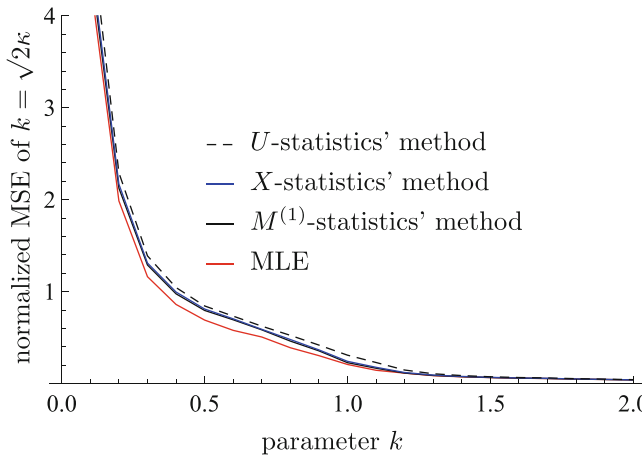


Fig. 7.5 Comparison of the normalized MSE statistics (—) and the U -statistics (---) in the case of the Rice distribution. The sample size is $N = 1000$

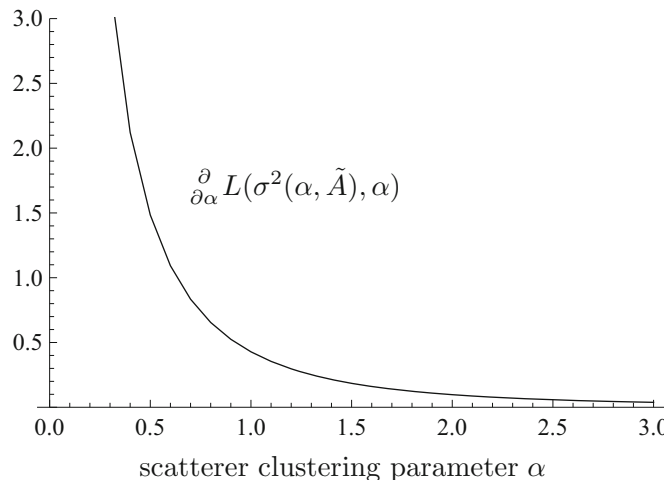


Fig. 7.6 Behavior of the function $\frac{\partial}{\partial \alpha} L_K(\sigma^2(\alpha, \tilde{A}), \alpha)$ for the K-distribution in the case where $\tilde{A} = \{\frac{1}{2}, \frac{\sqrt{7}}{2}\}$. The MLE is not defined in this case

posterior mean to define the MAP. The only requirement is a finite sum for the posterior distribution (i.e., $\int_0^\infty P(\alpha | \tilde{A}) d\alpha < \infty$). Now, taking the prior $1/\alpha^2$ (Abraham and Lyons 2010), the first statement is equivalent

to $\int_0^\infty \alpha \prod_{i=1}^N P(A_i | \sigma^2 \alpha) \frac{1}{\alpha^2} d\alpha < \infty$. On the other hand, taking the Jeffreys prior $1/\alpha$, the second statement is equivalent to $\int_0^\infty \prod_{i=1}^N P(A_i | \sigma^2 \alpha) \frac{1}{\alpha} d\alpha < \infty$. Thus, as

one can see, the two statements are equivalent (because two different priors are considered).

One may wish to simplify the above MAP estimator by considering a hybrid MAP. Namely, the

first moment of the intensity yields the identity $\sigma^2 = \bar{I}/(2\alpha)$. Substituting this expression into the difference of Eq. (7.40) with Eq. (7.41) yields the equation

$$\left\{ \alpha \frac{\partial}{\partial \alpha} L_K(\sigma^2, \alpha) - \sigma^2 \frac{\partial}{\partial \sigma^2} L_K(\sigma^2, \alpha) \right\} \Big|_{\sigma^2=\bar{I}/(2\alpha)} - 1 = 0. \quad (7.42)$$

The following result implies that a solution to Eq. (7.42) can be found with a binary search algorithm, provided that the sample size N is greater than 1.

-
- (a) $\lim_{\alpha \rightarrow 0} \left\{ \alpha \frac{\partial}{\partial \alpha} L_K(\sigma^2, \alpha) - \sigma^2 \frac{\partial}{\partial \sigma^2} L_K(\sigma^2, \alpha) \right\} \Big|_{\sigma^2=\bar{I}/(2\alpha)} = N$.
 - (b) $\lim_{\alpha \rightarrow \infty} \left\{ \alpha \frac{\partial}{\partial \alpha} L_K(\sigma^2, \alpha) - \sigma^2 \frac{\partial}{\partial \sigma^2} L_K(\sigma^2, \alpha) \right\} \Big|_{\sigma^2=\bar{I}/(2\alpha)} = 0$.
-

Concerning the estimation method based on the $M^{(v)}$ -statistics, in general, there is no closed form for a solution to the equation $M_K^{(v)}(\alpha) = M$, but one can use the following result, relevant for any $v \neq 2$. See Fig. 7.3, left column, for an illustration of the function $M_K^{(v)}(\alpha)$.

Theorem 21 *We have the following properties:*

- (a) *If $v < 2$, then $\lim_{\alpha \rightarrow 0} M_K^{(v)}(\alpha) = 0$, and if $v > 2$, then $\lim_{\alpha \rightarrow 0} M_K^{(v)}(\alpha) = \infty$.*
 - (b) $\lim_{\alpha \rightarrow \infty} M_K^{(v)}(\alpha) = \Gamma(v/2 + 1)$.
 - (c) *If $v < 2$, then $M_K^{(v)}(\alpha)$ is strictly increasing on its domain $(0, \infty)$, and if $v > 2$, then*
-

$$v < 2 \text{ and } 0 < M < \Gamma(v/2 + 1), \text{ or } v > 2 \text{ and } \Gamma(v/2 + 1) < M. \quad (7.43)$$

$M_K^{(v)}(\alpha)$ is strictly decreasing on its domain $(0, \infty)$.

So, let $M > 0$ be a real number (playing the role of the $M^{(v)}$ -statistics). If $v < 2$ and $0 < M < \Gamma(v/2 + 1)$, then an efficient binary search algorithm yields the unique solution to the equation $M_K^{(v)}(\alpha) = M$. Indeed, from Theorem 21, the function $M_K^{(v)}(\alpha)$ is increasing in that case and its range is the interval $(0, \Gamma(v/2 + 1))$. On the other

hand, if $v < 2$ and $\Gamma(v/2 + 1) \leq M < 1$, then there is no solution to the equation $M_K^{(v)}(\alpha) = M$. However, in that case, the distance between $M_K^{(v)}(\alpha)$ and M is minimal as $\alpha \rightarrow \infty$. Thus, it makes sense to take the Rayleigh distribution. Similarly, if $v > 2$ and $M > \Gamma(v/2 + 1)$, then there is a unique solution to the equation $M_K^{(v)}(\alpha) = M$, and this solution can be found efficiently with a binary search algorithm. On the other hand, if $v > 2$ and $1 < M < \Gamma(v/2 + 1)$, one may take $\alpha \rightarrow \infty$. For later reference, we introduce here what we call the K-distribution conditions

Thus, the equation $M_K^{(v)}(\alpha) = M$ has a solution if and only if the K-distribution conditions are satisfied. Note that the Rice conditions (7.29) and the K-distribution conditions (7.43) are mutually exclusive and they are exhaustive (that is to say, with the understanding that M plays the role of the $M^{(v)}$ -statistics).

Concerning the parameter estimation method (Dutt and Greenleaf 1995), the following result

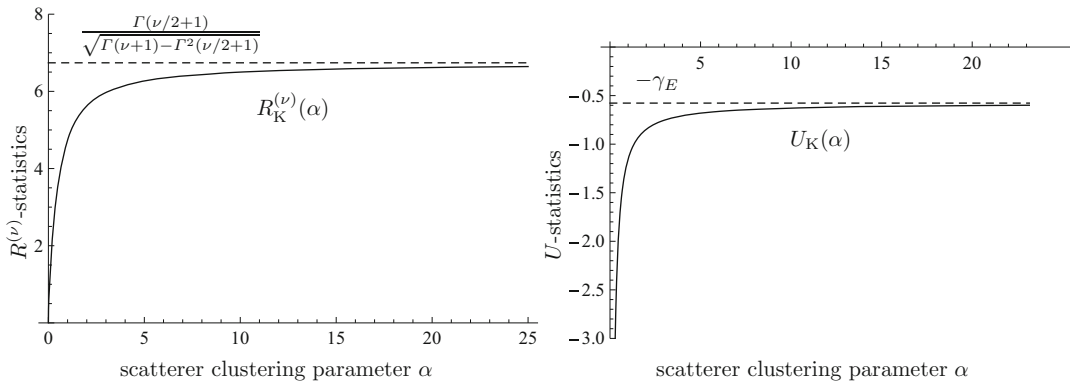


Fig. 7.7 Typical behavior of the $R^{(\nu)}$ -statistics (left image) and of the U -statistics (right image) for the K-distribution. Here, $\nu = 1/4$

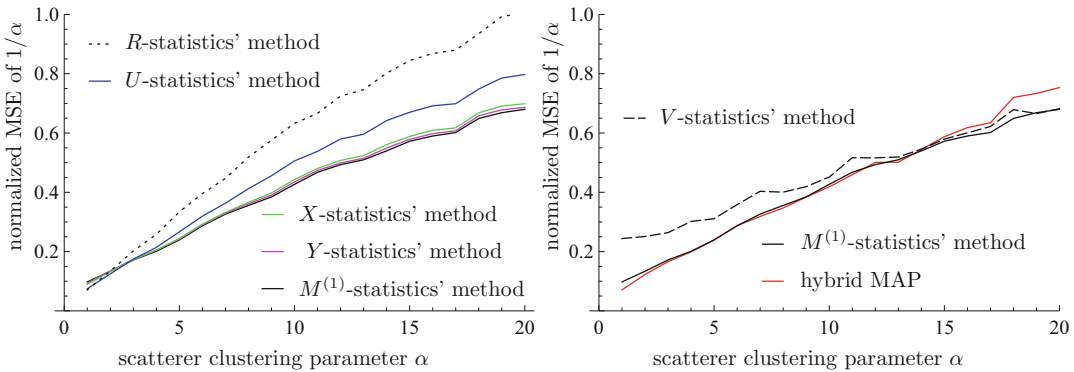


Fig. 7.8 Left: comparison between the normalized MSE $\sqrt{E[(\hat{\beta} - \beta)^2]}/\beta$, where $\beta = 1/\alpha$, of the estimators based on the $M^{(1)}$ -statistics (—), the Y -statistics (—), the X -statistics (—), the U -statistics (—), and the R -statistics

(···), for the K-distribution. Right: comparison between the normalized MSE of the estimators based on the $M^{(1)}$ -statistics (—), the V -statistics (---), and the hybrid MAP (—). The sample size is $N = 1000$

shows that the equation $R_K^{(v)}(\alpha) = R$, where $R > 0$ plays the role of the $R^{(v)}$ -statistics, has a solution if and only if $R < \frac{\Gamma(v/2+1)}{\sqrt{\Gamma(v+1)-\Gamma^2(v/2+1)}}$, and that there is at most one solution. Moreover, it shows that an efficient binary search algorithm can be used to find the solution, whenever it exists. Finally, one sees that the solution $\alpha = \infty$ is the one that minimizes the distance between $R_K^{(v)}(\alpha)$ and R , whenever the equation $R_K^{(v)}(\alpha) = R$ has no solution. This amounts to switch to the Rayleigh model, with parameter $a^2 = \lim_{\alpha \rightarrow \infty} \sigma^2 \alpha = \bar{I}$.

Theorem 22 *The following properties hold:*

- (a) $\lim_{\alpha \rightarrow 0} R_K^{(v)}(\alpha) = 0$.
- (b) $\lim_{\alpha \rightarrow \infty} R_K^{(v)}(\alpha) = \frac{\Gamma(v/2+1)}{\sqrt{\Gamma(v+1)-\Gamma^2(v/2+1)}}$.
- (c) $R_K^{(v)}(\alpha)$ is strictly increasing on its domain $(0, \infty)$.

Concerning the method (Oliver 1993), the following result shows that an efficient binary search algorithm can be used in order to find the unique solution to the equation $U_K(\alpha) = U$, whenever $U < -\gamma_E$. If ever $U \geq -\gamma_E$, Theorem 23 shows that it makes sense to adopt the Rayleigh model.

Theorem 23 *We have the following properties:*

- (a) $\lim_{\alpha \rightarrow 0} U_K(\alpha) = -\infty$.
- (b) $\lim_{\alpha \rightarrow \infty} U_K(\alpha) = -\gamma_E$.
- (c) $U_K(\alpha)$ is strictly increasing on its domain $(0, \infty)$.

Similarly, one may switch to the Rayleigh distribution, whenever $V \leq 2$ (cf. Sect. 7.4.4.3), or $Y \leq 1 + s$ (cf. Sect. 7.4.4.4), or $X \leq 1$ (cf.

Sect. 7.4.4.5). Theorems 22 and 23 are illustrated in Fig. 7.7.

In order to compare the various estimators, we considered the parameter α with values in the set $\{1, 2, \dots, 20\}$. For each value of α , 1000 datasets of $N = 1000$ elements each were simulated according to the corresponding K-distribution. As in Dutt and Greenleaf (1994), one may consider the estimation of the parameter $\beta = 1/\alpha$ instead of α itself. In that case, one does not need to discard values of $1/\alpha$ because whenever the method has no solution, one may switch to the Rayleigh model ($\alpha = \infty$), which corresponds to $1/\alpha = 0$. Thus, we could estimate the normalized mean squared error (MSE) of the estimator $\hat{\beta}$ as $\sqrt{E[(\hat{\beta} - \beta)^2]/\beta}$. The resulting normalized MSE curves are presented in Fig. 7.8. As one can see, the estimators based on the $M^{(1)}$, Y , or X statistics and the hybrid MAP are practically equivalent and are better than the estimators based on the U or the R statistics.

7.4.5 Parameter Estimation Methods for the Homodyned K-Distribution

7.4.5.1 Expression of Fractional Order Moments of the Amplitude

Theorem 24 *Assume that $A = \sqrt{I}$ is distributed according to the homodyned K-distribution, with parameters $\varepsilon \geq 0$, $\sigma^2 > 0$, and $\alpha > 0$. Let $\gamma = \varepsilon^2/(2\sigma^2)$. Then,*

- (a) (Prager 2002) *If $\gamma \geq 0$, the $M^{(v)}$ -statistics $E[A^v]/E[I]^{v/2}$ can be expressed in the following form:*

$$M_{HK}^{(v)}(\gamma, \alpha) = \frac{\Gamma(v/2 + 1)}{(\gamma + \alpha)^{v/2}} \int_0^\infty w^{v/2} {}_1F_1(-v/2, 1, -\frac{\gamma}{w}) G(w | \alpha, 1) dw, \quad (7.44)$$

where ${}_pF_q$ denotes the hypergeometric series (here, $p = q = 1$).

- (b) (Dutt and Greenleaf 1995) If $\gamma = 0$, the $M^{(v)}$ -statistics is equal to

$$M_{HK}^{(v)}(0, \alpha) = \Gamma(v/2 + 1) \frac{\Gamma(v/2 + \alpha)}{\alpha^{v/2} \Gamma(\alpha)}. \quad (7.45)$$

- (c) (Hruska and Oelze 2009) If $v/2 + \alpha$ is not an integer and $\gamma \geq 0$, the $M^{(v)}$ -statistics can be expressed as

$$\begin{aligned} M_{HK}^{(v)}(\gamma, \alpha) = & \frac{\Gamma(v/2 + 1)}{(\gamma + \alpha)^{v/2}} \left\{ \frac{\Gamma(v/2 + \alpha)}{\Gamma(\alpha)} {}_1F_2(-v/2; 1, 1 - v/2 - \alpha; \gamma) \right. \\ & + \frac{\Gamma(v/2 + 1) \sin(\pi v/2)}{\Gamma^2(1 + v/2 + \alpha) \sin(\pi(v/2 + \alpha))} \gamma^{v/2+\alpha} \\ & \left. \times {}_1F_2(\alpha; 1 + v/2 + \alpha, 1 + v/2 + \alpha; \gamma) \right\}. \end{aligned} \quad (7.46)$$

- (d) (Jakeman and Tough 1987) If $v/2 > 2$ is an integer and $\gamma \geq 0$, then the $M^{(v)}$ -statistics is equal to

$$M_{HK}^{(v)}(\gamma, \alpha) = \frac{(v/2)!(v/2)!}{(\gamma + \alpha)^{v/2} \Gamma(\alpha)} \sum_{i=0}^{v/2} \frac{\Gamma(v/2 - i + \alpha)}{i!i!(v/2 - i)!} \gamma^i. \quad (7.47)$$

7.4.5.2 A Method Based on the Moments of the Intensity

A moments' method for the estimation of the homodyned K-distribution was proposed in Dutt and Greenleaf (1994). Namely, one solves the system of equations

$$E[I] = \bar{I}; \quad E[I^2] = \bar{I^2}; \quad E[I^3] = \bar{I^3} \quad (7.48)$$

in order to estimate $(\varepsilon, \sigma^2, \alpha)$, where $I = A^2$ is the intensity. In Prager et al. (2003), the three moments $E[I]$, $E[I^2]$, and $E[I^3]$ are expressed analytically as functions of $\tau^2 = \sigma^2\alpha$ (denoted σ^2 in that reference), $k = \varepsilon/(\sigma\sqrt{\alpha})$, and $\beta = 1/\alpha$, as follows:

$$\begin{aligned} E[I] &= \tau^2[k^2 + 2]; \\ E[I^2] &= \tau^4[8(1 + \beta) + 8k^2 + k^4]; \\ E[I^3] &= \tau^6[48(1 + 3\beta + 2\beta^2) + 72k^2(1 + \beta) + 18k^4 + k^6]. \end{aligned} \quad (7.49)$$

In Prager et al. (2003, Appendix C, p. 712), an algebraic method is presented to solve the system (7.49) for τ^2 , k , and β , rejecting negative or imaginary values.

$$\mu = \bar{I}; \quad M_{HK}^{(4)}(\gamma, \alpha) = \bar{I}^2/\bar{I}^2; \quad M_{HK}^{(6)}(\gamma, \alpha) = \bar{I}^3/\bar{I}^3, \quad (7.50)$$

where $\mu = \varepsilon^2 + 2\sigma^2\alpha = E[I]$. Moreover, the values of ε and σ^2 can be recovered from γ , α , and μ with the change of variables

$$\varepsilon = \sqrt{\mu \frac{\gamma}{(\gamma + \alpha)}}; \quad \sigma^2 = \mu \frac{1}{2(\gamma + \alpha)}. \quad (7.51)$$

7.4.5.3 A Method Based on the Moments of the Amplitude

In Dutt (1995, Section 9.2.2, p. 116), it was suggested to use the first three moments of the ampli-

Observe that Eq.(7.48) is equivalent to the system of equations

$$E[A] = \bar{A}; \quad E[A^2] = \bar{A}^2; \quad E[A^3] = \bar{A}^3. \quad (7.52)$$

However, at that time, the authors could not find a closed-form expression of the moments of the amplitude. So, approximate expressions were used instead. As noted in Dutt (1995, p. 117), the parameter estimation might break down for small values of α and large values of k , due to the weakness of the approximations.

tude to estimate the homodyned K-distribution, namely, to solve the system of equations

Note that an explicit expression of an arbitrary moment of the amplitude was given in Hruska and Oelze (2009, Eq. (8), p. 2473). Thus, the estimation method based on the first three moments of the amplitude would likely need to be tested again with the exact expressions of those moments.

Observe that Eq.(7.52) is equivalent to the system of equations

$$\mu = \bar{I}; \quad M_{HK}^{(1)}(\gamma, \alpha) = \bar{A}/\bar{I}^{1/2}; \quad M_{HK}^{(3)}(\gamma, \alpha) = \bar{A}^3/\bar{I}^{3/2}. \quad (7.53)$$

7.4.5.4 Methods Based on the SNR of Fractional Order Moments of the Amplitude

In Dutt (1995, Section 9.2.4, p. 117), it was proposed to use the SNR R of the amplitude and of the intensity. It is reported in Dutt (1995, Section 9.5, p. 142) that the method based on SNRs gave better results than the three methods presented in Sects. 7.4.5.2, 7.4.5.3, and 7.4.5.5. But then, the

exact expression of Eq.(7.46) was not used, so that this conclusion is not necessarily valid.

In Martin-Fernandez and Alberola-Lopez (2007), the authors suggested to use the statistics R for two distinct values of ν (or more), using an exact expression of that statistics. In fact, the authors suggested the values 0.01, 0.03, 0.05, 0.075, 0.1, 0.25, 0.4, 0.5, 0.75, and 1. A solution is then found by inspection of the SNR level curves. Namely, for each value of the fractional

order ν , the statistics R is expressed analytically as a function of $k = \varepsilon/(\sigma\sqrt{\alpha})$ and α (denoted μ in that reference). One then considers the point (k, α) that is closest to all the corresponding SNR level curves, in the sense of the least mean squares (LMS). Thus, this method is an extension of the method based on the SNRs of Dutt (1995, Section 9.2.4).

7.4.5.5 A Method Based on the SNR and Skewness of the Amplitude

In Dutt (1995, Section 9.2.4, p. 117), it was proposed to use the SNR $R = \frac{E[A]}{(E[A^2] - E^2[A])^{1/2}}$ and the skewness $S = \frac{E[(A - E[A])^3]}{(E[A^2] - E^2[A])^{3/2}}$ of the amplitude for the estimation of the homodyned K-distribution. Again, that method should be tested with the exact expression of Eq. (7.46).

7.4.5.6 A Method Based on the SNR, Skewness, and Kurtosis of Fractional Order Moments of the Amplitude

In Hruska and Oelze (2009), the authors suggested the use of the SNR R , the skewness S , and the kurtosis $K = \frac{E[(A^\nu - E[A^\nu])^4]}{(E[A^{2\nu}] - E^2[A^\nu])^2}$, for two

to taking the numerous fractional orders 0.01, ..., 1 in Martin-Fernandez and Alberola-Lopez (2007).

7.4.5.7 Discussion

In this section, we present new results on the $M^{(\nu)}$ -statistics and the MLE for the homodyned K-distribution.

Concerning Theorem 24, the case where $\nu/2 + \alpha$ is not integer (with no restriction on γ) is covered by part (c), whereas part (b) covers the case where $\nu/2 + \alpha$ is an integer, but with the restriction $\gamma = 0$. So, what about the case where $\gamma > 0$ and $\nu/2 + \alpha$ is an integer. The following result answers that question. However, in practice, one may use linear interpolation to approximate the $M^{(\nu)}$ -statistics whenever $\nu/2 + \alpha$ is close to an integer (as is done in Hruska and Oelze 2009).

Theorem 25 Assume that $A = \sqrt{I}$ is distributed according to the homodyned K-distribution, with parameters $\varepsilon \geq 0$, $\sigma^2 > 0$, and $\alpha > 0$. Let $\gamma = \varepsilon^2/(2\sigma^2)$. Then, if $\gamma > 0$, the $M^{(\nu)}$ -statistics is expressed as

$$M_K^{(\nu)}(\alpha) = \frac{2}{(\gamma + \alpha)^{\nu/2}} \frac{\Gamma(\nu/2 + 1)}{\Gamma(\alpha)} \sum_{n=0}^{\infty} \frac{(1 + \nu/2)_n}{n! n!} \sqrt{\gamma}^{\nu/2 + \alpha + n} K_{\nu/2 + \alpha - n}(2\sqrt{\gamma}), \quad (7.54)$$

values of ν , namely 0.72 and 0.88. These statistics were expressed analytically as a function of $k = \varepsilon/(\sigma\sqrt{\alpha})$ and α (denoted μ in that reference). One then considers the point (k, α) that is closest to the six corresponding SNR, skewness, and kurtosis level curves in the sense of the LMS. In order to do so, the (k, α) -space was sampled at the points of the form $(i \times 0.01, 10^{-3+j \times 0.01})$, with $0 \leq i, j \leq 500$. The two methods (Martin-Fernandez and Alberola-Lopez 2007; Hruska and Oelze 2009) were not compared in Hruska and Oelze (2009). However, the choice of the fractional orders 0.72 and 0.88 was validated empirically in Hruska and Oelze (2009) (as opposed

where $(1 + \nu/2)_n$ denotes the rising factorial $\Gamma(1 + \nu/2 + n)/\Gamma(1 + \nu/2)$.

Theorems 9 and 21 on the behavior of the functions $M_{Ri}^{(\nu)}(\kappa)$ and $M_K^{(\nu)}(\alpha)$, respectively, can be extended to the following theorem.

Theorem 26 Assume that $A = \sqrt{I}$ is distributed according to the homodyned K-distribution, with parameters $\varepsilon \geq 0$, $\sigma^2 > 0$, and $\alpha > 0$. Let $\gamma = \varepsilon^2/(2\sigma^2)$. Then,

- (a) $\lim_{\gamma \rightarrow 0} M_{HK}^{(\nu)}(\gamma, \alpha) = M_K^{(\nu)}(\alpha)$ (the function introduced in Theorem 13).

- (b) $\lim_{\gamma \rightarrow \infty} M_{HK}^{(v)}(\gamma, \alpha) = 1$.
(c) For any $\alpha > 0$ and $\gamma > 0$, the function $M_{HK}^{(v)}(\gamma, \alpha)$ is increasing in the variable γ , if $v < 2$, whereas it is decreasing in the variable γ , if $v > 2$.

See Fig. 7.9 for an illustration of Theorem 26. Theorem 26 implies that the equation $M_{HK}^{(v)}(\gamma, \alpha) = M$, α being known, has at most one solution, and moreover, it gives sufficient and necessary conditions for a solution to exist, as expressed in the following corollary.

Corollary 2 Let $M > 0$ be a real number (playing the role of $M^{(v)}$). There exists at most one non-negative solution $\gamma = \gamma_M^{(v)}(\alpha)$ to the equation $M_{HK}^{(v)}(\gamma, \alpha) = M$, α being known.

So, given $\alpha > 0$, \bar{I} , and \bar{A} , one can recover ε and σ^2 as follows. First of all, we take $\gamma = \gamma_M^{(v)}(\alpha)$, where $M = \bar{A}/(\bar{I})^{1/2}$. Then, one uses Eq. (7.51), with $\mu = \bar{I}$ and $\gamma = \gamma_M^{(v)}(\alpha)$. In this manner, well-defined functions can be obtained

$$\varepsilon(\alpha, \bar{I}, \bar{A}); \quad \sigma^2(\alpha, \bar{I}, \bar{A}). \quad (7.55)$$

We now discuss briefly the MLE for the homodyned K-distribution. The following result is useful for the computation of the partial derivatives of that distribution.

Lemma 4 Let $\varepsilon \geq 0$, $\sigma^2 > 0$, and $\alpha > 0$.

- (a) The homodyned K-distribution $P_{HK}(A|\varepsilon, \sigma^2, \alpha)$ can be expressed as

$$\frac{1}{\pi} \int_0^\pi \frac{2A}{\sigma^2 \Gamma(\alpha)} \left(\frac{X(\theta)}{2} \right)^{\alpha-1} K_{\alpha-1}(X(\theta)) d\theta, \quad (7.56)$$

- (a) If the Rice conditions (7.29) are satisfied, then there exists a non-negative solution for any $\alpha > 0$.
(b) If the K-distribution conditions (7.43) are satisfied, then there exists a non-negative solution if and only if $\alpha \leq \alpha_0 = (M_K^{(v)})^{-1}(M)$.

where $X(\theta) = \sqrt{\frac{2}{\sigma^2}} \sqrt{A^2 + \varepsilon^2 - 2A\varepsilon \cos \theta}$.

- (b) The partial derivative $\frac{\partial}{\partial \varepsilon} P_{HK}(A|\varepsilon, \sigma^2, \alpha)$ can be expressed as

$$\frac{1}{\pi} \int_0^\pi \frac{2A}{\sigma^4 \Gamma(\alpha)} (A \cos \theta - \varepsilon) \left(\frac{X(\theta)}{2} \right)^{\alpha-2} K_{\alpha-2}(X(\theta)) d\theta. \quad (7.57)$$

- (c) The partial derivative $\frac{\partial}{\partial \sigma^2} P_{HK}(A|\varepsilon, \sigma^2, \alpha)$ can be expressed as

$$\begin{aligned} & -\frac{\alpha}{\sigma^2} \frac{1}{\pi} \int_0^\pi \frac{2A}{\sigma^2 \Gamma(\alpha)} \left(\frac{X(\theta)}{2} \right)^{\alpha-1} K_{\alpha-1}(X(\theta)) d\theta \\ & + \frac{1}{\sigma^2} \frac{1}{\pi} \int_0^\pi \frac{2A}{\sigma^2 \Gamma(\alpha)} \left(\frac{X(\theta)}{2} \right)^\alpha K_\alpha(X(\theta)) d\theta. \end{aligned} \quad (7.58)$$

- (d) The partial derivative $\frac{\partial}{\partial \alpha} P_{HK}(A | \varepsilon, \sigma^2, \alpha)$ can be expressed as

$$\begin{aligned} & \frac{1}{\pi} \int_0^\pi \frac{2A}{\sigma^2 \Gamma(\alpha)} \left(\frac{X(\theta)}{2} \right)^{\alpha-1} K_{\alpha-1}(X(\theta)) \\ & \times \left\{ -\psi(\alpha) + \log\left(\frac{X(\theta)}{2}\right) + \frac{\frac{\partial}{\partial \alpha} K_{\alpha-1}(X(\theta))}{K_{\alpha-1}(X(\theta))} \right\} d\theta, \end{aligned} \quad (7.59)$$

where ψ denotes the digamma function.

One could then extend Theorems 18 and 19 in the context of the homodyned K-distribution. In fact, we suspect that the MLE is not always well defined for the homodyned K-distribution. Thus, one would have to consider a MAP estimator. Since such an estimator results in a time-consuming algorithm, we will not develop further that topic here.

in the following form:

$$\Omega = \bar{I}; \quad m = \frac{\bar{I}^2}{\bar{I}^2 - \bar{I}^2}. \quad (7.61)$$

Note that the term $\frac{\bar{I}^2}{\bar{I}^2 - \bar{I}^2}$ is the square of the SNR of the intensity. This method is equivalent to the V-statistics' method (i.e., based on the $M^{(4)}$ -statistics \bar{I}^2/\bar{I}^2).

7.4.6 Parameter Estimation Methods for the Nakagami Distribution

7.4.6.1 The MLE for the Nakagami Distribution

Since a Nakagami distribution on the amplitude A is equivalent to a gamma distribution on the intensity $I = A^2$, the estimation of the Nakagami distribution parameters amounts to the well-known estimation problem of the gamma distribution. In particular, the MLE is the unique solution to the equation

$$\Omega = \bar{I}; \quad \psi(m) - \log m = \overline{\log I} - \log \bar{I}, \quad (7.60)$$

where ψ denotes the digamma function.

7.4.6.2 A Method Based on the First Two Moments of the Intensity

The most frequently used method for the parameter estimation of the Nakagami distribution is based on the first two moments of the intensity

7.4.6.3 Discussion

We first mention a relation between the MLE and the U -statistics for the Nakagami distribution. Then, new results on moments and log-moments-based methods are presented. Finally, a comparison of these estimators on simulated data is reported.

Concerning the MLE of the Nakagami distribution, note that the term $\log \bar{I} - \log \bar{I}$ is the U -statistics. Thus, it is negative unless all terms I_i are identical. Also, the term $\psi(m) - \log m$ is the analytical expression of the U -statistics for the Nakagami distribution, as stated in the following result.

Theorem 27 Let A be distributed according to the Nakagami distribution with parameters m and Ω . Then, the U -statistics $E[\log I] - \log E[I]$ is expressed as $U_{Na}(m) = \psi(m) - \log m$.

Thus, the MLE turns out to correspond to the U -statistics' method. But unlike the K-distribution, the equation $\psi(m) - \log m = U$ admits a solution for any $U < 0$. Indeed, the following result shows

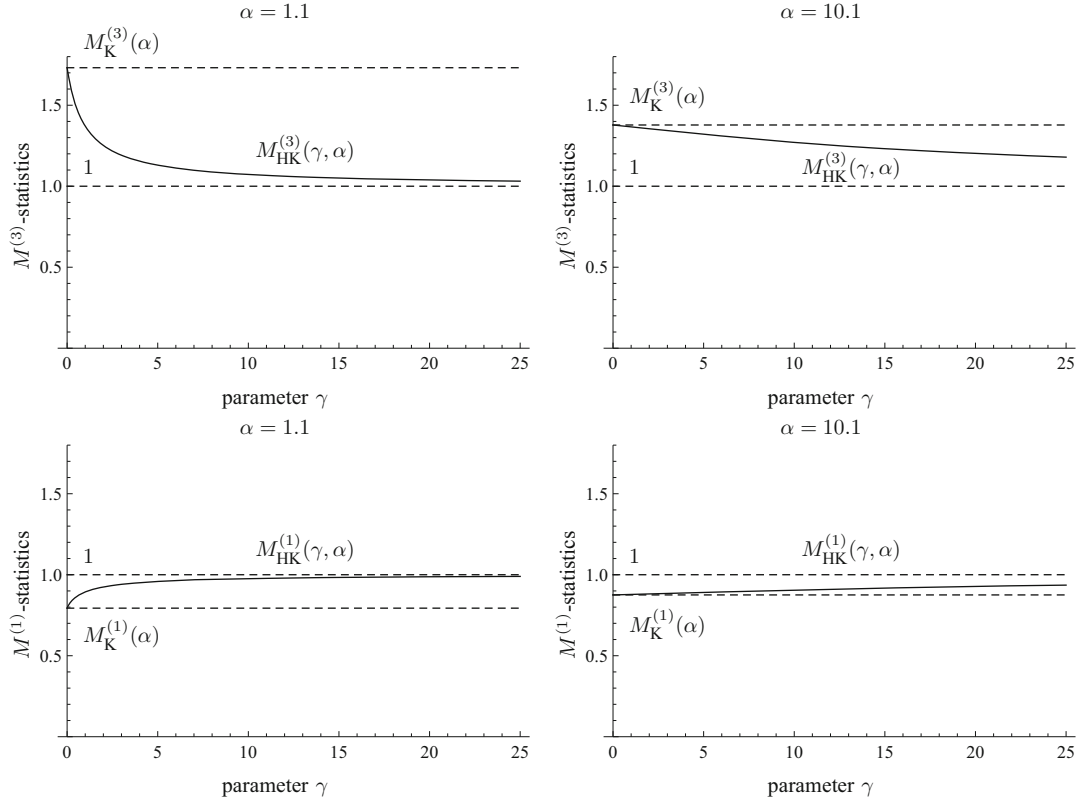


Fig. 7.9 Typical behavior of the $M^{(v)}$ -statistics for the homodyned K-distribution, α being fixed, when $v < 2$ (bottom row) and $v > 2$ (top row). In fact, we took here $v = 1$ (bottom row) and $v = 3$ (top row), as well as $\alpha = 1.1$ (left column) and $\alpha = 10.1$ (right column)

that a binary search can be used to compute the unique solution to that equation.

Theorem 28 (Destrempe et al. 2009) *The following properties hold:*

- (a) $\lim_{m \rightarrow 0} \psi(m) - \log m = -\infty$.
- (b) $\lim_{m \rightarrow \infty} \psi(m) - \log m = 0$.
- (c) *The function $\psi(m) - \log m$ is strictly increasing on its domain $(0, \infty)$.*

Proof (a) We have the identity (Abramowitz and Stegun 1972, p. 259, (6.3.21)) $\psi(m) = \log(m) - \frac{1}{2m} - 2 \int_0^\infty \frac{t}{(t^2+m^2)(e^{2\pi t}-1)} dt$, for $m > 0$. This yields $-\log(m) + \psi(m) \leq -\frac{1}{2m}$, and hence $\lim_{m \rightarrow 0} -\log(m) + \psi(m) = -\infty$.

- (b) The same identity as above yields the computation

$$\lim_{m \rightarrow \infty} -\log(m) + \psi(m) = -2 \lim_{m \rightarrow \infty} \int_0^\infty \frac{t}{(t^2+m^2)(e^{2\pi t}-1)} dt = 0.$$

- (c) We have $\frac{\partial}{\partial m} U_K(m) = -\frac{1}{m} + \psi^{(1)}(m)$. But from Abramowitz and Stegun (1972, p. 260, (6.4.1)), we have $\psi^{(1)}(m) = \int_0^\infty \frac{te^{-mt}}{1-e^{-t}} dt$. Now, $\frac{te^{-\alpha t}}{1-e^{-t}} > e^{-mt}$, since $e^{-t} > 1-t$, for $t > 0$. Therefore, $\psi^{(1)}(m) > \int_0^\infty e^{-mt} dt = \frac{1}{m}$, and we are done. ■

One can also show that the X -statistics is equal to $1/m$ for the Nakagami distribution.

Theorem 29 *Let A be distributed according to the Nakagami distribution with parameters m*

and Ω . Then,² the X -statistics $E[I \log I]/E[I] - E[\log I]$ is expressed as $X_{\text{Na}}(m) = \frac{1}{m}$.

Thus, the shape parameter of the Nakagami distribution can be estimated directly with the equation $m = 1/X$, where $X = \bar{I} \log \bar{I}/\bar{I} - \bar{\log} \bar{I}$.

Finally, one can compute explicitly the $M^{(1)}$ -statistics for the Nakagami distribution.

Theorem 30 Let A be distributed according to the Nakagami distribution with parameters m and Ω . Then, the $M^{(1)}$ -statistics $E[A]/\sqrt{E[I]}$ is expressed as $M_{\text{Na}}^{(1)}(m) = \frac{\Gamma(1/2+m)}{\sqrt{m}\Gamma(m)}$.

The equation $M_{\text{Na}}^{(1)}(m) = M$ can be estimated with a binary search algorithm, for any $0 < M < 1$.

Theorem 31 The following properties hold:

- (a) $\lim_{m \rightarrow 0} \frac{\Gamma(1/2+m)}{\sqrt{m}\Gamma(m)} = 0$.
- (b) $\lim_{m \rightarrow \infty} \frac{\Gamma(1/2+m)}{\sqrt{m}\Gamma(m)} = 1$.
- (c) The function $\frac{\Gamma(1/2+m)}{\sqrt{m}\Gamma(m)}$ is strictly increasing on its domain $(0, \infty)$.

Theorems 27, 29, 30, and 31 can be checked directly using the software Mathematica (Wolfram Research, Inc., Champaign, IL, USA, version 7.0).

In order to compare these four estimators, we considered the parameter m with values in the set $\{0.1, 0.2, \dots, 2.0\}$. For each value of m , 1000 datasets of $N = 1000$ elements each were simulated according to the corresponding Nakagami distribution. We could estimate the normalized MSE of the estimator \hat{m} as $\sqrt{E[(\hat{m} - m)^2]}/m$. The resulting normalized MSE curves are presented in Fig. 7.10. As one can see, the estimators based on the MLE (i.e., the U -statistics, in this case) or the X -statistics are practically equivalent. They are better than the estimator based on the $M^{(1)}$ -statistics, especially on the interval $m \in [0.0, 0.5]$. These three estimators are systemati-

cally better than the estimator based on the V -statistics.

7.5 Conclusion

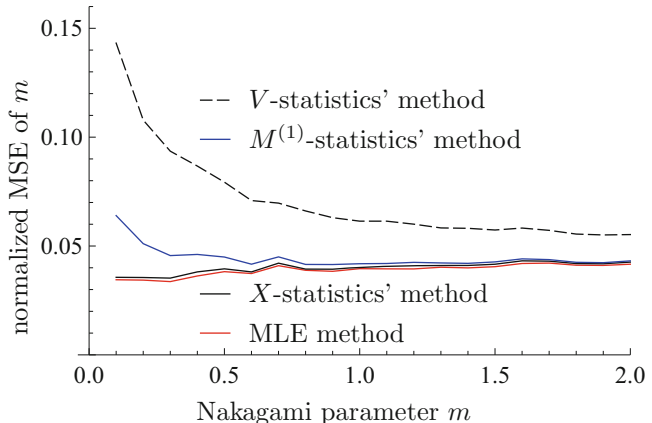
We conclude with the following issues:

- (1) It was argued that the homodyned K-distribution is a sound model for the first-order statistics of the echo envelope of the RF ultrasound signal, in the context where the backscattered echo signal received at the transducer of an ultrasound device is assumed to be the vector sum of the individual signals produced by the scatterers distributed in the medium (Wagner et al. 1983, 1987). The K-distribution is a special case where there is no coherent component (due to the absence of specular reflection). The Rice and the Rayleigh distributions are limit cases of the homodyned K-distribution or the K-distribution, respectively, corresponding to an infinite homogeneity of the diffuse scattering medium. The Nakagami is an approximation of the homodyned K-distribution. All these five distributions share two desirable properties: (1) the total signal power depends only on the coherent component in the case of a vanishing diffuse signal and (2) the intensity SNR is infinite in that case. The other models presented in Jakeman and Tough (1987), Shankar (2000), Barakat (1986), Eltoft (2005), Raju and Srinivasan (2002), Shankar (2003), and Agrawal and Karmeshu (2006) do not have these two properties. Thus, we recommend the homodyned K-distribution (or its related distributions, in special cases) as a model for the ultrasound echo envelope in that context, as was done in Dutt and Greenleaf (1994), Hruska and Oelze (2009), and Destrempe and Cloutier (2010).

- (2) It was shown that the methods based on the X -statistics and the mean intensity are practically as good as the MLE for the Rice and the Nakagami distributions or the proposed hybrid MAP for the

² Correction of a typo (“ $E[I \log I]/E[I] - \log E[I]$ ”) in the first edition.

Fig. 7.10 Comparison between the normalized MSE $\sqrt{E[(\hat{m} - m)^2]}/m$ of the estimators based on the MLE (—), the X -statistics (—), the $M^{(1)}$ -statistics (—), and the V -statistics (---), for the Nakagami distribution. The sample size is $N = 1000$



K-distribution. For the homodyned K-distribution, one may use a method based on the SNR, skewness, and kurtosis of fractional orders of the amplitude (Hruska and Oelze 2009).

- (3) A homodyned K-distribution with parameters (k, α) in the range $[0, 2] \times [1, 20]$ can be approximated by a Nakagami distribution with KL distance less than 0.072 (but for much larger values of k , the KL distance might be much larger). However, although one may express the two parameters Ω and m of the Nakagami distribution in terms of the three parameters ε , σ^2 , and α of the homodyned K-distribution in the form $\Omega = \varepsilon^2 + 2\sigma^2\alpha$ and $m = \frac{(\varepsilon^2 + 2\sigma^2\alpha)^2}{4\sigma^2\alpha(\varepsilon^2 + \sigma^2(2+\alpha))}$, as follows from Destrempe and Cloutier (2010, Eq. (23) and Tables 3 and 4), the converse statement is not true. Thus, the Nakagami distribution gives less information on the statistical properties of the echo envelope than the homodyned K-distribution. In particular, one may not retrieve the coherent or diffuse signal power from the parameters of the Nakagami distribution. For this reason, we recommend the use of the homodyned K-distribution, rather than the Nakagami distribution, in the context of tissue characterization. On the other hand, the Nakagami distribution may be used in the context of image segmentation, since in that application, the main property is a good fit of the

distribution with the data. This was the point of view adopted in Destrempe et al. (2009, 2011) and Bouhlel and Sevestre-Ghalila (2009).

- (4) When the product of the wave number with the mean size of the scatterers is much smaller than the wavelength and acoustic impedance of the scatterers is close to the impedance of the embedding medium, a high density of scatterers results in a packing organization that implies constructive and destructive wave interferences and a correlation between the individual signals produced by the scatterers (Hayley et al. 1967; Twersky 1975, 1978, 1987, 1988; Lucas and Twersky 1987; Berger et al. 1991). In such a case, the assumption made here on the randomness of the scatterers positions (or phase) might not be valid. The resulting first-order statistics might still be characterized with the proposed models, but the physical interpretation of the parameters should be done with caution in that case and should be further studied. See Wagner et al. (1987), Weng et al. (1990, 1992), and Narayanan et al. (1997) for further reading on that issue.
- (5) The distributions mentioned here concern the envelope of the RF signal. When a log-compression or other (nonlinear or linear) operators are applied to the envelope, the distribution of the gray levels no longer follows the distributions computed on the

RF echo envelope. In the case of log-compression, the resulting distribution has been modeled in Dutt and Greenleaf (1996), assuming the K-distribution for the envelope. In Prager et al. (2003), a decompression algorithm is proposed, assuming the homodyned K-distribution for the envelope. As mentioned before, operators other than log-compression can be applied on the envelope. In Nillesen et al. (2008), a linear filter was applied to the RF data before computing the envelope. Five distributions were tested to fit the data: the Rayleigh distribution, the K-distribution, the Nakagami distribution, the inverse Gaussian distribution, and the gamma distribution. The authors showed, based on empirical tests, that, overall, the gamma distribution best fit the data. See also Tao et al. (2002, 2006) and Shankar et al. (2003) for further reading on the gamma distribution model in ultrasound imaging. See also Keyes and Tucker (1999) for a comparison of the K-distribution with a few other models as well as Tsui et al. (2005, 2009c), Tsui and Wang (2004), and Tsui and Chang (2007) for the effect of log-compression or transducer characteristics on the parameters of the Nakagami distribution. Here, we were concerned with the statistical distributions of the amplitude of the unfiltered envelope of the RF image, and therefore we did not study such distributions.

- (6) The parameters of the homodyned K-distribution reveal the scattering properties of the underlying tissue, but they are also instrumentation and depth dependent. In particular, the transducer center frequency, the point spread function (PSF) real envelope, and the attenuation of the signal within the tissue play a role. A challenge consists in removing these dependencies. See Hruska (2009) for further reading on that matter.
- (7) The estimation problem is important, since the use of poor estimators might wash down

the performance of a method, otherwise fine. However, the mere study of the bias and variance of an estimator is not sufficient, since it assumes data distributed according to the distribution. Moreover, in the context of ultrasound imaging, various factors intervene, such as the presence of noise, the efficiency of the algorithm (in view of clinical applications, where the speed of execution of an algorithm is relevant). Thus, ideally, the study of an estimation method should include simulations of US data, as well as *in vitro* and *in vivo* experimental tests.

Perspective

In the future, it would be interesting to see a study of log-moments methods for the homodyned K-distribution. We believe that it would be instructive to establish relations between echo envelope statistics and spectral quantitative measures. See Oelze and O'Brien (2007) for an example of quantitative ultrasound assessment in the context of breast cancer that used the parameters of the homodyned K-distribution combined with an analysis of the normalized backscattered power spectrum. In the articles Shankar et al. (1993), Molthen et al. (1993, 1995), Narayanan et al. (1994), and Shankar (1995), an underlying physical model for the K-distribution was introduced. In the more recent article Saha and Kolios (2011), the Nakagami distribution was estimated on simulated tissues based on a scattering model. A challenge consists in deepening the understanding of an underlying physical model for the homodyned K-distribution. Finally, it would be desirable to take into account the effect of instrumentation and attenuation on the echo envelope statistics. Thus, there remain several challenging problems in that area of QUS imaging, which we believe will turn out to be useful in a clinical context.

Acknowledgments The authors acknowledge the continuous financial support of the Canadian Institutes of Health and Natural Sciences and Engineering Research Council of Canada.

Appendix: Proofs of the New Results

Proof of Theorem 8. From Theorem 6, there is exactly one critical point of $L(\varepsilon, \sigma^2)$ for which $\varepsilon > 0$, and it is the MLE (here, for L denotes L_{RI}). Therefore, using Theorem 5, the function $f(\kappa)$ has exactly one positive root κ_* and it corresponds to the MLE. Moreover, one can check that $\kappa = 0$ is also a root of the function f . Namely, we have $\lim_{\kappa \rightarrow 0} f(\kappa) = -1 + \frac{1}{N} \sum_{i=1}^N y_i^2$, and by construction, $\frac{1}{N} \sum_{i=1}^N y_i^2 = 1$.

We have $\lim_{\kappa \rightarrow \infty} f(\kappa) = 2(-1 + \frac{1}{N} \sum_{i=1}^N y_i) = 2(-1 + \sqrt{\bar{I}}/\sqrt{\bar{I}})$. A direct application of the Cauchy–Schwartz inequality ensures that

$\sqrt{\bar{I}}/\sqrt{\bar{I}} < 1$, so that $\lim_{\kappa \rightarrow \infty} f(\kappa) < 0$. In view of the Intermediate Value Theorem for continuous functions, it follows that $f(\kappa) < 0$, if $\kappa > \kappa_*$.

Next, we want to show that $f(\kappa) > 0$ for $\kappa \in (0, \kappa_*)$. Since κ_* is the only positive root of f and since $f(\kappa) < 0$ on (κ_*, ∞) , it is enough to show that $\frac{\partial f}{\partial \kappa} < 0$ at κ_* ; for then, $f(\kappa) > 0$ if $\kappa < \kappa_*$ is sufficiently near κ_* , and hence, $f(\kappa) > 0$ on $(0, \kappa_*)$ using the Intermediate Value Theorem.

First of all, we claim that $\frac{\partial f}{\partial \kappa} = \frac{1}{N} \frac{\partial^2 L}{\partial \kappa^2}$ at a critical point of $L(\varepsilon, \sigma^2) = \sum_{i=1}^N \log P_{\text{RI}}(A_i | \varepsilon, \sigma^2)$, whenever $\varepsilon > 0$ (i.e., $\kappa > 0$). Indeed, with the change of variable $\varepsilon = \sqrt{\frac{\mu \kappa}{(\kappa+1)}}$ and $\sigma^2 = \frac{\mu}{2(\kappa+1)}$, we obtain directly from Eq. (7.2)

$$\begin{aligned} \frac{1}{N} L(\mu, \kappa) &= \frac{1}{N} \sum_{i=1}^N \log A_i - \log \mu + \log 2 + \log(\kappa + 1) \\ &\quad - \frac{(\kappa + 1)}{\mu} \frac{1}{N} \sum_{i=1}^N A_i^2 - \kappa + \frac{1}{N} \sum_{i=1}^N \log I_0\left(\frac{2A_i}{\sqrt{\mu}} \sqrt{\kappa(\kappa + 1)}\right). \end{aligned} \tag{7.62}$$

Next, the derivative of $\frac{1}{N} L(\mu, \kappa)$ with respect to κ is equal to

$$\frac{1}{(\kappa + 1)} - \frac{1}{\mu} \frac{1}{N} \sum_{i=1}^N A_i^2 - 1 + \frac{(2\kappa + 1)}{\sqrt{\kappa(\kappa + 1)}} \frac{1}{N} \sum_{i=1}^N \frac{A_i}{\sqrt{\mu}} \frac{I_1\left(\frac{2A_i}{\sqrt{\mu}} \sqrt{\kappa(\kappa + 1)}\right)}{I_0\left(\frac{2A_i}{\sqrt{\mu}} \sqrt{\kappa(\kappa + 1)}\right)}. \tag{7.63}$$

But, from Talukdar and Lawding (1991), we have $\mu = \bar{I} = \frac{1}{N} \sum_{i=1}^N A_i^2$ at a critical point (ε, σ^2) of L_{RI} . Therefore, we obtain that $\frac{1}{N} \frac{\partial L}{\partial \kappa} = f(\kappa)$ at such a critical point (because $A_i/\sqrt{\mu}$ is then equal

to $y_i = A_i/\sqrt{\bar{I}}$). Taking the partial derivative of Eq. (7.63) with respect to κ , we also see that $\frac{\partial f}{\partial \kappa} = \frac{1}{N} \frac{\partial^2 L}{\partial \kappa^2}$ at a critical point (ε, σ^2) of L .

Now, recall that if $u = u(x, y)$ and $v = v(x, y)$ is a change of variable, then

$$\begin{aligned} \frac{\partial^2 L}{\partial u \partial v} &= \frac{\partial L}{\partial x} \frac{\partial^2 x}{\partial u \partial v} + \frac{\partial L}{\partial y} \frac{\partial^2 y}{\partial u \partial v} \\ &+ \frac{\partial^2 L}{\partial x^2} \frac{\partial x}{\partial u} \frac{\partial x}{\partial v} + \frac{\partial^2 L}{\partial y \partial x} \frac{\partial y}{\partial u} \frac{\partial x}{\partial v} + \frac{\partial^2 L}{\partial x \partial y} \frac{\partial x}{\partial u} \frac{\partial y}{\partial v} + \frac{\partial^2 L}{\partial y^2} \frac{\partial y}{\partial u} \frac{\partial y}{\partial v}; \\ \frac{\partial^2 L}{\partial^2 u} &= \frac{\partial L}{\partial x} \frac{\partial^2 x}{\partial u^2} + \frac{\partial L}{\partial y} \frac{\partial^2 y}{\partial u^2} \\ &+ \frac{\partial^2 L}{\partial x^2} \left(\frac{\partial x}{\partial u} \right)^2 + 2 \frac{\partial^2 L}{\partial x \partial y} \frac{\partial x}{\partial u} \frac{\partial y}{\partial u} + \frac{\partial^2 L}{\partial y^2} \left(\frac{\partial y}{\partial u} \right)^2. \end{aligned} \quad (7.64)$$

At this point, we find convenient to use the change of variable $\varepsilon^2 = \mu\kappa/(1 + \kappa)$ and $\sigma^2 = \mu/(2(1 + \kappa))$. We develop $\frac{\partial^2 L}{\partial \kappa^2} = (G_{11} - G_{12} + \frac{1}{4}G_{22})\frac{\mu^2}{(\kappa+1)^4}$ at a critical point of L , where $G_{11} = \frac{\partial^2 L}{\partial \varepsilon^2 \partial \varepsilon^2}$, $G_{12} = \frac{\partial^2 L}{\partial \varepsilon^2 \partial \sigma^2}$, and $G_{22} = \frac{\partial^2 L}{\partial \sigma^2 \partial \sigma^2}$ (we make use of the fact that $\frac{\partial L}{\partial \varepsilon^2} = 0 = \frac{\partial L}{\partial \sigma^2}$ at the critical point). Now, from Carrobi and Cati (2008, Appendix A, p.686–687), we have $H_{11}H_{22} - H_{12}^2 > 0$ and $H_{11} < 0$ at the critical point of interest, where $H_{11} = \frac{\partial^2 L}{\partial \varepsilon \partial \varepsilon}$, $H_{12} = \frac{\partial^2 L}{\partial \varepsilon \partial \sigma^2}$, and $H_{22} = \frac{\partial^2 L}{\partial \sigma^2 \partial \sigma^2}$ (σ^2 is viewed as a variable). From there, if one uses the change of variable $\varepsilon = \sqrt{\varepsilon^2}$ (and $\sigma^2 = \sigma^2$), one concludes that $G_{11}G_{22} - G_{12}^2 = (H_{11}H_{22} - H_{12}^2)\frac{1}{4\varepsilon^2} > 0$ and $G_{11} = H_{11}\frac{1}{4\varepsilon^2} < 0$, at that critical point. Thus, we obtain the upper bound $G_{22} < G_{12}^2/G_{11}$ (because $G_{11} < 0$), and therefore $\frac{\partial^2 L}{\partial \kappa^2} < (G_{11} - G_{12} + \frac{1}{4}G_{22}/G_{11})\frac{\mu^2}{(\kappa+1)^4}$.

But this is equal to $\frac{1}{G_{11}}\frac{\mu^2}{(\kappa+1)^4}(G_{11} - \frac{1}{2}G_{12})^2$, and it is non-positive since $G_{11} < 0$. Therefore, $\frac{\partial f}{\partial \kappa} = \frac{1}{N} \frac{\partial^2 L}{\partial \kappa^2} < 0$ at the point $\kappa = \kappa_*$ (with $\mu = \bar{I}$). This completes the proof of Theorem 8.

■

Proof of Theorem 9. (a) Setting $\kappa = 0$ in Theorem 7, we obtain directly $M_{\text{Ri}}^{(v)}(0) = \Gamma(v/2 + 1)$.

(b) From Luke (1962, pp. 7–8), we have the following asymptotic behavior:

$${}_1F_1(a_1; b_1; z) \propto \frac{\Gamma(b_1)}{\Gamma(a_1)} z^\chi e^z \left(1 + O(1/z) \right), \quad (7.65)$$

where $\chi = a_1 - b_1$, valid for $|\arg z| < \pi$ and $|z| \rightarrow \infty$. Therefore, we have

$$\begin{aligned} {}_1F_1(v/2 + 1; 1; \kappa) &\propto \frac{1}{\Gamma(v/2 + 1)} \kappa^{v/2} \\ &\times e^\kappa \left(1 + O(1/\kappa) \right). \end{aligned} \quad (7.66)$$

We conclude that $\lim_{\kappa \rightarrow \infty} M_{\text{Ri}}^{(v)}(\kappa) = \lim_{\kappa \rightarrow \infty} \frac{\Gamma(v/2+1)e^{-\kappa}}{(\kappa+1)^{v/2}} \times \frac{1}{\Gamma(v/2+1)} \kappa^{v/2} e^\kappa = 1$.

(c) From the definition $M_{\text{Ri}}^{(v)}(\kappa) = \Gamma(v/2 + 1) \frac{{}_1F_1(1+v/2, 1, \kappa)}{e^\kappa (\kappa+1)^{v/2}}$, we obtain after algebraic simplifications

$$\frac{d}{d \kappa} M_{\text{Ri}}^{(v)} = \Gamma(v/2 + 1) \frac{\frac{d}{d \kappa} {}_1F_1(1 + v/2, 1, \kappa) - {}_1F_1(1 + v/2, 1, \kappa) \left(1 + \frac{v}{2}(\kappa + 1)^{-1} \right)}{e^\kappa (\kappa + 1)^{v/2}}. \quad (7.67)$$

Now, from Gradshteyn and Ryshik (1994, 9.213, p.1086) and Gradshteyn and Ryshik (1994, 9.212(3), p.1086), we have $\frac{d}{d\kappa} {}_1F_1(1 +$

$v/2, 1, \kappa) = (1 + v/2) {}_1F_1(2 + v/2, 2, \kappa) = \frac{v}{2} {}_1F_1(1 + v/2, 2, \kappa) + {}_1F_1(1 + v/2, 1, \kappa)$. So, omitting the positive factor $\Gamma(v/2+1)e^{-\kappa}(\kappa+1)^{-v/2}$, we obtain

$$\frac{v}{2} {}_1F_1(1 + v/2, 2, \kappa) - \frac{v}{2} {}_1F_1(1 + v/2, 1, \kappa)(\kappa + 1)^{-1}. \quad (7.68)$$

Multiplying by $(\kappa + 1)$ and dividing by $v/2$ (both are positive numbers), we obtain

$${}_1F_1(1 + v/2, 2, \kappa)(\kappa + 1) - {}_1F_1(1 + v/2, 1, \kappa). \quad (7.69)$$

Using Gradshteyn and Ryshik (1994, 9.212(2), p.1086), we have $\kappa {}_1F_1(1 + v/2, 2, \kappa) - {}_1F_1(1 + v/2, 1, \kappa) = - {}_1F_1(v/2, 1, \kappa)$. Therefore, we finally obtain (up to a positive constant)

$${}_1F_1(1 + v/2, 2, \kappa) - {}_1F_1(v/2, 1, \kappa). \quad (7.70)$$

Now, by definition, the hypergeometric function ${}_1F_1(a, b, z)$ is equal to $\sum_{n=0}^{\infty} \frac{(a)_n}{(b)_n} \frac{z^n}{n!}$,

where $(a)_n = a(a + 1)\dots(a + n - 1)$ is the rising factorial. If $v/2 < 1$, then $\frac{(1+v/2)_n}{(2)_n} > \frac{(v/2)_n}{(1)_n}$ and hence ${}_1F_1(1 + v/2, 2, \gamma) - {}_1F_1(v/2, 1, \gamma) > 0$. On the other hand, if $v/2 > 1$, then $\frac{(1+v/2)_n}{(2)_n} < \frac{(v/2)_n}{(1)_n}$ and hence ${}_1F_1(1 + v/2, 2, \kappa) - {}_1F_1(v/2, 1, \kappa) < 0$. This completes the proof of the theorem. ■

Proof of Theorem 10. (a) First of all, using the change of variable $I = A^2$, one computes

$$\int_0^\infty \log A^2 P_{\text{Ri}}(A | \varepsilon, \sigma^2) dA = \int_0^\infty \log I \frac{1}{2\sigma^2} I_0\left(\frac{\varepsilon}{\sigma^2}\sqrt{I}\right) e^{-\varepsilon^2/(2\sigma^2)} e^{-I/(2\sigma^2)} dI, \quad (7.71)$$

which is a Laplace transform equal to $\Gamma(0, \frac{\varepsilon^2}{2\sigma^2}) + \log \varepsilon^2$, where $\Gamma(0, x)$ is the incomplete gamma function $\int_x^\infty \frac{e^{-t}}{t} dt$. Then, after subtraction by the term $\log(\varepsilon^2 + 2\sigma^2)$,

one obtains $\Gamma(0, \frac{\varepsilon^2}{2\sigma^2}) + \log(\frac{\varepsilon^2}{\varepsilon^2 + 2\sigma^2})$, which is equal to $\Gamma(0, \kappa) + \log(\frac{\kappa}{\kappa+1})$ (where $\kappa = \varepsilon^2/(2\sigma^2)$).

(b) Again, using the change of variable $I = A^2$, we compute

$$\begin{aligned} & \int_0^\infty A^2 \log A^2 P_{\text{Ri}}(A | \varepsilon, \sigma^2) dA \\ &= \int_0^\infty I \log I \frac{1}{2\sigma^2} I_0\left(\frac{\varepsilon}{\sigma^2}\sqrt{I}\right) e^{-\varepsilon^2/(2\sigma^2)} e^{-I/(2\sigma^2)} dI. \end{aligned} \quad (7.72)$$

This Laplace transform is equal to $4\sigma^2 - 2e^{-\frac{\varepsilon^2}{2\sigma^2}}\sigma^2 + (\varepsilon^2 + 2\sigma^2)(\Gamma(0, \frac{\varepsilon^2}{2\sigma^2}) + \log \varepsilon^2)$. Dividing by $\varepsilon^2 + 2\sigma^2$ and subtracting $E[\log I] = \Gamma(0, \frac{\varepsilon^2}{2\sigma^2}) + \log \varepsilon^2$ (from the proof of part (a)), one obtains $(4\sigma^2 - 2e^{-\frac{\varepsilon^2}{2\sigma^2}}\sigma^2) \div (\varepsilon^2 + 2\sigma^2)$, which is equal to $\frac{1}{\kappa+1}(2 - e^{-\kappa})$, after algebraic simplifications. ■

Proof of Theorem 11. (a) From Abramowitz and Stegun (1972), (6.5.15), p. 262, we have $\Gamma(0, \kappa) = E_1(\kappa)$ (the exponential integral). Moreover, from Abramowitz and Stegun (1972), (5.1.11), p. 229), $E_1(\kappa) = -\gamma_E - \log \kappa + \sum_{n=1}^{\infty} \frac{(-1)^n \kappa^n}{nn!}$. We conclude that $U_{\text{Ri}}(\kappa) = -\gamma_E - \log(1 + \kappa) + \sum_{n=1}^{\infty} \frac{(-1)^n \kappa^n}{nn!}$. Henceforth, $\lim_{\kappa \rightarrow 0} U_{\text{Ri}}(\kappa) = -\gamma_E$.

(b) Since $\Gamma(0, \kappa) = \int_{\kappa}^{\infty} \frac{e^{-t}}{t} dt$, it follows that $\lim_{\kappa \rightarrow \infty} \Gamma(0, \kappa) = 0$. Moreover, $\lim_{\kappa \rightarrow \infty} \log \frac{\kappa}{\kappa+1} = 0$.

(c) We compute $\frac{d}{d\kappa} U_{\text{Ri}}(\kappa) = -\frac{e^{-\kappa}}{\kappa} + \frac{1}{\kappa} - \frac{1}{\kappa+1}$. This is positive because $e^{\kappa} > 1 + \kappa$, for $\kappa > 0$. ■

Proof of Theorem 12. Parts (a) and (b) follow from basic Calculus.

(c) We compute $\frac{d}{d\kappa} X_{\text{Ri}}(\kappa) = \frac{e^{-\kappa}(\kappa+1)-(2-e^{-\kappa})}{(\kappa+1)^2}$. Ignoring the positive factor $1/(\kappa+1)^2$, we obtain $e^{-\kappa}(2+\kappa)-2$. This is negative since $e^{\kappa} > 1 + \kappa/2$, for $\kappa > 0$. ■

Lemma 5 Let $\alpha > 0$ be fixed. Denote any root of $\frac{\partial}{\partial \sigma^2} L(\sigma^2, \alpha)$ by $\sigma^2(\alpha, \tilde{A})$, where $\tilde{A} = \{A_1, A_2, \dots, A_N\}$.

- (a) If $0 < \alpha \leq 1/2$, then $\sigma^2(\alpha, \tilde{A}) \geq \frac{\alpha+\alpha^2+\sqrt{2\alpha^3+\alpha^4}}{\alpha^2} (\bar{A})^2$.
- (b) If $1/2 < \alpha \leq 3$, then $\sigma^2(\alpha, \tilde{A}) \geq \frac{1}{2\alpha^2} (\bar{A})^2$.
- (c) If $\alpha > 3$, then $\sigma^2(\alpha, \tilde{A}) \geq \frac{2\alpha-3+\sqrt{4\alpha-7}}{4(\alpha-2)^2} (\bar{A})^2$.
- (d) If $0 < \alpha \leq 1/2$, then $\sigma^2(\alpha, \tilde{A}) \leq \frac{1}{2\alpha^2} (\bar{A})^2$.
- (e) If $1/2 < \alpha \leq 3/2$, then $\sigma^2(\alpha, \tilde{A}) \leq \frac{1}{2(\alpha/2+1/4)^2} (\bar{A})^2$.
- (f) If $3/2 < \alpha \leq 3$, then $\sigma^2(\alpha, \tilde{A}) \leq \frac{1}{2} (\bar{A})^2$.

- (g) If $\alpha > 3$, then $\sigma^2(\alpha, \tilde{A}) \leq \frac{1}{2(\alpha-2)} \bar{A}^2$.
- (h) The function $\frac{\partial}{\partial \sigma^2} L(\sigma^2, \alpha)$ is positive at the lower bounds mentioned in parts (a) to (c), whereas it is negative at the upper bounds of parts (d) to (g).

Proof We compute

$$\begin{aligned} \sigma^2 \frac{\frac{\partial}{\partial \sigma^2} P_K(A | \sigma^2, \alpha)}{P_K(A | \sigma^2, \alpha)} &= -\alpha + \left(\frac{1}{\sqrt{2\sigma^2}} A \right) \\ &\times \frac{K_{\alpha}(\sqrt{\frac{2}{\sigma^2}} A)}{K_{\alpha-1}(\sqrt{\frac{2}{\sigma^2}} A)}. \end{aligned} \quad (7.73)$$

Part (a). If $0 < \alpha \leq 1/2$, then $K_{\alpha-1}(x) = K_{1-\alpha}(x) < K_1(x)$ and $K_{\alpha}(x) > K_0(x)$ for any $x > 0$. Also, the inequality $K_0(x)/K_1(x) > 1 - \frac{1}{(x+1)}$ holds for any $x > 0$. Therefore, from Eq.(7.73), we obtain $\sigma^2 \frac{\frac{\partial}{\partial \sigma^2} P_{\text{HK}}(A | \sigma^2, \alpha)}{P_{\text{HK}}(A | \sigma^2, \alpha)} > -\alpha + \frac{1}{2} f(\sqrt{\frac{2}{\sigma^2}} A)$, where $f(x) = x(1 - \frac{1}{(x+1)})$. Thus, we obtain that

$$\sigma^2 \frac{\partial}{\partial \sigma^2} L(\sigma^2, \alpha) > -N\alpha + \frac{1}{2} \sum_{i=1}^N f(\sqrt{\frac{2}{\sigma^2}} A_i). \quad (7.74)$$

Here, L denotes L_K . Now, the function $f(x)$ is convex. Therefore, from Jensen's inequality Jensen (1906), we conclude that

$$\sigma^2 \frac{\partial}{\partial \sigma^2} L(\sigma^2, \alpha) > -N\alpha + \frac{N}{2} f(\sqrt{\frac{2}{\sigma^2}} \bar{A}). \quad (7.75)$$

But the right-hand side of Eq. (7.75) is positive if $\sigma^2 < \frac{\alpha+\alpha^2+\sqrt{2\alpha^3+\alpha^4}}{\alpha^2} (\bar{A})^2$. This proves part (a).

Part (b). If $\alpha > 1/2$, then $K_{\alpha}(x) > K_{\alpha-1}(x)$ for any $x > 0$. Therefore, from Eq.(7.73), we

obtain $\sigma^2 \frac{\partial}{\partial \sigma^2} \frac{P_K(A | \sigma^2, \alpha)}{P_K(A | \sigma^2, \alpha)} > -\alpha + \frac{1}{\sqrt{2\sigma^2}} A$. Thus, we conclude that

$$\sigma^2 \frac{\partial}{\partial \sigma^2} L(\sigma^2, \alpha) > -N\alpha + \frac{1}{\sqrt{2\sigma^2}} \sum_{i=1}^N A_i. \quad (7.76)$$

But the right-hand side of Eq.(7.76) is positive if $\sigma^2 < \frac{1}{2\alpha^2} (\bar{A})^2$. This proves part (b).

Part (c). If $\alpha > 3$, then $\frac{x}{2} \frac{K_\alpha(x)}{K_{\alpha-1}(x)} > \frac{x}{2} \times (\frac{2(\alpha-1)}{x} + \frac{1}{\frac{2(\alpha-2)}{x} + 1})$. Thus, $\sigma^2 \frac{\partial}{\partial \sigma^2} \frac{P_K(A | \sigma^2, \alpha)}{P_K(A | \sigma^2, \alpha)}$ has lower bound $-1 + f(\frac{A}{\sqrt{2\sigma^2}})$, where $f(x) = (\frac{(\alpha-2)}{x^2} + \frac{1}{x})^{-1}$. Thus, we conclude that

Part (d). If $0 < \alpha \leq 1/2$, then $K_\alpha(x) < K_{\alpha-1}(x)$ for any $x > 0$. Therefore, from Eq.(7.73), we obtain $\sigma^2 \frac{\partial}{\partial \sigma^2} \frac{P_K(A | \sigma^2, \alpha)}{P_K(A | \sigma^2, \alpha)} < -\alpha + \frac{1}{\sqrt{2\sigma^2}} A$. This yields the inequality

$$\sigma^2 \frac{\partial}{\partial \sigma^2} L(\sigma^2, \alpha) < -N\alpha + \frac{1}{\sqrt{2\sigma^2}} \sum_{i=1}^N A_i. \quad (7.79)$$

But the right-hand side of Eq.(7.79) is negative if $\sigma^2 > \frac{1}{2\alpha^2} (\bar{A})^2$. This proves part (d).

Part (e). If $1/2 < \alpha \leq 3/2$, then $\frac{K_\alpha(x)}{K_{\alpha-1}(x)} < 1 + \frac{(\alpha-1/2)}{x}$ for any $x > 0$. Therefore, we have $\sigma^2 \frac{\partial}{\partial \sigma^2} \frac{P_K(A | \sigma^2, \alpha)}{P_K(A | \sigma^2, \alpha)} < -\frac{\alpha}{2} - \frac{1}{4} + \frac{1}{\sqrt{2\sigma^2}} A$. It follows that

$$\sigma^2 \frac{\partial}{\partial \sigma^2} L(\sigma^2, \alpha) < -N(\alpha/2 + 1/4) + \frac{1}{\sqrt{2\sigma^2}} \sum_{i=1}^N A_i. \quad (7.80)$$

$$\begin{aligned} \sigma^2 \frac{\partial}{\partial \sigma^2} L(\sigma^2, \alpha) &> -N \\ &+ \sum_{i=1}^N \frac{1}{\frac{2\sigma^2(\alpha-2)}{A_i^2} + \frac{\sqrt{2\sigma^2}}{A_i}}. \end{aligned} \quad (7.77)$$

From Jensen's inequality, we then obtain

$$\begin{aligned} \sigma^2 \frac{\partial}{\partial \sigma^2} L(\sigma^2, \alpha) &> -N \\ &+ N \frac{1}{\frac{2\sigma^2(\alpha-2)}{\bar{A}^2} + \frac{\sqrt{2\sigma^2}}{\bar{A}}}, \end{aligned} \quad (7.78)$$

because the function $f(x)$ above is convex. But the right-hand side of Eq.(7.78) is positive if $\sigma^2 < \frac{2\alpha-3+\sqrt{4\alpha-7}}{4(\alpha-2)^2} (\bar{A})^2$. This proves part (c).

But the right-hand side of Eq.(7.80) is negative if $\sigma^2 > \frac{1}{2(\alpha/2+1/4)^2} (\bar{A})^2$. This proves part (e).

Part (f). If $3/2 < \alpha \leq 3$, then $\frac{K_\alpha(x)}{K_{\alpha-1}(x)} < 1 + \frac{2(\alpha-1)}{x}$ for any $x > 0$. Thus, we obtain $\sigma^2 \frac{\partial}{\partial \sigma^2} \frac{P_K(A | \sigma^2, \alpha)}{P_K(A | \sigma^2, \alpha)} < -\alpha + (\alpha - 1) + \frac{1}{\sqrt{2\sigma^2}} A$. From there, we conclude that

$$\sigma^2 \frac{\partial}{\partial \sigma^2} L(\sigma^2, \alpha) < -N + \frac{1}{\sqrt{2\sigma^2}} \sum_{i=1}^N A_i. \quad (7.81)$$

But the right-hand side of Eq.(7.81) is negative if $\sigma^2 > \frac{1}{2} (\bar{A})^2$. Hence, part (f) of the theorem.

Part (g). If $3 < \alpha$, then $\frac{x}{2} \frac{K_\alpha(x)}{K_{\alpha-1}(x)} < (\alpha - 1) + \frac{x^2}{4(\alpha-2)}$ for any $x > 0$. Therefore, we obtain

$$\sigma^2 \frac{\partial}{\partial \sigma^2} L(\sigma^2, \alpha) < -N + \frac{1}{2\sigma^2(\alpha-2)} \sum_{i=1}^N A_i^2. \quad (7.82)$$

But the right-hand side of Eq.(7.82) is negative if $\sigma^2 > \frac{1}{2(\alpha-2)} \bar{A}^2$, hence, part (g) of the theorem.

Finally, part h) follows from the proof of parts (a) to (g). \blacksquare

Proof of Theorem 18. From Lemma 5, for any $\alpha > 0$, there exist two values $0 < \sigma_1^2 < \sigma_2^2$ for which $\frac{\partial}{\partial \sigma^2} L(\sigma_1^2, \alpha) > 0$ and $\frac{\partial}{\partial \sigma^2} L(\sigma_2^2, \alpha) < 0$, where L denotes L_K . Thus, by the Intermediate Value Theorem, there exists $\sigma^2 = \sigma^2(\alpha, \tilde{A})$ such that $\frac{\partial}{\partial \sigma^2} L(\sigma^2, \alpha) = 0$. \blacksquare

Proof of Theorem 19. Part (a). Let $0 < \alpha < 1/2$. In Eq.(7.32), the term $-\psi(\alpha) + \log\left(\frac{x}{2}\right) - \frac{\frac{\partial}{\partial \alpha} K_{1-\alpha}(x)}{K_{1-\alpha}(x)}$ is an increasing function of $x > 0$. Also, from Lemma 5 part (d), we have $\sigma^2(\alpha, \tilde{A}) \leq \frac{1}{2\sigma^2}(\tilde{A})^2$. Therefore, we obtain $\sqrt{\frac{2}{\sigma^2}} A_i \geq 2\alpha \frac{A_i}{\tilde{A}}$. It follows that $LB(\alpha) = -\psi(\alpha) + \log\left(\alpha \frac{A_i}{\tilde{A}}\right) - \frac{\frac{\partial}{\partial \alpha} K_{1-\alpha}\left(2\alpha \frac{A_i}{\tilde{A}}\right)}{K_{1-\alpha}\left(2\alpha \frac{A_i}{\tilde{A}}\right)}$ is a lower bound for that term. Now,

$$\begin{aligned} & -\alpha\psi(\alpha) + \alpha \log\left(\frac{1}{\sqrt{2\sigma^2}} A_i\right) + \alpha \frac{\frac{\partial}{\partial \alpha} K_{\alpha-1}\left(\sqrt{\frac{2}{\sigma^2}} A_i\right)}{K_{\alpha-1}\left(\sqrt{\frac{2}{\sigma^2}} A_i\right)} \\ & + \alpha - \left(\frac{1}{\sqrt{2\sigma^2}} A_i\right) \frac{K_\alpha\left(\sqrt{\frac{2}{\sigma^2}} A_i\right)}{K_{\alpha-1}\left(\sqrt{\frac{2}{\sigma^2}} A_i\right)}. \end{aligned} \quad (7.83)$$

from Abramowitz and Stegun (1972, Eq. (9.6.45), p. 377), we have $\frac{\frac{\partial}{\partial \alpha} K_{1-\alpha}(x)}{K_{1-\alpha}(x)} \approx \frac{\frac{\partial}{\partial \alpha} K_1(x)}{K_1(x)} = \frac{K_0(x)}{x K_1(x)}$ as $\alpha \rightarrow 0$. Moreover, from Abramowitz and Stegun (1972, Eqs. (9.6.8) and (9.6.9), p. 375), we have $\frac{K_0(x)}{x K_1(x)} \sim -\log x$ for small values of $x > 0$. But $x = 2\alpha \frac{A_i}{\tilde{A}}$ has small values for $\alpha \rightarrow 0$. Thus, we obtain $\lim_{\alpha \rightarrow 0} \alpha LB(\alpha) = \lim_{\alpha \rightarrow 0} \alpha \left\{ -\psi(\alpha) + \log\left(\alpha \frac{A_i}{\tilde{A}}\right) + \log\left(2\alpha \frac{A_i}{\tilde{A}}\right) \right\} = 1$. This proves part (a).

Part (b). First of all, we observe that there exist constants $0 < C_1 < C_2$, such that $\frac{1}{C_2} \leq \liminf_{\alpha \rightarrow \infty} \frac{\sigma^2(\alpha, \tilde{A})}{1/\alpha} \leq \limsup_{\alpha \rightarrow \infty} \frac{\sigma^2(\alpha, \tilde{A})}{1/\alpha} \leq \frac{1}{C_1}$. The first inequality follows from Lemma 5 part (c), whereas the third inequality follows from Lemma 5 part (g).

Let L denote L_K . Since by definition $\frac{\partial}{\partial \sigma^2} L(\sigma^2, \alpha)|_{\sigma^2(\alpha, \tilde{A})} = 0$, we might as well consider the expression $\alpha \frac{\partial}{\partial \alpha} L(\sigma^2, \alpha) - \sigma^2 \frac{\partial}{\partial \sigma^2} L(\sigma^2, \alpha)$. From Eqs. (7.32) and (7.33), each term of that expression is equal to

From Abraham and Lyons (2002, Eq. (46)), we have $\frac{\frac{\partial}{\partial \alpha} K_{\alpha-1}(x)}{K_{\alpha-1}(x)} \sim \psi(\alpha - 1) - \log(x/2) + \frac{x^2}{4\alpha^2}$ for large values of α . Also, from Abraham and Lyons (2002, Eq. (45)), we have $K_\alpha(x) \sim \frac{\Gamma(\alpha)}{2(x/2)^\alpha} \left(1 - \frac{(x/2)^2}{(\alpha-1)(\alpha-2)}\right)^{\alpha-2}$

for large values of α . Therefore, taking $\sigma^2 = 1/(C\alpha)$, we obtain the asymptotic expression

$$-\alpha\psi(\alpha) + \alpha\psi(\alpha - 1) + \frac{CA_i^2}{2} + \alpha - (\alpha - 1) \frac{\left(1 - \frac{C\alpha A_i^2}{2(\alpha-1)(\alpha-2)}\right)^{\alpha-2}}{\left(1 - \frac{C\alpha A_i^2}{2(\alpha-2)(\alpha-3)}\right)^{\alpha-3}}. \quad (7.84)$$

Finally, Eq. (7.84) tends to 0 as α tends to infinity. This proves part (b). ■

Proof of Theorem 20. Part (a). Let $0 < \alpha < 1$. We consider again Eq. (7.83). Using the asymptotic forms (for small values of x and

of α) $\frac{\frac{\partial}{\partial \alpha} K_{1-\alpha}(x)}{K_{1-\alpha}(x)} \approx \frac{K_0(x)}{x K_1(x)}$, $\frac{K_0(x)}{x K_1(x)} \sim -\log x$ and $(\frac{x}{2}) \frac{K_0(x)}{K_1(x)} \sim -\frac{x^2}{2} \log x$, and setting $x = \sqrt{\frac{2}{\sigma^2}} A_i$ with $\sigma^2 = 1/(C\alpha)$ and $C = 2/\bar{I}$, we obtain the asymptotic expression

$$-\alpha\psi(\alpha) + \alpha \log\left(\frac{1}{2}\sqrt{\alpha}\sqrt{C}A_i\right) + \alpha \log\left(\sqrt{\alpha}\sqrt{C}A_i\right) + \alpha + \alpha^2 CA_i^2 \log\left(\sqrt{\alpha}\sqrt{C}A_i\right). \quad (7.85)$$

Part (a) then follows by taking the limit of Eq. (7.85) as $\alpha \rightarrow 0$.

Part (b). Taking $\sigma^2 = 1/(C\alpha)$, where $C = 2/\bar{I}$, into Eq. (7.84), we obtain the limit 0 as $\alpha \rightarrow \infty$. This proves part (b). ■

Proof of Theorem 21. (a) At $\alpha = 0$, we have $\Gamma(\alpha + v/2) = \Gamma(v/2)$. Also, $\Gamma(\alpha)$ has a simple pole with residue 1 at $\alpha = 0$. Therefore, $\frac{\Gamma(\alpha+1/2)}{\alpha^{v/2}\Gamma(\alpha)} \sim \Gamma(v/2)\alpha^{1-v/2}$ at $\alpha \approx 0$, which shows part (a).

(b) Using Sterling's formula, we have $\frac{\Gamma(\alpha+v/2)}{\alpha^{v/2}\Gamma(\alpha)} \sim \frac{e^{-\alpha-v/2}(\alpha+v/2)^{\alpha+v/2-1/2}}{\alpha^{v/2}e^{-\alpha}\alpha^{\alpha-1/2}}$, which is equal to $e^{-v/2}\left(1 + \frac{v/2}{\alpha}\right)^\alpha \left(1 + \frac{v/2}{\alpha}\right)^{v/2-1/2}$. Therefore, $\lim_{\alpha \rightarrow \infty} \frac{\Gamma(\alpha+v/2)}{\alpha^{v/2}\Gamma(\alpha)} = 1$, and we are done.

(c) Using the logarithmic derivative, we have $\frac{d}{d\alpha} M_K^{(v)}(\alpha) = M_K^{(v)}(\alpha) \left(\psi(\alpha + v/2) - \psi(\alpha) - \frac{v}{2\alpha} \right)$. Now, we have $M_K^{(v)}(\alpha) > 0$. Also, $\frac{1}{\alpha} = \psi(\alpha + 1) - \psi(\alpha)$, and hence $\psi(\alpha + v/2) - \psi(\alpha) - \frac{v}{2\alpha} = \psi(\alpha + v/2) - \left(\frac{v}{2}\psi(\alpha + 1) + (1 - \frac{v}{2})\psi(\alpha)\right)$. Since the function ψ is convex, we

conclude that $\psi(\alpha + v/2) - \left(\frac{v}{2}\psi(\alpha + 1) + (1 - \frac{v}{2})\psi(\alpha)\right) > 0$, if $v/2 < 1$, whereas it is negative if $v/2 > 1$. ■

Proof of Theorem 22. (a) We consider the function $f(\alpha) = \frac{\Gamma(v+1)\Gamma(v+\alpha)\Gamma(\alpha)}{\Gamma^2(v/2+1)\Gamma^2(v/2+\alpha)}$, noting that $R_K^{(v)} = (f(\alpha) - 1)^{-1/2}$. Now, as $\alpha \rightarrow 0$, we have $\Gamma(\alpha) \rightarrow \infty$, whereas $\frac{\Gamma(v+1)\Gamma(v+\alpha)}{\Gamma^2(v/2+1)\Gamma^2(v/2+\alpha)} \rightarrow \frac{\Gamma(v+1)\Gamma(v)}{\Gamma^2(v/2+1)\Gamma^2(v/2)} > 0$. This proves part (a).

(b) Next, using directly Sterling's formula for $\Gamma(v + \alpha)$, $\Gamma(\alpha)$, and $\Gamma(v/2 + \alpha)$, one finds that $\lim_{\alpha \rightarrow \infty} f(\alpha) = \frac{\Gamma(v+1)}{\Gamma^2(v/2+1)}$, which proves part (b).

(c) Finally, taking the logarithmic derivative of $f(\alpha)$ yields $\frac{df}{d\alpha} = f(\alpha)(\psi(v + \alpha) + \psi(\alpha) - 2\psi(v/2 + \alpha))$. This is negative, since $f(\alpha) > 0$ and $\psi(v/2 + \alpha) > \frac{1}{2}(\psi(v + \alpha) + \psi(\alpha))$ (because ψ is a convex function). It follows that $f(\alpha) > \lim_{\alpha \rightarrow \infty} f(\alpha) = \frac{\Gamma(v+1)}{\Gamma^2(v/2+1)}$. We claim that $g(v) = \frac{\Gamma(v+1)}{\Gamma^2(v/2+1)} > 1$, for any $v > 0$. In fact, the function $g(v)$ is increasing (its

derivative is equal to $g(v)(\psi(v+1) - \psi(v/2 + 1))$ and $g(0) = 1$. Therefore, $f(\alpha) > 1$, and it follows that $(f(\alpha) - 1)^{-1/2}$ is an increasing function. This completes the proof of part (c). ■

Proof of Theorem 23. This is an immediate consequence of Theorem 28. ■

Proof of Theorem 25. Starting with Eq. (7.44), we compute

$$\begin{aligned} M_{HK}^{(v)}(\gamma, \alpha) &= \frac{\Gamma(v/2 + 1)}{(\gamma + \alpha)^{v/2}} \int_0^\infty w^{v/2} {}_1F_1(-v/2, 1, -\frac{\gamma}{w}) \mathcal{G}(w | \alpha, 1) dw \\ &= \frac{\Gamma(v/2 + 1)}{(\gamma + \alpha)^{v/2}} \int_0^\infty w^{v/2} e^{-\gamma/w} {}_1F_1(1 + v/2, 1, \frac{\gamma}{w}) \mathcal{G}(w | \alpha, 1) dw \\ &= \frac{1}{(\gamma + \alpha)^{v/2}} \frac{\Gamma(v/2 + 1)}{\Gamma(\alpha)} \sum_{n=0}^{\infty} \frac{(1 + v/2)_n}{n! n!} \gamma^n \int_0^\infty w^{v/2 + \alpha - n - 1} e^{-\gamma/w} e^{-w} dw. \end{aligned} \quad (7.86)$$

Using Erdélyi (1954, I, p. 146, (29)), this is equal to

$$\begin{aligned} &\frac{1}{(\gamma + \alpha)^{v/2}} \frac{\Gamma(v/2 + 1)}{\Gamma(\alpha)} \sum_{n=0}^{\infty} \frac{(1 + v/2)_n}{n! n!} \gamma^n 2(\sqrt{\gamma})^{v/2 + \alpha - n} K_{v/2 + \alpha - n}(2\sqrt{\gamma}) \\ &= \frac{2}{(\gamma + \alpha)^{v/2}} \frac{\Gamma(v/2 + 1)}{\Gamma(\alpha)} \sum_{n=0}^{\infty} \frac{(1 + v/2)_n}{n! n!} (\sqrt{\gamma})^{v/2 + \alpha + n} K_{v/2 + \alpha - n}(2\sqrt{\gamma}). \end{aligned} \quad (7.87)$$

This completes the proof of Theorem 25. ■

Proof of Theorem 26. (a) This follows from Theorem 24, part (b), and Theorem 13.

(b) From Theorem 24, part (a), we know that $M_{HK}^{(v)}(\gamma, \alpha)$ is equal to $\frac{\Gamma(v/2 + 1)}{(\gamma + \alpha)^{v/2}} \int_0^\infty w^{v/2} {}_1F_1(-v/2, 1, -\gamma/w) \mathcal{G}(w | \alpha, 1) dw$. From Luke (1962, pp. 7–8), we have $\Gamma(v/2 + 1) {}_1F_1(-v/2, 1, -z) = \Gamma(v/2 + 1) e^{-z} {}_1F_1(1 + v/2, 1, z) = z^{v/2} (1 + O(1/z))$, for large values of z . Let $\eta > 0$ be a real number (arbitrarily small). Take z_0 sufficiently large so that $(1 - \eta)z^{v/2} \leq \Gamma(v/2 + 1) {}_1F_1(-v/2, 1, -z) \leq (1 + \eta)z^{v/2}$, for any $z \geq z_0$. Then, if $\gamma/w \geq z_0$, i.e., $w \leq \gamma/z_0$, we have $(1 - \eta)\gamma^{v/2} \leq \Gamma(v/2 + 1)w^{v/2} {}_1F_1(-v/2, 1, -\gamma/w) \leq (1 + \eta)\gamma^{v/2}$. Therefore, the integral $\frac{\Gamma(v/2 + 1)}{(\gamma + \alpha)^{v/2}} \int_0^{\gamma/z_0} w^{v/2} {}_1F_1(-v/2, 1, -\gamma/w)$

$\mathcal{G}(w | \alpha, 1) dw$ has lower bound $(1 - \eta) \frac{\gamma^{v/2}}{(\gamma + \alpha)^{v/2}}$ $Pr(w \leq \gamma/z_0)$ and upper bound $(1 + \eta) \frac{\gamma^{v/2}}{(\gamma + \alpha)^{v/2}} Pr(w \leq \gamma/z_0)$. On the other hand, the function ${}_1F_1(-v/2, 1, -z)$ equals 1 at $z = 0$, and hence there is a real number $C > 0$ such that $0 < {}_1F_1(-v/2, 1, -\gamma/w) \leq C$ for any $w > \gamma/z_0$. Thus, the integral $\frac{\Gamma(v/2 + 1)}{(\gamma + \alpha)^{v/2}} \int_{\gamma/z_0}^\infty w^{v/2} {}_1F_1(-v/2, 1, -\gamma/w) \mathcal{G}(w | \alpha, 1) dw$ has lower bound 0 and upper bound $\frac{\Gamma(v/2 + 1)}{(\gamma + \alpha)^{v/2}} C \frac{\Gamma(v/2 + \alpha)}{\Gamma(\alpha)}$. But now, $\lim_{\gamma \rightarrow \infty} \frac{\gamma^{v/2}}{(\gamma + \alpha)^{v/2}} = 1$, $\lim_{\gamma \rightarrow \infty} Pr(w \leq \gamma/z_0) = 1$, and $\lim_{\gamma \rightarrow \infty} \frac{1}{(\gamma + \alpha)^{v/2}} = 0$. Therefore, we obtain $\liminf_{\gamma \rightarrow \infty} M_{HK}^{(v)}(\gamma, \alpha) \geq 1 - \eta$ and $\limsup_{\gamma \rightarrow \infty} M_{HK}^{(v)}(\gamma, \alpha) \leq 1 + \eta$. Since η is arbitrarily small, we conclude that $\lim_{\gamma \rightarrow \infty} M_{HK}^{(v)}(\gamma, \alpha) = 1$.

(c) We consider the function $f(\gamma, w) = \frac{{}_1F_1(1+\nu/2, 1, \gamma/w)}{e^{\gamma/w}(\gamma+\alpha)^{\nu/2}}$. From Theorem 24, part (a), we have $M_{\text{HK}}^{(\nu)}(\gamma, \alpha) = \Gamma(\nu/2 + 1) \int_0^\infty w^{\nu/2} f(\gamma, w) \mathcal{G}(w | \alpha, 1) dw$. Thus, we obtain $\frac{\partial}{\partial \gamma} M_{\text{HK}}^{(\nu)}(\gamma, \alpha) = \Gamma(\nu/2 + 1) \int_0^\infty w^{\nu/2} \frac{\partial}{\partial \gamma} f(\gamma, w) \mathcal{G}(w | \alpha, 1) dw$. We compute the value of $\frac{\partial}{\partial \gamma} f(\gamma, w)$ as

$$\frac{\frac{d}{dz} {}_1F_1(1 + \nu/2, 1, \gamma/w) w^{-1} - {}_1F_1(1 + \nu/2, 1, \gamma/w) \left(w^{-1} + \frac{\nu}{2} (\gamma + \alpha)^{-1} \right)}{e^{\gamma/w} (\gamma + \alpha)^{\nu/2}}. \quad (7.88)$$

Using Gradshteyn and Ryshik (1994, 9.213, p. 1086) and Gradshteyn and Ryshik (1994, 9.212(3), p. 1086), we have $\frac{d}{dz} {}_1F_1(1 + \nu/2, 1, \gamma/w) = (1 + \nu/2) {}_1F_1(2 + \nu/2, 2, \gamma/w) = \frac{\nu/2}{2} {}_1F_1(1 + \nu/2, 2, \gamma/w) + {}_1F_1(1 + \nu/2, 1, \gamma/w)$. So, we obtain after algebraic simplifications

$$\frac{\nu/2}{e^{\gamma/w} (\gamma + \alpha)^{\nu/2+1}} \left\{ {}_1F_1(1 + \nu/2, 2, \gamma/w) \left(\frac{\gamma}{w} + \frac{\alpha}{w} \right) - {}_1F_1(1 + \nu/2, 1, \gamma/w) \right\}. \quad (7.89)$$

Using Gradshteyn and Ryshik (1994, 9.212(2), p. 1086), we have $\frac{\gamma}{w} {}_1F_1(1 + \nu/2, 2, \gamma/w) - {}_1F_1(1 + \nu/2, 1, \gamma/w) = - {}_1F_1(\nu/2, 1, \gamma/w)$. Therefore, we finally obtain

$$\frac{\alpha \nu/2}{e^{\gamma/w} (\gamma + \alpha)^{\nu/2+1} w} \left\{ {}_1F_1(1 + \nu/2, 2, \gamma/w) - \frac{w}{\alpha} {}_1F_1(\nu/2, 1, \gamma/w) \right\}. \quad (7.90)$$

Now, let $\nu/2 < 1$. Then, we obtain the strict lower bound for $\frac{\partial}{\partial \gamma} f(\gamma, w)$

$$\frac{\alpha \nu/2}{e^{\gamma/w} (\gamma + \alpha)^{\nu/2+1} w} \left\{ {}_1F_1(1 + \nu/2, 2, \gamma/w) - \frac{w}{\alpha} {}_1F_1(\nu/2, 1, \gamma/w) \right\}. \quad (7.91)$$

Consider the function $g(\gamma, w) = \frac{\alpha \nu/2}{e^{\gamma/w} (\gamma + \alpha)^{\nu/2+1} w} {}_1F_1(1 + \nu/2, 2, \gamma/w)$. We have shown that

$$\frac{\partial}{\partial \gamma} M_{\text{HK}}^{(\nu)}(\gamma, \alpha) > \int_0^\infty g(\gamma, w) \mathcal{G}(w | \alpha, 1) dw - \int_0^\infty \frac{w}{\alpha} g(\gamma, w) \mathcal{G}(w | \alpha, 1) dw. \quad (7.92)$$

But $\frac{w}{\alpha} \mathcal{G}(w | \alpha, 1) = \mathcal{G}(w | \alpha + 1, 1)$. So, we obtain

$$\frac{\partial}{\partial \gamma} M_{HK}^{(v)}(\gamma, \alpha) > \int_0^\infty g(\gamma, w) \mathcal{G}(w | \alpha, 1) dw - \int_0^\infty g(\gamma, w) \mathcal{G}(w | \alpha + 1, 1) dw. \quad (7.93)$$

Thus, we want to show that $\int_0^\infty g(\gamma, w) \mathcal{G}(w | \alpha, 1) dw - \int_0^\infty g(\gamma, w) \mathcal{G}(w | \alpha + 1, 1) dw \geq 0$. Ignoring the positive factor $\Gamma(v/2 + 1) \frac{\alpha v/2}{(\gamma + \alpha)^{v/2+1}}$, we are thus lead to the function $h(\gamma, w) = \frac{w^{v/2-1} {}_1F_1(1+v/2, 2, \gamma/w)}{e^{\gamma/w} (\gamma + \alpha)^{v/2+1} w}$, and we show that $\int_0^\infty h(\gamma, w) \mathcal{G}(w | \alpha, 1) dw - \int_0^\infty h(\gamma, w) \mathcal{G}(w | \alpha + 1, 1) dw \geq 0$ as follows. In

Lemma 6, we show that $h(\gamma, w)$ is decreasing in the variable w , if $v/2 < 1$. Then, in Lemma 7, we show that for any decreasing positive function $H(w)$, we have $\int_0^\infty H(w) \mathcal{G}(w | \alpha, 1) dw - \int_0^\infty H(w) \mathcal{G}(w | \alpha + 1, 1) dw \geq 0$.

Next, let $v/2 > 1$. Then, we obtain the strict upper bound for $\frac{\partial}{\partial \gamma} f(\gamma, w)$

$$\frac{\alpha v/2}{e^{\gamma/w} (\gamma + \alpha)^{v/2+1} w} \left\{ {}_1F_1(1 + v/2, 2, \gamma/w) - \frac{w}{\alpha} {}_1F_1(1 + v/2, 2, \gamma/w) \right\}. \quad (7.94)$$

The same argument as above (but with reversed inequalities) leads to

$$\frac{\partial}{\partial \gamma} M_{HK}^{(v)}(\gamma, \alpha) < \int_0^\infty g(\gamma, w) \mathcal{G}(w | \alpha, 1) dw - \int_0^\infty g(\gamma, w) \mathcal{G}(w | \alpha + 1, 1) dw, \quad (7.95)$$

where the function $g(\gamma, w)$ is defined as above. So, in this case, we want to show that $\int_0^\infty h(\gamma, w) \mathcal{G}(w | \alpha, 1) dw - \int_0^\infty h(\gamma, w) \mathcal{G}(w | \alpha + 1, 1) dw \leq 0$, where $h(\gamma, w)$ is defined as above. But this is implied by Lemmas 6 and 7 (case $v/2 > 1$). This completes the proof of the theorem. ■

Lemma 6 (a) If $v/2 < 1$, the function $h(\gamma, w) = \frac{w^{v/2-1} {}_1F_1(1+v/2, 2, \gamma/w)}{e^{\gamma/w}}$ is decreasing in the variable w .

(b) If $v/2 > 1$, the function $h(\gamma, w)$ is increasing in the variable w .

Proof Using the change of variable $x = \gamma/w$, we consider the function $F(x) = \frac{{}_1F_1(1+v/2, 2, x)}{e^x x^{v/2-1}}$. So, we want to show that $F(x)$ is increasing if $v/2 < 1$ and $F(x)$ is decreasing if $v/2 > 1$ (the function $x = \gamma/w$ is decreasing in the variable w).

We compute

$$\frac{d}{dx} F(x) = \frac{\frac{d}{dz} {}_1F_1(1 + v/2, 2, x) - {}_1F_1(1 + v/2, 2, x) \left(1 + \left(\frac{v}{2} - 1\right)x^{-1}\right)}{e^x x^{v/2-1}}. \quad (7.96)$$

Using Gradshteyn and Ryshik (1994, 9.213, p. 1086) and Gradshteyn and Ryshik (1994, 9.212(3), p. 1086), we have $\frac{d}{dz} {}_1F_1(1 +$

$$\nu/2, 2, x) = \frac{(1+\nu/2)}{2} {}_1F_1(2 + \nu/2, 3, x) = \frac{(\nu/2-1)}{2} {}_1F_1(1 + \nu/2, 3, x) + \frac{2}{2} {}_1F_1(1 + \nu/2, 2, x).$$

So, we obtain after algebraic simplifications

$$\frac{(\nu/2 - 1)}{e^x x^{\nu/2}} \left\{ \frac{x}{2} {}_1F_1(1 + \nu/2, 3, x) - {}_1F_1(1 + \nu/2, 2, x) \right\}. \quad (7.97)$$

Using Gradshteyn and Ryshik (1994, 9.212(2), p. 1086), we finally obtain

$$-\frac{(\nu/2 - 1)}{e^x x^{\nu/2}} {}_1F_1(1 + \nu/2, 1, x). \quad (7.98)$$

The result is now clear. ■

Lemma 7 (a) Let $H(w)$ be a decreasing positive function. Then, one has

$$\int_0^\infty H(w)\mathcal{G}(w|\alpha, 1) dw - \int_0^\infty H(w)\mathcal{G}(w|\alpha+1, 1) dw \geq 0.$$

(b) Let $H(w)$ be an increasing positive function. Then, one has

$$\int_0^\infty H(w)\mathcal{G}(w|\alpha, 1) dw - \int_0^\infty H(w)\mathcal{G}(w|\alpha+1, 1) dw \leq 0.$$

Proof (a) Since $H(w)$ is a positive decreasing function, we can approximate it by functions of the form $\sum_{n=1}^N a_n B(b_n, w)$, where $a_n \geq 0$, $b_n > 0$, and $B(b, w)$ is equal to 1, if $w \in [0, b]$, and $B(b, w) = 0$, if $w > b$. Now, $\int_0^\infty B(b, w)\mathcal{G}(w|\alpha, 1) dw = \int_0^b \mathcal{G}(w|\alpha, 1) dw = 1 - \frac{\Gamma(\alpha, b)}{\Gamma(\alpha)}$, where $\Gamma(\alpha, b)$ is the incomplete Euler gamma function. But the function $1 - \frac{\Gamma(\alpha, b)}{\Gamma(\alpha)}$ is decreasing. Therefore, $\int_0^\infty B(b, w)\mathcal{G}(w|\alpha, 1) dw > \int_0^\infty B(b, w)\mathcal{G}(w|\alpha+1, 1) dw$, and we are done.

(b) Since $H(w)$ is a positive increasing function, we can approximate $H(w)$ by functions of the form $\sum_{n=1}^N a_n (1 - B(b_n, w))$, where $a_n \geq 0$, $b_n > 0$. Now, $\int_0^\infty (1 -$

$B(b, w))\mathcal{G}(w|\alpha, 1) dw = \frac{\Gamma(\alpha, b)}{\Gamma(\alpha)}$, and we are done. ■

Proof of Corollary 2. Let $\nu/2 < 1$. Since $0 < M < 1$, we conclude from Theorem 26, using the Intermediate Value Theorem, that for any $\alpha > 0$ such that $M_K(\alpha) \leq M$, there is a unique value of $\gamma \geq 0$ for which $M_{HK}^{(\nu)}(\gamma, \alpha) = M$. Thus, if $M \geq \Gamma(\nu/2 + 1)$, α has no restrictions, because $M_K^{(\nu)}(\alpha) < \Gamma(\nu/2 + 1)$ for any $\alpha > 0$ (Theorem 21). On the other hand, if $M_K(\alpha) < M$, let α_0 be the unique solution to the equation $M_K^{(\nu)}(\alpha_0) = M$ (Theorem 21). Then, using once more Theorem 21, we obtain that $M_K^{(\nu)}(\alpha) < M$ if and only if $\alpha \leq \alpha_0$. Henceforth, if $M_K^{(\nu)}(\alpha) < M$, the domain of the function $\gamma_M^{(\nu)}(\alpha)$ is the interval $(0, \alpha_0]$.

The case $\nu/2 > 1$ is handled similarly, but with reversed inequalities. ■

Proof of Lemma 4. Part (a). From the definition in Eq. (7.6), the distribution $P_{HK}(A | \varepsilon, \sigma^2, \alpha)$ is equal to $\int_0^\infty P_{Ri}(A | \varepsilon, \sigma^2 w) \mathcal{G}(w|\alpha, 1) dw$. Using the identity $I_0(z) = \frac{1}{\pi} \int_0^\pi e^{z \cos \theta} d\theta$ from Abramowitz and Stegun (1972, Eq. (9.6.16), p. 376) and the definition of the Rice distribution (7.2), we can express $P_{Ri}(A | \varepsilon, \sigma^2 w)$ in the form $\frac{1}{\pi} \int_0^\pi \frac{A}{\sigma^2 w} \exp\left(-\frac{\varepsilon}{\sigma^2 w} A \cos \theta\right) \exp\left(-\frac{(\varepsilon^2 + A^2)}{2\sigma^2 w}\right) d\theta$. It follows that $P_{HK}(A | \varepsilon, \sigma^2, \alpha)$ can be written as

$$\frac{1}{\pi} \int_0^\pi \left\{ \int_0^\infty \frac{A}{\sigma^2 w} \exp\left(-\frac{\varepsilon}{\sigma^2 w} A \cos \theta\right) \exp\left(-\frac{(\varepsilon^2 + A^2)}{2\sigma^2 w}\right) \mathcal{G}(w|\alpha, 1) dw \right\} d\theta, \quad (7.99)$$

which yields Eq. (7.56) after evaluation of the inner integral.

Part (b). Using Eq. (7.56), the partial derivative of the homodyned K-distribution with respect to ε is equal to

$$\begin{aligned} & \frac{1}{\pi} \int_0^\pi \frac{2A}{\sigma^2 \Gamma(\alpha)} \frac{\partial}{\partial \varepsilon} \left\{ \left(\frac{X(\theta)}{2} \right)^{\alpha-1} K_{\alpha-1}(X(\theta)) \right\} d\theta \\ &= \frac{1}{\pi} \int_0^\pi \frac{2A}{\sigma^2 \Gamma(\alpha)} \left\{ \frac{(\alpha-1)}{2} \left(\frac{X(\theta)}{2} \right)^{\alpha-2} K_{\alpha-1}(X(\theta)) \right. \\ &\quad \left. + \left(\frac{X(\theta)}{2} \right)^{\alpha-1} \frac{d}{dz} K_{\alpha-1}(X(\theta)) \right\} \frac{\partial}{\partial \varepsilon} X(\theta) d\theta \\ &= -\frac{1}{\pi} \int_0^\pi \frac{2A}{\sigma^2 \Gamma(\alpha)} \left(\frac{X(\theta)}{2} \right)^{\alpha-1} K_{\alpha-2}(X(\theta)) 2 \frac{(\varepsilon - A \cos \theta)}{\sigma^2 X(\theta)} d\theta. \end{aligned} \quad (7.100)$$

Here, we have used the identity $z \frac{d}{dz} K_{\alpha-1}(z) + (\alpha-1)K_{\alpha-1}(z) = -z K_{\alpha-2}(z)$ (Abramowitz and Stegun 1972, Eq. (9.6.26), 2nd identity, p. 376) and algebraic simplifications.

Part (c). Using Eq. (7.56), the partial derivative of the homodyned K-distribution with respect to σ^2 is equal to

$$\begin{aligned} & \frac{1}{\pi} \int_0^\pi \frac{2A}{\Gamma(\alpha)} \frac{\partial}{\partial \sigma^2} \left\{ \frac{1}{\sigma^2} \left(\frac{X(\theta)}{2} \right)^{\alpha-1} K_{\alpha-1}(X(\theta)) \right\} d\theta \\ &= -\frac{1}{\sigma^2} \frac{1}{\pi} \int_0^\pi \frac{2A}{\sigma^2 \Gamma(\alpha)} \left(\frac{X(\theta)}{2} \right)^{\alpha-1} K_{\alpha-1}(X(\theta)) d\theta \\ &\quad + \frac{1}{\pi} \int_0^\pi \frac{2A}{\sigma^2 \Gamma(\alpha)} \left\{ \frac{(\alpha-1)}{2} \left(\frac{X(\theta)}{2} \right)^{\alpha-2} K_{\alpha-1}(X(\theta)) \right. \\ &\quad \left. + \left(\frac{X(\theta)}{2} \right)^{\alpha-1} \frac{d}{dz} K_{\alpha-1}(X(\theta)) \right\} \frac{\partial}{\partial \sigma^2} X(\theta) d\theta \\ &= -\frac{1}{\sigma^2} \frac{1}{\pi} \int_0^\pi \frac{2A}{\sigma^2 \Gamma(\alpha)} \left(\frac{X(\theta)}{2} \right)^{\alpha-1} K_{\alpha-1}(X(\theta)) d\theta \\ &\quad - \frac{1}{\sigma^2} \frac{1}{\pi} \int_0^\pi \frac{2A}{\sigma^2 \Gamma(\alpha)} \left\{ (\alpha-1) \left(\frac{X(\theta)}{2} \right)^{\alpha-2} K_{\alpha-1}(X(\theta)) \right. \\ &\quad \left. - \left(\frac{X(\theta)}{2} \right)^{\alpha-1} K_\alpha(X(\theta)) \right\} \left(\frac{X(\theta)}{2} \right) d\theta \\ &= -\frac{\alpha}{\sigma^2} \frac{1}{\pi} \int_0^\pi \frac{2A}{\sigma^2 \Gamma(\alpha)} \left(\frac{X(\theta)}{2} \right)^{\alpha-1} K_{\alpha-1}(X(\theta)) d\theta \\ &\quad + \frac{1}{\sigma^2} \frac{1}{\pi} \int_0^\pi \frac{2A}{\sigma^2 \Gamma(\alpha)} \left(\frac{X(\theta)}{2} \right)^\alpha K_\alpha(X(\theta)) d\theta. \end{aligned} \quad (7.101)$$

Here, we have used the identity $\frac{z}{2} \frac{d}{dz} K_{\alpha-1}(z) = -\frac{z}{2} K_\alpha(z) + \frac{(\alpha-1)}{2} K_{\alpha-1}(z)$ (Abramowitz and Stegun 1972, Eq. (9.6.26), 4th identity, p. 376) and algebraic simplifications.

Part (d). Eq. (7.59) follows from part (a) upon taking the logarithmic derivative of the integrand in Eq. (7.56). ■

References

- Abraham DA, Lyons AP (2002) Novel physical interpretation of K-distributed reverberation. *IEEE J Oceanic Eng* 27(4):800–813
- Abraham DA, Lyons AP (2010) Reliable methods for estimating the K-distribution shape parameter. *IEEE J of Oceanic Eng* 35(2):288–302
- Abramowitz M, Stegun IA (eds) (1972) Handbook of mathematical functions with formulas, graphs, and mathematical tables. Dover, New York
- Agrawal R, Karmeshu (2006) Ultrasonic backscattering in tissue: characterization through Nakagami-generalized inverse Gaussian distribution. *Comput Biol Med* 37:166–172
- Barakat R (1986) Weak-scatterer generalizations of the K-density function with application to laser in atmospheric turbulence. *J Opt Soc Am A* 3:401–409
- Berger NE, Lucas RJ, Twersky V (1991) Polydisperse scattering theory and comparisons with data for red blood cells. *J Acoust Soc Am* 89(3):1394–1401
- Blacknell D, Tough RJA (2001) Parameter estimation for the K-distributed based on $[z \log(z)]$. *IEE Proc-Radar Sonar Navig* 148(6):309–312
- Bouhlel N, Sevestre-Ghalila S (2009) Nakagami Markov random field as texture model for ultrasound RF envelope image. *Comput Biol Med* 39:535–544
- Burckhardt CB (1978) Speckle in ultrasound B-mode scans. *IEEE Trans Son Ultrason SU-25(1)*:1–6
- Carrobi CFM, Cati M (2008) The absolute maximum of the likelihood function of the Rice distribution: existence and uniqueness. *IEEE Trans Instrum Meas* 57(4):682–689
- Chung P-J, Roberts WJJ, Bohme JF (2005) Recursive K-distribution parameter estimation. *IEEE Trans Signal Process* 53(2):397–402
- Destrempe F, Cloutier G (2010) A critical review and uniformized representation of statistical distributions modeling the ultrasound echo envelope. *Ultrasound Med Biol* 36(7):1037–1051
- Destrempe F, Meunier J, Giroux M-F, Soulez G, Cloutier G (2009) Segmentation in ultrasonic B-mode images of healthy carotid arteries using mixtures of Nakagami distributions and stochastic optimization. *IEEE Trans Med Imag* 28(2):215–229
- Destrempe F, Meunier J, Giroux M-F, Soulez G, Cloutier G (2011) Segmentation of plaques in sequences of ultrasonic B-mode images of carotid arteries based on motion estimation and a Bayesian model. *IEEE Trans Biomed Eng* 58(8):2202–2211
- Dumane VA, Shankar PM (2001) Use of frequency diversity and Nakagami statistics in ultrasonic tissue characterization. *IEEE Trans Ultrason Ferroelectr Freq Control* 48(5):1139–1146
- Dutt V (1995) Statistical analysis of ultrasound echo envelope. Ph.D. Thesis, Mayo Graduate School
- Dutt V, Greenleaf JF (1994) Ultrasound echo envelope analysis using a homodyned K distribution signal model. *Ultrason Imaging* 16:265–287
- Dutt V, Greenleaf JF (1995) Speckle analysis using signal to noise ratios based on fractional order moments. *Ultrason Imaging* 17:251–268
- Dutt V, Greenleaf JF (1996) Statistics of the log-compressed echo envelope. *J Acoust Soc Am* 99(6):265–287
- Edgeworth FY (1908) On the probable errors of frequency-constants I, II, III. *J Roy Statist Soc* 71:381–397, 499–512, 651–678
- Edgeworth FY (1909) On the probable errors of frequency-constants. Addendum. *J Roy Statist Soc* 72:81–90
- Eltoft T (2005) The Rician inverse gaussian distribution: a new model for non-Rayleigh signal amplitude statistics. *IEEE Trans Image Process* 14:1722–1735
- Erdélyi A (1954) Tables of integral transforms. McGraw-Hill, New York, NY
- Fisher RA (1912) On an absolute criterion for fitting frequency curves. *Messenger Math* 41:155–160
- Fisher RA (1922) On the mathematical foundations of theoretical statistics. *Philos Trans Roy London Ser A* 222:309–368
- Fisher RA (1925) Theory of statistical estimation. In: *Proceedings of the Cambridge Philosophical Society*, vol 22, pp 700–725
- Fisher RA (1956) Statistical methods and scientific inference. Oliver and Boyd, Edinburgh
- Gradshteyn IS, Ryzhik IM (eds) (1994) Table of integrals, series, and products. Academic Press, London
- Hao X, Bruce CJ, Pislaru C, Greenleaf JF (2002) Characterization of reperfused infarcted myocardium from high-frequency intracardiac ultrasound imaging using homodyned K distribution. *IEEE Trans Ultrason Ferroelectr Freq Control* 49(11):1530–1542
- Hayley SW, Kays TH, Twersky V (1967) Comparison of distribution functions from scattering data on different sets of spheres. *IEEE Trans Antennas Propag AP-15(1)*:118–135
- Hruska DP (2009) Improved techniques for statistical analysis of the envelope of backscattered ultrasound using the Homodyned K distribution. M.Sc. Thesis, University of Illinois at Urbana-Champaign
- Hruska DP, Oelze ML (2009) Improved parameter estimates based on the Homodyned K distribution. *IEEE Trans Ultrason Ferroelectr Freq Control* 56(11):2471–2481
- Hruska DP, Sanchez J, Oelze ML (2009) Improved diagnostics through quantitative ultrasound imaging. In: *IEEE conference of the engineering in medicine and biology society*, pp 1956–1959
- Huang C-C, Wang S-H (2007) Statistical variations of ultrasound signals backscattered from flowing blood. *Ultrasound Med Biol* 33(12):1943–1954
- Huang C-C, Tsui P-H, Wang S-H (2007) Detection of coagulating blood under steady flow by statistical analysis of backscattered signals. *IEEE Trans Ultrason Ferroelectr Freq Control* 54(2):435–442
- Insana MF, Wagner RF, Garra BS, Brown DG, Shawker TH (1986) Analysis of ultrasound image texture via generalized Rician statistics. *Opt Eng* 25(6):743–748

- Iskander DR, Zoubir AM (1999) Estimation of the parameters of the K-distribution using higher order and fractional moments. *IEEE Trans Aerosp Electron Syst* 35(4):1453–1457
- Jakeman E (1980) On the statistics of K-distributed noise. *J Phys A* 13:31–48
- Jakeman E, Pusey PN (1976) A model for non-Rayleigh sea echo. *IEEE Trans Antennas Propag* 24:806–814
- Jakeman E, Tough RJA (1987) Generalized k distribution: a statistical model for weak scattering. *J Opt Soc Am A* 4:1764–1772
- Jeffreys H (1946) An invariant form for the prior probability in estimation problems. In: *Proceedings of the royal society of london (Ser A)*, vol 186, pp 453–461
- Jensen J (1906) Sur les fonctions convexes et les inégalités entre les valeurs moyennes. *Acta Math* 30:175–193
- Joughin IR, Percival DB, Winebrenner DP (1993) Maximum likelihood estimation of K distribution parameters for SAR data. *IEEE Trans Geosci Remote Sens* 31(5):989–999
- Keyes TK, Tucker WT (1999) The K-distribution for modeling the envelope amplitude of a backscattered signal. *IEEE Trans Ultrason Ferroelectr Freq Control* 46(4):883–887
- Kullback S, Leibler RA (1951) On information and sufficiency. *Ann Math Stat* 22:79–86
- Lord RD (1954) The use of the Hankel transform in statistics. I. *Biometrika* 41:44–55
- Lucas RJ, Twersky V (1987) Inversion of ultrasonic scattering data for red blood cell suspension under different flow conditions. *J Acoust Soc Am* 82(3):794–799
- Luke YL (1962) Integrals of bessel functions. McGraw-Hill, New York, NY
- Mamou J, Coron A, Oelze ML, Saegusa-Beecroft E, Hata M, Lee P, Machi J, Yanagihara E, Laugier P, Feleppa EJ (2011) Three-dimensional high-frequency backscatter and envelope quantification of cancerous human lymph nodes. *Ultrasound Med Biol* 37(3):2055–2068
- Mamou J, Coron A, Oelze ML, Saegusa-Beecroft E, Hata M, Lee P, Machi J, Yanagihara E, Laugier P, Feleppa EJ (2010) Three-dimensional high-frequency spectral and envelope quantification of excised human lymph nodes. In: *IEEE ultrasonics symposium*, pp 604–607
- Martin-Fernandez M, Alberola-Lopez C (2007) Parameter estimation of the Homodyned K distribution based on signal to noise ratio. In: *IEEE ultrasound symposium*, pp 158–161
- Molthen RC, Narayanan VM, Shankar PM, Reid JM, Genis V, Vergara-Dominguez L (1993) Ultrasound echo evaluation by K-distribution. In: *IEEE ultrasonics symposium*, pp 957–960
- Molthen RC, Shankar PM, Reid JM (1995) Characterization of ultrasonic B-scans using non-Rayleigh statistics. *Ultrasound Med Biol* 21:161–170
- Nakagami M (1940) Study of the resultant amplitude of many vibrations whose phases and amplitudes are at random. *J Inst Elec Commun Engrs Japan* 24(202):17–26
- Nakagami M (1943) Statistical character of short-wave fading. *J Inst Elec Commun Engrs Japan* 27:145–150
- Nakagami M (1960) The m distribution: a general formula of intensity distribution in rapid fading. In: Hoffman WC (ed) *Statistical methods on radio wave propagation*. Pergamon Press, New York, pp 3–36
- Narayanan VM, Shankar PM, Reid JM (1994) Non-Rayleigh statistics of ultrasonic backscattered signals. *IEEE Trans Ultrason Ferroelectr Freq Control* 41(6):845–852
- Narayanan VM, Molthen RC, Shankar PM, Vergara L, Reid JM (1997) Studies on ultrasonic scattering from quasi-periodic structures. *IEEE Trans Ultrason Ferroelectr Freq Control* 44(1):114–124
- Nillesen MM, Lopata RGP, Gerrits IH, Kapusta L, Thussen JM, de Korte CL (2008) Modeling envelope statistics of blood and myocardium for segmentation of echocardiographic images. *Ultrasound Med Biol* 34(4):674–680
- Oelze ML, O'Brien WD Jr (2007) Quantitative ultrasound assessment of breast cancer using a multiparameter approach. In: *IEEE ultrasound symposium*, pp 981–984
- Oliver CJ (1993) Optimum texture estimators for SAR clutter. *J Phys D Appl Phys* 26(11):1824–1835
- Prager RW, Gee AH, Treece GM, Berman LH (2002) Analysis of speckle in ultrasound images using fractional order statistics and the homodyned K-distribution. *Ultrasonics* 40:133–137
- Prager RW, Gee AH, Treece GM, Berman LH (2003) Decompression and speckle detection for ultrasound images using the homodyned K-distribution. *Pattern Recogn Lett* 24(4–5):705–713
- Pratt JW, Edgeworth FY (1976) R. A. Fisher on the efficiency of maximum likelihood estimation, *Ann Stat* 4:501–514
- Raju BI, Srinivasan MA (2002) Statistics of envelope of high-frequency ultrasonic backscatter from human skin in vivo. *IEEE Trans Ultrason Ferroelectr Freq Contr* 49(7):871–882
- Rayleigh L (1880) On the resultant of a large number of vibrations of the same pitch and of arbitrary phase. *Philos Mag* 10:73
- Redner R (1981) Note on the consistency of the maximum likelihood estimate for nonidentifiable distributions. *Ann Stat* 9(1):225–228
- Redner RA, Walker HF (1984) Mixture densities, maximum likelihood and the EM algorithm. *SIAM Rev* 26(2):195–239
- Rice SO (1945) Mathematical analysis of random noise. *Bell Syst Techn J* 24:46–156
- Rice SO (1954) Mathematical analysis of random noise. In: Wax N (ed) *Selected papers on noise and stochastic processes*. Dover, New York, pp 133–294
- Roberts WJJ, Furui S (2000) Maximum likelihood estimation of K-distribution parameters via the expectation-maximization algorithm. *IEEE Trans Signal Process* 48(12):3303–3306
- Saha RK, Kolios MC (2011) Effects of cell spatial organization and size distribution on ultrasound backscattering. *IEEE Trans Ultrason Ferroelectr Freq Control* 58(10):2118–2131

- Shankar PM (1995) A model for ultrasonic scattering from tissues based on the K distribution. *Phys Med Biol* 40:1633–1649
- Shankar PM (2000) A general statistical model for ultrasonic backscattering from tissues. *IEEE Trans Ultrason Ferroelectr Freq Control* 47(3):727–736
- Shankar PM (2003) A compound scattering pdf for the ultrasonic echo envelope and its relationship to K and Nakagami distributions. *IEEE Trans Ultrason Ferroelectr Freq Contr* 50(3):339–343
- Shankar PM, Reid JM, Ortega H, Piccoli CW, Goldberg BB (1993) Use of non-Rayleigh statistics for the identification of tumors in ultrasonic B-scans of the breast. *IEEE Trans Med Imag* 12(4):687–692
- Shankar PM, Dumane VA, Reid JM, Genis V, Forsberg F, Piccoli CW, Goldberg BB (2001) Classification of ultrasonic B-mode images of breast masses using Nakagami distribution. *IEEE Trans Ultrason Ferroelectr Freq Control* 48(2):569–580
- Shankar PM, Forsberg F, Lown L (2003) Statistical modeling of atherosclerotic plaque in carotid B mode images—a feasibility study. *Ultrasound Med Biol* 29(9):1305–1309
- Talukdar KK, Lawding WD (1991) Estimation of the parameters of the Rice distribution. *J Acoust Soc Am* 89(3):1193–1197
- Tao Z, Beaty J, Jaffe CC, Tagare HD (2002) Gray level models for segmenting myocardium and blood in cardiac ultrasound images. In: IEEE international symposium on biomedical imaging, pp 265–268
- Tao Z, Tagare HD, Beaty JD (2006) Evaluation of four probability distribution models for speckle in clinical cardiac ultrasound images. *IEEE Trans Med Imag* 25(11):1483–1491
- Tsui P-H, Wang S-H, Huang C-C (2005) The effect of logarithmic compression on estimation of the Nakagami parameter for ultrasonic tissue characterization: a simulation study. *Phys Med Biol* 50(14):3235–3244
- Tsui P-H, Chang C-C (2007) Imaging local scatterer concentrations by the nakagami statistical model. *Ultrasound Med Biol* 33(4):608–619
- Tsui P-H, Wang S-H (2004) The effect of transducer characteristics on the estimation of Nakagami parameter as a function of scatterer concentration. *Ultrasound Med Biol* 30(10):1345–1353
- Tsui P-H, Yeh C-K, Chang C-C (2009a) Microvascular flow estimation by contrast-assisted ultrasound B-scan and statistical parametric images. *IEEE Trans Inf Technol Biomed* 13(3):360–369
- Tsui P-H, Yeh C-K, Chang C-C (2009b) Microvascular flow estimation by microbubble-assisted nakagami imaging. *Ultrasound Med Biol* 35(4):653–671
- Tsui P-H, Huang C-C, Chang C-C, Wang S-H, Shung K-K (2007) Feasibility study of using high-frequency ultrasonic Nakagami imaging for characterizing the cataract lens in vitro. *Phys Med Biol* 52(21):6413–6425
- Tsui P-H, Yeh C-K, Chang C-C, Liao Y-Y (2008a) Classification of breast masses by ultrasonic Nakagami imaging: a feasibility study. *Phys Med Biol* 53:6027–6044
- Tsui P-H, Yeh C-K, Chang C-C (2008b) Feasibility exploration of blood flow estimation by contrast-assisted Nakagami imaging. *Ultrason Imaging* 30(3):133–150
- Tsui P-H, Chang C-C, Ho M-C, Lee Y-H, Chen Y-S, Chang C-C, Huang N-E, Wu Z-H, Chang K-J (2009c) Use of Nakagami statistics and empirical mode decomposition for ultrasound tissue characterization by a nonfocused transducer. *Ultrasound Med Biol* 35(12):2055–2068
- Tsui P-H, Hsu C-W, Ho M-C, Chen Y-S, Lin J-J, Chang C-C, Chu C-C (2010a) Three-dimensional ultrasonic Nakagami imaging for tissue characterization. *Phys Med Biol* 55(19):5849–5866
- Tsui P-H, Liao Y-Y, Chang C-C, Kuo W-H, Chang K-J, Yeh C-K (2010b) Classification of benign and malignant breast tumors by 2-D analysis based on contour description and scatterer characterization. *IEEE Trans Med Imag* 29(2):513–522
- Tsui P-H, Yeh C-K, Liao Y-Y, Chang C-C, Kuo W-H, Chang K-J, Chen C-N (2010c) Ultrasonic Nakagami imaging: a strategy to visualize the scatterer properties of benign and malignant breast tumors. *Ultrasound Med Biol* 36(2):209–217
- Twersky V (1975) Transparency of pair-correlated random distributions of small scatterers with applications to the cornea. *J Opt Soc Am* 65(5):524–530
- Twersky V (1978) Acoustic bulk parameters in distributions of pair-correlated scatterers. *J Opt Soc Am* 64:1710–1719
- Twersky V (1987) Low-frequency scattering by correlated distributions of randomly oriented particles. *J Acoust Soc Am* 81(7):1609–1618
- Twersky V (1988) Low-frequency scattering by mixtures of correlated nonspherical particles. *J Acoust Soc Am* 84(1): 409–415
- Wagner RF, Smith SW, Sandrick JM, Lopez H (1983) Statistics of speckle in ultrasound B-scans. *IEEE Trans Sonics Ultras* 30(3):156–163
- Wagner RF, Insana MF, Brown DG (1987) Statistical properties of radio-frequency and envelope-detected signals with applications to medical ultrasound. *J Opt Soc Am A* 4(5):910–922
- Weng L, Reid J, Shankar P, Soetanto K (1990) Non-uniform ultrasound speckle phase distribution applied to scatterer spacing estimation. In: IEEE ultrasonics symposium, pp 1593–1596
- Weng L, Reid JM, Shankar PM, Soetanto K, Lu X-M (1992) Nonuniform phase distribution in ultrasound speckle analysis—part I: background and experimental demonstration. *IEEE Trans Ultrason Ferroelectr Freq Control* 39(3):352–359
- Yamaguchi T, Zenbutsu S, Igarashi Y, Kamiyama N, Mamou J, Hachiya H (2011) Echo envelope analysis method for quantifying heterogeneity of scatterer distribution for tissue characterization of liver fibrosis. In: IEEE ultrasonics symposium, pp 1412–1415



Information Entropy and Its Applications

8

Po-Hsiang Tsui

Abstract

Ultrasound is a first-line diagnostic tool for imaging many disease states. A number of statistical distributions have been proposed to describe ultrasound backscattering measured from tissues having different disease states. As an example, in this chapter we use non-alcoholic fatty liver disease (NAFLD), which is a critical health issue on a global scale, to demonstrate the capabilities of ultrasound to diagnose disease. Ultrasound interaction with the liver is typically characterized by scattering, which is quantified for the purpose of determining the degree of liver steatosis and fibrosis. Information entropy provides an insight into signal uncertainty. This concept allows for the analysis of backscattered statistics without considering the distribution of data or the statistical properties of ultrasound signals. In this chapter, we examined the background of NAFLD and the sources of scattering in the liver. The fundamentals of information entropy and an algorithmic scheme for ultrasound entropy imaging are then presented. Lastly, some examples of using ultrasound entropy imaging to grade hepatic steatosis and evaluate the risk

of liver fibrosis in patients with significant hepatic steatosis are presented to illustrate future opportunities for clinical use.

Keywords

Information entropy · Fatty liver · Liver fibrosis · Nonalcoholic fatty liver disease · Backscattering · Signal uncertainty

8.1 Introduction

Nonalcoholic fatty liver disease (NAFLD) is a disorder characterized by excessive and abnormal intracellular triglyceride accumulation within hepatocytes. In terms of histology, NAFLD refers to macrovesicular steatosis and is associated with nonalcoholic steatohepatitis, fibrosis, cirrhosis, and hepatocellular carcinoma (Yu and Keeffe 2002; Loomba et al. 2012). Globally, the incidence and prevalence of NAFLD are rapidly increasing. NAFLD is prevalent worldwide at the rate of approximately 25%, ranging from 13% in Africa to 42% in southeast Asia (Huang et al. 2021). Children with obesity are also more likely to develop NAFLD and its incidence has increased rapidly over the past decade; the estimated prevalence of NAFLD in children with obesity is 26% (Shapiro et al.

P.-H. Tsui (✉)

Department of Medical Imaging and Radiological Sciences, Chang Gung University, Taoyuan City, Taiwan
e-mail: tsuiph@mail.cgu.edu.tw

2021). Additionally, research has linked NAFLD to metabolic syndrome, which is a cluster of metabolic disorders that are associated with diabetes and heart disease (Yki-Järvinen 2014). As a consequence, NAFLD may be considered a critical health problem, whose early detection, follow-up, and management can prevent the progression of advanced liver diseases and metabolic diseases.

Ultrasound imaging has been widely used as a first-line diagnostic modality because of its advantages in terms of non-ionizing radiation, real-time capabilities, and the fact that it can be applied in a variety of different clinical settings. NAFLD should be diagnosed using ultrasound, according to the guidelines of the European Association for the Study of the Liver (Pandyarajan et al. 2019). Physicians often use B-mode ultrasound imaging features to evaluate liver diseases. For example, the surface of the liver (smooth, undulated, or irregular), the parenchyma of the liver (homogenous, heterogeneous, or coarse), the hepatic vessels (smooth, obscure, or narrow), and the spleen size (20 cm^2 or $>20\text{ cm}^2$) are the factors that correlate well with the level of fibrosis in the liver (Lin et al. 1993; Hung et al. 2003; Choong et al. 2012). The liver-diaphragm differentiation in the echo amplitude, the penetration of ultrasound waves, and the visibility of hepatic vessels in B-mode images are associated with the degree of fatty liver (Chan et al. 2004; Gerstenmaier and Gibson 2014). Notably, the features and textures of B-mode images may vary depending on the operator and can be affected by certain system settings (e.g., gain, time gain compensation, and signal and image processing). Interpretations may differ among physicians. A quantitative computational analysis of raw images could therefore contribute to the evaluation of liver diseases in a more objective manner.

In this chapter, we discussed the information entropy and its applications to the ultrasound diagnosis of NAFLD. Information entropy is a new concept in quantitative ultrasound that has significant potential for tissue characterization and liver disease diagnosis. We begin by introducing the liver and explaining how the ultrasonic waves interact with the microstructures within the liver to produce ultrasound backscattered signals. Next,

we discuss the advantages of information entropy over conventional statistical distributions in the quantitative analysis of backscattered signals. Finally, some clinical examples are presented to demonstrate the value of information entropy in parametric imaging of NAFLD, including steatosis and fibrosis.

8.2 The Liver and Its Scattering Sources

An individual's liver is the largest gland in the body; it is found in the upper right side of the abdomen, just beneath the diaphragm, and above the stomach, right kidney, and intestines; it comprises 70–85% parenchymal hepatocytes (Zhou et al. 2016). Parenchyma of the liver can typically be viewed as a three-dimensional structure with a large number of scatterers. When an ultrasound wave propagates through the liver, backscattered echo signals from acoustic scatterers are received by the transducer to produce an image. In general, diffuse scatterers may be defined as objects that are smaller than the wavelength such that their amplitudes and phases are insensitive to their orientation (Szabo 2004). A hepatocyte is a cell of the liver's main parenchymal tissue; it is approximately cubical, with side lengths of 20–30 μm and volume of $3.4 \times 10^{-6}\text{ mm}^3$ (Lodish et al. 2000), and thus liver cells behave as diffuse scatterers that contribute to ultrasound scattering. There are also many small vessels with diameters of only a few tenths of a millimeter that are potentially diffuse scattering sources to form ultrasonic speckle (Shung and Thieme 1993). Several research studies have demonstrated that the portal triads serve as a source of ultrasound coherent scattering in the liver (Fellingham and Sommer 1984; Insana et al. 1986; Garra et al. 1989; Rubert and Varghese 2013). There are three to six portal triads per liver lobule, which is a polygonal mass of tissue composed of a central vein surrounded by plates and hepatocytes. The hexagonal diameter of liver lobules is approximately 1–1.5 mm, and the lobule length is 1.5–2 mm (Pike and Sabatier 2001). The portal triad located at the corners of the lobule contains a bile duct, a portal venule, a portal arteriole, and lymphatic

vessels. All of these structures are surrounded by a sheath of connective tissue. The connective tissue network (Nicholas 1982), veins, arteries, ducts (Pike and Sabatier 2001), and hepatocytes (Fei and Shung 1985; Shung and Thieme 1993) are able to contribute ultrasound backscattered signals. Therefore, the liver lobule is not only a structural and functional component of the liver (Rappaport 1958; Young et al. 2006) but may also be considered as the effective scattering unit (Mamou and Oelze 2013) that simultaneously involves diffuse and coherent scatterers for interpreting the interaction between ultrasound wave and the liver tissue.

8.3 Statistical Analysis of Ultrasound Backscattering

An ultrasound wave will be scattered if its wavelength matches or exceeds the dimensions of scatterers in biological tissues. An ultrasonic backscattered echo from tissues can be expressed as the sum of the phasors of each scatterer within the resolution cell. In the case where scatterers in tissue have random positions and random scattering cross-sections, both the amplitude and phase of the echo returned by each scatterer are random. In other words, the ultrasonic backscattered signals can be considered a stochastic process, resulting in small dots or granular patterns in the ultrasonic B-mode image, called speckle. Speckle is a random, deterministic, and interference texture feature in an image produced by a medium that contains many sub-resolution scatterers. Speckle features were regarded as potential sources of physiological data related to the characteristics of biological tissues. As a result of the random nature of ultrasonic backscattering, many researchers use mathematically statistical distributions to model the probability density function (PDF) of the echoes. Further quantitative assessment of the properties of tissues can be performed by estimating the associated parameters of the applied statistical model from the ultrasonic envelope of backscattered signals.

The goals all lie in the additional acquisition of valuable information relating to the number, size, shape, spacing, concentration, and scattering cross-section of scatterers constituting the tissues for assisting in clinical diagnosis.

The Rayleigh distribution was the first model used to describe the envelope statistics of ultrasound signals (Burckhardt 1978). Backscattered envelopes follow the Rayleigh distribution when the resolution cell of the ultrasound transducer contains numerous randomly distributed scatterers (≥ 10 scatterers) (Tuthill et al. 1988). The scatterers in most biological tissues are arranged in a variety of ways. Therefore, some non-Rayleigh distributions, such as Rician (Wagner et al. 1987), K (Weng et al. 1991), generalized K (Jakeman and Tough 1987), homodyned K (HK) (Dutt and Greenleaf 1994), and Nakagami distribution (Shankar 2000) have been applied to encompass different scattering conditions. The Nakagami distribution, which has been proposed as a useful approximation of backscatter statistics, is the most commonly adopted statistical model for tissue characterization because of its simplicity and low computational complexity (Mamou and Oelze 2013). Several studies have investigated ultrasound parametric imaging based on the Nakagami parameter for hepatic steatosis assessment and have found that the Nakagami parameter is associated with the stage of fatty liver disease in rats (Ho et al. 2013) and humans (Wan et al. 2015). Apart from the Nakagami distribution, the homodyned K (HK) distribution has also been extensively studied for ultrasound tissue characterization. The HK distribution adequately describes the backscattering characteristics of biological tissues and has been recommended as a general model for ultrasound backscattering (Destrempe and Cloutier 2010). Interestingly, HK parameters can still be used to characterize tissues when the region of interest under investigation is a fully developed speckle, as in the case of concentrated media (Cristea et al. 2015; Cristea et al. 2020). This indicates that HK parameters can detect hepatic steatosis and offer additional information to aid in the evaluation of severe fatty liver disease. It has been shown that HK imaging allows grading hepatic steatosis in rats (Fang et al. 2018; Zhou

et al. 2020). HK imaging provided improved diagnostic performance for the early detection of liver fibrosis in conjunction with moderate to severe liver steatosis as well (Tsai et al. 2021). For patients with significant hepatic steatosis, ultrasound HK imaging is recommended as a strategy to assess fibrosis risk.

8.4 Fundamentals of Information Entropy

With respect to the analysis of ultrasound backscatter from tissues, information entropy is more flexible than statistical distribution models. In using physically based statistical models to fit the backscatter envelopes, one constraint is that the distribution of the backscatter envelope data must agree with the distribution used. In certain circumstances, this requirement may not be met because adjusting the settings of an ultrasound system or utilizing nonlinear signal processing techniques (e.g., logarithmic compression) may alter the statistical distribution of raw data. It is also possible to obtain different envelope statistics by using different demodulation methods (Tuthill et al. 1988). Even when operators use the same system configuration and demodulation method, obtaining output signals that match a specific statistical distribution can pose a challenge because different manufacturers utilize different hardware and software techniques to process the output data. Particularly, not all system manufacturers release raw image data to users. A more flexible parameter that is independent of any statistical model must be applied to backscattering analysis in order to address this limitation. Recall that ultrasound backscattered signals are the source of information associated with scatterer properties of tissues. Information, which is not a physical entity but an abstract concept, presented a difficult challenge for quantification until Shannon introduced entropy as a fundamental measure of information (Shannon 1948). Information is essentially uncertain, not deterministic (Yeung 2002), and therefore an information source is naturally

modeled as a random variable or a random process, and probability is employed to develop the theory of information. Considering a variety of possibilities for determining information uncertainty or the degree of disorder within a system, several types of entropy have been defined (Borowska 2015) (see Fig. 8.1). Next, we introduce two commonly encountered entropy forms: Shannon and sample entropies, which can be used to describe the statistical properties of backscattered signals in terms of PDF patterns and time-series patterns, respectively.

Hughes first proposed the use of Shannon entropy for analyzing ultrasound signals, showing that entropy could be used to quantify changes in microstructures of scattering media (Hughes 1992, 1993, 1994; Hughes et al. 2007, 2013). In ultrasound imaging, the Shannon entropy (denoted by ShanEn) of backscattered radiofrequency (RF) signals $y = f(t)$ is defined as the negative of the logarithm of the backscattered probability distribution, and it can be expressed as follows:

$$\text{ShanEn} \equiv - \int_{y_{\min}}^{y_{\max}} w(y) \log_2 [w(y)] dy, \quad (8.1)$$

where t represents time, y means the amplitude of $f(t)$, $w(y)$ means the PDF of $f(t)$, and y_{\min} and y_{\max} represent the minimum and maximum values of $f(t)$, respectively. In practice, the Shannon entropy is obtained using digitized versions of the underlying continuous waveform in a discrete form of Eq. (8.1).

Before performing Shannon entropy estimations, $w(y)$, the PDF of raw RF data must be obtained. Ideally, $w(y)$ is obtained from the continuous waveform of backscattered RF signals, which is not accurately known in practice because of a finite sampling rate (Hughes 1993). Therefore, an efficient and robust scheme is required for reconstructing $w(y)$ from a digital waveform. Hughes proposed an algorithmic scheme based on Fourier analysis for establishing the PDF of RF data, which can be expressed as follows (Hughes 1993):

$$w(y) = \sum_{-\infty}^{\infty} a_n e^{i\pi n(y-\mu)/\lambda}, \quad (8.2)$$

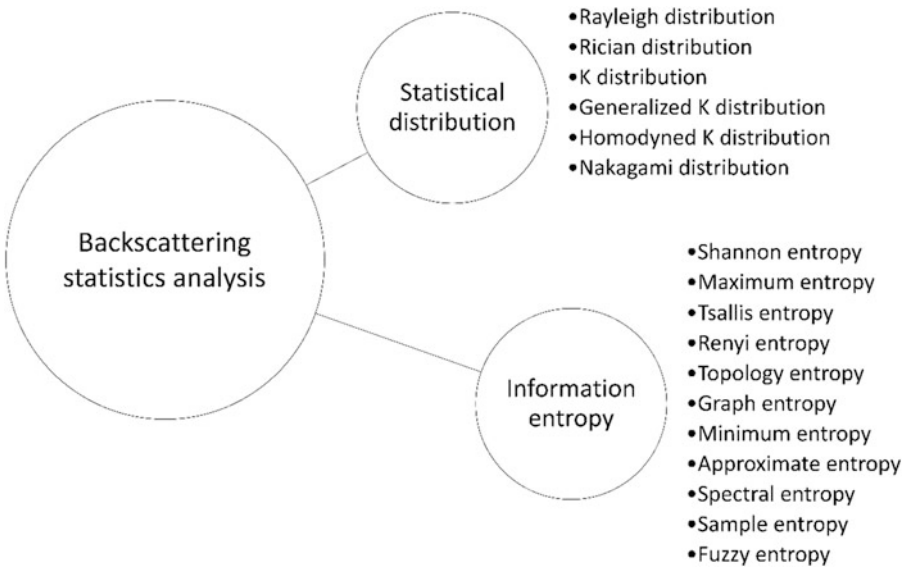


Fig. 8.1 Due to the random nature of ultrasound backscattering, statistical distributions and information entropies can be used to describe the properties of backscattered signals for tissue characterization. Infor-

mation entropy is not a model-based approach but rather a mathematical formulation of signal uncertainty or complexity

where $\lambda = (y_{\max} - y_{\min})/2$, $\mu = (y_{\max} + y_{\min})/2$, and a_n represents the Fourier coefficients calculated using Eq. (8.3):

$$a_n = \frac{e^{i\pi n \mu / \lambda}}{(y_{\max} - y_{\min})} \int_a^b e^{-i\pi n f(t) / \lambda} dt \quad (8.3)$$

where $[a, b]$ is the interval of $f(t)$. Different ultrasound systems may produce different dynamic ranges of RF signals (i.e., $y_{\max} - y_{\min}$); therefore, signal normalization could be performed to limit the variance of signal amplitudes between -1 and 1 . Moreover, Eq. (8.2) illustrates that to approximate the infinite sum, a finite number of Fourier terms must be introduced on the bounds of the summation (Hughes 1993). According to the mentioned considerations, the approximations of Eqs. (8.2) and (8.3) can be expressed as follows:

$$w(y) = \sum_{n=-N_{\text{co}}}^{N_{\text{co}}} a_n e^{i\pi n y}, \quad (8.4)$$

and

$$a_n = \frac{1}{2} \int_a^b e^{-i\pi n f(t)} dt. \quad (8.5)$$

According to Eq. (8.4), two parameters affect the reconstruction of $w(y)$, including N_{co} (the number of terms in the Fourier series is determined by $2N_{\text{co}} + 1$) and Δy (i.e., the interval between discrete sample points in the reconstructed $w(y)$). To reduce the computational complexity of reconstructing the PDF of ultrasound signals, the statistical histogram might be used as an alternative method, which would increase the practical applicability of Shannon entropy (Smolikova et al. 2004; Zhou et al. 2014). Entropy measures the degree of uncertainty associated with information content. The minimum Shannon entropy is obtained when all the amplitude values are equal in the backscatter signals; it is maximized when every value of amplitude occurs exactly once. The Shannon entropy also reflects the physical

meaning of backscattered statistics because it is a function of the probability density and correlates with the statistical distribution parameters (Tsui 2015). Essentially, entropy is a measure of signal uncertainty (a non-model-based statistical parameter); the estimation of entropy does not require the backscattered data to follow a specific distribution and the estimation can be performed using any type of backscattered data (Tsui et al. 2017). In the analysis of ultrasound backscattering, information entropy has a high potential for application, which gives the opportunity to develop more flexible methods in practice.

Shannon entropy has some limitations. The Shannon entropy measures the average amount of information contained in a message (i.e., backscattered signals). Standard definitions of Shannon entropy provide an objective measure of information since it is determined by the PDF of the message and is not related to the values of the symbols within the message (i.e., amplitude). When Shannon defined entropy as a measure of uncertainty in information, an objective consideration based on probability was indeed a primary consideration. Nevertheless, this does not mean that the symbols in the message are inadequate for interpreting information. The Shannon entropy may lose some information, resulting in inferior performance in information analysis (Nawrockia and Harding 1986; Yang et al. 2005; Khan and Bhuiyan 2014). The symbols in the message or some subjective factors may play a critical role in quantifying information. In light of this, a previous study proposed a highly flexible weighted entropy, which is an indication of the amount of information contained within a probabilistic experiment in which elementary events are characterized both by their objective probabilities and some qualitative (objective or subjective) weights (Guas 1971). In addition, Shannon entropy does not take into account the time-series causality of ultrasound backscattered signals. It is possible for different scattering microstructures to produce the same probability distribution, resulting in the ambiguity of physical meaning. As opposed to Shannon and other PDF-based entropies, approximate entropy and sample

entropy provide computational solutions for entropic measures of finite time series; sample entropy is a data-length independent entropy and offers better computation consistency during the determination of information regularity based on patterns in the data (Richman and Moorman 2000).

To measure the irregularity of a unidimensional series, the sample entropy is defined as the negative natural logarithm of the probability that a subseries will remain similar when its data length increases, in which self-matches are not included (Richman and Moorman 2000). We assume time-series data of length N with a constant time interval τ for an ultrasound backscattered RF signal, as given by

$$Y = \{y_1, y_2, y_3, \dots, y_N\} \quad (8.6)$$

where y_i are the discrete random variables representing the backscattered signals. Template vectors (i.e., subseries) with length m (the dimension parameter) are

$$Y_m(i) = \{y_i, y_{i+1}, y_{i+2}, \dots, y_{i+m-1}\}, \quad (8.7)$$

and their distance function (based on the Chebychev distance) is

$$d[Y_m(i), Y_m(j)], i \neq j. \quad (8.8)$$

The sample entropy (denoted by SampEn) is then defined as

$$\text{SampEn}(m, r, N) = -\ln \left(\frac{A}{B} \right), \quad (8.9)$$

where r is the tolerance value, A represents the number of template vector pairs for which $d[Y_{m+1}(i), Y_{m+1}(j)] < r$, and B is the number of template vector pairs for which $d[Y_m(i), Y_m(j)] < r$. The tolerance value r is a percentage multiplied by the standard deviation of the original sequence; thus, the time series should be normalized before analysis (Delgado-Bonal and Marshak 2019). For signals with highly periodic patterns, sample entropy approaches zero, whereas it increases for

irregular signals (Delgado-Bonal and Marshak 2019; Silva et al. 2016). In the following section, we will discuss an algorithmic scheme for ultrasound entropy parametric imaging, which allows for quantification and visualization of the uncertainty associated with backscattered signals.

8.5 A Basic Scheme for Ultrasound Entropy Imaging

Ultrasound parametric imaging is a useful technique for characterizing tissues with quantitative parameters in a visual manner. A sliding window processing is a typical algorithm used to produce ultrasound parametric images corresponding to B-scans using ultrasound data that may be beamformed RF signals, uncompressed envelopes, or log-compressed envelopes when information entropy is estimated. A combination of parametric imaging and commercial scanners can fulfill clinical screening, observation, display of information, and quantitative analysis through visualization of quantitative parameters. An ultrasound entropic parametric image is typically constructed through the following steps: (i) A square window is generated within the image data to acquire local data for determining the PDF and calculating the entropy value, which is a new pixel in the window location; (ii) the window is moved across the entire range of image data in steps of the number of pixels corresponding to a window overlap ratio (WOR), and step 1 is repeated to obtain an entropy parametric map; (iii) since the parametric map is smaller than the original data because of the sliding window processing, the parametric map may be further resized using two-dimensionally linear interpolation in order to have the same data size as the original data; (iv) a pseudocolor is employed to display the entropy map, which is superimposed onto the B-mode image to reveal morphological information and signal uncertainty of speckle patterns; and (v) the final entropy image superimposed onto the B-scan is converted into a fan-shaped image according to the geometry of the curve probe

(for liver and abdominal examinations). A basic scheme of ultrasound parametric imaging using Shannon and sample entropies is illustrated in Fig. 8.2.

Choosing an appropriate sliding window size for the construction of a parametric image is necessary for reliable parameter estimation and satisfactory resolution. Generally, a stable estimation of a parameter requires a sufficient number of data points and a finite length of the signal to describe the trend in the waveform. The signal waveform can be reconstructed without the effect of aliasing as soon as the sampling rate of the imaging system satisfies the Nyquist theory. In this condition, the key to a stable estimation of the parameter is the practical length of the signal, not the number of data points or the length of the lateral sides of the window (Tsui and Chang 2007; Zhang et al. 2012; Wan et al. 2015). The image data obtained from the scanner under a curved probe geometry will not be uniformly sampled along the lateral axis. The distance between scan lines increases as the distance from the transducer increases. In this case, however, it does not affect the axial sampling, which is determined by the analog-to-digital converter in the imaging system. Because information entropy is not a model-based parameter, the issue of stability in estimating parameters may be ignored, and this is why information entropy enables using a small window with a side length corresponding to one pulse length of the transducer for implementing high-resolution ultrasound parametric imaging (Tsui et al. 2017). The WOR is another consideration when constructing parametric images using the sliding window. A low WOR results in a low line density in a parametric image. As the line density decreases, the spatial resolution of an image decreases, making spatial information insufficient to describe the region of interest (ROI). When the WOR is high, the line density is high. Nevertheless, because of the large amount of data to be processed, computational efficiency and speed may be affected. In order to achieve a balance between the image resolution and the computation time, $WOR = 50\%$ has been recommended (Tsui et al. 2017).

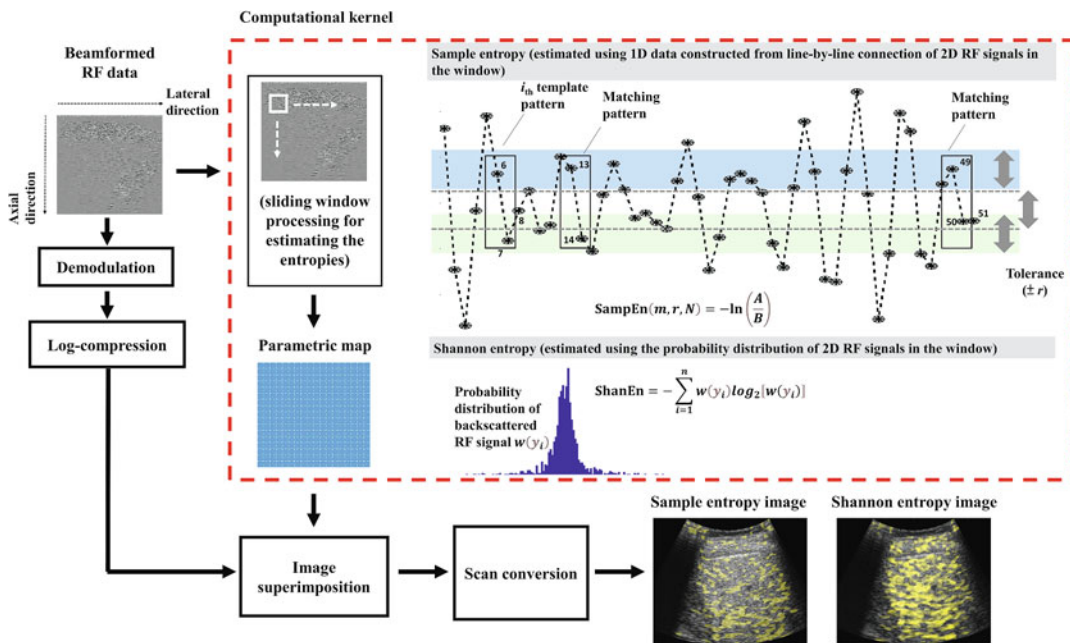


Fig. 8.2 Algorithmic scheme for ultrasound parametric imaging using sample and Shannon entropies. This illustration presents an example of the sample entropy calculation process with the dimension $m = 2$. The data points

x_6 and x_7 are used as the i th template pattern ($i = 6$). The 2-point sequences x_{13} , x_{14} and x_{49} , x_{50} are matched, and x_{49} , x_{50} , x_{51} is a 3-point matched sequence. In this case, SampEn = $-\ln(1/2)$

8.6 Clinical Examples of Ultrasound Entropy Imaging in Characterizing NAFLD

An animal experiment (Fang et al. 2018) and clinical validation (Tsui and Wan 2016; Zhou et al. 2018; Lin et al. 2018; Chen et al. 2020; Chang et al. 2021; Chan et al. 2021) have been reported to reveal the usefulness of ultrasound entropy parametric imaging in characterizing NAFLD. We present a few representative clinical examples in this section to illustrate the use of Shannon and sample entropies in ultrasound parametric imaging of hepatic steatosis and liver fibrosis. We also discuss the physical interpretations and biological significance of entropy in imaging the liver with steatosis and fibrosis.

Data used for this chapter were collected from clinical measurements conducted at Chang Gung Memorial Hospital in Taiwan. This study was approved by the Institutional Review Board (IRB), all participants signed informed consent

forms, and experimental methods followed approved guidelines. Liver donors were enrolled in Group I ($n = 72$). Patients scheduled to undergo liver biopsy due to confirmed chronic hepatitis B infection or partial liver resection were enrolled in Groups II ($n = 286$). The hepatic fat fraction (HFF) of the liver (right lobe) in each liver donor in Group I was measured through hydrogen-1 (^1H) proton MR spectroscopy (i.e., ^1H -MRS) (GE Signa HDXT, Waukesha, WI, USA). The HFF was defined as (fat mass)/(fat mass + water mass) and expressed as a percentage. For patients in Group II, we obtained specimens from the right liver lobe by adopting an intercostal approach and sent them to the Department of Pathology for histological examination. Hepatic steatosis was graded according to the percentage of involved hepatocytes: normal (<5%), mild (5–33%), moderate (33–66%), and severe (>66%). Considering that hepatic steatosis is a risk factor for nonalcoholic steatohepatitis, which causes liver fibrosis (Brunt et al. 1999), additional 65

patients histologically graded as having moderate or severe hepatic steatosis were included in Group III to undergo METAVIR scoring; these scores were classified as F0, no fibrosis; F1, portal fibrosis with no septa; F2, portal fibrosis with few septa; F3, bridging fibrosis with many septa; and F4, cirrhosis (nodular stage).

Each subject underwent standard-care ultrasound examinations of the liver. According to the Couinaud model of hepatic anatomy, the liver consists of eight segments (Skandalakis et al. 2004) that have their own vascular inflow, outflow, and biliary drainage (Couinaud 1999). The left, middle, and right hepatic veins are typically used as the margins to divide the liver grossly into the left (segments I–IV) and right (segments V–VIII) lobes (Pauli et al. 2012). Consequently, different lobes and segments have various characteristics and structures that may affect the measurement of backscattered signals. Intercostal scanning has been recommended for imaging the liver parenchyma of the right lobe because relatively thin subcutaneous tissue and minimal intestinal gas are encountered; intercostal scanning also provides technicians with high imaging stability because the rib serves as a suitable support that enables the image quality to be unaffected by compression force during scanning (Lin et al. 2019). When scanning, major vessels, structures, and acoustic shadowing artifacts should be excluded from the image (Tsui et al. 2016). A clinical ultrasound scanner (Model 3000, Terason, Burlington, MA, USA) equipped with a convex array

transducer with a 3-MHz central frequency (Model 5C2A, Terason) was used. The system-default time-gain compensation curve in terms of an exponentially increasing function constructed using an attenuation coefficient of 0.3 dB/MHz·cm (a conservative assumption generally used in commercial ultrasound systems) was used to reduce the acoustic attenuation effect. The pulse length obtained from the pulse-echo measurement of the transducer was approximately 2.3 mm, and the focus and depth for imaging were set at 4 and 8 cm, respectively. For each scan, the imaging data were saved in ULT file format. No apodization, filtering, or any kind of signal processing were used during ultrasound transmission and data acquisition. The software kit provided by Terason was then used to convert the image data into raw beamformed RF signals (sampling rate: 12 MHz; 128 scan lines) for offline ultrasound entropy imaging using the sliding window processing. The ROI on the B-scan of the liver parenchyma were manually outlined by an experienced radiologist, and the pixel values in both Shannon and sample entropy images corresponding to the ROI were used to calculate the average entropy values for quantitative analysis. A typical ultrasound image of the liver obtained using intercostal scanning is shown in Fig. 8.3.

A typical Shannon entropy image and sample entropy image of a healthy liver, hepatic steatosis, and liver fibrosis with coexisting steatosis are shown in Fig. 8.4. When liver steatosis is present, Shannon entropy images appear brighter and

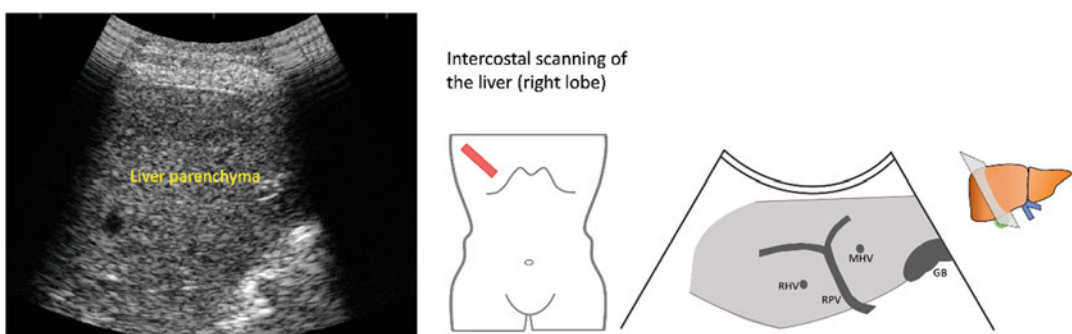


Fig. 8.3 A typical ultrasound B-mode (left) image acquired by using the intercostal scanning approach (right). The abbreviations: *MHV* middle hepatic vein, *GB* gall bladder, *RPV* right portal vein, *RHV* right hepatic vein

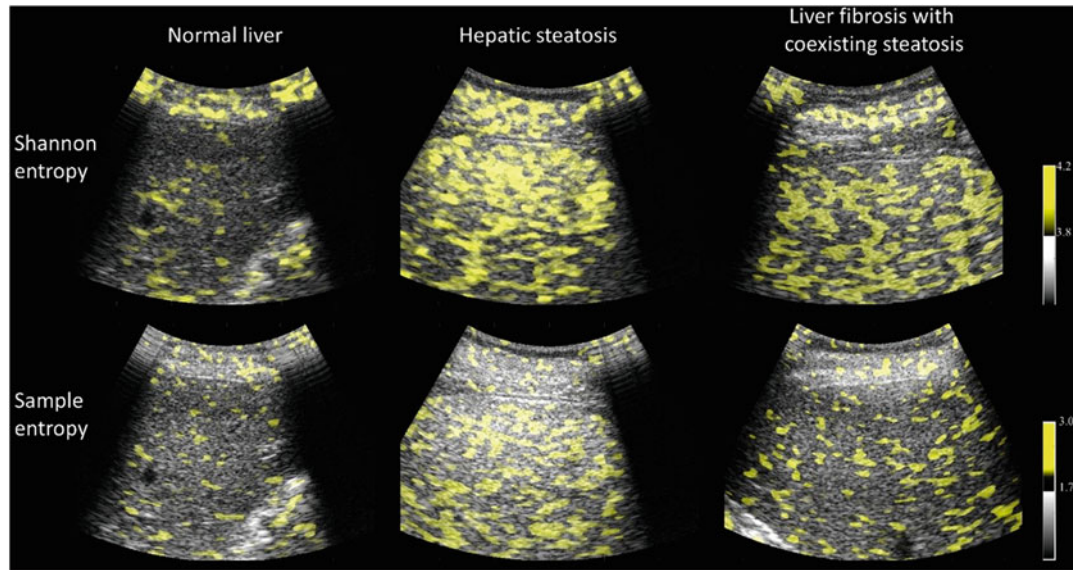


Fig. 8.4 Examples of Shannon and sample entropy images showing a normal liver, liver steatosis, and liver fibrosis with coexisting steatosis

more evenly distributed than when normal liver tissue exists; similar findings were observed in sample entropy images. The brightness of ultrasound entropy images decreased when fatty infiltration accompanied liver fibrosis. According to the previous study (Chan et al. 2021), the Pearson correlation coefficient r_p value of the sample entropy was proportional to the logarithmic transform of the HFF ($r_p = 0.70$; $p < 0.05$), as was the r_p value of the Shannon entropy ($r_p = 0.60$; $p < 0.05$). From normal to severe grades of hepatic steatosis, the median and interquartile range (IQR) of the sample entropy increased from 1.75 (IQR: 0.07) to 1.87 (IQR: 0.06) (the Spearman correlation coefficient $r_s = 0.73$; $p < 0.05$), and those of the Shannon entropy increased from 3.69 (IQR: 0.10) to 3.81 (IQR: 0.06) ($r_s = 0.67$; $p < 0.05$). The areas under the receiver operating characteristic (ROC) curves of (SampEn, ShanEN) for classifying hepatic steatosis as \geq mild, \geq moderate, and \geq severe were (0.86, 0.80), (0.90, 0.89), and (0.88, 0.87), respectively. The median sample entropy decreased from 2.07 (IQR: 0.31) to 1.85 (IQR: 0.06) as the METAVIR score increased from F0 to F4 ($r_s = -0.44$; $p < 0.05$). The Shannon entropy values were widely distributed and had

no significant association with the METAVIR score ($r_s = -0.03$; $p > 0.05$). The areas under the ROC curves of (SampEn, ShanEN) for classifying liver fibrosis as \geq F1, \geq F2, \geq F3, and \geq F4 were (0.87, 0.59), (0.77, 0.48), (0.71, 0.48), and (0.68, 0.55), respectively. The results suggest that Shannon and sample entropies are able to grade the hepatic steatosis. Sample entropy outperformed Shannon entropy for the detection of liver fibrosis in patients with significant hepatic steatosis.

The underlying mechanism is illustrated in Fig. 8.5. The entropy values increased with the progression of hepatic steatosis, representing an increase in irregularities or uncertainties in ultrasound backscattered RF signals, which were specifically interpreted by changes in the signal waveform and PDF. In a fat-infiltrated liver, a single large fat droplet in a hepatocyte can push the nucleus to the periphery (i.e., macrovesicular steatosis) (Tandra et al. 2011). The single large fat droplet in macrovesicular steatosis is believed to form from the fusion of multiple small- to medium-sized fat droplets (Martin and Parton 2006). These fat-infiltrated hepatocytes are newly added acoustic scatterers with not only increased density but also increased scattering

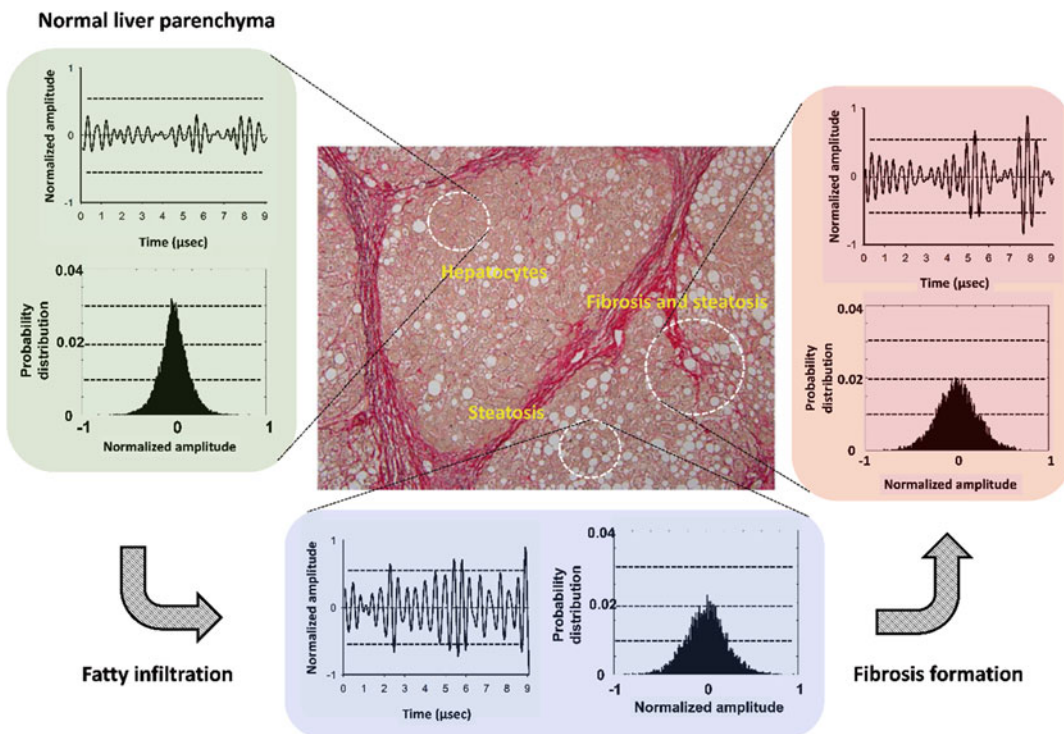


Fig. 8.5 The RF data amplitude increases with increasing steatosis grade when the liver changes from normal to hepatic steatosis, leading to an increase in the PDF width. The echo amplitude of RF data for the steatosis case with liver fibrosis exhibits a higher degree of variations in

signal amplitude; however, the signal PDF is not affected significantly. In this case, the Shannon entropy is not as effective as the sample entropy in the assessment of liver fibrosis in patients with hepatic steatosis

cross-section areas to strengthen constructive wave interference, increasing ultrasound signal amplitudes, broadening PDFs, and elevating entropies. However, we should note that hepatic steatosis and liver fibrosis produce opposite effects on backscattered statistics, especially hepatic steatosis typically coexists with liver fibrosis according to clinical experiences. Fibrous structures (including cirrhotic nodules) existing in the liver parenchyma with hepatic steatosis make the tissue properties complex, resulting in a relatively high degree of variance in the scattering cross-sections of the scatterers (Tsai et al. 2021). Thus, such an inhomogeneity of tissue tends to result in destructive wave interference, variations in the signal waveform, and narrow PDFs for the time-domain signals (Tsui et al. 2015), reducing the informational

complexity corresponding to a decrease in entropy.

It is noteworthy that conventional Shannon entropy was not associated with liver fibrosis severity in patients with liver steatosis; comparatively, the sample entropy was sensitive to the detection of liver fibrosis. This implies a common problem with PDF-based entropies in that the probability distributions of ultrasound RF signals may exhibit similarly in different scattering microstructures, causing physical ambiguity in interpreting the fact that ultrasound backscattering occurs. For example, a tissue with few scatterers or a homogeneous medium with strong scatterers can cause variation in the scattering cross-section, which may result in the same type of backscattering statistics (Shankar 2000). In addition, because fibrous structures in the liver are acoustically weaker scatterers than fatty droplets, the forma-

tion of backscattered signals is dominated by fatty droplets. In these circumstances, changes in the PDF of the backscattered signals caused by liver fibrosis may not be evident, causing the Shannon entropy and other PDF-based entropies to exhibit information-mixing problems which would inhibit the detection of liver fibrosis. In contrast, sample entropy is an adaptive method used to measure the irregularity of raw time-series data without too much information mixing or loss caused by the transformation of the signal into a probability distribution. Furthermore, in this chapter, sample entropy was calculated directly using RF signals, which are generated as a result of ultrasound interaction with liver tissue; therefore, the physical interpretations of sample entropy imaging may be more relevant to altered microstructures to some degree. Despite the fact that steatosis and fibrosis could coexist in the liver, the time-domain RF signal exhibited a greater ability to pick up changes in scatterer properties, which were not reflected in the PDF. It is likely that these advantages account for the superior performance of sample entropy over Shannon entropy in grading early hepatic steatosis and detection of liver fibrosis in patients with significant hepatic steatosis.

Besides histological validations of information entropy, it has also been shown that information entropy is strongly associated with biologically metabolic information. NAFLD is a hepatic manifestation of metabolic syndrome (MetS). For this reason, a new-generation ultrasound biosignature of NAFLD should include the ability to describe MetS risk in addition to being associated with the histological findings. The entropy value appears to be associated with metabolic indices, as shown in a previous study (Lin et al. 2018), indicating that even after adjusting for confounding factors, ultrasound entropy imaging provided a more significant link to MetS risk. Information entropy has also been demonstrated to be a potential imaging biomarker during first-line community screening of hepatic steatosis and insulin resistance (Chang et al. 2021). On the other hand, deep learning algorithms and pretrained models have become commonly used in the assessment of hepatic steatosis with the advancement of

artificial intelligence. Interestingly, preliminary results showed that ultrasound entropy imaging was more effective than deep learning based on VGG models for grading moderate to severe liver steatosis (Chen et al. 2020). Currently, it is difficult to determine whether information entropy is superior to deep learning in NAFLD examinations. It is clear that ultrasound entropy imaging and deep learning have different theoretical foundations and require different considerations in practice. In the former, physical descriptions and mathematical computations of backscattered signals are used to establish a relationship between the entropy and the properties of scatterers, while in the latter, pretrained CNNs are used for feature extraction and classification. However, we recommend physics-based information entropy for ultrasound diagnosis of NAFLD to improve not only the accuracy of grading but also the accuracy of clinical interpretations. The other consideration is that the use of information entropy or another rule-based method does not require a very large volume of data for training, validation, and testing. If necessary, deep learning could be an additional solution to compensate for possible deficiencies of ultrasound entropy imaging. A software algorithm for ultrasound entropy imaging is also totally compatible with ultrasound pulse-echo imaging systems, allowing the upgrade of general B-scan machines to an advanced diagnostic system. The advantages of information entropy may facilitate the implementation and commercialization of ultrasound expert systems for NAFLD diagnosis. As an example, quantitative ultrasound-based parametric imaging based on Nakagami distribution has been introduced in Samsung Medison systems for the diagnosis of hepatic steatosis (Cloutier et al. 2021; Park et al. 2022).

8.7 Conclusions and Perspectives

This chapter has presented information entropy and its clinical applications with regard to grading hepatic steatosis and liver fibrosis. Compared to statistical distribution models, information

entropy allows ultrasound backscattering analysis regardless of the characteristics of data distributions. Imaging with ultrasound entropy allows a visual representation of signal uncertainty, which is a representation of the physical interpretations associated with changes found in the liver's microstructure. It is important to stress that there are many types of entropies available even though we only presented the basic Shannon entropy and the sample entropy as typical examples. It is indeed challenging to clarify the pros and cons of each type of information entropy in ultrasound tissue characterization, but it is also very interesting and could be a long-term research topic. Non-model-based information entropy and statistical distributions may complement each other with a more flexible and general approach for analysis of ultrasound backscattering. Toward the future, quantitative ultrasound techniques based on statistical models and information entropy should be investigated and developed for use in ultrasound expert systems of NAFLD diagnosis.

References

- Borowska M (2015) Entropy-based algorithms in the analysis of biomedical signals. *Stud Logic Grammar Rhetoric* 43(56):21–32
- Brunt EM, Janney CG, Di Bisceglie AM, Neuschwander-Tetri BA, Bacon BR (1999) Nonalcoholic steatohepatitis: a proposal for grading and staging the histological lesions. *Am J Gastroenterol* 94(9):2467–2474
- Burckhardt CB (1978) Speckle in ultrasound B-mode scans. *IEEE Trans Sonics Ultrason* 25(1):1–6
- Chan DF, Li AM, Chu WC, Chan MH, Wong EM, Liu EK, Chan IH, Yin J, Lam CW, Fok TF, Nelson EA (2004) Hepatic steatosis in obese Chinese children. *Int J Obes Relat Metab Disord* 28(10):1257–1263
- Chan HJ, Zhou Z, Fang J, Tai DI, Tseng JH, Lai MW, Hsieh BY, Yamaguchi T, Tsui PH (2021) Ultrasound sample entropy imaging: a new approach for evaluating hepatic steatosis and fibrosis. *IEEE J Trans Eng Health Med* 9:1800612
- Chang TY, Chang SH, Lin YH, Ho WC, Wang CY, Jeng WJ, Wan YL, Tsui PH (2021) Utility of quantitative ultrasound in community screening for hepatic steatosis. *Ultrasonics* 111:106329
- Chen JR, Chao YP, Tsai YW, Chan HJ, Wan YL, Tai DI, Tsui PH (2020) Clinical value of information entropy compared with deep learning for ultrasound grading of hepatic steatosis. *Entropy* 22:1006
- Choong CC, Venkatesh SK, Siew EPY (2012) Accuracy of routine clinical ultrasound for staging of liver fibrosis. *J Clin Imaging Sci* 2:58
- Cloutier G, Destrempe F, Yu F, Tang A (2021) Quantitative ultrasound imaging of soft biological tissues: a primer for radiologists and medical physicists. *Insights Imaging* 12(1):127
- Couinaud C (1999) Liver anatomy: portal (and suprahepatic) or biliary segmentation. *Dig Surg* 16:459–467
- Cristea A, Franceschini E, Lin F, Mamou J, Cachard C, Bassett O (2015) Quantitative characterization of concentrated cell pellet biophantoms using statistical models for the ultrasound echo envelope. *Phys Procedia* 70:1091–1095
- Cristea A, Collier N, Franceschini E, Mamou J, Cachard C, Bassett O (2020) Quantitative assessment of media concentration using the homodyned K distribution. *Ultrasonics* 101:105986
- Delgado-Bonal A, Marshak A (2019) Approximate entropy and sample entropy: a comprehensive tutorial. *Entropy* 21(6):541
- Destrempe F, Cloutier G (2010) A critical review and uniformized representation of statistical distributions modeling the ultrasound echo envelope. *Ultrasound Med Biol* 36(7):1037–1051
- Dutt V, Greenleaf JF (1994) Ultrasound echo envelope analysis using a homodyned K distribution signal model. *Ultrason Imaging* 16:265–287
- Fang J, Chang NF, Tsui PH (2018) Performance evaluations on using entropy of ultrasound log-compressed envelope images for hepatic steatosis assessment: an in vivo animal study. *Entropy* 20(2):120
- Fei DY, Shung KK (1985) Ultrasonic backscatter from mammalian tissues. *J Acoust Soc Am* 78:871–876
- Fellingham LL, Sommer FG (1984) Ultrasonic characterization of tissue structure in the in vivo human liver and spleen. *IEEE Trans Sonics Ultrason* 31(4):418–428
- Garra BS, Insana MF, Shawker TH, Wagner RF, Bradford M, Russell M (1989) Quantitative ultrasonic detection and classification of diffuse liver disease. Comparison with human observer performance. *Investig Radiol* 24:196–203
- Gerstenmaier JF, Gibson RN (2014) Ultrasound in chronic liver disease. *Insights Imaging* 5:441–455
- Guisas S (1971) Weighted entropy. *Rep Math Phys* 2:165–179
- Ho MC, Lee YH, Jeng YM, Chen CN, Chang KJ, Tsui PH (2013) Relationship between ultrasound backscattered statistics and the concentration of fatty droplets in livers: an animal study. *PLoS One* 8(5):e63543
- Huang DQ, El-Serag HB, Loomba R (2021) Global epidemiology of NAFLD-related HCC: trends, predictions, risk factors and prevention. *Nat Rev Gastroenterol Hepatol* 18:223–238
- Hughes MS (1992) Analysis of ultrasonic waveforms using Shannon entropy. *IEEE Ultrason Symp Proc* 1:1205–1209

- Hughes MS (1993) Analysis of digitized waveforms using Shannon entropy. *J Acoust Soc Am* 93:892–906
- Hughes MS (1994) Analysis of digitized waveforms using Shannon entropy. II High speed algorithms based on Green's functions. *J Acoust Soc Am* 95:2582–2588
- Hughes MS, McCarthy JE, Marsh JN, Arbeit JM, Neumann RG, Fuhrhop RW, Wallace KD, Znidarsic DR, Maurizi BN, Baldwin SL, Lanza GM, Wickline SA (2007) Properties of an entropy-based signal receiver with an application to ultrasonic molecular imaging. *J Acoust Soc Am* 121:3542–3557
- Hughes MS, McCarthy JE, Marsh JN, Wickline SA (2013) Joint entropy of continuously differentiable ultrasonic waveforms. *J Acoust Soc Am* 133:283–300
- Hung CH, Lu SN, Wang JH, Lee CM, Chen TM, Tung HD et al (2003) Correlation between ultrasonographic and pathologic diagnoses of hepatitis B and C virus-related cirrhosis. *J Gastroenterol* 38:153–157
- Insana MF, Wagner RF, Garra BS, Momenan R, Shawker TH (1986) Pattern recognition methods for optimizing multivariate tissue signatures in diagnostic ultrasound. *Ultrason Imaging* 8:165–180
- Jakeman E, Tough RJA (1987) Generalized K distribution: a statistical model for weak scattering. *J Opt Soc Am A* 4:1764–1772
- Khan JF, Bhuiyan SM (2014) Weighted entropy for segmentation evaluation. *Opt Laser Technol* 57:236–242
- Lin DY, Sheen IS, Chiu CT, Lin SM, Kuo YC, Liaw YF (1993) Ultrasonographic changes of early liver cirrhosis in chronic hepatitis B: a longitudinal study. *J Clin Ultrasound* 21:303–308
- Lin YH, Liao YY, Yeh CK, Yang KC, Tsui PH (2018) Ultrasound entropy imaging of nonalcoholic fatty liver disease: association with metabolic syndrome. *Entropy* 20:893
- Lin YH, Wan YL, Tai DI, Tseng JH, Wang CY, Tsai YW, Lin YR, Chang TY, Tsui PH (2019) Considerations of ultrasound scanning approaches in non-alcoholic fatty liver disease assessment through acoustic structure quantification. *Ultrasound Med Biol* 45(8):1955–1969
- Lodish H, Berk A, Zipursky SL, Matsudaira P, Baltimore D, Darnell J (2000) Molecular cell biology, 4th edn. W. H. Freeman, New York
- Loomba R, Abraham M, Unalp A, Wilson L, Lavine J, Doo E, Bass NM (2012) Association between diabetes, family history of diabetes, and risk of nonalcoholic steatohepatitis and fibrosis. *Hepatology* 56:943–951
- Mamou J, Oelze ML (2013) Quantitative ultrasound in soft tissues. Springer, Dordrecht
- Martin S, Parton RG (2006) Lipid droplets: a unified view of a dynamic organelle. *Nat Rev Mol Cell Biol* 7(5):373–378
- Nawrockia DN, Harding WH (1986) State-value weighted entropy as a measure of investment risk. *Appl Econ* 18:411–419
- Nicholas D (1982) Evaluation of backscattering coefficients for excised human tissues: results, interpretation and associated measurements. *Ultrasound Med Biol* 8:17–28
- Pandyarajan V, Gish RG, Alkhouri N, Noureddin M (2019) Screening for nonalcoholic fatty liver disease in the primary care clinic. *Gastroenterol Hepatol* 15(7):357–365
- Park J, Lee JM, Lee G, Jeon SK, Joo I (2022) Quantitative evaluation of hepatic steatosis using advanced imaging techniques: focusing on new quantitative ultrasound techniques. *Korean J Radiol* 23(1):13–29
- Pauli EM, Staveley-O'Carroll KF, Brock MV, Efron DT, Efron G (2012) A handy tool to teach segmental liver anatomy to surgical trainees. *Arch Surg* 147:692–693
- Pike R, Sabatier P (2001) Scattering and inverse scattering in pure and applied science. Academic Press, New York
- Rappaport AM (1958) The structural and functional unit in the human liver (liver acinus). *Anat Rec* 130:673–689
- Richman J, Moorman J (2000) Physiological time-series analysis using approximate entropy and sample entropy. *Am J Physiol Heart Circ Physiol* 278:H2039–H2049
- Rubert N, Varghese T (2013) Mean scatterer spacing estimation using multi-taper coherence. *IEEE Trans Ultrason Ferroelectr Freq Contr* 60:1061–1073
- Shankar PM (2000) A general statistical model for ultrasonic backscattering from tissues. *IEEE Trans Ultrason Ferroelectr Freq Control* 7(3):727–736
- Shannon CE (1948) A mathematical theory of communication. *Bell Syst Tech J* 27:379–423
- Shapiro WL, Noon SL, Schwimmer JR (2021) Recent advances in the epidemiology of nonalcoholic fatty liver disease in children. *Pediatr Obes* 16(11):e12849
- Shung KK, Thieme GA (1993) Ultrasonic scattering in biological tissues. CRC Press, Boca Raton
- Silva LE, Senra F, Antonio C, Fazan V, Felipe J, Murta L (2016) Two-dimensional sample entropy: assessing image texture through irregularity. *Biomed Phy Eng Exp* 2:045002
- Skandalakis JE, Skandalakis LJ, Skandalakis PN, Mirilas P (2004) Hepatic surgical anatomy. *Surg Clin North Am* 84:413–435
- Smolikova R, Wachowiak MP, Zurada JM (2004) An information-theoretic approach to estimating ultrasound backscatter characteristics. *Comput Biol Med* 34:355–370
- Szabo TL (2004) Diagnostic ultrasound imaging: inside out. Elsevier, Oxford
- Tandra S, Yeh MM, Brunt EM, Vuppalauchi R, Cummings OW, Ünalp-Arida A, Wilson LA, Chalasani N (2011) Presence and significance of microvesicular steatosis in nonalcoholic fatty liver disease. *J Hepatol* 55(3):654–659
- Tsai YW, Zhou Z, Gong CA, Tai DI, Cristea A, Lin YC, Tang YC, Tsui PH (2021) Ultrasound detection of liver fibrosis in individuals with hepatic steatosis using the homodyned K distribution. *Ultrasound Med Biol* 47(1):84–94
- Tsui PH (2015) Ultrasound detection of scatterer concentration by weighted entropy. *Entropy* 17:6598–6616
- Tsui PH, Chang CC (2007) Imaging local scatterer concentrations by the Nakagami statistical model. *Ultrasound Med Biol* 33:608–619

- Tsui PH, Wan YL (2016) Effects of fatty infiltration of the Liver on the Shannon entropy of ultrasound backscattered signals. *Entropy* 18:341
- Tsui PH, Wan YL, Tai DI, Shu YC (2015) Effects of estimators on ultrasound Nakagami imaging in visualizing the change in the backscattered statistics from a Rayleigh distribution to a pre-Rayleigh distribution. *Ultrasound Med Biol* 41(8):2240–2251
- Tsui PH, Ho MC, Tai DI, Lin YH, Wang CY, Ma HY (2016) Acoustic structure quantification by using ultrasound Nakagami imaging for assessing liver fibrosis. *Sci Rep* 8(6):33075
- Tsui PH, Chen CK, Kuo WH, Chang KJ, Fang J, Ma HY, Chou D (2017) Small-window parametric imaging based on information entropy for ultrasound tissue characterization. *Sci Rep* 7:41004
- Tuthill TA, Sperry RH, Parker KJ (1988) Deviations from Rayleigh statistics in ultrasonic speckle. *Ultrasound Imaging* 10:81–89
- Wagner RF, Insana MF, Brown DG (1987) Statistical properties of radio-frequency and envelope detected signals with applications to medical ultrasound. *J Opt Soc Am* 4:910–922
- Wan YL, Tai DI, Ma HY, Chiang BH, Chen CK, Tsui PH (2015) Effects of fatty infiltration in human livers on the backscattered statistics of ultrasound imaging. *Proc Inst Mech Eng H J Eng Med* 229(6):419–428
- Weng L, Reid JM, Shankar PM, Soetanto K (1991) Ultrasound speckle analysis based on the K distribution. *J Acoust Soc Am* 89:2992–2995
- Yang L, Yang J, Peng N, Ling J (2005) Weighted information entropy: a method for estimating the complex degree of infrared images' backgrounds. *Lect Notes Comput Sci* 3656:215–222
- Yeung RW (2002) A first course in information theory. Kluwer Academic/Plenum Publishers, New York
- Yki-Järvinen H (2014) Non-alcoholic fatty liver disease as a cause and a consequence of metabolic syndrome. *Lancet Diabetes Endocrinol* 2(11):901–910
- Young B, Woodford P, O'Dowd G (2006) Wheater's functional histology: a text and colour atlas. Elsevier, Oxford
- Yu AS, Keeffe EB (2002) Nonalcoholic fatty liver disease. *Rev Gastroenterol Disord* 2:11–19
- Zhang S, Zhou F, Wan M, Wei M, Fu Q, Wang X, Wang S (2012) Feasibility of using Nakagami distribution in evaluating the formation of ultrasound-induced thermal lesions. *J Acoust Soc Am* 131:4836–4844
- Zhou Z, Huang CC, Shung KK, Tsui PH, Fang J, Ma HY, Wu S, Lin CC (2014) Entropic imaging of cataract lens: an in vitro study. *PLoS One* 9:e96195
- Zhou Z, Xu MJ, Gao B (2016) Hepatocytes: a key cell type for innate immunity. *Cell Mol Immunol* 13:301–315
- Zhou Z, Tai DI, Wan YL, Tseng JH, Lin YR, Wu S, Yang KC, Liao YY, Yeh CK, Tsui PH (2018) Hepatic steatosis assessment with ultrasound small-window entropy imaging. *Ultrasound Med Biol* 44(7): 1327–1340
- Zhou Z, Fang J, Cristea A, Lin YH, Tsai YW, Wan YL, Yeow KM, Ho MC, Tsui PH (2020) Value of homodyned K distribution in ultrasound parametric imaging of hepatic steatosis: an animal study. *Ultrasonics* 101(7):106001

Part IV

Ultrasound Computed Tomography



Ultrasound Tomography

9

Nicole V. Ruiter, Michael Zapf, Torsten Hopp,
and Hartmut Gemmeke

Abstract

Ultrasound tomography (USCT) is a promising imaging modality, mainly aiming at early diagnosis of breast cancer. It provides three-dimensional, reproducible images of higher quality than conventional ultrasound methods and additionally offers quantitative information on tissue properties. This chapter provides an introduction to the background and history of USCT, followed by an overview of image reconstruction algorithms and system design. It concludes with a discussion of current and future applications as well as limitations and their potential solutions.

Keywords

Ultrasound tomography · State of the art · Reconstruction methods · System design · Clinical applications

N. V. Ruiter (✉) · M. Zapf · T. Hopp · H. Gemmeke
Institute for Data Processing and Electronics, Karlsruhe
Institute of Technology, Karlsruhe, Germany
e-mail: nicole.ruiter@kit.edu; michael.zapf@kit.edu;
Torsten.hopp@kit.edu; Hartmut.gemmeke@kit.edu

9.1 Introduction

Ultrasound Tomography (USCT) is an exciting technology with several active research groups investigating new algorithms, devices, and applications around the globe. The basic idea of USCT is to surround the object to be imaged as much as possible with many ultrasound transducers and collect unfocused ultrasound data from many different angles. An exemplary setup is shown in Fig. 9.1.

The main application of the method is imaging of the female breast for early cancer detection. In the following sections, most examples will be given from breast cancer diagnosis. However, other applications are also possible and will be presented in later sections.

The potential benefits of USCT have been known for a long time. First publications in this field date back to the 1970s, e.g., Schomberg (1978). The main advantages of USCT systems are simultaneous recording of two or three-dimensional images of reflection, attenuation and speed of sound, high image quality, and fast data acquisition of a large volume.

The construction of such a device for clinical practice was not successful for a long time—mainly because of the huge data rate and the time-consuming image reconstruction. Currently, the first 2D and 2.5D systems have become available

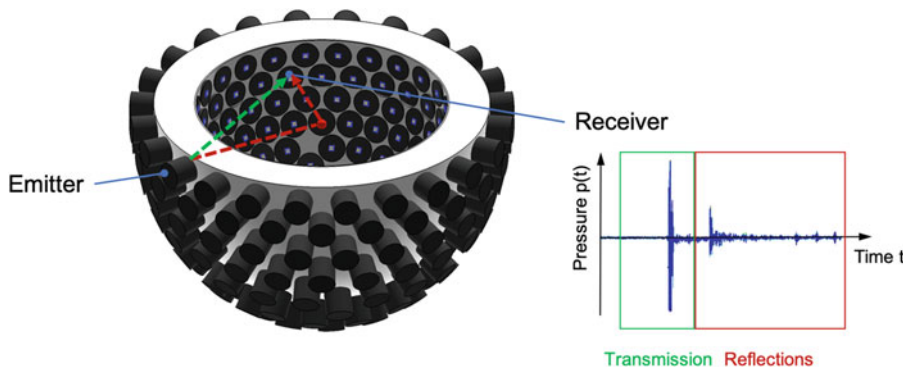


Fig. 9.1 Example of an USCT setup: A point scatterer (red sphere) in water is surrounded by ultrasound transducers (gray) in a fixed setup. One emitter emits a pulsed spherical wave. The pulse is scattered at the point scatterer. All transducers receive the resulting field. One exemplary A-scan is depicted on the right for the indicated emitter-

receiver combination as pressure signal versus time. The first pulse corresponds to the pulse traveling on the fastest path from emitter to receiver (green, transmission), the second pulse is scattered at the point (red). More scattered and reflected pulses can occur, e.g., reflections on the water surface or other objects

for clinical evaluation (Duric et al. 2014; André et al. 2013) and the Delphinus system was FDA approved for screening in October 2021 (Delphinus Medical Technologies Inc 2021).

9.1.1 Advantages of USCT

Ultrasound tomography offers the possibility to generate 3D volumes of the imaged object; deformation of soft tissue is not necessary due to non-contact imaging. Unlike X-ray procedures, the patient and operator are not exposed to radiation.

USCT produces multimodal images in one acquisition step, i.e., three different properties of the tissue can be reconstructed from one data set: Reflectivity, speed of sound, and attenuation. Reflectivity images show qualitative changes in acoustic impedance and thus represent interfaces between tissues in a manner similar to sonography.

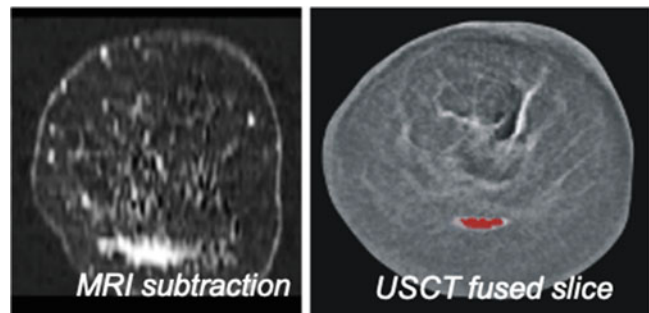
Speed of sound and attenuation are quantitative values and can therefore be used to classify different tissue types (Greenleaf and Bahn 1981). For breast cancer diagnosis, initial experiments have shown that increased speed of sound values can separate cancer from normal tissue, e.g., Hopp (2012); in combination with attenuation

this might be a good classifier for breast cancer (Calderon et al. 1976; Johnson et al. 2007). This type of quantitative information is only acquired with the USCT method and not with conventional sonography. Figure 9.2 shows an example for the KIT 3D USCT system of a fused reflectivity image overlaid with thresholded speed of sound image indicating a large cancer in comparison with the magnetic resonance imaging (MRI) contrast enhancement of the same patient.

Due to the defined patient positioning without deformation of the soft tissues, the volume images of the patients are reproducible and operator-independent. This is a major advantage for follow-up examinations: Older images can easily be compared with new ones in order to detect small tissue changes for cancer diagnosis at an early stage.

The USCT device itself, device maintenance, and the imaging are very cost-effective. The costs for breast imaging can be comparable to mammography and are therefore significantly lower than, for example, MRI. The image acquisition can be carried out by a medical-technical assistant without the presence of a doctor. This enables the method to be used very widely, e.g., also by resident doctors.

Fig. 9.2 Example of an USCT fused information: On the left side, the MRI subtraction image indicates the position of the cancer. The right image shows a reflectivity slice approximately at the same position with overlayed region of high speed of sound for this patient



9.1.2 Challenges of USCT

The challenges of building and operating an ultrasound tomography device are due to the large volume of a complex object being imaged, e.g., the female breast, compared to the wavelength of the ultrasound. Additionally a large number of unfocused ultrasound transducers is required to image the object, which need to be as identical as possible.

In order to approximate spherical waves (3D systems) or cylindrical (2D systems), the individual transducers have to be very small, resulting in low sound level pressures and a low signal-to-noise ratio.

The large number of ultrasound transducers that have to be recorded in parallel leads to a large number of parallel channels required and a high data rate in order to avoid patient motions with the shortest possible data acquisition times.

Due to the complex interaction of ultrasound with tissue, reconstruction algorithms for high image quality are complex (Duric et al. 2011). A compromise has to be found between clinically relevant computing time and resulting image quality. Suitable three-dimensional reconstruction algorithms and parallel computing have to be investigated and further developed.

The overall design of the devices should be robustly applicable in clinical practice, low cost and designed to have a low power consumption.

9.1.3 Definition of USCT and Differences to Sonography

In order to differentiate USCT as precisely as possible from conventional ultrasound applications in medicine, a few key aspects need to be pointed out. Ultrasound tomography is a diagnostic procedure with its main application in the diagnosis of breast cancer. Contrary to conventional sonography, the object to be imaged is surrounded in a fixed setup by ultrasound transducers and sonicated in such a way that both reflection and transmission images of the speed of sound and attenuation distribution can be reconstructed.

Reflectivity tomography, as applied in conventional sonography, does generate a qualitative representation of the gradient of the body's acoustic impedance. However, the resolution of the resulting B-scans in sonography is anisotropic and spatially highly variable. This can be overcome with USCT by optimizing the transducer distribution and using unfocussed emission and reception. A diagram of the different acquisition modes is given in Fig. 9.3.

The relatively high speckle noise of sonography can, on the one hand, provide indirect information about the tissue as a diagnostic tool and, on the other hand, can obstruct important features. Speckle is the typical grainy background pattern in sonography images and is caused by interference effects (Szabo 2014). Speckle can be reduced by spatial compounding. Compounding means that B-scans from different acquisition

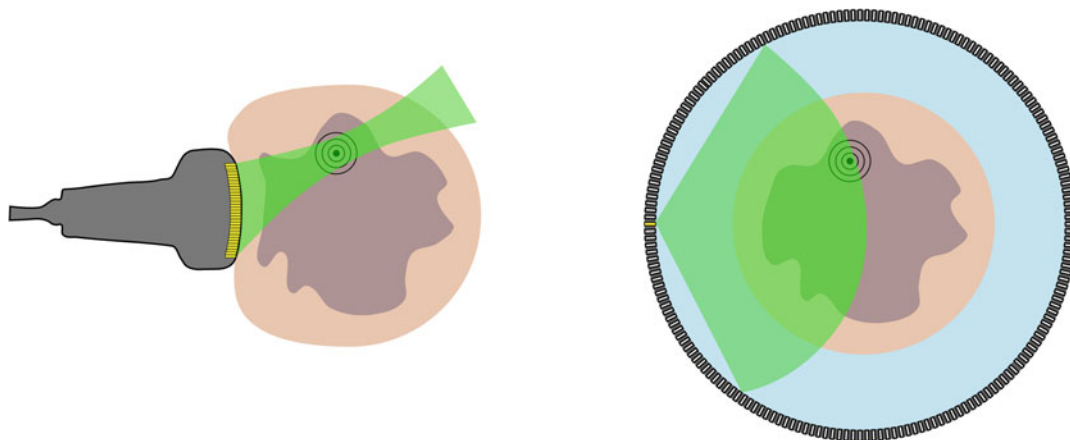


Fig. 9.3 Sonography (left) and USCT (right) acquisition modes. For sonography, a phased array focuses on one point in the imaged object. The focused beam is steered

to acquire a slice image. For USCT, unfocused waves are emitted by each transducer sequentially. The acquired signals are then focused during the reconstruction

angles are added together. USCT systems include compounding due to their surrounding aperture, i.e., the object is imaged from many sides with ultrasound transducers.

3D ultrasound systems allow imaging of a 3D volume. However, the 3D volume at an imaging position corresponds to only a small part of the imaged object. If the entire volume has to be represented, many volumes must be recorded over the entire body region of interest. These partial volumes are then subsequently assembled. A recent development in breast ultrasound is, for example, Automated Whole-Breast Ultrasound (AWBU, SonoCine) (Kelly and Richwald 2011), which images reflectivity volumes of the entire breast. This procedure results in more objective images and structured documentation than is common with ultrasound examinations. However, the systems only image from one side with conventional US scanners, resulting in anisotropic and spatially variable resolution and decreasing signal-to-noise ratio with penetration depth.

neurologist K. Dussik of the University Hospital of Vienna as “hyperfonography” (Dussik 1942). The transmission-only system recorded so-called ventriculograms, i.e., attenuation projections of ultrasound pulses through the human skull. The application was intended to examine the ventricles in the brain. For this purpose, the back of the patient’s head was placed in a water bath and transilluminated by two opposing single transducers. A photograph of the apparatus can be found, e.g., in Woo (2015). However, the strong attenuation and reflection of ultrasound from the skull bone meant that this method was not pursued.

Holmes et al. (1955); Howry and Bliss (1952) developed several prototypes, so-called compound scanners, which used a single focused transducer to compose B-scans from A-scan lines. USCT-like features were the placement of the patient in a water bath and the ability to move the transducer in a circular path around the patient. The “sonoscope” of 1954 is, e.g., reprinted in Woo (2015).

From the mid-1950s onwards, further research was almost entirely limited to pulse-echo systems. Transmission devices or surrounding systems no longer played a role (Woo 2015). In the late 1970s and early 1980s, the idea of tomography for reflection slice images was revisited and analyzed theoretically and with computer simulations by Norton and Linzer, among others. In par-

9.2 State of the Art of Ultrasound Tomography

The first use of ultrasound in medical diagnostics was published in 1942 by the psychiatrist and

ticular, they discussed how the aperture type affects the point spread function (PSF) of the resulting images. Different aperture types were considered, from spherical (Norton and Linzer 1979a) to planar and cylindrical (Norton and Linzer 1981) to circular apertures (Norton and Linzer 1979b).

At the same time, the idea of transmission imaging in the form of transmission tomography was revived by several groups for various applications (Schomberg 1978; Carson et al. 1977; Glover 1977; Greenleaf et al. 1974; Klepper et al. 1977; O'Donnell et al. 1977). Greenleaf and Bahn published clinical results on transmission tomography of the breast (Greenleaf and Bahn 1981), in which they showed a diagram, still often cited today, see Fig. 9.11, of the relationships between speed of sound and attenuation of normal and abnormal tissues of the breast. Further experiments were performed on Doppler and reflectivity tomography (Greenleaf et al. 1987).

Combined systems that provided both transmission and reflection data from the breast were described by Mueller et al. (1979) and by Carson and colleagues in Carson et al. (1981). Carson et al. used two directional, opposing ultrasound transducers with 3.5 MHz center frequency and 40% bandwidth. These were rotated and lifted around the patient's breast in the prone position to produce slice images in the frontal plane of the breast.

9.2.1 Current Systems

Most current USCT systems acquire both reflectivity and transmission data and focus on breast cancer diagnosis. Basically, systems can be divided into three types according to their aperture: 2D ring apertures, 2.5D segment, or 3D apertures. They operate at frequencies from 0.35 to 8 MHz and transmit unfocused ultrasound pulses in 2D or 3D. Acquisition times of the more sophisticated systems are in the range of minutes. The total time is dominated by the duration of the movements of the apertures; the travel times of the pulses are almost negligible with current systems.

Image reconstruction is computed offline in minutes to hours, often using massive paralleliza-

tion in clinical trials, e.g., André et al. (2012), Duric et al. (2013), Kretzek et al. (2013), Pellegretti (2011), and Roy et al. (2013). Since most groups do not provide detailed information on the acquisition time, only an approximate overview can be given. From the available system parameters, it is estimated that recordings with patients take between two and ten minutes per breast. Clinical trials have been described for systems from QT Imaging, Inc. (formerly QT Ultrasound and TechniScan) (André et al. 2013; Malik et al. 2020a), Delphinus Medical Systems (Duric et al. 2014, 2010), MastoScopia (Zografos et al. 2015), and KIT (Ruiter et al. 2013). Delphinus stands out for reporting by far the largest number of patients.

The used reconstruction algorithms for transmission images are iterative algorithms, whereby the Algebraic Reconstruction Technique (ART) (Natterer 2001) is mostly preferred. This reconstruction method assumes straight rays in the simplest case or, in extended implementations, can also represent refraction effects (Dapp 2013). Neglecting diffraction leads to a limited resolution of transmission volumes, see Sect. 9.4. This is where QT Ultrasound and Delphinus stand out. The system of QT uses a transmission reconstruction based on the paraxial approximation (Wiskin et al. 2012), which offers much higher resolution than ART. Delphinus even uses 2D full-waveform inversion tomography (Sandhu et al. 2015). However, these approaches have the disadvantage that the required computation time is increased massively. Most systems use the Synthetic Aperture Focusing Technique (SAFT) (Doctor et al. 1986) or spatial compounding for reflectivity imaging. Reconstructions are performed on multiple parallel GPUs for clinical use, e.g., Duric et al. (2013); Kretzek et al. (2013).

For 2D systems the resolution is anisotropic in the image plane and in the slice direction. It depends on the bandwidth of the used pulses, the used aperture shape and is location dependent (Schwarzenberg et al. 2008). The 2D approaches result in images with slice thicknesses in the millimeter range. In addition, the images show limited depth of field. Focusing the transducers in the slice direction results in loss of out-of-plane reflections. Due to the required motion me-

chanics, the acquisition time cannot be reduced to sound-only time. A full 3D aperture using spherical wave fronts for imaging solves these limitations.

An overview of current USCT systems and their properties are listed in Table 9.1.

9.3 Ultrasound Propagation in Tissue

Imaging procedures are based on the interaction of energy with matter. Most medical procedures introduce energy into the body and record its interaction with the imaged structures. A certain imaging procedure thereby maps one or more defined physical properties of the tissues. This mapping can be qualitative or quantitative. For accurate medical diagnosis, the mapping of physical properties for normal and abnormal tissues have to be as well known and distinguishable as possible (Webb 1988).

Ultrasound propagation in soft tissue is characterized by complex interaction. According to Linzer and Norton (1982), these diverse interactions between ultrasound and tissue are the greatest advantage of ultrasound-based diagnosis and, at the same time, its greatest weakness: They enable many applications and modalities of diagnostic ultrasound from Doppler to elastography to pulse-echo sonography. However, individual effects are difficult to isolate. Therefore, quantitative imaging is often not possible.

9.3.1 Acoustic Wave Equation and Assumptions

Ultrasound describes the phenomenon of propagation of density and pressure fluctuations in an elastic medium at frequencies greater than 20 kHz. Typical assumptions for the description of wave propagation in soft tissue are (Greenleaf 1986; Szabo 2014):

1. The medium “soft body tissue” behaves like a liquid. Thus, ultrasound waves propagate approximately only as longitudinal waves, i.e.,

compressional waves. Shear waves can be ignored.

2. The propagation is described by a linear wave equation as the amplitudes of the sound pressure and the particle displacement are very small.
3. The energy loss in the propagation of the sound wave is so small that absorption can be modeled in a simplified way. Dispersion effects can be neglected.
4. The medium is approximately isotropic, so that the material properties in homogeneous tissue can be described by a direction-independent scalar.

With the above assumptions, ultrasound propagation in soft tissue can be described by the acoustic wave equation (Greenleaf 1986):

$$\nabla^2 p(\mathbf{x}) + k_0^2 \eta(\mathbf{x})^2 p(\mathbf{x}) - \frac{1}{\rho(\mathbf{x})} \nabla \rho(\mathbf{x}) \nabla p(\mathbf{x}) = 0, \quad (9.1)$$

where $p(\mathbf{x})$ is the spatially dependent pressure, $\rho(\mathbf{x})$ is the spatially dependent density, and $\eta(\mathbf{x})$ is the spatially dependent refractive index; k_0 is the wave number of the background medium.

If lossless propagation is assumed, the refractive index can be calculated as

$$\eta(\mathbf{x}) = \frac{c_0}{c(\mathbf{x})} = \sqrt{\frac{K_0}{\rho_0}} \sqrt{\frac{\rho(\mathbf{x})}{K(\mathbf{x})}}, \quad (9.2)$$

where c_0 is the speed of sound of the background medium, $c(\mathbf{x})$ is the spatially dependent speed of sound, ρ_0 is the density of the background without sound propagation, and K_0 and $K(\mathbf{x})$ are the compression moduli of the background and medium, respectively.

If absorption is assumed to be small over the distance of a wavelength, the refractive index can be written as

$$\eta(\mathbf{x}) \approx \frac{c_0}{c(\mathbf{x})} + i \frac{\mu(\mathbf{x})}{k_0} \quad (9.3)$$

with μ as the spatial and frequency-dependent absorption coefficients. Attenuation α is often cal-

Table 9.1 Overview of a selection of current USCT systems

System	Modality	Aperture	Freq. range (Bandwidth)	No. elements	Motion	In vivo or clinical test
ANAÏS (Rouyer et al. 2012)	Transmission reflection	Semicircle	3.0 MHz (75%)	1024	Rotation translation	no André et al. (2013; Malik et al. (2020a))
	Transmission reflection	Planar arrays circular segments	0.9 MHz (100%) 3.6 MHz (70%)	8×256 3×192	Rotation translation	
MUT (Marmarelis et al. 2007; Tae-Seong 2005)	Transmission	Planar arrays	8 MHz (50%)	128	Rotation translation	Zografos et al. (2015)
SoftVue (Duric et al. 2013; Roy et al. 2013)	Transmission reflection	Ring	2.75 MHz (100%)	2048	Translation	Duric et al. (2010, 2014)
Prototype us CT (Suzuki et al. 2021)	Transmission reflection	Ring	3 MHz (unk.)	2048	Translation	Suzuki et al. (2021)
BUTIS (Ding et al. 2018)	Transmission reflection	Ring	2.25 MHz (unk.)	1024	Translation	Ding et al. (2018)
3D USCT II (Ruijer et al. 2011)	Transmission reflection	Semi-ellipsoid	2.5 MHz (60%)	2041	Rotation translation	Ruijer et al. (2013)

culated instead of the absorption. This describes the total of the energy loss due to absorption and scattering (Sehgal and Greenleaf 1984). The attenuation is thus partly also dependent on the aperture, since scattered energy components play a role, which are not detected by the finite active area of the aperture (Linzer and Norton 1982).

With these assumptions, sound propagation in inhomogeneous media depends on three parameters (Günter 2002): the density ρ , the adiabatic compression modulus K , and the absorption μ . Mostly these or derived properties such as the speed of sound $c = \sqrt{\frac{K}{\rho}}$, the attenuation α , and the gradient of acoustic impedance, $Z = \rho c$, as “reflectivity” I , are reconstructed during image generation.

Wave equations that model tissue not as a fluid but as an elastic solid, and thus include shear waves, can be found, e.g., in Greenleaf (1986).

9.4 Image Reconstruction

The image formation algorithm reconstructs the object properties from the measured values such as ultrasound amplitude and phase. In general, if the relationship can be described relatively simply, the reconstruction can be performed quickly and effectively. When the relationship is complex, as in the case of ultrasound propagation in tissue, either limitations in the quality of reconstructed images have to be accepted or more sophisticated reconstruction algorithms have to be used, provided that current technology can compute them in finite time. For a given imaging system, the “quality,” i.e., the resolution, the contrast and the correspondence with the true values of the reconstructed images, mainly depends on the reconstruction method used. The reconstructed values can be either quantitative or qualitative.

The reconstruction methods of USCT are based on the acoustic wave equation for inhomogeneous media with the assumptions described in Sect. 9.3.1. The resulting main effects for the propagation of a wave are often modeled in a simplified manner as diffraction, refraction, scattering, and absorption. Table 9.2 summarizes

the approximations of the reconstruction methods described below and their properties.

Wave-based reconstruction methods, distinguished here as Full-Waveform, Paraxial, and Diffraction Tomography, can be grouped into two categories (Taskin 2021): Full-Waveform Tomography which uses (almost) all information of the received waves and Paraxial and Diffraction Tomography, which use approximations for the reconstruction.

9.4.1 Full-Waveform Tomography

Full-waveform inversion (FWI) or waveform tomography (Virieux and Operto 2009) uses a forward model that approximates the measured data based on an initial estimate of the object properties to be reconstructed. A new model of the object properties is generated from the difference between the measured and simulated data. These steps are iterated using a suitable optimization algorithm until a termination criterion is reached, i.e., the difference of the object model and the measured data is small. The advantage of this method is that the wave equation does not need to be linearized and therefore all effects of wave propagation, within the stated assumptions in Sect. 9.3.1, are modeled. The object itself is discretized, which allows, for example, the solution of the wave equation using finite elements (Virieux and Operto 2009). A disadvantage is that this method requires the highest computational effort.

First implementations for ultrasound tomography have been published in recent years, e.g., Natтерер (2008), Özmen et al. (2015), and Zhang et al. (2004). However, these methods are currently limited to low frequencies below 0.5 MHz or 2D reconstructions (Sandhu et al. 2015; Özmen et al. 2015; Goncharsky and Romanov 2013). Most of these approaches assume that the density in the tissue is constant and only the compressibility varies. Results with simulated data for simultaneous reconstruction of density and compressibility can be found in Hesse et al. (2013) and van Dongen and Wright (2007).

Table 9.2 Overview of USCT reconstruction methods using approximations based on Dapp (2013). λ is the wavelength, L is the distance between emitter and receiver, p is the ultrasound pressure, y a direction normal to the

Method	Approximation	Resolution	Complexity	Assumption
Paraxial	Anisotropic field	$\lambda/2$	High	$\partial^2 p / \partial y^2$ small
Born	Linearization of pressure	$\lambda/2$	High	$p_s \ll p$
Rytov	Linearization of phase	$\lambda/2$	High	$\delta p \ll 1$
Eikonal	Infinite frequency	$\sqrt{L\lambda}$	Middle	k small
Ray propagation	Infinite frequency	$\sqrt{L\lambda}$	Low	c_0 const.

In detail the published methods vary greatly, especially in the underlying formulation of wave equation, e.g., with or without absorption, and whether the forward model is calculated in the time or in the frequency domain. The following brief introduction to the theory and the reconstruction methods closely follows (Özmen et al. 2015) by applying Contrast Source Inversion in the frequency domain. For simplicity, the introduction is done without modeling absorption and the density is assumed to be constant, i.e., only the spatially varying speed of sound $c(\mathbf{x})$ is considered. The theory and reconstruction for this particular method, including absorption and density reconstruction, can be found in Taskin (2021).

The Helmholtz equation for heterogeneous media in the frequency domain is

$$\nabla^2 \hat{p}(\mathbf{x}) + \frac{\omega^2}{c^2(\mathbf{x})} \hat{p}(\mathbf{x}) = -\hat{S}(\mathbf{x}), \quad (9.4)$$

where $\hat{p}(\mathbf{x})$ is the pressure field at location \mathbf{x} in the frequency domain. $\hat{S}(\mathbf{x})$ is the primary source generating the sound field. ω is the angular frequency and ∇^2 the Laplace operator.

The total pressure field is separated into the incident field $\hat{p}^{inc}(\mathbf{x})$ and the scattered field $\hat{p}^{sct}(\mathbf{x})$ as

$$\hat{p}(\mathbf{x}) = \hat{p}^{inc}(\mathbf{x}) + \hat{p}^{sct}(\mathbf{x}). \quad (9.5)$$

The incident field is the part of the pressure field generated by the source \hat{S} which is traveling through homogeneous background medium with c_0 and the scattered field is a correction term which accounts for the deviations due to the imaged object with $c(\mathbf{x}) = c_0 + \Delta c(\mathbf{x})$.

main propagation direction, p_s is the scattered pressure, ∂p the change of pressure, k the wave number and c_0 the speed of sound

The scattered field can be written as

$$\hat{p}^{sct}(\mathbf{x}) = \omega^2 \int_{\mathbf{x}' \in \mathbb{D}} \hat{G}(\mathbf{x} - \mathbf{x}') \hat{p}(\mathbf{x}') \chi(\mathbf{x}') dV(\mathbf{x}'), \quad (9.6)$$

where \mathbb{D} is the spatial domain, i.e., the reconstructed area or volume (V), \hat{G} is the Green's function, and the contrast function $\chi(\mathbf{x}')$ is the deviation from the background medium caused by the object, with

$$\chi(\mathbf{x}') = \frac{1}{c^2(\mathbf{x}')} - \frac{1}{c_0^2}. \quad (9.7)$$

For Contrast Source Inversion in two dimensions, i.e., $\mathbf{x} = (x, y)^T$, the total field in Eq. (9.5) and the scattered field in Eq. (9.6) are modified such that the contrast function $\chi(\mathbf{x}')$ and the total field are combined in one variable $\hat{w}(\mathbf{x}') = \hat{p}(\mathbf{x}') \chi(\mathbf{x}')$, i.e.,

$$\begin{aligned} \hat{p}(\mathbf{x}) &= \hat{p}^{inc}(\mathbf{x}) + \omega^2 \int_{\mathbf{x}' \in \mathbb{D}} \hat{G}(\mathbf{x} - \mathbf{x}') \\ &\quad \times \hat{w}(\mathbf{x}') dA(\mathbf{x}'), \end{aligned} \quad (9.8)$$

with $\mathbf{x} \in \mathbb{S}$ and

$$\hat{p}^{sct}(\mathbf{x}) = \omega^2 \int_{\mathbf{x}' \in \mathbb{D}} \hat{G}(\mathbf{x} - \mathbf{x}') \hat{w}(\mathbf{x}') dA(\mathbf{x}'), \quad (9.9)$$

with $\mathbf{x} \in \mathbb{S}$ and \mathbb{S} the surface of the domain \mathbb{D} .

After discretization and in operator notation, the Eq. (9.8) is written as

$$\hat{\mathbf{p}}_j = \hat{\mathbf{p}}_j^{inc} + \mathbf{L}^{\mathbb{D}}[\hat{\mathbf{w}}_j], \quad (9.10)$$

where $\hat{\mathbf{p}}_j$ is the discretized total field, $\hat{\mathbf{p}}_j^{inc}$ the discretized incident field, \mathbf{L}^D the integral operator on D , and $j = 1, 2, \dots, J$ denote the unique emitter and receiver combinations.

If the Eq. (9.10) is multiplied by χ and solved for the incident field, the resulting equation is called object equation

$$\chi \hat{\mathbf{p}}_j^{inc} = \hat{\mathbf{w}}_j - \chi \mathbf{L}^D[\hat{\mathbf{w}}_j], \quad (9.11)$$

where $\hat{\mathbf{w}}_j$ are the contrast sources.

Equation (9.9) can be rewritten in a similar way and expressed as the so-called data equation

$$\hat{\mathbf{f}}_j = \mathbf{L}^S[\hat{\mathbf{w}}_j], \quad (9.12)$$

where $\hat{\mathbf{f}}_j$ is the measured data, i.e., a set of measurements of the scattered field at S , and \mathbf{L}^S is the integral operator over S .

The aim is to reconstruct the contrast function χ for given $\hat{\mathbf{f}}_j$. This is done iteratively by minimizing the error for the object equation (9.11) and the error for the data equation (9.12), which is a measure of how well a current estimate of $\hat{\mathbf{w}}_{j,n}$ predicts $\chi \hat{\mathbf{p}}_j^{inc}$ and $\hat{\mathbf{f}}_j$, respectively. The initial values of the contrast source $\hat{\mathbf{w}}_{j,0}$, the total field $\hat{\mathbf{p}}_{j,0}$, and the contrast function χ_0 are calculated directly from the data equation (9.12) using the measured values. In the following iteration, first the contrast source $\hat{\mathbf{w}}_{j,n}$ is updated based on the current error. Then, the total field $\hat{\mathbf{p}}_{j,n}$ is calculated for the updated contrast source. Finally, the contrast function χ_n is calculated by direct minimization from $\hat{\mathbf{w}}_{j,n}$ and $\hat{\mathbf{p}}_{j,n}$. This is repeated until a threshold for the total error or a certain number of iterations is reached.

Finally, the speed of sound values of the domain are calculated from the resulting χ as

$$\mathbf{c} = \frac{1}{\sqrt{\chi + c_0^{-2}}}. \quad (9.13)$$

9.4.2 Diffraction Tomography

The term diffraction tomography is also used in the literature for full-wave(form) methods.

Here, the classification according to Duric et al. (2011) is used, which distinguishes diffraction tomography from FWI tomography by applying additional simplifying approximations.

Typical reconstruction methods are based on the Born or the Rytov approximation in the first order of the wave equation (Keller 1969). Diffraction tomography has so far been used mainly on simulated 2D data sets with low frequencies, e.g., Greenleaf et al. (1987), André et al. (1997), Chenevert et al. (1984), and Simonetti et al. (2009). The Born approximation assumes that objects to be reconstructed are small and their acoustic parameters are only weakly distinguishable from the background. The Rytov approximation constrains the maximum contrast of objects. Both assume non-absorbing media, so absorption or attenuation has to be modeled additionally. The advantage of diffraction tomography is that the reconstructions can be up to a hundred times faster than the FWI methods (Hardt 2012). However, the assumptions are of limited use for imaging breast tissue (Duric et al. 2011; Özmen et al. 2015) and other tissues with highly varying speed of sound. Extensions of the Born approximation such as the Distorted Wave Born Approximation can improve this, e.g., Lavarello and Oelze (2009), but are again more complex to compute.

The following short introduction focuses on the Born approximation in two dimensions as described in Özmen et al. (2015). The Born approximation simplifies the scattered field in Eq. (9.6) to

$$\begin{aligned} \hat{p}^{sct}(\mathbf{x}) &= \omega^2 \int_{\mathbf{x}' \in D} \hat{G}(\mathbf{x} - \mathbf{x}') \hat{p}^{inc}(\mathbf{x}') \\ &\times \chi(\mathbf{x}') dA(\mathbf{x}'), \end{aligned} \quad (9.14)$$

where the total field $\hat{p}(\mathbf{x}')$ is approximated by the incident field $\hat{p}^{inc}(\mathbf{x}')$.

Discretized and in operator notation, the scattered field can be rewritten as

$$\hat{\mathbf{p}}_j^{sct} = \mathbf{M}[\chi], \quad (9.15)$$

where \mathbf{M} is the integral operator.

The aim of the reconstruction is again to calculate χ from the measured data, denoted here as $\hat{\mathbf{p}}_j^{sct}$.

Simple Backpropagation reconstructs χ directly from the scattered field

$$\chi = \mathbf{M}^\dagger[\hat{\mathbf{p}}_j^{sct}], \quad (9.16)$$

where $\mathbf{M}^\dagger[\hat{\mathbf{p}}_j^{sct}] = \sum_{j,\omega} \omega^2 [\hat{\mathbf{p}}_j^{inc}(\mathbf{x}') \hat{G}(\mathbf{x}' - \mathbf{x}')]^* \hat{\mathbf{p}}_j^{sct}(\mathbf{x}')$ is the adjoint of the integral operator \mathbf{M} and $*$ denoting the complex conjugate.

In the so-called Born inversion χ is calculated iteratively, e.g., by minimizing $E_n = \|\hat{\mathbf{p}}_j^{sct} - \mathbf{M}[\chi_n]\|$. This corresponds to finding a contrast function that best fits the measured data. Before the first iteration step, χ_0 is set to 0. Then χ_n is calculated based on the previous difference E_{n-1} between measured data and contrast function. This is repeated until E_n is smaller than a threshold or a certain number of iterations is reached.

In both cases, the speed of sound distribution of the reconstructed image can be calculated using χ_n in Eq. (9.13).

9.4.3 Paraxial Tomography

Reconstructions based on the paraxial approximation are often used in geophysics (Hung et al. 2000). In paraxial tomography, the wave propagation is computed mainly in one direction and the contributions from other directions are neglected. This reduces the required computational power since the wave propagation can be computed by an iterative layer-by-layer wave transport. Refraction, diffraction, and forward scattering are taken into account. Absorption can be modeled additionally. This reconstruction method has already been successfully applied to clinical data for speed of sound and attenuation reconstructions of a 2.5D system (André et al. 2013) that emits approximately plane waves. It has been extended for the use with spherical waves (Althaus 2015) recently, which will allow broader application to the more common USCT setups with cylindrical and spherical waves in future.

A quite effective method is to learn the forward model and to reconstruct the paraxial tomography with a neural network (Wang et al. 2020).

The brief introduction in the theory follows (Althaus 2015). For simplicity, the density is considered constant, the problem to be two-dimensional, and the medium lossless. Note that for the paraxial approximation, the 2D problem is usually denoted by x and z , where z is the direction in which the plane wave travels, i.e., the paraxial direction.

The inhomogeneous Helmholtz equation (9.4) may then be rewritten as

$$\nabla^2 \hat{p}(\mathbf{x}) + k_0^2 (1 + \eta(\mathbf{x}))^2 \hat{p}(\mathbf{x}) = 0, \quad (9.17)$$

where $k_0 = \frac{\omega}{c_0}$ is the wave number of the background and η is the refractive index.

The paraxial approximation of the Helmholtz equation is found by first transforming the pressure \hat{p} with $\hat{p} = e^{ik_0 z} \hat{u}$ to an equation of its envelope with

$$\begin{aligned} \partial_{xx} \hat{u} + \partial_{zz} \hat{u} + 2ik_0 \partial_z \hat{u} \\ + k_0^2 ((1 + \eta(\mathbf{x}))^2 - 1) \hat{u} = 0. \end{aligned} \quad (9.18)$$

The envelope \hat{u} contains the deviation of \hat{p} from a plane wave. Introducing operator $Q = \sqrt{1 + (\frac{1}{k_0^2} \partial_{xx} + (1 + \eta)^2 - 1)}$ and assuming that η varies only very slowly in z direction ($\partial_{zz} \approx 0$), the Eq. (9.18) can be factorized into two parts

$$(\partial_z + ik_0 + ik_0 Q)(\partial_z + ik_0 - ik_0 Q)\hat{u} = 0. \quad (9.19)$$

The first part on the left-hand side describes the propagation of the wave in $-z$, i.e., the reflected wave, and the right part in $+z$ direction, i.e., the transmitted wave.

Considering only the wave propagation in $+z$ direction, the paraxial approximation can be written as

$$\partial_z \hat{u} + ik_0 (1 - Q)\hat{u} = 0. \quad (9.20)$$

The forward problem, i.e., the calculation of \hat{p} for given η and \hat{p}^{inc} , can now be solved numerically by the split step formulation. The pressure \hat{p}_{n+1} at position z_{n+1} is calculated based on \hat{p}_n at

$z_n, n = 1 \dots N$,

$$\hat{\mathbf{p}}_{n+1} = e^{ik_0\eta_n\Delta z} \times \mathcal{F}^{-1}\{e^{i k_0 \sqrt{1 - (\frac{2\pi}{\Delta x N k_0})^2} \Delta z} \mathcal{F}\{\hat{\mathbf{p}}_n\}\}, \quad (9.21)$$

with \mathcal{F} the (discrete) Fourier transformation over space. Setting $\hat{\mathbf{p}}_0 = \hat{\mathbf{p}}^{inc}$, one can incrementally calculate the pressure at discrete z_n .

Different approaches have been proposed for the backward problem of reconstructing c from known $\hat{\mathbf{p}}^{inc}$ and measured data $\hat{\mathbf{f}}$. In Althaus (2015), the problem is solved similarly to the Born inversion described in the previous subsection by iteratively minimizing the error between the measured data and the simulated data for the current estimate of η with $E_n = \|\hat{\mathbf{p}}_j^{sct} - \mathbf{p}_N\|$. For this simple case, it is assumed that the receivers are located at z_N .

9.4.4 Ray Tomography

In ray tomography, an ultrasound pulse is assumed to travel on an infinitely thin beam. Diffraction and scattering are thus neglected. This assumption is based on the limiting case for infinitely small wavelengths or infinitely high frequencies, similar to the assumptions for geometrical optics. Allowing for refraction of the ray, the Eikonal ray approximation is obtained. For rays traveling directly from emitter to receiver without refraction, the straight ray approximation is obtained, see Fig. 9.4. Both approaches are used for transmission tomography, i.e., either the speed of sound or the attenuation distribution can be calculated using the pulses received on the fastest or shortest paths from emitter to receiver, respectively.

In Eikonal tomography, the refracted path between transmitter and receiver is calculated iteratively on a current voxel model of the object. The model of the object is then recomputed for these new paths. Examples of Eikonal tomography for 2D systems are Schomberg (1978), Andersen (1990), Li et al. (2009) and for 3D systems Dapp et al. (2012).

Straight ray tomography is based on the most limiting approximation, neither refraction, diffraction nor scattering are considered. However, since it is very fast to compute, it is widely used, e.g., Glover (1977), Greenleaf et al. (1974), Dapp (2013), and Li et al. (2008).

In contrast to previous methods, the achievable resolution of the resulting images is very limited in ray tomography techniques. Because diffraction and scattering are neglected, effects from the first Fresnel zone around the direct path are ignored (Spetzler and Snieder 2004). The first Fresnel zone corresponds in 2D to an ellipse with emitter and receiver at the focal points and includes all scatterers that can interfere with transmission, see Fig. 9.5. The position of scatterers located in this zone cannot be unambiguously determined without modeling diffraction and scattering. This leads to uncertainty in the position reconstruction, which in the worst case corresponds to the maximum width of the first Fresnel zone of $\sqrt{L\lambda}$, where L is the distance from emitter to receiver and λ is the wavelength of the wave (Williamson 1991). Thus, for 2.5 MHz in water, an L of 20 cm results in a position uncertainty of about 1 cm.

One method for reconstructing sound speed images (Dapp et al. 2011) is to discretize the problem and write the forward problem as

$$\mathbf{As} = \mathbf{b}. \quad (9.22)$$

Here, the matrix \mathbf{A} describes the paths the rays travel through the slowness map \mathbf{s} to generate the arrival time measurements in \mathbf{b} . The slowness map is the inverse of the speed of sound map, i.e., $s_j = 1/c_j$.

Since \mathbf{A} is usually very large and sparse and the problem is often ill-posed, direct inversion is often not possible. Hence the speed of sound distribution of the imaged object is then iteratively calculated by minimizing an error term describing the differences between the simulated and measured arrival times, e.g., $E = \|\mathbf{As} - \mathbf{b}\|^2$.

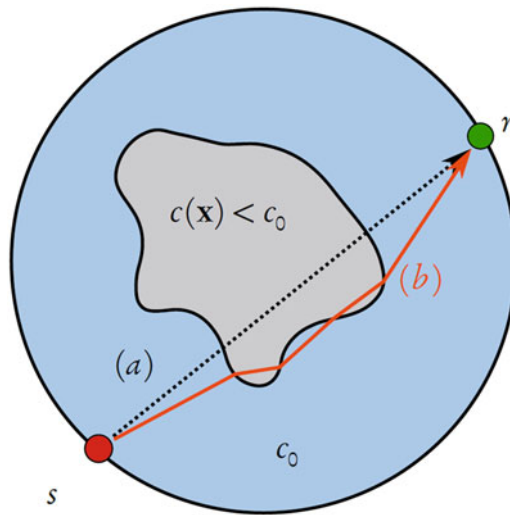


Fig. 9.4 Example for straight and refracted beams from Dapp (2013): Path (a) is the shortest and path (b) the fastest path connecting emitter e (red) and receiver r (green)

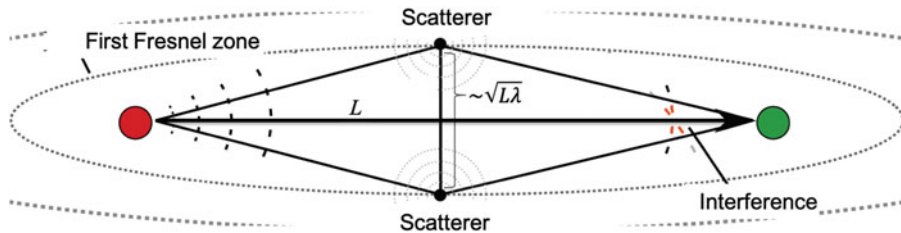


Fig. 9.5 First Fresnel zone of emitter (red) and receiver (green): L is the distance of emitter and receiver. (Adapted from Dapp 2013)

9.4.5 Reflection Tomography

Reflection tomography (Norton and Linzer 1981) also assumes straight rays between the emitter, reflector, and receiver. However, the reflected amplitude of the ultrasound is used to reconstruct images. Reflection tomography is based on the Born approximation. In the simplest case, this assumes constant speed of sound, negligible attenuation, and single scattering. Reflection tomography is related to the B-scan method of conventional sonography. There, however, the optimal focus is only achieved at the focal point of the beam during transmission, whereas with USCT reflection tomography an ideal focus can be generated at any point in the image. This is due to acquiring fully unfocused data which is then focused to each point during the reconstruction. Many USCT systems use the Synthetic Aperture

Focusing Technique (SAFT) (Doctor et al. 1986) for reconstruction of reflectivity images.

The reconstruction can be performed in one step, e.g., in Özmen et al. (2015) described as

$$\chi = \sum_{j,t} \mathbf{p}_j^{sct}(\mathbf{t}) \delta(c_0 t - ||\mathbf{x}^s - \mathbf{x}|| - ||\mathbf{x}^r - \mathbf{x}||), \quad (9.23)$$

with j all combinations of emitters \mathbf{x}^s and receivers \mathbf{x}^r and t the discrete time samples of the measured field \mathbf{p}_j^{sct} .

9.4.6 Clinical Applicability of Reconstruction Methods

So far USCT devices with their algorithms are aimed at high image quality and are used for image-based diagnosis. In contrast to sonography,

it is not mandatory to acquire and reconstruct the images in real-time, because comparable to MRI, a structured volume is generated that can be stored and analyzed without the patient. The main challenge is to acquire the raw data fast enough to prevent blurring due to patient motion and enabling clinical applicability by reconstructions in the range of minutes to hours.

Since there is a certain amount of time available for reconstruction, the best possible image quality should be the main goal in the selection of possible algorithms. However, reconstructions based on the wave equation are very computationally expensive. Currently, only a few algorithms are available that have been tested with real data, and only two examples are used with clinically relevant timing with parallel hardware (Wiskin et al. 2012; Sandhu et al. 2015). They trade off by using frequencies well below 1 MHz, limiting the possible resolution.

The reconstruction methods, with the exception of simple ray and reflection tomography, generally use time-consuming iterative methods to solve the inverse problem. The two simpler methods can, in principle, be computed directly without iteratively estimating the object to be imaged. An exception is the algebraic reconstruction method (ART) for ray-based transmission tomography, where the iterative solution is used to solve an ill-posed inverse problem. Figure 9.6 shows a simplified comparison of the computational complexity of the algorithms as a function of the number of pixels or voxels in one direction (N) and the non-parallelized time duration. Not included in this overview is the potential of the algorithms for parallelization or use of alternative reconstruction methods. Some examples can be found in Hardt (2012), Kretzsch and Ruiter (2014), and Wang et al. (2020).

The O-notation (Thomas et al. 1990) is used to classify the complexity of the algorithms. It describes how the runtime and memory requirements change as a function of the size of the input parameters. The following assumptions were made for the input parameters:

- Number of discrete image points: in 3D $N = n_x = n_y = n_z$ with n_x, n_y, n_z the number of

points in each direction. An overall number of N^3 voxels have to be reconstructed. In 2D $N = n_x = n_y$ and $N_s = n_z$ number of slices in z direction and $N_s \ll N$. An overall number of $N_s \cdot N^2$ pixels have to be reconstructed.

- Number of emitters and receivers: $N = N_e = N_r$ with N_e number of emitting positions and N_r number of receiving positions per emission. The number is each assumed to be equal to N , which fits roughly the Nyquist theorem in 2D and results in N^2 A-scans.
- Number of iterations for iterative algorithms: N_{iter} , with $N_{iter} \ll N$.
- Number of swept frequencies for algorithms which use discrete frequencies: N_f , with $N_f \ll N$.
- Number of time samples in each A-Scan: N_t , with $N_t = N$.

Given these assumptions simple ray and reflection tomography algorithms are in the range of $O(N^2 \log N)$ to $O(N^5)$ which equals, e.g., a calculation in the range of seconds to minutes for 2D systems. On the other end, full-waveform tomography has a complexity of $O(N^6)$ in the 2D and $O(N^7)$ in the 3D case resulting in computation times in the range of days to months and years depending on the image resolution.

The system design strongly influences the computational complexity and limits the applicability of certain methods. For example, a fully unfocused 3D system (Ruiter et al. 2013) offers better 3D point spread function and less artifacts, but the third dimension increases the computational requirements for reconstruction by a significant factor. In comparison, for a 2D system (Duric et al. 2013) only 20 slices per breast need to be computed, but for a 3D system more than 1000 slices are generated. Thus, additional accelerations and approximations are necessary for reconstruction in a clinically applicable time frame (Hardt 2012).

9.4.7 Resources for USCT Data

A direct comparison of different implementations of algorithms is difficult, since they

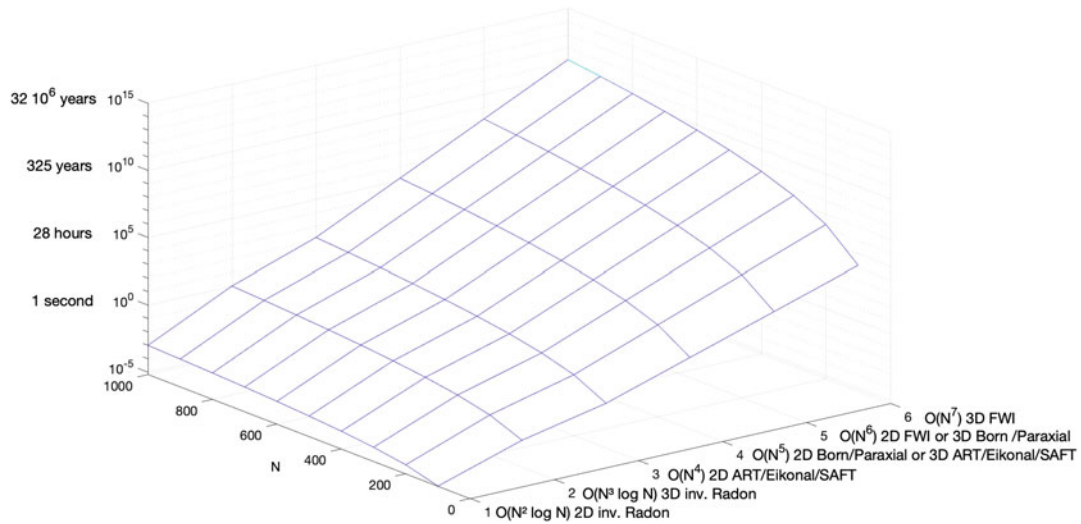


Fig. 9.6 Simplified comparison of the complexity of reconstruction algorithms used for USCT based on the assumption that 3D Fourier transform could be calculated in 1 s for $N = 1000$

are usually applied to custom simulated data or—if available—real data. The relatively few experimental data sets are usually not widely available. Also, the different experimental setups usually require many adjustments for data processing and system modeling for the reconstruction algorithms. To address this gap, a USCT data exchange and collaboration initiative was launched to provide open and easy-to-use data and code interfaces and to stimulate the exchange of available reconstruction algorithms and raw data sets from different USCT instruments.

The reference database USCT Exchange and Collaboration Platform (2021) was established with freely available and openly licensed USCT data. It provides a tool for direct comparison of algorithms using the same data for reconstruction. Simulated data as well as real-world data sets are available. Figure 9.7 shows the real-world data sets. The first three phantoms were imaged using KIT’s 3D USCT, the fourth using TU Delft’s DBUS with a 2D low-frequency setup, and the last using the 2D system MUBI from the Spanish National Research Council and Complutense University Madrid (Ruiter et al. 2018). In addition, feedback on data and system architecture

from scientists working on the reconstruction will help drive further development of measurement setups.

9.5 Technical Challenges and System Design

A USCT device should both generate data that enables optimal imaging results and be suitable for clinical use, including patient safety and comfort, high patient throughput, and low cost of acquisition and operation. The practical challenges in developing such a system are summarized below.

9.5.1 Transducer Distribution

The 3D distribution of ultrasound waves in the measured volume has to be sampled temporally and spatially to obtain digitized data for the reconstruction. Similar to the sampling theorem for temporal signals, where the sampling rate and time window of an A-scan has to match the bandwidth and time duration used, the spatial sampling has to match the spatial frequencies of the imaged object, i.e., the inverse of the required resolution, and the object volume. The po-

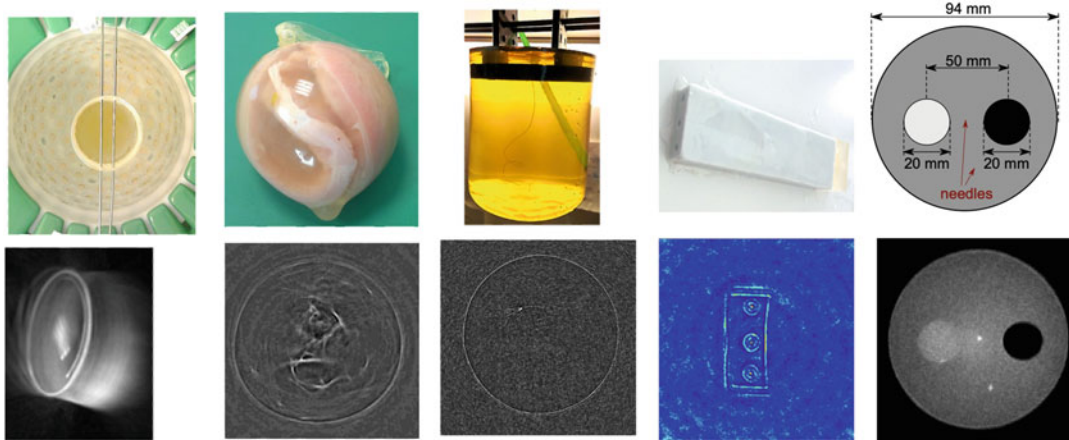


Fig. 9.7 Real-world phantoms of the USCT exchange platform (from left to right): gelatin, turkey, thread, agar, and tissue mimicking phantom with each SAFT reconstructions or spatial compounding (bottom right)

sitions of the transducers during data acquisition define the spatial sampling points of the data. This is usually a compromise between optimal distribution and number of available transducers, either real available transducers or virtual positions, usually obtained by multiple movements of available transducers.

Ideally, for a 3D volume such as the female breast, spatial sampling points would completely surround the object and sample at distances of $\Delta x/2$, where Δx is the resolution of the resulting images. However, this is practically impossible due to the accessibility of the object to be imaged and constraints imposed by the cost and complexity of the device, the resulting data size, and the reconstruction time. Therefore, various approximations of such apertures, i.e., the set of physically available and virtual transducer positions, have been proposed so far. Figure 9.8 shows diagrams and Fig. 9.9 shows realizations of such setups. Virtual transducer positions are created by mechanically moving either individual transducers, sets of transducers, or all transducers to additional positions and repeating the measurements with these new positions. The disadvantage of this method is a longer data acquisition time and, if the transducers cannot be positioned individually, a limited pattern of overall positions.

Simple laboratory experiments use only a few individual transducers or conventional sonogra-

phy scanners focused on azimuth direction. They are mechanically moved to many virtual positions and acquire the data from one 2D slice, e.g., Medina-Valdés et al. (2015). Typical data acquisition times are many minutes to several hours. They are therefore mostly used for imaging phantoms.

For the use in paraxial tomography, systems with linearly grouped transducers have been used in 1D (Chen et al. 2016) and 2D arrays (Wiskin et al. 2011). The transducers have to be rotated around the object and also moved in the azimuth direction to obtain virtual positions. It has been reported that data acquisition will take several minutes.

The most commonly used aperture design is grouping transducers on a ring, e.g., Roy et al. (2013). The ring is usually densely populated with transducers, e.g., 2048 transducers on a ring of 22 cm diameter for 3 MHz center frequency. The transducers are unfocused in x-y direction and focused on z (azimuth) direction. The ring is mechanically moved in z-direction and acquires data for 2D slices, with, for example, 20 to 40 slices. Typical duration for data acquisition is 1 to 5 minutes per breast. An interesting approach was proposed by Rouyer et al. (2012). There, the transducers were grouped on a semicircle with diameter 20 cm and the semicircle could be

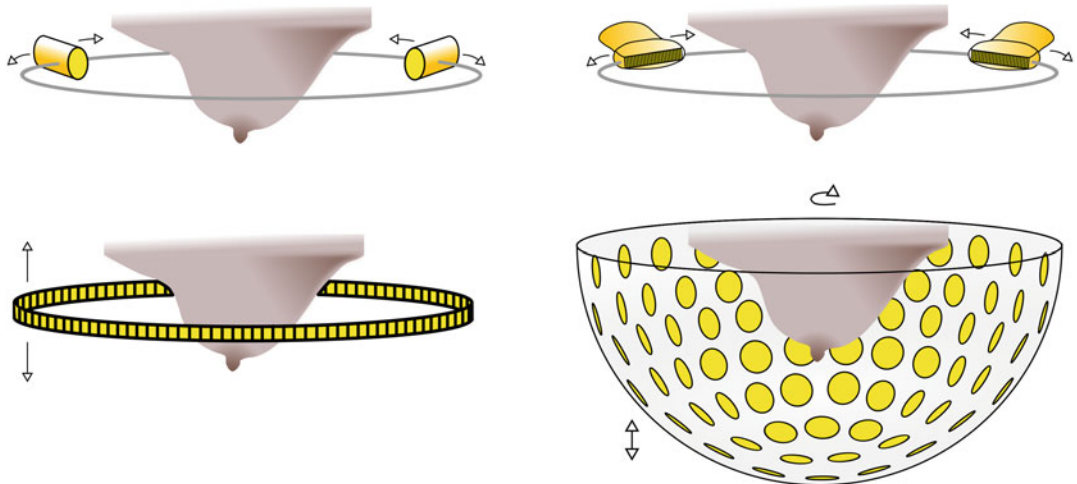


Fig. 9.8 Different setups for USCT systems imaging a breast are shown in this diagram. Top left: 2D slice acquisition with individual and freely positioned transducers (yellow). Top right: 2D slice acquisition with individual and freely positioned linear transducer arrays. Bottom left:

2D slice acquisition with a ring of transducers. Bottom right: 3D acquisition with hemispherical array. Arrows indicate the typical degrees of freedom for mechanical motion of the transducers

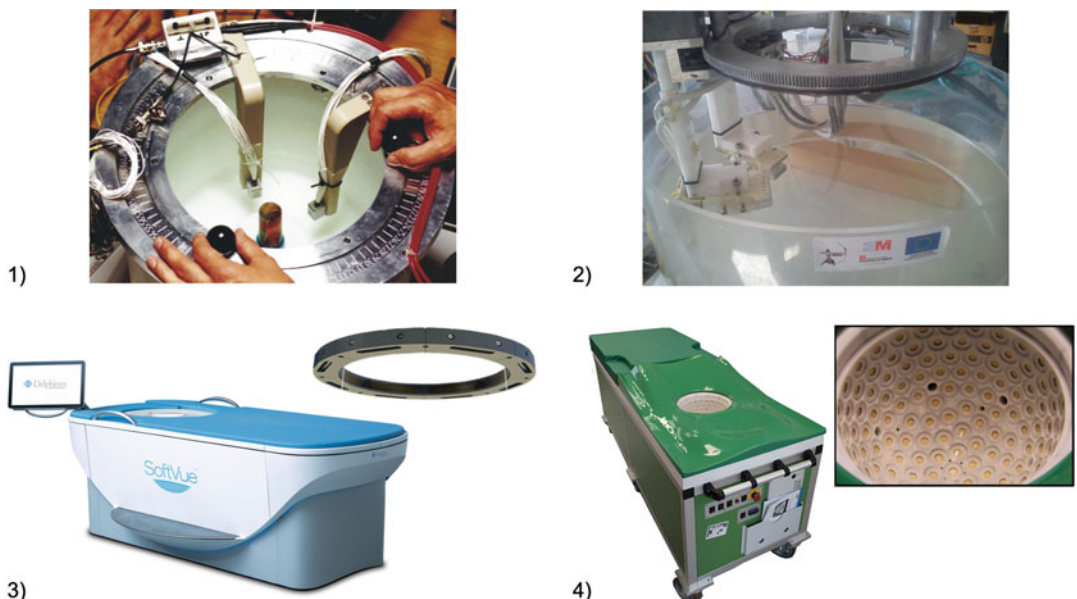


Fig. 9.9 Top left (1): 2D slice acquisition with individual and freely positionable transducers of the first experimental USCT at KIT (Stotzka et al. 2004). Top right (2): 2D slice acquisition with individual and freely positionable linear transducer arrays of the first MUBI system (Camacho et al. 2012). Bottom left (3): 2D slice acqui-

sition with a ring of transducers in Delphinus' SoftVue system (Courtesy of Neb Duric, CTO, Delphinus Medical Technologies). Bottom right (4): 3D acquisition with semiellipsoidal array of KIT's 3D USCT II (Ruiter et al. 2011)

moved with two degrees of freedom, allowing also sagittal slices.

3D systems based on a cylinder, a half ellipsoid (Ruiter et al. 2011), and a hemisphere (Gemmek et al. 2018) have been presented. The number of transducers ranges up to 2304, so mechanical repositioning of the entire transducer aperture is also used to achieve denser sampling. The transducers transmit and receive approximately spherical waves for full 3D imaging. Data acquisition time ranges from 1 to 6 minutes. Due to the unfocused transducers, no reflections are lost between layers and isotropic resolution in 3D is possible.

9.5.2 Ultrasound Transducers for USCT

The ultrasound transducers that usually operate in the lower frequency range, i.e., 1 to 3 MHz, are required to have a large bandwidth and either emit or receive spherical waves for 3D imaging or cylindrical waves with azimuthal focus for 2D slice imaging. Typically, trade-offs are made between the resulting low local acoustic pressure and the need for an acceptable signal-to-noise ratio.

The frequency range and the 3D distribution of the generated ultrasound field is mainly dependent on the geometry of the active elements of the transducers. The thickness of the elements in the main direction of vibration determines the resonance frequency. The radiating area and diameter determine the angular characteristic, see Fig. 9.10 for examples.

The frequency range of most systems is centered around 2 to 3 MHz, with a wide bandwidth, i.e., more than 50%. The center frequency is a compromise between image resolution and size of the imaged volume. The higher the frequencies, i.e., the smaller the wavelength λ , the higher the possible resolution, see Table 9.2. However, ultrasound absorption also increases with frequency. The local sound pressure is additionally reduced by the propagation of the wave as a function of the distance traveled. Thus, the use of high frequencies is limited by the size and absorption of the object and the total distance of the transducers in

the aperture, since the sensitivity of the receivers is limited. Currently, systems operating at lower frequencies around 1 MHz are becoming more popular (Sandhu et al. 2015; Wiskin et al. 2013). This is because FWI and paraxial tomography have become computationally feasible at these lower frequencies. They also have additional advantages, e.g., they can be applied to body parts that contain bone, such as joints or the skull, due to the lower absorption, and also reduce the overall complexity of the system by allowing for less dense spatial sampling.

A 2D system would typically use a rod-shaped active element, see Fig. 9.10 top row, with large opening angle in xy direction and narrow angle in azimuth direction to image approximately 2D slices. The thickness of the slice can be further reduced with acoustic lenses. Note that the layer thickness is smaller near the transmitter and increases with distance. Thus, the total layer thickness is an average value. A 3D system usually uses square or disk-shaped transducers, see Fig. 9.10 bottom row, to achieve large opening angles in 3D.

Since the transducers in most systems have small active areas and are fired individually, the amplitude of the emitted pressure and the sensitivity of the receivers is low, resulting in a low signal-to-noise ratio. For this reason, the area of the active element is often set as a compromise between ultrasound pressure and opening angle. Also, amplification electronics may be present near the transducers and the gain of the channels can be set individually or object-specific and time-dependent. Some systems additionally use a so-called coded excitation (Misaridis and Jensen 2005). The advantage of coded excitation is that the emitted ultrasound energy can be distributed over time and recovered in the form of a much shorter decoded pulse, which significantly increases the SNR.

9.5.3 Data Acquisition and Processing

For a short duration of imaging and especially to avoid blurring of data due to patient movement,

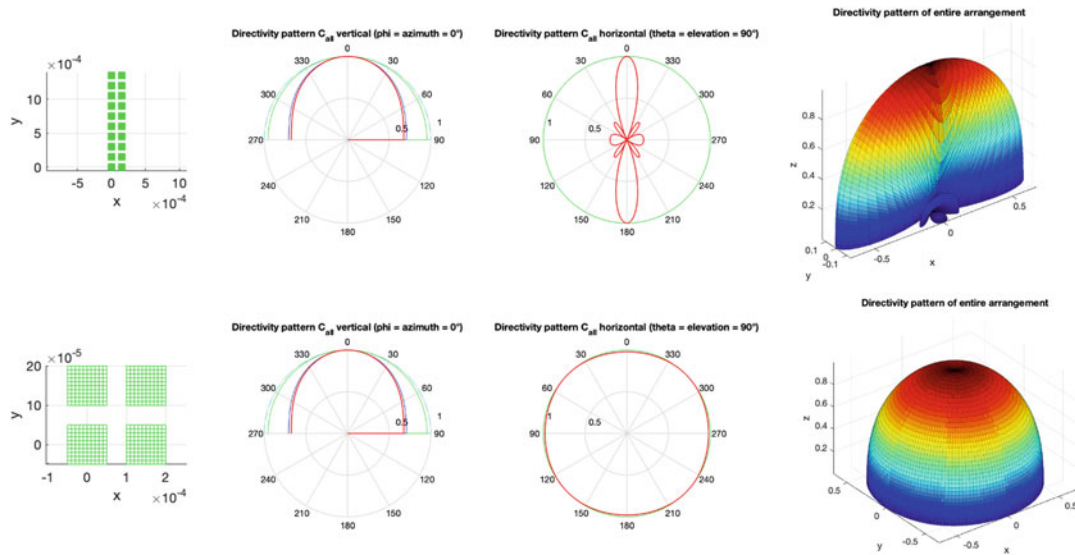


Fig. 9.10 Beam patterns of a rectangular and a quadratic transducer element: Top: Rectangular element with $0.25 \text{ mm} \times 1.45 \text{ mm}$ area. Bottom: Quadratic element with $0.25 \text{ mm} \times 0.25 \text{ mm}$ area. Both for a 2.5 MHz excitation in

water. Left: Active area in m. Left center: -3 dB intensity limit in xy-plane (red). Right center: -3 dB intensity limit in yz-plane (red). Right: -3 dB surface in 3D. Both elements emit in z-direction

data acquisition in systems for medical use must be fast and is performed with hundreds of parallel channels. Computing power for reconstruction has to be high to obtain images in clinically relevant time.

Data acquisition and image reconstruction are often performed separately in USCT devices: After the fastest possible data acquisition, the data are stored in the device or on an external storage medium for offline image processing.

After data acquisition, the signals are preprocessed and image reconstruction is performed. The separation into two systems has several advantages: The development of the data acquisition hardware can be decoupled from the development of the reconstruction algorithms and their platform. Heat generation and appropriate countermeasures in the device need only be considered for the data acquisition (DAQ) hardware. The reconstruction algorithms and corresponding acceleration hardware can be adapted to some extent during the clinical trial, since changes to the device itself are often only possible with renewed approval. For more complex reconstruction algorithms with longer computation times,

the device can be used to continuously image patients without waiting for the reconstruction to finish. One drawback is the additional time required to transfer data from the USCT device to the reconstruction hardware, which can be significant due to the large amount of raw data acquired.

9.5.4 Calibration

Calibration is an important part of initialization and maintenance of USCT systems. It can be divided into spatial calibration, temperature calibration, and calibration of the measurement chain of signals.

Spatial calibration involves determining the position of the transducers. For high resolution imaging, the position must be known better than $\lambda/2$, e.g., for 2.5 MHz this would correspond to an accuracy better than 0.3 mm. This could be achieved by building the aperture and transducers with high precision. Alternatively, the positions can be determined by measurements, see e.g., Rouyer et al. (2012); Tan et al. (2015).

Since ultrasound travels through water over long distances and the speed of sound in water depends on temperature, this must also be monitored. Here, calibration of the internal temperature measurement devices may be necessary, or temperature or speed of sound can be calculated from empty measurements using known transducer positions.

The measurement chain of the signal contains the individual system responses of the transducers and the measurement channels. The transducers can differ in center frequency, bandwidth, sensitivity, and aperture angle. The DAQ channels can introduce delays and also have frequency-dependent transfer functions. Options for calibration of these channels are: 3D hydrophone measurements of the transducers, short-time measurements of the transfer functions of the channels, and the use of empty measurements. More detailed information can be found, for example, in Cueto et al. (2021).

9.5.5 Medical Products and Standards

Finally, the device must comply with the standards for medical devices in order to be applicable to the patient. These include the use of biocompatible materials, hygiene concepts for the water bath and other surfaces, ultrasound safety with limitation of the applied ultrasound energy and maximum pressure values, electrical and mechanical safety and electromagnetic compatibility (EMC). For the clinical use of the method, extensive clinical studies have to be performed to demonstrate the advantages and limitations of the method.

9.6 Applications and Current Limitations of USCT

The USCT method opens up exciting new possibilities for ultrasound imaging, providing high-quality images comparable to MRI with the added benefit of being quantitative. USCT is being developed primarily as a tool for

imaging in breast cancer prognosis, with other applications, e.g., joint and brain imaging, currently being explored. Other potential applications include combination with other modalities, e.g., photoacoustics, Doppler, etc., and use in therapy.

Nevertheless, the method is currently limited by the fundamentally different transducer setup compared to conventional sonography and the relatively long duration of data acquisition and image reconstruction, especially when compared to the real-time imaging capabilities of sonography.

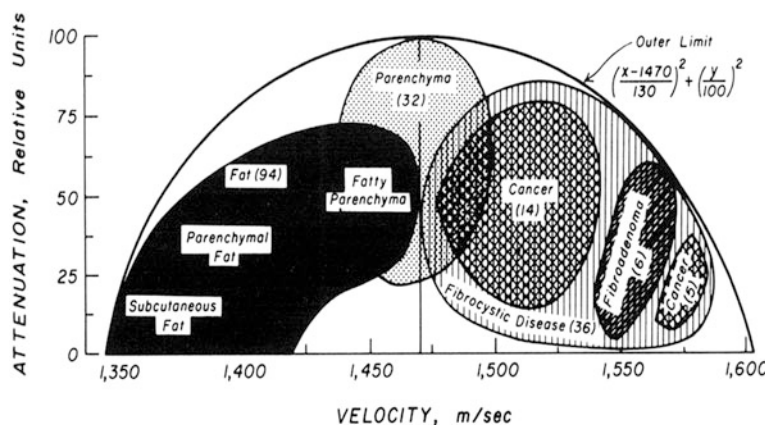
9.6.1 USCT and the Breast

Breast cancer is one of the most common cancers in women in the Western world (Fischer et al. 2007). Approximately one in ten women will develop breast cancer during their lifetime. Because early and mid-stage breast cancer is usually asymptomatic, screening is offered in many countries. The central goal of breast cancer screening is to detect tumors as early as possible and to avoid false positive diagnoses. Currently, the main method is X-ray mammography with sonography or MRI as a secondary diagnostic procedure. The USCT method is a promising candidate to improve the sensitivity and specificity of the current method, as it can also image the attenuation and speed of sound.

A number of early studies were performed to distinguish breast and cancer tissues based on their attenuation coefficients and speed of sound values (Calderon et al. 1976; Greenleaf 1977; D'Astous and Foster 1986; Edmonds et al. 1991; Mortensen et al. 1996). Greenleaf and Bahn (1981) published a correlation between attenuation and speed of sound with a USCT system in 1981, see Fig. 9.11. Here, different tissue types can be roughly classified by their combined values for attenuation and speed of sound. Similar results have been found with more recent USCT scanners, e.g., André et al. (2009), Hopp et al. (2015), and Duric et al. (2009).

Based on these results, several research groups are currently working on USCT systems

Fig. 9.11 Diagram of attenuation over speed of sound for normal and suspicious tissues of the female breast from Greenleaf and colleagues, reproduced from Greenleaf and Bahn (1981). Speed of sound is shown on the x-axis and normalized attenuation on the y-axis



for breast cancer diagnosis. In some cases, companies have been formed that are developing commercial systems and have FDA approval. Smaller clinical trials have been conducted by several groups and larger clinical trials have been started to show how effective the method is.

Delphinus Medical Technologies were founded in 2010 as a spin-off from the Barbara Ann Karmanos Cancer Institute (Duric et al. 2013). They reported successful smaller studies (Duric et al. 2014) and also engaged tracking the progress of chemotherapy (Duric et al. 2020) and breast density estimation for risk classification (Sak et al. 2020). Their large clinical study (Yamashita 2021) with approx. 8500 asymptomatic patients was completed in July 2021 and the system was FDA approved for screening in October 2021 (Delphinus Medical Technologies Inc 2021). A very impressive comparison between MRI and speed of sound images of different patients is given in Fig. 9.12.

QT Imaging, Inc. (formerly Techniscan and QT Ultrasound) reported successful clinical studies, the most recent publication being comparing speed of sound images with mammograms (Malik et al. 2020a). They have also conducted a smaller study on estimating breast density for risk classification (Malik et al. 2020). They completed a large study with approx. 750 patients in March 2021 (Case collection study to determine the accuracy 2021).

The 3D USCT II of KIT was evaluated in a smaller pilot study (Ruiter et al. 2013) and is currently employed in a concordance study. The successor system is aimed at a larger multi-center study to be started in 2023 (Gemmeke et al. 2018).

For the MUT system of Mastoscopia good results in distinguishing benign and malignant smaller lesions (< 15 mm) with 71 patients (Zografos et al. 2015) was reported.

Other upcoming systems are planning or have started trials, e.g., Suzuki et al. (2021) and Ding et al. (2018).

Although USCT is not yet a standard of clinical practice, clinical trial results and FDA approval of the first device for breast cancer screening demonstrate the method's potential for the future.

9.6.2 Beyond the Breast: More Applications of USCT

The female breast has been the main application of USCT systems because it is relatively easy to access from many angles and does not contain bone or other ultrasonically hard structures. Bone is highly attenuating to ultrasound at high frequencies, and because of its high density, the assumptions in Sect. 9.3 are not tenable. Nevertheless, the following experimental applications

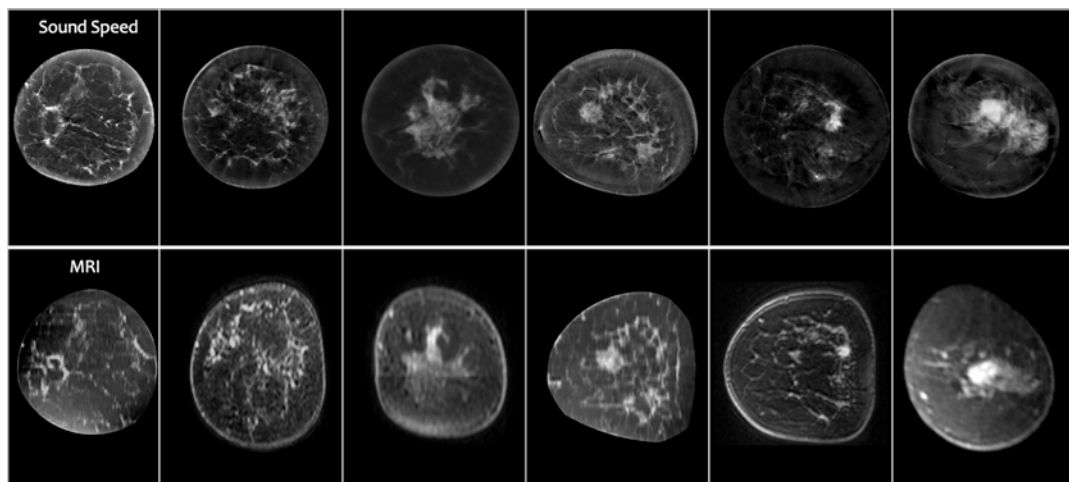


Fig. 9.12 Comparison of coronal speed of sound and MRI slices of different patients for the Delphinus SoftVue system. Speed of sound in the top row and MRI in the

bottom row. Courtesy of Neb Duric, CTO, Delphinus Medical Technologies

of USCT systems show that imaging is possible with some adjustments. This pioneering work could open the application to many other parts of the body.

9.6.3 Joints

First, Lasaygues et al. (2018) published several papers on USCT of ex vivo bones and obtained impressive results. Ding et al. (2018) and colleagues demonstrated initial slice images of the arm and leg of a living subject.

Wiskin and colleagues examined imaging of a cadaveric knee (Wiskin et al. 2019, 2020a). They used fused images from reflectivity and paraxial tomography and compared them to MRI. They were able to reproduce the 3D geometry of the knee in great detail and the sound velocity values of the soft tissues (fat, muscle, tendon, cartilage) agreed very well with values from the literature. They extended this work in a study of limited angle tomography (Wiskin et al. 2020b). The applications of these images could be in the diagnosis, monitoring, and grading of muscular dystrophy and osteoarthritis.

9.6.4 Brain Imaging

Guasch et al. (2020) investigated 3D FWI tomography of the brain in simulations and real experiments. They simulated a hemispherical 3D array of 1024 low-frequency transducers in the range of 100–850 kHz. Brain structures including a simulated hemorrhage could be imaged with high resolution and high contrast. In addition, it was shown that ultrasound signals could be received with sufficient SNR through the skull of a subject at the low frequencies used.

Applications of this method could be in rapid diagnosis of stroke and head trauma as well as routine monitoring of various neurological diseases.

9.6.5 Ultrasound Therapy and USCT

Thermoablation is a therapeutic method in which focused ultrasound induces high temperatures above 60 °C in a focal region, resulting in cell death within seconds (Dubinsky et al. 2008). The method is completely noninvasive and has the potential to replace conventional surgery of small tumors (Yu et al. 2006).

Conventional thermal ablation is currently at the stage of clinical trials and initial applications. Limiting factors are the long duration of up to several hours, difficult-to-control ultrasound focusing, local hot spots, and the need for image-guided monitoring (Qian et al. 2006).

USCT could directly monitor ablation using the change in speed of sound due to heating. It could also significantly speed up thermal ablation by applying multiple focal points similar to the method proposed by Fab (Fan and Hynynen 1996). The complex 2D phased array used there to generate the multiple foci could be replaced by a USCT system. In particular, 3D USCT with its many transducers positioned around the imaged object can be considered as a huge non-planar 2D array. With simultaneous application of all emitters and focusing on one point, the total acoustic pressure of all available transducers in such a system would result in foci with several megapascals of acoustic pressure, sufficient for thermal ablation (Dubinsky et al. 2008). Currently, the electronics of USCT systems are not designed to be triggered as a 2D phased array. Adapting the electronics is a task that is challenging but feasible.

9.6.6 Modalities beyond Reflectivity, Speed of Sound and Attenuation

Conventional ultrasound systems can usually provide Doppler and sometimes elastography modes in addition to B-scan images. Doppler maps the local blood flow distribution and elastography images the tissue stiffness distribution. Both modalities provide valuable additional diagnostic information for cancer diagnosis and functional imaging. The modalities are feasible in principle with USCT systems. For Doppler, methods similar to those used by Jensen et al. (2016) for SAFT-based Doppler imaging, i.e., synthetic aperture flow imaging, could be used. Currently, the major limitation is the DAQ speed of the USCT systems.

Spatial compounding for breast ARFI images was first developed and analyzed by Salido et al.

(2016). A proposal and simulations how to perform elastography with a USCT system was given by Hopp and Ruiter (2021). There, strain elastography was realized using two USCT images of an undeformed and a mechanically deformed breast.

Microbubbles are tiny air bubbles used as contrast agents in conventional sonography (Szabo 2014). The bubbles are injected into the patient and ultrasound is strongly reflected off the bubbles. They are used to image cavities, such as the heart or blood vessels, or to create nonlinear effects to increase image contrast. Alternatively, high sound pressure can be applied to destroy the bubbles. This is mostly used for therapy, e.g., local drug delivery or opening the blood-brain barrier.

Recent applications include rapid imaging of microbubbles and tracking their movements to produce super-resolution images of small vessels (Chen et al. 2021). For this purpose, the so-called ultrafast ultrasound imaging methods (Tanter and Fink 2014) are used. There, plane waves from different angles are used to image the object with high repetition rates. Initial publications showed impressive results in imaging microvessels in a rat brain (Errico et al. 2015). The use of ultrafast Doppler showed the possibility for functional imaging of the brain, which was previously only possible with MRI (Tanter and Fink 2014). Similarly, Doppler imaging of microbubbles or super-resolution imaging can theoretically be applied in USCT systems but is currently limited by the DAQ rate and, to some extent, the low acoustic pressures used in USCT.

Photoacoustics is a promising imaging technique based on laser-induced ultrasound. Short laser pulses locally cause the tissue to oscillate and are thus a source of ultrasound waves. The emissions are recorded with ultrasound transducers in setups similar to USCT systems. The intensity of the emitted ultrasound depends on the absorbed light, i.e., the wavelength of the laser and the illuminated tissue type. In particular, red lasers can be used to produce impressive images of vascularization, i.e., the distribution of blood vessels, of structures such as cancerous tumors. However, the method is limited by the penetration depth of the light into the body. Therefore, and

because of the similarity of the receiving aperture to USCT systems, combinations of the methods are currently being investigated, e.g., Manohar and Dantuma (2019).

Beyond the already existing ultrasound modalities, additional information can be retrieved from the rich USCT data due to the complex interaction of the waves with the tissue, see Sect. 9.3. For example, the data can be used to generate scatter characteristics of pixels (Kretzek et al. 2015). For reflectivity tomography, the reflected amplitudes of an image point are simply summed up. Thus, for directional scattering, the characteristic information of the scatterers is lost. SAFT can be extended to obtain reflectivity characteristics. Instead of summing over all A-scans, the two-dimensional reflectivity characteristics can be reconstructed for each voxel over angles. In the long term, this modality could also be used to obtain information similar to tissue-specific speckle texture in sonography.

9.6.7 Current Limitations and Possible Solutions

The current advantages of conventional sonography over USCT are the many applications, multiple established modalities, and real-time imaging.

The many applications, i.e., imaging of different body structures, are possible because sonography uses back reflection for imaging with linear arrays and the array are mainly in direct contact with the structure to be analyzed.

As a result, ultrasound travels smaller distances and body parts that are partially shadowed by bone or air-filled structures can be imaged without having to traverse these areas. However, as shown previously, it is possible to extend USCT imaging to areas that contain bone. Thus, this disadvantage of USCT may be overcome in the future at least partly, especially with the use of lower frequency ranges and advanced image reconstruction algorithms.

Enclosing the body with ultrasound transducers is challenging, and coupling to the patient by a water bath is also not very practical. This could be solved, for example, with water-filled contact

balloons or a flexible transducer aperture that can be placed directly on the patient surface. A hybrid approach could be to extend USCT image reconstruction methods to the use with limited angle view reconstructions, as shown by Wiskin et al. (2020b).

In the future, the established modalities of sonography can either be implemented, improved, or extended with speed of sound and attenuation tomography. For future implementation of established modalities such as Doppler, the main challenges are the low acoustic pressure of USCT and the relatively slow data acquisition.

An established method of dealing with low sound pressure is the use of phased arrays to generate so-called virtual sources (Nikolov and Jensen 2002). In contrast to focusing the sound beam as used in conventional sonography, the virtual sources are generated near the array and act as sources of approximately spherical waves. Since the entire active area of the phased array can be used to generate the virtual source, the total radiated sound pressure is approximately the same as in sonography. For this purpose, the transmitting electronics of the USCT systems have to be adapted to allow the individually delayed excitation of multiple transducers.

The current duration of data acquisition for USCT systems is limited primarily by the need to mechanically move the transducers. Other factors that increase the duration of data acquisition are multiplexing and the averaging factor of the systems. Multiplexing is used when more than one receiver shares a DAQ channel. Averaging involves acquiring the same A-scan from the same transmitter-receiver combination multiple times to add these A-scans together to increase SNR.

The lower limit for the duration of data acquisition is the time it takes for the ultrasound pulses to travel through the imaged volume. Since ultrasound is reflected and scattered in tissue, this is usually estimated by the longest distance from a transmitter to the furthest point plus the distance from that point to the furthest receiver. It depends on the spatial dimensions of the imaged volume or slice, the speed of sound range, and the transducer distribution. An additional waiting time is usually added to allow the sound intensity in the volume

to decay to a certain threshold. This duration is then multiplied by the number of emissions for the device.

In sum the data acquisition time T of most systems can be calculated by:

$$T = N_s \cdot N_{em} \cdot T_{prop} \cdot N_{mult} \cdot N_{ava} + (N_s - 1) \cdot T_{mo}$$

with N_{em} the number of emissions, T_{prop} the propagation time of the ultrasound wave, N_{mult} the multiplex factor, N_{ava} the averaging factor, N_s the number of slices in a 2D ring system or the number of aperture positions in a 3D system, and T_{mo} the time for the mechanical motion. In Table 9.3 some examples are given. The first six rows give examples for a 2D system with a ring of transducers, the last six rows for a 3D system with a hemispherical aperture. The numbers given are based on current systems, and for each type of system the last rows estimate the values for existing systems, i.e., previous 2D ring of Delphinus (Roy et al. 2013) (row 6) and the two 3D systems of KIT (Ruiter et al. 2011; Gemmeke et al. 2018) (rows 11 and 12).

T_{prop} was simplified and calculated as $T_{prop} = 2 \cdot (2d)/c$ with d diameter of the ring, c speed of sound of water at 1500 m/s and doubling the time to fade the ultrasonic intensity.

In general, for all configurations, the data acquisition time is dominated by the time required to mechanically move the transducers, i.e., T_{mo} and especially for 2D systems by the averaging N_{ava} and the multiplex N_{mult} factors (row 5). Reducing the diameter d (rows 4) and the number of emitters N_{em} by a factor of 2 (row 3) does lead to a slight increased speed. As expected, the 3D system is faster compared to the 2D acquisition (e.g., rows 2 and 8), although it should be noted that the acquired amount of data is much sparser in most examples, i.e., for the 3D example (rows 8), only 10 % of the A-scans are acquired. For a hypothetical 3D system (row 10) with no motion and the same number of A-scans and diameter as the real 2D system (row 6), the DAQ time is less than 3 seconds compared to 1 minute.

The duration of data acquisition is limited only by the transit time of the ultrasound and

the number of transmitting positions if the acquisition hardware and number of transducers are optimized. However, for the given examples without motion (rows 1, 7, 10), the duration is still greater than 1 second. To approach higher frame rates, further developments are necessary, e.g., by simultaneous transmission at multiple positions with coded pulses as described by Misaridis and Munk (2004).

The challenges of using the advanced image reconstruction algorithms are currently addressed by parallel computation (GPUs or FPGAs) using either simpler algorithms or 2D lower frequency systems. In the future, this could only be addressed by improved computational speed and more memory (Moore's law) or by advances in the reconstruction algorithms. A promising approach is to use neural networks for the advanced reconstruction algorithms, e.g., Wang et al. (2020), since these require an enormous computational effort for training but, once trained, can perform reconstructions very quickly.

9.7 Summary

USCT is an old concept from the early days of medical ultrasound imaging, but only became technically feasible for clinical application in the last decade. Currently, several research groups around the globe are working on improving reconstruction algorithms, developing optimal setups, and are conducting clinical evaluation.

A major breakthrough in recent years has been the application of reconstruction methods that completely solve the acoustic wave equation, i.e., FWI and paraxial tomography. They now allow speed of sound imaging at high resolution and are beginning to rival MRI in contrast and diagnostic information. However, due to the large computational requirements, there are still many challenges to be solved before these methods can be widely used.

System design of an optimal device is still a subject of research. Due to the simplicity of the design, 2D ring systems are the most commonly built systems. However, they limit the overall

Table 9.3 Example duration of DAQ for different system specifications (rounded)

Row	System	d in cm	N_{em}	T_{prop} in ms	N_{mult}	N_{ava}	N_s	T_{mo} in s	T in s
1	2D ring	30	2048	0.8	1	1	1	–	1.6
2		30	2048	0.8	1	1	40	0.5	85.0
3		30	1024	0.8	1	1	40	0.5	52.3
4		20	2048	0.5	1	1	40	0.5	63.2
5		30	2048	0.8	4	4	40	0.5	1068.1
6		22	1024	1.0	2	1	20	1	59.0
7	3D hemi-sphere	30	2048	0.8	1	1	1	–	1.6
8		30	2048	0.8	1	1	4	0.5	8.1
9		30	2048	0.8	4	1	4	0.5	106.4
10		22	4579	0.6	1	1	1	–	2.7
11		24	628	0.6	3	8	10	30	360.4
12		36	2304	0.8	6	4	2	20	108.5

measurement speed because many mechanical motion steps are required and lead to large layer thickness and artifacts due to 2D data acquisition. Other setups will certainly become popular in the future, but the additional cost and complexity of the more sophisticated hardware has to be justified by significantly improved imaging results.

The clinical performance of the method is currently being evaluated for breast cancer diagnosis. The initial results are very promising. An extension to other application areas, e.g., imaging of joints or the human brain, seems possible but is still a field of early research.

References

- Althaus L (2015) On acoustic tomography using paraxial approximations. Master thesis, Universität Darmstadt
- Andersen AH (1990) A ray tracing approach to restoration and resolution enhancement in experimental ultrasound tomography. *Ultrasound Imaging* 12(4):268–291
- André MP, Janee HS, Martin PJ, Otto GP, Spivey BA, Palmer DA (1997) High-speed data acquisition in a diffraction tomography system employing large-scale toroidal arrays. *Int J Imaging Syst Technol* 8(1):137–147
- André MP, Barker CH, Sekhon N, Wiskin J, Borup D, Callahan K (2009) Pre-clinical experience with full-wave inverse-scattering for breast imaging. In: Akiyama I (ed) Acoustical imaging, volume 29 of acoustical imaging. Springer, Netherlands, pp 73–80
- André M, Wiskin J, Borup D, Johnson S, Ojeda-Fournier H, Olson L (2012) Quantitative volumetric breast imaging with 3D inverse scatter computed tomography. In: Proceedings of the annual international conference of the IEEE engineering in medicine and biology society, EMBS, pp 1110–1113
- André M, Wiskin J, Borup D (2013) Clinical results with ultrasound computed tomography of the breast. Quantitative ultrasound in soft tissues. Springer, Berlin, pp 395–432
- Calderon C, Vilkomerson D, Mezrich R, Etzold KF, Kingsley B, Haskin M (1976) Differences in the attenuation of ultrasound by normal, benign, and malignant breast tissue. *J Clin Ultrasound* 4:249–254
- Camacho J, Medina L, Cruza J, Moreno J, Fritsch C (2012) Multimodal ultrasonic imaging for breast cancer detection. *Arch Acoust* 37(3):253–260. <https://acoustics.ippt.pan.pl/index.php/aa/article/view/89>
- Carson PL, Oughton TV, Hendee WR, Ahuja S (1977) Imaging soft tissue through bone with ultrasound transmission tomography by reconstruction. *Med Phys* 4(4):302–309
- Carson PL, Meyer CR, Scherzinger AL, Oughton TV (1981) Breast imaging in coronal planes with simultaneous pulse echo and transmission ultrasound. *Science* (New York, NY) 214(4525):1141–1143
- Case collection study to determine the accuracy, call back and cancer detection rates of qt ultrasound in breast imaging (accrue) (2021). <https://www.clinicaltrials.gov/ct2/show/NCT03052166>. Accessed: 2021-11-08
- Chen T, Shin J, Huang L (2016) Ultrasound transmission attenuation tomography using energy-scaled amplitude ratios. In: Duric N, Heyde B (eds) Medical imaging 2016: ultrasonic imaging and tomography, vol 9790. International Society for optics and Photonics, SPIE, Bellingham, pp 324–330

- Chen Q, Song H, Yu J, Kim K (2021) Current development and applications of super-resolution ultrasound imaging. *Sensors* (Basel, Switzerland) 21(7):2417
- Chenevert TL, Bylski DI, Carson PL, Meyer CR, Bland PH, Adler DD, Schmitt RM (1984) Ultrasonic computed tomography of the breast. Improvement of image quality by use of cross-correlation time-of-flight and phase-insensitive attenuation measurements. *Radiology* 152(1):155–159
- Cueto C, Guasch L, Cudeiro J, Agudo OC, Bates O, Strong G, Tang M-X (2021) Spatial response identification enables robust experimental ultrasound computed tomography. *IEEE Trans Ultrason Ferroelectr Freq Control* 69(1):27–37
- D'Astous FT, Foster FS (1986) Frequency dependence of ultrasound attenuation and backscatter in breast tissue. *Ultrasound Med Biol* 12(10):795–808
- Dapp R (2013) Abbildungsmethoden für die Brust mit einem 3D-Ultraschall-Computertomographen. Dissertation, Karlsruher Institut für Technologie
- Dapp R, Zapf M, Ruiter NV (2011) Geometry-independent speed of sound reconstruction for 3D USCT using a priori information. In: 2011 IEEE international ultrasonics symposium, pp 1403–1406
- Dapp R, Gemmeke H, Ruiter NV (2012) 3D refraction-corrected transmission reconstruction for 3D Ultrasound Computer Tomography. In: Bosch JG, Doyle MM (eds) SPIE medical imaging 2012: ultrasonic imaging, tomography, and therapy, pp 832014–832014–7
- Delphinus Medical Technologies Inc (2021) Delphinus receives FDA approval for its SoftVue 3D whole breast ultrasound tomography system. <https://www.delphinusmt.com/news/delphinus-receives-fda-approval-for-its-softvue-3d-whole-breast-ultrasound-tomography-system/>. Accessed: 2021-11-08
- Ding M, Song J, Zhou L, Wang S, Yuchi M (2018) In vitro and in vivo evaluations of breast ultrasound tomography imaging system in HUST. In: Duric N, Byram BC (eds) Medical imaging 2018: ultrasonic imaging and tomography, vol 10580. International Society for Optics and Photonics, SPIE, Bellingham, pp 162–169
- Doctor SR, Hall TE, Reid LD (1986) SAFT—the evolution of a signal processing technology for ultrasonic testing. *NDT Int* 19(3):163–167
- Dubinsky TJ, Cuevas C, Dighe MK, Kolokythas O, Hwang JH (2008) High-intensity focused ultrasound: Current potential and oncologic applications. *AJR Am J Roentgenol* 190(1):191–199
- Duric N, Littrup P, Li C, Rama O, Bey-Knight L, Schmidt S, Lupinacci J (2009) Detection and characterization of breast masses with ultrasound tomography: clinical results. In: McAleavey SA, D'hooge J (eds) SPIE proceedings vol. 7265: medical imaging 2009: ultrasonic imaging and signal processing, vol 7265. p 72651G
- Duric N, Littrup P, Chandiwala-Mody P, Li C, Schmidt S, Myc L, Rama O, Bey-Knight L, Lupinacci J, Ranger B, Szczepanski A, West E (2010) In-vivo imaging results with ultrasound tomography: report on an ongoing study at the Karmanos cancer institute. In: SPIE proceedings vol. 7629: medical imaging 2010: ultrasonic imaging, tomography, and therapy, p 76290M
- Duric N, Li C, Roy O, Schmidt S (2011) Acoustic tomography: promise versus reality. In: IEEE international ultrasonics symposium, IUS, pp 2033–2041
- Duric N, Littrup P, Schmidt S, Li C, Roy O, Bey-Knight L, Janer R, Kunz D, Chen X, Goll J, Wallen A, Zafar F, Allada V, West E, Jovanovic I, Li K, Greenway W (2013) Breast imaging with the SoftVue imaging system: First results. In: SPIE proceedings vol. 8675: medical imaging 2013: ultrasonic imaging, tomography, and therapy, vol 8675. p 86750K
- Duric N, Littrup P, Li C, Roy O, Schmidt S, Cheng X, Seamans J, Wallen A, Bey-Knight L (2014) Breast imaging with SoftVue: initial clinical evaluation. In: Bosch JG, Doyle MM (eds) Medical imaging 2014: ultrasonic imaging and tomography, vol 9040. International Society for Optics and Photonics, SPIE, pp 208–215
- Duric N, Littrup P, Sak M, Li C, Chen D, Roy O, Bey-Knight L, Brem R (2020) A novel marker, based on ultrasound tomography, for monitoring early response to neoadjuvant chemotherapy. *J Breast Imaging* 2(6):569–576
- Dussik KT (1942) Über die Möglichkeit hochfrequente mechanische Schwingungen als diagnostisches Hilfsmittel zu verwerten. *Z Neurol Psychiat* 174(183):153–168
- Edmonds PD, Mortensen CL, Hill JR, Holland SK, Jensen JF, Schattner P, Valdes AD (1991) Ultrasound tissue characterization of breast biopsy specimens. *Ultrasound Imaging* 13(2):162–185
- Errico C, Pierre J, Pezet S, Desailly Y, Lenkei Z, Couture O, Tanter M (2015) Ultrafast ultrasound localization microscopy for deep super-resolution vascular imaging. *Nature* 527(7579):499–502
- Fan X, Hynynen K (1996) Ultrasound surgery using multiple sonications—treatment time considerations. *Ultrasound Med Biol* 22(4):471–482
- Fischer T, Bick U, Thomas A (2007) Mammographie-Screening in Deutschland. *Vis J* 15:62–67
- Günter A (2002) Quantitative Analyse und objektive Darstellung von Ultraschallbildern zur medizinischen Diagnose. Dissertation, Universität Karlsruhe
- Gemmeke H, Berger L, Hopp T, Zapf M, Tan W, Blanco R, Leys R, Peric I, Ruiter NV (2018) The new generation of the kit 3D USCT. In: Proceedings of the international workshop on medical ultrasound tomography: 1.–3. Nov. 2017, Speyer, Germany. Hrsg.: T. Hopp. KIT Scientific Publishing, pp 271–282. 54.02.02; LK 01
- Glover GH (1977) Characterization of in vivo breast tissue by ultrasonic time of flight computed tomography. In: Proceeding of the national bureau of standards 2nd international symposium on ultrasonic tissue characterization, p 221
- Goncharsky AV, Romanov SY (2013) Supercomputer technologies in inverse problems of ultrasound tomography. *Inverse Prob* 29:075004

- Greenleaf JF (1977) Quantitative cross-sectional imaging of ultrasound parameters. In: Ultrasonics symposium proceedings, pp 989–995
- Greenleaf JF (1986) A graphical description of scattering. *Ultrasound Med Biol* 12(8):603–609
- Greenleaf J, Bahn RC (1981) Clinical imaging with transmissive ultrasonic computerized tomography. *IEEE Trans Biomed Eng* 28(2):177–185
- Greenleaf JF, Johnson SA, Lee SL, Herman GT, Wood EH (1974) Algebraic reconstruction of spatial distributions of acoustic absorption within tissue from their two-dimensional acoustic projections. In: Acoustic holography, vol 5. Springer, New York, pp 591–603
- Greenleaf JF, Ylitalo J, Gisvold JJ (1987) Ultrasonic computed tomography for breast examination. *IEEE engineering in medicine and biology magazine: the quarterly magazine of the engineering in medicine & biology society* 6(4):27–32
- Guasch L, Agudo OC, Tang M-X, Nachev P, Warner M (2020) Full-waveform inversion imaging of the human brain. *NPJ Digital Med* 3(1):28
- Hardt M (2012) Distributed simulations for 3D ultrasound computer tomography. Acoustic wave simulations for a new breast cancer imaging device. Ph.d. thesis, University of Karlsruhe
- Hesse MC, Salehi L, Schmitz G (2013) Nonlinear simultaneous reconstruction of inhomogeneous compressibility and mass density distributions in unidirectional pulse-echo ultrasound imaging. *Phys Med Biol* 58(17):6163–6178
- Holmes JH, Howry DH, Posakony GJ, Cushman CR (1955) The ultrasonic visualization of soft tissue structures in the human body. *Trans Am Clin Climatol Assoc* 66(C):208–225
- Hopp T (2012) Multimodal registration of x-ray mammography with 3D volume datasets. Ph.d. thesis, University Mannheim
- Hopp T, Ruiter NV (2021) Strain elastography with ultrasound computer tomography: a simulation study based on biomechanical models. In: Byram BC, Ruiter NV (eds) Medical imaging 2021: ultrasonic imaging and tomography, vol 11602. International Society for Optics and Photonics, SPIE, Bellingham, pp 194–201
- Hopp T, Duric N, Ruiter NV (2015) Image fusion of ultrasound computer tomography volumes with x-ray mammograms using a biomechanical model based 2D/3D registration. *Comput Med Imaging Graph* 40:170–181
- Howry DH, Bliss WR (1952) Ultrasonic visualization of soft tissue structures of the body. *J Lab Clin Med* 40:579–592
- Hung S-H, Dahlen FA, Nolet G (2000) Frechet kernels for finite-frequency traveltimes-II. Examples. *Geophys J Int* 141:175–203
- Jensen J, Nikolov SI, Yu A, Garcia D (2016) Ultrasound vector flow imaging: II: parallel systems. *IEEE Trans Ultrason Ferroelectr Freq Control* 63:1–1
- Johnson SA, Abbott T, Bell R, Berggren M, Borup D, Robinson D, Wiskin J, Olsen S, Hanover B (2007) Non-invasive breast tissue characterization using ultrasound speed and attenuation. In: Acoustical imaging. Springer, Netherlands, pp 147–154
- Keller JB (1969) Accuracy and validity of the Born and Rytov approximations. *J Opt Soc Am* 59(8):1003–1004
- Kelly KM, Richwald GA (2011) Automated whole-breast ultrasound: advancing the performance of breast cancer screening. *Semin Ultrasound CT MR* 32(4):273–280
- Klepper JR, Brandenburger GH, Busse LJ, Miller JG (1977) Phase cancellation, reflection, and refraction effects in quantitative ultrasonic attenuation tomography. In: 1977 ultrasonics symposium, pp 182–188
- Kretzek E, Ruiter NV (2014) GPU based 3D SAFT reconstruction including phase aberration. In: Bosch JG, Doyley MM (eds) Proceeding SPIE 9040, medical imaging 2014: ultrasonic imaging and tomography, p 90400W
- Kretzek E, Zapf M, Birk M, Gemmeke H, Ruiter NV (2013) GPU based acceleration of 3D USCT image reconstruction with efficient integration into MATLAB. In: Bosch JG, Doyley MM (eds) Proceedings of SPIE 8675, medical imaging 2013: ultrasonic imaging, tomography, and therapy, p 867500
- Kretzek E, Hucker P, Zapf M, Ruiter NV (2015) Evaluation of directional reflectivity characteristics as new modality for 3D Ultrasound Computer Tomography. In: 2015 IEEE international ultrasonics symposium (IUS)
- Lasaygues P, Rouyer J, Mensah S, Franceschini E, Rabau G, Guillermin R, Bernard S, Monteiller V, Komatitsch D (2018) Non-linear ultrasonic computed tomography (USCT) for soft and hard tissue imaging. In: Proceedings of the international workshop on medical ultrasound tomography, pp 77–88
- Lavarello RJ, Oelze ML (2009) Tomographic reconstruction of three-dimensional volumes using the distorted Born iterative method. *IEEE Trans Med Imaging* 28(10):1643–1653
- Li C, Duric N, Huang L (2008) Breast imaging using transmission ultrasound: reconstructing tissue parameters of sound speed and attenuation. In: BioMedical engineering and informatics: new development and the future - proceedings of the 1st international conference on bioMedical engineering and informatics, BMEI 2008, vol 2. pp 708–712
- Li C, Duric N, Littrup P, Huang L (2009) In vivo breast sound-speed imaging with ultrasound tomography. *Ultrasound Med Biol* 35(10):1615–1628
- Linzer M, Norton, SJ (1982) Ultrasonic tissue characterization. *Annu Rev Biophys Bioeng* 11(4):303–329
- Malik B, Terry R, Wiskin J, Lenox M (2018) Quantitative transmission ultrasound tomography: imaging and performance characteristics. *Med Phys* 45(7):3063–3075
- Malik B, Iuanow E, Klock J (2020) An exploratory multi-reader, multi-case study comparing transmission ultrasound to mammography on recall rates and detection rates for breast cancer lesions. *Acad Radiol* 29:S10–S18
- Malik B, Lee S, Natesan R, Wiskin J (2020) Clustering based quantitative breast density assessment using 3D transmission ultrasound. In: Byram BC, Ruiter NV

- (eds) Medical imaging 2020: ultrasonic imaging and tomography, vol 11319. International Society for Optics and Photonics, SPIE, Bellingham, pp 91–96
- Manohar S, Dantuma M (2019) Current and future trends in photoacoustic breast imaging. *Photoacoustics* 16:100134
- Marmarelis VZ, Jeong J, Shin DC, Do S (2007) High-resolution 3-D imaging and tissue differentiation with transmission tomography. In: André MP et al (eds) Acoustical imaging, volume 28 of acoustical imaging. Springer, Netherlands, pp 195–206
- Medina-Valdés L, Pérez-Liva M, Camacho J, Udías JM, Herraiz JL, González-Salido N (2015) Multi-modal ultrasound imaging for breast cancer detection. *Phys Procedia* 63:134–140. 43rd Annual UIA Symposium 23–25 April 2014 CSIC Madrid, Spain
- Misaridis T, Jensen JA (2005) Use of modulated excitation signals in medical ultrasound. Part I: basic concepts and expected benefits. *IEEE Trans Ultrason Ferroelectr Freq Control* 52(2):177–191
- Misaridis T, Munk P (2004) High frame rate imaging using parallel transmission of focused coded fields [medical ultrasound imaging applications]. In: IEEE ultrasonics symposium 2004, vol 2. pp 1417–1420
- Mortensen CL, Edmonds PD, Gorfu Y, Hill JR, Jensen JF, Schattner P, Shifrin LA, Valdes AD, Jeffrey SS, Esserman LJ (1996) Ultrasound tissue characterization of breast biopsy specimens: expanded study. *Ultrason Imaging* 18(3):215–230
- Mueller RK, Kaveh M, Wade G (1979) Reconstructive tomography and applications to ultrasonics. *Proc IEEE* 67(4):567–587
- Natterer F (2001) The mathematics of computerized tomography. Society for industrial and applied mathematics, Philadelphia
- Natterer F (2008) Acoustic mammography in the time domain. Technical report, University Muenster
- Nikolov S, Jensen JA (2002) Virtual ultrasound sources in high-resolution ultrasound imaging. In: Insana MF, Walker WF (eds) Medical imaging 2002: ultrasonic imaging and signal processing, vol 4687. International Society for Optics and Photonics, SPIE, Bellingham, pp 395–405
- Norton SJ, Linzer M (1979) Ultrasonic reflectivity imaging in three dimensions: reconstruction with spherical transducer arrays. *Ultrason Imaging* 1:210–231
- Norton SJ, Linzer M (1979) Ultrasonic reflectivity tomography: reconstruction with circular transducer arrays. *Ultrason Imaging* 1(2):154–184
- Norton SJ, Linzer M (1981) Ultrasonic reflectivity imaging in three dimensions: exact inverse scattering solutions for plane, cylindrical, and spherical apertures. *IEEE Trans Biomed Eng* BME-28(2):202–220
- O'Donnell M, Mimbs JW, Sobel BE, Miller JB (1977) Ultrasonic attenuation in normal and ischemic myocardium. In: Proceeding of the national bureau of standards 2nd international symposium on ultrasonic tissue characterization, p 63
- Özmen N, Dapp R, Zapf M, Gemmeke H, Ruiter NV, van Dongen KWA (2015) Comparing different ultrasound imaging methods for breast cancer detection. *IEEE Trans Ultrason Ferroelectr Freq Control* 62(4):637–646
- Pellegretti P, Vicari M, Zani M, Weigel M, Borup D, Wiskin J, Saueressig U, Kotter E, Langer M (2011) A clinical experience of a prototype automated breast ultrasound system combining transmission and reflection 3D imaging. In: IEEE international ultrasonics symposium, IUS, p 1407–1410
- Qian ZW, Xiong L, Yu J, Shao D, Zhu H, Wu X (2006) Noninvasive thermometer for HIFU and its scaling. *Ultrasonics* 44:e31–e35. Proceedings of Ultrasonics International (UI'05) and World Congress on Ultrasonics (WCU)
- Rouyer J, Mensah S, Franceschini E, Lasaygues P, Lefebvre J-P (2012) Conformal ultrasound imaging system for anatomical breast inspection. *IEEE Trans Ultrason Ferroelectr Freq Control* 59(7):1457–1469
- Roy O, Schmidt S, Li C, Allada V, West E, Kunz D, Duric N (2013) Breast imaging using ultrasound tomography: from clinical requirements to system design. In: 2013 IEEE international ultrasonics symposium (IUS), p 1174–1177
- Ruiter NV, Göbel G, Berger L, Zapf M, Gemmeke H (2011) Realization of an optimized 3D USCT. In: D'hooge J, Doyley MM (eds) Proceeding SPIE 7968, medical imaging 2011: ultrasonic imaging, tomography, and therapy, p 796805
- Ruiter NV, Zapf M, Dapp R, Hopp T, Kaiser WA, Gemmeke H (2013) First results of a clinical study with 3D ultrasound computer tomography. In: 2013 IEEE international ultrasonics symposium (IUS), pp 651–654
- Ruiter NV, Zapf M, Hopp T, Gemmeke H, van Dongen KWA, Camacho J, Fritsch C, Cruza JF, Herraiz JL, Perez Liva M, Udias JM (2018) The USCT reference database. In: Proceedings of the international workshop on medical ultrasound tomography: 1.- 3. Nov. 2017, Speyer, Germany. Hrsg.: T. Hopp. KIT Scientific Publishing, pp 385–394. 54.02.02; LK 01
- Sak M, Duric N, Pfeiffer R, Sherman M, Littrup P, Simon M, Gorski D, Albrecht T, Ali H, Brem R, Fan S, Gierach G (2020) Abstract p3-08-28: tissue sound speed is more strongly associated with breast cancer risk than mammographic percent density: a comparative case-control study. *Cancer Res* 80(4 Supplement):P3–08
- Salido N, Medina L, Camacho J (2016) Full angle spatial compound of ARFI images for breast cancer detection. *Ultrasonics* 71:161–171
- Sandhu GY, Li C, Roy O, Schmidt S, Duric N (2015) Frequency domain ultrasound waveform tomography: breast imaging using a ring transducer. *Phys Med Biol* 60(14):5381–5398
- Schomberg H (1978) An improved approach to reconstructive ultrasound tomography. *J Phys D Appl Phys* 11(15):L181–L185
- Schwarzenberg GF, Gemmeke H, Ruiter NV (2008) 3D PSF analysis for arbitrary transducer geometries and SAFT-based image reconstruction. In: McAlevey SA, D'hooge J (eds) SPIE proceedings vol. 6920: medical imaging 2008: ultrasonic imaging and signal processing, p 69200A

- Sehgal CM, Greenleaf JF (1984) Scattering of ultrasound by tissues. *Ultrason Imaging* 6(1):60–80
- Simonetti F, Huang L, Duric N (2009) A multiscale approach to diffraction tomography of complex three-dimensional objects. *Appl Phys Lett* 95:061904
- Spetzler J, Snieder R (2004) The Fresnel volume and transmitted waves. *Geophysics* 69(3):653–663
- Stotzka R, Widmann H, Müller TO, Schlotbe-Holubek K, Gemmeke H, Ruiter NV, Göbel G (2004) Prototype of a new 3D ultrasound computer tomography system: transducer design and data recording. In: Walker WF, Emelianov SY (eds) Proceeding SPIE. 5373, medical imaging 2004: ultrasonic imaging and signal processing, pp 70–79
- Suzuki A, Tsubota Y, Terada T, Yamashita H, Kato F, Nishida M, Satoh M, and Kawabata K (2021) Optimized source estimation for full waveform inversion in ultrasound computed tomography. In: Byram BC, Ruiter NV (eds) Medical imaging 2021: ultrasonic imaging and tomography, vol 11602. International Society for Optics and Photonics, SPIE, Bellingham, pp 32–39
- Szabo TL (2014) Diagnostic ultrasound imaging: inside out. Academic Press, New York
- Tae-Seong K (2005) 3-D high resolution ultrasonic transmission tomography and soft tissue differentiation. *J Biomed Eng Res* 26(1):55–63
- Tan WY, Steiner T, Ruiter NV (2015) Newton's method based self calibration for a 3D Ultrasound Tomography System. In: 2015 IEEE international ultrasonics symposium (IUS), pp 1–4
- Tanter M, Fink M (2014) Ultrafast imaging in biomedical ultrasound. *IEEE Trans Ultrason Ferroelectr Freq control* 61:102–119
- Taskin U (2021) Full-waveform inversion for breast ultrasound. PhD thesis, Delft University of Technology
- Cormen TH, Leiserson CE, Rivest RL, Stein C (1990) Introduction to Algorithms. MIT Press, Cambridge
- USCT Exchange and Collaboration Platform (2021) <http://ipeusctdb1.ipe.kit.edu/~usct/challenge/>. Accessed: 2021-04-21
- van Dongen KWA, Wright WMD (2007) A full vectorial contrast source inversion scheme for three-dimensional acoustic imaging of both compressibility and density profiles. *J Acoust Soc Am* 121:1538–1549
- Virieux J, Operto S (2009) An overview of full-waveform inversion in exploration geophysics. *Geophysics* 74(6):WCC1–WCC26
- Wang H, Qian X, Gemmeke H, Hopp T, Ruiter NV, Hesser J (2020) Fast image reconstruction in ultrasound transmission tomography by U-net. In: 2020 virtual IEEE nuclear science symposium and medical imaging conference
- Webb S (1988) The physics of medical imaging. Hilger, Bristol Philadelphia
- Williamson PR (1991) A guide to the limits of resolution imposed by scattering in ray tomography. *Geophysics* 56(2):202–207
- Wiskin J, Borup D, Johnson S (2011) Inverse scattering theory. In André MP, Jones JP, Lee H (eds) Acoustical imaging, vol 30. Springer, Netherlands, pp 53–59
- Wiskin J, Borup DT, Johnson SA, Berggren M (2012) Non-linear inverse scattering: high resolution quantitative breast tissue tomography. *J Acoust Soc Am* 131(5):3802–3813
- Wiskin J, Borup D, Johnson S, André M, Greenleaf J, Parisky Y, Klock J (2013) Three-dimensional non-linear inverse scattering: quantitative transmission algorithms, refraction corrected reflection, scanner design and clinical results. In: Proceedings of meetings on acoustics, vol 19
- Wiskin J, Malik B, Natesan R, Pirshafiey N, Klock J, Lenox M (2019) 3D full inverse scattering ultrasound tomography of the human knee (conference Presentation). In: Byram BC, Ruiter NV (eds) Medical imaging 2019: ultrasonic imaging and tomography, vol 10955. International Society for Optics and Photonics, SPIE, Bellingham
- Wiskin J, Malik B, Theendakara V, Klock J (2020) Orthopedic and myopathic imaging with transmission ultrasound tomography: experimental verification, quantitative accuracy and clinical implications. In: Byram BC, Ruiter NV (eds) Medical imaging 2020: ultrasonic imaging and tomography, vol 11319. International Society for Optics and Photonics, SPIE, Bellingham, pp 175–182
- Wiskin J, Malik B, Pirshafiey N, Klock J (2020) Limited view reconstructions with transmission ultrasound tomography: clinical implications and quantitative accuracy. In: Byram BC, Ruiter NV (eds) Medical imaging 2020: ultrasonic imaging and tomography, vol 11319. International Society for Optics and Photonics, SPIE, Bellingham, p 167–174
- Woo J (2015) A short history of the development of ultrasound in obstetrics and gynecology. <http://www.ob-ultrasound.net/history1.html>. Accessed: 2015-11-09.
- Yamashita M (2021) Delphinus SoftVue prospective case collection - arm 1 (SV PCC ARMI). <https://www.clinicaltrials.gov/ct2/show/record/NCT03257839>. Accessed: 2021-11-08
- Yu T, Fan X, Xiong S, Hu K, Wang Z (2006) Microbubbles assist goat liver ablation by high intensity focused ultrasound. *Eur Radiol* 16(7):1557–1563
- Zhang X, Broschat SL, Flynn PJ (2004) A numerical study of conjugate gradient directions for an ultrasound inverse problem. *J Comput Acoust* 12(4): 587–604
- Zografos G, Liakou P, Koulocheri D, Liovarou I, Sofras M, Hadjiagapis S, Orme M, Marmarelis V (2015) Differentiation of BI-RADS-4 small breast lesions via multimodal ultrasound tomography. *Eur Radiol* 25(2):410–418



Full Wave Inversion and Inverse Scattering in Ultrasound Tomography/Volography

10

James Wiskin

Abstract

Ultrasound breast tomography has been around for more than 40 years. Early approaches to reconstruction focused on simple algebraic reconstructions and bent ray techniques. These approaches were not able to provide high-quality and high spatial-resolution images. The advent of inverse scattering approaches resulted in a shift in image reconstruction approaches for breast tomography and a subsequent improvement in image quality. Full wave inverse solvers were developed to improve the reconstruction times without sacrificing image quality. The development of GPUs has markedly decreased the time for reconstruction using inverse scattering approaches. The development of fully 3D image solvers and hardware capable of capturing out of plane scattering have resulted in further improvement in breast tomography. This chapter discusses the state-of-the-art in ultrasound breast tomography, its history, the theory behind inverse scattering, approximations that are included to improve convergence, 3D image reconstruction, and hardware implementation of the constructions.

Keywords

Full-wave inversion · Scattering · Tomography · Regularization · Volography

10.1 Introduction

There is a long history of methods for imaging with ultrasound using tomography. The excellent review by Lavarello and Hesford in Oelze and Mamou [2013, first edition of Quantitative Ultrasound in Soft Tissues] covers a multitude of methods that are relevant:

1. Integral equations, linear (Born, Rytov approximations).
2. Ray tracing – straight ray tomography.
3. Finite difference frequency domain.
4. Time domain methods, finite difference, and integral equation methods.
5. Bent ray tomography.
6. Multipole expansions, fast multipole methods.
7. Algebraic reconstruction methods.

Some of these are more effective than others in terms of accuracy and numerical stability, and some are computationally less efficient while yielding accurate results. Note also that the heart of the problem is implementing a fast method for

J. Wiskin (✉)
QT Imaging, Novato, CA, USA
e-mail: james.wiskin@qtimaging.com

the forward problem that can be generalized to the Jacobian and adjoint Jacobian operations, as will be seen below.

Indeed there are a very large number of excellent works, e.g., Devaney (Angular-spectrum and multipole expansions 2012), that give clear comprehensive foundations for imaging with wave energy in general, and many more papers, chapters and books that discuss medical imaging with wave energy as well. Therefore, any additional treatise in this space must be a niche contribution. The emphasis we take is to summarize an operator theory approach to the inverse scattering paradigm, followed immediately by a fast method for inversion that itself has been used in some form or another in geophysics, oceanography, and ultrasound tomography. The remarkable thing is that the approach taken here is mathematically congruent to training a fully connected convolutional neural network with complex valued weights and some symmetry properties. This fact means that it takes full advantage of the NVIDIA™ GPU technology and leads to a speed of approximately 60–100X over published algorithms while using 64 times fewer compute nodes (i.e., 2 NVIDIA GPU cards instead of 128 compute nodes).

Furthermore, the chapter emphasizes the fact that 2D algorithms that create images “slice by slice” (tomography) are inadequate when dealing with ultrasound at medically relevant frequencies, because the energy cannot be constrained to a single slice as an X-ray, e.g., can be. That is a collection of levels of data (a volume of data) must be transformed into a collection of slices of the image (i.e., a volume of the image). This “volume to volume” mapping is termed vugraphy. While the term is perhaps superfluous to those familiar with inverse scattering mathematics, it is extremely helpful in the pre-clinical or clinical environment where medical professionals may not be cognizant of this important difference.

This chapter explains in detail the geometry of k-space, the spatial Fourier transform space ubiquitous in this area of study. We will utilize the Lippmann-Schwinger equation (Fredholm integral equation (IE) of the second kind) to gain in-

sight into the relation between the incident acoustic energy field, the scattered field, and the scattering potential (the object to be imaged). Although not always a practical method of inversion, the IE formulation gives a good intuitive feel for the scattering processes and lays a good foundation for an operator theory approach to imaging.

After this, we’ll transition to the finite difference frequency domain methods, and the paraxial approximation in particular, and split-step methods to explore practical methods in more detail. This last method has many advantages for breast imaging, and has been recently generalized to imaging in the presence of high contrast (i.e., in the presence of bone where traditionally ultrasound tomography has failed) (Wiskin et al. 2020). There is further evidence that even in the presence of air and bone, ultrasound vugraphy (3D algorithm, see below) works (Wiskin et al. in press).

We are concerned with “seeing” internal structure to the breast, or extremities or even whole body images so we focus on the inverse medium problem as opposed to the inverse obstacle problem, where the boundary conditions of an obstacle are important and only the boundary of the object is to be determined.

The last 20 years have witnessed a veritable explosion of mathematical techniques, data acquisition methods and devices and algorithms that would be impossible to review adequately. Focusing on the ultrasound tomography problem is fruitful because the scalar Helmholtz equation and its approximations give insight into the mathematical difficulties associated with imaging (inverting the data) that is also applicable to microwave and electromagnetic wave imaging in general.

Furthermore, it may be said that while all manner of medical imaging has exploded in recent years, the idea of using such a benign energy source as ultrasound is attractive in the context of twenty-first-century medicine. MR imaging has difficulties associated with specificity and contrast agent toxicity and X-rays are carcinogenic to some degree, etc. While progress is being made, the attractive nature of ultrasound lends itself to medical imaging with less potential side effects.

10.1.1 Breast Cancer

Although full-field digital mammography (FFDM) and digital breast tomosynthesis (DBT) are used for breast cancer screening, recent work (Malik et al. 2020) has highlighted some recognized shortcomings of these methods. In particular, fibroglandular tissue can decrease the sensitivity for breast cancer detection in particular for dense breasted women. It can also lead to false-positives by superposing dense tissue yielding an abnormally high localized density in projection interpreted as an apparent mass.

Some of these issues are partially addressed with DBT but it is a very limited angle approach and not truly tomographic even with enhanced algorithms (Rodriguez-Ruiz et al. 2018) wherein a standard filtered back-projection algorithm (FBP) is enhanced with Iterative Reconstruction (e.g., Siemens EMPIRE from 2016). The iterative algorithm reduces noise and artifacts while not substantially increasing reconstruction times and while it has advantages over FBP, a full tomographic (360-degree aperture) has significant advantages over even this algorithm.

Of course, MRI and Hand-Held Ultrasound (HHUS) have also historically been useful as secondary (adjunct) methods. We investigate here QUANTITATIVE methods of imaging.

10.1.2 Historical Development in Last 40 Years

Due to space constraints, we focus on imaging problems encountered in practice in ultrasound tomography and not rigor. The mathematical discussion of inverse scattering problems is carried out in Colton and Kress (1992) and Kirsch. The latter has a very useful appendix on functional analysis.

Even focusing on the ultrasound inverse scattering problem (ultrasound tomography) is difficult. There are a large number of researchers who have contributed substantially over the past 4 decades: Greenleaf and Johnson (Greenleaf et al. 1974, 1975; Johnson et al. 1982, 1992; Johnson and Tracy 1983) were certainly pioneers

in this area, and applied inverse scattering in the acoustic approximation to Oceanography by Johnson, Borup, and Wiskin (Johnson et al. 1992; Wiskin et al. 1993, 1997). In the 1990s and new millennium, there was increased interest in breast imaging using ultrasound tomography as witnessed in Wiskin et al. (1997) and the Duric group employed a ray tracing approach (Duric et al. 2003) and inverse scattering more recently. The ray-tracing approach is distinguished from “Full Wave” methods in that only the time of arrival of the total field is measured, so vast amounts of information are lost.

10.1.3 Caveat

We live in the age of information explosion and so it is impossible to adequately cover all of the researchers who have contributed to this area. A partial list would include the Duric group, N. Ruiter, H. Gemmeke and students, Koen van Dongen, early work of Natterer, Oelze, Lavarello, M. Andre, and many others (Huthwaite et al. 2012; Li et al. 2009; Li and Duric 2013; Wang et al. 2015; Sandhu et al. 2015; Duric et al. 2013; Matthews et al. 2017; Jirik et al. 2012; Ozmen et al. 2015; Ruiter et al. 2012; Van Dongen and Wright 2006; Natterer and Wubbeling 1995; Lavarello and Oelze 2009a; Andre et al. 1997). Several researchers from the geophysics community made the transition to breast imaging a few decades ago (Duric et al. 2005). The use of geophysical tools (Pratt et al. 1998) has recently been championed by Fichtner (Ulrich et al. 2021) and coworkers, and others (Guasch et al. 2020) with success. The lack of comprehensive references is unfortunate because there have been multiple papers and abstracts over the past few years and there is substantial foundational work being carried out in many academic institutions worldwide. Lack of reference here is not to be construed as an indication of lack of merit at all.

Also, although mathematical rigor is important, for the purposes of this chapter notation will be somewhat loose and not all statements will be proven completely. Rather, the goal of the chapter is to show the geometric and intuitive reason for

certain statements and how they can influence the construction of fast and quantitatively accurate inversion algorithms in medically relevant scenarios.

The inverse problem in scattering is best summarized as shown in Fig. 10.1.

10.2 Inverse Scattering

Examples of the kind of images we have achieved are provided in Fig. 10.2.

The images in Fig. 10.2 were obtained from the QT Imaging scanner – a water bath-based

scanner originally developed for breast imaging, but which has recently been used successfully for imaging in the presence of bone and air. Figure 10.3 shows an image of the QT scanner.

10.2.1 Theory of Acoustic Wave Propagation

Density is allowed to vary.

We start with the equation governing wave propagation (acoustic) in fluids:

$$\nabla^2 p + \frac{\omega^2}{c_o^2} p = \nabla \cdot (\gamma_\rho \nabla p) - \frac{\omega^2}{c_o^2} \gamma_\kappa p$$

or

$$\nabla^2 p + k_o^2 p = \nabla \cdot (\gamma_\rho \nabla p) - k_o^2 \gamma_\kappa p$$

where $\gamma_\kappa \equiv \left(\frac{\kappa - \kappa_o}{\kappa_o} \right)$, $\gamma_\rho \equiv \left(\frac{\rho - \rho_o}{\rho} \right)$, represent the scattering potential due to the adiabatic compressibility $\kappa = \kappa(\mathbf{x})$ and density $\rho = \rho(\mathbf{x})$ respectively, and are spatially dependent. Further, the (square of the) speed of sound is given by $c^2(\mathbf{x}) = \left(\frac{1}{\rho(\mathbf{x})\kappa(\mathbf{x})} \right)$. Note that when density is allowed to vary, a dipole scattering term results on the right-hand side (RHS) of the above equations.

This equation allows for variable density, but there is no shear wave term (only compressional) and there is no viscosity term – this is a fluid that does not support shear stress. This equation is the result of three equations in three unknowns: equation of state, equation of continuity (preservation

of mass), and Euler's equation (preservation of momentum).

Note: We use conservation of specific entropy, S , only to remove entropy from the equation of state: See Colton and Kress (1992), their classic “Inverse Acoustic and Electromagnetic Scattering Theory”, for a succinct derivation. For this reason, we don't include it in the above equations. Note also, these equations are themselves the result of linearization of the non-linear Navier-Stokes equations.

Putting $\gamma_\rho \equiv \left(\frac{\rho - \rho_o}{\rho} \right) = 0$ gives the standard Helmholtz equation,

This also utilizes $\rho = \text{constant} = \rho_o$

$$\nabla^2 p + (k_o^2 + k_o^2 \gamma_\kappa) p = 0$$

$$\gamma_\kappa \equiv \left(\frac{\kappa - \kappa_o}{\kappa_o} \right)$$

$$k_o^2 (1 + \gamma_\kappa) = \frac{\omega^2}{c^2} = k^2$$

$$\nabla^2 p(\mathbf{x}) + k^2(\mathbf{x}) p(\mathbf{x}) = 0$$

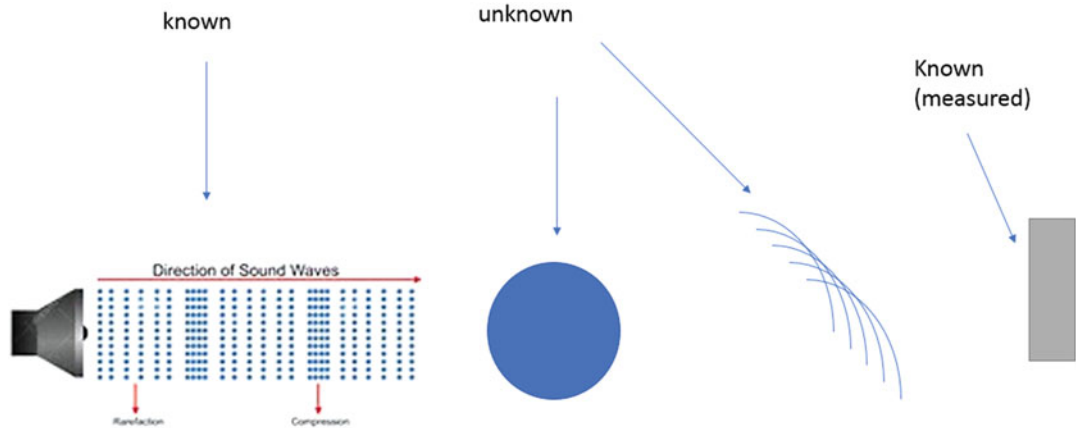


Fig. 10.1 Pictorial representation of the inverse scattering problem. The mathematical discussion is below, but intuitively a known acoustic field impinges upon an un-

known object. The received field is collected at various azimuth angles and heights and used to determine the internal characteristics of the object

That is, the object function for the compressibility is = object function for speed:

$$\gamma_\kappa \equiv \left(\frac{\kappa - \kappa_o}{\kappa_o} \right) = \left(\frac{\rho_o \kappa - \rho_o \kappa_o}{\rho_o \kappa_o} \right) = \left(\frac{c_o^2}{c^2} - 1 \right),$$

where we use $\rho \equiv \rho_o$ and definition of c :
 $c^2(\mathbf{x}) = \left(\frac{1}{\rho(\mathbf{x}) \kappa(\mathbf{x})} \right) = \left(\frac{1}{\rho_o \kappa(\mathbf{x})} \right)$.

Upon using the substitution $p' \equiv \frac{p}{\rho^\alpha}$, a straightforward calculation yields, after dividing by the common factor ρ^α :

$$\nabla^2 p' + \frac{2\alpha-1}{\rho} \nabla p' \bullet \nabla \rho + \left(k^2 + \alpha \frac{\alpha-2}{\rho^2} (\nabla \rho)^2 + \frac{\alpha}{\rho} \nabla^2 \rho \right) = 0.$$

Defining the “wave number” k' by: $k'^2(\mathbf{x}) \equiv k^2(\mathbf{x}) + \alpha \frac{\alpha-2}{\rho^2} (\nabla \rho)^2 + \frac{\alpha}{\rho} \nabla^2 \rho$, and putting $\alpha = 1/2$ to remove the middle term in the above equation, we get the Helmholtz equation again:

$$\nabla^2 p' + k'^2(\mathbf{x}) = 0$$

However, it has the distorted wave number $k'^2(\mathbf{x}) \equiv k^2(\mathbf{x}) - \frac{3}{4\rho^2} (\nabla \rho)^2 + \frac{1}{2\rho} \nabla^2 \rho$, and with “pressure field” $p' \equiv \frac{p}{\sqrt{\rho}}$. From the form of the “wave number”: k' , it is clear that the perturbation in wavenumber is small if there is relatively little variation in density ρ . So mathematically we can use the Helmholtz equation as long as we recognize we are not solving for the pressure field alone, and the “wave-number” is perturbed. This clearly fails at interfaces but is useful elsewhere.

$$\nabla^2 p + k_o^2 p = \nabla \bullet (\gamma_\rho \nabla p) - k_o^2 \gamma_\kappa p,$$

or using

$$k_o^2 (1 + \gamma_\kappa) = k_o^2 \frac{c_o^2}{c^2} = k^2 = \frac{\omega^2}{c^2} :$$

$$\begin{aligned} \nabla^2 p - \nabla \bullet (\gamma_\rho \nabla p) + k_o^2 (1 + \gamma_\kappa) p \\ = \nabla^2 p - \nabla \bullet (\gamma_\rho \nabla p) + k^2(\mathbf{x}) p = 0. \end{aligned}$$

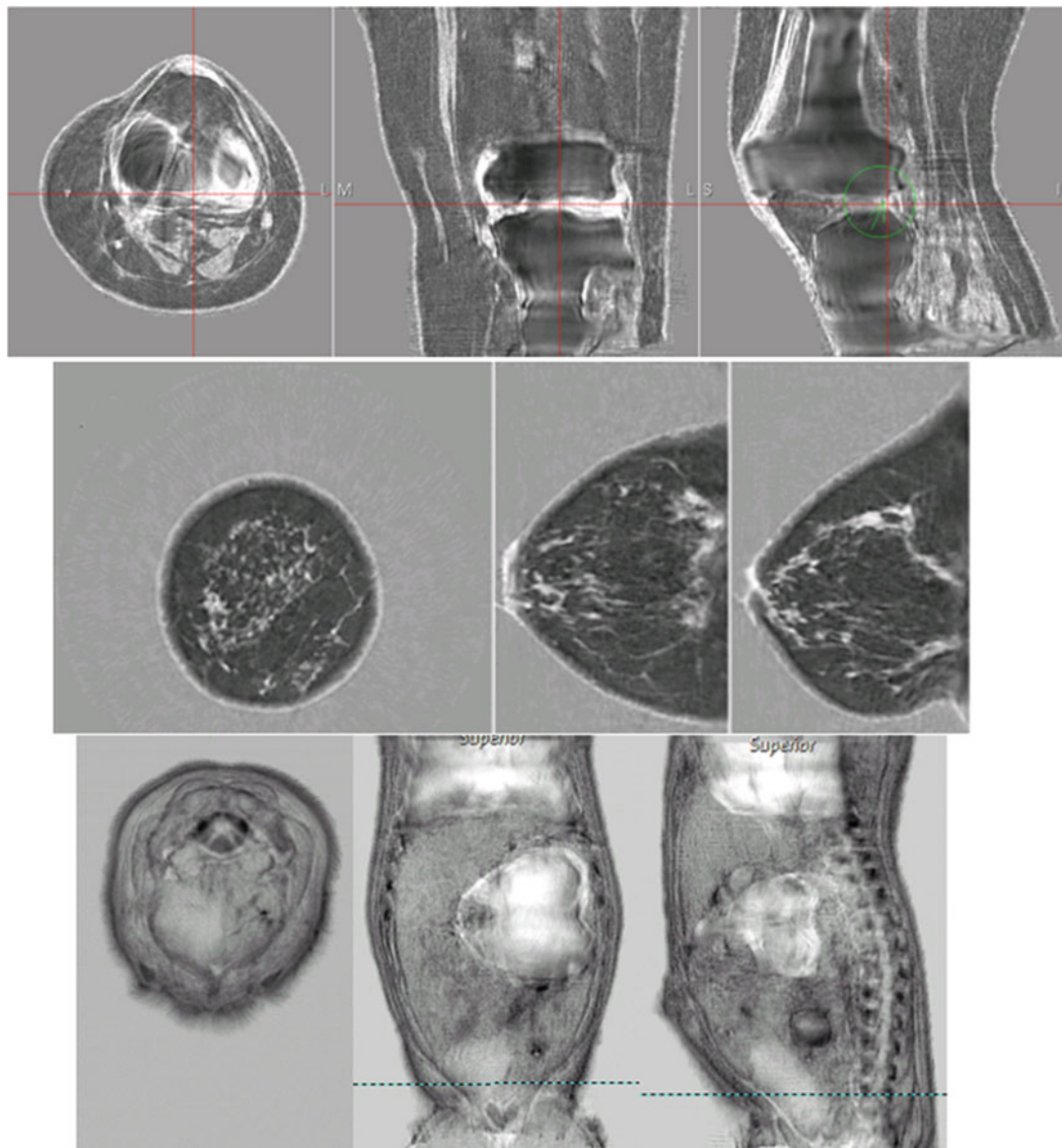


Fig. 10.2 Representative images from 3D ultrasound tomography/volugraphy. The top row shows orthopedic views of knee (cadaver), axial, coronal, and sagittal views. Middle Row: breast (human) *in vivo*, in coronal, axial, and sagittal views. Bottom Row: fused speed of sound and reflection images of pig (neonate). axial, coronal, and

sagittal views. (Images reprinted with permission from “Full wave 3D inverse scattering transmission ultrasound tomography in the presence of high contrast,” Scientific Reports, vol. 10, p. 20166, 2020, and “Whole body imaging using low frequency transmission ultrasound”, Acad. Rad., in press)

10.2.3 Attenuation

We note that the attenuation can be dealt with as a part of a complex wavenumber $k(\mathbf{x}) \equiv \frac{\omega}{c(\mathbf{x})} + i\alpha(\mathbf{x})$, where $\alpha(\mathbf{x})$ is the attenuation in Np/mm.

The object function in this case is $\gamma(\mathbf{x}) \equiv \frac{k(\mathbf{x})}{k_o} - 1 = \frac{c_o}{c(\mathbf{x})} - 1 + i \frac{\alpha(\mathbf{x}) c_o}{2\pi f}$. The conversion factor 8.686 converts the attenuation in Np to dB, i.e., $\alpha^{dB}(\mathbf{x}) = \alpha(\mathbf{x}) * 8.686$.



Fig. 10.3 Left is the water bath-based QT Imaging, Inc. scanner that is fairly representative of several such scanners that have arisen recently. The patient lies on the table (prone) with the breast hanging into and secured in the water bath. Right: the chassis containing the receiver array (right side) with 8 rows and 256 columns of receivers for true 3D transmission field reception. The transmitter array

With this definition, $\text{Im } \gamma = \frac{\alpha^{dB}(\mathbf{x})c_o}{2\pi * 8.686f}$, and $\text{Re } \gamma = \frac{c_o}{c(\mathbf{x})} - 1$ give the speed and attenuation in terms of the real and imaginary parts of the object function. For example: $\alpha^{dB}(\mathbf{x}) = \frac{2\pi * 8.686f(\text{Im } \gamma)}{c_o}$.

Note the Wirtinger calculus can be used to carry out the calculations effectively, using

$$\frac{\partial}{\partial \bar{z}} F(z, \bar{z}) \equiv \frac{1}{2} \left(\frac{\partial}{\partial x} F(x, y) + i \frac{\partial}{\partial y} F(x, y) \right)$$

for an objective function that is non-holomorphic as is the case below for the optimization/minimization approach to inverse scattering, where $z = x + iy$.

The general objective function at frequency ω will be:

$$\frac{\partial}{\partial \bar{\gamma}} F_\omega(\gamma, \bar{\gamma}) \equiv \frac{1}{2} \sum_{\theta, l} \left(\frac{\partial \bar{\mathbf{r}}_{\omega\theta}^l}{\partial \bar{\gamma}} (\bar{\gamma}) \right)^T \mathbf{r}_{\omega\theta}^l(\gamma)$$

where the sum is over all levels, l , and angles θ , and the residual \mathbf{r} is the difference between the forward problem (predicted data) and the measured data for a given receiver array (e.g., having 2048 elements). Note also, the holomorphic nature of the forward problem yields the above convenient result. Also, in the calculation of the step length in the Ribiere Polak nonlinear conjugate

is on the left side of the chassis and the three reflection arrays are seen in the back, in this view. The reflection arrays collect the data for refraction-corrected reflection imaging which is described below. (Images reprinted with permission from “Full wave 3D inverse scattering transmission ultrasound tomography in the presence of high contrast,” Scientific Reports, vol. 10, p. 20166, 2020)

gradient method, the inner product is required. This is easily accomplished using the formula $\text{Re}(\mathbf{u}'\bar{\mathbf{v}}) = \text{Re } \mathbf{u} \cdot \text{Re } \mathbf{v} + \text{Im } \mathbf{u} \cdot \text{Im } \mathbf{v}$, where \mathbf{u}, \mathbf{v} are complex valued vectors. In the following discussion we sometimes discuss results in terms of a real-valued objective function γ , and at other times, in terms of the complex-valued object function, depending on what is to be emphasized. Of course, any calculus of complex n-dimensional functionals can be turned into a corresponding calculus of $2n$ functions, but the Wirtinger calculus is a natural shortcut.

10.2.4 1D, 2D, 3D

The analysis of the one-dimensional inverse scattering problem is extremely instructive and leads to an exact solution using the Gel'fand-Levitman or Marchenko equations. See also Kay and Moses (1961). These equations in turn lead historically to the “inverse scattering transform” and soliton mathematics, which is an important area of research in its own right. See Lamb (Wallis 1981) for a nice introduction to this area (though a bit dated). This area also has close ties to modern mathematics (Lie groups, algebras, and their representations) and physics, but also gives in-

sight into what can happen in physical scattering. In fact, some underappreciated work of Cheney, Rose et al., e.g., (Cheney et al. 1989) and others (Newton 1966) have resulted in formulas that are not necessarily practical but give insight into data character and what is required for the inversion process.

The 2D inverse scattering problem is different in character in some ways due to the qualitatively different behavior of the 2D wave equation as opposed to the wave equation in odd dimensions. However, it has similar constructions (e.g., the Lippmann-Schwinger equation discussed below) and serves as a useful practice area for ultrasound tomography algorithms. In reality, also discussed below, it has become apparent in recent years that the full 3D algorithm (forward problem, Jacobian action, and adjoint Jacobian action) is required to handle real-world inversions due to the 3D nature of the scattering process with ultrasound.

This 3D character is a curse and a blessing: The problem is much more difficult to solve, but there is greater redundancy of data due to the overlap of domain of influence of different data levels in the image and the overlap of data levels affected by a single layer of the image. This is discussed below.

10.2.5 Linearized Inverse Scattering

It will be made clear below that the inverse scattering problem for acoustic waves is not only ill-posed but also nonlinear. In contradistinction, the MRI reconstruction and CT reconstruction problems can be considered linear to very high accuracy. This is essentially due to the fact that the acoustic field itself changes shape when the object potential is changed (see below for clarification). This nonlinearity is clearly manifest in the integral equation solution discussed below.

The linear approach to inverse scattering is due primarily to Devaney (Devaney 1982; Devaney and Oristaglio 1983) and the comprehensive book (Angular-spectrum and multipole expansions 2012). This approach is based on the Born (or Rytov) approximation and is discussed

(along with its limitations and some generalizations) in (Lavarello and Oelze 2007, 2009a, b). This mathematically attractive method, unfortunately, fails for most practical situations in ultrasound imaging.

10.2.6 Ray-Based Methods

The early work of Greenleaf and Johnson was soon supplemented by the bent ray approach of the Duric group (Duric et al. 2003, 2005, 2009). The problem with these methods is they account for refraction effects but not for diffraction or multiple scattering. These groups have since moved to full wave inversion (FWI) methods, in fact.

10.2.7 Full Wave Inversion

Standard B-mode assumes in its “reconstruction” that acoustic energy propagates in a straight line and is not subject to bending (refraction) or scattering (diffraction) of energy. Historically the algorithms that fully utilize these phenomena have been developed in oceanography and geophysical applications where time of reconstruction is often secondary. These utilize the Helmholtz wave equation which is a partial differential equation that fully accounts for the refraction, scattering, and diffraction phenomena mentioned above.

The difficulty with these methods is they are 100 times too slow even with a cluster of 128 computers connected in parallel to create a supercomputer used by geophysicists (Guasch et al. 2020).

There has been a virtual explosion of FWI (full wave inversion) algorithms over the past 20 years that have been applied to the breast imaging problem, especially from the geophysics community (Pratt et al. 1998). However, they generally have one flaw in common: they are often based on 2D algorithms. The reason for this is the computational cost of 3D imaging which has been alleviated substantially in the manner discussed below.

10.2.8 NVIDIA Graphics Processing Units (GPUs) and a Mathematical Trick

NVIDIA has developed its GPUs to optimally train convolution neural networks (CNNs), which are a part of the artificial intelligence (AI) revolution. The algorithm used in Wiskin et al. (2017) is mathematically congruent to training a special type of CNN (a gauge invariant fully connected deep NN with complex weights – gauge invariant FCNN-c) and therefore 100 times faster than similar algorithms, though using only 2 GPU cards, when implemented on NVIDIA GPUs.

This congruence means that there is an optimal utilization of the NVIDIA GPUs which are designed in part to optimally train deep CNNs. Therefore, increases in the speed of the NVIDIA GPUs are often directly translated into a similar speedup for the imaging algorithm discussed below.

10.2.9 Interlude on Ray Tracing

We will also review ray tracing methods below for completeness because it is used in bent-ray inversion methods and in reflection mode imaging. The bent-ray method can be used to give a good starting estimate in the inverse scattering process. Furthermore, ray-tracing is the foundation for a refraction-corrected reflection image that utilizes the speed of sound (SOS) map resulting from the transmission inverse scattering algorithm.

10.3 Introduction to Inverse Scattering

This is an overview of the data acquisition and image reconstruction system at a high level. We will see that the direct solution of the Helmholtz equation will prove to be extremely computationally intensive. The paraxial approximation (which assumes energy propagates in essentially one direction) will prove useful (Fig. 10.4).

Our paraxial approximation is based on the assumption that the majority of energy propagates in one direction. Other such approximations result from conversion to cylindrical coordinates, for example, in Oceanography. While this assumption may seem unrealistic, the resulting algorithm has proven remarkably accurate in pre-clinical studies (Malik et al. 2018).

10.4 Specially Designed Breast Scanner for Tomography/Volography

This method is based on a 360-degree aperture. A specially developed 2048-element array receiver is placed opposite a transmitter array designed to send out a tailored signal optimized to increase signal-to-noise ratios. See Fig. 10.3 to see how the arrays are placed in holder that rotates 360 degrees emitting acoustic ultrasound energy as it rotates. This ultrasound signal progresses through the breast interacting in a unique way with human tissue and progresses to the receiver array which is constructed from state-of-the-art in piezo-electric materials.

The array holder also contains 3 linear arrays for reflection mode imaging. This reflection mode imaging is similar to B-mode. However, it is refraction corrected thereby yielding sub-mm resolution and the ability to compound the image over 360 degrees.

10.4.1 Specially Designed Algorithms

Not only are the motion control, arrays and data acquisition systems (DA) specifically designed, the algorithms that reconstruct the image from raw data are similarly unique. They take advantage of certain mathematical reformulations and the NVIDIA CUDA RTX 6000 and A100 cards to optimize performance.

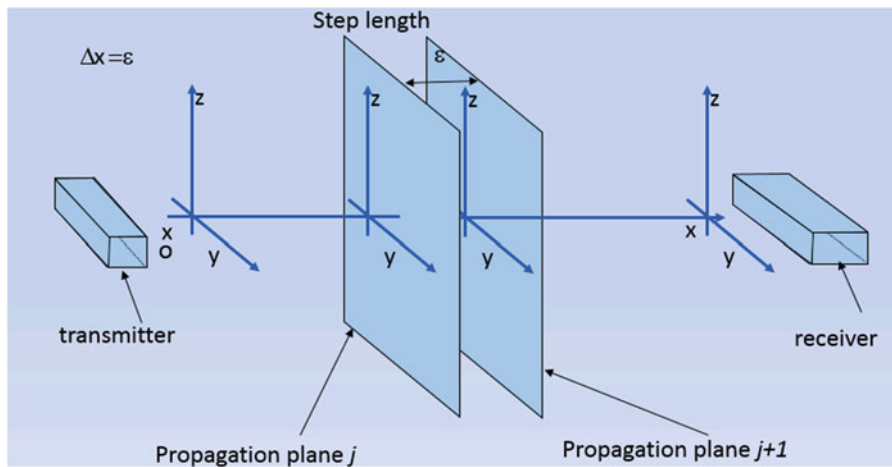


Fig. 10.4 Schematic of the propagation of the field slice from one plane to another in one incarnation of the paraxial method. The propagation of the field has vertical extent, since the true field does. The z coordinate here requires

that a 2D FFT (fast Fourier transform) is carried out at each propagation step. Care must be exercised to avoid “wrap around” due to the FFT that will introduce extraneous sources/reflections in the propagating field

10.4.2 Physics of Ultrasound – Why 2D Ultrasound Tomography Is Not Enough

In Fig. 10.5, the ultrasound field is shown propagating from the transducer (emitter) and propagating through the water bath to the ultrasound receiver array. Note that the energy is NOT CONFINED to a horizontal plane. If this was a high-energy X-ray field it would be confined to a single plane. Similarly, while the magnetic field in MRI is also space filling, the reconstruction algorithm is able to reconstruct a single slice at a time due to the field gradient. Such slice-by-slice reconstructions are not viable with ultrasound tomography.

10.5 Tomography (2D) Vs Volumography (3D)

The importance of the 2D vs 3D field is related to:

1. 3D algorithms are typically two orders of magnitude slower than the fast 2D algorithms.
2. 2D algorithms, although fast (seconds), result in artifacts and noisy images.

3. 3D fields require a 2D array (or minimally a 1.25D array) in order to capture the full extent of the field at the receiver array.
 - (a) A 1D receiver array has a single row of 256 or 192 receiver elements.
 - (b) The receiver array in the QT imaging scanner has 8 rows of 256 receiver elements.
4. The transmitter must emit a carefully tailored incident field into the breast in order to reduce noise and artifacts.

Figure 10.6 shows how one level of the data in CT and MRI contributes to a single level of the image and a single level of the image contributes to only one data level in the data acquisition DA process.

Figure 10.7 shows how with ultrasound a single level of the data acquired contributes to multiple levels of the image in the reconstruction process. Similarly, one level of the image contributes to multiple levels of data in the data acquisition process (DA).

Therefore, the 3D algorithm is fundamentally different from the 2D method, even though they both result in a 3D image. One (2D) merely concatenates the levels together to yield the 3D

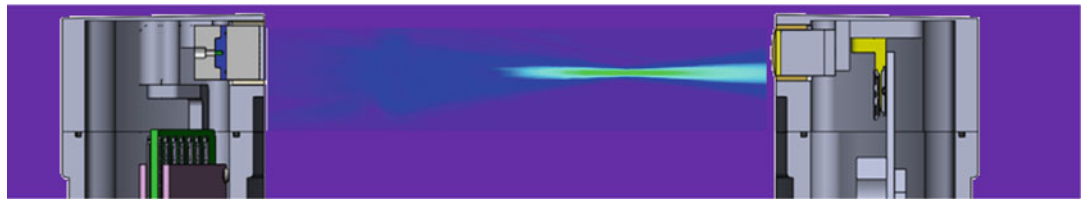


Fig. 10.5 Cross section of ultrasound field energy showing the vertical extent of the field which requires a full 3D wave model. (Reprinted with permission from Wiskin et al. “3D Ultrasound tomography timing validation for clinical deployment,” in 2022 IEEE International Ultrasonics Symposium (IUS), 2022, pp. 1–3)

2D: A series of 2D mappings

2D → 2D

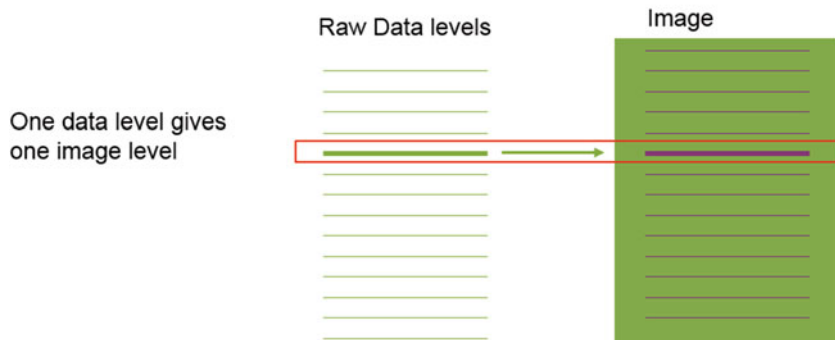


Fig. 10.6 A single layer of data gives a single layer of the image. A single level of the image contributes to one level of the data

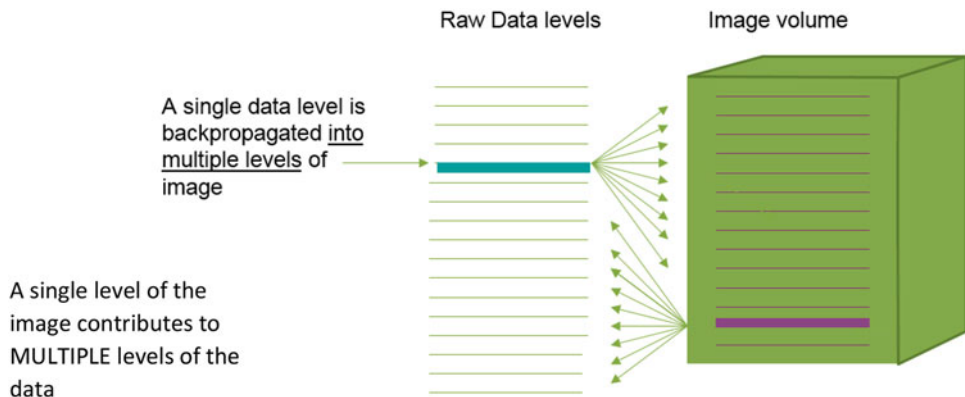


Fig. 10.7 Multiple data levels contribute to a single layer of the image and a single layer of the image contributes to multiple levels of the data. For these reasons a volume of data must correspond to a volume of the image. (Reprinted

with permission from Wiskin et al. “3D Ultrasound tomography timing validation for clinical deployment,” in 2022 IEEE International Ultrasonics Symposium (IUS), 2022, pp. 1–3)

image, whereas the other (3D) forms the image VOLUME by VOLUME: a VOLUME of data

(multiple levels) is used to simultaneously create a VOLUME image of the breast. Hence the

term “vography” to quickly differentiate between these two distinct processes.

10.6 Inverse Obstacle Problem

In this case, the far field pattern (defined below) for several incident waves and knowing the boundary conditions (Dirichlet or Neumann – defined below) are used to determine the shape of the scattering object. This problem is both improperly posed (in the sense of Hadamard) and nonlinear, and is discussed extensively in Colton and Kress (1992) and the associated book in the Springer Applied Math Sciences Series (vol 93). See also Kirsch (1996). We focus here on the more relevant problem (to medical imaging) of the inverse medium problem.

10.7 Well-Posed and Ill-Posed Problems in the Sense of Hadamard

We will come across this concept occasionally. Hadamard suggested that a correctly formulated mathematical problem should meet 3 requirements to be considered “well-posed”.

1. Existence of a solution.
2. Uniqueness of the solution.
3. The unique solution should vary “continuously” on supplied (measured) data.

This definition arose out of considerations in mathematical physics and research historically was focused on “well-posed” problems. However, in the course of time investigations involving inverse scattering problems arose. The forward problem for scattering is well-posed, but the inverse scattering problem is not. However, there are uniqueness results that give insight into the characterization of the problem (Colton and Kress 1992).

10.8 Direct Scattering

When the scattering object (scattering potential) is known and the incident field and boundary conditions are known it is desired to solve a partial differential equation (PDE) to determine the scattered and total field at some receiver locations outside of the scattering body. This is predicting the measurements. Here $f(\mathbf{x})$ is the total field, and is composed of the incident field and scattered field: $f(\mathbf{x}, y) = f^i(\mathbf{x}, y) + f^s(\mathbf{x}, y)$, $f^i(\mathbf{x}, y)$ is the incident field, and $f^s(\mathbf{x}, y)$ is the field resulting from interaction with the scattering potential. The total field satisfies the Helmholtz equation

$$\nabla^2 f(\mathbf{x}) + k^2(\mathbf{x}) f(\mathbf{x}) = 0.$$

10.9 Inverse Medium Problem

This is the inverse problem in the medical sense (primarily), because we wish to determine the internal structure of the human breast (for example). This is portrayed in Fig. 10.1 and as stated, involves measuring scattered field data and using this to build a model for the scattering object.

10.10 Integral Equation Formulation

10.10.1 Lippmann-Schwinger Equation and Its Implications

Start with a simple geometry as shown in Fig. 10.8.

Start with the Helmholtz equation:

$$\nabla^2 f(\mathbf{x}) + k^2(\mathbf{x}) f(\mathbf{x}) = 0. \quad (10.1)$$

Define γ , the object function, or scattering potential as (recall the wavenumber k may have an imaginary part representing attenuation):

$$\gamma(k(\mathbf{x})) \equiv \frac{k^2(\mathbf{x})}{k_o^2} - 1.$$

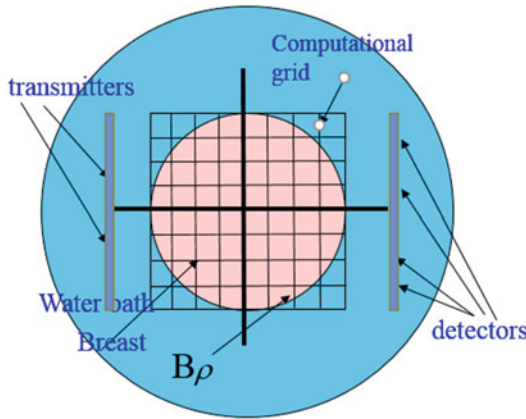


Fig. 10.8 Top view looking down upon the water bath. The transmitter and receiver arrays are seen in the water bath. They rotate around the object placed where the computational grid is shown. The chassis rotates 360 degrees collecting data every 2 degrees, moves up 2 mm, then repeats the rotation in the opposite direction. (Reprinted with permission from Wiskin, et al., “Full-Wave, Non-Linear, Inverse Scattering,” in Acoustical Imaging 28, M. P. André, Ed., ed. Dordrecht: Springer Netherlands, 2007, pp. pp. 183–193)

Rewrite the Helmholtz or “reduced” wave equation

$$\nabla^2 f(\mathbf{x}) + k_o^2 f(\mathbf{x}) = -k_o^2 \gamma(\mathbf{x}) f(\mathbf{x}).$$

Recall that the incident field satisfies:

$$\nabla^2 f^i(\mathbf{x}) + k_o^2 f^i(\mathbf{x}) = 0.$$

Now, we have,

$$\nabla^2 f^{sc}(\mathbf{x}) + k_o^2 f^{sc}(\mathbf{x}) = -k_o^2 \gamma(\mathbf{x}) f(\mathbf{x}),$$

for the scattered field.

Now, define the Green’s function $G(\mathbf{x}; \mathbf{x}')$ as the solution to the following equation:

$$(\nabla^2 + k_o^2) G(\mathbf{x}; \mathbf{x}') = -\delta(\mathbf{x} - \mathbf{x}')$$

Suppose we have the geometric set up seen in Fig. 10.8. The scattered field is then (for a particular azimuth angle θ and frequency ω):

$$f_{\omega\theta}^{sc}(\mathbf{r}) = k_0^2 \iiint_{\Gamma} \gamma(\mathbf{r}') f_{\omega\theta}(\mathbf{r}') G_{\omega}(|\mathbf{r} - \mathbf{r}'|) dx'dy'dz'$$

This can be observed in a “formal” way (i.e., this does not constitute a proof but can be made into one, see Colton and Kress for mathematical details (Colton and Kress 1992) or Kirsch (1996)).

Applying the Helmholtz operator, and assuming that the differentiation can be passed under the integral we obtain the following:

$$\begin{aligned} & (\nabla^2 + k_o^2) f_{\omega\theta}^{sc}(\mathbf{r}) \\ &= k_0^2 \iiint_{\Gamma} \gamma(\mathbf{r}') f_{\omega\theta}(\mathbf{r}') (\nabla^2 + k_o^2) G_{\omega}(|\mathbf{r} - \mathbf{r}'|) dx'dy'dz' \end{aligned}$$

(the following is more involved since the delta distribution should be treated as a distribution – not a function – and the Green’s function is L_2 – i.e., a square integrable singular function). This can be made rigorous by breaking the 3D integral into the sphere surrounding the singularity and the rest of space. The spherical volume integral is then converted into a surface integral by Gauss’ theorem and then the radius taken to zero in a controlled way.

We get

$$\begin{aligned} & (\nabla^2 + k_o^2) f_{\omega\theta}^{sc}(\mathbf{r}) \\ &= -k_0^2 \iiint_{\Gamma} \gamma(\mathbf{r}') f_{\omega\theta}(\mathbf{r}') \delta(\mathbf{x} - \mathbf{x}') dx'dy'dz'. \end{aligned}$$

The characteristic property of the delta distribution yields

$$\nabla^2 f^{sc}(\mathbf{x}) + k_o^2 f^{sc}(\mathbf{x}) = -k_o^2 \gamma(\mathbf{x}) f(\mathbf{x})$$

as required.

So now we can, using the definition of $f_{\omega\theta}^{sc}$, write

$$\begin{aligned} f_{\omega\theta}^{\text{inc}}(\mathbf{r}) &= f_{\omega\theta}(\mathbf{r}) - k_0^2 \iiint_{\Gamma} \gamma(\mathbf{r}') f_{\omega\theta}(\mathbf{r}') G_{\omega}(|\mathbf{r} - \mathbf{r}'|) dx'dy'dz'. \end{aligned} \quad (10.2)$$

Or equivalently in operator notation:

$f_{\omega\theta}^{\text{inc}} = (I - k_0^2 G_{\omega}[\gamma]) f_{\omega\theta}$, where the operator: $G_{\omega}[\gamma]$ signifies

$$G_{\omega}[\gamma] f_{\omega\theta} \equiv \iiint_{\Gamma} G_{\omega}(|\mathbf{r} - \mathbf{r}'|) \gamma(\mathbf{r}') f_{\omega\theta}(\mathbf{r}') dx'dy'dz'.$$

Symbolically, we can rewrite this as:

$$f_{\omega\theta} = (I - k_0^2 G_\omega [\gamma])^{-1} f_{\omega\theta}^{\text{inc}}.$$

From this representation of the solution we see that the problem is manifestly nonlinear. The square brackets surrounding the γ represent a conversion of the matrix of object function values to a linearly ordered vector in the discretized representation (through the method of moments, for example). The Green's function in the discretized version is likewise converted to a matrix by linearly ordering spatial coordinates.

Alternatively, we define $(G_\omega [\gamma])_{ijk} \equiv \sum_{l,m,n} (G_\omega)_{ijk,lmn} \gamma_{lmn}$, and note this defines a linear operator defined on a vector space (finite dimensional in the case of discretization), where the elements are the γ_{lmn} . This applies to 2D as well, and the infinite dimensional case is merely the same notation with the summation replaced by an integral.

The ball of radius ρ is denoted $B_\rho \equiv \{\mathbf{x} \in R^2 | |\mathbf{x}| < \rho\}$, for the 2D problem, as shown in the general geometry repeated in Fig. 10.9 for convenience:

For a fixed frequency $\omega = 2\pi f$, and scattering potential γ , the “scattering operator” $[\phi_\omega(\gamma)]$ maps a known incident field into the scattered field: $\phi_\omega(\gamma) : f^{\text{inc}} \rightarrow f^{\text{sc}}$. Specifically: $\phi_\omega(\gamma) \in \text{Hom}(C(B_\rho), C^2(R^N))$, $N = 2, 3$.

Here, $C(B_\rho)$ = continuous functions on B_ρ , and $C^2(B_\rho)$, $C^2(R^N)$ = continuous functions on B_ρ , R^N respectively with continuous second derivatives, and.

$\text{Hom}(V_1, V_2)$ is the set of linear maps from one linear (Banach) space to another: $(V_1 \rightarrow V_2)$.

A more complete mathematical description including the appropriate Sobolev spaces shows that the Far-Field Operator $\mathbf{F} : H_0^2(B_\rho) \rightarrow L^2(S^2 \times S^2)$, is well defined in the following way:

When the incident field is a plane wave: $f_{\omega\theta}^{\text{inc}}(\mathbf{r}) \equiv e^{ik_\theta \mathbf{r} \cdot \hat{\mathbf{r}}}$, where $\hat{\mathbf{r}} \equiv (\cos \theta, \sin \theta)$, is the direction vector of propagation. The Sommerfeld radiation condition [5] implies that asymptotically the scattered field behaves

like an outgoing spherical wave: $f_{\omega\theta}^{\text{sc}}(\mathbf{x}) = \frac{e^{-ik_\theta |\mathbf{x}|}}{|\mathbf{x}|} \left(f^\infty(\hat{\mathbf{x}}) + O\left(\frac{1}{|\mathbf{x}|}\right) \right)$, where $\hat{\mathbf{x}} \equiv \frac{\mathbf{x}}{|\mathbf{x}|} \in S^2$ is a unit vector.

The map

$$\mathbf{F} : \gamma \in H_0^2(B_\rho) \rightarrow f^\infty(\hat{\mathbf{x}}) \in L^2(S^2 \times S^2). \quad (10.3)$$

is the required (nonlinear) map.

It can be shown that the Frechet derivative of $\mathbf{F}, \mathbf{A} \equiv \mathbf{F}'(\gamma_0)$, at a solution γ_0 , is a compact operator, indicating that the inversion problem will be severely ill-posed. In fact, the singular values of this operator actually decrease exponentially (Hohage 2001).

This is in accord with the fact that the far-field pattern is guaranteed to be an analytic function on $S^2 \times S^2$ (Kirsch 1996). Recall, by the residue theorem for the complex plane, that the value of an analytic (holomorphic) function in \mathbb{C} (for simplicity), is determined by its values on a surrounding closed path. Thus, the values in a region of the plane with non-zero measure are determined uniquely by values on a set of measure zero (in the sense of measure theory). This is a strong constraint and thus it is not surprising that the far-field operator is compact. This argument can be generalized using charts (standard manifold theory) to the complex structure on $S^2 \times S^2$.

The numerical process by which the scattered field f^{sc} is determined can be viewed as a two-step process because the solution of the Helmholtz scattering problem with Sommerfeld-Wilcox radiation condition is equivalent to the “Lippmann-Schwinger equation”:

First step: Solve the Lippmann-Schwinger equation (Fredholm Integral Equation of the second kind) for the total field $f_{\omega\theta}(\mathbf{x})$.

$$f_{\omega\theta}^{\text{inc}}(\mathbf{r}) = f_{\omega\theta}(\mathbf{r}) - k_0^2 \iint_{\Gamma} \gamma(\mathbf{r}') f_{\omega\theta}(\mathbf{r}') G_\omega(|\mathbf{r} - \mathbf{r}'|) dx' dy' dz' \quad (10.4)$$

where, is the support of the “object function” γ and $\mathbf{r}, \mathbf{r}' \in \Gamma$.

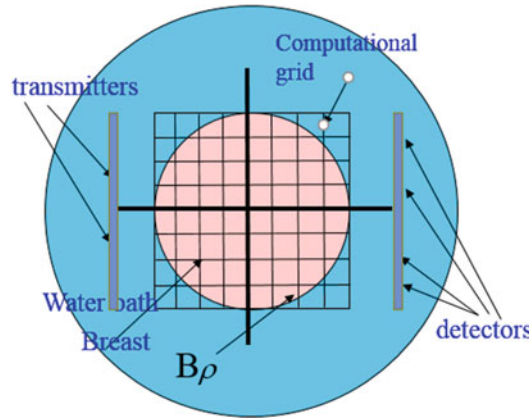


Fig. 10.9 Water bath and breast as seen from above. This is the water bath shown in Fig. 10.3. The Green's operator and the object function γ are defined on the computational grid as noted. (Reprinted with permission from Wiskin et al.

al. "Full-Wave, Non-Linear, Inverse Scattering," in Acoustical Imaging 28, M. P. André, Ed., ed. Dordrecht: Springer Netherlands, 2007, pp. pp. 183–193)

$G_\omega(|\mathbf{r} - \mathbf{r}'|)$ is the Green's function, the solution to: $\nabla^2 G_\omega(|\mathbf{r} - \mathbf{r}'|) + k_0^2 G_\omega(|\mathbf{r} - \mathbf{r}'|) = -\delta(\mathbf{r} - \mathbf{r}'), \delta(\mathbf{r}')$, being the Dirac distribution. It represents a source at \mathbf{r}' .

Second Step: The solution to (10.4) gives the total field, $f_{\omega\theta}$, which is then converted to the measured scattered field measured on the detectors by (10.2) computing the integral:

$$f_{\omega\theta}^{sc}(\mathbf{r}_i) = k_0^2 \iiint_{\Gamma} \gamma(\mathbf{r}') f_{\omega\theta}(\mathbf{r}') G_\omega(|\mathbf{r}_i - \mathbf{r}'|) dx'dy'dz', \quad (10.5)$$

where i is the position of the i th receiver.

These equations are the basis of the method employed in (Wiskin et al. 1997) – the Conjugate Gradient FFT method – and is prohibitively expensive, as it involves the inversion of a dense matrix. We use these definitions to elucidate the action of the Jacobian and the Adjoint operators below, but the actual calculations are carried out for (10.4) by solving parabolic approximations to the Helmholtz equation, as discussed below.

We introduce the operator theoretic notation:

$$(k_0^2 G_{\omega j} [\gamma]) f_{\omega\theta} \equiv k_0^2 \iiint_{\Gamma} \gamma(\mathbf{r}') f_{\omega\theta}(\mathbf{r}') G_\omega(|\mathbf{r}_j - \mathbf{r}'|) dx'dy'dz'$$

$G_\omega(|\mathbf{r}_j - \mathbf{r}'|)$ is the Green's function (propagator) from image space to a receiver at j . $[\gamma]$ is a diagonal operator (matrix in finite-dimensional form), given by (after sampling to convert to a computer-ready problem).

$$\gamma_{ij} \equiv \gamma(\Delta(i-1), \Delta(j-1)),$$

where Δ is the pixel size. Note that the scattered field is now:

$$\begin{aligned} f_{\omega\theta}^{sc}(\mathbf{r}_j) &= k_0^2 G_{\omega r} [\gamma] f_{\omega\theta} \\ &= k_0^2 G_{\omega r} [\gamma] (I - k_0^2 G_\omega [\gamma])^{-1} f_{\omega\theta}^{\text{inc}}. \end{aligned}$$

10.11 Born Approximation

Given the Lippmann-Schwinger equation with Born approximation in the special case of a plane

wave traveling in the y direction (see Fig. 10.10): we get

$$\begin{aligned} u^{sc} &= \int_{\Omega} d\mathbf{r}' G(\mathbf{r} - \mathbf{r}') \gamma(\mathbf{r}') u(\mathbf{r}') \\ &\rightarrow (\text{Born approximation}) \rightarrow u^{sc} \\ &\approx \int_{\Omega} d\mathbf{r}' G(\mathbf{r} - \mathbf{r}') \gamma(\mathbf{r}') u^{inc}(\mathbf{r}'). \end{aligned}$$

This last can be shown to be related to the Jacobian of the scattering operator as a function of the object function γ .

Using a plane wave incident field: $u^{inc}(\mathbf{r}') = e^{ik_0 y'}$, gives immediately $u^{sc} \approx \int_{\Omega} d\mathbf{r}' G(\mathbf{r} - \mathbf{r}') \gamma(\mathbf{r}') e^{ik_0 y'}$.

10.11.1 Weyl Decomposition

The Weyl decomposition of the Green's function into plane waves (for 2D) is:

$$\begin{aligned} G(k_o |\mathbf{r} - \mathbf{r}'|) &= \frac{i}{4} H_o^{(1)}(k_o |\mathbf{r} - \mathbf{r}'|) \\ &= \frac{i}{4} \frac{1}{\pi} \int d\alpha \frac{e^{i\alpha(x-x')+i\beta|y-y'|}}{\beta}, \end{aligned}$$

where

$$\beta = \sqrt{k_o^2 - \alpha^2},$$

(Here we use the Hankel function of the first kind, because the asymptotic behavior is $e^{ik|\mathbf{r}|}$, which is correct for an assumed time variation of $e^{-i\omega t}$.)

This gives immediately (receiver array is assumed to be at $y = y_o$)

$$u^{sc}(x) \approx \frac{i}{2} \frac{1}{2\pi} \int_R d\alpha \frac{e^{i\beta y_o}}{\beta} e^{i\alpha x} \int_{\Omega} d\mathbf{r}' e^{-ix'\alpha + iy'(k_0 - \beta)} \gamma(\mathbf{r}')$$

The inner integral is a 2D Fourier transform:

$$\int_{\Omega} d\mathbf{r}' e^{-ix'\alpha + iy'(k_0 - \beta)} \gamma(\mathbf{r}') \equiv \mathbf{F}\gamma(\alpha, (k_0 - \beta)),$$

that is, it is a Fourier transform of the objection function.

Therefore, the integral

$$u^{sc}(x) \approx \frac{i}{2} \frac{1}{2\pi} \int_R d\alpha \frac{e^{i\beta y_o}}{\beta} e^{i\alpha x} \int_{\Omega} d\mathbf{r}' e^{-ix'\alpha + iy'(k_0 - \beta)} \gamma(\mathbf{r}')$$

has the form of a 2D Fourier Transform followed by an *inverse* 1D Fourier Transform $\alpha \rightarrow x$, except for the $\frac{ie^{i\beta y_o}}{2\beta} \equiv \frac{ie^i\sqrt{k_o^2 - \alpha^2} y_o}{2\sqrt{k_o^2 - \alpha^2}}$ term, where y_o is the position of the receiver array.

Therefore, applying a Fourier transform in x to $u^{sc}(x)$ therefore gives

$$\begin{aligned} \hat{u}^{sc}(\alpha) &\equiv F[u^{sc}(x)] \\ &\approx \frac{i}{2} \frac{e^{i\beta y_o}}{\sqrt{k_o^2 - \alpha^2}} F[\gamma](\alpha, \beta - k_0), \end{aligned}$$

where F is the Fourier Transform. This is a specialized geometry, but by symmetry this is true irrespective of the angle of incidence of the plane wave, and receiver, as long as they face each other directly. The generalization to the case where the transmitter is at an angle to the receiver is straightforward.

This is a linearization of the problem (Born Approximation), nevertheless it is clear that multiplying the Fourier transformed (in x direction) received field: $\hat{u}^{sc}(\alpha)$, by $2\sqrt{k_o^2 - \alpha^2}$ yields an inversion problem that involves inverting a Unitary matrix (with eigenvalues of unit modulus). Note also that the value of the Fourier transform of the data along the array length at a particular point α on the receiver corresponds to a particular point in the 2D Fourier transform space (k -space) of the object as shown in Fig. 10.11.

10.11.2 Comments on Weyl Decomposition

Although authors generally make use of the integral representation of the Hankel function, in reality the Weyl or plane wave decomposition of the function is by virtue of the fact that *it*

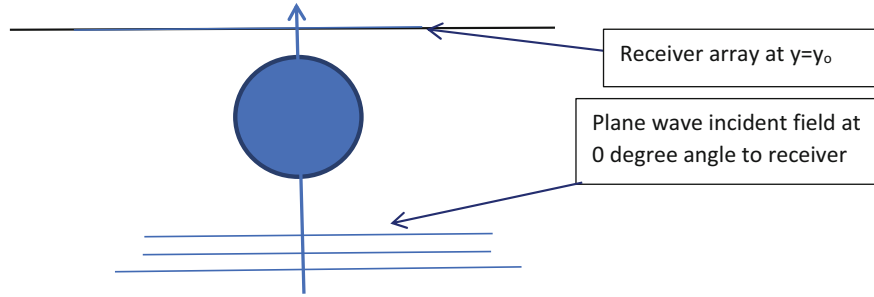


Fig. 10.10 Diagram of the scattering of a plane wave incident on an object with plane wave normal to the receivers. This geometry gives a simple proof of the diffraction tomography algorithm under the Born approximation

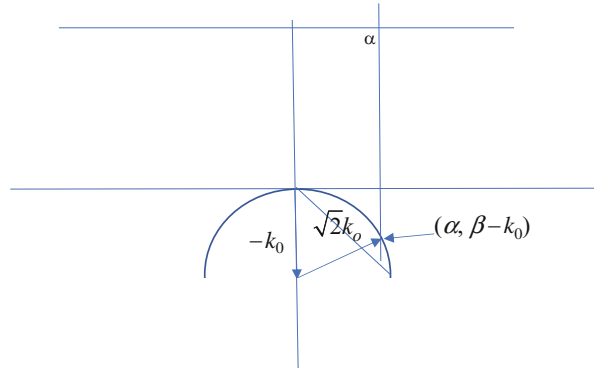


Fig. 10.11 Showing geometric relation between the position on the receiver array in k-space corresponding to a particular point on the Ewald circle in the Fourier transform of the object function Note that the above geometry

can be rotated around the origin in k-space (following the rotation in real space of the transmitter/receiver pair) and the resulting coverage of k-space indicates the maximum k value is $\sqrt{2k_0}$

is the Green's function of the Helmholtz equation. It is incidental that it is the Hankel function.

In fact, the formula is proved merely by taking the inverse 2D/3D Fourier Transform of the Fourier transform of the Helmholtz equation with the spatial Green's function (the fact that it is Hankel in 2D is incidental). Indeed:

$$\nabla^2 G_\omega(k_o |\mathbf{r} - \mathbf{r}'|) + k_o^2 G_\omega(k_o |\mathbf{r} - \mathbf{r}'|) = -\delta(\mathbf{r} - \mathbf{r}'),$$

becomes

$$-\mathbf{k} \cdot \mathbf{k} \hat{G}_\omega + k_o^2 \hat{G}_\omega = -e^{-i\mathbf{k} \cdot \mathbf{r}'}$$

and

$$\hat{G}_\omega = -\frac{e^{-i\mathbf{k} \cdot \mathbf{r}'}}{-\mathbf{k} \cdot \mathbf{k} + k_o^2} = -\frac{e^{-i\mathbf{k} \cdot \mathbf{r}'}}{-(k_z^2 + k_y^2 + k_x^2) + k_o^2}.$$

In 3D, the inverse Fourier transform can be carried out and explicitly evaluated in one direction:

$\int_{-\infty}^{\infty} \left(\iint \frac{e^{i\mathbf{k} \cdot (\mathbf{r} - \mathbf{r}')}}{\mathbf{k} \cdot \mathbf{k} - k_o^2} dk_x dk_y \right) dk_z$, the k_z integral is carried out by contour integration in the complex plane and use of Jordan's lemma.

$$\begin{aligned} & \int_{-\infty}^{\infty} \left(\iint \frac{e^{i\mathbf{k} \cdot (\mathbf{r} - \mathbf{r}')}}{\mathbf{k} \cdot \mathbf{k} - k_o^2} dk_x dk_y \right) dk_z \\ &= \int_{-\infty}^{\infty} \left(\iint \frac{e^{i\mathbf{k} \cdot (\mathbf{r} - \mathbf{r}')}}{(k_z + \sqrt{k_o^2 - k_y^2 - k_x^2})(k_z - \sqrt{k_o^2 - k_y^2 - k_x^2})} dk_x dk_y \right) dk_z \end{aligned}$$

The singularity at $k_z = \sqrt{k_o^2 - k_x^2 - k_y^2}$ is moved to the first quadrant by an addition of some attenuation, and evaluation of the residue gives the Weyl (plane wave) decomposition mentioned above.

Note this applies in 2D in the same manner.

As mentioned, the attenuation is dealt with in this model in a similar way. That is the wave number can be defined as $k = \frac{\omega}{c} + i\alpha$. Note that the sign of α is positive for $e^{-i\omega t}$ and negative for $e^{i\omega t}$ sign convention for conservation of energy reasons.

10.12 Summary: Utility of Integral Equation Approach

We see that the Integral equation method gives a unified point of view along with:

1. Gives a solution method with coarse ($\lambda/2$) sampling (using Whittaker Cardinal sinc functions) and convolutional Green's function (FFT) (Wiskin et al. 1997).
 - (a) Use of Green's function means it involves trying to invert a dense matrix (LU methods prefer sparse matrices).
 - (b) The use of BiCG or BiCG Stabilized – even with pre-conditioner is slow to converge or may not converge (note BiCG is not guaranteed to converge).
2. Shows clearly the Diffraction tomography theorem (Ewald circle) and allows estimation of resolution in various geometries.
 - (a) Linear approximation to nonlinear problem (Born or Rytov) is immediate.
3. The Green's function has a “plane wave” decomposition – which is extremely powerful (Weyl decomposition).
 - (a) Merely an explicit inverse Fourier transform of the solution to the Fourier-transformed Helmholtz equation, using an explicit contour integration that avoids singularities.
4. The singularities of the Green's function tell us where the evanescent waves begin in the spectrum.

5. Can be used to show the equivalence of different solution methods:
 - (a) The Newton-Raphson approach attempts to zero the gradient (perturb and solve).
 - (b) The iterated Distorted Wave Born series.
 - (i) Carry out successive Born approximations with increasingly complicated Green's functions.
 - (ii) Start with Homogeneous Green's function (standard Born).
 - (iii) One may hope that this method would converge when Born does not.
 - (iv) An integral equation method approach shows that the two methods a. and b. are mathematically identical to first order. (see below – they may differ at second order).
 - (c) Digital Implementation: Large-scale minimization of error term via nonlinear conjugate gradients.
 - (d) Digital Implementation: Large-scale minimization of error term with Quasi-Newton methods (Variable Metric methods) – L-BFGS.
 - (i) Successive approximation of the inverse Hessian.
 - (ii) Has some relationship with nonlinear conjugate gradients in special cases.

10.13 The Gradient of the Functional Is the Product of Two “Total” Fields

Before proceeding further we show that the gradient of our error term functional is the pointwise product of two fields:

1. The total field as calculated with the “forward problem”.
2. The “adjoint field”: which is the field generated when the receivers are treated as sources and their strength is precisely the residual at that receiver element.

We will show this using the parabolic (or paraxial) approximation below. Let's show

this is not restricted to that approximation, but is in fact, a general statement valid for the Helmholtz equation which accounts for all multiple scattering and diffraction phenomena:

Recall now the Lippmann-Schwinger (LS) equation, for a given fixed frequency ω and azimuth angle θ :

$$f_{\omega\theta}^{\text{inc}}(\mathbf{r}) = f_{\omega\theta} - k_0^2 \iiint_{\Gamma} G_{\omega}(|\mathbf{r} - \mathbf{r}'|) dx' dy' dz' f_{\omega\theta}(\mathbf{r}')$$

Symbolically this can be written using operator notation:

$$(I - k_0^2 G_{\omega}[\gamma]) f_{\omega\theta} = f_{\omega\theta}^{\text{inc}}.$$

$$f_{\omega\theta} = (I - k_0^2 G_{\omega}[\gamma])^{-1} f_{\omega\theta}^{\text{inc}}.$$

The scattered field is found to be, in the same notation:

$$G_{\omega}[\gamma] f_{\omega\theta} \equiv \iiint_{\Gamma} G_{\omega}(|\mathbf{r} - \mathbf{r}'|) \gamma(\mathbf{r}') f_{\omega\theta}(\mathbf{r}') dx' dy' dz'$$

Therefore, the scattered field at the receiver is:

$$\begin{aligned} & ((k_0^2 G_{\omega}[\gamma]) f_{\omega\theta})(\mathbf{r}_j) \\ & \equiv k_0^2 \iiint_{\Gamma} \gamma(\mathbf{r}') f_{\omega\theta}(\mathbf{r}') G_{\omega}(|\mathbf{r}_j - \mathbf{r}'|) dx' dy' dz', \end{aligned}$$

where \mathbf{r}_j is the position of the j th receiver.

The operator T_k can be applied to account for the characteristics of the k th receiver:

$$[\phi_{\omega}(\gamma) f_{\omega\theta}^{\text{inc}}]_k \equiv T_k k_0^2 G_2[\gamma] (I - k_0^2 G_{\omega}[\gamma])^{-1} f_{\omega\theta}^{\text{inc}}.$$

Now, ignoring for the moment the third dimension z , and defining the functional as:

$$F_{\omega}(\gamma, \bar{\gamma}) \equiv \frac{1}{2} \sum_{\theta} \bar{\mathbf{r}}_{\omega\theta}^T \mathbf{r}_{\omega\theta},$$

we can use Wirtinger calculus, in particular the Dolbeault, derivative: $\frac{\partial}{\partial \bar{\gamma}} F_{\omega}(\gamma, \bar{\gamma}) = \frac{1}{2} \left(\frac{\partial F}{\partial \gamma_R} + i \frac{\partial F}{\partial \gamma_I} \right)$, to give, using explicitly the

analytic (holomorphic) nature of the forward problem and residual function $\mathbf{r}_{\omega\theta}(\gamma)$, i.e., $\mathbf{r}_{\omega\theta}(\gamma) \equiv (\hat{\mathbf{d}}_{\omega\theta}(\gamma) - \mathbf{d}_{\omega\theta})$, and in our case the predicted data at angle θ is $[\hat{\mathbf{d}}_{\omega\theta}(\gamma)]_k \equiv T_k k_0^2 G_2[\gamma] (I - k_0^2 G_{\omega}[\gamma])^{-1} f_{\omega\theta}^{\text{inc}}$, which is manifestly holomorphic. When this equation is

$$\text{discretized } [\gamma] \equiv \begin{bmatrix} \gamma_1 & 0 & \cdots & 0 \\ 0 & \ddots & & \vdots \\ \vdots & & \gamma_{N-1} & 0 \\ 0 & \cdots & 0 & \gamma_N \end{bmatrix}, \text{ where}$$

$N = N_x N_y$ in the 2D case and is the linearly ordered components of the scattering potential. That is, we represent the vector of γ values as a diagonal matrix to keep the formulas consistent. The data are now holomorphic functions of the vector γ ,

$$\frac{\partial}{\partial \bar{\gamma}} F_{\omega}(\gamma, \bar{\gamma}) \equiv \frac{1}{2} \sum_{\theta} \left(\frac{\partial \bar{\mathbf{r}}_{\omega\theta}}{\partial \bar{\gamma}}(\bar{\gamma}) \right)^T \mathbf{r}_{\omega\theta}(\gamma).$$

We need to calculate the derivative of the forward operator: $\mathbf{r}_{\omega\theta}(\gamma) \equiv (\hat{\mathbf{d}}_{\omega\theta}(\gamma) - \mathbf{d}_{\omega\theta})$.

Calculating the gradient requires: $\left(\frac{\partial \bar{\mathbf{r}}_{\omega\theta}}{\partial \bar{\gamma}}(\bar{\gamma}) \right)^T \mathbf{r}_{\omega\theta} \equiv \overline{\left[\frac{\partial \hat{\mathbf{d}}_{\omega\theta}}{\partial \gamma} \right]^T} \mathbf{r}_{\omega\theta}$ and we will incorporate k_0^2 into the Green's symbol, and f is total field (incident plus scattered).

The direct calculation gives:

$$\begin{aligned} [\hat{\mathbf{d}}_{\omega\theta}(\gamma)]_k & \equiv T_k k_0^2 G_2[\gamma] (I - k_0^2 G_{\omega}[\gamma])^{-1} f_{\omega\theta}^{\text{inc}} \\ & \equiv T_k k_0^2 G_2[\gamma] f_{\omega\theta} \\ \frac{\partial \hat{\mathbf{d}}_{\omega\theta}(\gamma)}{\partial \gamma} & = T_k G_2(I - G_{\omega}[\gamma])^{-1} f_{\omega\theta}^{\text{inc}} \\ & + T_k G_2[\gamma] \frac{\partial f_{\omega\theta}}{\partial \gamma}. \end{aligned}$$

Next, we determine by differentiating the forward LS equation with respect to (wrt) vector γ .

$$\frac{\partial f}{\partial \gamma} : (I - k_0^2 G_{\omega}[\gamma]) f_{\omega\theta} = f_{\omega\theta}^{\text{inc}},$$

to get the formula, using $f \equiv f_{\omega\theta}$, for the total field.

$$\frac{\partial f}{\partial \gamma} - k_0^2 G_{\omega} f - k_0^2 G_{\omega}[\gamma] \frac{\partial f}{\partial \gamma} = 0,$$

or rearranging terms,

$$(I - k_0^2 G_\omega[\gamma]) \frac{\partial f}{\partial \gamma} = k_0^2 G_\omega f,$$

such that

$$\begin{aligned} \frac{\partial \hat{\mathbf{d}}_{\omega\theta}(\gamma)}{\partial \gamma} &= T_k G_2 f + T_k G_2 [\gamma] \\ &\quad ((I - G_\omega[\gamma])^{-1} G_\omega f) \\ &= T_k G_2 (I + [\gamma] (I - G_\omega[\gamma])^{-1} G_\omega) f. \end{aligned}$$

Note that we have Proposition 1:

$$[\gamma] (I - G_\omega[\gamma])^{-1} = (I - [\gamma] G_\omega)^{-1} [\gamma]$$

Proof:

Note that $(I - [\gamma] G_\omega)[\gamma] = [\gamma](I - G_\omega[\gamma])$, multiply by $(I - G_\omega[\gamma])^{-1}$ on the right and $(I - [\gamma] G_\omega)^{-1}$ on the left to get the result.

Hence, we have

$$\frac{\partial \hat{\mathbf{d}}_{\omega\theta}(\gamma)}{\partial \gamma} = T_k G_2 (I + (I - [\gamma] G_\omega)^{-1} [\gamma] G_\omega) f.$$

However:

$$I + (I - [\gamma] G_\omega)^{-1} [\gamma] G_\omega = (I - [\gamma] G_\omega)^{-1}.$$

As can be observed by multiplying both sides by $(I - [\gamma] G_\omega)$, yielding:

$$(I - [\gamma] G_\omega) + [\gamma] G_\omega = I,$$

which is clearly true.

So finally:

$$\frac{\partial \phi_\omega}{\partial \gamma} = T_k G_2 (I - [\gamma] G_\omega)^{-1} f.$$

Note that everything that has been done up to this point has used the fact that the forward operator is analytic in γ (as a complex map).

Let's look at this equation more closely:

$$\frac{\partial \phi_\omega}{\partial \gamma} = T_k G_2 (I - [\gamma] G_\omega)^{-1} f.$$

From now on we will incorporate the T_k operator into the G_2 Green's operator scattering the

total field to the receivers. See below for how this is done explicitly.

Therefore, $\left[\frac{\partial \phi_\omega}{\partial \gamma} \right]^H \mathbf{r}$ (our gradient for the L2 norm functional) is:

$$\begin{aligned} &\left[G_2 (I - [\gamma] G_\omega)^{-1} f \right]^H \mathbf{r} \\ &= \overline{[f]} (I - \overline{G_\omega[\gamma]})^{-1} G_2^H \mathbf{r}, \end{aligned}$$

(it helps to treat everything as finite-dimensional operators after discretization).

However, $\sum_r G_2^H (|\mathbf{x}_r - \mathbf{x}_j|) \mathbf{r}_r = \sum_r \overline{G_2} (|\mathbf{x}_j - \mathbf{x}_r|) \mathbf{r}_r$, $r = 1, \dots, N_R$.

Note that $\sum_r \overline{G_2} (\mathbf{x}_j - \mathbf{x}_r) \mathbf{r}_r$ is the field generated by all of the receivers evaluated at pixel j , with strength \mathbf{r}_r , the value of the residual at that receiver – just as $\overline{G_2} (|\mathbf{x}_j - \mathbf{x}_r|)$ is the (complex conjugate) of the field generated by receiver r and measured at image pixel j , since it is the solution to the Helmholtz equation:

$$\nabla^2 G_\omega (|\mathbf{r} - \mathbf{r}'|) + k_0^2 G_\omega (|\mathbf{r} - \mathbf{r}'|) = -\delta(\mathbf{r} - \mathbf{r}').$$

Moreover, it is the incident field generated by that source, because the Green's function is the free-space Green's function. The conjugate guarantees that the wave propagates in the correct direction from receivers to breast (or scattering body).

Now apply $(I - \overline{G_\omega[\gamma]})^{-1}$, the forward operator on the image space, to get a kind of total field associated with this special incident field,

$$f^{\text{adj}} \equiv (I - \overline{G_\omega[\gamma]})^{-1} G_2^H \mathbf{r}.$$

This is the total field generated by using the receivers as sources, since it is the total field operator applied to the incident field generated by the receiver elements acting as sources.

This is what we have called the adjoint field in the past. Note that since we are using the complex conjugate of the Green's function, for a given wave number, and given the sign convention for the time \rightarrow frequency decomposition, the field is propagating in the opposite direction to the standard total field.

Finally: $\left[\frac{\partial \phi_\omega}{\partial \gamma} \right]^H \mathbf{r} = [G_2(I - [\gamma] G_\omega)^{-1} f]^H \mathbf{r} = \overline{[f]}(I - \overline{G_\omega[\gamma]})^{-1} G_2^H \mathbf{r}$.
 That is: $\left[\frac{\partial \phi_\omega}{\partial \gamma} \right]^H \mathbf{r} = \overline{[f]} f^{adj}$.

The pointwise product of the (complex conjugate of the) total field * “adjoint” field is the gradient of the objective functional.

Note that this is seen independently below in the context of the paraxial approximation. This is due to the fact that it represents a physical reality. We are only establishing this through several different equations (Parabolic, elliptic) which are approximations to the physical reality with varying assumptions. The fact that the same relationship holds true, is a *partial*, practical vindication of the accuracy of these models, in particular it is reassuring in the paraxial approximation context.

10.14 Newton Raphson/Gauss Newton Method (NR/GN)

We will derive the NR method and show its equivalence to the Distorted Born Iterative Method (DBIM) *to first order*. This is an important caveat, since the DBIM has been tried in the literature extensively (and shown to fail for high contrast, large objects). The derivation is for the real case. A similar argument can be made with complex γ .

Minimizing

$$F = \frac{1}{2} \mathbf{r}^H \mathbf{r},$$

the Newton-Raphson method says that

$$\frac{\partial F}{\partial \gamma} (\gamma_o + \delta\gamma) = 0.$$

Expanding

$$\frac{\partial F}{\partial \gamma} (\gamma_o) + \frac{\partial^2 F}{\partial \gamma^2} (\gamma_o) \delta\gamma = 0, \quad (10.6)$$

use

$$\frac{\partial F}{\partial \gamma} = \left[\frac{\partial \phi_\omega}{\partial \gamma} \right]^T \mathbf{r},$$

and approximate the Hessian by neglecting $\left[\frac{\partial^2 \phi_\omega}{\partial \gamma^2} \right] \mathbf{r}$ since \mathbf{r} is presumed small. Using

$$\frac{\partial^2 F}{\partial \gamma^2} \approx \frac{1}{2} \left[\frac{\partial \phi_\omega}{\partial \gamma} \right]^T \left[\frac{\partial \phi_\omega}{\partial \gamma} \right],$$

Equation (10.6) becomes

$$\left[\frac{\partial \phi_\omega}{\partial \gamma} \right]^T \left[\frac{\partial \phi_\omega}{\partial \gamma} \right] \delta\gamma = - \left[\frac{\partial \phi_\omega}{\partial \gamma} \right]^T \mathbf{r}.$$

This is the minimum norm solution to the minimization of the non-square system

$$\min \left\| \left[\frac{\partial \phi_\omega}{\partial \gamma} \right] \delta\gamma + \mathbf{r} \right\|.$$

Using the fact that we know the Jacobian of the forward problem analytically: (see above).

$\frac{\partial \phi_\omega}{\partial \gamma} = T_k G_2(I - [\gamma] G_\omega)^{-1} [f]$, or incorporating the T_k operator into the G_2 Green's operator, the NR/GN method follows.

1. Start with γ_j , determine $\delta\gamma_j$ as the solution to the minimization problem:

$$\min \|G_2(I - [\gamma] G_\omega)^{-1} [f] \delta\gamma + \mathbf{r}\|$$

Note the presence of the *total field* in this calculation.

2. Then evaluate:

$$\gamma_{j+1} \equiv \gamma_j + \delta\gamma_j$$

3. Repeat until minimum norm is small $F = \frac{1}{2} \mathbf{r}^H \mathbf{r}$.

This can be amended with regularization as required. See below.

10.15 Distorted Born Iterative and Related Methods (DBIM)

The DBIM has been discussed by multiple authors. We take the point of view that we create new scattering Green's operator that incorporates the present estimate of the object.

We show also that *to first order* the Newton-Raphson method is equivalent to the DBIM update. See also (Remis and van den Berg 2000) for a similar analysis, though longer.

We desire to minimize:

$$\min \sum_k \left\| \overline{(\hat{d}_k - d_k)} (\hat{d}_k - d_k) \right\|,$$

where the simulated data is (by definition).

$\hat{d}_k \equiv (G_S^0 [\gamma_n] [f_n])_k$, *kth receiver, nth iteration*, $G_S^0 \equiv G_2$ is the scattering operator (Green's function) from the image space to the receivers.

Recall the Newton-Raphson method derived above:

$\min \|T_k G_2(I - [\gamma] G_\omega)^{-1} [f] \delta\gamma + \mathbf{r}\|$, T_k is the propagator from the edge to the receivers. This has now been replaced by the G_2 which propagates from the image space to the receivers directly. Thus T_k can be ignored.

Define $G_S^0 \equiv G_2$.

The reason for the zero will become clear below.

$\min \sum_k \left\| \overline{(\hat{d} - d)_k} (\hat{d} - d)_k \right\|$: *k* is a multi-vector index representing all possible views and data levels, d is the vector of receivers on the receiver array, define the *nth* iterate $\hat{d}_n \equiv G_S^0 [\gamma_n] [f_n]$. Therefore

$$\hat{d}_{n+1} \equiv G_S^0 [\gamma_n + \delta\gamma] [f_n + \delta f],$$

thus:

$$\begin{aligned} \hat{d}_{n+1} &\approx G_S^0 [\gamma_n] [f_n] + G_S^0 [\gamma_n] [\delta f] \\ &+ G_S^0 [\delta\gamma] [f_n], \end{aligned}$$

to first order in perturbation of object function and field.

We wish to create a G_S^n such that

$$G_S^n [\delta\gamma_n] [f_n] \approx G_S^0 [\gamma_n] [\delta f] + G_S^0 [\delta\gamma] [f_n].$$

From Chew and Wang (1990), we can write the required G_S^n as

$$[G_S^n]^T \equiv (I - G_\omega [\gamma_n])^{-1} G_S^0. \quad (10.7)$$

The transpose is determined from the derivation in Chew. Note, a given row (note transpose) of this $[G_S^n]$ is the total field in the image space when the incident field is from a point source at a receiver and object approximation $[\gamma_n]$ is present to scatter the incoming incident field. That is, this Green's operator is obtained by the forward operator acting on the free space Helmholtz Green's function. If I fix a column of the linearly ordered free space Green's function then the corresponding column in $(I - G_\omega [\gamma_n])^{-1} G_S^0$ is the total field resulting from treating the original fixed column in G_S^0 as the incident field and the “scattering potential” is the *nth* iteration of the object to be imaged (also called the scattering potential).

So, to find $\delta\gamma_n$, the *nth* update, the following minimization is carried out

$$\min \sum_k \left\| \left((G_S^0 [\gamma_n] [f_n])_k + (G_S^n [\delta\gamma_n] [f_n])_k - d_k \right) \right\|^2.$$

But this is, using $\hat{d}_n \equiv G_S^0 [\gamma_n] [f_n]$, just:

$$\min \sum_{j=1, \dots, N_R} \|\mathbf{r}_j + (G_S^n [\delta\gamma_n] [f_n])_k\|^2,$$

where taking the transpose of (10.7) gives $G_S^n \equiv (G_S^0)^T (I - [\gamma_n]^T G_\omega^T)^{-1}$.

Using the symmetry of the free space Green's function and the diagonal matrix $[\gamma_n]$, we get

$$(G_S^k) = G_S^0 (\mathbf{I} - [\gamma_k] G_\omega)^{-1},$$

using *k* in place of *n* to correspond to the iteration count.

Also,

$$\gamma_{j+1} \equiv \gamma_j + \delta\gamma_j,$$

is the update and

$$\mathbf{r}_k \equiv \hat{d}_k - d_k,$$

is the residual error between the predicted data and the measured data.

Because

$$(G_S^k) = G_S^0(\mathbf{I} - [\gamma_k] G_\omega)^{-1},$$

the minimization is

$$\min \sum_{j=1, \dots, N_R} \|\mathbf{r}_j + (G_S^n [\delta \gamma_n] [f_n])_k\|^2, \\ \text{or min } \|\mathbf{r} + G_S^n [\delta \gamma_n] [f_n]\|^2,$$

which can be rewritten as:

$$\min \|(\mathbf{r} + G_S^0(\mathbf{I} - [\gamma_n] G_\omega)^{-1} [\delta \gamma_n] [f_n])\|.$$

Comparing this to the Newton-Raphson formula:

$$\min \|G_2(I - [\gamma] G_\omega)^{-1} [f] \delta \gamma + \mathbf{r}\|.$$

Now, using $G_2 \equiv G_S^0$, and the commutativity of two diagonal matrices $[\delta \gamma_n][f_n] = [f_n][\delta \gamma_n]$, we see the NR formula is identical to the Distorted Born approximation. Even though the NR formula is a bona-fide nonlinear optimization procedure and the DBIM is an ad-hoc interpretation.

Note that these methods are only equal *up to first order*. A method that estimated the Hessian (such as Limited memory BFGS – Broyden, Fletcher, Goldfarb, and Shannon) would result in different behavior.

Note also that the equivalence is based on the result by Chew mentioned above.

1968):

$$f(\mathbf{r}) \equiv \iint_{S_o} f(\mathbf{r}') \frac{\partial}{\partial \hat{n}} G(|\mathbf{r} - \mathbf{r}'|) \\ - G(|\mathbf{r} - \mathbf{r}'|) \frac{\partial}{\partial \hat{n}} f(\mathbf{r}') dS, \text{ i.e.} \\ f(\mathbf{r}) \equiv \iint_{S_o} f(\mathbf{r}') G(|\mathbf{r} - \mathbf{r}'|) \left(ik_o - \frac{1}{R}\right) \cos \theta \\ - G(|\mathbf{r} - \mathbf{r}'|) \frac{\partial}{\partial \hat{n}} f(\mathbf{r}') dS.$$

where the surface S_o is extended to a plane perpendicular to the direction of propagation, see Fig. 10.2 for $\mathbf{r} \equiv (x, y, z)$, and \mathbf{r}' definitions, and where G is any Green's function that satisfies $\nabla'^2 G(|\mathbf{r} - \mathbf{r}'|) = -k_o^2 G(|\mathbf{r} - \mathbf{r}'|) + \delta(\mathbf{r} - \mathbf{r}')$. In particular define:

$$G_-(\mathbf{r}, \mathbf{r}') \equiv \frac{e^{ik_o R^+}}{4\pi R^+} - \frac{e^{ik_o R^-}}{4\pi R^-},$$

where $(x_c, y_c, z_c) = (x - 2\Delta, y, z)$ $\Delta \equiv x - x'$ and

$$R^- = \|(x_c - x', y_c - y', z_c - z')\| \\ R^+ = \|(x - x', y - y', z - z')\|.$$

Thus:

$G_-(\mathbf{r}, \mathbf{r}') \equiv \frac{e^{ik_o R^+}}{4\pi R^+} - \frac{e^{ik_o R^-}}{4\pi R^-} = 0$, for $(x', y', z') \in S_o \equiv \{\mathbf{r}, x = x_o\}$, since $R^- = R^+$, by symmetry. On the other hand, direct calculation gives that the normal derivative at the boundary is

$$\nabla' G(|\mathbf{r} - \mathbf{r}'|) \cdot \hat{n} \\ \equiv \frac{e^{ik_o R^+}}{4\pi R^+} \left(ik_o - \frac{1}{R^+}\right) \cos \theta \\ - \frac{e^{ik_o R^-}}{4\pi R^-} \left(ik_o - \frac{1}{R^-}\right) \cos(\pi - \theta),$$

which by symmetry, collapses to $\frac{e^{ik_o R^+}}{2\pi R^+} (ik_o - \frac{1}{R^+}) \cos \theta$, and the field at a point \mathbf{r} , is given by:

$$f(\mathbf{r}) \equiv \iint_{S_o} f(\mathbf{r}') \frac{e^{ik_o R^+}}{2\pi R^+} \left(ik_o - \frac{1}{R^+}\right) \cos \theta dS.$$

If the integration is carried out over points on the transducer element face, i.e., over \mathbf{r} , we get the total field contribution, which is proportional to the voltage received at that element (receiver R

10.16 Discussion of Propagation Formula

The field at a point \mathbf{r} is expressible in the very general (Green's) formula (Morse and Ingard

in Fig. 10.2). That is,

$$\int_{R_k} f(\mathbf{r}) dy \equiv \int_{R_k} \iint_{S_o} f(\mathbf{r}') \frac{e^{ik_o R^+}}{2\pi R^+} (ik_o - \frac{1}{R^+}) \cos \theta dS_{\mathbf{r}'} dS_{\mathbf{r}},$$

where

R_k support of k th transducer element, the interchange of the two-dimensional integrations above leads to (for 3D):

$$\iint_{S_o} f(\mathbf{r}') \left(\int_{R_k} \frac{e^{ik_o R^+}}{2\pi R^+} (ik_o - \frac{1}{R^+}) \cos \theta dS_{\mathbf{r}'} \right) dS_{\mathbf{r}'},$$

where

$$R^+ = \|(x - x', y - y', z - z')\|.$$

Now, the inner integral:

$f_{R_k}(\mathbf{r}') \equiv \int_{R_k} \frac{e^{ik_o R^+}}{2\pi R^+} (ik_o - \frac{1}{R^+}) \cos \theta dS_{\mathbf{r}'}$ is the field at \mathbf{r}' , due to the receiver element R_k -acting as a source. This can also be derived from Green's theorem by putting the surface of integration (the bounding surface) at the transducer (receiver) face, and the field point at the point at which the total field is evaluated in the first case.

The voltage generated by the R_k receiver, is therefore, $V_{R_k} \propto \iint_{S_o} f(\mathbf{r}') f_{R_k}(\mathbf{r}') dS_{\mathbf{r}'}$, i.e., proportional to the inner product in L_2 , of the total field:

$$V_{R_k} \propto \iint_{S_o} f(\mathbf{r}') f_{R_k}(\mathbf{r}') dS_{\mathbf{r}'} \\ \equiv \langle f_{x'} | f_{x', R_k} \rangle_{L_2(\mathbb{R}^2)},$$

which is what we wished to show.

10.17 Paraxial Approximation

The paraxial approximation has been used extensively in Oceanography, photonics, and microwave imaging. We apply it here and find that the resulting algorithm is mathematically congruent to training a special type of fully connected (CNN). Thus, the deployment of the NVIDIA GPUs is optimal in some sense. Indeed, we will verify this below with some actual numbers.

We start with the Helmholtz equation (note this could also apply to light wave propagation in the scalar approximation) $\nabla^2 f(\mathbf{x}) + k^2(\mathbf{x})f(\mathbf{x}) = 0$, i.e.

$$\frac{\partial^2 f(\mathbf{x})}{\partial x^2} + \frac{\partial^2 f(\mathbf{x})}{\partial y^2} + \frac{\partial^2 f(\mathbf{x})}{\partial z^2} + (k(\mathbf{x}) - i\alpha(\mathbf{x}))^2 f(\mathbf{x}) = 0.$$

This can be written in the following manner:

$$[(A + iB)(A - iB) - i[B, A]] f(\mathbf{x}) = 0$$

where $A \equiv \frac{\partial}{\partial x}$, and $B \equiv \sqrt{\frac{\partial^2}{\partial y^2} + \frac{\partial^2}{\partial z^2} + k^2(x, y, z)}$ is a pseudo-differential operator in sense of Booss & Bleeker's "Topology and Analysis" or other standard text in Analysis, and $[B, A] \equiv BA - AB$ is the commutator of two operators. If the commutator is small and ignored and we Fourier transform in the transverse direction (y, z) coordinates, we obtain:

$$\frac{\partial}{\partial x} \hat{f}(x, \mathbf{k}_\perp) = -i\mathbf{H}(x, \mathbf{k}_\perp) \hat{f}(x, \mathbf{k}_\perp).$$

The conditions under which this assumption is valid are discussed in Wiskin et al. (2012) but intuitively when the rate of change in the wavenumber $k(x, k_y, k_z)$ is small in the x or range direction.

The equation is thus (where the square root is a symbolic representation of a pseudo-differential operator)

$$\left(\frac{\partial}{\partial x} + i\sqrt{k^2(x, k_y, k_z) \otimes -k_y^2 - k_z^2} \right) \hat{f}(x, k_y, k_z) = 0.$$

This can be *formally* integrated from x to $x + \varepsilon$, to yield

$$\hat{f}(x + \varepsilon, k_y, k_z) = e^{-i\varepsilon\sqrt{\hat{k}^2(x', k_y) \otimes -k_y^2}} \hat{f}(x, k_y, k_z),$$

where

$$x < x' < x + \varepsilon.$$

Note that we still have to interpret the operator, $e^{-i\varepsilon\sqrt{\hat{k}^2(x', k_T) \otimes -k_T^2}}$, where the transverse wave vector is $\mathbf{k}_T \equiv (k_y, k_z)$ and $k_T^2 \equiv k_y^2 + k_z^2$. Formally

this is the “flow” associated with the operator acting on a Hilbert space. In the standard way (from operator theory or quantum field theory) we break up the x (direction of propagation) coordinate to $x_0 < x_1 < \dots < x_{N-1} < x_N$.

The field is propagated from $x = x_o$ to $x = x_N$. The propagation action, then, is given by:

$$f(x_{j+1}, \mathbf{r}_T) = \mathbf{F}^{-1} e^{i\epsilon\sqrt{k^2(x', \mathbf{k}_T) \otimes -k_T^2}} \mathbf{F} f(x_j, \mathbf{r}_T),$$

where $\Delta x \equiv x_{j+1} - x_j = \epsilon$, and \mathbf{F} is the Fourier transform. This is approximated by $f(x_{j+1}, y) = \mathbf{t}_j(y) \mathbf{F}^{-1} P_0(k_y) \mathbf{F} f(x_j, y)$, where the phase mask is $\mathbf{t}_j(\mathbf{r}_T) \equiv e^{i\epsilon(k(x_j, \mathbf{r}_T) - k_o)}$, and the free space propagator $P_0(k_y) \equiv e^{i\epsilon\sqrt{k_o^2 - k_T^2}}$. Note that k_o can be replaced by a constant suitable k_j that is range dependent but not dependent on the transverse $\mathbf{k}_T \equiv (k_y, k_z)$ or \mathbf{r}_T .

We define $(\mathbf{f}_j)_{kl} \equiv f(x_j, y_k, z_l)$, the field at the j th propagation level. Now define the free space propagation operator as $\mathbf{A} \equiv \mathbf{F}^{-1} P_0(k_T) \mathbf{F} f(x_j, \mathbf{r}_T)$, this propagates the field through water to the next level. Thus, the full propagation step is

$$\begin{aligned} f(x_{j+1}, \mathbf{r}_T) &= \mathbf{t}_j(\mathbf{r}_T) \mathbf{F}^{-1} P_0(k_T) \mathbf{F} f(x_j, \mathbf{r}_T) \\ &= \mathbf{t}_j(\mathbf{r}_T) \mathbf{A} f(x_j, \mathbf{r}_T) \end{aligned}$$

or in case the propagator is level dependent, $P_j(k_T) \equiv e^{i\epsilon\sqrt{k_j^2 - k_T^2}}$,

$$\begin{aligned} f(x_{j+1}, \mathbf{r}_T) &= \mathbf{t}_j(\mathbf{r}_T) \mathbf{F}^{-1} P_j(k_T) \mathbf{F} f(x_j, \mathbf{r}_T) \\ &= \mathbf{t}_j(\mathbf{r}_T) \mathbf{A}_j f(x_j, \mathbf{r}_T). \end{aligned}$$

The propagation step can be written as $\mathbf{f}_j = (\mathbf{t}_j) \circ \mathbf{A}(\mathbf{f}_{j-1})$, where the operator $\mathbf{A} : C^{N_z \times N} \rightarrow C^{N_z \times N}$, N_z is the vertical dimension, N is the horizontal dimension. This operator takes the spatial field to the spatial field at the next propagation level *through empty water* (free space). The phase mask operator \mathbf{t}_j is applied after the propagation to account for phase shifts caused by the breast (or imaged object).

Note, the phase mask operator $(\mathbf{t}_j \circ) : C^{N_z \times N} \rightarrow C^{N_z \times N}$ is point-wise or component-wise multiplication: $(\mathbf{v} \circ \mathbf{w})_i \equiv v_i w_i$. This is also referred to as Hadamard or Schur multiplication and corresponds to Fig. 10.12.

10.18 Inverse Scattering in the Paraxial Approximation

There are many ways of formulating the inverse scattering problem. For conciseness, we focus on one formulation, the one involving the residuals

$$\mathbf{r}_{\omega_j \theta}^l(\gamma) \equiv \left(\hat{\mathbf{d}}_{\omega_j \theta}^l(\gamma) - \mathbf{d}_{\omega_j \theta}^l \right) \in \mathbb{C}^{N_R},$$

where N_R is the number of receivers on the receiver array. The object function is defined as:

$$\gamma(\mathbf{x}) \equiv \frac{k(\mathbf{x})}{k_o} - 1,$$

$\hat{\mathbf{d}}_{\omega_j \theta}^l(\gamma) \equiv \hat{\mathbf{d}}_\theta^l$, is the *predicted* data at level l , and view θ , (for a fixed frequency ω_j). $\mathbf{d}_{\omega_j \theta}^l \equiv \mathbf{d}_\theta^l$, is the *measured data*, at a particular frequency ω_j . Note also we define: $k(\mathbf{x}) \equiv \omega/c(\mathbf{x}) - i\alpha(\mathbf{x})$, $k_o \equiv \omega/c_o$ and that the field at the rightmost level in the image space is:

$$\begin{aligned} f(x_N, \mathbf{r}_N^\perp) \\ = \prod_{j=1}^N t(x_j, \mathbf{r}_j^\perp) \circ \mathbf{F}^{-1} P \circ \mathbf{F} f(x_o, \mathbf{r}_o^\perp), \end{aligned}$$

where $\mathbf{r}_j^\perp \equiv \mathbf{r}_T(x_j)$ are the transverse coordinates at the j th propagation level. This rightmost level can be propagated to the receivers in a manner discussed below, using Green’s identity.

The minimization that will result in an image is given by (at a fixed frequency),

$$\min F_{\omega_j}(\gamma(\mathbf{x})) = \min \frac{1}{2} \sum_{\theta=1, \dots, N_{\text{views}}} \sum_{l=1, \dots, N_{\text{levels}}} \overline{\mathbf{r}_{\omega_j \theta}^l(\gamma)} \mathbf{r}_{\omega_j \theta}^l(\gamma).$$

In the determination of the minima, a gradient-based algorithm is used. The two most popular are the Limited memory BFGS – Broyden-Fletcher-Goldfarb-Shannon method and the conjugate gradient method. The L-BFGS method uses gradient information sequentially to iteratively estimate the Hessian of the objective functional. The *non-linear* conjugate gradient method uses sequential estimates of the descent direction based on

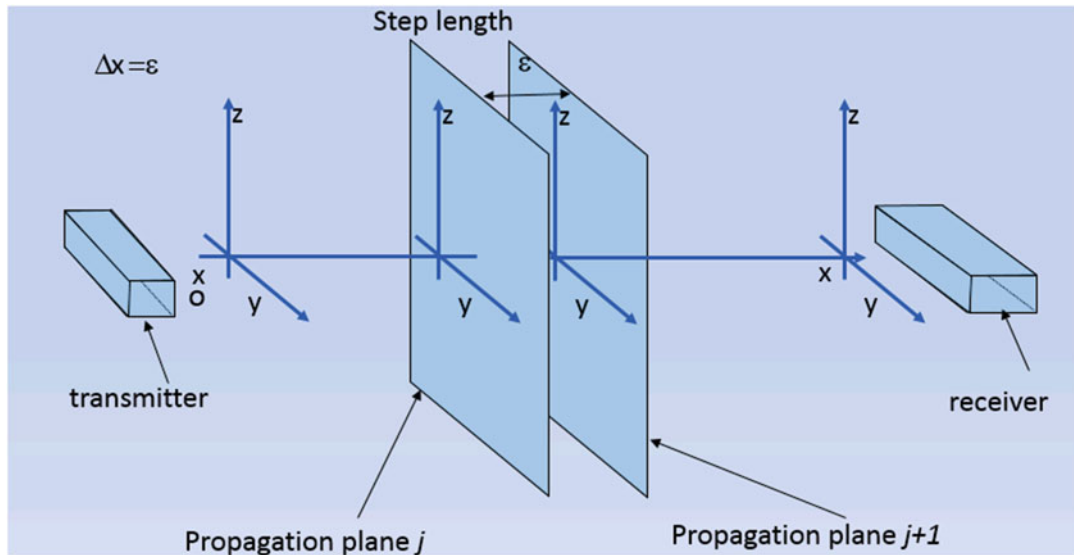


Fig. 10.12 Propagation of the total field from plane (level) j to $j + 1$, from transmitter to receiver. L to R in figure above. This constitutes the forward problem

the gradient of F to avoid hemstitching behavior in the gradient descent. There are several other approaches, such as stochastic gradient methods, and methods adapted from large-scale minimizations from other fields. We focus here on calculation of the gradient and a step length, because these are relevant to the *nonlinear* Polyak-Ribiere-Polak method, which has variations due to Fletcher and others.

We utilize the known analytic nature of the forward problem and the following representation of the derivative of a real scalar with respect to (wrt) a complex variable γ :

$$\frac{\partial}{\partial \bar{\gamma}} F_\omega(\gamma, \bar{\gamma}) = \frac{1}{2} \left(\frac{\partial F}{\partial \gamma_R} + i \frac{\partial F}{\partial \gamma_I} \right),$$

here $\frac{\partial F}{\partial \gamma_R}(\gamma, \bar{\gamma}), \frac{\partial F}{\partial \gamma_I}(\gamma, \bar{\gamma})$ are the derivatives of the object function wrt the real and imaginary parts of γ .

10.18.1 Jacobian Action

The gradient of F will require the adjoint action of the Jacobian operator, and this operator will also be required for a quick estimate of the step length.

The Jacobian of the forward problem is (because the measured data are fixed (see Fig. 10.13) and do not depend on the object γ):

$$J_n \equiv \left(\frac{\partial \mathbf{r}_{l\theta}}{\partial \gamma} \right)_n,$$

The Jacobian action on a particular variation/perturbation of the transmission coefficient \mathbf{t} , $\delta \mathbf{t}_j$ is obtained by perturbation argument as:

$$\delta \mathbf{f}_j = \delta \mathbf{t}_j \circ \mathbf{A} \mathbf{f}_{j-1} + \mathbf{t}_j \circ \mathbf{A} (\delta \mathbf{f}_{j-1}), \text{ with } \mathbf{t}_j(\mathbf{r}_T) \equiv e^{i\varepsilon(k(x_j, \mathbf{r}_T) - k_0)} = e^{i\varepsilon k_0(\gamma(x_j, \mathbf{r}_T))}.$$

Note that both the total field \mathbf{f}_j and the perturbation $\delta \mathbf{f}_j$ are required and that $\delta \mathbf{t}_j(\mathbf{r}_T) = i\varepsilon k_0 e^{i\varepsilon k_0(\gamma(x_j, \mathbf{r}_T))} \delta \gamma(x_j, \mathbf{r}_T)$.

10.18.2 The Gradient of Functional

Given the objective functional

$$F_\omega(\gamma, \bar{\gamma}) \equiv \frac{1}{2} \sum_{l\theta} \bar{\mathbf{r}}_{l\theta}^T \mathbf{r}_{l\theta},$$

then the gradient of the functional is given by direct calculation (using the analyticity of the

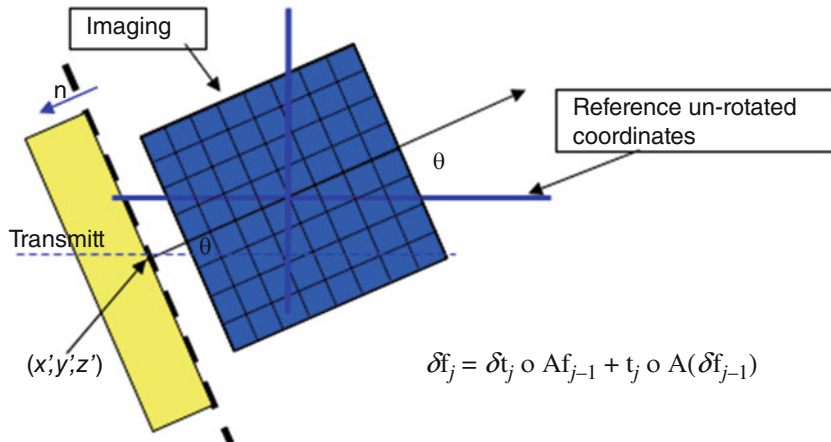


Fig. 10.13 Pictorial representation of the action of the Jacobian on a perturbation of γ , the object function. (Reprinted with permission from Wiskin et al.,

“Non-linear inverse scattering: high-resolution quantitative breast tissue tomography,” J Acoust Soc Am, vol. 131, pp. 3802–13, May 2012)

forward problem):

$$\frac{\partial}{\partial \bar{\gamma}} F_\omega(\gamma, \bar{\gamma}) = \sum_{l\theta} \left(\overline{\frac{\partial}{\partial \gamma} \mathbf{r}_{l\theta}} \right)^T \mathbf{r}_{l\theta} \equiv \bar{J}_\omega^T \mathbf{r},$$

where we've used the fact that

$$\begin{aligned} \frac{\partial}{\partial \bar{\gamma}} F_\omega(\gamma, \bar{\gamma}) &= \frac{\partial}{\partial \bar{\gamma}} \sum_{l\theta} \mathbf{r}_{l\theta}^T (\bar{\gamma}) \mathbf{r}_{l\theta} (\gamma) \\ &= \sum_{l\theta} \left[\frac{\partial}{\partial \bar{\gamma}} \mathbf{r}_{l\theta}^T (\bar{\gamma}) \right] \mathbf{r}_{l\theta} (\gamma) \\ &= \sum_{l\theta} \left[\frac{\partial \mathbf{r}_{l\theta}}{\partial \gamma} (\gamma) \right]^T \mathbf{r}_{l\theta} (\gamma) \equiv \bar{J}_\omega^T \mathbf{r}. \end{aligned}$$

The actual form of the Hermitian (conjugate transpose) of the Jacobian is determined by the following two-step process (this is easily validated by noting that the Jacobian is a linear operator – we seek the adjoint as a linear operator, which is adjoint to the recursion formula for the action of the Jacobian on a perturbation of the transmission coefficients above).

1. $J_n : \mathbf{C}^{N_x N_y N_z} \rightarrow \mathbf{C}^{N_R}$: A back-propagated field is formed from the receiver elements to the last level of the image grid, $(f_{\mathbf{r}_{l\theta}}^{back})_N$ as in Fig. 10.14.
2. This field is “back-propagated” into the entire image space (a level at a time) by the backward recursion using the complex conjugation of the transmission coefficient which guar-

antees proper behavior of attenuative (non-unitary components) of the coefficient. Similarly, the conjugation of the propagator guarantees proper behavior of “evanescent” wave components going in the backward direction. Finally, the action of the adjoint on a “residual” at the receiver (data space) is given by the product of the total field with the “back-propagated field”. See (Wiskin et al. 2020).

Figure 10.14 shows this process pictorially.

This formula agrees with the Banach space operator calculations carried out above in the *case that the infinitesimal distance ϵ goes to zero*. See also (Wiskin et al. 2017) for further discussion.

10.18.3 Spatial Resolution

The spatial resolution resulting from the transmission and reflection algorithm are discussed in (Malik et al. 2018). Specifically, the results are reflection: < 1 mm (coronal plane), transmission: <1.5 mm (coronal plane FWHM – almost isotropic in 3D). The point spread function (PSF) is almost isotropic due to the model-based nature of the reconstruction (imaging) process, although the vertical PSF is slightly larger than x or y directions.

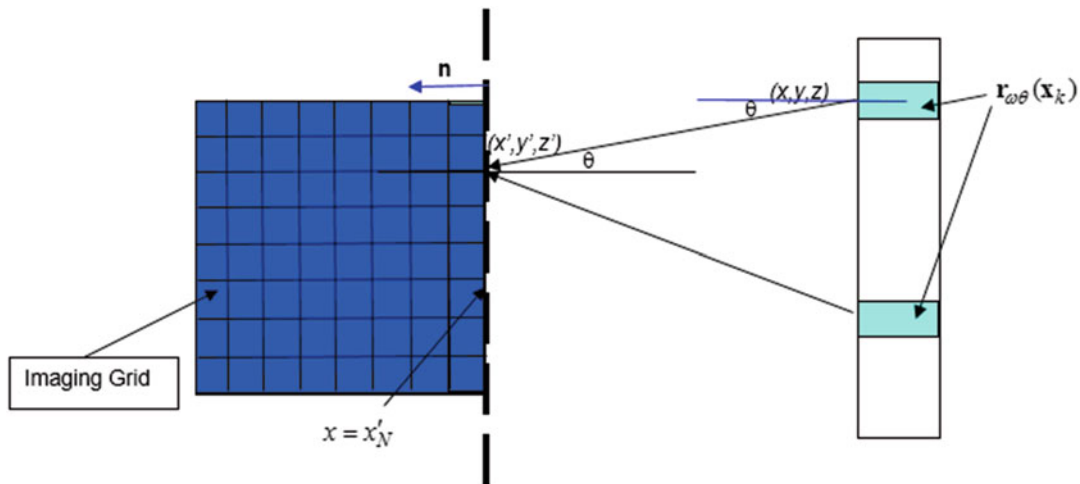


Fig. 10.14 Back-projecting the residual to the image space is a two-step process: 1. Propagate from receiver to image space, 2. Propagate through image space recursively. (Reprinted with permission from Wiskin et al.,

“Non-linear inverse scattering: high resolution quantitative breast tissue tomography,” J Acoust Soc Am, vol. 131, pp. 3802–13, May 2012)

These results are of course improving every year.

10.18.4 NVIDIA GPUs

It turns out this algorithm is mathematically congruent to training a gauge invariant fully connected CNN with complex coefficients (Wiskin 2022). The convolutional nature of the paraxial approximation algorithm is represented in the use of the FFTs. The result of this is that NVIDIA GPUs and CUDA implementations are close to optimal. This is demonstrated in the following graphs (Figs. 10.15 and 10.16), which show the variation of the time to reconstruct as a function of the data levels in the data collection process (e.g., if the data levels are 2 mm apart, the breast size is 120 mm for a 60 data level case). The NVIDIA RTX gives results that vary nonlinearly with mammographically dense breasts (i.e., breasts that have a relatively large percentage of total breast volume and are composed of fibroglandular material) due to the adaptive nature of the algorithm. However, even large breasts (14 cm tall in water bath, for example) take on the order of 30 min.

This number compares favorably with non-paraxial methods that also utilize NVIDIA cards (Guasch et al. 2020), which take 32 h on a 128 node supercomputer. Note the results below were carried out on only two GPUs. The new A100 GPUs have a verified speed up of 3X over the RTX 6000. This indicates that images for even the larger sized breasts will be available in 10 min, with only two A100’s.

In Fig. 10.16 we isolate medium to large dense breasts and observe an almost linear relationship with approximately 15 s added for each additional data level. These are carried out with the RTX NVIDIA card. The times are consistently approximately three times faster with the NVIDIA A100 cards.

The following section discusses the refraction-corrected reflection algorithm.

10.19 The Reflection Algorithm

This algorithm supplies the refraction-corrected image, which is used in parallel with the speed of sound map in diagnostic situations. Indeed, these two images are displayed in correlated fashion in the QT Imaging viewer and are also available in DICOM format.

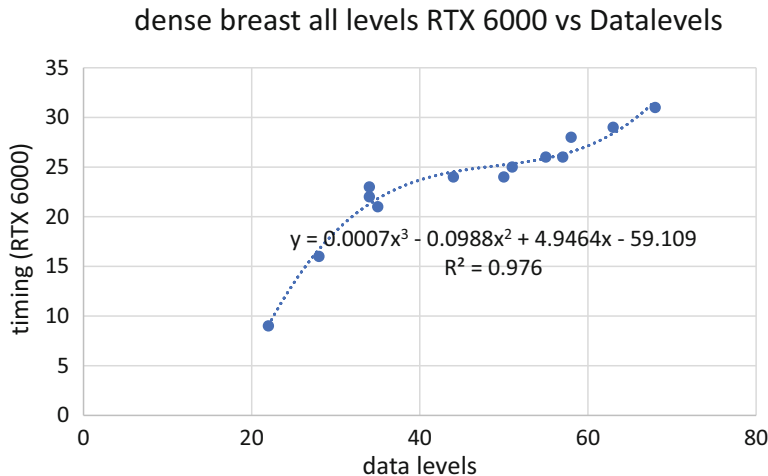


Fig. 10.15 The behavior of reconstruction times vs size of dense breasts, i.e., when the ratio of fibroglandular tissue to total breast volume is 30% or larger. The timing is not a linear function of size due to the adaptive nature

of the algorithm. (Reprinted with permission from Wiskin and J. Klock, “3D Ultrasound tomography timing validation for clinical deployment,” in 2022 IEEE International Ultrasonics Symposium (IUS), 2022, pp. 1–3)

RTX timing vs data levels

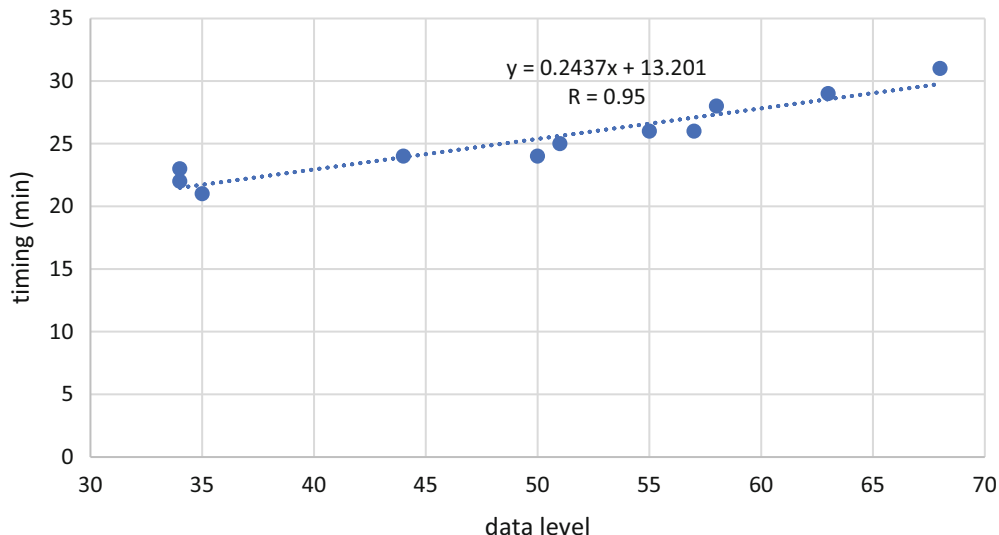


Fig. 10.16 The timing behavior for medium to large size breasts is almost linear with approximately 15 s added for each additional data level, unlike behavior for all breast sizes (Fig. 10.15)

The speed of sound map is created first, and the refraction-corrected nature of the reflection image allows for 360-degree compounding. The refraction-corrected reflection algorithm begins with the eikonal equation, and the definition of the index of refraction: $n(\mathbf{r}) = \frac{c_o}{c(\mathbf{r})}$ and the phase

ϕ , given by the ansatz:

$$\begin{aligned} \mathbf{u}(\mathbf{r}, t) &= A(\mathbf{r}) e^{-i\omega(t-T(\mathbf{r}))} \\ &= A(\mathbf{r}) e^{-i\omega t} e^{ik_o T(\mathbf{r})} \\ &= A(\mathbf{r}) e^{-i\omega t} e^{i\phi(\mathbf{r})}. \end{aligned}$$

Here, $T(\mathbf{r}) = \frac{\phi(\mathbf{r})}{c_o}$, $k_o = \frac{\omega}{c_o}$, describe the “travel time”, T , and wavenumber k_o . The eikonal equation then

$$(\nabla\varphi \bullet \nabla\varphi) = n^2(\mathbf{r})$$

comes directly as the first term in an asymptotic expansion in frequency of the Helmholtz equation. Thus, it is a high-frequency approximation to wave propagation. The form most conducive to computer implementation is the ray-tracing form which is as follows (derived below), and \mathbf{r} is the position of the ray being traced, s is arclength,

$$\frac{d}{ds} \left(n \frac{d\mathbf{r}}{ds} \right) = \nabla n.$$

From Fig. 10.17, we note that the ray tracing path will have a tangent vector that is parallel to the normal to the wavefront, which is given by the gradient of the phase function ϕ .

Because the magnitude of the gradient is $n(\mathbf{r})$ (the eikonal equation is $|\nabla\varphi| = |n(\mathbf{r})|$), the unit vector perpendicular to the wavefront is set equal to the unit vector obtained by differentiating the position vector on the ray, \mathbf{u} , by arc-length s ,

$$\frac{1}{n(\mathbf{r})} \nabla\varphi(\mathbf{r}) = \frac{d\mathbf{r}}{ds},$$

both are unit vectors.

In component form this is

$$\frac{1}{n(\mathbf{r})} \frac{\partial}{\partial x^j} \varphi(\mathbf{r}) = \frac{dx^j}{ds}.$$

Now differentiating wrt arclength s gives:

$$\frac{d}{ds} \left(n(\mathbf{r}) \frac{dx^j}{ds} \right) = \frac{\partial}{\partial x^j} \left(\frac{d}{ds} \varphi(\mathbf{r}) \right).$$

Expanding the RHS

$$\begin{aligned} \text{RHS} &= \frac{\partial}{\partial x^j} \left(\frac{dx^i}{ds} \frac{\partial}{\partial x^i} \varphi(\mathbf{r}) \right) \\ &= \frac{\partial}{\partial x^j} \left(\frac{1}{n(\mathbf{r})} \frac{\partial}{\partial x^i} \varphi(\mathbf{r}) \frac{\partial}{\partial x^i} \varphi(\mathbf{r}) \right). \end{aligned}$$

Which in light of $\frac{\partial}{\partial x^i} \varphi(\mathbf{r}) \frac{\partial}{\partial x^i} \varphi(\mathbf{r}) = \nabla\varphi(\mathbf{r}) \bullet \nabla\varphi(\mathbf{r}) = n^2(\mathbf{r})$, gives

$$\frac{d}{ds} \left(n(\mathbf{r}) \frac{dx^j}{ds} \right) = \frac{\partial}{\partial x^j} (n(\mathbf{r})), \text{ i.e.,}$$

$$\frac{d}{ds} \left(n \frac{d\mathbf{r}}{ds} \right) = \nabla n,$$

the form we desire.

This last form is very convenient for numerical calculation on the NVIDIA cards, because each ray can be traced independently. This results in a massive speedup, although the original eikonal can also be used and has some conceptual advantages.

The refraction-corrected reflection algorithm allows for 360-degree compounding which gives a high-resolution image, due to the transverse PSF being relevant. It is also a priori *2D isotropic* by virtue of this compounding.

The following diagram gives a geometric interpretation of the ray path formalism derivation from the wavefront formulation. In this diagram (Figs. 10.17 and 10.18) slowness $S(\mathbf{r}) = \frac{1}{c(\mathbf{r})} = \frac{n(\mathbf{r})}{c_o}$, and $T(\mathbf{r}) = \text{const}$ describes the wavefront, where $T(\mathbf{r}) = \frac{\phi(\mathbf{r})}{c_o}$ is a measure of time.

10.20 Examples of Inverse Scattering Images

Now that the theory has been laid out to some degree, we show some typical images (Figs. 10.19, 10.20 and 10.21) that verify the clinical utility of the method. Three things are important clinically: 1. The quantitative accuracy, 2. The high resolution, and 3. The availability in reasonable time of the images.

10.21 Limited View

There are certain clinically relevant situations where the 360-degree compounding is not relevant. This requires a reconstruction with limited view angles. Below we document some effects of

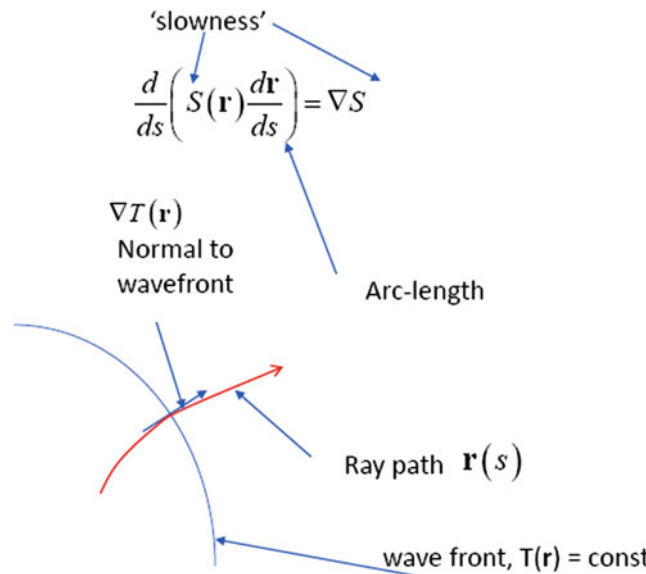


Fig. 10.17 Gradient of phase function is normal to wave front and therefore parallel to tangent to ray tracing. Normalizing by the index of refraction gives a unit vector

by virtue of the eikonal equation in partial differential equation form

$$\nabla T(\mathbf{r}) \bullet \nabla T(\mathbf{r}) = S^2(\mathbf{r}), \quad T(\mathbf{r}) \equiv \frac{\phi(\mathbf{r})}{c_o}, \quad S(\mathbf{r}) = \frac{1}{c(\mathbf{r})}$$

$$\frac{d}{ds} \left(S(\mathbf{r}) \frac{d\mathbf{r}}{ds} \right) = \nabla S$$

Fig. 10.18 The eikonal equations can be written in terms of travel time or slowness, as well as the phase function ϕ

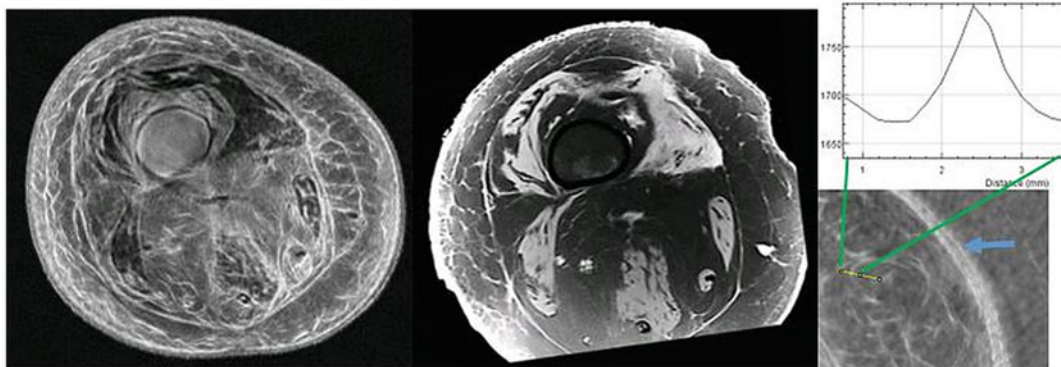


Fig. 10.19 The ultrasound volography image is on left. The MRI at the same level is in the middle panel. Note the inverted grayscale on the ultrasound volography – USV image. Note the USV has more detail in the fat region (right side of left image). The right most panel shows

the FWHM (top) estimation based on a visible structure (bottom). (Reprinted with permission from Wiskin et al., “Full wave 3D inverse scattering transmission ultrasound tomography in the presence of high contrast,” Scientific Reports, vol. 10, p. 20166, 2020)

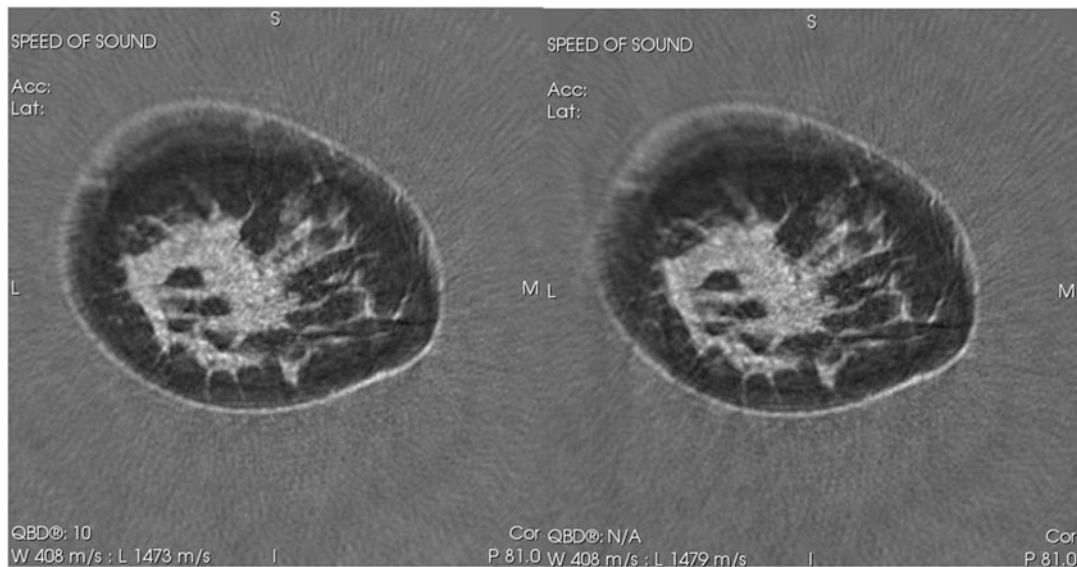


Fig. 10.20 Comparison of full aperture(left) with limited view reconstruction (right). 32 degrees are missing in this case. The degradation is seen in the lack of definition of the skin. Quantitative accuracy is minimally compromised at the skin. The image\adjust{vprotect\newpage} is just

beginning to deteriorate. Some degradation can be seen on close inspection. "Limited view reconstructions with transmission ultrasound tomography: clinical implications and quantitative accuracy", vol. 11,319: SPIE, 2020

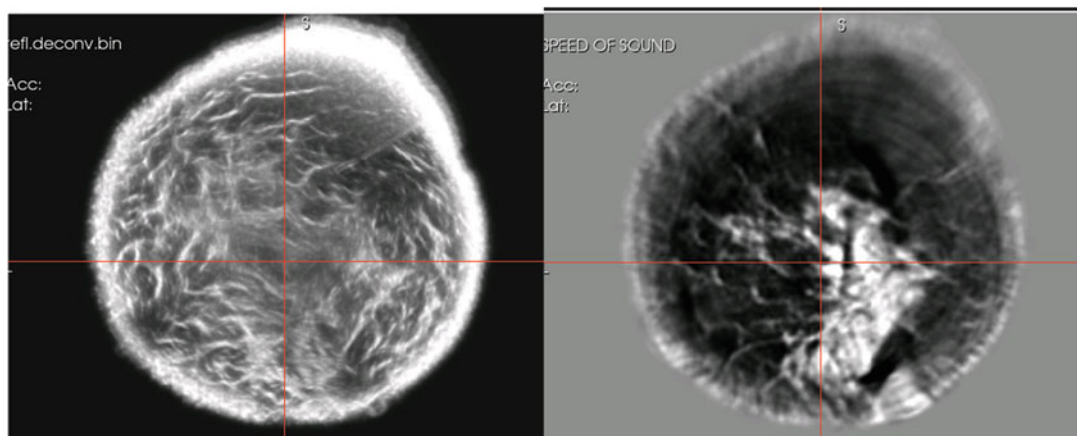


Fig. 10.21 Left is the refraction corrected 360-degree compounded reflection image. The grayscale is L: 17 W: 40. The right is the speed of sound for a typical breast

image. The grayscale is L:1473 W: 200 (m/s). L central Level, W width. Reflection has no units

missing angles in the tomographic reconstruction. The importance lies in the azimuthal missing angles, so coronal views are shown.

10.22 Important Topics

10.22.1 Timing, Stopping Criteria, L₁ Norms, Frequency Hopping, Attenuation, and Regularization

Time does not permit an exhaustive study of the importance of stopping criteria for the iterative process at each frequency and these other important topics. However, it is important to mention these and quickly summarize how they are dealt with.

10.22.2 Stopping Criteria

The iterative process is ended when the residual is below some predetermined value. This rather crude criterion can be supplemented with the behavior of the gradient or statistical analysis of the image properties on the fly. The process must definitely be adaptive because, for example, a fatty breast will converge more quickly than a dense breast and the overall size will have an effect on the image quality for a fixed number of iterations. Generally, the behavior of the magnitude of the residual and the magnitude of the gradient are relevant to finding a correct stopping criterion. Alternative indices, such as stochastic behavior can be used as well. The different stopping criteria provide a test or tests to determine when sufficient iterations have been carried out. Note that over convergence can be deleterious to image quality (and in fact almost always is). It has been observed that iteration counts are quite different for different imaged objects, knees vs whole-body images, and dense (mammographically dense)

breasts behave differently than fatty breasts for example.

10.22.3 L₁,L₀ Norms

The use of L_1 norms in tomography has increased dramatically over the past decades due to the work of Chambolle (2004) and the Fast Iterative Shrinking Algorithm (FISTA) and adaptions related to it (Accelerated FISTA) (Babapour et al. 2021). The literature on this is large. The discussion above is the foundation for further investigation using these tools. There are trade-offs with image quality that can be non-trivial when these methods are applied so care must be exercised with advice of a radiologist or trained medical diagnostician to verify that changes in image quality will not adversely affect diagnoses in a clinical setting (this is a regulatory problem well beyond our scope here). Note that the total variation regularization uses the L_1 norm of the gradient of the image, and has some advantages. The L_0 norm is used in Compressed sensing, which is a large area of research of particular value in certain cases where the image is not sampled adequately from a Nyquist point of view.

10.22.4 Frequency Hopping

Often referred to cycle skipping in the geophysics literature (where inverse scattering is referred to as full wave inversion – FWI) (Pratt et al. 1998) this is the tendency of large-scale optimizations (40 million or more unknowns for a large breast) to fall into local minima if the frequency is chosen too high or if one moves upward in frequency in large jumps. This local minimum problem can have severe consequences as shown in Fig. 10.22.

The local minimum problem can be observed to cause artifacts that may affect diagnosis and therefore are unacceptable.

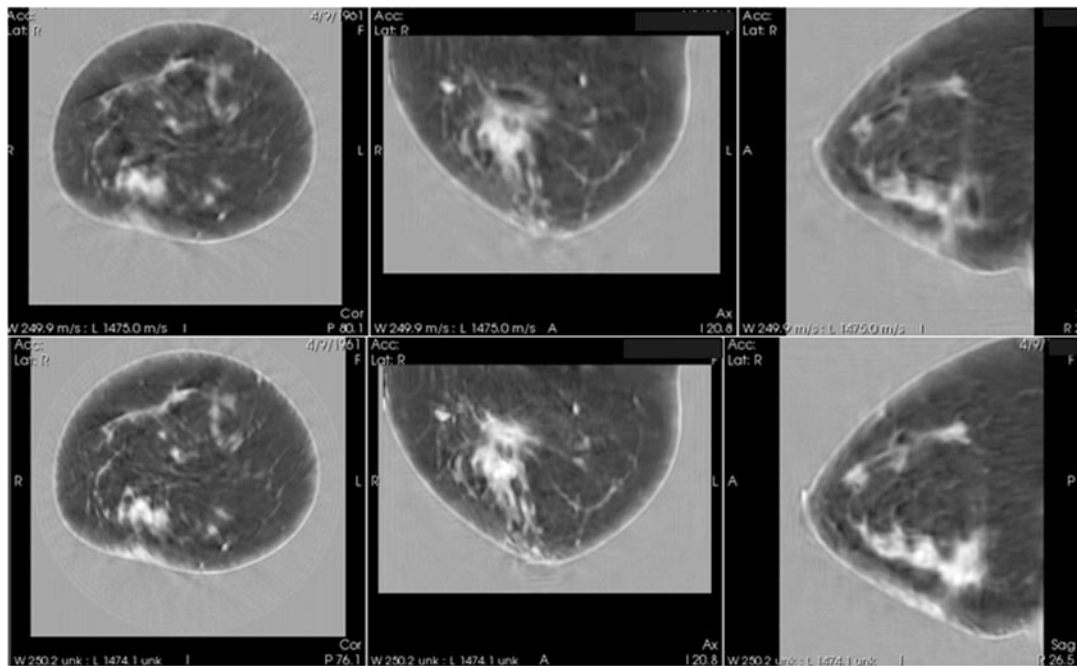


Fig. 10.22 Top is speed of sound image at local minimum. Note the dark region (low speed of sound) which appears to be a fat cyst or other structure. The grayscale is 1350 → 1700 (black → white). Bottom: same data

reconstructed to avoid cycle skipping. The region is now showing up correctly as a high-speed region. (Data and image from TechniScan 2006 internal study)

10.22.5 Attenuation

Attenuation is dealt with in the paraxial approximation as the complex part of the wavenumber as described above. The proper treatment for attenuation is relatively straightforward for frequency domain methods as opposed to time domain methods where fractional derivatives are sometimes employed.

10.22.6 Regularization

Regularization is another vast topic that can be addressed now that a solid foundation for the inverse scattering or FWI imaging problem has been laid. The various regularizing terms can involve a priori information or gradient information of the present iteration of the image.

10.22.7 Artificial Intelligence

It would be impossible to cover the application of AI to ultrasound tomography/vogography to any degree here. However, the geometric increase in the number of abstracts submitted to IEEE International Ultrasound symposium, and publications that deal with machine and deep learning indicate it is rapidly becoming de facto normative in inverse scattering applications.

We will only mention that the use of artificial neural networks (ANN) and specifically CNN's has transcended image enhancement and analysis, which have been historically the areas of applicability. There are a large number of reviews discussing enhancement and analysis presently. We focus on image generation.

Fan et al. (2021) have employed dual domain network architecture to create 2D images with high resolution with fast reconstruction times.

The dual nature referred to here is the simultaneous use of the image and data domain. They also avoid the use of fully connected layers. This is important as it has memory-saving repercussions.

It is important to note that it has been shown that there is a mathematical congruence between a fully connected CNN with complex weights and certain Lie group symmetries among the weights, and the paraxial approximation approach to the inverse scattering problem. Thus, the training of the CNN and the formation of the 3D volume of speed of sound are mathematically the same. The problems are dual though, in the sense that the important result for the CNN are the images, and the weights are unimportant. Conversely in the inverse scattering problem the “weights” play the role of the 3D image and are thus ultimately important. The fields in this case correspond to the “images” being processed in CNN, but in the inverse scattering problem are ultimately not important.

Finally, both of these problems are equivalent to immersion of a smaller manifold into a larger one, which in the case of the inverse scattering problem, the larger dimensional manifold is non-Euclidean (it is an n-dimensional torus, where n is the number of receivers on the array). Certain manifestations of CNNs also have this property. The map need only be an immersion, not an embedding (i.e., the target space may not be a manifold). This point of view has data acquisition implications.

The IEEE Transactions Medical Imaging special issue (Wang et al. 2018), for example, discusses multiple examples of image reconstruction algorithms based on Deep Learning that are a complement to those used in imaging analysis and processing. This issue and the introduction (Wang et al. 2018) in particular are a valuable source of information, though somewhat dated due to the fast-developing nature of the field. These methods are associated with MR, CT, and PET imaging which involve the inversion of linear models. They are therefore much easier problems than the nonlinear inversion associated with the problem we have just investigated. The U-net architecture and generational adversarial networks (GAN) are used for image reconstruction in Fan et al. (2021).

These approaches are required due to the inherent nonlinearity of the full imaging problem. Using the data acquisition geometry and code for the paraxial approximation is more amenable than a full-blown all-view reconstruction utilizing both forward and reflected data. This helps explain the success of Fan et al. (2021). The paraxial approach is in some sense the next level generalization of the geometry and algorithm of the Radon transform. Indeed, the linearization of the forward problem in inverse scattering yields the well-known algorithm of diffraction tomography (Devaney and Oristaglio 1983).

Both the standard minimization-based inversion algorithms that have been historically used in inverse scattering and the relatively recent use of the CNNs can benefit from the duality mentioned above, in that skip-connections, down/up sampling, pooling, stochastic gradients, etc., in training CNNs have counterparts in inverse scattering and vice versa.

10.23 Summary: Clinical Importance of 3D Volography

Applications involve breast imaging related to breast cancer, imaging of knees and joints for orthopedic applications, and whole-body imaging for pediatrics. While these applications are under development, this and the following chapter, and multiple research papers presented at the IEEE International Ultrasound Symposium, the SPIE Medical Imaging symposium, and other venues attest to the growing importance and utility of ultrasound tomography/volography. The further advantage of ultrasound tomography/volography as very safe (no ionizing radiation, no contrast agents) coupled with the quantitative accuracy, low cost, and high resolution indicate that this modality is truly a twenty-first-century technology.

We have observed how the operator approach shows clearly the nonlinear and ill-posed nature of the inverse scattering medium problem, which is at the heart of ultrasound tomography/volography. We also summarized

why the full 3D algorithm is generally recognized as important in this context as opposed to a “slice by slice” reconstruction. This facilitates the need for a term (volography) to indicate this difference, not necessarily to mathematically informed theorists, but to medical personal who may not appreciate this difference that leads to clinically acceptable images.¹

References

- Andre M, Janee H, Otto G, Martin P, Spivey B, Palmer D (1997) High speed data acquisition in a diffraction tomography system employing large-scale toroidal arrays. *Int J Imaging Syst Technol* 8:137–147
- Devaney AJ (2012) Angular-spectrum and multipole expansions. Mathematical foundations of imaging, tomography and wavefield inversion. Cambridge University Press, Cambridge, pp 118–168
- Babapour S, Lakestani M, Fatholahzadeh A (2021) AFISTA: accelerated FISTA for sparse signal recovery and compressive sensing. *Multimed Tools Appl* 80:20707–20731
- Chambolle A (2004) An algorithm for Total variation minimization and applications. *J Math Imaging Vision* 20:89–97
- Cheney M, Rose JH, Defacio B (1989) A new equation of scattering theory and its use in inverse scattering. *Wave Motion* 11:175–184
- Chew WC, Wang YM (1990) Reconstruction of two-dimensional permittivity distribution using the distorted Born iterative method. *IEEE Trans Med Imaging* 9:218–225
- Colton D, Kress R (1992) Inverse acoustic and electromagnetic scattering theory. Springer-Verlag, Berlin
- Devaney AJ (1982) A filtered backpropagation algorithm for diffraction tomography. *Ultrason Imaging* 4:336–350
- Devaney AJ, Oristaglio ML (1983) Inversion procedure for inverse scattering within the distorted-wave born approximation. *Phys Rev Lett* 51:237–240
- Duric N, Littrup PJ, Holsapple E, Babkin A, Duncan R, Kalinin A et al (2003) Ultrasound tomography of breast tissue. In: Medical imaging 2003: ultrasonic imaging and signal processing, pp 24–32
- Duric N, Littrup P, Babkin A, Chambers D, Azevedo S, Kalinin A et al (2005) Development of ultrasound tomography for breast imaging: technical assessment. *Med Phys* 32:1375–1386
- Duric ND, Li C, Littrup P, Huang L, Glide-Hurst CK, Ramsa O et al (2009) Detection and characterization of breast masses with ultrasound tomography: clinical results. In: Medical imaging 2009: ultrasonic imaging, tomography and therapy. SPIE 72651G: detection and characterization of breast masses with ultrasound tomography: clinical results, pp 1–8
- Duric N, Littrup P, Roy O, Schmidt S, Li C, Bey-Knight L et al (2013) Breast imaging with ultrasound tomography: initial results with SoftVue. In: 2013 IEEE International Ultrasonics Symposium (IUS), pp 382–385
- Fan Y, Wang H, Gemmeke H, Hopp T, Hesser J (2021) DDN: dual domain network architecture for non-linear ultrasound transmission tomography reconstruction, vol 11602. SPIE
- Greenleaf JF, Johnson SA, Lee SL, Herman GT, Woo EH (1974) Algebraic reconstruction of spatial distributions of acoustic absorption within tissue from their two-dimensional acoustic projections. In: Green PS (ed) Acoustical holography: volume 5. Springer, Boston, pp 591–603
- Greenleaf JF, Johnson SA, Samayoa WF, Duck FA (1975) Algebraic reconstruction of spatial distributions of acoustic velocities in tissue from their time-of-flight profiles. In: Booth N (ed) Acoustical holography: volume 6. Springer, Boston, pp 71–90
- Guasch L, Calderón Agudo O, Tang M-X, Nachev P, Warner M (2020) Full-waveform inversion imaging of the human brain. *npj Digit Med* 3:28
- Hohage T (2001) On the numerical solution of a three-dimensional inverse medium scattering problem. *Inverse Prob* 17:1743–1763
- Huthwaite P, Simonetti F, Duric N (2012) Combining time of flight and diffraction tomography for high resolution breast imaging: initial invivo results (I). *J Acoust Soc Am* 132:1249–1252
- Jirik R, Peterlik I, Ruiter N, Fousek J, Dapp R, Zapf M et al (2012) Sound-speed image reconstruction in sparse-aperture 3-D ultrasound transmission tomography. *IEEE Trans Ultrason Ferroelectr Freq Control* 59:254–264
- Johnson SA, Tracy ML (1983) Inverse scattering solutions by a Sinc basis, multiple source, moment method – part I: theory. *Ultrason Imaging* 5:361–375
- Johnson SA, Stenger F, Wilcox C, Ball J, Berggren MJ (1982) Wave equations and inverse solutions for soft tissue. In: Powers JP (ed) Acoustical imaging. Springer, Boston, pp 409–424
- Johnson SA, Borup DT, Berggren MJ, Wiskin JW, Eiedens R (1992) Modeling of inverse scattering and other tomographic algorithms in conjunction with wide bandwidth acoustic transducer arrays for towed or autonomous sub-bottom imaging systems. In: OCEANS 92 proceedings@m_Mastering the Oceans through technology, pp 294–299
- Kay I, Moses HE (1961) The determination of the scattering potential from the spectral measure function. *Il Nuovo Cimento (1955–1965)* 22:689–705

¹ Note: The references are inadequate due to the fast-growing nature of the field. However, hopefully they will aid the reader in beginning their investigation in ultrasound tomography/volography, and any omissions do not reflect the quality of the work being done in this area by numerous research groups.

- Kirsch A (1996) An introduction to the mathematical theory of inverse problems. Springer, New York
- Lavarello R, Oelze M (2007) A study on the reconstruction of moderate contrast targets using the distorted born iterative method. *IEEE Trans Ultrason Ferroelectr Freq Control* 55:112–124
- Lavarello RJ, Oelze ML (2009a) Density imaging using inverse scattering. *J Acoust Soc Am* 125:793–802
- Lavarello RJ, Oelze M (2009b) Tomographic reconstruction of three dimensional volumes using the distorted born approximation. *IEEE Trans Med Imaging* 28:1643–1653
- Li C, Duric N (2013) Resolution limitation of travel time tomography: beyond the first Fresnel zone, pp 86751D–86751D-10. <https://doi.org/10.1117/12.2006978>
- Li C, Duric N, Littrup P, Huang L (2009) In vivo breast sound-speed imaging with ultrasound tomography. *Ultrasound Med Biol* 35:1615–1628
- Malik B, Terry R, Wiskin J, Lenox M (2018) Quantitative transmission ultrasound tomography: imaging and performance characteristics. *Med Phys* 45:3063–3075
- Malik B, Iuanow E, Klock J (2020) An exploratory multi-reader, multi-case study comparing transmission ultrasound to mammography on recall rates and detection rates for breast cancer lesions. *Acad Radiol* 29(Suppl 1):S10–S18
- Matthews TP, Wang K, Li C, Duric N, Anastasio MA (2017) Regularized dual averaging image reconstruction for full-wave ultrasound computed tomography. *IEEE Trans Ultrason Ferroelectr Freq Control* 64:811–825
- Natterer F, Wubbeling F (1995) A propagation-backpropagation method for ultrasound tomography. *Inverse Prob* 11:1225–1232
- Newton RG (1966) Scattering theory of waves and particles. The University of Michigan
- Ozmen N, Dapp R, Zapf M, Gemmeke H, Ruiter NV, Van Dongen KWA (2015) Comparing different ultrasound imaging methods for breast cancer detection. *IEEE Trans Ultrason Ferroelectr Freq Control* 62:637–646
- Pratt RG, Shin C, Hick GJ (1998) Gauss–Newton and full Newton methods in frequency–space seismic waveform inversion. *Geophys J Int* 133:341–362
- Remis RF, van den Berg PM (2000) On the equivalence of the Newton-Kantorovich and distorted Born methods. *Inverse Prob* 16:L1–L4
- Rodriguez-Ruiz A, Teuwen J, Vreemann S, Bouwman RW, van Engen RE, Karssemeijer N et al (2018) New reconstruction algorithm for digital breast tomosynthesis: better image quality for humans and computers. *Acta Radiol* 59:1051–1059
- Ruiter NV, Zapf M, Hopp T, Dapp R, Kretzek E, Birk M et al (2012) 3D ultrasound computer tomography of the breast: a new era? *Eur J Radiol* 81:S133–S134
- Sandhu GY, Li C, Roy O, Schmidt S, Duric N (2015) Frequency domain ultrasound waveform tomography: breast imaging using a ring transducer. *Phys Med Biol* 60:5381–5398
- Ulrich IE, Zunino A, Boehm C, Fichtner A (2021) Sparsifying regularizations for stochastic sample average minimization in ultrasound computed tomography, vol 11602. SPIE
- Van Dongen KWA, Wright WMD (2006) A forward model and conjugate gradient inversion technique for low-frequency ultrasonic imaging. *J Acoust Soc Am* 120:2086–2095
- Wallis G (1981) Lamb, G. L., jr., Elements of soliton theory, New York-Chichester-Brisbane-Toronto, John Wiley & Sons 1980, XII, 289 S., £ 16.00. ISBN 0-471-04559-4. ZAMM – J Appl Math Mech/Zeitschrift für Angewandte Mathematik und Mechanik 61:603–603
- Wang K, Matthews T, Anis F, Li C, Duric N, Anastasio MA (2015) Waveform inversion with source encoding for breast sound speed reconstruction in ultrasound computed tomography. *IEEE Trans Ultrason Ferroelectr Freq Control* 62:475–493
- Wang G, Ye JC, Mueller K, Fessler JA (2018) Image reconstruction is a new frontier of machine learning. *IEEE Trans Med Imaging* 37:1289–1296
- Wiskin J (2022) Ultrasound tomography as a gauge invariant fully connected convolutional neural network: repercussions. SPIE, PC12038
- Wiskin J, Johnson SA, Borup DT, Berggren M, Eidens R (1993) Full inverse scattering vs. born-like approximation for imaging in a stratified Ocean. Proceedings of OCEANS '93 453:450–455
- Wiskin JW, Borup DT, Johnson SA (1997) Inverse scattering from arbitrary two-dimensional objects in stratified environments via a Green's operator. *J Acoust Soc Am* 102:853–864
- Wiskin J, Borup DT, Johnson SA, Berggren M (2012) Non-linear inverse scattering: high resolution quantitative breast tissue tomography. *J Acoust Soc Am* 131:3802–3813
- Wiskin JW, Borup DT, Iuanow E, Klock J, Lenox MW (2017) 3-D nonlinear acoustic inverse scattering: algorithm and quantitative results. *IEEE Trans Ultrason Ferroelectr Freq Control* 64:1161–1174
- Wiskin J, Malik B, Borup D, Pirshafiey N, Klock J (2020) Full wave 3D inverse scattering transmission ultrasound tomography in the presence of high contrast. *Sci Rep* 10:20166
- Wiskin J et al (in press) Whole body imaging using low frequency transmission ultrasound. *Acad Radiol*



Clinical Importance of 3D Volumography in Breast Imaging

11

John Klock

Abstract

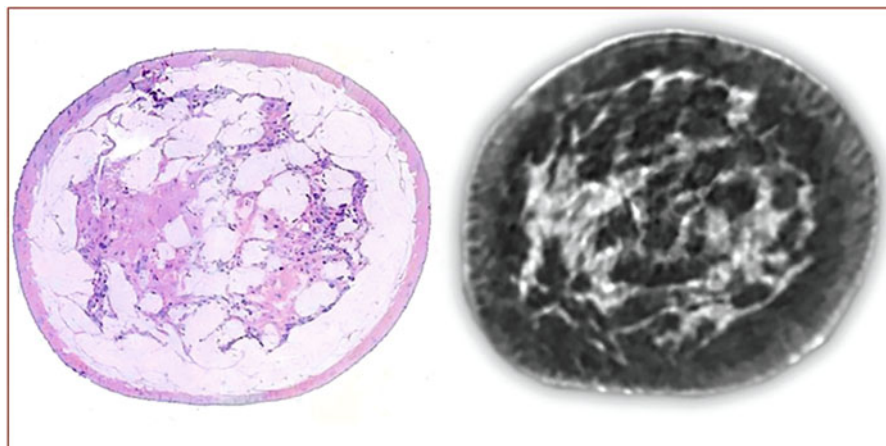
The clinical applications of the volumography algorithm and concomitant refraction-corrected reflection algorithm as described in Chap. 10 are discussed here. Comparisons with an H&E stained image, discussion of glandular tissue visibility, related biomarkers, segmentation accuracy and capabilities, microcalcification and cyst detection and analysis, and various VGA and clinical studies show the unique capabilities of the method. The accuracy of the fibroglandular segmentation and its relevance to breast density in imaging is mentioned. The compatibility with artificial intelligence (AI) is shown and clinical results discussed, concluding that low-frequency 3D ultrasound volumography is a powerful 3D ultrasound imaging technique for microanatomic and quantitative features of the breast with good potential for AI utilization to provide an imaging technique that will quantitatively improve clinical performance.

Keywords

Breast cancer · Ultrasound tomography · Speed-of-sound imaging · Microcalcification

J. Klock (✉)
QT Imaging, Novato, CA, USA
e-mail: john.klock@qtimaging.com

Transmitted sound 3D volumography of the breast sends a low-frequency (0.3–1.8 MHz) pulse pressure-wave of sound through the breast and the resulting sound energy is measured at one of a number of destinations as the wave is propagated and refracted through the breast. The multi-modality nature of transmitted sound 3D volumography is very complementary, as the speed map generated with transmission can be used to correct the reflection images for refraction and the refraction-corrected image provides detail unavailable to the speed map. This refraction correction has further advantages in that it puts every voxel in the reflection images in the correct location in 3D space. After the compounding process, all structures (e.g., Cooper ligaments) line up correctly and structures within the imaging volume are not duplicated, as is sometimes the case in ultrasound compounding without refraction and speed correction. For clinical evaluation of breast tissue, it is clear that duplication of structures that are not actually present could create an inaccurate image of the true anatomic structures, which could lead to misdiagnoses or even inaccurate measurements of findings. Furthermore, with refraction correction, contrast resolution under 100 μm is achieved in these ‘360-degree compounded’ B-



H & E WHOLE BREAST SECTION

QT SPEED IMAGE

Fig. 11.1 Histological cross section of a human breast using H&E stain (left) with corresponding transmitted sound coronal image (right). (Reprinted with permission: “Exploratory Multi-reader, Multi-case Study Comparing

Transmission Ultrasound to Mammography on Recall Rates and Detection Rates for Breast Cancer Lesions,” Academic Radiology, vol. 29, pp. S10–S18, 2022)

Mode reflection images (Klock et al. 2016). An example of a transmitted sound 3D v holography image of the human breast is shown in Fig. 11.1.

The result of each scan are volumes of speed of sound and reflection containing 30 million voxels or more, with unique quantitative speed of sound values for each voxel within the entirety of that volume (Malik et al. 2018a). This allows (1) accurate and reproducible measurements due to 3D quantitative accuracy, (2) accurate segmentation ($\pm 0.2\%$) of skin, fat, connective tissue, ducts, glands, cysts, fibroadenomas, and cancers, (3) quantitation of all structures throughout the breast volume, (4) high resolution, (5) visualization of microcalcifications, and (6) scanning to the chest wall and lower axilla. The speed of sound and reflection modality images are both presented to the clinician in the work station for review in the coronal, axial, and sagittal planes.

11.1 Microanatomy

Visualization of normal breast anatomy is crucial for accurate diagnosis in breast imaging. Defining normal anatomy informs the radiologist about

structures that are present and any abnormalities that may arise. Transmitted sound 3D v holography uses both speed of sound and reflection imaging to evaluate breast tissue. Transmitted sound 3D v holography with refraction-corrected reflection provides a stable measure of both geometry and speed-of-sound on objects as small as 0.4 mm in diameter, and evidence indicates higher resolution is possible. Clinical trials have been done using receiver-operating-characteristic analysis of a QT Imaging® system in evaluating all breast structures including microcalcifications. The technology has been tested in clinical settings and the images are unique to the methods used as seen in Figs. 11.2 and 11.3.

11.2 Biomarkers

Because the transmission mode of the scanner gives a quantitative speed of sound value for each voxel within the 3D breast dataset, there is the potential for that speed of sound value to be used as a discriminator of breast tissue type. In the published studies of transmitted sound 3D v holography, it was shown that the quantitative speed of sound value can be used as a biomarker

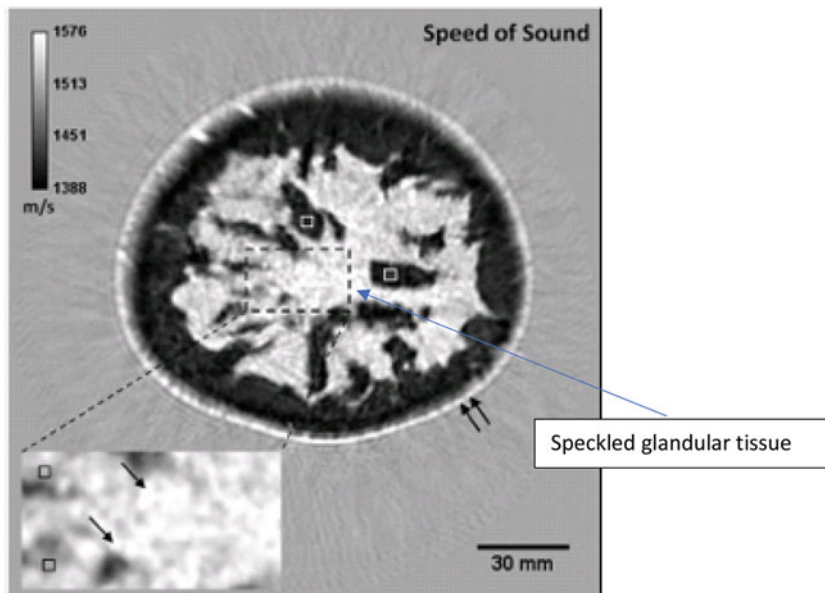
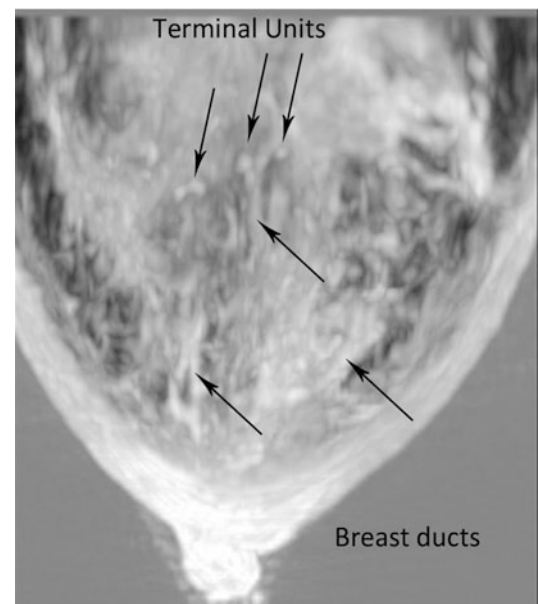


Fig. 11.2 Transmission ultrasound image (coronal view) showing “speckled” glandular tissue (left arrow) and the terminal ducto-lobular units (TDLU) of the breast as marked with 2 black pointers. Double black arrows point

to skin. (Reprinted with permission from “Objective breast tissue image classification using Quantitative Transmission ultrasound tomography,” Scientific Reports, vol. 6, p. 38857, 12/09/online 2016)

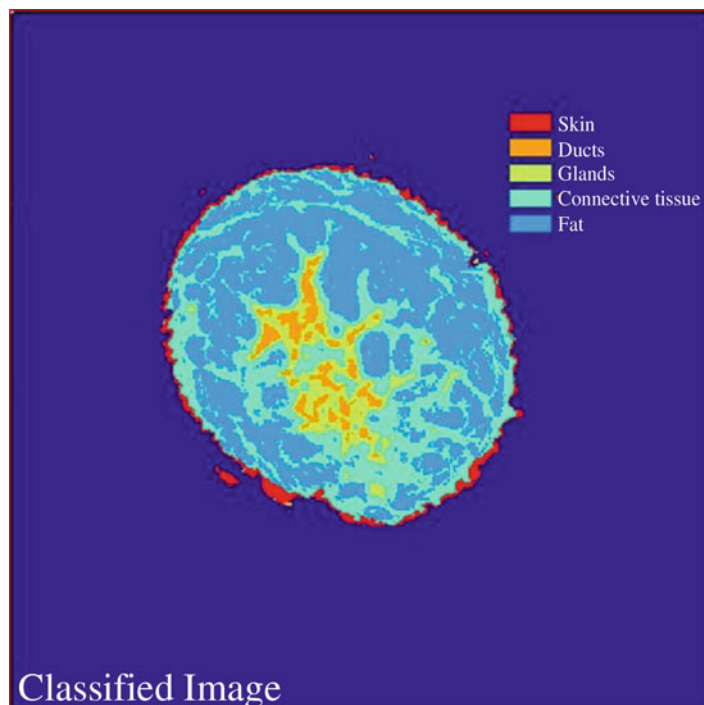
Fig. 11.3 Transmission ultrasound image (axial view) showing ductal and glandular tissue and the terminal ducto-lobular units (TDLU) of the breast. (Reprinted with permission: “Anatomy-Correlated Breast Imaging and Visual Grading Analysis Using Quantitative Transmission Ultrasound,” International Journal of Biomedical Imaging, vol. 2016, p. 9, 2016)



to further inform the radiologist as to the significance of findings, in addition to the actual speed of sound images provided to the radiologist for interpretation (Malik et al. 2016). It was shown that using a support vector machine (SVM) classi-

fier, it was possible to differentiate features of all the normal breast tissue types including skin, fat, glands, ducts, or connective tissue with an overall accuracy of greater than 90%. While the SVM algorithm showed high classification accuracy, it

Fig. 11.4 Tissue classifier using speed of sound, attenuation, and reflection as data in a support vector machine (SVM) allows tissue classification as a tool for CAD development. (Reproduced with permission: “Objective breast tissue image classification using Quantitative Transmission ultrasound tomography,” Scientific Reports, vol. 6, p. 38857, 12/09/online 2016)



is important to note that the strength of the transmission ultrasound images as a biomarker is such that most machine learning algorithms provided high accuracy. Such a visual model can be instructive in the evaluation of breast pathologies and serve as a tool to guide further CAD development. CAD has been shown to moderately improve the interpretations of experienced and inexperienced radiologists, but with a volumetric transmission ultrasound technology, we expect the level of improvement with CAD to be even greater. Colored overlay depicting the various anatomical components of the breasts with transmission ultrasound is shown in Fig. 11.4.

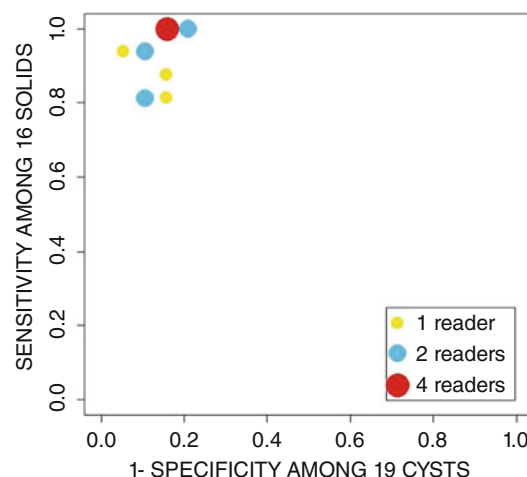
This classification system has been used to classify cystic versus solid lesions (Iuanow et al. 2017) and examples of normal tissue from abnormalities. Using the readers’ binary classification of cyst or solid lesions, the mean sensitivity and specificity were 0.933 [95% CI: 0.837, 0.995] and 0.858 [95% CI: 0.701, 0.985], respectively. When the readers’ confidence scores were used to distinguish a cyst versus solid, the mean receiver operating characteristic area was 0.920 [95% CI: 0.827, 0.985]. This is shown in Fig. 11.5.

11.3 Visual Grading Analysis (VGA)

To compare the image quality of transmitted sound 3D v holography with digital mammography and hand-held ultrasound, multiple readers scored the image quality of quantitative transmission (QT) ultrasound compared to mammography (XRM) and HHUS using an ordinal rating scale (Klock et al. 2017). The proportion of breasts where the image quality was rated better on QT was reported for each feature including different ACR BI-RADS® breast density classes. QT images were scored as equivalent or better than XRM in more than 90% of breasts. Readers scored transmission ultrasound images as equivalent or better than HHUS in more than 80% of breasts. In the analysis by breast density, there was no significant change in the performance by transmission ultrasound for any density subtype, as shown in Figs. 11.6 and 11.7.

Transmitted sound 3D v holography can see all the major anatomical features of the human breast that cannot be seen as well by

Fig. 11.5 Estimated sensitivity and false positive results among 13 readers for transmission ultrasound. The red circle corresponds to reads from 4 readers, the blue circle to 2 readers, and the yellow circle to 1 reader.
 (Reprinted with permission “Accuracy of Cyst Versus Solid Diagnosis in the Breast Using Quantitative Transmission (QT) Ultrasound,” Academic Radiology, vol. 24)



other routinely used clinical imaging methods (e.g., mammography and hand-held ultrasound (HHUS)), including accurately visualizing ductal and glandular tissue detail which is especially true even in dense breasts. This finding again emphasizes the strength of transmitted sound 3D volography in its ability to visualize breast microanatomy and hence detect any aberrations to the normal tissue that can be further classified as benign or malignant.

11.4 Breast Microcalcification Detection

Presently, a significant number of non-palpable breast cancers are detected on mammography by examining the morphology and distribution of microcalcifications. Studies show that failing to call back calcifications can lead to missed cancers in a substantial number of patients. HHUS which has been a mainstay of diagnostic breast imaging is limited and results do not support the clinical use of HHUS for this application. Transmitted sound 3D volography addresses these limitations in detecting microcalcifications, and it has been applied to detection of microcalcifications. Specifically, it has been shown that QT reflection imaging (using refraction correction supplied by the QT speed volume) can detect microcalcifications an

order of magnitude smaller than the intrinsic resolution of the system (Malik et al. 2018b). Custom fabricated phantoms show the ability of transmitted sound 3D volography to detect calcium, as measured by the contrast to noise ratio (CNR), which is superior to mammography. Specifically, a two-layer agar phantom with glass beads was created to quantify the visualization of calcium particles using QT reflection imaging. The 3% agar gel was prepared by dissolving 21 g of agar in 700 ml of DI water. Several 3 mm, 2 mm, 1 mm, 0.5 mm, and 0.1–0.3 mm calcium particles (calcium carbonate) were used as high-reflection objects within agar background. While the dimensions of the phantom were measured using a caliper, the dimensions of glass beads within the phantom were measured and verified using a calibrated X-ray image (on GE Senographe Essential). Cadaveric tissue and in-clinic breast imaging demonstrate the strength of QT to detect microcalcifications. Figure 11.8 demonstrates how this is performed.

11.5 Breast Cyst Detection and Analysis

Breast imaging with high specificity is critical to avoid additional testing and unnecessary biopsies in women who have benign disease. Ultrasound

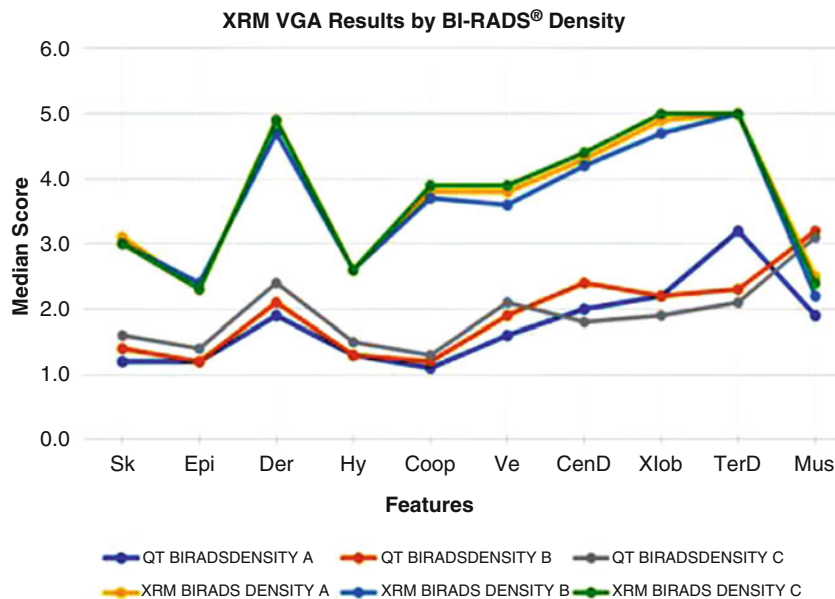


Fig. 11.6 Reader's median image quality score by modality (X-ray Mammography vs QT Ultrasound), BI-RADS® density and breast feature: skin (overall), epidermis, dermis, hypodermis, Cooper's ligaments, superficial veins, central ducts entering nipple, intermediate or peripheral ducts (extra-lobular ducts), terminal ductal lobular units, and pectoralis muscle (chest wall). A

scanning is used routinely to determine whether a lesion is solid or cystic. The accuracy of cyst vs solid has been found to be one of the hallmarks of ultrasound in breast imaging. The radiologist can detect large cysts with anechoic characteristics on traditional hand-held ultrasound because of their smooth, circumscribed margins, and their pronounced through transmission of sound and posterior enhancement, but with internal echoes, the lesion becomes harder to diagnose. Transmitted sound 3D volegraphy provides high-fidelity and spatial resolution and quantitative measurements. This is useful because closely packed cellular components in a cyst (such as cells in a suspension) exhibit a higher effective refractive index. Furthermore, higher cell counts within breast cysts result in a correspondingly higher value of refractive index, with a consequent increase in the speed of sound within the cyst. A cyst without internal proteinaceous material has a lower speed of sound

higher score indicates LESS visibility. (Reprinted with permission from "Visual Grading Assessment of Quantitative Transmission Ultrasound Compared to Digital X-ray Mammography and Hand-held Ultrasound in Identifying Ten Breast Anatomical Structures," BAOJ Clinical Trials, vol. 3, 2017)

relative to a complicated cyst or even lower than a solid lesion. This is demonstrated in Fig. 11.9.

Also, as is clear from Fig. 11.10, there is a significant correlation between cell count observed cytologically and the effective speed of sound in macro-cysts with the speed of sound increasing by 2 m/s for every additional 1000 cells.

It is important to note that no other imaging modalities can capture such quantitative variation as a function of cell count. Using QT-based classification, one can define a spectrum of breast macro cysts from fluid-filled to highly cellular with high-speed cysts being mature macro cysts with high cell counts and many cellular clumps that correlate with cyst anatomy as seen by transmission ultrasound. This technique will allow the breast imaging radiologists to have a quantitative basis for describing breast cysts and for following changes in these masses over time, if necessary, to confirm benignity (Malik and Klock 2019).

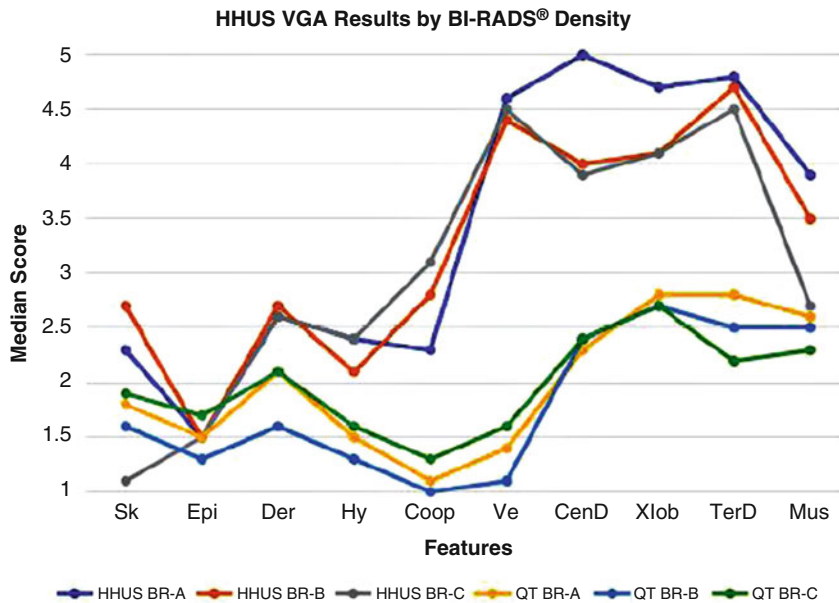


Fig. 11.7 Reader's median image quality score by modality (Hand-Held Ultrasound (HHUS) vs QT Ultra-sound), BI-RADS® density and breast feature: skin (overall), epidermis, dermis, hypodermis, Cooper's ligaments, superficial veins, central ducts entering nipple, intermediate or peripheral ducts (extra-lobular ducts), terminal ductal lobular units, and pectoralis muscle (chest wall).

A higher score indicates LESS visibility. (Reprinted with permission from “Visual Grading Assessment of Quantitative Transmission Ultrasound Compared to Digital X-ray Mammography and Hand-held Ultrasound in Identifying Ten Breast Anatomical Structures,” BAOJ Clinical Trials, vol. 3, 2017)

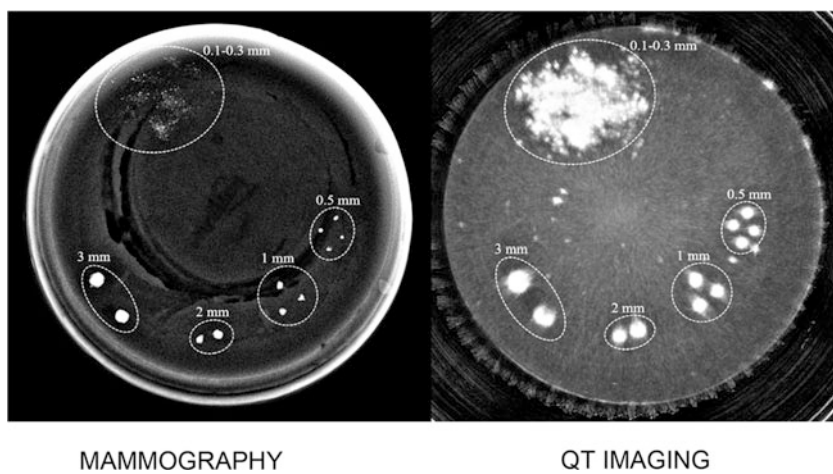


Fig. 11.8 The QT imaging system is highly sensitive to detecting calcifications as shown in these phantom studies. The detection of different sizes and shapes of calcifications are shown comparing Mammography (left) and QT imag-

ing (right). (Reprinted with permission from: “Detection of microcalcifications in anatomy using quantitative transmission ultrasound tomography,” USA Patent, 2019)

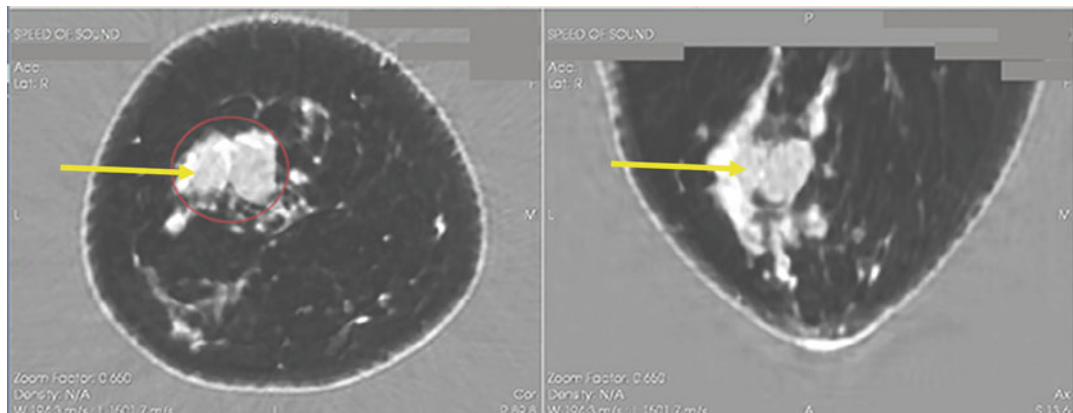


Fig. 11.9 This figure demonstrates a breast macro-cyst containing relatively high-speed “speckled” contents indicating clumps of cells within cyst fluid. Average speed value of 1554 m/s. (Reprinted with permission. “Accuracy

of Cyst Versus Solid Diagnosis in the Breast Using Quantitative Transmission (QT) Ultrasound.” Academic Radiology, vol. 24, pp. 1148–1153, <https://doi.org/10.1016/j.acra.2017.03.024>, 2017)

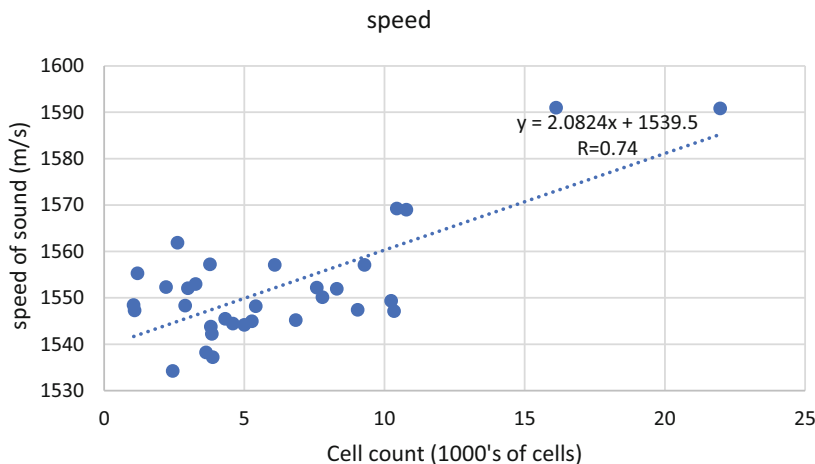


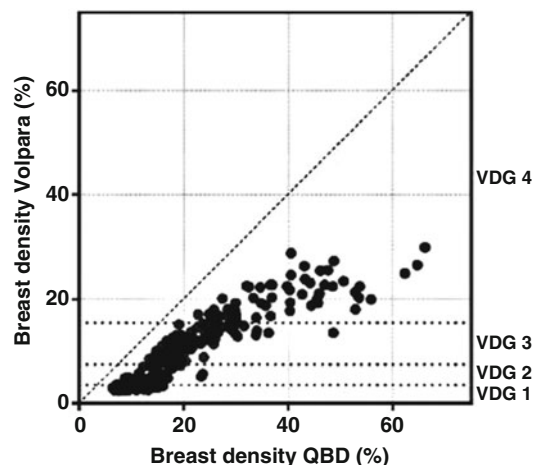
Fig. 11.10 Plot of the speed of sound as measured by QT as a function of cell count. The correlation coefficient “r” was calculated to be 0.74. The speed increases by 2 m/s for every additional 1000 cells

11.6 Measurement of Dense Fibroglandular Tissue Volume In Vivo Using Transmitted Sound 3D Volumography Imaging

Three-dimensional speed of sound maps generated by transmission ultrasound imaging can quantitatively identify tissue types. In the speed of sound images, there is a substantial

difference in the speed of sound of fat and fibroglandular tissue, and that difference is the most significant source of contrast in the images. This in turn allows the measurement of volumetric breast glands and ducts using a continuous scale termed percent fibroglandular volume, which is the ratio of total fibroglandular tissue volume to the total breast volume. Dense breast tissue is an established risk factor for the development of breast cancer (Destounis et al., 2020; Lee et al., 2017; Melnikow et al., 2016;

Fig. 11.11 Scatter plot of values calculated by Volpara Density and QBD (FGV) algorithms for breast density.
 (Reproduced with permission: “Quantitative assessment of breast density: transmission ultrasound is comparable to mammography with tomosynthesis,” Cancer Prevention Research, p. canprevres.0268.2019)



Vourtsis and Berg 2019). Since breast density may be a risk factor for breast cancer because of its masking effect on cancer detection, as well as a primary risk factor in and of itself for cancer development, having an accurate assessment of breast density is extremely important. Studies have been performed to validate that the QT technology can provide accurate breast density assessment as compared with VolparaDensity (VDG) scores based on mammography with 3D tomosynthesis (Fig. 11.11) (Natesan et al. 2019a). Low-frequency transmitted ultrasound volography was cleared for clinical use of this function by the FDA in 2022 (510 K 220933).

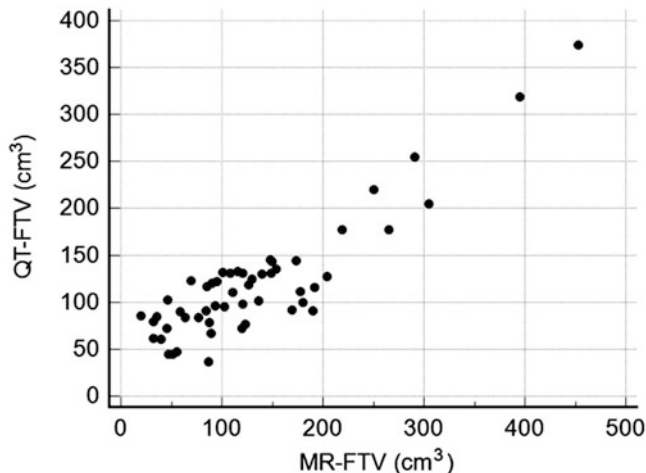
As can be seen in Fig. 11.11, the range of QBD (FGV) values is approximately twice the range of Volpara Density values. This suggests that the breast density determined by QT ultrasound provides a greater level of detail with the ability to more specifically determine breast density. A similar trend is seen when ground-truth MRI-based breast density is compared with digital QT (Fig. 11.12). This indicates that QBD (FGV) may exhibit higher absolute accuracy than Volpara Density in estimating breast density, especially within the dense breast cohort.

Further research will be performed to understand how QBD (FGV) may contribute to the output of risk models such as the Tyrer-Cuzick and Breast Cancer Surveillance Consortium (BCSC) models.

11.7 Use of AI to Differentiate Between Benign and Malignant Breast Masses

In the present time, artificial intelligence is taking center stage for improving the accuracy of imaging technologies. Radiomic features extract image-level data to derive quantitative biomarkers which could be related to tissue characteristics and pathology and have proved to be helpful in aiding in the characterization of tumor biology. “Combined approaches where visual assessment made by the radiologist is augmented by quantitative imaging biomarkers are gaining attention”. As noted above, an abundance of imaging biomarkers are encoded in the speed-of-sound maps of breast tissue, which can be used to characterize breast masses. We identified and utilized such features and applied them to the speed of sound images (Natesan et al. 2019b). We identified several morphological parameters and speed of sound as imaging biomarkers and tested their ability to differentiate benign from malignant breast masses. We randomly selected 90 pathology-proven cases with space-occupying breast masses (49 benign and 41 malignant). After segmentation of masses using a semi-automated connected components method, radiomic features, including morphological parameters such as irregularity and circularity, and first-order statistics of the pixel distribution, were calculated. These features

Fig. 11.12 Scatterplot of fibroglandular tissue volumes as assessed by QT and MRI



were used in several mainstream machine learning-based classifiers to differentiate benign from malignant masses. Using both irregularity and circularity of the masses along with the speed of sound derived directly from the images, our algorithm testing found that K-nearest neighbor (KNN) method with ten-fold cross-validation provided the highest accuracy of 86.7% (ROC-AUC of 0.85). Results demonstrate that imaging phenotypes derived from transmission ultrasound images of the breast can successfully differentiate between benign and malignant breast masses. This study uncovers the clinical potential for transmission ultrasound-based decision support systems (artificial intelligence) for breast imaging.

11.8 Clinical Trial Results

Over 14,000 women have been scanned with the QT Breast scanner and over 1000 of these women have participated in blinded clinical trials. These trials directly compare transmission ultrasound breast imaging with X-ray mammography for breast cancer screening. Results show that transmission ultrasound imaging shows improvement in sensitivity, specificity in breast cancer detection in women (Malik et al. 2021). The study also showed a decrease in false-positives (call-back rate). The complete results of these trials were published in Academic Radiology in 2021¹⁰.

11.9 Conclusions

Transmitted sound 3D v holography is a novel imaging modality with important applications in breast imaging for diagnostic and screening purposes. Clinical studies show that this technology is capable of visualizing breast microanatomy and breast microcalcifications at sub-mm resolution. It provides data for tissue classification using biomarkers via machine learning. This modality is also effective for imaging dense breasts due to the full wave modeling and is an accurate method for determining breast fibroglandular volume. Transmitted sound 3D v holography offers powerful 3D ultrasound imaging of the breast defining microanatomic and quantitative features of the breast, with the additional use of artificial intelligence, providing radiologists a new alternative for breast imaging that is poised to measurably improve clinical performance.

References

- Destounis SV, Santacroce A, Arieno A (2020) Update on breast density, risk estimation, and supplemental screening. Am J Roentgenol 214:296–305
- Iuanow E, Smith K, Obuchowski NA, Bullen J, Klock JC (2017) Accuracy of cyst vs. solid diagnosis in the breast using quantitative transmission (QT) ultrasound. Acad Rad 24:1148–1153. <https://doi.org/10.1016/j.acra.2017.03.024>. Epub 2017 May 23;

- PubMed ID 28549870. Academic Radiology has posted the study in full for free. <http://www.healthimaging.com/topics/womens-health/breast-imaging/and-coming-ultrasound-technology-shows-prowess-mammography-adjunct>
- Klock JC, Iuanow E, Malik B, Obuchowski NA, Wiskin J, Lenox M (2016) Anatomy-correlated breast imaging and visual grading analysis using quantitative transmission ultrasound. *Int J Biomed Imaging* 2016, Article ID 7570406, 9 pages. <https://doi.org/10.1155/2016/7570406>
- Klock JC, Iuanow E, Smith K, Obuchowski (2017) Visual grading assessment of quantitative transmission ultrasound compared to digital x-ray mammography and hand-held ultrasound in identifying ten breast anatomical structures. *BAOJ Clinical Trials* 3
- Lee CI, Chen LE, Elmore JG (2017) Risk-based breast cancer screening: implications of breast density. *Med Clin North Am* 101:725–741
- Malik B, Klock JC (2019) Breast cyst fluid analysis correlations with speed of sound using transmission ultrasound. *Acad Radiol* 26:76–85. <https://www.sciencedirect.com/science/article/pii/S1076633218301788>
- Malik B, Klock J, Wiskin J, Lenox M (2016) Objective breast tissue image classification using quantitative transmission ultrasound tomography. *Nat Sci Rep* 6:38857. <https://doi.org/10.1038/srep38857>. <https://www.ncbi.nlm.nih.gov/pmc/articles/PMC5146962/>
- Malik B, Terry R, Wiskin J, Lenox M (2018a) Quantitative transmission ultrasound tomography: Imaging and performance characteristics. *Med Phys* 45(7) <https://aapm.onlinelibrary.wiley.com/doi/epdf/10.1002/mp.12957>
- Malik B, Terry A, Klock J, Lenox M (2018b) Sensitivity of quantitative transmission ultrasound to detection of microcalcifications. SPIE (International Society for Optics and Photonics) Meeting Houston Texas February 20, 2018
- Malik B, Iuanow E, Klock J (2021) An exploratory multi-reader, multicase study comparing transmission ultrasound to mammography on recall rates and detection rates for breast cancer lesions. *Acad Radiol*. <https://www.sciencedirect.com/science/article/pii/S1076633220306462>. <https://doi.org/10.1016/j.acra.2020.11.011>
- Melnikow J, Fenton JJ, Whitlock EP, Miglioretti DL, Weyrich MS, Thompson JH et al (2016) Supplemental screening for breast cancer in women with dense breasts: a systematic review for the U.S. preventive services task force. *Ann Intern Med* 164:268–278
- Natesan R, Wiskin JW, Lee S, Malik B (2019a) Quantitative assessment of breast density: transmission ultrasound is comparable to mammography with tomosynthesis. *Cancer Prevent Res*. <https://doi.org/10.1158/1940-6207.CAPR-19-068>. <https://cancerpreventionresearch.aacrjournals.org/content/early/2019/10/23/1940-6207.CAPR-19-0268>
- Natesan R, Lee S, Navarro D, Anaje C, Malik B (2019b) Radiomics in transmission ultrasound improve differentiation between benign and malignant breast masses. In: Radiological Society of North America 2019 Scientific Assembly and Annual Meeting. <http://archive.rsna.org/2019/19011296.html>, Chicago, IL, 2019
- Vourtsis A, Berg WA (2019) Breast density implications and supplemental screening. *Eur Radiol* 29:1762–1777

Part V

Acoustic Microscopy



Advanced Topics in Quantitative Acoustic Microscopy

12

Cameron Hoerig and Jonathan Mamou

Abstract

Quantitative acoustic microscopy (QAM) reconstructs two-dimensional (2D) maps of the acoustic properties of thin tissue sections. Using ultrahigh frequency transducers (≥ 100 MHz), unstained, micron-thick tissue sections affixed to glass are raster scanned to collect radiofrequency (RF) echo data and generate parametric maps with resolution approximately equal to the ultrasound wavelength. 2D maps of speed of sound, mass density, acoustic impedance, bulk modulus, and acoustic attenuation provide unique and quantitative information that is complementary to typical optical microscopy modalities. Consequently, many biomedical researchers have great interest in utilizing QAM instruments to investigate the acoustic and biomechanical properties of tissues at the micron scale. Unfortunately, current state-of-the-art QAM technology is costly, requires operation by a trained user, and is accompanied by substantial experimental challenges, many of which become more onerous as the transducer frequency is increased. In this

chapter, typical QAM technology and standard image formation methods are reviewed. Then, novel experimental and signal processing approaches are presented with the specific goal of reducing QAM instrument costs and improving ease of use. These methods rely on modern techniques based on compressed sensing and sparsity-based deconvolution methods. Together, these approaches could serve as the basis of the next generation of QAM instruments that are affordable and provide high-resolution QAM images with turnkey solutions requiring nearly no training to operate.

Keywords

Quantitative · Compressed sensing · Super-resolution · Ultrahigh frequency · Machine learning · Deconvolution

12.1 Introduction

Quantitative acoustic microscopy (QAM) builds upon scanning acoustic microscopy (SAM) to form quantitative images of scanned samples. SAM forms fine-spatial-resolution images of raster-scanned specimens using very high-

C. Hoerig · J. Mamou (✉)
Department of Radiology, Weill Cornell Medicine, New York, NY, USA
e-mail: cah4016@med.cornell.edu;
jom4032@med.cornell.edu

frequency ultrasonic excitations (i.e., >100 MHz) (Daft and Briggs 1989; Quate et al. 1979; Kessler and Yuhas 1979). SAM is well established in non-destructive testing (Briggs 1985; Lemons 1974) and in studies of hard biological samples (e.g., bones; Raum 2008). Over the last 30 years, SAM has also been used in soft-tissue studies that provide quantitative images of acoustic properties at frequencies typically near 100 MHz (Miura et al. 2013; Sasaki et al. 1997; Litniewski and Bereiter-Hahn 1990), though commercial SAM systems exist that provide qualitative images at frequencies as high as 1 GHz (<https://www.honda-el.co.jp/en/medical/AMS-50SI-1.html>, <https://www.kbero.com>). QAM provides novel information that is not available with any other microscopic imaging modality. Our group and others have used QAM to acquire new knowledge about diseases affecting bone, cartilage, brain, skin, heart, eye, liver, tumors, and lymph nodes (Raum 2008; Rohrbach et al. 2017a; Kobayashi et al. 2014; Rohrbach et al. 2015a, 2016c; Mamou et al. 2015; Rohrbach et al. 2015b; Ito et al. 2017; Irie et al. 2016; Ojanen et al. 2016; Hofmann et al. 2016; Saijo et al. 2000; Weiss et al. 2007). Optical microscopy approaches provide images related to optical or staining properties; conversely, QAM provides valuable and complementary information of inherent biomechanical properties. Optical microscopy and QAM used together can provide important optical and mechanical microscopic information to researchers. The microscopic imaging modality with capabilities closest to those of QAM is atomic force microscopy (AFM) (Binnig et al. 1986), which provides quantitative, fine-resolution images of surface topography and mechanical properties (Last et al. 2010) by exerting and measuring forces on the order of pico-Newton. Although AFM has the ability to determine properties such as Young's modulus and provide exquisite topological images of a small specimen, it cannot reconstruct a microscopic image that can be co-registered with an optical image. This limitation of atomic force microscopy necessitates an imaging mode such as QAM. Furthermore, AFM cannot provide the bulk modulus of a material under investigation.

The bulk modulus is an important descriptor of elastic media like biological tissues. It is particularly valuable for soft-tissue studies because many diseases alter the elastic properties of tissues.

In the past ten years, our group contributed numerous experimental, theoretical, and preclinical studies to the QAM research field (Rohrbach et al. 2015c, 2016b, 2015a, 2016c; Mamou et al. 2015; Rohrbach et al. 2015b,d, 2016a, 2014; Ito et al. 2017; Irie et al. 2016; Basarab et al. 2017b; Mamou and Rohrbach 2017; Rohrbach et al. 2017b, 2018; Kim et al. 2020a; Rohrbach and Mamou 2018). We have acquired QAM data from a wide range of soft-tissue samples, such as fresh and fixed lymph nodes; eyes of mice, pigs, guinea pigs (GPs), and humans; mouse cerebellum; human cartilage; chicken tendons; and rat livers. Our group possesses QAM systems operating at frequencies of 250 MHz, 500 MHz, and 1 GHz providing spatial resolutions of 7 μm , 4 μm , and 2 μm , respectively. A recent signal processing algorithm allows simultaneously forming 2D images of acoustic impedance, mass density, bulk modulus, speed of sound, bulk modulus, and acoustic attenuation (Rohrbach and Mamou 2018).

Our existing fully operational laboratory QAM systems require trained users and expensive components including an ultrahigh frequency transducer, pulser, amplifier, digitizer, and motor stages. Scanning time can be long (e.g., \sim 5 min to scan an area of 1 mm by 1 mm), and experiments can be challenging because of the required precision in stage position. Temperature changes as small as $< 0.5^\circ\text{C}$ in the drop of water used as an acoustic coupling medium affects the QAM parameters. Furthermore, given the acoustic wavelength at these ultrahigh frequencies, vibration amplitudes in the 100-nm range introduce errors in reconstructed parametric maps. However, we already possess tools to address these and other challenges, many of which can be further mitigated by the use of more expensive equipment like isolated and levitated tables, high-precision motor stages, and temperature-controlled scanning tanks.

The goal of this chapter is to propose solutions for the next generation of QAM instruments pro-

viding the best possible performance and robustness by employing ultramodern signal and image processing methods and experimental approaches never used to this extent in QAM, thereby reducing or eliminating the need for costly measures. Several of these new ideas are discussed in the remainder of this chapter with the rationale that successful development and implementation of these methods will generate better quality images for a given QAM system as well as enable development of simpler, lower cost, more reliable, easier-to-use QAM systems. These advanced methods have the potential to revolutionize QAM imaging, making QAM a widely used tool in industrial, clinical, and academic research laboratories. Ultimately, our hypothesis is that QAM technology could become turnkey and be as easy to use as an optical microscopy system while providing quantitative tissue information not available by any other microscopy modality.

12.2 Current State-of-the-Art QAM Technology

12.2.1 Industrial Systems

Many SAM systems exist for non-destructive testing, many of which are designed with custom instrumentation for specific applications. Few industrial systems are available that offer turnkey solutions, but even those are costly and require trained users. One of the most used SAM systems is the AMS-50SI from Honda Electronics Co. (Toyoashi, Japan), which can operate at three distinct center frequencies: 80, 160, and 320 MHz. The system—shown in Fig. 12.1—is very compact and includes an optical microscope.

Few industrial QAM systems are on the market. Kibero, GmbH, sells QAM transducers and systems with frequencies up to 1 GHz. Most units offered by Kibero are not fully quantitative but can be easily integrated with optical microscopy systems (<https://www.kbero.com>). Recently, they also developed an instrument for optoacoustic imaging. Their transducers are of excellent quality and could be easily integrated into custom-designed QAM instruments such as those of our

group. Nevertheless, their QAM instruments remain expensive, require expert users, and do not always provide 2D quantitative maps of tissue sections. There is still a need for QAM instruments capable of providing fine-resolution quantitative maps at affordable prices and without the need for expert users.

12.2.2 Laboratory Systems

Several research groups have designed their own SAM or QAM instruments operating at a wide range of frequencies, each having their own features and limitations. The focus of this section is the three QAM systems developed by our group because they are state of the art, provide straightforward illustration of a QAM system's inner-workings, and detail the necessary system components.

QAM instruments are conceptually simple to understand as they are based on raster scanning a single-element transducer over the surface of a sample. At each scan location, an electrical signal is generated to excite the transducer to produce an ultrasound wave. The wave then propagates in the coupling medium (e.g., saline) and the tissue under investigation, reflects off the glass plate, and propagates back toward the transducer through the tissue and coupling medium. The transducer transforms the ultrasound echo into an electric signal which is amplified before being digitized. Figure 12.2 shows a block diagram of a typical QAM system with all components and Fig. 12.3 shows a picture of a current QAM system in our laboratory. Pictured is the 1-GHz system; the 250-MHz and 500-MHz systems are nearly identical. The transducer, pulse generator, and transmit-receive electronics (i.e., cable lengths, filters, and pre-amplifier) are chosen to optimize system performance based on the transducer in use.

Building an operational QAM system is challenging and expensive. First, the transducer must be sensitive and have sufficient bandwidth. Because only a handful of groups have the capabilities to make such devices, they are expensive and require long lead times. Our three transducers

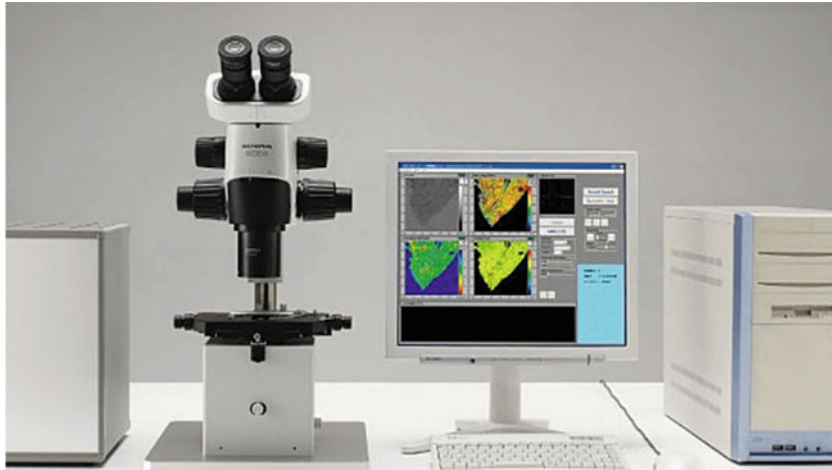


Fig. 12.1 Commercial QAM system (AMS-50SI from Honda Electronics)

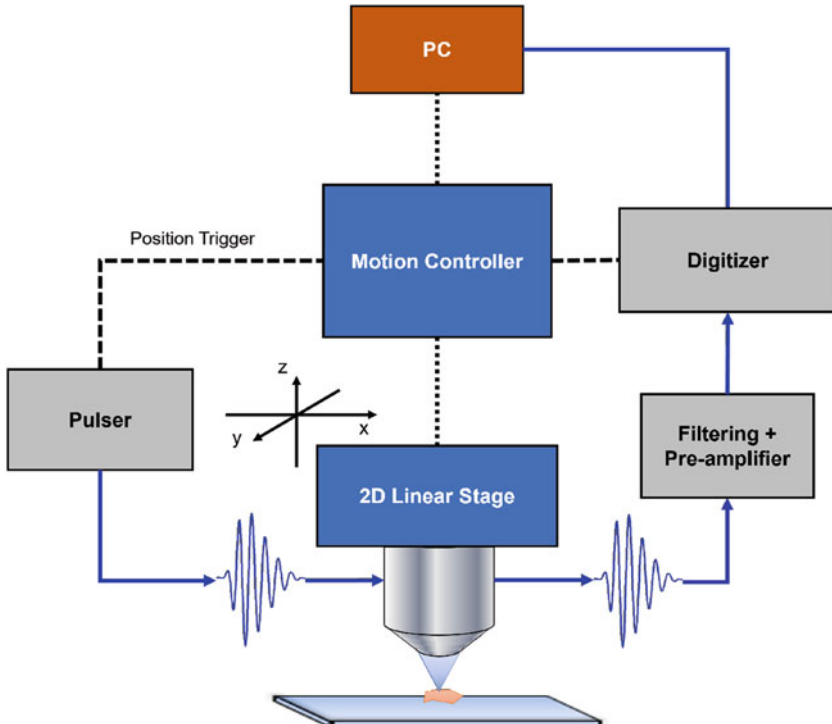


Fig. 12.2 Block diagram of a typical QAM instrument

are pictured in Fig. 12.4 along with the associated time signals and spectra obtained from a glass-plate reflector. As evidenced by these plots, the three transducers are broadband and provide satisfactory SNR even at 1 GHz. All three were

purchased directly from the Fraunhofer Institute in St. Ingbert.

Second, motor stages must be ultra-precise: the step size must be at most half the bandwidth of the transducer, preferably smaller. For

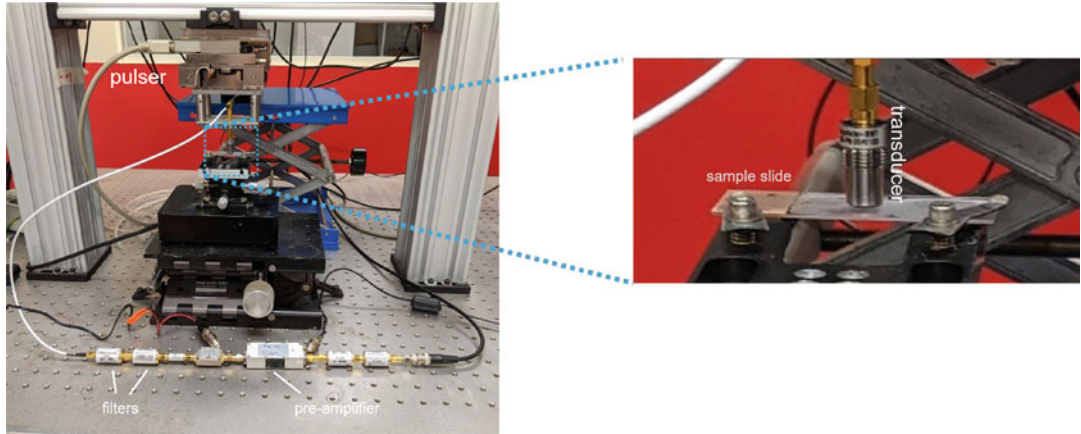


Fig. 12.3 Picture of the 1-GHz QAM system along with a magnified view of the transducer and glass slide

instance, our motor stages have $0.1\text{ }\mu\text{m}$ precision, but we typically sample every $0.2\text{ }\mu\text{m}$ for the 1-GHz QAM system which has a theoretical beamwidth of approximately $1.7\text{ }\mu\text{m}$. Generally, increasing precision in the step size implies increased cost.

Third, each transducer has a dedicated monocyte pulser because it is impossible to design an impulse generator which would cover such a wide range of frequencies. Our pulsers were manufactured by Geozondas (Vilnius, Lithuania) to generate broadband, monocyte excitation pulses and are straightforward to use. On the receiving end, the echo signal must be amplified. While low-power amplifiers will provide satisfactory gain (typically going from μV to mV), they must also be low-noise broadband and have an impedance as close as possible to exactly $50\ \Omega$.

Finally, the last key piece of hardware is the analog to digital converter (ADC), which must not only be fast enough to handle the bandwidths of the ultrasound signals but also provide adequate digitization precision (i.e., bit count). The Nyquist theorem drives the minimum sampling frequency required to avoid aliasing. For example, if one assumes that the useful signal exists between 0.5 and 1.5-GHz for the 1-GHz QAM system, then a minimum sampling rate of 3-GHz is needed. A higher sampling rate is

recommended in practice to obtain better SNR; a rough rule of thumb is that adequate high-quality data can be obtained by sampling at 10 times the center frequency. The data we acquire from the 1-GHz QAM system is typically sampled at 10-GHz. In addition to sampling rate, the precision of the digitizer is a complex practical issue because QAM signals have large dynamic range. As it will be clearly explained in the next section, QAM echo signals are composed of two main reflections: the water/tissue interface reflections and the tissue/glass/plate reflection. The former is small because the acoustic impedance contrast between water and tissue is marginal whereas the latter is larger because of the large impedance mismatch between glass and tissue, causing a nearly complete reflection of the ultrasound wave (even though the signal ultimately received by the transducer suffers round-trip attenuation through the tissue). A reasonable recommendation is to have a digitizer with at least 12-bit precision.

Another caveat of ADC selection is the ability to adjust the reference voltage. Many of the new generation PCIe-based digitizers only allow for a fixed reference voltage, which puts pressure on ensuring that the signal to be digitized has low enough amplitude to avoid saturating the ADC but large enough to utilize the most significant bits and avoid diminishing the SNR. Essentially,

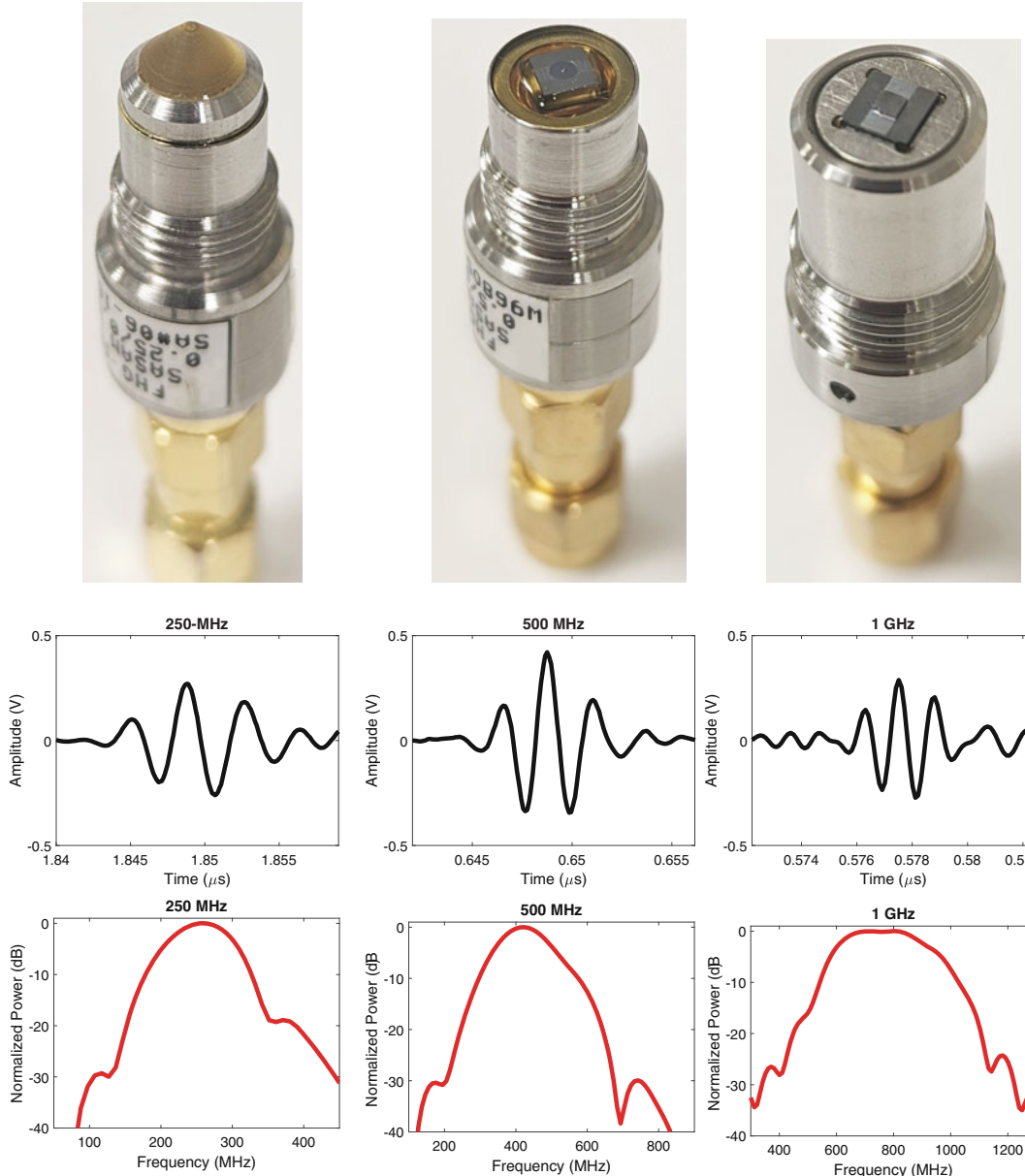


Fig. 12.4 Pictures of the 250-MHz transducer (top left), 500-MHz transducer (top middle), 1-GHz transducer (top right), and associated time signals (middle row) and spec-

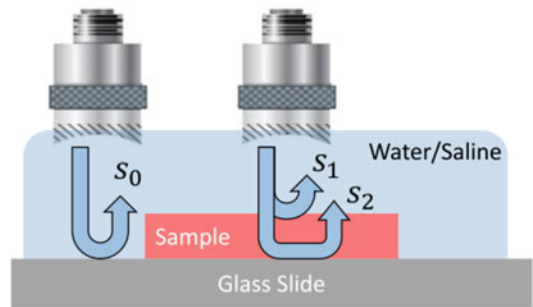
tra (bottom row). As evidenced by these plots, the three transducers are broadband and provide satisfactory SNR even at 1-GHz

the gain of the amplifier must be chosen to make full use of the bit precision of a digitizer with a fixed reference voltage.

The primary point of the preceding discussion is that the operating principles of a QAM system are easy to understand, but the implemen-

tation requires specialized, expensive equipment and system optimization can be tedious. Then, once the system is built, it requires a trained user and remains highly sensitive to vibration and temperature change. Overall, these state-of-the-art QAM instruments provide valuable and

Fig. 12.5 The measured signal s is comprised of two signals s_1 and s_2 which correspond to the water–tissue and tissue–glass reflections, respectively. Both of these signals are in turn scaled and time-shifted versions of the reference signal s_0



quantitative information not available with any other imaging modality, but they are not ready for wide acceptance in microscopy suites and do not provide turnkey solutions. In the following sections, we discuss new ways of thinking to exploit ultra-modern signal processing and experimental methods. These ideas could possibly yield a new generation of low-cost QAM instruments that produce high-quality images and are much simpler to use.

12.3 Forward Model in QAM

The forward model assumed in QAM imaging treats each scan location independently. A simplified representation of the reflected signal at one scan location is illustrated on the right side of Fig. 12.5. It is composed of two main reflections: the water/tissue reflection s_1 and the sample/glass slide reflection s_2 . In actuality, additional signals will exist because of multiple reflections at these interfaces, but they will be much lower in amplitude and occur later in time. Therefore, at a specific scan location, the *sample signal* $s(t)$ is assumed to be the sum of many reflected signals as the wave propagates through the water and tissue,

$$s(t) = s_1(t) + s_2(t) + \dots + s_n(t). \quad (12.1)$$

We define the *reference signal* s_0 as the measured reflection of the pulse from the glass plate when propagating only through the water; the reference

signal is illustrated on the left side of Fig. 12.5 (reference signals from our three QAM instruments are shown in Fig. 12.4).

The next approximation made in the QAM forward model is that each reflection is an amplitude-weighted, time-delayed, and attenuated version of the reference signal. This assumes that the beam properties are identical throughout the thickness of the sample and that the wavefront is planar. Both assumptions are true in the focal region of the transducer. Therefore, each reflection in Eq. 12.1 can be expressed as follows:

$$\begin{aligned} s_1(t) &= C_1 s_0^*(t - t_1) \\ s_2(t) &= C_2 s_0^*(t - t_2) \\ &\dots \\ s_n(t) &= C_n s_0^*(t - t_n), \end{aligned} \quad (12.2)$$

where the $*$ symbol represents frequency-dependent attenuation effects. Of these, two signals s_{k_1} and s_{k_2} ($k_1 \neq k_2$ and $t_{k_1} < t_{k_2}$) are the reflections from the water–tissue and tissue–glass interfaces, respectively. The reference time (t_0) can be defined somewhat arbitrarily, for instance, t_0 could be the time at which the reference signals reach its peak magnitude. However, the time differences are explicit in the sense that, for example, $t_2 - t_0$ is the actual time difference (i.e., delay) between s_2 and the reference signal.

The final assumption made at this point is the attenuation model which we can explicitly express by taking the Fourier transform (FT) of

Eq. (12.1), using Eq. (12.2), and assuming the frequency attenuation is linear with frequency and travelled distance. The basic Fourier transform properties yield

$$\begin{aligned} S(f) &= \text{FT}\{s(t)\} \\ &= S_0(f) [C_1 \exp(f(\beta_1 \\ &\quad + j2\pi(t_1 - t_0))) + \dots C_n \\ &\quad \times \exp(f(\beta_n + j2\pi(t_n - t_0)))] \end{aligned} \quad (12.3)$$

where transform pairs are expressed by lower case letters and upper case letters in the time and frequency domains, respectively. The “*” symbols were dropped and explicit frequency-dependent attenuation coefficients are introduced (i.e., β_i in Np/MHz). We also assume that $\beta_{k_1} = 0$ Np/MHz, which means that signals reflected from the water/tissue interface do not suffer significant attenuation effects.

Dividing $S(f)$ by the Fourier transform of the reference signal gives the normalized spectrum that serves as the starting point for two inverse models described in the next section:

$$N(f) = \frac{S(f)}{S_0(f)} \quad (12.4)$$

$$= \sum_{k=1}^n C_k \exp(f[\beta_k + j2\pi(t_k - t_0)]) \quad (12.5)$$

12.4 Inverse Models in QAM

This section deals with extracting quantitative acoustic and mechanical properties by fitting experimental measurements to Eq. (12.5). We discuss below two typical inverse models. Before diving into the details of both approaches, it is important to understand that while Eq. (12.5)

is—in theory—valid at all frequencies, in practice, one can only measure a reliable normalized spectrum within the bandwidth of the transducer where sufficiently high SNR can be achieved. Depending on the sensitivity of the transducer and system technology, the usable bandwidth might be composed of those frequencies somewhere –6 to –12 dB below the center (i.e., peak) frequency obtained from $S_0(f)$.

12.4.1 Hozumi Inverse Method

The Hozumi inverse model assumes that the measured echo signal is comprised of exactly two signals s_{k_1} and s_{k_2} , which correspond to the water/tissue and tissue/glass reflections. This assumption is often reasonable because the echo signals can be appropriately cropped in time to limit multiple reflections which would arrive at later times. Furthermore, multiple reflections would be at least an order of magnitude smaller in amplitude. In this section, for simplicity and without loss of generality, we assume $k_1=1$ and $k_2=2$.

The Hozumi inverse model considers first the squared magnitude of the normalized spectrum, Eq. (12.5), which under the above assumptions reduces to

$$\begin{aligned} |N(f)|^2 &= \left| \frac{S_1(f) + S_2(f)}{S_0(f)} \right|^2 \\ &= C_1^2 + 2C_1C_2 \cdot e^{f\beta_2} \cdot \cos(2\pi f(t_2 - t_1)) \\ &\quad + C_2^2 e^{2f\beta_2} \end{aligned} \quad (12.6)$$

Remember that attenuation effects are considered only for s_2 and are represented by β_2 in (12.6); i.e., $\beta_1 = 0$ Np/MHz.

Equation (12.6) implies that the normalized spectrum is an oscillatory function with minima and maxima occurring at frequencies f_{min}

and f_{max} , respectively. The extrema are found by identifying the frequencies at which the cosine term equals -1 or $+1$:

$$2\pi f_{min} \cdot (t_2 - t_1) = (2p + 1)\pi, p \in \mathbb{N}_0 \quad (12.7)$$

$$2\pi f_{max} \cdot (t_2 - t_1) = 2p\pi, p \in \mathbb{N}_0. \quad (12.8)$$

Locations of these extrema are experimentally found with a peak detection algorithm operating within the usable bandwidth of the transducer. The values of the integers p are determined from the estimated periodicity of f_{min} and f_{max} and the fact that 0 MHz is the first maximum ($p = 0$). The next step comes from a theoretical derivation applied to N ; specifically, the unwrapped phase $\phi_u(N)$ at the extrema frequencies are equal to

$$\phi_u(N) = 2\pi \left(f_{max} \frac{2d}{c_w} - q \right), q \in \mathbb{Z} \quad (12.9)$$

and

$$\phi_u(N) = 2\pi \left(f_{min} \frac{2d}{c_w} - q + \frac{1}{2} \right), q \in \mathbb{Z}, \quad (12.10)$$

where d is the tissue sample thickness and c_w is the (known) speed of sound in the water. From Eqs. (12.9) and (12.10), the sample thickness can be estimated in two ways,

$$d = \frac{\phi_u(N)}{4\pi f_{max} \left(\frac{1}{c_w} - \frac{1}{c} \right)} \quad (12.11)$$

or

$$d = \frac{c_w}{4\pi f_{min}} (\phi_u(N) + \pi(2q - 1)). \quad (12.12)$$

By first estimating sample thickness with Eq. (12.12), an initial value of speed of sound in the sample c can be estimated from Eq. (12.11). However, this procedure neglects the effects of attenuation, which alters the locations of f_{min} and f_{max} . An alternative is to obtain an initial estimate of c from Eq. (12.11), computed as the average value over all d estimates for each found f_{min} and f_{max} within the usable bandwidth.

Estimates of C_1 , C_2 , and β_2 can be obtained by fitting the normalized measured spectra to the forward model in Eq. (12.6), but the optimization can be difficult. An alternative is to estimate β_2 directly from the normalized spectrum using a dichotomy method based on simple algebraic considerations. Define the extrema of $|N|^2$ to be S_{M1} , S_{M2} , and S_{m1} , with Mi and mi indicating the i th maximum and minimum, respectively, and $S_{Mi} = (C_1 + C_2 e^{-2df_{Mi}\beta_2})^2$, $S_{mi} = (C_1 - C_2 e^{-2df_{mi}\beta_2})^2$. It can be found that

$$\frac{\sqrt{S_{M2}} - \sqrt{S_{M1}}}{\sqrt{S_{M2}} + \sqrt{S_{m1}}} = \frac{e^{-2df_{M2}\beta_2} - e^{-2df_{M1}\beta_2}}{e^{-2df_{M2}\beta_2} + e^{-2df_{m1}\beta_2}}. \quad (12.13)$$

An iterative method can then be used to estimate β_2 from Eq. (12.13). The values of C_1 and C_2 are then found from Eq. (12.6) using two maxima and β_2 .

Using the estimated value of the attenuation parameter, the initial estimate of c can be updated by using β_2 to mitigate the effects of attenuation on Eq. (12.6) and obtain corrected values of f_{min} and f_{max} . Final estimates of c (and d) can then be obtained from Eqs. (12.11) and (12.12).

Acoustic impedance Z_s can be computed from the amplitude C_1 of the reflection from the water-tissue interface, amplitude C_{ref} of the water-glass reflection in the reference signal, the known acoustic impedances Z_w and Z_{ref} of water and the substrate, respectively, and first principles. Given the reflection coefficient R_{ref} of the reference signal, Z_s is calculated using

$$Z_s = \frac{Z_w R_{ref} + \frac{C_1}{C_{ref}} Z_w}{R_{ref} - \frac{C_1}{C_{ref}}}. \quad (12.14)$$

Parameters Z , β_2 , and c are estimated independently for each RF signal to yield 2D parameter maps. The attenuation, α , in Np/m/MHz is equal to $\beta_2/2d$. Additional parameters can be derived through relationship between these acoustic properties. Specifically, the mechanical properties mass density $\rho = Z/c$ (expressed as g/cm³) and bulk modulus $K = c \cdot Z$ (in GPa) (Briggs et al. 2010).

12.4.2 Autoregressive Inverse Model

Unlike the Hozumi method, the auto-regressive (AR) inverse model assumes that the measured sample signals are composed of two or more signals ($n \geq 2$), which provides robustness and stability because the additional signals account for possible multiple reflections and noise. The aim of the AR method is to find the two signals related to the water–tissue and tissue–glass interfaces. A full discussion of the AR method, including the Cadzow denoising procedure and extension to the nonlinear AR model, is beyond the scope of this chapter, but the reader is encouraged to see Rohrbach and Mamou (2018) for full details (note that the paper also demonstrates the superiority of the AR model over the Hozumi model in cases with low SNR, multiple reflections or when the two echo signals overlap significantly in the time domain (i.e., small d)). In this section, the AR model will be introduced and parameter estimation methods covered to provide the necessary foundation for the compressed sensing methods presented in Sect. 12.5.2.

The AR inverse model consists of rewriting the normalized spectrum in Eq. (12.5) at discrete frequencies denoted by $f_i = i\Delta f$. The step size $\Delta f = f_s/(2M)$ between discrete frequencies is determined by the number of points M in the sampled signal and the sampling rate f_s .¹ Rewriting the discretized normalized spectrum yields

$$N_i = N(i\Delta f) = \sum_{k=1}^n C_k \left(\exp\left(i\Delta f(\beta_k + j2\pi(t_k - t_0))\right) \right) \quad (12.15)$$

$$= \sum_{k=1}^n C_k \lambda_k^i, \quad (12.16)$$

¹ The step size will be reduced if the time domain signal is zero-padded prior to application of the FFT. However, no new information is provided by zero padding and is therefore unnecessary and typically omitted in the AR inverse method. Zero padding also increases computation time.

where $\lambda_k = \exp(\Delta f[\beta_k + j2\pi(t_k - t_0)])$. The AR process is then introduced by assuming each N_i can be estimated by a linear combination of the \hat{n} ² previous frequencies (Makhoul 1975). Given AR coefficients x_k and an error ϵ_i , N_i is expressed as

$$N_i = \sum_{k=1}^{\hat{n}} x_k N_{i-k} + \epsilon_i. \quad (12.17)$$

Using this model, the AR inverse method proceeds in four steps: (1) estimation of C_k and λ_k , (2) Cadzow denoising, (3) determination of k_1 and k_2 , and (4) estimation of all acoustic parameters from C_1 , C_2 , λ_1 , λ_2 . The full details of steps 1–3 can be found in Rohrbach and Mamou (2018). Assuming, without loss of generality, that the parameter sets (C_1, λ_1) and (C_2, λ_2) corresponding to signals at the water–tissue and tissue–glass interfaces, respectively, the sample thickness, speed of sound, and acoustic attenuation, are computed as

$$d = \frac{c_w}{2} \frac{\text{imag}(\log(\lambda_1))}{\Delta f} \quad (12.18)$$

$$c = c_w \frac{\text{imag}(\log(\lambda_1))}{\text{imag}(\log(\lambda_1)) + \text{imag}(\log(\lambda_2))}, \quad (12.19)$$

$$\alpha = \frac{\beta_{k_2}}{2d} = \frac{\text{real}(\log(\lambda_2))}{2d\Delta f}. \quad (12.20)$$

The remaining parameters Z , ρ , and K are estimated in the same way as described in Sect. 12.4.1.

12.5 Compressive Sensing in QAM

This section presents two compressive sensing (CS) approaches to reduce sampling in the spatial and temporal domains independently. Both approaches are later combined to provide drastic spatio-temporal compression without detrimental effects to the final QAM maps, but first we explain here why these methods have tremendous value in QAM and could pave the way toward

² For reference, $\hat{n} = n$ was used in Rohrbach and Mamou (2018).

the next generation of QAM instruments. The methods presented below are valid options to improve QAM technology, but they are by no means comprehensive, and it is quite likely that other CS-based methods exist to further improve QAM technology. However, we firmly believe that they represent a new way of thinking—one which will be part of the next generation of QAM instruments.

In QAM, acquisition time is directly related to the number of scan lines in a 2D raster scan of a sample. The motors can move fast along one line, but they must decelerate, reach zero velocity, and then accelerate in the opposite direction, leading to a lot of lost time. Scanning time could be significantly improved by using a continuous scanning trajectory that permits a constant and fast speed with no abrupt change of direction. A spiral is such a pattern and is illustrated in the next section. Acquisition time can be further reduced by decreasing the number of scan locations. For this type of spatial sampling reduction, we assume the 2D QAM images are sparse in some transform domain. This knowledge can then be exploited to reconstruct QAM maps without meeting the Nyquist spatial sampling requirements. Beyond breaking classical sampling requirements, CS methods could relax demands on the motor stage precision and reduce system costs. As briefly discussed above, QAM motor stages are typically ultra-precise because we require small step sizes and very specific scan locations. Less precise—and therefore less expensive—motor stages can be used by employing CS methods to reconstruct images even if the spatial sampling occurs at “noisy” spatial positions, so long as the position information is available. In summary, spatial sampling and motor requirements can be drastically lessened using appropriate CS approaches, resulting in reduced costs and decreased scan time.

In the temporal domain, high sampling rates are required and should be at least twice the largest usable frequency in the bandwidth used for imaging. A drastic reduction in sampling frequency can be obtained by using CS methods that take advantage of the forward model in QAM signals, e.g., Eq. (12.16). Specifically, the number

of unknowns in Eq. (12.16) is much smaller (i.e., 3 per signal component, $3n$) than the number of sampled points one would obtain at an appropriate sampling frequency. Below we discuss an elegant approach to take advantage of the QAM signal modal and dramatically reduce the required temporal sampling rate, thereby reducing costs associated with using a high-frequency digitizer.

12.5.1 Spatial Sampling Reduction via Wavelets and Approximate Message Passing

In this section, we present a CS method which has been successfully applied to reduce spatial sampling requirements in QAM. The approach employs wavelets and an approximate message passing (AMP) algorithm to find a sparse set of wavelet coefficients to reconstruct QAM images with little loss in quality. AMP has produced interesting results and provides a nice way to illustrate our rationale that CS has a significant role to play in improving QAM instruments. This section is an educational summary of a previous publication which provides much greater detail (Kim et al. 2018).

Typical CS spatial sampling schemes applied to imaging usually rely on random sampling of the spatial domain, which typically provide random samples also in a transformed space from which a satisfactory image can be reconstructed. However, random spatial sampling in QAM is not realistic because we are constrained by the fact that motor motion must be continuous and that, as explained in the inverse models above, each spatial location is essentially independent by providing acoustic parameter values at that location only. Therefore, in our AMP work, we developed QAM specific methods. First, as depicted in Fig. 12.6, we tried three distinct realistic spatial sampling schemes which reduced the number of total samples. Second, we empirically determined that QAM acoustic parameter maps were sparse in a specific wavelet domain and that the distribution of wavelet coefficients could be modeled by a Cauchy distribution. With

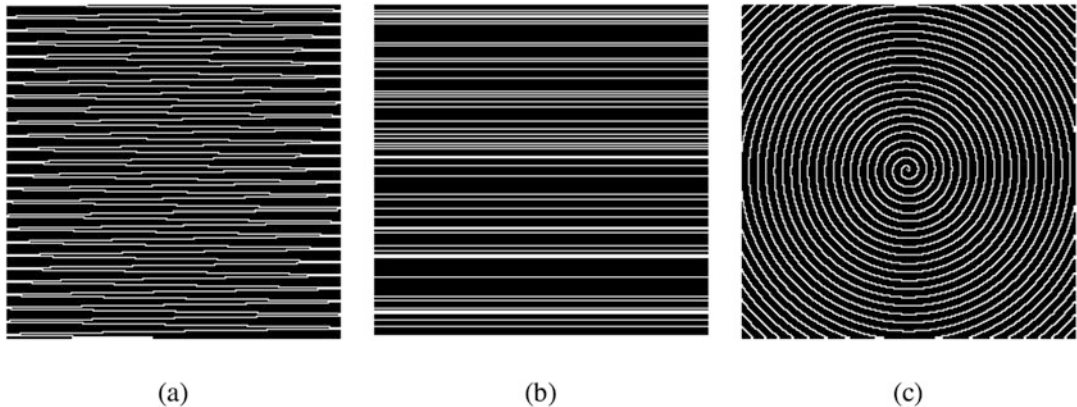


Fig. 12.6 Example sampling masks. (a) Diagonal scan lines. (b) Randomly selected rows. (c) Spiral

this empirical knowledge, a bespoke shrinkage function was created for the AMP algorithm to find an appropriate sparse set of wavelet coefficients.

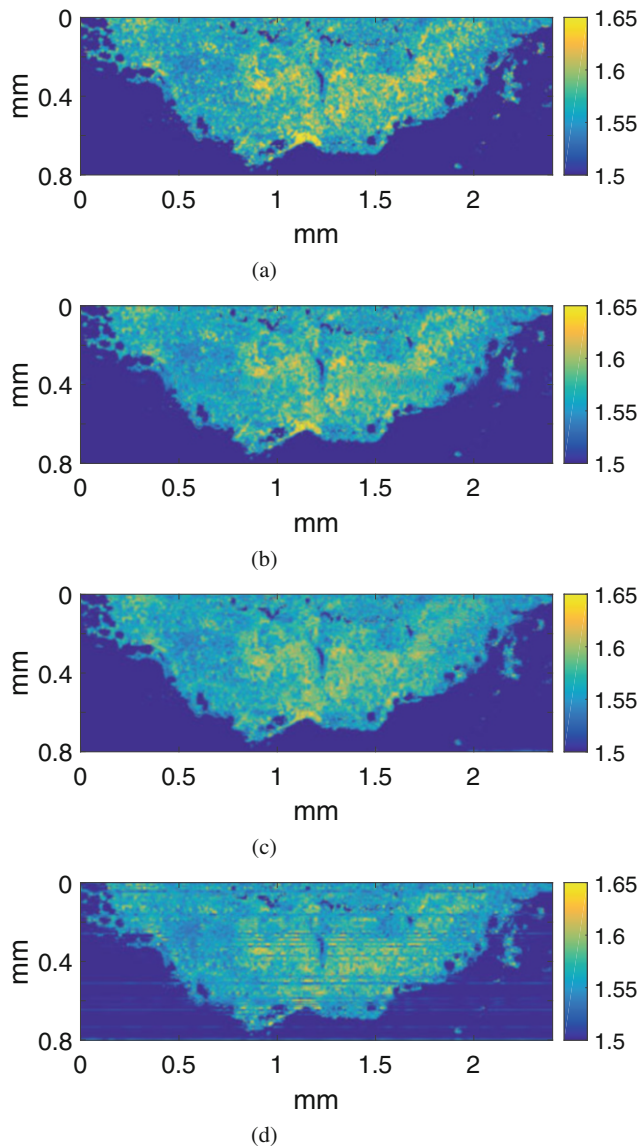
In this previous work, the AMP-based algorithm was designed to reconstruct QAM maps of acoustic parameters from spatially undersampled measurements. AMP is a simplified version of MP (message passing) derived from belief propagation in graphical models (Dabov et al. 2007) and is characterized not only by dramatically reduced convergence times but also by a reconstruction performance equivalent to l_p -based methods. AMP uses an iterative process consisting of a sparse representation-based image denoising algorithm performed at each iteration. Our proposed AMP-based QAM imaging framework consists of two major tasks: (i) for data acquisition, we propose novel techniques for QAM data sampling, by choosing scanning patterns (Fig. 12.6) that simultaneously meet CS requirements and take into account the peculiarities of practical QAM systems, and (ii) for QAM map formation, we design and test a wavelet domain AMP-based algorithm which exploits underlying data statistics.

For task (i), we investigated the three scanning patterns shown in Fig. 12.6. Although all three patterns reduce the number of sampled locations, the first two patterns (diagonal and row random) do not reduce the total scan time significantly

compared to full raster scanning because they still require deceleration at the end of a straight line. However, the spiral pattern is continuous and not only allows reducing the total number of samples but also significantly reduces scanning time by allowing the motion stage to maintain a constant speed through the scan over the sample. For the details pertaining to task (ii), the reader is referred to the publication which provides all the details of the algorithm elegantly capitalizing on the sparsity of the QAM maps in a wavelet domain (Kim et al. 2018). Note that the sparsity was found empirically by observing the distribution of wavelet coefficients obtained from several QAM images acquired from lymph node samples.

Figure 12.7 shows illustrative results obtained with the AMP algorithm using the three sampling patterns of Fig. 12.6 with only 40% of the original raw data. Visual inspection of Fig. 12.7 reveals that the spiral pattern produces the best results; this observation was confirmed by quantitative analyses (see Table IV in Ref. Kim et al. 2018). Intuitively, it was expected that the spiral pattern would provide the better reconstruction because it covered the 2D space more uniformly than the other two patterns, which both contain regions of dense and sparse pixels. As outlined above, the spiral has the additional advantage to be a continuous pattern which allows acquiring the entire scan data at near constant speed without regular acceleration and deceleration. Furthermore,

Fig. 12.7 Reconstruction results of 2D impedance (MRayl) map from human lymph node samples acquired at 250 MHz: (a) original fully sample data at pixel resolution of 2 μm per 2 μm , (b–d) reconstructed images with the proposed AMP algorithm for spiral, diagonal, and row random sampling patterns, respectively. All the results correspond to a compression ratio of 40%



the spiral sampling approach could be implemented on cheap, potentially less precise, servo motors.

In summary, the AMP-based algorithm paved the way for a reduction in spatial sampling by a factor of 2.5 and commensurate decrease in scanning time by a factor of at least 5 at no detriment to QAM map quality. This is a huge improvement on current state-of-the art QAM systems.

12.5.2 Temporal Sampling Reduction via Finite Rate of Innovation

In this section, we present a CS scheme which is applied to reduce the number of recorded samples of each A-line. AMP exploited sparsity in the wavelet domain based on empirical observations to reduce spatial sampling constraints; here, we will employ a more mathematically rigorous ap-

proach, but the rationale is very similar. An RF A-line acquired with a QAM system requires accurately sampling the two reflected signals, but these signals belong to very sparse space because they are fully defined by two times of flight, two amplitudes, and one attenuation coefficient in addition to the knowledge of the reference signal (i.e., 5 unknown parameters can be used to fully reconstruct the echo signals). The temporal CS scheme we developed is rigorously exploiting these properties to sample the signals at much lower sampling frequency than those required by the Nyquist theory. Reducing the sampling rates has two main benefits to QAM instruments: (1) it allows reducing costs by permitting the use of a digitizer operating at lower sampling frequencies (also often improving precision by having a larger bit count) and (2) allows reducing the total amount of data associated with a QAM dataset (also enabling faster image reconstruction).

Signals with a limited number of degrees of freedom occur in various applications such as astronomy, radar, or medical imaging (Oñativia et al. 2013; Rudresh and Seelamantula 2017; Wei and Dragotti 2016; Pan et al. 2017; Tur et al. 2011). Generally called signals with finite rate of innovation (FRI), they are typically expressed as a τ -periodic parametric form:

$$x(t) = \sum_{m \in Z} \sum_{l=1}^L a_l h(t - t_l - m\tau), \quad (12.21)$$

where $h(t)$ is a possibly non-bandlimited pulse supposed to be known and repeated L times at the time instants t_l and scaled by the amplitudes a_l . Starting from the seminal paper of Vetterli et al. (2002), a rich literature exists on the reconstruction of these kinds of signals from a limited number of samples. In contrast to the classical sampling theory based on the Nyquist theorem that relates the number of samples required to the signal bandwidth, the number of measurements in the FRI framework is dictated by the rate of innovation, i.e., the number of parameters able to

completely describe $x(t)$ over one period. Given the parametric representation in Eq. (12.2) of a QAM echo signal of interest, the canonical FRI processes can be directly applied to QAM data under the assumed forward model; it involves the design of a relevant sampling kernel and the development of effective recovery strategies, which are beyond the scope of this chapter but can be found in our published work Kim et al. (2020b).

Before showing some illustrative results, an interesting feature of the FRI implementation we developed is that although it could be used to reconstruct RF echo signals which would then be sent through the AR inverse model to form 2D maps of acoustic properties, the FRI implementation directly provides the normalized spectrum at discretized frequencies within the transducer bandwidth (see Eq. (12.16)). This refinement further reduces the time required for QAM map formation.

Figure 12.8 compares results applying our FRI approach to QAM data acquired from a chicken tendon using the 250-MHz QAM system. Overall, the results presented in this figure and our publication demonstrate that even at an effective sampling rate of 150 MHz, satisfactory QAM images are obtained with excellent values for the normalized mean squared error (NRMSE) and the peak signal-to-noise ratio (PSNR). The implications are tremendous because assuming the usable bandwidth of the 250-MHz QAM system extends from 100 to 400 MHz, the Nyquist rate would be 800 MHz (note that we actually sample at 2.5 GHz to increase SNR), and therefore 150 MHz is smaller than the Nyquist rate by a factor of 5.3. High-quality digitizers operating at 150 MHz are much cheaper than those operating in the GHz range and often come with variable input voltage and a larger bit count. Finally, in terms of data reduction, the gains are also tremendous: at 150-MHz sampling rate, we would obtain only 13 temporal samples per pixel instead of 200 currently, leading a total data size reduction by a factor of more than 15.

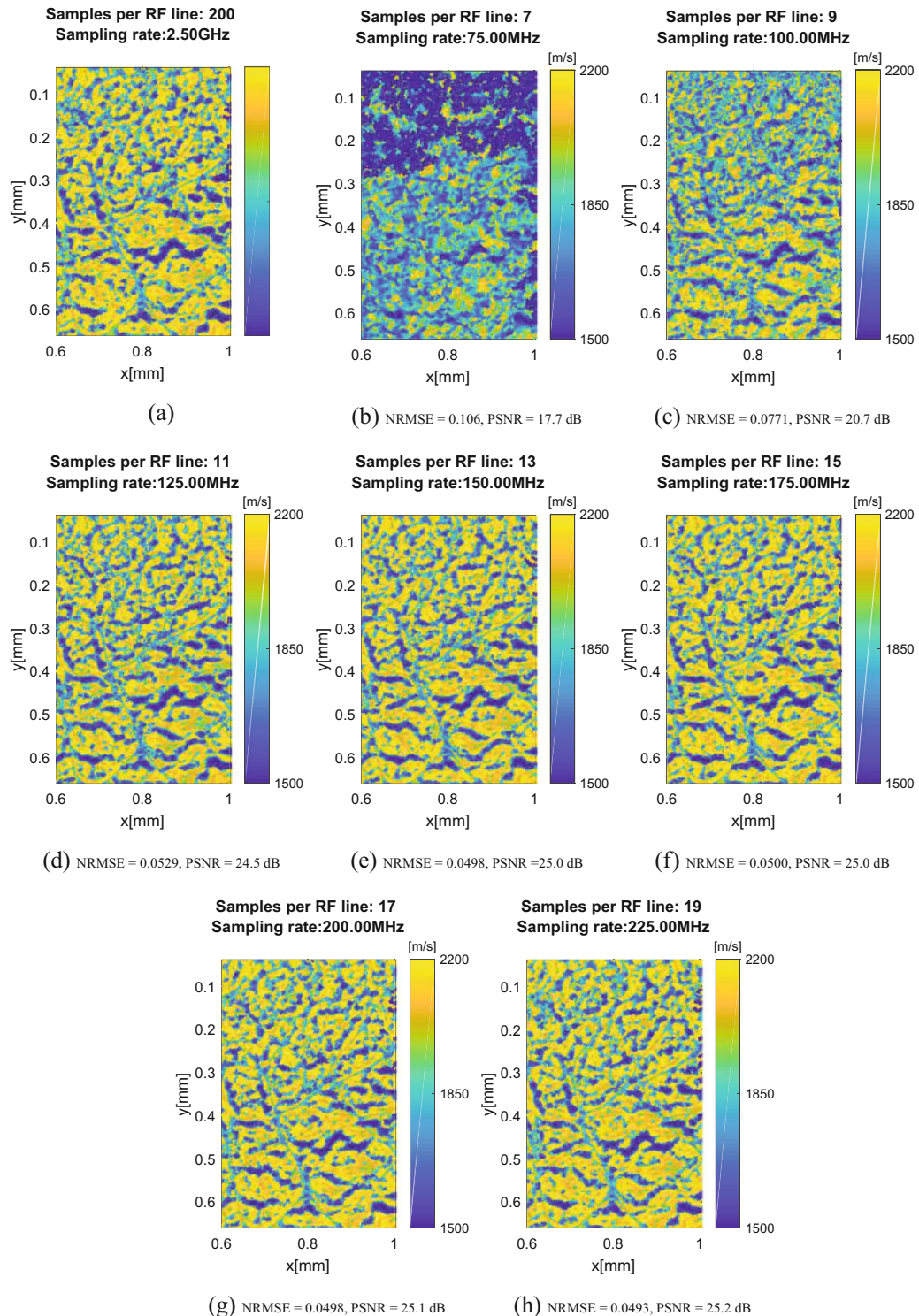


Fig. 12.8 2D speed of sound maps obtained from a thin chicken tendon tissue section. (a) The map created from fully sampled RF data cube (200 samples per RF signal).

(b-h) Maps estimated following the proposed approach corresponding to, respectively, 7, 9, 11, 13, 15, 17, and 19 samples per RF signal

12.5.3 Spatio-Temporal Data Reduction

The AMP and FRI CS sampling schemes are independent and operate in different dimensions of a 3D block of QAM RF data. Therefore, the spiral spatial sampling scheme using AMP can be used simultaneously with FRI temporal sampling providing tremendous data reduction. For instance, using the spiral sampling with 40% of the original data and sampling at 150 MHz instead of 2.5 GHz for the 250-MHz QAM instrument would reduce the total data size by a factor of approximately 39. Or equivalently, we can reconstruct 2D maps of equivalent quality with only 2.6% of the original 3D block of RF data.

Figure 12.9 displays 2D speed of sound maps obtained from a chicken tendon at full sampling and using CS approaches in the spatial domain only, temporal domain only, or combining both. It is visually nearly impossible to see differences between the four 2D maps. Table 12.1 provides quantitative assessments associated with Fig. 12.9. Overall, Table 12.1 provides a nice summary of this section on applying novel CS methods to QAM. The numbers demonstrate that the various methods can reduce data size and scanning time tremendously without being detrimental to the image quality. Moreover, the presented CS methods are tunable and spatial and temporal sampling rates can be chosen to meet specific criteria for a given application, providing tremendous flexibility.

12.6 Super-resolution (SR) Methods in QAM

Another way to reduce costs and improve ease of use for QAM systems can be achieved by using lower frequency transducers and postprocessing the data using methods to increase spatial resolution. Before discussing several so-called super-resolution (SR) methods in QAM, let us consider the implications of using a 250-MHz transducer to reconstruct QAM images with the same spatial resolution and properties as those acquired using a 500-MHz or even a 1-GHz transducer.

Generally speaking, challenges and expense increase with transducer center frequency. These challenges include:

- Transducer cost increases with frequency.
- Transducer sensitivity and SNR decrease with frequency.
- Water path attenuation effects increase with f^2 and further reduce signal strength at high frequencies.
- Depth of field and focal length decrease with increasing frequency.
- Dependence on room temperature; speed of sound is a function of temperature and small errors in speed of sound values will have more impact in higher frequency measurements because travel distances are shorter.
- Sensitivity to vibration; as frequency increases, axial wavelength decreases and vibration becomes more challenging.
- Electronics speed and costs; digitizer, pulser, amplifier, etc. all need to work faster and are more expensive.
- High frequency requires more precise motors; lateral resolution becomes finer with increasing frequency, and therefore scan steps must be smaller to fully exploit the finer resolution.
- Sensitivity to the level and flatness of the glass slide.
- Total scan area is approximately proportional to fixed total number of pixels, and therefore, decreasing step size will lead to smaller total scan areas.

As evidenced by the above list, if one can achieve the same final QAM images using a 250-MHz transducer instead of a 1-GHz transducer, tremendous ease of use and cost reductions will be achieved. Below are a few SR methods investigated by our group. Just like the CS methods, these are an illustrative sample of SR methods, but numerous others could be considered. Nevertheless, we believe that SR could have a tremendous role to play in QAM. It is also one of the few instances where the physics is actually on our side compared to conventional B-mode imaging at clinical frequencies. QAM images are slices at constant depth of a 3D block of RF data; as such,

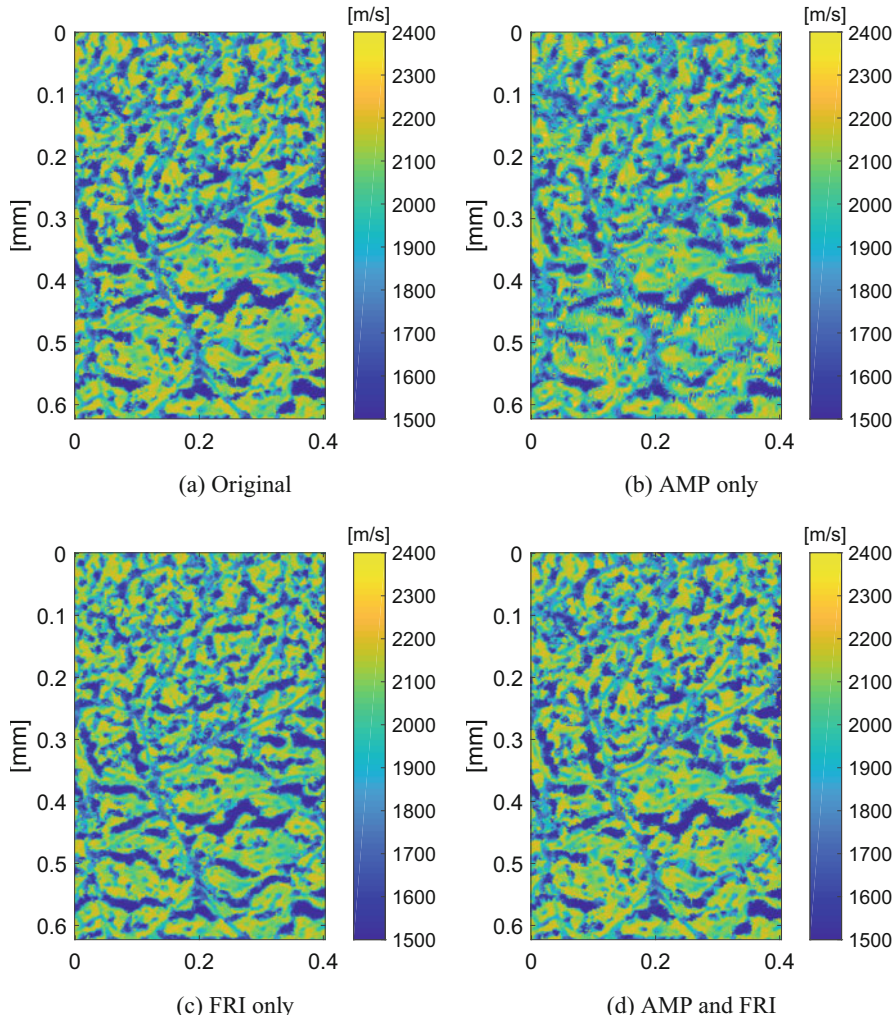


Fig. 12.9 2D speed of sound maps obtained from a thin section of a chicken tendon. (a) Fully sampled reconstruction (the same as Fig. 12.8a), (b) AMP reconstruction only

with spiral, (c) FRI reconstruction only with 250 MHz effective sampling rate (the same as Fig. 12.8e), and (d) AMP and FRI together

Table 12.1 Quantitative results computed between the 2D map from fully sampled RF data cube and those obtained from QAM RF signal sampled at low rates. Compression compares the size of the data volume when

compared to the fully sampled acquisition. Similarly, scanning time is the relative time required to perform a QAM scan compared to the fully sampled acquisition

Method	PSNR (dB)	NRMSE	Compression	Scanning time
Full sampling	NA	NA	100%	100%
AMP only	26.3	0.0483	40%	20%
FRI only	24.2	0.0617	6.5%	100%
AMP and FRI	23.4	0.0678	2.6%	20%

the point spread function (PSF) of the instrument is expected to be nearly constant, whereas in B-mode images the PSF varies strongly with imaging depth.

12.6.1 Regularized Deconvolution

Single-image SR is a well-established research field in image processing. The goal of these postprocessing methods is to obtain a fine-resolution image from a coarse-resolution observed image, i.e., a blurred, decimated, and noisy version of the fine-resolution image (Park et al. 2003). Reconstruction-based approaches are among the most popular techniques of SR. They formulate the SR problem as an ill-posed inverse problem that is solved by incorporating application-dependent regularization terms. In this section, we present the potential of such a reconstruction method (Zhao et al. 2016) to improve the spatial resolution and quality of 2D QAM images of acoustic impedance (2DZMs). The remainder of this section is a brief summary of a previous study by our group (Basarab et al. 2017a).

In Basarab et al. (2017a), we modeled the inadequate spatial resolution by two blurring and decimation operators and by an additive white Gaussian noise to imitate the image degradation process. Let us denote by \mathbf{y}_t the vectorized version, using a standard lexicographic order, of one slice from the QAM volume data \mathbf{y} corresponding to time t , where t is an integer between 1 and $N = Tf_s$, with T the time duration of the acquired RF signals and f_s the sampling frequency. The direct model for a given time t can then be written as

$$\mathbf{y}_t = \mathbf{S}\mathbf{H}\mathbf{x}_t + \mathbf{n}_t, \quad (12.22)$$

where the vector $\mathbf{y}_t \in \mathbb{R}^{N_t \times 1}$ ($N_t = m_t \times n_t$) is the measured data at time t , $\mathbf{x}_t \in \mathbb{R}^{N_h \times 1}$ ($N_h = m_h \times n_h$) is the vectorized super-resolved slice to be estimated, with $N_h = D^2 N_t$ (D is an integer representing the super-resolution factor, fixed at 2 here) and $\mathbf{n}_t \in \mathbb{R}^{N_t \times 1}$ is the Gaussian noise. The matrices $\mathbf{S} \in \mathbb{R}^{N_t \times N_h}$ and $\mathbf{H} \in \mathbb{R}^{N_h \times N_h}$ stand

for the decimation and blurring (convolution) operators. \mathbf{H} is a block circulant matrix modeling the 2D convolution between the super-resolved slice and the PSF, and left-multiplying by \mathbf{S} corresponds to down-sampling with an integer factor D in each spatial direction.

Interestingly, because QAM forms images at constant depth in the (x_1, x_2) plane, there is no axial range-dependent change in the PSF. In fact, a reasonable approximation to the PSF can be obtained from first principles and published equations for spherically focused transducers in their focal plane (Kino 1987). Therefore, the PSF is assumed to be known for QAM.

Following traditional image reconstruction problems, the super-resolved slice $\hat{\mathbf{x}}_t$ (the subscript corresponding to the time variable is omitted in the following) is estimated using a numerical optimization procedure to minimize the following function (Zhao et al. 2016):

$$\hat{\mathbf{x}} = \arg \min_{\mathbf{x}} \frac{1}{2} \|\mathbf{y} - \mathbf{S}\mathbf{H}\mathbf{x}\|_2^2 + \tau \phi(\mathbf{A}\mathbf{x}), \quad (12.23)$$

where τ is a regularization parameter manually tuned, $\phi(\mathbf{Ax}) = \sqrt{\|\mathbf{D}_h\mathbf{x}\|^2 + \|\mathbf{D}_v\mathbf{x}\|^2}$ is the total variation penalization (Ng et al. 2010) and $\mathbf{A} = [\mathbf{D}_h, \mathbf{D}_v]^T \in \mathbb{R}^{2N_h \times N_h}$, with \mathbf{D}_h and \mathbf{D}_v standing for horizontal and vertical numerical derivative operators. The decision to use total variation regularization was based on the piecewise constant nature of QAM slices. However, exploring other regularization terms is of high interest in QAM and represents an important perspective of our future work.

The algorithm to solve Eq. (12.23) is beyond the scope of this chapter but is described in great detail in Basarab et al. (2017a). The algorithm operates independently on each slice, for each time t , resulting in a super-resolved QAM volume \mathbf{X} . This data volume is further used as input in the AR or Hozumi inverse models to obtain 2D quantitative maps of acoustic parameters.

This approach shows promising results in acoustic simulations of tissue data (Fig. 12.10) and experimental data from a USAF 1951 resolution target (Fig. 12.11). Although these

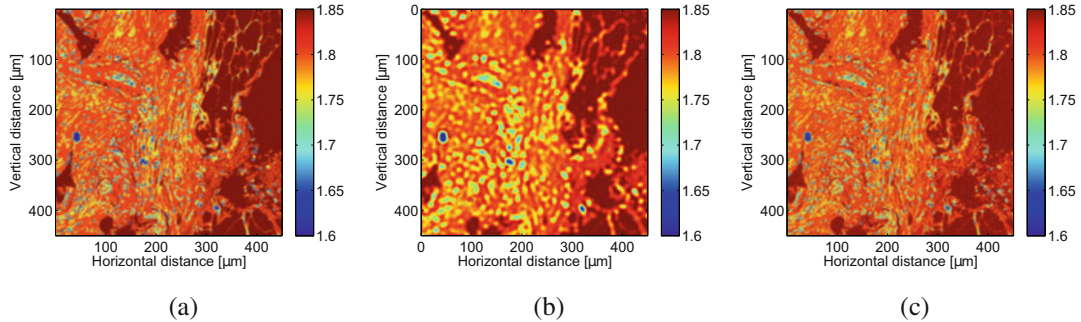


Fig. 12.10 Simulation result showing impedance maps in MRayl estimated using (a) the true fine resolution, (b) the observed coarse resolution (LR), and (c) the estimated super-resolved data volumes

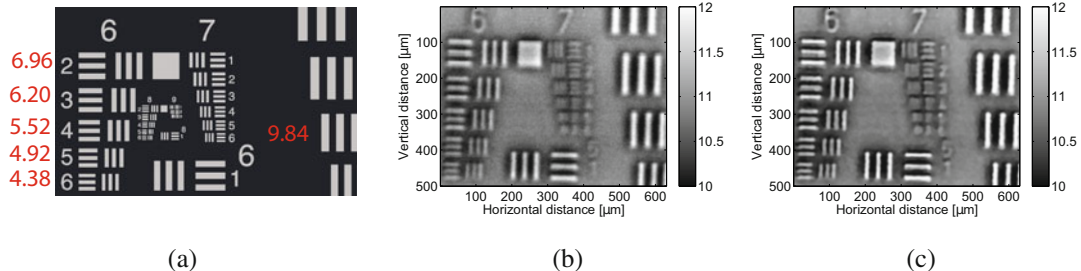


Fig. 12.11 Amplitude maps estimated from (b) the original and (c) the super-resolved RF volume acquired on the USAF 1951 resolution test chart (cartoon image shown

in (a)). The red numbers in (a) indicate the width in μm (equal to the pitch) between the bars

results provide encouraging preliminary evidence for the use of SR in QAM, results were less satisfactory in experimental data from soft tissues. Better regularization methods (such as those presented in the next section) or novel PSF estimation approaches may further improve results achieved with SR.

and can be applied to tissue sections following QAM data acquisition. Hematoxylin stains cell nuclei between purple and blue, whereas eosin stains cytoplasm and extracellular matrix pink. Overall, H&E stain provides a good layout of cell and tissue structure permitting pathologists to diagnose numerous diseases. Although it is a challenging hypothesis to rigorously test, it is reasonable to expect that some structural boundaries visible in H&E-stained histology images may also have boundaries in QAM maps. Therefore, in a recent study, a single-image SR approach using total variation regularization with bilateral weights based on a digital histology image of the same sample acquired at finer spatial resolution was investigated (Khalilian-Gourtani et al. 2018).

Briefly, the inversion is formulated as an optimization problem using the bilateral weights and approximation of the total variation (TV) norm as shown in Eq. (12.24), which is very

12.6.2 Histology-Based Regularization

Digital pathology images with better native resolution than those allowed by QAM are easy to obtain, albeit with different contrast mechanisms. Another SR approach was implemented using an original regularization method under the assumption that some structures are visible in both QAM and optical microscopy of stained tissue sections. For example, hematoxylin and eosin (H&E) stain is the most used in clinical diagnosis

similar to Eq. (12.23):

$$\hat{\mathbf{x}} = \arg \min_{\mathbf{x}} \left[\|\mathbf{y} - \mathbf{S}\mathbf{H}\mathbf{x}\|_2^2 + \lambda \sum_{m,n} \|\mathbf{w}_{m,n} \odot (\mathbf{I} - \mathbf{D}_x^m \mathbf{D}_y^n) \mathbf{x}\|_1 \right]. \quad (12.24)$$

The formulation in Eq. (12.24) consists of an ℓ_2 -norm as data fidelity term and a set of ℓ_1 -norm regularization terms to enforce sparsity of the image gradient in different directions. Additionally, \mathbf{D}_x^m and \mathbf{D}_y^n are the shifting operators that shift the image by m and n pixels in the horizontal and vertical directions, respectively (Farsiu et al. 2004). Note that the zero value for m or n means no shift in the corresponding direction. In this formulation, $\mathbf{w}_{m,n}$ are sets of weights that are determined using the histology image and the \odot operator corresponds to the Hadamard product. The general idea is to relax the penalty applied to a nonzero derivative in a given direction at a pixel location if the corresponding pixel in the histology image also exhibits large derivative in the same direction.

To make the weights $\mathbf{w}_{m,n}$ inversely proportional to the gradient magnitude in the direction defined by (m, n) in the histology image, we define the weights using the sigmoid function:

$$\mathbf{w}_{m,n} = \text{sigmoid}((\mathbf{I} - \mathbf{D}_x^m \mathbf{D}_y^n) \mathbf{v}), \quad (12.25)$$

where \mathbf{v} is the vectorized histology image and the sigmoid() function is defined as

$$\text{sigmoid}(x) = 1 - \frac{1}{1 + e^{-a(x-c)}}. \quad (12.26)$$

Setting the weights to equal values will reduce the formulation to a reliable approximation of the TV prior (Li et al. 1996).

Solving the optimization problem of Eq. (12.24) is beyond the scope of this chapter, but the reader can find the elegant algorithm in our published study (Khalilian-Gourtani et al. 2018). An illustrative result is shown in Fig. 12.12 where standard bicubic interpolation, standard total variation regularization, and the proposed approach are compared. The sharpness and the

new small features shown only in Fig. 12.12c, d strongly exemplify the power of the proposed SR approach.

This SR approach provides excellent resolution enhancement and could be part of a set of available methods to improve spatial resolution of QAM maps. However, this SR approach also has some limitations. While nothing prevents staining and acquiring optical microscopy images after QAM data acquisition, this process can be costly and time consuming. In addition, H&E-stained optical microscopy images and QAM images have very different contrast mechanisms, meaning it is possible that artificial edges may appear in QAM images or that true edges will not appear because they are between structures having no contrast with H&E or other stains.

12.6.3 Machine Learning Super-Resolution

Finally, machine learning was investigated to improve the spatial resolution of QAM images. The goal was to generate impedance maps matching the resolution achieved by a 500-MHz transducer from impedance maps reconstructed using 250-MHz acquisition data. To do this, a deep neural network was trained with data acquired from the same samples at both frequencies. In a published study, a classical U-net architecture was used and satisfactory results were obtained (Mamou et al. 2019). The specific architecture of the trained network is shown in Fig. 1 of Mamou et al. (2019), and the reader is also referred to the publication for the details of the training and testing of the network. In this study, nothing original was done from the machine learning point of view; a standard architecture was used with

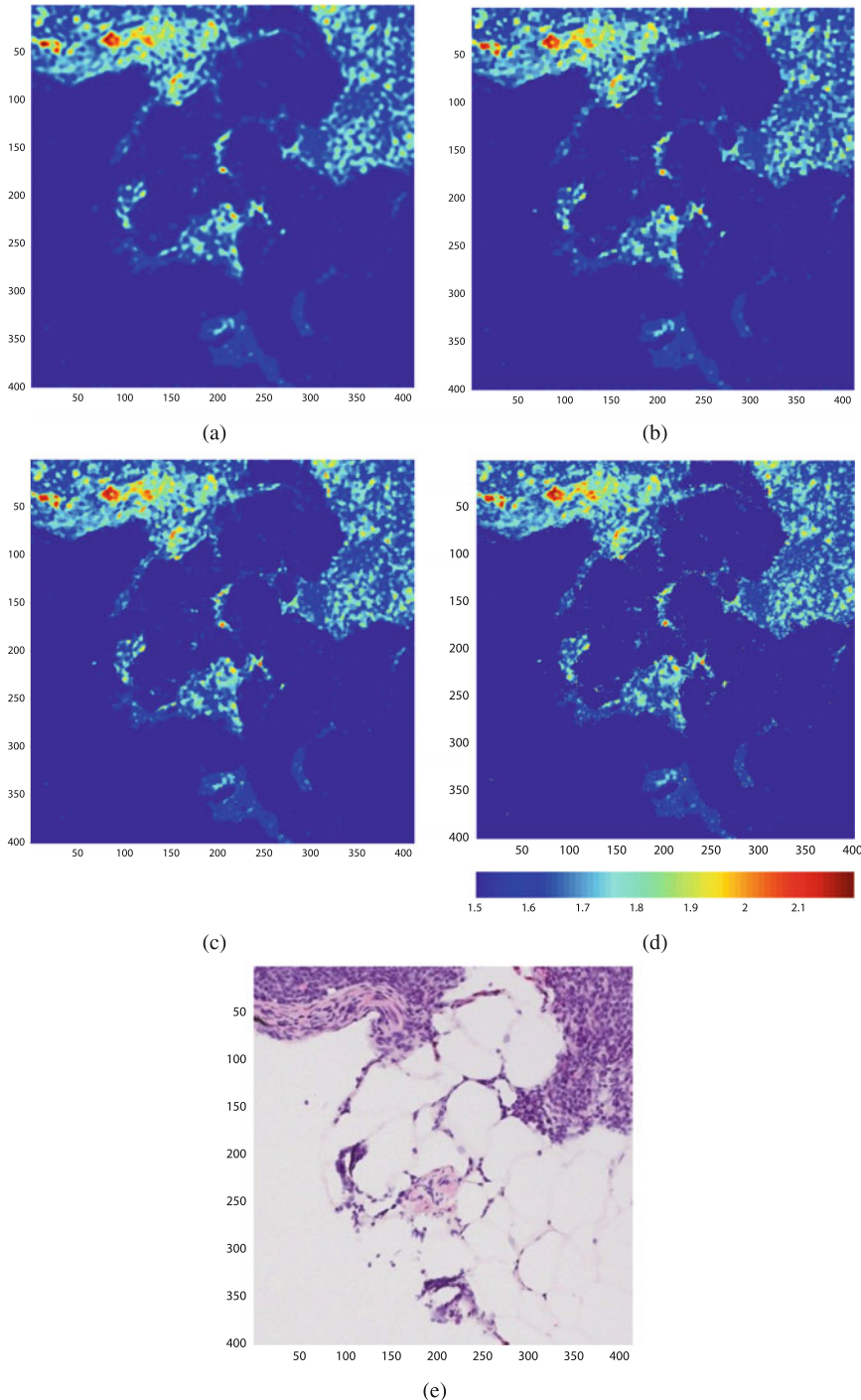


Fig. 12.12 (a) The interpolated 250-MHz QAM image of human lymph node using bicubic interpolation, (b) SR image without bilateral weights (conventional TV norm in two directions), (c) SR image with bilateral weights,

(d) the same region in the 500-MHz QAM image, and [scale=1 μm] (e) registered corresponding histology image of the same region

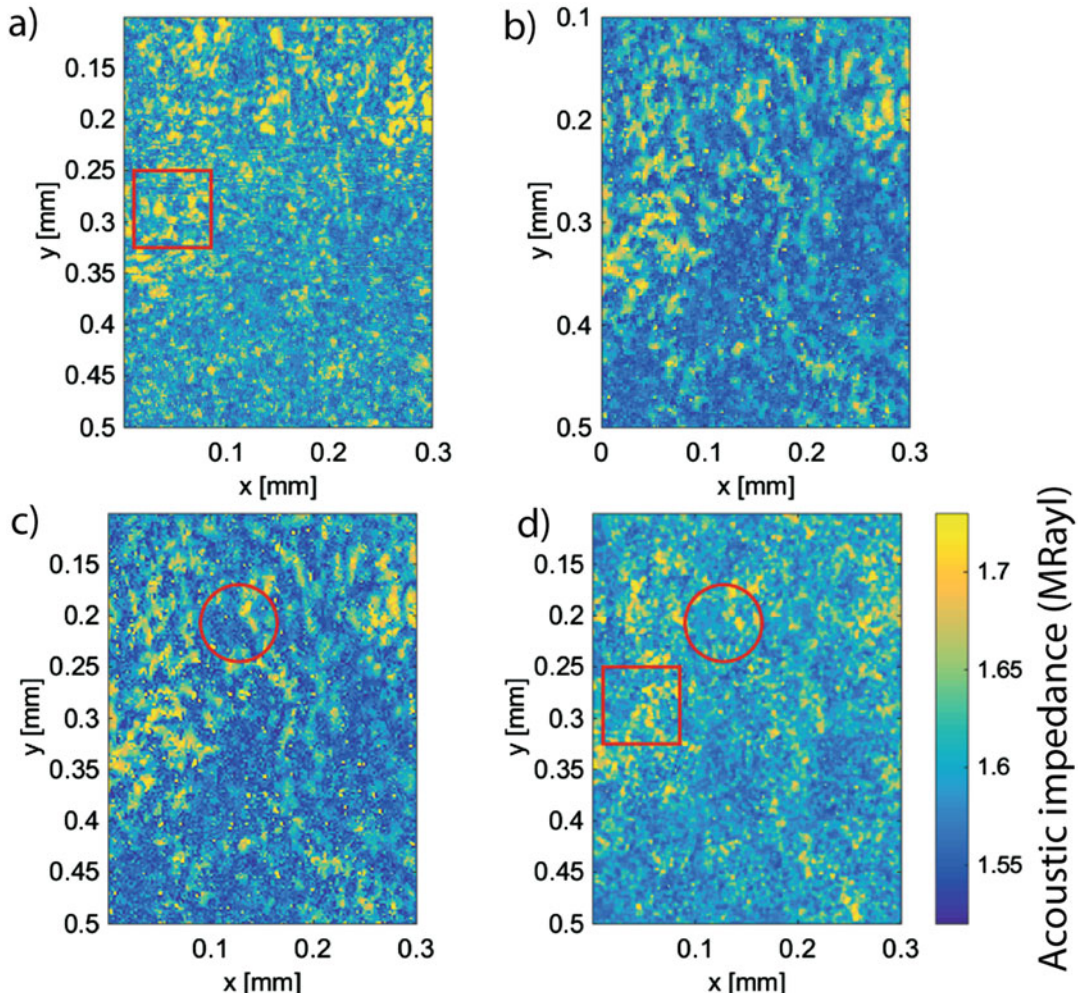


Fig. 12.13 Illustrative 2D acoustic impedance maps: (a) original at 500 MHz, (b) Original at 250 MHz, (c) the SR approach from Sect. 12.6.1 applied to (b), and (d) proposed machine learning approach applied to (b)

conventional metrics to optimize and assess performance.

Figure 12.13 displays results obtained on a previously unseen 250-MHz impedance map from a human lymph node. Visual inspection of Fig. 12.13c, d reveals novel fine details not visible in Fig. 12.13b, but the spatial resolution improvement seems far better in Fig. 12.13d obtained with the machine learning methods presented herein. See for example the area within the small red circle where more detailed structures are visible, in particular in the background (e.g., small acoustic impedance) regions and also in the regions exhibiting large

acoustic impedance values. Similarly, the area within the red squares is similar even though the 500-MHz 2D impedance map contains a lot of fine structures.

Even though this deep learning approach was simple and used limited training data, it did provide encouraging results that imply machine learning—in particular deep learning—have a role to play in improving spatial resolution in QAM images. The drawbacks here reflect many of the same issues of machine learning applied to challenging tasks: the black box aspect and the need for training data, which may be tissue specific. This latter point may be a

major drawback for investigators whose QAM systems cannot provide images with the required resolution to generate adequate training data for machine learning algorithms.

12.6.4 Discussion and Conclusions

This chapter provided an in-depth review of the concept of QAM data acquisition and image formation. In doing so, we highlighted how 2D QAM maps are valuable in biomedical research, but the systems come bundled with several challenges. Of particular note are the associated expense arising from specialty, high-precision components, a sensitivity to small vibrations and temperature change that increases with operating bandwidth, and the need for trained users to operate the system. Together these limitations make QAM use in soft tissues limited to research laboratories with the necessary experience. The wide acceptance of the technology remains challenging. Without a significant improvement in costs and ease of use, it remains unlikely that we will see QAM instruments join optical instruments in microscopy suites in academic and industrial settings. Theoretical and experimental challenges cannot be mitigated using standard methods, and in this chapter, elegant computational techniques were illustrated to break the Nyquist theorem limit or improve spatial resolution.

Together, these methods will deliver the next generation of QAM instrument. Super-resolution methods will allow using lower frequency transducers while delivering satisfactory spatial resolution. Based on our own studies, we expect SR methods to yield a resolution improvement by a factor between 2 and 3. Using lower frequency transducers makes the QAM instrument cheaper, easier to use, and less sensitive to vibration and water temperature. CS methods in the temporal domain allow using sampling rates at a fraction of those dictated by the Nyquist theory, reducing the total data size and digitizer cost. Moreover, FRI methods directly deliver normalized spectrum values, reducing parameter computation time. In fact, we believe the reduction in

computation time is so substantial that real-time image formation is within reach. CS methods in the spatial domain allow collecting data faster and enable the use of cheaper and less precise motor stages. These approaches are highly modular and can be used together, separately, or even with a pick-and-choose approach, providing tremendous flexibility to the user in terms of scanning time, image reconstruction time, image quality, and spatial resolution.

References

- Basarab A, Rohrbach D, Zhao N, Tourneret J-Y, Kouamé D, Mamou J (2017a) Enhancement of 250-MHz quantitative acoustic-microscopy data using a single-image super-resolution method. In: 2017 IEEE 14th international symposium on biomedical imaging (ISBI 2017), pp 827–830
- Basarab A, Rohrbach D, Zhao N, Tourneret J-Y, Kouamé D, Mamou J (2017b) Enhancement of 250-MHz quantitative acoustic-microscopy data using a single-image super-resolution method (regular paper). In: IEEE international symposium on biomedical imaging, Melbourne, 18/04/17–21/04/17. IEEE <http://www.ieee.org/>
- Binnig G, Quate CF, Gerber C (1986) Atomic force microscope. *Phys Rev Lett* 56(9):930–933
- Briggs A (1985) An introduction to scanning acoustic microscopy. Series microscopy handbooks. Oxford University Press, Oxford. [Online]. Available: <https://books.google.com/books?id=olqqAAAAIAAJ>
- Briggs A, Briggs G, Kolosov O (2010) Acoustic microscopy, vol 67. Oxford University Press, Oxford
- Dabov K, Foi A, Katkovnik V, Egiazarian K (2007) Image denoising by sparse 3-d transform-domain collaborative filtering. *IEEE Trans Image Process* 16(8):2080–2095
- Daft CW, Briggs GD (1989) Wideband acoustic microscopy of tissue. *IEEE Trans Ultrason Ferroelectr Freq Control* 36(2):258–263
- Farsiu S, Robinson MD et al (2004) Fast and robust multiframe super resolution. *IEEE Trans Image Process* 13(10):1327–1344
- Hofmann M, Pflanzer R, Habib A, Shelke A, Bereiter-Hahn J, Bernd A, Kaufmann R, Sader R, Kippenberger S (2016) Scanning acoustic microscopy—a novel non-invasive method to determine tumor interstitial fluid pressure in a xenograft tumor model. *Transl Oncol* 9(3):179–183
- Irie S, Inoue K, Yoshida K, Mamou J, Kobayashi K, Maruyama H, Yamaguchi T (2016) Speed of sound in diseased liver observed by scanning acoustic microscopy with 80 MHz and 250 MHz. *J Acoust Soc Am* 139(1):512–519

- Ito K, Yoshida K, Maruyama H, Mamou J, Yamaguchi T (2017) Acoustic impedance analysis with high-frequency ultrasound for identification of fatty acid species in the liver. *Ultrasound Med Biol* 43(3):700–711
- Kessler LW, Yuhas DE (1979) Acoustic microscopy. *Proc IEEE* 67(4):526–536
- Khalilian-Gourtani A, Wang Y, Mamou J (2018) Scanning acoustic microscopy image super-resolution using bilateral weighted total variation regularization. In: Annual International Conference of the IEEE Engineering in Medicine and Biology Society - Proceedings, vol 2018, pp 5113–5116
- Kim J, Mamou J, Hill PR, Canagarajah N, Kouame D, Basarab A, Achim A (2018) Approximate message passing reconstruction of quantitative acoustic microscopy images. *IEEE Trans Ultrason Ferroelectr Freq Control* 65(3):327–338
- Kim J, Mamou J, Kouamé D, Achim A, Basarab A (2020) Autoregressive model-based reconstruction of quantitative acoustic maps from RF signals sampled at innovation rate. *IEEE Trans Comput Imaging* 6:993–1006
- Kim J-H, Mamou J, Kouamé D, Achim A, Basarab A (2020) Autoregressive model-based reconstruction of quantitative acoustic maps from RF signals sampled at innovation rate. *IEEE Trans Comput Imaging* 6:993–1006
- Kino G (1987) Acoustic waves: devices, imaging, and analog signal processing, Series Prentice-Hall signal processing series. Prentice Hall PTR, Hoboken
- Kobayashi K, Yoshida S, Saijo Y, Hozumi N (2014) Acoustic impedance microscopy for biological tissue characterization. *Ultrasonics* 54(7):1922–1928
- Last JA, Russell P, Nealey PF, Murphy CJ (2010) The applications of atomic force microscopy to vision science. *Invest Ophthalmol Vis Sci* 51(12):6083–6094
- Lemons RA (1974) Acoustic microscope—scanning version. *Appl Phys Lett* 24(4):163
- Li Y et al (1996) A computational algorithm for minimizing total variation in image restoration. *IEEE Trans Image Process* 5(6):987–995
- Litniewski J, Bereiter-Hahn J (1990) Measurements of cells in culture by scanning acoustic microscopy. *J Microsc* 158(1):95–107
- Makhoul J (1975) Linear prediction: a tutorial review. *Proc IEEE* 63(4):561–580
- Mamou J, Rohrbach, D (2017) Image formation methods in quantitative acoustic microscopy. In: 2017 IEEE international conference on acoustics, speech and signal processing (ICASSP)
- Mamou J, Rohrbach D, Saegusa-Beecroft E, Yanagihara E, Machi J, Feleppa EJ (2015) Ultrasound-scattering models based on quantitative acoustic microscopy of fresh samples and unstained fixed sections from cancerous human lymph nodes. In: Ultrasonics symposium (IUS), 2015 IEEE International, pp 1–4
- Mamou J, Pellegrini T, Kouame D, Basarab A (2019) A convolutional neural network for 250-MHz quantitative acoustic-microscopy resolution enhancement. In: Annual International Conference of the IEEE Engineering in Medicine and Biology Society, vol 2019, pp 6212–6215
- Miura K, Nasu H, Yamamoto S (2013) Scanning acoustic microscopy for characterization of neoplastic and inflammatory lesions of lymph nodes. *Sci Rep* 3:1255
- Ng MK, Weiss P, Yuan X (2010) Solving constrained total-variation image restoration and reconstruction problems via alternating direction methods. *SIAM J Sci Comput* 32:2710–2736
- Oñativia J, Schultz SR, Dragotti PL (2013) A finite rate of innovation algorithm for fast and accurate spike detection from two-photon calcium imaging. *J Neural Eng* 10(4):046017. [Online]. Available: <http://stacks.iop.org/1741-2553/10/i=4/a=046017>
- Ojanen X, Toyras J, Inkkinen SI, Malo MK, Isaksson H, Jurvelin JS (2016) Differences in acoustic impedance of fresh and embedded human trabecular bone samples—scanning acoustic microscopy and numerical evaluation. *J Acoust Soc Am* 140(3):1931
- Pan H, Blu T, Vetterli M (2017) Towards generalized FRI sampling with an application to source resolution in radioastronomy. *IEEE Trans Signal Process* 65(4):821–835
- Park SC, Park MK, Kang MG (2003) Super-resolution image reconstruction: a technical overview. *IEEE Signal Process Mag* 20:21–36
- Quate CF, Atalar A, Wickramasinghe HK (1979) Acoustic microscopy with mechanical scanning—A review. *Proc IEEE* 67(8):1092–1114
- Raum K (2008) Microelastic imaging of bone. *IEEE Trans Ultrason Ferroelectr Freq Control* 55(7):1417–1431
- Rohrbach D, Mamou J (2018) Autoregressive signal processing applied to high-frequency acoustic microscopy of soft tissues. *IEEE Trans Ultrason Ferroelectr Freq Control* 65(11):2054–2072
- Rohrbach D, Saegusa-Beecroft E, Yanagihara E, Machi J, Feleppa EJ, Mamou J (2014) Fine-resolution maps of acoustic properties at 250 MHz of fresh samples and unstained fixed 12- μ m thin sections from cancerous human lymph nodes. IEEE, pp 624–627. [Online]. Available: <http://ieeexplore.ieee.org/lpdocs/epic03/wrapper.htm?arnumber=6931943>
- Rohrbach D, Hoang QV, Wen Q, McFadden SA, Silverman RH, Mamou J (2015). Fine-resolution elastic-property maps of myopic sclera by means of acoustic microscopy. In: Ultrasonics symposium (IUS), 2015 IEEE international, pp 1–4
- Rohrbach D, Lloyd HO, Silverman RH, Mamou J (2015) Fine-resolution maps of acoustic properties at 250 MHz of unstained fixed murine retinal layers. *J Acoust Soc Am* 137(5):EL381–EL387
- Rohrbach D, Lloyd HO, Silverman RH, Urs R, Mamou J (2015) Acoustic-property maps of the cornea for improved high-frequency ultrasound corneal biometric accuracy. In: Ultrasonics symposium (IUS), 2015 IEEE international, pp 1–4
- Rohrbach D, Lloyd HO, Silverman RH, Urs R, Mamou J (2015) Acoustic-property maps of the cornea for improved high-frequency ultrasound corneal biometric accuracy. IEEE, pp 1–4. [Online]. Available: <http://ieeexplore.ieee.org/lpdocs/epic03/wrapper.htm?arnumber=7290000>

- able: <http://ieeexplore.ieee.org/lpdocs/epic03/wrapper.htm?arnumber=7329192>
- Rohrbach D, Inkinen S, Hradilova J, Kadow-Romacker A, Joukainen A, Malo MK, Mamou J, Töyräs J, Raum K (2016) Ultrasound biomicroscopy reveals chondrocyte layer spacing in human articular cartilage. In: IEEE international ultrasonics symposium, vol conference proceeding, no. Abstract ID: 1074
- Rohrbach D, Jakob A, Lloyd H, Tretbar S, Silverman RH, Mamou J (2016) A novel quantitative 500-MHz acoustic-microscopy system for ophthalmologic tissues. *IEEE Trans Biomed Eng* 64:715–724
- Rohrbach D, Wen ASRQ, McFadden SA, Silverman RH, Hoang QV, Mamou J (2016) Microstructural assessment of the guinea pig sclera using quantitative acoustic microscopy. In: Ultrasonics symposium (IUS), 2016 IEEE international
- Rohrbach D, Inkinen SI, Zatloukalova J, Kadow-Romacker A, Joukainen A, Malo MK, Mamou J, Toyras J, Raum K (2017) Regular chondrocyte spacing is a potential cause for coherent ultrasound backscatter in human articular cartilage. *J Acoust Soc Am* 141(5):3105
- Rohrbach D, Ito K, Lloyd HO, Silverman RH, Yoshida K, Yamaguchi T, Mamou J (2017) Material properties of human ocular tissue at 7-microm resolution. *Ultrasound Imaging*, 39:313–325
- Rohrbach D, Silverman RH, Chun D, Lloyd HO, Urs R, Mamou J (2018) Improved high-frequency ultrasound corneal biometric accuracy by micrometer-resolution acoustic-property maps of the cornea. *Transl Vis Sci Technol* 7(2):21
- Rudresh S, Seelamantula CS (2017) Finite-rate-of-innovation-sampling-based super-resolution radar imaging. *IEEE Trans Signal Process* 65(19):5021–5033
- Saijo Y, Okawai H, Sasaki H, Yambe T, Nitta S, Tanaka M, Kobayashi K, Honda Y (2000) Evaluation of the inner-surface morphology of an artificial heart by acoustic microscopy. *Artif Organs* 24(1):64–69
- Sasaki H, Saijo Y, Tanaka M, Nitta S, Terasawa Y, Yambe T, Taguma Y (1997) Acoustic properties of dialysed kidney by scanning acoustic microscopy. *Nephrol Dial Transplant* 12(10):2151–2154
- Tur R, Eldar YC, Friedman Z (2011) Innovation rate sampling of pulse streams with application to ultrasound imaging. *IEEE Trans Signal Process* 59(4):1827–1842
- Vetterli M, Marziliano P, Blu T (2002) Sampling signals with finite rate of innovation. *IEEE Trans Signal Process* 50(6):1417–1428
- Wei X, Dragotti PL (2016) Fresh x2014;fri-based single-image super-resolution algorithm. *IEEE Trans Image Process* 25(8):3723–3735
- Weiss EC, Lemor RM, Pilarczyk G, Anastasiadis P, Zinin PV (2007) Imaging of focal contacts of chicken heart muscle cells by high-frequency acoustic microscopy. *Ultrasound Med Biol* 33(8):1320–1326
- Zhao N, Wei Q, Basarab A, Dobigeon N, Kouamé D, Tourneret J-Y (2016) Fast single image super-resolution using a new analytical solution for ℓ_2 - ℓ_2 problems. *IEEE Trans Image Process* 25(8):3683–3697

Part VI

Phantoms for Quantitative Ultrasound



Phantoms for Quantitative Ultrasound

13

Timothy A Stiles

Abstract

Tissue-mimicking materials and phantoms have an important role in quantitative ultrasound. These materials allow for investigation of new techniques with the ability to design materials with properties that are stable over time and available for repeated measurements to refine techniques and analysis algorithms. This chapter presents an overview of the history of phantoms, methods of creation of materials with a variety of acoustic properties, and methods of measurement of those properties. It includes a section addressing the measurement of variance in those techniques using interlaboratory comparisons. There is a wide range of existing tissue-mimicking materials that exhibit properties similar to those of most soft tissues. Ongoing work is part of the expansion of QUS as materials are developed to better mimic specific tissues, geometries, or pathologies.

Keywords

Phantom · Tissue mimicking · Attenuation · Backscatter coefficient · Speed of sound

13.1 Overview of Ultrasound Phantoms

As with other imaging modalities, ultrasound phantoms are widely used for routine quality assurance, acceptance testing, and research into new uses of ultrasound for diagnosis or treatment. In general, phantoms must have:

1. Physical properties that match those of tissue
2. Known and calibrated geometry
3. Little or no change over time

The key physical properties for ultrasound phantoms are:

1. Speed of sound
2. Acoustic impedance
3. Attenuation, both magnitude and frequency dependence
4. Backscatter coefficient, both magnitude and frequency dependence

T. A. Stiles (✉)
Department of Physics, Kettering University, Flint, MI,
USA
e-mail: tstiles@kettering.edu

Additional properties that may be important depending on the specific use of the phantom include mechanical properties such as elastic moduli, speed of shear wave propagation, and nonlinearity parameter B/A .

A variety of materials have been produced. Several reviews of tissue-mimicking materials for ultrasound are available (Culjat et al. 2010; Zell et al. 2007; Browne et al. 2003a). This section will review some of these techniques, with an emphasis on those that are most suitable for use in quantitative ultrasound of soft tissues. In particular, this chapter will not discuss the rather large body of literature on bone or dental ultrasound phantoms. It will not discuss materials that have been designed for use in elastographic or shear wave measurements.

13.1.1 Acoustic Properties of TM Materials

The speed of sound of the material refers here to the propagation speed of longitudinal waves in the material. The speed of sound of most soft tissues is very nearly independent of frequency in the frequency range used by diagnostic ultrasound. Ultrasound scanners have traditionally assumed a speed of sound of 1540 m/s. This value is used in several ways by a scanner. The speed of sound is used to determine appropriate delays between transducer elements in beamforming for both transmit and receive focusing. The speed of sound is also used to convert the measured time delay between transmission and reception of a signal into the distance from the transducer to the structure producing the detected echo. Many modern ultrasound scanners have the ability to change the assumed speed of sound in the material and can measure the speed of sound of the tissue using a variety of techniques (Szabo 2013).

The characteristic specific acoustic impedance of a material is the product of the speed of sound and mass density of the material. This name is often shortened to “acoustic impedance.” The units of acoustic impedance are $\text{kg m}^{-2}\text{s}^{-1}$ which can be defined as the rayl. The acoustic impedance

determines the reflection and transmission coefficients of ultrasound at the boundary between two materials (Szabo 2013).

Attenuation coefficient refers to the rate of the loss of energy from an ultrasound beam. In a plane wave model, the intensity of an ultrasound beam will decrease as the beam propagates due to absorption and scattering of ultrasound out of the beam. The combined effects of these two physical processes are the attenuation of the ultrasound beam. It is typically measured in reference to a loss in the pressure amplitude of the beam of the form:

$$p(z) = p_0 e^{-\alpha z} \quad (13.1)$$

where z is the distance along the propagation axis, p_0 is the initial pressure amplitude, $p(z)$ is the pressure amplitude at location z , and α is the attenuation coefficient. Typically, the attenuation coefficient is measured in decibels, as in dB/cm. Attenuation coefficient varies substantially with frequency. One method to express this variation is to fit measurements of attenuation coefficient to a power law model of the form

$$\alpha(f) = \alpha_0 f^n \quad (13.2)$$

where f is the frequency (in MHz) and α is the attenuation coefficient (.). The term α_0 then is a measure of the overall magnitude of attenuation and has units of $\text{dB cm}^{-1} \text{MHz}^{-n}$. It should be noted that this power law relationship may exist only over a particular range of frequencies. However, it has been found to be broadly applicable to frequencies in the range from 1 to 20 MHz. It is common to report the value of the attenuation coefficient at a particular frequency divided by that frequency in units of $\text{dB cm}^{-1} \text{MHz}^{-1}$. This value is often somewhat erroneously called the “attenuation coefficient slope” (IEC 2010). Mathematically, this value is not the slope since the slope would refer to the slope of the tangent line and would be $n\alpha_0 f^{n-1}$. In this chapter, we propose the use of the term “specific attenuation coefficient” and the symbol ζ , such that

$$\zeta = \frac{\alpha}{f}$$

which is measured in units $\text{dB cm}^{-1} \text{MHz}^{-1}$. For a power-law relationship, $\zeta = \alpha_0 f^{n-1}$ and is different from the slope of the tangent line by a factor of n . The slope and the specific attenuation coefficient are the same only if $n = 1$. For many materials, this difference is small, however there are materials for which $n \approx 2$ and the difference is substantial. For example, corn oil has a reported attenuation coefficient for frequencies between 1 and 60 MHz of $\alpha = (0.0703 \text{ dB cm}^{-1} \text{ MHz}^{-1.85}) f^{1.85}$ with f in MHz (Chanamai and McClements 1998). At 1.0 MHz, this corresponds to a specific attenuation coefficient of $0.0703 \text{ dB cm}^{-1} \text{ MHz}^{-1}$. At 10 MHz, the specific attenuation coefficient is $0.498 \text{ dB cm}^{-1} \text{ MHz}^{-1}$. However, normal human liver *in vivo* exhibits an attenuation coefficient described by $\alpha = (0.47 \text{ dB cm}^{-1} \text{ MHz}^{-1.05}) f^{1.05}$ (Parker et al. 1988), which implies a specific attenuation coefficient of $0.47 \text{ dB cm}^{-1} \text{ MHz}^{-1}$ at 1.0 MHz and $0.53 \text{ dB cm}^{-1} \text{ MHz}^{-1}$ at 10 MHz.

Typical values of speed of sound, acoustic impedance, and attenuation fit parameters for soft tissues and materials are given in Table 13.1. Note that there may be substantial variations from these values for various diseases and conditions. The values of tissue are listed at normal body temperature, while phantoms are typically measured at room temperature.

The backscatter coefficient (BSC) refers to the relative amount of ultrasound energy that is scattered in the backward direction, that is at 180° from the initial propagation direction. Assuming an incident plane wave and randomly positions, independent scatterers under the Born approximation, the BSC is defined as the number density of scatterers times the power of the scattered

ultrasound signal per unit solid angle divided by the incident intensity. The units of BSC are inverse distance times inverse solid angle and are often reported as $\text{cm}^{-1} \text{ sr}^{-1}$. The BSC is the differential cross section per solid angle (units of area per solid angle) divided by the volume of the region from which the scattering occurs. Additional details about the BSC are discussed below. Note that the BSC is highly dependent on frequency. In some cases, BSC can be fit to a power law model over a limited range of frequencies. As described below, the BSC depends greatly on the size, shape, and composition of the scattering material. Very small scatterers compared to the wavelength of ultrasound will exhibit Rayleigh scattering in which the BSC is proportional to frequency to the fourth power. If the size of the scatterers is on the order of the wavelength, there will be substantial resonance effects that are difficult to model mathematically. Because of the random nature of scattering, the characterization of the scattering properties of tissue or phantom materials require stochastic approaches.

13.1.2 Development of TM Materials

Early ultrasound phantoms consisted of a container with thin steel rods at known positions. An example of this is the “AIUM (American Institute of Ultrasound in Medicine) Standard 100 mm Test Object” (AIUM 1975). This phantom could be produced in two forms: an “open” configuration that was designed to be placed in a separate container of fluid and an “enclosed” configuration that was sealed on all sides with fluid within. In either case, the phantom con-

Table 13.1 Values of relevant physical properties of normal soft tissues (Szabo 2013;)

Tissue/Material	Speed of sound (m/s)	Acoustic impedance (MRayl)	Attenuation parameter α_0 (dB/cm/MHz ⁿ)	Attenuation power n (unitless)
Water (20 °C)	1480	1.48	0.0022	2
Corn oil	1460	1.39	0.073	1.85
Soft tissue (average)	1540	1.63	0.3–0.8	0.9–1.2
Fat	1450–1480	1.40	0.5–1.8	1.1
Breast glandular	1510	1.54	0.75	1.1
Liver	1550–1600	1.68	0.4–0.7	1.1

sisted of 28 stainless steel rods with a diameter of 0.75 mm. The fluid portion of the phantom could be water or saline, with the temperature adjusted to match the speed of sound of the fluid to that of tissue. A speed of sound of 1540 m/s would require a water bath to have a temperature of 47 °C. Optionally, a solution of water with sodium chloride or water with ethyl alcohol could be used to create a fluid with the appropriate speed of sound at room temperature. While simple, this phantom could be used for measurements of depth calibration, axial resolution, dead zone, lateral resolution, time-gain characteristics, A-Mode and B-Mode linearity, and scanned B-Mode alignment.

Some of the first tissue-mimicking (TM) materials were developed at the University of Wisconsin-Madison. An early success was the production of gelatin or agar-based material with the addition of n-propanol to increase the speed of sound and microscopic graphite grains to increase attenuation (Madsen et al. 1978; Burlew et al. 1980). The speed of sound of this material at room temperature could be varied from 1500 to 1650 m/s and attenuation from about 0.4 to 1.5 dB/cm/MHz with nearly linear frequency dependence. This material did not have substantial scattering as noted in Madsen et al. (1978): “Gray scale patterns obtained with [B-scans] indicate a lower level of scatter occurs from within the sample than occurs from liver parenchyma.” A later article built on this material to produce a TM material with very low intrinsic scatter by replacing the powdered graphite with evaporated milk (Madsen et al. 1998). Madsen et al. (1998) includes detailed instructions for the production of this material. One liter of TM liquid is produced from 600 mL evaporated milk, 370 mL of distilled water, 30 mL of n-propanol, and 1.0 gram of thimerosal as a preservative. A

similar solid form can be produced using agar (Madsen et al. 1998).

The material described in Madsen et al. (1998) allows for mostly independent control of the three key acoustic parameters. Since the intrinsic backscatter of the evaporated milk and agar material is very low (reported as $(4.59 \pm 0.50) \times 10^{-7} \text{ cm}^{-1} \text{ sr}^{-1}$ at 4.0 MHz), backscatter coefficient is controlled by the addition of independent scattering material, such as microscopic glass or ceramic beads. The amount of attenuation can be controlled by the addition of various amounts of evaporated milk with results described in Table 13.2. The authors suggest a practical upper limit of specific attenuation coefficient of $0.70 \text{ dB cm}^{-1} \text{ MHz}^{-1}$ due to the practical issues of mixing evaporated milk with agarose solution. The speed of sound of the material is close to 1540 m/s. If needed, the speed of sound can be increased by the addition of n-propanol.

In recent years, a substantial amount of work has used what is often termed the “IEC agar” material (IEC 2009, 2007). A detailed set of instructions for creating this material has also been published (Souza et al. 2016). This material uses a mixture of very small scatterers to produce attenuation and larger scatterers to produce substantial backscatter. This material is composed of 82.97% deionized water, 11.21% glycerol, 3.00% agar, 0.53% 400 grit silicon carbide particles, 0.88% 0.3 μm aluminum oxide particles, 0.94% 3 μm aluminum oxide particles, and 0.47% benzalkonium chloride as a preservative (all percentages are weight/weight) (Souza et al. 2016). The properties of this material have been measured over a broad range of frequencies with a speed of sound of 1542 m/s, specific attenuation coefficient of $0.50 \text{ dB cm}^{-1} \text{ MHz}^{-1}$, and

Table 13.2 Attenuation of samples described in Madsen et al. (1998), results of fitting to power law model done by the author based on results reported in Table 6 of Madsen et al. (1998)

Sample designation from Madsen et al. (1998)	Percentage of evaporated milk	$\alpha_0 (\text{dB cm}^{-1} \text{ MHz}^{-n})$	Power n
Sample B	0%	0.0265	1.52
Sample C	20%	0.205	1.03
Sample D	50%	0.468	1.03

BSC near soft tissue (Brewin et al. 2008; Sun et al. 2012). This material has been extended to mimic fat and aorta tissue (Maia et al. 2021) by changing the relative amounts of the constituents.

13.1.3 Commercially Available Materials

There are a number of commercial companies that produce ultrasound phantoms. These include Sun Nuclear (Middleton, WI), CIRS (Norfolk, VA), and Kyota Kagaku (Tokyo, Japan). Several other companies produce training phantoms with anatomical likeness. Sun Nuclear uses a material known as “High Equivalency Gel” or HE Gel. This material is marketed as having a speed of sound of 1540 m/s and attenuation coefficient of either 0.5 or 0.7 dB/cm/MHz with the attenuation coefficient being linear with frequency over the range from 2 to 18 MHz. CIRS manufactures phantoms with one of the two base materials: Zerdine or ATS Urethane. Zerdine is described as a hydrogel polymer with a speed of sound of 1540 m/s and can be produced with any of several attenuation coefficients. ATS Urethane has an advantage of being resistant to desiccation or other changes over time but had a speed of sound of 1450 m/s, substantially lower than most soft tissue.

Several studies have been conducted to independently measure the properties of the materials used by commercial phantom manufacturers. Browne et al. (2003b) measured speed of sound and attenuation coefficient of five materials: IEC agar (Ramnarine et al. 2001; IEC 2001), Zerdine, ATS Urethane, and two versions of the condensed milk gel that is the basis for HE Gel. Results of their measurements at 20 °C are presented in Table 13.3. The conclusions of this study indicate that the sound speed of ATS Urethane may cause diffraction errors when used with ultrasound scanners that assume a sound speed of 1540 m/s. The authors note that the manufacturer

states that the placement of targets within ATS Urethane phantoms is adjusted such that the target location appears correct on when scanned with a system that assumes a sound speed of 1540 m/s. With the advent of technology that allows beam-formers to adjust sound speed, it is not clear if this remains a substantial issue. The study also concludes that highly nonlinear dependence of attenuation coefficient on frequency of both ATS Urethane and Zerdine may result in a decrease in measurements of penetration depth and axial resolution results at frequencies greater than 7 MHz.

13.1.4 Other Materials

Many other materials have been investigated for possible use as ultrasound TM materials. Several of these materials have speed of sound that is substantially less than 1540 m/s. These materials are not appropriate mimics for most soft tissues but may have a role in producing materials that mimic the properties of fat or fatty tissue. Several articles report on using a copolymer in oil gel such as styrene-ethylene/butylene-styrene mixed with mineral oil (Oudry et al. 2009; Cabrelli et al. 2016). This produces a material with mechanical properties very close to those of tissue. However, as with urethane, the speed of sound is substantially lower than most soft tissue (1420 to 1480 m/s) and attenuation coefficient has a power law dependence that is substantially larger than that of soft tissue (Cabrelli et al. 2016 reports n between 1.66 and 1.85). Similarly, gel-wax materials have been proposed for photo-acoustic imaging but again have acoustic properties that do not match those of soft tissue with a speed of sound of about 1445 m/s and attenuation coefficient that is nearly proportional to frequency squared (Maneas et al. 2018). Silicone rubber-based materials offer ease of fabrication and long-term stability but have extremely low speed of sound, in the range from 970 to 1250 m/s (Cabrelli et al. 2016) much lower than soft tissue. It

Table 13.3 Speed of sound and attenuation results at 20°C from Browne et al. (2003b)

Material	Speed of sound at 7.5 MHz (m/s)	α_0 (dB cm ⁻¹ MHz ⁻ⁿ)	Power <i>n</i>
Agar	1540	0.53	1.01
Zerdine	1540	0.48	1.30
Urethane	1460	0.19	1.83
0.5 dB/cm/MHz condensed milk	1535	0.49	1.10
0.7 dB/cm/MHz condensed milk	1540	0.72	1.08

may be possible to combine these materials with others to produce materials that mimic both the speed and attenuation of fatty tissues.

Other materials have properties that are fairly close to soft tissues. Polyvinyl alcohol (PVA) gel has a speed of sound of about 1570 m/s and attenuation coefficient of about 0.4 dB cm⁻¹ MHz⁻¹ with a gel composed of 15% PVA and 85% water/DMSO (Zell et al. 2007; Kharine et al. 2003). The production of gels using PVA is a longer process and may require multiple cycles of freezing and thawing. Polyacrylamide gel can be produced with a speed of sound of 1580 m/s and attenuation coefficient of (0.15 dB cm⁻¹ MHz^{-1.15}) $f^{1.15}$ (Zell et al. 2007). It is likely that the attenuation could be increased using techniques similar to hydrogel (i.e., addition of materials such as evaporated milk or powdered graphite). Varying the amount of polyacrylamide from 5 to 20% can result in a speed of sound between 1512 and 1595 m/s (Cafarelli et al. 2017; Prokop et al. 2003) without a substantial change in attenuation. It should be noted that the monomer acrylamide is carcinogenic and neurotoxic. Therefore, care should be taken during the preparation and handling of polyacrylamide gels. A combination of 98% ballistics gel, 1% mineral oil, and 1% 50 μ m cellulose powder has been reported to have a speed of sound of 1537 m/s and specific attenuation coefficient of 1.07 dB cm⁻¹ MHz⁻¹ (Alves et al. 2020). However, other measurements of similar materials result in a much lower speed of sound, around 1455 m/s, and that the attenuation coefficient is nearly proportional to frequency squared (Sjöstrand et al. 2020). These materials show promise of being useful in a variety of applications for tissue-mimicking materials.

There is a good deal of ongoing research into creating tissue-mimicking materials for use in ultrasound. Many of the most successful materials are based on agarose gels or polyacrylamide hydrogels. Rubber and similar materials have an advantage in that they do not have long-term changes in acoustic properties from the evaporation of water. However, the rubber- and urethane-based materials have a much lower speed of sound than most soft tissues. Agarose and polyacrylamide materials need to be stored in a container that inhibits evaporation of water. That container can be mostly made from solid plastic or similar waterproof materials. At least one surface of the container must allow for transmission of ultrasound into and out of the tissue mimicking material. That side is often composed of a thin flexible plastic membrane and called the acoustic window of the phantom. As detailed below, the presence of that window does reduce the transmission of ultrasound and care must be taken to correct for its presence in measurements of the acoustic properties of the phantom.

13.2 Measurements of Acoustic Properties

Standard methods for measuring the acoustics properties of TM materials are published by several organizations, including the AIUM (2014) and IEC (2019). This section presents an overview of the most common methods for measuring relevant acoustic properties of tissue-mimicking materials.

13.2.1 Speed and Attenuation

The speed of sound and attenuation of TM materials are often measured using an “insert-substitution” technique. In this technique, a measurement of an ultrasound signal is performed in a reference medium (typically, degassed deionized water,) and a second measurement is made with part of the reference medium replaced by the test object. The speed of sound and attenuation can be measured in either through-transmission configuration (as shown in Fig. 13.1) or pulse-echo with a reflector (Fig. 13.2). The reflector method may result in

a smaller signal-to-noise ratio because the signal must propagate through four transmissions, a reflection, and through the sample twice. The through-transmission experiment requires only a single pass through the sample and the two transmissions into and out of the sample. In either case, the presence of the sample affects the ultrasound signal by shifting the time of arrival and amplitude of the received signal. Because acoustic properties depend on temperature, the water bath should be carefully temperature controlled.

The through-transmission technique is often used in a narrowband measurement using

Fig. 13.1 Schematic of insert-substitution technique for measuring speed of sound and attenuation of a sample

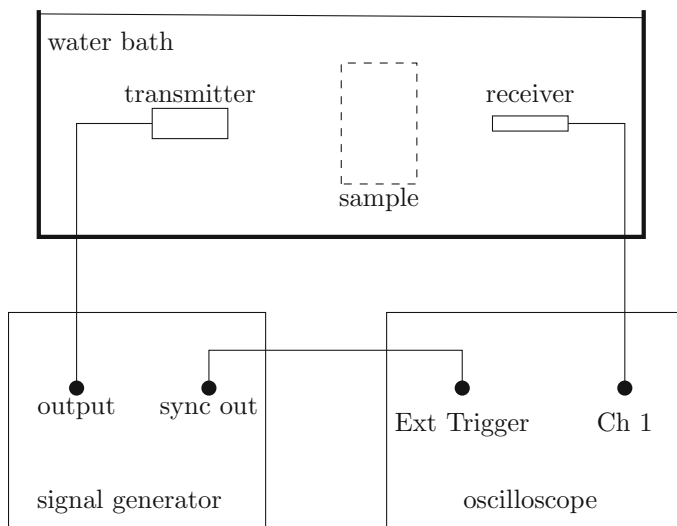
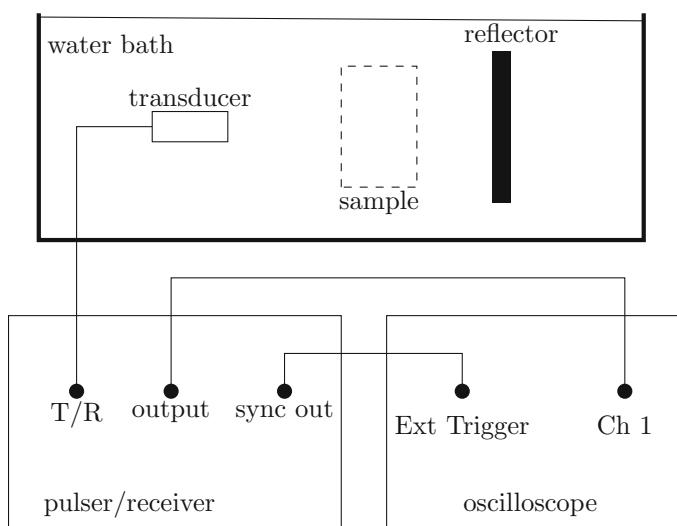


Fig. 13.2 Schematic of insert-substitution technique for measuring speed of sound and attenuation of a sample in pulse-echo configuration



quasi-continuous wave signals created using a tone burst from the signal generator. In this setup, both the transmitter and receiver may be unfocused (flat) transducers. Care must be taken to properly align the transducers coaxially. The receiver is placed in the far field of the transmitter, at a distance greater than a^2/λ from the transmitter, where a is the radius of the transmitter and λ is the wavelength of the ultrasonic signal in water. The signal from the transmitter is recorded with and without the sample in the beam bath. An example is depicted in Fig. 13.3.

The presence of the sample changes the amount of time required for the acoustic signal to propagate from the transmitter to receiver. Without the sample in place, the propagation time is

$$t_{\text{water only}} = \frac{L}{c_w} \quad (13.3)$$

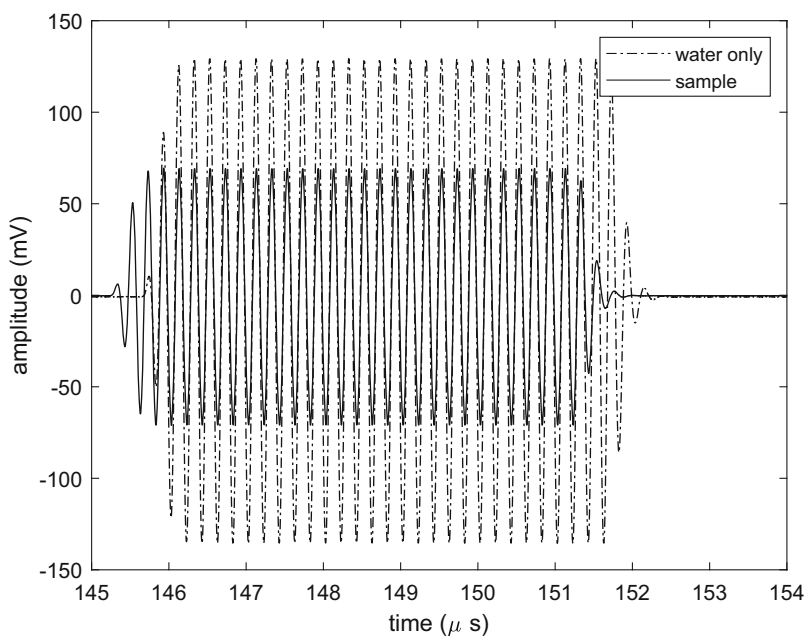
where L is the equivalent distance between the transducers and c_w is the speed of sound in water. With the sample in place, the propagation time becomes

$$t_{\text{sample}} = \frac{L-d}{c_w} + \frac{d}{c_s} = \frac{L}{c_w} - \frac{d}{c_w} + \frac{d}{c_s} \quad (13.4)$$

where d is the thickness of the sample and c_s is the speed of sound in the sample. Note that any system-dependent time intervals (such as cabling length or delays in the transducers) are identical for both measurements. Also note that this assumes that any time interval or phase change associated with the propagation of sound into or out of the sample is negligible. The difference between Eqs. 13.3 and 13.4 will eliminate any of these effects:

$$\Delta t = t_{\text{sample}} - t_{\text{water only}} = -\frac{d}{c_w} + \frac{d}{c_s} \quad (13.5)$$

Fig. 13.3 Example data from narrowband speed of sound and attenuation insert-substitution through-transmission experiment



which can be solved for the unknown sound speed in the sample:

$$c_s = \frac{c_w}{1 + \Delta t \frac{c_w}{d}} \quad (13.6)$$

This method requires knowledge of the sample thickness and the speed of sound in water. In practice, the speed of sound is temperature dependent, but only weakly frequency dependent for ultrasonic frequencies for most materials relevant to soft tissue diagnostic imaging. The speed of sound in pure water can be estimated from any of several sources such as (Wilson 1959)

$$c_w = (1403 + 5 T - 0.06 T^2 + 3.0 \times 10^{-4} T^3) \quad (13.7)$$

where T is the temperature in degrees Celsius and c_w is the speed of sound in m/s. With this method, the speed of sound in a sample can be measured to within about 2 m/s. With a digital oscilloscope, it is possible to measure Δt to within 10 ns. The uncertainty is largely due to the uncertainty in the thickness of the sample. There may also be

$$A_{\text{sample}}(f) = B(f)e^{-\alpha_w(f)(L-d)}T_{\text{in}}(f)e^{-\alpha_s(f)d}T_{\text{out}}(f) \quad (13.9)$$

some uncertainty in the speed of sound of the water bath due to presence of minor impurities. In practice, the uncertainty from the water quality can be eliminated by additional measurements of well-known standard samples such as castor oil or ethylene glycol.

Attenuation measurements similarly can be determined by comparison of the amplitudes of the received signal with and without the sample present. However, there are two significant complicating factors: (1) the attenuation coefficient is highly frequency dependent and (2) unlike the phase, the magnitude of the transmission coefficient into and out of the sample is substantial and must be included in the determination of the attenuation coefficient of the sample. In some instances, the word attenuation refers to intensity attenuation, that is, the rate of loss of intensity

within a medium. In this chapter, and usually in medical ultrasonics, attenuation refers to amplitude attenuation. That is, for a plane wave of initial pressure amplitude p_0 , the pressure amplitude at a distance z further along the propagation is given by

$$p(z) = p_0 e^{-\alpha z}$$

where α is the attenuation coefficient.

To first order, the measured amplitude of the electrical signal produced by the receiver without the sample in place is

$$A_{\text{water only}}(f) = B(f)e^{-\alpha_w(f)L} \quad (13.8)$$

where $B(f)$ is a frequency-dependent function that describes the combined effects of the conversion of the initial electrical signal into ultrasound by the transmitter and conversion of the received pressure signal back into an electrical signal by the receiver and $\alpha_w(f)$ is the frequency-dependent attenuation coefficient of water. With the sample in place, the received amplitude becomes

where $T_{\text{in}}(f)$ is the amplitude of the frequency-dependent transmission coefficient for transmission from water into the sample and $T_{\text{out}}(f)$ is the amplitude of the transmission coefficient for transmission from the sample back into water. Dividing Eq. 13.9 by 13.8 will cancel the system-dependent factor $B(f)$, resulting in

$$\frac{A_{\text{sample}}(f)}{A_{\text{water only}}(f)} = e^{\alpha_w(f)d} T_{\text{in}}(f) e^{-\alpha_s(f)d} T_{\text{out}}(f) \quad (13.10)$$

which can be solved for the attenuation coefficient of the sample measured in nepers/m:

$$\begin{aligned} \alpha_s(f) &= \frac{1}{d} \ln \left(\frac{T_{\text{in}}(f)T_{\text{out}}(f)A_{\text{water}}(f)}{A_{\text{sample}}(f)} \right) \\ &\quad + \alpha_w(f) \end{aligned} \quad (13.11)$$

or converted to decibels:

$$\alpha_{s,\text{dB}}(f) = \frac{20}{d} \log_{10} \left(\frac{T_{\text{in}}(f) T_{\text{out}}(f) A_{\text{water}}(f)}{A_{\text{sample}}(f)} \right) + \alpha_{w,\text{dB}}(f) \quad (13.12)$$

The attenuation of water is quite small compared to tissue. At 20 °C, the attenuation of water in neper/cm or dB/cm is given by

$$\alpha_w(f) = (2.54 \times 10^{-4} \text{ np cm}^{-1} \text{ MHz}^{-2}) f^2 \quad (13.13)$$

or

$$\alpha_{w,\text{dB}} = (2.2 \times 10^{-3} \text{ dB cm}^{-1} \text{ MHz}^{-2}) f^2 \quad (13.14)$$

which is very small compared to the attenuation of most tissue-mimicking materials. Because of the low attenuation of water, Eqs. 13.11 and 13.12 are often used without correcting for the attenuation of water.

The transmission coefficient calculations can become complicated depending on the interface between the sample and water. If the sample is in direct contact with water and the sample is aligned so that the ultrasound beam is incident perpendicular to the surface of the sample, the transmission coefficient between two materials is

$$T = \frac{2Z_2}{Z_2 + Z_1} \quad (13.15)$$

where Z_1 is the specific acoustic impedance of medium 1 and Z_2 is that of the second medium. This equation assumes the direction of propagation of the plane sound wave is perpendicular to the surface of the sample. Care must be taken to ensure proper alignment of the transmitter, receiver, and sample. If attenuation is not significant, the specific acoustic impedance is the product of the speed of sound and physical density of the medium: $Z = \rho c$. In this case, the transmission coefficient is independent of frequency. The combined transmission coefficient into and out of the sample is given by

$$T_{\text{in}} T_{\text{out}} = \frac{4Z_{\text{water}} Z_{\text{sample}}}{(Z_{\text{water}} + Z_{\text{sample}})^2} \quad (13.16)$$

$$T(f) = \frac{2Z_3}{(Z_1 + Z_3) \cos(k_2 \ell) + j \left(Z_2 + \frac{Z_1 Z_3}{Z_2} \right) \sin(k_2 \ell)} \quad (13.17)$$

Note that to calculate the effects of transmission coefficient, one must know the specific acoustic impedance, which usually requires a prior mea-

surement of the speed of sound and density of the material.

Because many of the tissue-mimicking materials are prone to desiccation, the samples are often enclosed in a container with “acoustic windows” to allow acoustic transmission into and out the sample while preventing water vapor from passing through the material. A traditional choice for the window material is Saran (TM) or similar single-layer plastic membrane. Other choices include polyethylene and polymethylpentene (Madsen et al. 2011). For a thin layer, the transmission coefficient at perpendicular incidence becomes

where the subscripts 1, 2, and 3 refer to the initial medium, thin layer, and final medium, respectively; j is the complex unit ($j = \sqrt{-1}$); k_2 is the wavenumber in the layer; and ℓ is the thickness of

the layer (Brekhovskikh 2012). For a thin layer, the transmission coefficient is complex, indicating a change in both magnitude and phase as the ultrasound wave passes through the layer. Attenuation within the materials can be included by treating the acoustic impedance and wavenumber as complex values:

$$k = \frac{2\pi f}{c} - j\alpha(f) \quad \text{and} \quad Z = \frac{\rho c}{1 - j\frac{\alpha(f)c}{2\pi f}}$$

$$\begin{aligned} & \text{abs} \left(\frac{2Z_{\text{sample}}}{(Z_{\text{water}} + Z_{\text{sample}}) \cos(k_{\text{layer}}\ell) + j \left(Z_{\text{layer}} + \frac{Z_{\text{water}}Z_{\text{sample}}}{Z_{\text{layer}}} \right) \sin(k_{\text{layer}}\ell)} \right) \times \\ & \text{abs} \left(\frac{2Z_{\text{water}}}{(Z_{\text{sample}} + Z_{\text{water}}) \cos(k_{\text{layer}}\ell) + j \left(Z_{\text{layer}} + \frac{Z_{\text{sample}}Z_{\text{water}}}{Z_{\text{layer}}} \right) \sin(k_{\text{layer}}\ell)} \right) \end{aligned} \quad (13.18)$$

As with thin layers for optics, such as anti-reflection coatings on eyeglasses, the transmission coefficient for a thin layer exhibits alternating constructive and destructive interference as a function of frequency. To better protect the tissue mimicking material, the commercial ultrasound phantom manufacturers utilize acoustic windows that contain several layers. For example, a layer of metalized plastic film is well known to reduce water vapor transmission as in food packaging for snack foods. The transmission coefficient for thin

The complete effect from transmission into and out of the sample is the product of the absolute value of two versions of Eq. 13.17, one with $Z_1 = Z_{\text{water}}$ and $Z_3 = Z_{\text{sample}}$ and one with $Z_1 = Z_{\text{sample}}$ and $Z_3 = Z_{\text{water}}$:

films with multiple layers becomes increasingly complicated and may be very difficult to effectively model. In this case, measurements of the transmission coefficient in water may offer some guidance about correcting for the presence of the acoustic window.

As an example of these measurements, consider the data shown in Fig. 13.3. The measurement was performed with a 30 cycle bursts at 5.0 MHz. Measurements from the oscilloscope supply the following values:

$$\Delta t = -0.422 \mu\text{s} \quad A_{\text{water}} = 133.4 \text{ mV} \quad \text{and} \quad A_{\text{sample}} = 69.9 \text{ mV}$$

The sample thickness was measured by digital calipers to be 2.65 cm. The data were collected in water bath with a constant temperature of 22.0°C. From Eq. 13.7, the speed of sound in pure water at this temperature is

$$c_w = 1487 \text{ m/s}$$

Therefore, using Eq. 13.6, we have

$$c_s = \frac{1487 \text{ m/s}}{1 + (-0.422 \times 10^{-6} \text{ s}) \frac{1487 \text{ m/s}}{0.0265 \text{ m}}} = 1523 \text{ m/s}$$

This sample has acoustic windows made from Saran with a thickness of 18.6 μm, measured by digital micrometer. Previous measurements of Saran film have shown Saran to have a speed of sound of 2400 m/s and attenuation of 5.0 neper $\text{m}^{-1} \text{ MHz}^{-1.5} f^{1.5}$ (Wear et al. 2005). The density of the sample material is 1050 kg/m³, so the specific acoustic impedance of the sample is

$$\begin{aligned} Z_{\text{sample}} &= (1050 \text{ kg/m}^3)(1523 \text{ m/s}) \\ &= 1.60 \times 10^6 \text{ kg/(m}^2\text{s)} \end{aligned}$$

Using Eq. 13.18, the magnitude of the total transmission coefficient into and out of the sample at 5.0 MHz is

$$T_{\text{total}} = 0.9130$$

the attenuation coefficient of water at 5.0 MHz is

$$(2.2 \times 10^{-3}) \times 5^2 = 0.055 \text{ dB/cm}$$

and the attenuation coefficient of the sample in dB/cm is calculated from Eq. 13.12:

$$\alpha_{s,\text{dB}}(f) = \frac{20}{2d} \log_{10} \left(\frac{T_{\text{in}}(f)T_{\text{out}}(f)A_{\text{water}}(f)}{A_{\text{sample}}(f)} \right) + \alpha_{w,\text{dB}}(f) \quad (13.19)$$

$$\begin{aligned} & \frac{20}{2.65 \text{ cm}} \log_{10} \left(\frac{(0.9130)(133.4 \text{ mV})}{(69.9 \text{ mV})} \right) \\ & + 0.055 \text{ dB/cm} = 1.87 \text{ dB/cm} \end{aligned}$$

Note that if the attenuation of water is neglected, the result would be about 3% less. This material has a fairly small specific attenuation of 0.37 dB/cm/MHz. The effect of attenuation in water is less significant for higher attenuation materials.

The reflection method has similar analysis for the equations. In this method, the ultrasound signal passes through the sample, reflects from the reflector, and then passes back through the sample before returning to the transducer. The pulses used in this method are generally short time duration and therefore broad bandwidth. The speed of sound can be estimated by determining the unwrapped phase shift of the signal with and without the sample in place. Since

$$\Delta t = \frac{\Delta\phi}{\omega}$$

where $\Delta\phi$ is the phase shift with and without the sample in place, the speed of sound is given by

$$c_s = \frac{c_w}{1 + \frac{c_w \Delta\phi}{2\omega d}}$$

where the factor of 2 in the denominator of the denominator accounts for the passage of the ultrasound signal during both the outward and reflected portions of its beam-path. Similarly, the attenuation coefficient can be found using Eqs. 13.11 or 13.12 if the amplitude of the signal with and without the sample in place is replaced by the amplitude of the Fourier Transform of the signal with and without the sample in place, as in

The chief advantage of the broadband pulse-echo techniques is the accumulation of many attenuation coefficient values at various frequencies with only a single recording. Additionally, these methods may be adapted to eliminate the need to independently measure the thickness of the sample (Tsuji et al. 2019) or estimate the window transmission from measurements of the reflection coefficient of an intact sample (Nagabhushana et al. 2020).

There are several common potential complications in measuring the speed of sound and attenuation coefficient with these methods. Diffraction effects can be significant, especially with thicker samples or samples that have speed of sound substantially different from that of water. Diffraction effects can cause the ultrasound beam to become de-focused and may result in spurious changes of time shift or amplitude in the received signal. Samples with flat and parallel sides will minimize diffraction effects. Similarly, nonlinear propagation may substantially alter the amplitude of the received signals. One can check for nonlinear propagation effects by repeating the measurement at a different driving amplitude and examining the results for any change. Decreasing the driving signal to the transmitter decreases the probability of nonlinear propagation effects; therefore, the smallest driving am-

plitude that produces sufficient signal to noise should be used for speed and attenuation measurements.

13.2.2 Backscatter Measurements

There are several methods available to measure the backscatter coefficient. The method by Madsen et al. (1984), Madsen (1992) is based on the Sigelman–Reid technique (Sigelmann and Reid 1973; Reid 1992). This method has been well tested on tissue-mimicking materials with verified accuracy over a broad range of values of backscatter coefficient (Wear et al. 1989; Chen et al. 1993). The Madsen technique uses a broad bandwidth pulse and a time gate to select echo signal from within the sample material. The bandwidth of the time gate is much smaller than the frequency range of the echo signals. This assumption simplifies the analysis by ignoring the effects of convolution of the gate function with the system frequency response (Chen et al. 1993). Echo signals from a large number of independent positions are collected to allow for averaging of the spectral density function to acquire an accurate estimate of the spectral density. The backscatter coefficient is given by

$$\eta(\omega) \approx \frac{\langle V_g(\omega) V_g^*(\omega) \rangle}{C^2 |T(\omega)B(\omega)| \iiint_{\Omega} |A(\mathbf{r}, \omega)|^4 d\mathbf{r}} \quad (13.20)$$

The numerator is the measured echo signal spectral density function (the * indicates complex conjugate and the brackets indicate averaging over many independent position). The constant C is the energy correction factor due to any gating function used in its calculation of the signal spectral density. For a rectangular gate, $C = 1$, for a Hamming window $C = 0.63$. Values for other gates can be found in the literature (Marple et al. 1989). The function $T(\omega)B(\omega)$ accounts for the frequency response of the system, including transmit and receive properties of the transducer and frequency dependence of the excitation signal. The function $A(\mathbf{r}, \omega)$ represents the trans-

ducer field in the sample, and the integral of this field is taken over the volume, Ω , of all scatterers which can contribute to the time-gated signal. This integral corrects for the diffraction effects of the transducers. By including the sample attenuation in the calculation of $A(\mathbf{r}, \omega)$, the correction for attenuation is also incorporated. In Madsen's original formulation, the integral is performed numerically. Chen, et. al. incorporated an approximate analytical formulation of the diffraction correction (Chen et al. 1997). Chen's formulation and two other analytical approaches were extensively tested by Lavarello et al. (2011). Those measurements found differences between those formulations that were less than 3 dB.

The system frequency response is measured by recording one or more signals from a planar reflector (Madsen et al. 1984), hence the common name of “planar-reflector” method for this technique.

$$T(\omega)B(\omega) = \frac{V_r(\omega)}{R \iint_{S_{\text{mirror}}} A_0(\mathbf{r}, \omega) d\mathbf{r}} \quad (13.21)$$

where $V_r(\omega)$ is the Fourier Transform of a pulse-echo signal recorded from the planar reflector, R is the reflection coefficient of the planar reflector, and S_{mirror} is the surface of a “mirror image” transducer.

13.3 Scattering Prediction

A key component of designing phantoms for quantitative ultrasound studies is the specification of the predicted backscatter coefficient. The study of acoustic scattering has a long history dating back to early solutions by Lord Rayleigh for rigid cylinders and spheres. This theory was extended to include compressional and shear waves within the scatterers by Faran and James (1951). This article includes experimental tests of the theory with metal cylinders and spheres. These results were extended and a typographical error in Faran's equations was corrected in an article by Hickling (1962). Combined, the equations in this article predict

the scattered pressure waveform from a single sphere and are often referred to as “Faran theory” or “Faran–Hickling theory.” These equations have been tested in numerous publications as both a function of angle and frequency (for example, see Burke et al. 1984 and Baddour et al. 2005).

The Faran–Hickling theory assumes a plane wave in a fluid incident upon a solid scatterer. The incident and scattered waves must satisfy the boundary conditions at the surface of the scatterer. The boundary conditions are:

1. The pressure in the fluid is equal to the normal component of stress in the solid scatterer.
2. The normal component of the displacement in the fluid is equal to the normal component of displacement of the solid scatterer.
3. The tangential components of the shearing stress in the solid scatterer are zero at its surface.

Faran writes the solution to the scattered wave from a spherical scatterer in terms of the amplitude of the pressure wave at position (r, θ, ϕ) relative to the scatterer at distances that are large compared to the radius of the scatterer:

$$|p_s| = \frac{P_0}{k_3 r} \left| \sum_{n=0}^{\infty} (2n+1) \sin(\eta_n) \right. \\ \times \exp(j\eta_n) P_n(\cos(\theta)) \left. \right| \quad (13.22)$$

where η_n is a phase shift angle, P_0 is the pressure of the incident plane wave, k_3 is the wavenumber

in the fluid, and P_n is the n th Legendre polynomial. The equations for determining η_n are very complicated and are not included in this chapter. The interested reader is referred to Faran’s original article Faran and James (1951). However, note that equation (30) of Faran’s article contains a typographical error. The correct form is in the unnumbered equation directly above equation (30) or in equation (8) of Hickling (1962). Since the solution is in the form of an infinite series, the solution must be truncated at some upper value of n . Typically, this can be done by computing the series term by term until including additional terms results in negligible change in the value of the summation. The value of η_n depends on the following properties of the scattering and surrounding fluid medium:

- Wavenumber in the surrounding fluid
- Radius of the sphere
- Longitudinal speed of sound in the scatterer
- Speed of sound in the fluid
- Density of the scatterer
- Density of the fluid
- Poisson’s ratio of the scatterer

Note that Poisson’s ratio effectively allows one to compute the shear wave speed in the scatterer.

Equation 13.22 provides the amplitude of the scattered pressure. The scattering cross section of a single scatterer is defined as the total power scattered divided by the incident intensity (Morse et al. 1986). If we write the intensity of the scattered wave as a function of position in spherical coordinates, the scattered power can be written as

$$\Pi_{\text{scattered}} = \int_{\theta=0}^{\pi} \int_{\phi=0}^{2\pi} I_{\text{scattered}}(r, \theta, \phi) r^2 \sin(\theta) d\theta d\phi$$

so the cross section is

$$\sigma = \frac{\Pi_{\text{scattered}}}{I_{\text{incident}}} = \int_{\theta=0}^{\pi} \int_{\phi=0}^{2\pi} \left(\frac{I_{\text{scattered}}(r, \theta, \phi) r^2}{I_{\text{incident}}} \right) \sin(\theta) d\theta d\phi$$

The differential cross section per solid angle can be defined as the term in parenthesis:

$$\frac{d\sigma}{d\Omega} = \frac{I_{\text{scattered}}(r, \theta, \phi) r^2}{I_{\text{incident}}}$$

For both spherical and plane waves, the intensity of a sound wave is the square of the pressure amplitude divided by two times the density times the speed of sound of the medium. Therefore, the differential cross section per solid angle can be written as

$$\frac{d\sigma}{d\Omega} = \frac{P_{\text{scattered}}^2 r^2}{P_0^2}$$

with $P_{\text{scattered}}$ computed by Faran's theory as in Eq. 13.22.

In practice, any volume of material contains many individual scatterers. The backscatter coefficient is the differential cross section per solid angle evaluated at $\theta = 180^\circ$ per volume of scatterers. If scattering is incoherent and multiple scattering is not substantial, on average each scatterer will contribute the same amount of scattered intensity. In this case, the backscatter coefficient is the number density of scatterers multiplied by the differential cross section per solid angle evaluated at $\theta = 180^\circ$:

$$\eta = N_V \left. \frac{d\sigma}{d\Omega} \right|_{\theta=180^\circ}$$

where N_V is the number of scatterers per unit volume. Units for the backscatter coefficient are inverse distance inverse solid angle and are often reported in units of $\text{cm}^{-1} \text{sr}^{-1}$.

The range of scattering can be characterized by the value of the dimensionless value ka , where k is the wavenumber in the surrounding fluid and a is the radius of the spherical scatterer. For very small values of ka , the BSC follows Raleigh scattering and is proportional to frequency to the fourth power. For large values of ka , the scattered intensity is independent of frequency and becomes equivalent to reflection from a plane surface. Figure 13.4 is a predication of BSC vs ka for glass beads in a tissue-mimicking background material.

13.4 Creating Phantoms with Specific Acoustic Properties

To use phantoms for QUS, one must be able to create phantoms with specified acoustics properties. Therefore, TM materials need to be able to be created with a range of speed of sound, attenuation coefficient, and scattering properties. Ideally, the values of each of these three properties would be able to be varied without affecting the values of the other two. For example, one could change the speed of sound of the material without substantially changing either the attenuation or scattering. The following sections detail several methods for altering each of these acoustic properties and the limitations and effectiveness of these methods.

13.4.1 Speed of Sound

For many hydrogel- and agar-based materials, the speed of sound can be varied over the range of values applicable to human tissue. Note from above that the speed of sound in soft tissue varies from about 1400 m/s for fat to 1650 m/s for liver. Thus, it is desirable to have TM materials that exhibit a similar range of values.

In early ultrasound phantoms, a mixture of water and ethanol was used to create a fluid with the desired speed of sound. At room temperature, the speed of sound in such a mixture is a linear function with respect to proportion of ethanol. Martin et al. (2001) report data that indicate that at 20 °C the speed of sound in water and ethanol mixture is given by

$$1481.1 \text{ m/s} + (6.25 \text{ m/s})x$$

where x is the percent of ethanol by volume in the mixture over the range of ethanol concentrations from 6 to 12%. They recommend a solution of 9.5% of ethanol in water to achieve a speed of sound 1540 m/s at 20 °C. They also note that this speed of sound is dependent on temperature and

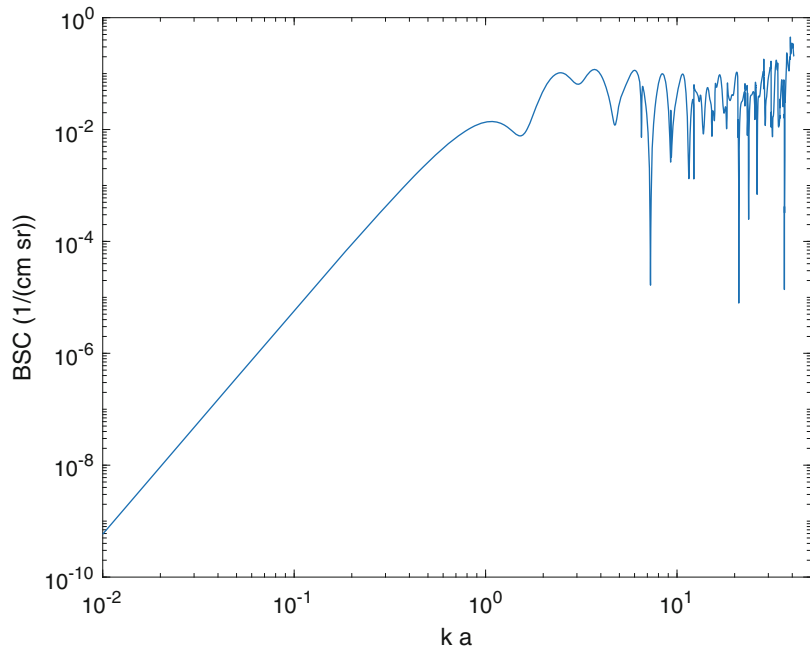


Fig. 13.4 Predicted BSC for spherical glass beads. Parameters used in this prediction are $c_{\text{medium}} = 1540 \text{ m/s}$, $\rho_{\text{medium}} = 1.05 \text{ g/cm}^3$, $c_{\text{scatterer}} = 5340 \text{ m/s}$, $\rho_{\text{scatterer}} =$

2.54 g/cm^3 , $a = 20 \mu\text{m}$, and $v_{\text{scatterer}} = 0.22$ with a bead density of $47 \times 10^9 \text{ beads/mm}^3$ (equal to 4.0 g/liter). Note that this a log-log scaled plot

recommend temperature be controlled to within 0.75°C . Earlier researchers Giacomini (1947); Burton (1948) noted that there is a maximum speed of sound in water ethanol mixtures of about 1620 m/s at about 25% ethanol by volume, so there are limitations to using water ethanol mixtures to achieving high speeds of sound.

Madsen's early phantoms (Madsen et al. 1978) using gelatin to create a solid material varied the speed of sound through the addition of n-propanol. That work created samples with speed of sound that could be varied from 1550 to 1650 m/s by adding up to 21% n-propanol. They note that the addition of propanol did not substantially change the attenuation or scattering properties of the material. Madsen also produced phantoms composed of agarose gel and concentrated milk (Madsen et al. 1998). A liquid TM material with a speed of sound of 1540 m/s and attenuation coefficient slope of 0.50 dB/cm/MHz was described that is composed of 60% (by volume) evaporated milk, 37% water, and 3% n-propanol. The article notes that the

liquid can be made with greater attenuation coefficient but that more propanol would be needed to keep the speed of sound at 1540 m/s . It is implied that larger speeds could be created using a greater proportion of propanol. Other additives that have been used to increase the speed of sound of a TM material include table salt (sodium chloride), glycerol, and propylene glycol.

Additives that decrease the speed of sound are slightly more difficult to realize in practice. Decreasing the speed of sound below 1540 m/s is important in the production of TM materials designed to mimic tissue with substantial fat content. One technique that has been successful is to emulsify some type of oil into the molten gel. As the gel solidifies, the oil components are frozen into the gel as small droplets. Madsen referred to these materials as "oil in gelatin dispersions" (Madsen et al. 1982). Various oils have been used including kerosene, olive oil, castor oil, and safflower oil. The use of olive oil is described in US Patent 4,277,367 using up to 60% by volume

olive oil to reduce the speed of sound to 1492 m/s (Madsen et al. 1981).

Hydrogel type materials such as Zerdine (TM, CIRS) can similarly have the speed of sound adjusted to larger or smaller values. US Patent 5,196,343 describes the addition of up to 30% ethylene glycol (weight of ethylene glycol per weight of water content in the sample) to increase the speed of sound from 1525 to 1650 m/s (Zerhouni et al. 1993). To decrease the speed of sound below 1525 m/s, this patent uses turpentine oil. The addition of up to 50% turpentine oil (weight of turpentine per weight of water content in the sample) decreases the speed of sound from 1525 to 1420 m/s. Similar work has been reported using the IEC agar-based materials as a base with the addition of up to 20% olive oil to reduce speed of sound to 1460 m/s while maintaining a specific attenuation coefficient of about $0.5 \text{ dB cm}^{-1} \text{ MHz}^{-1}$ (Kim et al. 2014).

13.4.2 Attenuation Coefficient

Altering the attenuation coefficient of the TM material is generally focused on increasing the attenuation above that of the background material. Gels composed of animal-hide gelatin, agarose, or acrylamide have attenuation coefficients that are much smaller than those of tissue.

Many early gelatin-based phantoms made use of graphite powder to increase attenuation and scattering. Madsen et al. (1978) produced a sample with graphite concentration varying from 0.049 to 0.187 g/cm³, producing attenuation in the samples that when fitted to a power-law relationship (Eq. 13.2) yielded values of α_0 that increased from 0.368 to 1.453 dB cm⁻¹ MHz⁻ⁿ with values of n that decreased from 1.24 for low concentrations of graphite to about 1.00 for high concentrations of graphite. This article also demonstrates a negligible change in the speed of sound in the materials with different amounts of graphite, all samples have a speed of sound of 1578 ± 2 m/s. The graphite powder in this study consisted of irregularly shaped grains that had been passed through a sieve with 43 μm openings. However, the mean size of the

particles was only about 6 μm , much smaller than the wavelength of ultrasound used in this study (which included measurements up to 10 MHz). The increased attenuation was largely due to increased scattering from the graphite particles.

Similar studies have been performed with other small particles to increase attenuation, including one micron diameter alumina powder (Zerhouni et al. 1993) mixed in acrylamide gels. That patent describes a method utilizing up to approximately 15% by weight alumina particles in acrylamide gel. The resulting attenuation coefficient increases from $(0.05 \text{ dB cm}^{-1} \text{ MHz}^{-n}) f^{0.933}$ with no alumina particles to $(1.475 \text{ dB cm}^{-1} \text{ MHz}^{-n}) f^{0.81}$ with 15% alumina particles. This same patent describes the use 10 μm diameter boron nitride powders producing results with attenuation of $(0.677 \text{ dB cm}^{-1} \text{ MHz}^{-n}) f^{1.073}$ with 15% boron nitride powder. Similarly, the IEC agar material (Ramnarine et al. 2001) includes aluminum oxide particles with sizes of 3.0 μm and 0.30 μm to increase attenuation up to about $0.50 \text{ dB cm}^{-1} \text{ MHz}^{-1}$ (Brewin et al. 2008).

Although the small particles described so far result in increased attenuation, those particles will also increase scattering (Wu et al. 1992). Madsen also describes the creation of a TM material that has very low scatter (Madsen et al. 1998). This material uses concentrated milk; the protein and fat globules in milk contribute to the attenuation of this material. Due to their size (less than 15 μm) and acoustic properties, the fat globules contribute very little scattering to the material. This material has a backscatter coefficient of $3.37 \times 10^{-7} \text{ sr}^{-1} \text{ cm}^{-1}$ at 4.0 MHz, compared to the lowest scattering graphite TM material with backscatter of $3.87 \times 10^{-5} \text{ sr}^{-1} \text{ cm}^{-1}$ at 4.0 MHz. This represents a decrease in the background scattering by a factor of 100. This decrease in scattering allows for direct control of backscatter coefficient as described below.

13.4.3 Scattering

As with attenuation, BSC is largely controlled by the addition of small particles that cause

scattering within the material. A very common material has been microscopic glass spheres. These spheres have many industrial uses, including sandblasting and use as a light reflecting component in paints designed for use in highway signs and markings. A number of manufacturers produce these beads. Typically, the size range of the beads may be quite large. This range can be reduced by mechanically sieving the beads to have a desired size range. The resulting distribution of sizes may still be quite large. In practice, the diameters of the beads must be measured using optical microscopy, Coulter counter, or similar techniques. The fact that the beads are from a continuum of sizes slightly complicates the prediction of BSC based on Faran calculations. The combined BSC can be found by summing over the bead distribution as in

$$\eta = \sum_i N_{V,i} \left(\frac{d\sigma}{d\Omega} \Big|_{\theta=180^\circ} \right)_i$$

where the i index runs over the various sized beads contained in the material, $N_{V,i}$ is the volume bead density of the i th size, and $(\frac{d\sigma}{d\Omega} \Big|_{\theta=180^\circ})_i$ is the differential scattering cross section per solid angle, evaluated in the backward direction, for the i th size.

Calculating the predicted BSC is typically performed with a histogram of the size distribution of beads within the sample. The size distribution can be measured by optical microscope. This can be a time-intensive process, and many hundreds of measurements are needed for an accurate histogram. Monodisperse bead sizes are available but can be quite expensive for use in a typical phantom.

13.5 Review of Interlaboratory Comparisons

One method to determine the accuracy of measurements of tissue-mimicking materials is to conduct an interlaboratory comparison using the same or identically prepared samples. This section presents an overview of some of the studies of this type that have been conducted.

One of the first interlaboratory comparisons occurred in 1986 and focused only on speed of sound and attenuation coefficient measurements (Madsen et al. 1986). Identical samples composed of gelatin and graphite powder were prepared and distributed to seven laboratories for measurement of speed of sound and attenuation. The samples were measured before and after distribution at the University of Wisconsin–Madison to measure the inter-sample variability and ensure the sample properties did not significantly change during the process of sending the samples to the various laboratories. The speed of sound values agreed very well, within 0.5 per cent, when correcting for slight variations in temperature at the various laboratories. The attenuation coefficient measurements varied some between the laboratories in this study, with most of the values differing from the group average by less than $\pm 20\%$.

In 1999, another study was conducted (Madsen et al. 1999). This study was larger, involving 10 laboratories and also included measurements of the backscatter coefficient of the samples. Two different types of samples were used. Both types of samples were based on agar with powdered graphite and glass beads for attenuation and scattering. Both samples had a speed of sound near 1540 m/s. Sample Type A had attenuation near $0.45 \text{ dB cm}^{-1} \text{ MHz}^{-1}$ and BSC near $1.0 \times 10^{-3} \text{ cm}^{-1} \text{ sr}^{-1}$ at 4.0 MHz. Sample Type B had attenuation of $0.60 \text{ dB cm}^{-1} \text{ MHz}^{-1}$ and BSC near $2.0 \times 10^{-3} \text{ cm}^{-1} \text{ sr}^{-1}$ at 4.0 MHz. This study found a larger variation in speed of sound than the 1986 study but comparable variation in attenuation coefficient measurements. This study found a tendency for many of the sites to substantially underestimate the BSC, by more than an order of magnitude. This study concluded that “uniformity does not exist among laboratories in the determination of fundamental ultrasonic properties in tissue-like media.”

A larger study was reported in 2005 with three types of samples sent to eight laboratories (Wear et al. 2005). Two of the samples (named A and B in the study) were composed of glass beads in agarose with concentrated milk providing attenuation. Sample A was 25% concentrated milk with 0.889 g/L of 75 to 90 micron diameter glass

beads. Sample B was 50% concentrated milk with 18g/L of 26 micron mean diameter glass beads. The third set of samples (C) was composed of 0.6 to 1.7 mm diameter gelatin sphere in an oil in gelatin dispersion. Again there was considerable variation in the speed of sound with values of Sample A values ranging from 1525 to 1580 m/s. Attenuation coefficients were consistent, except for sample C which showed substantial variation. The BSC values varied by up to three orders of magnitude for sample C. The authors note that the laboratories do show considerable agreement regarding the frequency dependence of BSC.

As part of an attempt to understand the source of this large discrepancy in BSC, two of the laboratories involved undertook a detailed study of BSC measurements with nine different samples (Anderson et al. 2010). Their results demonstrate good agreement in speed of sound, attenuation, and BSC values. Furthermore, the BSC values agree with predictions using the Faran model. Additional work on analyzing the BSC using single element transducers showed agreement in BSC values using several analysis algorithms (Lavarello et al. 2011).

We are nearing the stage in which standardized methods of creating phantoms and for measuring the acoustics properties of those samples may be possible. Two recent studies have focused on the feasibility of certifying tissue-mimicking materials using ISO guidelines (Santos et al. 2017; Maia et al. 2021). These studies have focused only on speed of sound and attenuation measurements of the IEC agar material. However, this may be extended to measurements of BSC and other types of materials.

13.6 Discussion and Conclusions

The creation and measurement of the properties of tissue-mimicking materials has an important role to play in quantitative ultrasound. These materials allow us to validate methods using pulse-echo ultrasound scanners. They play an especially important role in clinical measurements of attenuation and BSC. Some algorithms for attenuation and most algorithms for BSC rely on reference

phantom methods that require a calibrated phantom to correct for system-dependent factors.

There is a long history of investigating tissue-mimicking materials. Many current materials that mimic soft tissues are based on agarose or polyacrylamide to provide mechanical rigidity to the material. The speed of sound can be raised or lowered with the addition of substances such as propanol or safflower oil, respectively. Attenuation can be separately controlled by the addition of very fine powders or protein rich substances such as concentrated milk. BSC can then also be separately controlled by the addition of large (but still microscopic) scatterers such as glass beads with a known diameter distribution. Continuing efforts in this area are needed to work with substances that may have combinations of properties that mimic particular tissues or pathologies.

References

- AIUM (1975) The AIUM 100 mm test object and recommended procedures for its use. *Reflections* 1:74–91
- AIUM Technical Standards Committee (2014) Methods for specifying acoustic properties of tissue-mimicking phantoms and objects, 2nd edn. AIUM Technical Standards Committee, Laurel, MD
- Alves N, Kim A, Tan J, Hwang G, Javed T, Neagu B, Courtney BK (2020) Cardiac tissue-mimicking ballistic gel phantom for ultrasound imaging in clinical and research applications. *Ultrasound Med Biol* 46(8):2057–2069
- Anderson JJ, Herd MT, King MR, Haak A, Hafez ZT, Song J, Oelze ML, Madsen EL, Zagzebski JA, O'Brien WD Jr, Hall TJ Jr (2010) Interlaboratory comparison of backscatter coefficient estimates for tissue-mimicking phantoms. *Ultrason Imaging* 32(1):48–64
- Baddour RE et al (2005) High-frequency ultrasound scattering from microspheres and single cells. *J Acoust Soc Am* 117(2):934–943
- Brekhovskikh L (2012) Waves in layered media, vol. 16. Elsevier, Amsterdam
- Brewin MP et al (2008) The acoustic properties, centered on 20 MHz, of an IEC agar-based tissue-mimicking material and its temperature, frequency and age dependence. *Ultrasound Med Biol* 34(8):1292–1306
- Browne JE et al (2003a) Assessment of the acoustic properties of common tissue-mimicking test phantoms. *Ultrasound Med Biol* 29(7):1053–1060
- Browne, J. E., et al (2003) Assessment of the acoustic properties of common tissue-mimicking test phantoms. *Ultrasound in medicine & biology* 29(7):1053–1060

- Burke TM et al (1984) Angular distribution of scattered ultrasound from a single steel sphere in agar gelatin: a comparison between theory and experiment. *Ultrason Imaging* 6(3): 342–347
- Burlew MM, Madsen EL, Zagzebski JA, Banjovic RA, Sum SW (1980) A new ultrasound tissue-equivalent material. *Radiology* 134:517–520
- Burton CJ (1948) A study of ultrasonic velocity and absorption in liquid mixtures. *J Acoust Soc Am* 20(2):186–199
- Cabrelli LC et al (2016) Stable phantom materials for ultrasound and optical imaging. *Phys Med Biol* 62(2):432
- Cafarelli A et al (2016) Speed of sound in rubber-based materials for ultrasonic phantoms. *J Ultrasound* 19(4):251–256
- Cafarelli A et al (2017) Tuning acoustic and mechanical properties of materials for ultrasound phantoms and smart substrates for cell cultures. *Acta Biomater* 49:368–378
- Chanamai R, Julian McClements D (1998) Ultrasonic attenuation of edible oils. *J Am Oil Chem Soc* 75(10):1447–1448
- Chen JF, Zagzebski JA, Madsen EL (1993) Tests of a backscatter coefficient measurement method using broadband pulses. *IEEE Trans Ultrason Ferroelectr Freq Control* 40:603–607
- Chen X et al (1997) The measurement of backscatter coefficient from a broadband pulse-echo system: a new formulation. *IEEE Trans Ultrason Ferroelectr Freq Control* 44(2):515–525
- Culjat MO et al (2010) A review of tissue substitutes for ultrasound imaging. *Ultrasound Med Biol* 36(6):861–873
- Duck FA (2013) Physical properties of tissues: a comprehensive reference book. Academic press, London
- Faran JJ Jr (1951) Sound scattering by solid cylinders and spheres. *J Acoust Soc Am* 23(4):405–418
- Giacomini A (1947) Ultrasonic velocity in ethanol-water mixtures. *J Acoust Soc Am* 19(4):701–702
- Hickling R (1962) Analysis of echoes from a solid elastic sphere in water. *J Acoust Soc Am* 34(10):1582–1592
- International Electrotechnical Commission (2001) Ultrasonics—Flow measurement systems—Flow test object, Publication number 61685. IEC, Geneva. IEC 61685
- International Electrotechnical Commission (2007) Part 2–37: Particular requirements for the basic safety and essential performance of ultrasonic medical diagnostic and monitoring equipments, 2nd edn. IEC, Geneve, p 82. IEC 60601-2-37:2007
- International Electrotechnical Commission (2009) Part 2–5: Particular requirements for the basic safety and essential performance of ultrasonic physiotherapy equipment, 3rd edn. IEC, Geneve, p 66. IEC 60601-2-5: 2009
- International Electrotechnical Commission (2010) Ultrasonics - pulse-echo scanners - part 2: measurement of maximum depth of penetration and local dynamic range. IEC, Geneve, pp 61391–61392. IEC 61391-2: 2010
- IEC (2019) TS 63081: Ultrasonics—Methods for the characterization of the ultrasonic properties of materials. Danish Standards Foundation, Denmark
- Kharine A et al (2003) Poly (vinyl alcohol) gels for use as tissue phantoms in photoacoustic mammography. *Phys Med Biol* 48(3):357
- Kim MS et al (2014) A fat-tissue mimic phantom for therapeutic ultrasound. *IEE Trans. Smart Process Comput* 3(3):153–159
- Lavarello RJ, Ghoshal G, Oelze ML (2011) On the estimation of backscatter coefficients using single-element focused transducers. *J Acoust Soc Am* 129(5):2903–2911
- Madsen E (1992) Method of determination of acoustic backscatter and attenuation coefficients independent of depth and instrumentation. In: Shung K, Thieme G (eds) Ultrasonic scattering in biological tissue. CRC Press, Boca Rota, FL, pp 204–249
- Madsen EL, Zagzebski JA, Banjovic RA, Jutila RE (1978) Tissue mimicking materials for ultrasound phantoms. *Med Phys* 5:391–394
- Madsen EL et al (1981) Phantom material and method. U.S. Patent No. 4,277,367
- Madsen EL, Zagzebski JA, Frank GR (1982) Oil-in-gelatin dispersions for use as ultrasonically tissue-mimicking materials. *Ultrasound Med Biol* 8(3):277–287
- Madsen EL, Insana MF, Zagzebski JA (1984) Method of data reduction for accurate determination of acoustic backscatter coefficients. *J Acoust Soc Am* 76:913–923
- Madsen EL, Frank GR, Carson PL, Edmonds PD, Frizzell LA, Herman BA, Kremkau FW, O'Brien WD Jr, Parker KJ, Robinson RA (1986) Interlaboratory comparison of ultrasonic attenuation and speed measurements. *J Ultrasound Med* 5(10):569–576
- Madsen EL, Frank GR, Dong F (1998) Liquid or solid ultrasonically tissue-mimicking materials with very low scatter. *Ultrasound Med Biol* 24(4):535–542
- Madsen EL, Dong F, Frank GR, Garra BS, Wear KA, Wilson T, Zagzebski JA, Miller HL, Shung KK, Wang SH, Feleppa EJ (1999). Interlaboratory comparison of ultrasonic backscatter, attenuation, and speed measurements. *J Ultrasound Med* 18(9):615–631
- Madsen EL, Deaner ME, Mehi J (2011) Properties of phantom tissue-like polymethylpentene in the frequency range 20–70 MHz. *Ultrasound Med Biol* 37(8):1327–1339
- Maia TQS et al (2021) Feasibility of reference material certification for speed of sound and attenuation coefficient based on standard tissue-mimicking material. *Ultrasound Med Biol* 47(7):1904–1919
- Maneas E et al (2018) Gel wax-based tissue-mimicking phantoms for multispectral photoacoustic imaging. *Biomed Opt Express* 9(3):1151–1163
- Marple SL Jr, Carey WM (1989) Digital spectral analysis with applications. Prentice Hall, Hoboken, pp 2043–2043
- Martin K, Spinks D (2001) Measurement of the speed of sound in ethanol/water mixtures. *Ultrasound Med Biol* 27(2):289–291

- Morse PM, Uno Ingard K (1986) Theoretical acoustics. Princeton university press, Princeton, NJ
- Nagabhusana K, O'Brien WD, Han A (2020) Technique to compensate for unknown laminate transmission loss in phantom attenuation measurements. In: 2020 IEEE international ultrasonics symposium (IUS). IEEE, London
- Oudry J et al (2009) Copolymer-in-oil phantom materials for elastography. *Ultrasound Med Biol* 35(7):1185–1197
- Parker KJ et al (1988) In-vivo measurements of ultrasound attenuation in normal or diseased liver. *Ultrasound Med Biol* 14(2):127–136
- Prokop AF et al (2003) Polyacrylamide gel as an acoustic coupling medium for focused ultrasound therapy. *Ultrasound Med Biol* 29(9):1351–1358
- Ramnarine KV, Tom A, Hoskins PR (2001) Construction and geometric stability of physiological flow rate wall-less stenosis phantoms. *Ultrasound Med Biol* 27(2):245–250
- Reid J (1992) Standard substitution methods for measuring ultrasonic scattering in tissues. In: Shung K, Thieme G (eds) Ultrasonic scattering in biological tissue. CRC Press, Boca Rota, FL, pp 171–204
- Santos TQ, Alvarenga AV, Oliveira DP, Costa-Felix RP (2017) Metrological validation of a measurement procedure for the characterization of a biological ultrasound tissue-mimicking material. *Ultrasound Med Biol* 43(1):323–331
- Sigelmann RA, Reid JM (1973) Analysis and measurement of ultrasonic backscattering from an ensemble of scatterers excited by sine-wave bursts. *J Acoust Soc Am* 53:1351–1359
- Sjöstrand S et al (2020) Tuning viscoelasticity with minor changes in speed of sound in an ultrasound phantom material. *Ultrasound Med Biol* 46(8):2070–2078
- Souza RM et al (2016) Standard operating procedure to prepare agar phantoms. In: Journal of physics: conference series (vol 733(1)). IOP Publishing
- Sun C et al (2012) The speed of sound and attenuation of an IEC agar-based tissue-mimicking material for high frequency ultrasound applications. *Ultrasound Med Biol* 38(7):1262–1270
- Szabo T (2013) Diagnostic ultrasound imaging: inside out. 2nd edn. Academic Press, London
- Tsuji K et al (2019) Simultaneous measurements of ultrasound attenuation, phase velocity, thickness, and density spectra of polymeric sheets. *Ultrasonics* 99:105974
- Wear KA, Milunski MR, Wickland SA, Perez JE, Sobel BE, Miller JG (1989) Differentiation between acutely ischemic myocardium and zones of complete infarction in dogs on the basis of frequency-dependent backscatter. *J Acoust Soc Am* 85:2634–2641
- Wear KA, Stiles TA, Frank GR, Madsen EL, Cheng F, Feleppa EJ, Hall CS, Kim BS, Lee P, O'Brien Jr WD, Oelze ML (2005) Interlaboratory comparison of ultrasonic backscatter coefficient measurements from 2 to 9 MHz. *J Ultrasound Med* 24(9):1235–1250
- Wilson W (1959) Speed of sound in distilled water as a function of temperature and pressure. *J Acoust Soc Am* 31:1067–1072
- Wu EX, Goodsitt MM, Madsen EL (1992) Microscopic mechanism of attenuation of compressional ultrasonic waves in tissue-mimicking phantom materials. *Ultrason Imaging* 14(2):121–133
- Zell K et al (2007) Acoustical properties of selected tissue phantom materials for ultrasound imaging. *Phys Med Biol* 52(20):N475
- Zerhouni MB, Rachedine M (1993) Ultrasonic calibration material and method. U.S. Patent No. 5,196,343

Index

A

Absorption
ultrasonic, 46, 188

Acoustical properties
of tissue, 30, 40

Acoustic concentration, 8, 9, 52, 67, 68, 74, 75, 97, 100

Acoustic impedance
reflections in, 261, 282

Algebraic reconstruction methods, 184, 201

Algebraic reconstruction technique (ART), 175, 184

American College of Radiology (ACR), 242

Arrays

linear arrays, 194, 209

Artificial neural networks (ANNs), 234

Attenuation

backscattered power spectrum, impact on, 68–70

effect of, 292

local (*see* Local attenuation)

of signal within tissue, 137

statistical estimation, 78

total (*see* Total attenuation)

Attenuation coefficients

energy loss mechanisms, 178

percent error of, 76, 96, 99

Attenuation compensation, 31–32, 67–83

backscattered power spectrum, 68–70

local attenuation, 67, 69 (*see also* Local attenuation)

local attenuation estimation algorithms

comparison of algorithms, 75

hybrid method for, 75

spectral difference method for, 72–73

spectral log difference method for, 73–74

total attenuation estimation algorithms

comparison of algorithms, 82–83

multiple filter algorithm for, 76–79

spectral fit algorithm for, 79–82

Attenuation correction

frequency-dependent, 8, 31–33, 79, 86

function, 31

Average power spectrum, 30

B

Backscatter
amplitudes, 157

function, 69, 79, 158

intercept, 7

ultrasound

radiofrequency, 43

Backscatter coefficient (BSC)

based QUS, 27, 37, 43, 44

calculation

attenuation correction, 31, 46

flowchart, 30

methods to, 40

single-element sources, 299

definition, 20

estimation of, 20, 24, 26, 27, 29–40, 49, 67, 90, 95, 96, 99–101

in soft tissues, 285

variation, 38

Backscattered power spectrum

local attenuation

attenuation, impact of, 68, 69

estimation algorithms (*see* Local attenuation)

total attenuation

attenuation, impact of, 68

estimation algorithms (*see* Total attenuation)

Backscattering, 33, 45, 46, 50, 51, 55, 155–158, 163–165

Bandwidth, 6–8, 12, 13, 20, 31, 40, 56, 71, 75–78, 81, 86, 87, 89, 94, 99, 175, 177, 185, 188, 190, 255–257, 260, 261, 263, 266, 275, 292, 293

Beam diffraction, 40

Benign fibroadenoma, 88

Bessel function

modified Bessel function, 110, 118, 119

*m*th order, 35

Bias, 27, 36, 38, 39, 75, 81–83, 86–94, 97, 99, 100, 137

Binary search algorithm, 114, 119–121, 124, 126, 128, 135

Biological media, 30, 47

Biological tissue

acoustic scattering theories, 45, 47

Biopsy

location, 4

tissue sample, 6

B-mode images

conventional, 88

conventional ultrasound, 29

- RF data, 10, 43
 spatial resolution of, 7
 speckle, 7, 155
 speckle pattern in, 108
 ultrasound images, 4, 154
 B-mode imaging, 3, 268
 B-mode ultrasound, 4, 154
 Born approximation
 distorted, 223
 Distorted Wave, 180
 first-order, 34
 B-scan
 ultrasound, 159
 Bulk modulus
 and sound speed, 254
- C**
 Calibration, 5–7, 26, 30, 32–38, 44, 189–190, 284
 Cauchy-Schwartz' inequality, 138
 Center frequency, 7, 38, 56, 70, 71, 77, 78, 81, 86, 88, 99–101, 137, 175, 186, 188, 190, 255, 257, 268
 Clinical applications, 36, 37, 88, 90, 137, 164, 195
 Clinical ultrasound imaging, 88
 Coherent component, 27, 109, 113, 115, 135
 Coherent scatter, 23, 27, 38, 55, 154, 155
 Coherent scattering, 23, 27, 38, 55, 154
 Compressed sensing, 97, 98, 233, 262
 Computed tomography (CT), 14, 15, 177, 208, 210, 235
See also Single photon emission computed tomography (SPECT); Ultrasound computed tomography (USCT)
 Continuum model (CM), 21–24, 27
 Conventional B-mode images, 4, 88, 268
 Cost function, 95, 96, 99–101
- D**
 Data block
 image of, 30, 31
 Deconvolution, 38, 270–271
 Detection index, 124
 Diagnostic ultrasound imaging, 176, 282
 Diffraction tomography
 advantages and limitations, 180
 image reconstruction, 178, 180–181
 Digamma function, 123, 133
 Discrete model, 21, 24, 27
- E**
 Echo(es)
 backscattered, 69, 78, 88, 96, 135, 154, 155
 RF signals, 4, 5, 7, 10, 86, 89–91, 93, 97, 99, 266
 ultrasound, 3, 45, 299
 Effective acoustic concentration (EAC), 52, 53, 56
 Effective number of scatterers, 109, 112, 113
 Effective scatterer diameter (ESD), 52–54, 56, 75
 Eikonal equation, 229–231
- Envelope statistics
 homodyned K distribution, 110–111, 128–133
 K distribution, 110, 121–128
 Rayleigh distribution, 109–110, 117
 Erythrocyte, *see* Red blood cells (RBCs)
 Euclidean plane, 112
 Euler gamma function, 110, 113, 148
- F**
 Fatty liver, 13, 56, 154, 155
 Fibrosis, 108, 153, 154, 156, 160–164
 First-order Rytov approximation, 180
 Form factor, 9, 24, 26, 52–54, 68, 73, 77–79, 97, 100
 Form factor model, 26, 100
 Fourier transform
 discrete, 98, 182
 fast Fourier transform (FFT), 210, 215, 218, 228, 262
 spatial, 50, 51
 three-dimensional (3D), 23, 51, 185, 217
 two-dimensional (2D), 216, 217
 Frequency dependence
 backscatter, 79, 96, 100
 scattering, 68, 73–75, 78
 total attenuation, 75–77, 99
 Frequency-dependent attenuation, 8, 31–33, 79, 86
 Frequency-dependent backscatter, 9, 26
 Frequency domain, 29, 33, 70, 71, 88, 179, 201, 202, 234, 260
 Full-wave inversion (FWI), 201–236
 Full wave inversion methods
 conjugate gradient methods, 207, 225
- G**
 Gamma distribution, 12, 54, 55, 110, 111, 113–115, 133, 137
 Gaussian filters, 76, 78–83
 Gaussian form factor, 68, 79, 97, 100
 Gaussian function, 32, 51, 69–72, 74
- H**
 Hanning window
 spectral resolution of, 5
 Hematoxylin and eosin (H&E) stain, 271, 272
 Hitachi EUB-525 scanner, 4, 5
 Homodyned K-distribution, 10–12, 108–116, 128–137, 149
 (2-dimensional) homodyned K-distribution, 110
 K-distribution, 10–12, 108–116, 128–137, 149, 155
 M^(v)-statistics for, 117, 120, 134
 Nakagami distribution, 10, 11, 108, 112–116, 133–137, 155
 parameter estimation method for
 fractional order moments of amplitude, 128–129
 log-moments methods, 116–117
 methods on moments of amplitude, 130–131
 methods on moments of intensity, 129–130
 SNR and skewness of amplitude, 131

- SNR of fractional order moments of amplitude, 130, 131
 SNR, skewness and kurtosis of fractional order moments of amplitude, 131
 Rayleigh distribution, 109–111, 135, 137
 Rice distribution, 110, 111, 115, 116
 Human liver, 91, 283
 Hybrid method, 74–77, 86, 92–95
 Hybrid method, for local attenuation method, 74–75
- I**
Impedance
 acoustic, 4, 5, 7, 8, 14, 21, 24, 50, 136, 172, 173, 178, 254, 257, 261, 274, 281–283, 290, 291
 scatterer and background, mismatch between, 49
 Incoherent scatter, 23, 27, 48, 54–56, 89
 Incoherent scattering, 23, 27, 48, 54–56, 89, 295
 Incomplete Euler gamma function, 148
 Incomplete gamma function, 121, 140
 Information entropy, 153–165
 Integrated backscatter coefficient, 56
 Intermediate Value Theorem
 for continuous functions, 138
 Inverse scattering
 applications, 234
 optimizations, 207, 233
 In vivo experiments
 with in vitro experiments, 40, 137
- J**
 Jensen’s inequality, 116, 117, 141, 142
- K**
K-distribution
 M(v)-statistics for, 118
 parameter estimation method for
 fractional order moments of amplitude, 122, 128–129
 log-moments methods, 123–124
 MLE for, 124, 131, 132
 and Rice distribution conditions, 116, 122
 Kidney, 9, 154
 Kullback-Leibler distance, 112–114
 Kullback-Leibler (K-L) divergence, 113
See also Kullback-Leibler distance
- L**
 Laplace transform, 140, 141
 Linear-discriminant analysis, 10
 Linear regression analysis, 7
 Liver fibrosis, 108, 156, 160–164
 Liver lobules, 154, 155
 Local attenuation
 algorithms, comparison of, 75, 82–83
 attenuation, impact of, 69
 estimation algorithms
- hybrid method, 74–75
 spectral difference method, 72–73
 spectral log difference method, 73–74
 spectral shift algorithm, 70–72
 Log-moments, 108, 117, 137
- M**
 Machine learning, 44, 242, 248, 249, 272–275
 Magnetic resonance imaging (MRI), 172, 173, 184, 190–193, 195, 203, 208, 210, 232, 248
 Maximum a posteriori (MAP), 108, 115, 116, 124–128, 133, 135
 Maximum likelihood estimator (MLE)
 for homodyned K-distribution, 131–133
 for K-distribution, 121–122, 124, 133
 for Nakagami distribution
 and U-statistics, 133
 for Rice distribution, 118, 119
 Mean squared error (MSE), 81–83, 121, 125, 127, 128, 135, 136, 266
 Microcalcification, 240, 243, 245, 248
 Moment-based methods
 least mean square (LMS), 117
 log moment based methods, 117
 Moments, 108, 112, 116–119, 122–124, 126, 128–131, 133, 204, 214
 Multiple filter algorithm
 challenges, 77
 form factor, 77–79
 power spectra, 76–78
 statistical analysis study, 78
 theoretical and calculated standard deviation, 79
 Multiple filter method, 80–82
 Multi-taper method, 27, 39, 93
- N**
Nakagami distribution
 generalized distribution, 115
 Kullback-Leibler distance, 112, 113
 M(1)-statistics for, 114, 134–136
 Nakagami-gamma distribution, 12, 115
 parameter estimation method for
 methods on moments of amplitude, 133
 MLE for, 133
 moments of intensity, 133
 signal-to-noise ratio (SNR), 113, 115, 133
n-distribution, 110
 Newton, Isaac, 25
 Nonalcoholic fatty liver disease (NAFLD), 153, 154, 160–165
 Noninvasive surgery, 192
 Non-Rayleigh distributions, 108, 155
 Normalized backscattered power spectra, 137
- P**
 Parameters estimation, 115–135, 159, 262
 Parameters estimation methods

- for homodyned K-distribution
 fractional order moments of amplitude, 128–129
 methods on moments of amplitude, 130
 methods on moments of intensity, 129–130
 SNR and skewness of amplitude, 131
 SNR of fractional order moments of amplitude, 130–131
 SNR, skewness and kurtosis of fractional order moments of amplitude, 131
- K-distribution
 fractional order moments of amplitude, 122–123
 log-moments methods, 123–124
 methods on moments of intensity, 122–123
 MLE for, 121–122
- log moment based methods, 117
- MAP, 115–116
- MLE, 115–116
- moments based methods, 116–117
- Nakagami distribution
 MLE for, 133
 moments of intensity, 133
- for Rayleigh distribution, 117
- for Rice distribution
 fractional order moments of amplitude, 118
 methods on moments of amplitude, 118–119
 MLE for, 118
- Parametric imaging, 8, 154, 155, 159, 160, 164
- Phantom, 5, 9, 32, 35, 36, 39, 40, 68, 72, 86–101, 185, 186, 243, 245, 281–299
- glass bead, 40
- reference technique, 36
- tissue mimicking, 40, 68, 72, 86, 87, 90, 91, 93, 98, 100–102, 186
- Planar reference, 32–35, 37
- Planar reflector, definition, 293
- Point compensation, 69, 70
- Point spread function (PSF), 11, 92, 137, 175, 227, 230, 270, 271
- Polak-Ribiere version
 step length calculation, 207, 226
- Positron emission tomography (PET) imaging, 14, 235
- Power spectra, 4, 7, 13, 32, 34, 38, 39, 56, 69, 72–74, 76–78, 91, 93, 95–97, 99
- Precision, 23, 78, 80, 85, 92, 93, 96, 102, 189, 254, 257, 258, 263, 266
- Probability density functions (PDFs), 54, 94, 113, 155–158, 162–164
- Prostate-specific antigen (PSA), 10
- Pulse-echo ultrasound technique, 3, 45
- Q**
- Quantitative, 7, 15, 108, 137, 154, 155, 159, 165, 172, 176, 178, 190, 203, 227, 228, 230, 232, 235, 240, 241, 246–248, 253–255, 259, 264, 268–270
- R**
- Radio frequency (RF)
 data, 4–6, 10, 11, 43, 137, 156, 163, 267–269
 echo signals, 4–7, 10, 43, 86, 89–91, 93, 97, 99, 266
 ultrasound-backscatter, 158, 162
- Ray-based acoustic tomography
 reflection mode tomography, 209
 straight-ray propagation
 straight-ray acoustic tomography, 182, 201
- Rayleigh distribution
 and homodyned K-distribution conditions, 108–111, 116, 135, 137, 155
 parameter estimation method for, 117
- Reconstruction methods, 175, 178–181, 183–184, 194, 195, 201, 270
- Red blood cells (RBCs)
 aggregation (*see* Ultrasound backscatter model)
- Reference phantom, 30, 35–36, 40, 44, 69, 72–76, 79, 86–88, 90–94, 96, 97, 99, 299
- Reflection tomography, 183, 184
- Regularization, 92, 95–102, 221, 233, 234, 270–272
- Rice distribution
 inverse Gaussian (IG) distribution, 114
 and K-distribution conditions, 109, 113–116, 122
 $M^{(v)}$ -statistics for, 118, 120
 parameter estimation method for
 fractional order moments of amplitude, 118
 methods on moments of amplitude, 118–119
 MLE for, 118
 (2-dimensional) Rice distribution, 110
- Rician distribution, 10, 12
- S**
- Scanning acoustic microscopy (SAM), 253–255, 275
- Scatterer clustering parameter, 109, 113, 120, 122, 125, 127
- Scatterers
 acoustic impedance of, 7, 136
 glass beads as, 40
 properties, 7, 25, 27, 38, 39, 156, 164
 size estimates, effective, 12, 54
- Scattering, 4, 19, 29, 44, 67, 89, 108, 154, 178, 201, 282
- Signal-to-noise ratio (SNR)
 methods based on
 fractional order moments of amplitude, 123, 130–131
 skewness and kurtosis of fractional order moments of amplitude, 131
 and skewness of amplitude, 131
- Signal uncertainty, 157–159, 165
- Single photon emission computed tomography (SPECT), 14, 15
- Spatial autocorrelation function (SAF), 23, 51
- Spatial compounding technique, 27, 173, 175, 186, 193
- Spatial resolution
 B-mode image, 7

- limitations, 272
 QUS image, 27
- Speckle**
 pattern, 108, 159
- Spectral difference method, 72–73, 75, 86, 87, 89, 90, 92–94, 97–100
- Spectral-fit algorithm, 79–83
- Spectral-fit method, 82–83
- Spectral intercept (SI), 7, 56
- Spectral log difference method, 73–75, 86, 88, 94–96, 100
- Spectral-shift algorithm**
 center frequency and bandwidth, 71
 error in attenuation estimate, 72
 Gaussian function, 71, 72
 Gaussian transformation, 71
 usable frequency range, 71, 75
- Spectral slope (SS), 7, 56
- Spectrum, 4–14, 27, 30, 33–39, 67–73, 78, 79, 82, 83, 86, 88–96, 99, 100, 137, 218, 244, 260–262, 266, 275
- Spectrum-analysis method, 14
- Speed-of-sound, 240, 248
- Speed-of-sound imaging, 240
- Standard deviation (STD), 76, 78–83, 89, 92, 93, 96, 97, 100, 101, 158
- State of the art, v, 174–176, 209, 255–259, 265
- Statistics**
 envelope
 bias and variance, estimates of, 27, 39
 homodyned K distribution, 109–115
 K distribution, 110
 Rayleigh distribution, 109–110
 scattered property, improvement of
 angular compounding technique, 89
 discrete model analysis, 21, 24–27
 spatial compounding technique, 27
- Structure function, 54–56, 60
- Super-resolution (SR), 193, 268–275
- Support-vector machines (SVMs), 242
- System design, 184–190, 195
- T**
- Talukdar-Lawing estimator, 119
- Tissue characterization**
 local attenuation (*see* Local attenuation)
 performing ultrasound, illustration of tissue, 68
 purpose of, 67
 QUS on, 44, 107–149
- Tissue-mimicking (TM), 40, 68, 72, 86, 87, 90, 91, 93, 98, 100, 101, 186, 282–287, 290, 291, 293, 295–299
- Tissue-type images (TTI)
 likelihood of cancer, 10, 11
- Tissue-typing, 4, 8, 10–12, 14, 172, 190, 193, 241, 242, 246
- Tomography, 174, 201–236
- Total attenuation
 attenuation, impact of, 68–70
 estimation algorithms
- multiple filter algorithm, 76–79
 spectral fit algorithm, 79–82
- Transducer**
 array designs, 36
 radiation pattern, 34
 single-element, 9, 33, 35, 36, 44, 86, 88, 255, 299
- Transducer center frequency, 137, 268
- U**
- Ultra-high frequency, 254
- Ultrasonic scattering, 19–27
- Ultrasound backscatter model
 aggregated RBCs
 characterization of, 165
 in vitro experiments, 137
 in vivo experiments, 137
See also Backscattering coefficient (BSC)
- Ultrasound computed tomography (USCT)
 breast sonography, 190
 current breast cancer imaging, 175
 diffraction tomography
 clinical DT prototype design, 177
 imaging reconstruction, 178
 results, 185, 190, 191
 ray-based backprojection tomography, 184
 3D-USCT systems, 172, 177, 187
- Ultrasound imaging
 characterization, 107–150
 interpretation of distribution, 111–113
 probability density function, 113
 speckle, 108
- Ultrasound tissue characterization, 39, 68, 76, 155, 165
- Usable frequency range, 71, 75, 77, 81, 83
- U-statistics**
 for K-distribution, 107–116, 120–137, 149
 for Rice distribution, 107–111, 113–116, 118–122, 125, 148
- V**
- Volumography, 201–236, 239–248
- W**
- Wave propagation model, *see* Rayleigh distribution; Rice distribution
- Welch' technique, 39
- Window functions, 4, 7
- X**
- X-statistics
 for K-distribution, 122, 124
 Nakagami distribution, 134
 for Rice distribution, 121, 122
- Y**
- Young's modulus, 254